applied sciences

Special Issue Reprint

New Advances, Challenges, and Illustrations in Applied Geochemistry

Edited by
Qingjie Gong and Zeming Shi

mdpi.com/journal/applsci

MDPI

New Advances, Challenges, and Illustrations in Applied Geochemistry

New Advances, Challenges, and Illustrations in Applied Geochemistry

Guest Editors

Qingjie Gong
Zeming Shi

MDPI

Basel • Beijing • Wuhan • Barcelona • Belgrade • Novi Sad • Cluj • Manchester

Guest Editors

Qingjie Gong
School of Earth Sciences and Resources
China University of Geosciences (Beijing)
Beijing
China

Zeming Shi
College of Earth and Planetary Sciences
Chengdu University of Technology
Chengdu
China

Editorial Office
MDPI AG
Grosspeteranlage 5
4052 Basel, Switzerland

This is a reprint of the Special Issue, published open access by the journal *Applied Sciences* (ISSN 2076-3417), freely accessible at: https://www.mdpi.com/journal/applsci/special_issues/33Y7428L9J.

For citation purposes, cite each article independently as indicated on the article page online and as indicated below:

Lastname, A.A.; Lastname, B.B. Article Title. *Journal Name* **Year**, *Volume Number*, Page Range.

ISBN 978-3-7258-3781-6 (Hbk)
ISBN 978-3-7258-3782-3 (PDF)
https://doi.org/10.3390/books978-3-7258-3782-3

Contents

About the Editors

Qingjie Gong

Qingjie Gong is professor and doctoral supervisor of geochemistry from China University of Geosciences (Beijing) and acts as the Director of the Committee of Applied Geochemistry, Chinese Society for Mineralogy, Petrology and Geochemistry (CSMPG), and as Associate Editor of the Applied Geochemistry journal hosted by the International Association of Geochemistry. Dr. Gong is an expert at geochemical exploration, environmental geochemistry and experimental geochemistry at high temperatures and pressures. Dr. Gong presents (i) the 19-level fixed-value method to classify elemental concentrations of geological materials, (ii) an innovative equation to calculate the native values of trace elements based on the contents of major oxides in a sample, and a method called seven-level classification of geochemical anomaly to determine and classify geochemical anomalies based on two rulers: the native value and the cutoff grade of a trace element in a sample, and (iii) a promising concept called geochemical gene to discriminate, evaluating and tracing the geological materials in the system of rock–soil–sediment. In order to calculate geochemical backgrounds and anomaly levels, a software called GBAL and another called GGC were developed by Dr. Gong to calculate geochemical gene codes and the gene similarities of samples, respectively.

Zeming Shi

Zeming Shi is a professor and doctoral supervisor of geochemistry from the Chengdu University of Technology and acts as the Communist Party secretary of the College of Earth and Planetary Sciences, Head of the Applied Nuclear Techniques in Geosciences Key Laboratory of Sichuan Province, Academic and Technical Leader of Sichuan Province, the Tianfu famous teacher of Tianfu Qingcheng Plan, and the Executive Member of the Society of Chinese Mineralogy, Petrology and Geochemistry. He is mainly engaged in environmental geochemistry and mineral deposit geochemistry research and is responsible for more than 20 provincial and ministerial level projects such as the National Natural Science Foundation of China (NSFC) and the National Key Research and Development Program of China (subprojects). He has published more than 200 academic papers, compiled 2 textbooks and published 3 monographs, and has been awarded 3 provincial and ministerial science and technology awards.

applied sciences

MDPI

Editorial

New Advances, Challenges, and Illustrations in Applied Geochemistry

Qingjie Gong [1,*] and Zeming Shi [2,*]

[1] School of Earth Sciences and Resources, China University of Geosciences, Beijing 100083, China
[2] College of Earth and Planetary Sciences, Chengdu University of Technology, Chengdu 610059, China
* Correspondence: qjiegong@cugb.edu.cn (Q.G.); shizm@cdut.edu.cn (Z.S.)

1. Introduction

The Special Issue 'New Advances and Illustrations in Applied Geochemistry in China' was organized for the presentation of ideas from the 9th National Conference on Applied Geochemistry in China held in Chengdu, Sichuan Province, in October 2023. A new Special Issue, 'New Advances, Challenges, and Illustrations in Applied Chemistry', is currently being organized, which aims to facilitate the academic exchange and presentation of new ideas in the field of applied geochemistry, particularly those presented at the 10th National Conference on Applied Geochemistry, which was held in Kunming, Yunnan Province, in November 2024. This Special Issue is edited by the Committee of Applied Geochemistry of the Chinese Society for Mineralogy, Petrology, and Geochemistry (CSMPG).

This Special Issue contains 12 scientific papers that reflect various advances, challenges, and illustrations in applied geochemistry. These articles cover to the following three broad fields: (i) geochemical exploration, including traditional and non-traditional exploration methods and determination methods for geochemical background values; (ii) environmental geochemistry, including risk assessment, provenance tracing, and the remediation of heavy metals; and (iii) basic applications in geology, including magmatism, mineralization, and tectonic thermal evolution, etc.

2. Geochemical Exploration

2.1. Methods for the Geochemical Exploration of Mineral Resources

Geochemical exploration mainly focuses on prospecting for mineral resources; its methods are commonly divided into the following two groups: traditional methods and non-traditional methods [1].

Traditional methods have developed from the denudation principle of mineralized exposed materials, and the commonly used sampling materials for traditional methods include stream sediments, soils, and rocks. For example, the RGNR (regional geochemistry–national reconnaissance) project in China collects stream sediment from mountainous and hilly areas [2]; the NMPRGS (national multi-purpose regional geochemical survey) project in China collects soils from plains and basins [3]; and primary halo surveys on a specific deposit mainly focus on rock samples taken from an outcropped area [4]. On the contrary, few geochemical survey projects have been conducted in deserts and sandy areas. Wen et al. (contribution 1) reported the results of a geochemical survey, including the geochemical background and baseline values of 61 indicators for 344 composite samples in 12 desert and sandy areas in China. These background and baseline data greatly enriched the elemental abundance database within applied geochemistry [5].

Received: 15 March 2025
Accepted: 18 March 2025
Published: 20 March 2025

Citation: Gong, Q.; Shi, Z. New Advances, Challenges, and Illustrations in Applied Geochemistry. *Appl. Sci.* **2025**, *15*, 3407. https://doi.org/10.3390/app15063407

Non-traditional methods have developed from the penetration principle of mineralized concealed materials, the common sampling materials for which include gas, water, plants, and other materials which are analyzed differently from traditional total concentrations [6]. Geogas [7], geoelectrochemical technology [8], gas analyzers [9], and partial extraction methods [10] are commonly used approaches for prospecting buried ore deposits. Zhou et al. (contribution 2) compared traditional and non-traditional exploration methods on a concealed gold deposit. In their illustration, non-traditional methods, including the chemical form analysis of gold, a soil halogen survey, and a heat-released mercury survey, were utilized, which were found to be applicable and efficient in targeting potential gold mineralization zones. Sun et al. (contribution 3) introduced a geoelectrochemical method, but they aimed to remove the heavy metal Cd from a sample of paddy soil rather than to target mineral resources. This illustrates the wider applications of geoelectrochemical technology.

2.2. Methods for the Determination of Geochemical Background Values

Contribution 1, a study on geochemical background values, is an important foundational work in earth sciences. The types of methods used to determine geochemical background values can be classified as fixed-value and unfixed-value methods. Fixed-value methods define a fixed value as an elemental background value in a specific area, whereas unfixed-value methods indicate that different values are determined as the elemental background values within a specific area, with even each background value corresponding to each sample within a specific area.

Utilizing fixed-value methods, Wen et al. (contribution 1) introduced three ways in which to determine geochemical background values, as follows: the iterative method [11], the frequency histogram method, and the multifractal concentration-area method [12]. In this paper (contribution 1), the final geochemical background value was obtained by averaging the values calculated using the three methods for each analytical item.

For the unfixed-value method, which is the ideal method to use, each geological sample has a different geochemical background value due to different degrees of weathering and lithology in each sample, as proposed by Gong et al. [13]. In their study [13], the geochemical background values of 27 trace elements in a sample could be calculated from the sample's major oxide contents using empirical equations. Recently, the equations for Li [14] and Cr [15] were further improved, to help determine their geochemical backgrounds more accurately.

3. Environmental Geochemistry

Studies on environmental geochemistry mainly focus on aspects of pollution risk assessment, elemental bioaccumulation, and heavy metal remediation.

3.1. Methods for Heavy Metal Risk Assessments

Methods for assessing the pollution risk of heavy metals in soils have been used and discussed for several decades and can be classified into two types: those with standards and those without standards.

Assessment methods without standards for heavy metal soil pollution were reviewed and summarized by Gong et al. [16] and are currently widely used, albeit with some new revised versions. For example, Luo et al. (contribution 4) adopted the indices of the Pollution Load Index (PLI) [17], the Geoaccumulation index (I_{geo}) [18], and the Nemero index [19] to assess the pollution risk of heavy metals in the soils of an industrial park in Kunming, China.

Methods with standards are also commonly used to assess the pollution risk of soils and other geological materials, and are based on promulgated standards, such as GB15618-2018 [20] in China, among others. Xu et al. (contribution 5) proposed single and integrated indices for the assessment of the pollution risk of heavy metals in soils and crops based on the Chinese standards GB15618-2018 and GB2762-2022 [21], respectively. They found two inconsistent assessments, indicating a new challenge in maintaining consistency between the assessment standards for soils and crops. This inconsistent assessment was also found by Sun et al. (contribution 3). In contrast, concerning atmospheric deposition, Wei et al. (contribution 6) adopted the criteria of non-carcinogenic and carcinogenic risk assessment methods used by the United States Environmental Protection Agency (USEPA) in order to assess the risk of potential toxic elements (PTE) in a ion-adsorption rare earth mining area in Ganzhou City, Southeast China.

3.2. Elemental Bioaccumulation

Elemental bioaccumulation refers to transfer of elements from soils to crops or the crop uptake of elements from soils, which is measured by conducting a geochemical survey on the soils and the crops grown. The bioconcentration factor (BCF) is often used to quantitatively calculate the accumulation of heavy metals in plant tissues relative to the environmental soils [22].

Li et al. (contribution 7) studied the bioaccumulation of arsenic in the soil–rice system, using paired soil–rice samples from karst regions in Guangxi, China. They indicate that concentrations of As in the rice are inconsistent with the total concentrations of As in the soils, and the low bioavailability of As by rice in the karstic paddy soil was attributed to its residual form being present in Fe-Mn oxides. This low bioavailability of heavy metals can explain the inconsistent assessment results for soils and their crops (contribution 5).

Although inconsistent assessments and uncorrelated concentrations between soils and crops are widespread findings, many studies aiming to predict heavy metal concentrations in crops based on their concentrations in soils have been carried out. Geng et al. (contribution 8) established a prediction model for zinc concentration in rice from farmland soil, using 371 paired rice–soil samples from the Pear River Delta and Heyuan regions in Guangdong, China, and machine learning models. Ma et al. [23] also presented a prediction model for cadmium concentrations in paired rice–soil samples, using paddy soil samples from Guangxi Province, China, and machine learning algorithms. Besides rice, heavy metal contamination levels in other crops, such as maize [24] and peanut [25], have also been predicted on the contamination levels of the soil in which they were grown. However, these prediction models are only pilot studies and primarily data-driven, and knowledge-based models have not been well developed.

3.3. Remediation of Heavy Metals

Alongside the risk assessment of heavy metals, the remediation of heavy metals in soils is another important topic in environmental geochemistry. Remediation methods are categorized as agronomic control or soil amendment techniques. The agronomic control methods include crop variation, optimized fertilization, and foliar obstruction control ([26] and contribution 3), and the soil amendment methods include chemical leaching, in situ passivation, plant enrichment, and electrokinetic techniques ([27] and contribution 3).

Sun et al. (contribution 3) introduced the geo-electrochemical technology to remove the heavy metal Cd from paddy soil in Guilin, China. The results indicated that the new method is effective, not only at removing the Cd from the paddy soil but also at reducing the contents of Cd in the tissues and organs of the rice. This contribution is a good illustration of new in situ electrokinetic remediation methods.

4. Basic Applications in Geology

The main sample materials used in geochemical exploration and environmental geochemistry are soils and stream sediments [2,3], while rock and mineral samples are mainly used within basic geology, specifically when studying magmatism, mineralization, and tectonic thermal evolution, etc. [28,29].

Abd El-Naby and Dawood (contribution 9) studied peralkaline granites and related pegmatites in the Arabian shield in order to discover their geochemistry, petrogenesis, and rare-metal mineralization. Liu et al. (contribution 10) analyzed the trace elements in the minerals chalcopyrite and cassiterite, taken from the Shuangjianzishan super-large silver deposit in Inner Mongolia, in order to shed light on the genesis of Cu-Sn mineralization. In addition to the geochemistry of minerals, basic geology is also concerned with minerals' signatures. Wu et al. (contribution 11) analyzed the apatite fission-track and zircon fission-track in the Helanshan Mountain tectonic belt, Northwest China, to reveal the tectonic activities in this area. Huang et al. (contribution 12) studied the characteristics of luminescence in high-temperature- and high-pressure-treated diamonds in order to explore a new rapid and nondestructive identification method. These contributions are very interesting and attractive for applications in the field of basic geology.

As a conclusion, the new advances and studies in applied geochemistry are mainly focused on the typical topics covered in the field, namely geochemical exploration and environmental geochemistry; some new challenges are also found and proposed in this Special Issue. The innovative studies presented here have great application potential in the fields of resources, environments, and social services. We thank the authors and reviewers for their contribution to this Special Issue and hope that more in-depth research in applied geochemistry will be illustrated in the future National Conferences on Applied Geochemistry.

Author Contributions: Conceptualization, Q.G. and Z.S.; Formal analysis, Q.G. and Z.S.; Writing—original draft preparation, Q.G. and Z.S.; Writing—review and editing, Q.G. and Z.S. All authors have read and agreed to the published version of the manuscript.

Acknowledgments: We are grateful to all contributors who made this Special Issue a success. Our thanks and congratulations are extended to all the authors for submitting their work. Our sincere gratefulness is also given to all the reviewers for the effort and time they spent helping the authors to improve their papers. We want to express our gratitude to the editorial team of *Applied Sciences* for their effective and untiring editorial support of the success of this Special Issue. We hope this Issue serves as an inspiration for future research in applied geochemistry.

Conflicts of Interest: The authors declare no conflicts of interest.

List of Contributions

1. Wen, W.; Yang, F.; Xie, S.; Wang, C.; Song, Y.; Zhang, Y.; Zhou, W. Determination of Geochemical Background and Baseline and Research on Geochemical Zoning in the Desert and Sandy Areas of China. *Appl. Sci.* **2024**, *14*, 10612.
2. Zhou, W.; Lei, L.; Gong, Y.; Liu, D.; Xie, S.; Chen, Z.; Xia, Q.; Wang, M.; Awadelseid, S.; Yaisamut, O. A Deep-Penetrating Geochemical Prospecting Experiment of Mahuagou Gold Deposit in the Core of the Huangling Anticline, Western Hubei, China. *Appl. Sci.* **2023**, *13*, 12279.
3. Sun, Y.; Wen, M.; Liu, P.; Jiang, Y. Removal of Heavy Metal Cd Element from Paddy Soil by Geo-Electrochemical Technology. *Appl. Sci.* **2023**, *13*, 11685.
4. Luo, W.; Wei, P.; Zhang, Y.; Sun, C. Characterization and Source Analysis of Heavy Metal(loid)s Pollution in Soil of an Industrial Park in Kunming, China. *Appl. Sci.* **2024**, *14*, 6547.
5. Xu, S.; Huang, Z.; Huang, J.; Wu, S.; Dao, Y.; Chen, Z.; Yang, B.; Xu, Y.; Liu, N.; Gong, Q. Environmental Pollution Assessment of Heavy Metals in Soils and Crops in Xinping Area of Yunnan Province, China. *Appl. Sci.* **2023**, *13*, 10810.

6. Wei, J.; Liu, S.; Chu, T.; Yuan, G.; Xie, M.; Huang, Y.; Sun, Q.; Ma, C.; Xue, Q. The Distribution and Health Risk Assessment of Potential Toxic Elements in Atmospheric Deposition from Ion-Adsorption Rare Earth Mining Areas in the Ganzhou City of Southeast China. *Appl. Sci.* **2024**, *14*, 3585.
7. Li, X.; Ma, X.; Hou, Q.; Xia, X.; Li, B.; Lin, K.; Liu, X.; Wu, Z.; Ji, W.; Wang, L.; Yu, T.; Yang, Z. Arsenic in a Karstic Paddy Soil with a High Geochemical Background in Guangxi, China: Its Bioavailability and Controlling Factors. *Appl. Sci.* **2024**, *14*, 1400.
8. Geng, W.; Li, T.; Zhu, X.; Dou, L.; Liu, Z.; Qian, K.; Ye, G.; Lin, K.; Li, B.; Ma, X.; Hou, Q.; Yu, T.; Yang, Z. Predicting the Zinc Content in Rice from Farmland Using Machine Learning Models: Insights from Universal Geochemical Parameters. *Appl. Sci.* **2025**, *15*, 1273.
9. Abd El-Naby, H.; Dawood, Y. The Geochemistry, Petrogenesis, and Rare-Metal Mineralization of the Peralkaline Granites and Related Pegmatites in the Arabian Shield: A Case Study of the Jabal Sayid and Dayheen Ring Complexes, Central Saudi Arabia. *Appl. Sci.* **2024**, *14*, 2814.
10. Liu, Y.; Jiang, B.; Chen, Y.; Wu, L.; Zuo, Y.; Liu, Z. Genesis of Cu-Sn Mineralization in the Shuangjianzishan Super-Large Silver Deposit, Inner Mongolia: Trace Element Constraints from Chalcopyrite and Cassiterite. *Appl. Sci.* **2024**, *14*, 3822.
11. Wu, C.; Wang, Y.; Yuan, W.; Zhou, L. A Complex Meso–Cenozoic History of Far-Field Extension and Compression: Evidence from Fission Track Analysis in the Helanshan Mountain Tectonic Belt, NW China. *Appl. Sci.* **2024**, *14*, 3559.
12. Huang, M.; He, X.; Du, M.; Jiang, P.; Wang, X. The Characteristics of Luminescence from High-Temperature- and High-Pressure-Treated Diamonds. *Appl. Sci.* **2024**, *14*, 3071.

References

1. Xie, X.; Wang, X. Geochemical Exploration for Gold: A New Approach to an Old Problem. *J. Geochem. Expl.* **1991**, *40*, 25–48.
2. Xie, X.; Cheng, H. Sixty Years of Exploration Geochemistry in China. *J. Geochem. Explor.* **2014**, *139*, 4–8.
3. Li, M.; Xi, X.; Xiao, G.; Cheng, H.; Yang, Z.; Zhou, G.; Ye, J.; Li, Z. National Multi-purpose Regional Geochemical Survey in China. *J. Geochem. Explor.* **2014**, *139*, 21–30.
4. Shatov, V.V.; Moon, C.J.; Seltmann, R. Discrimination between Volcanic Associated Massive Sulphide and Porphyry Mineralization Using a Combination of Quantitative Petrographic and Rock Geochemical Data: A Case Study from the Yubileinoe Cu-Au Deposit, Western Kazakhstan. *J. Geochem. Explor.* **2014**, *147*, 26–36. [CrossRef]
5. Chi, Q.H.; Yan, M.C. *Handbook of Element Abundance for Applied Geochemistry*; Geological Publishing House: Beijing, China, 2007.
6. Wang, X.; Zhang, B.; Lin, X.; Xu, S.; Yao, W.; Ye, R. Geochemical Challenges of Diverse Regolith-Covered Tterrains for Mineral Exploration in China. *Ore Geol. Rev.* **2016**, *73*, 417–431.
7. Wang, Q.; Wang, X.; Cheng, Z.; Zhang, B.; Du, Z.; Yan, T.; Yuan, H.; Li, X.; Qiao, Y.; Liu, H. Geogas-Carried Metal Prospecting for Concealed Ore Deposits: A Review of Case Studies in China. *Minerals* **2023**, *13*, 1553. [CrossRef]
8. Liu, P.; Luo, X.; Wen, M.; Zhang, J.; Zheng, C.; Gao, W.; Ouyang, F. Geoelectrochemical Anomaly Prosepcting for Uranium Deposits in Southeastern China. *Appl. Geochem.* **2018**, *97*, 226–237.
9. Cheng, Z.; Wang, Q.; Lin, C.; Qiu, C.; Yan, T.; Yuan, H. Application of Portable Multi-Component Gas Analyzer to Mineral Exploration in Semi-Arid Steppes of Northern China: A Case Study from the Qinjiaying Ag-Pb-Zn Prospect. *Appl. Geochem.* **2024**, *166*, 105996. [CrossRef]
10. van Geffen, P.W.G.; Kyser, T.K.; Oates, C.J.; Ihlenfeld, C. Evaluation of Partial Digestions for Soils to Detect a Deeply Burried VMS Cu-Zn Prospect in Boreal Forests. *Geochem. Explor. Environ. Anal.* **2015**, *15*, 27–38.
11. Zhang, J.; Huang, C.; Chen, K.; Gao, Z.; Huang, Q. The Soil Background Values of Heavy Metals and Ecological Risk Assessment Based on the Geo-statistical Analysis. *Environ. Sci. Technol.* **2021**, *44*, 218–225.
12. Cheng, Q.; Agterberg, F.P.; Ballantyne, S.B. The Separation of Geochemical Anomalies from Background by Fractal Methods. *J. GeoChem. Expl.* **1994**, *51*, 109–130.
13. Gong, Q.; Deng, J.; Jia, Y.; Tong, Y.; Liu, N. Empirical Equations to Describe Trace Element Behaviors Due to Rock Weathering in China. *J. Geochem. Explor.* **2015**, *152*, 110–117.
14. Chen, S.; Gong, Q.; Li, P.; Xu, S.; Liu, N. Describing Geochemical Backgrounds of Lithium in Rock-Soil-Sediment Systems. *Appl. Geochem.* **2024**, *162*, 105908. [CrossRef]
15. Zhou, S.; Gong, Q.; Zhang, Z.; Lv, Z.; Chen, S.; An, Y. Innovative Equation for Determining the Geochemical Background Values of Chromium Based on Major Components in Rock–Soil–Sediment Systems. *Appl. Sci.* **2025**, *15*, 182. [CrossRef]
16. Gong, Q.; Deng, J.; Xiang, Y.; Wang, Q.; Yang, L. Calculating Pollution Indices by Heavy Metals in Econological Geochemistry Assessment and a Case Study in Parks of Beijing. *J. China Univ. Geosci.* **2008**, *19*, 230–241.

17. Cabrera, F.; Clemente, L.; Barrientos, E.D.; Lopez, R.; Murillo, J.M. Heavy Metal Pollution of Soils Affected by the Guadiamar Toxic Flood. *Sci. Total Environ.* **1999**, *242*, 117–129.
18. Liu, P.; Wu, Z.; Luo, X.; Wen, M.; Huang, L.; Chen, B.; Zheng, C.; Zhu, C.; Liang, R. Pollution Assessment and Source Analysis of Heavy Metals in Acidic Farmland of the Karst Region in Southern China—A Case Study of Quanzhou County. *Appl. Geochem.* **2020**, *123*, 104764.
19. Xiang, M.T.; Li, Y.; Yang, J.Y.; Li, Y.; Li, F.; Hu, B.F.; Cao, Y. Assessment of Heavy Metal Pollution in Soil and Classification of Pollution Risk Management and Control Zones in the Industrial Developed City. *Env. Manag.* **2020**, *66*, 1105–1119. [CrossRef]
20. *GB 15618-2018*; Soil Environmental Quality—Risk Control Standards for Soil Contamination of Agricultural Land. MEEC (Ministry of Ecology and Environment of the People's Republic of China): Beijing, China, 2018.
21. *GB2762-2017*; Maximum Level of Contaminants in Food. MHC (Ministry of Health of the People's Republic of China) Chinese National Standard Agency: Beijing, China, 2017.
22. McKone, T.E.; Maddalena, R.L. Plant Uptake of Organic Pollutants from Soil: Bioconcentration Estimates Based on Models and Experiments. *Environ. Toxico. Chem.* **2007**, *26*, 2494–2504.
23. Ma, X.; Yu, T.; Guan, D.-X.; Li, C.; Li, B.; Liu, X.; Lin, K.; Li, X.; Wang, L.; Yang, Z. Prediction of Cadmium Contents in Rice Grains from Quaternary Sediment-Distributed Farmland Using Field Investigations and Machine Learning. *Sci. Total Environ.* **2023**, *898*, 165482.
24. Yang, Y.; Li, C.; Yang, Z.; Yu, T.; Jiang, H.; Han, M.; Liu, X.; Wang, J.; Zhang, Q. Application of Cadmium Prediction Moddels for Rice and Maize in the Safe Utilization of Framland Associated with Tin Mining in Hezhou, Guangxi, China. *Environ. Ploout.* **2021**, *285*, 117202.
25. Gu, Q.; Yu, T.; Yang, Z.; Ji, J.; Hou, Q.; Wang, L.; Wei, X.; Zhang, Q. Prediction and Risk Assessment of Five Heavy Metals in Maize and Peanut: A Case Study of Guangxi, China. *Environ. Toxicol. Pharmacol.* **2019**, *70*, 103199. [PubMed]
26. Yang, Z.; Guo, W.; Cheng, Z.; Wang, G.; Xian, J.; Yang, Y.; Liu, L.; Xu, X. Possibility of Using Combined Compost-Attapulgite for Remediation of Cd Contaminated Soil. *J. Clean. Prod.* **2022**, *368*, 133216.
27. Luan, Y.; Xu, J.; Zhou, J.; Wang, H.; Han, F.; Wang, K.; Lv, Y. Migration and Removal of Labile Cadmium Contaminants in Paddy Soils by Electrokinetic Remediation without Changing Soil pH. *Int. J. Environ. Res. Public Health* **2022**, *19*, 3812. [CrossRef]
28. Liu, X.; Qiu, N.; Søager, N.; Fu, X.; Liu, R. Geochemistry of Late Permian Basalts from Boreholes in the Sichuan Basin, SW China: Implications for an Extension of the Emeishan Large Igneous Province. *Chem. Geol.* **2022**, *588*, 120636.
29. Zhang, Q.-Q.; Chen, Y.-W.; Gao, J.-F. Trace Elements in Magmatic and Hydrothermal Quartz: Implications on the Genesis of the Xingluokeng Tungsten Deposit, South China. *Acta Geochim.* **2024**, *43*, 441–458.

applied sciences

MDPI

Article

Determination of Geochemical Background and Baseline and Research on Geochemical Zoning in the Desert and Sandy Areas of China

Weiji Wen [1], Fan Yang [2,*], Shuyun Xie [1,*], Chengwen Wang [2], Yuntao Song [2], Yuepeng Zhang [1] and Weihang Zhou [1]

[1] State Key Laboratory of Geological Processes and Mineral Resources (GPMR), Faculty of Earth Sciences, China University of Geosciences, Wuhan 430074, China; cugwenweiji@163.com (W.W.); zwh15671032170@126.com (W.Z.)
[2] Institute of Geophysical and Geochemical Exploration, Chinese Academy of Geological Sciences, Langfang 065000, China; wchengwen@mail.cgs.gov.cn (C.W.); songyuntao@mail.cgs.gov.cn (Y.S.)
* Correspondence: yangf@mail.cgs.gov.cn (F.Y.); tinaxie@cug.edu.cn (S.X.)

Abstract: Resources in deserts and sandy landscapes have potential for development, but existing surveys and sampling have not collected desert soil samples. As such, the geochemical background of these spaces remains unexplored due to the vastness and desolation of deserts. Therefore, researching the geochemical background values and geochemical baseline values of deserts is of long-term significance. Our research indicates that in addition to macrostructural environmental divisions, microelement geochemistry can also be used for geological unit zoning. In this paper, geochemical background and geochemical baseline values of 61 desert elements were calculated using the iterative method, frequency histograms method, and multifractal concentration-area method. It also analyzes the distribution characteristics of major, trace, and rare earth elements, and divides the 12 desert sand regions into different geochemical zones. This paper determines, for the first time, the geochemical background values of elements in Chinese deserts, filling the gap in the study of desert background values. By combining machine learning methods, different deserts have been divided into three geochemical zones. This research will greatly enhance our ability to interpret the geochemical distribution and evolutionary patterns of desert elements in China, and it has important scientific significance and practical value for desert research.

Keywords: geochemical background; geochemical baseline; geochemical zoning machine learning; multifractal method

Citation: Wen, W.; Yang, F.; Xie, S.; Wang, C.; Song, Y.; Zhang, Y.; Zhou, W. Determination of Geochemical Background and Baseline and Research on Geochemical Zoning in the Desert and Sandy Areas of China. *Appl. Sci.* **2024**, *14*, 10612. https://doi.org/10.3390/app142210612

Academic Editor: Valerio Comerci

Received: 4 September 2024
Revised: 9 November 2024
Accepted: 13 November 2024
Published: 18 November 2024

1. Introduction

Most studies are related to background values, which can be divided into geochemical background values and environmental background values. The "Geochemical background" is proposed to distinguish whether the content of elements in a geological unit or a certain area is normal and whether the data outside the background range are abnormal (positive or negative) data [1]. The study of geochemical background values is an important foundational work in the field of Earth sciences. The concept of geochemical background originated in exploration geochemistry, and was initially proposed for mineral exploration purposes [2]. However, with the rise of environmental science, this concept began to be introduced into the field of environmental geochemistry in the early 21st century [3]. For exploration geochemistry, the anomaly data may be an indication of the existence of a certain deposit or the element migration caused by alteration process [4]. Unlike its traditional meaning in exploration geochemistry, in environmental geochemistry, geochemical background values typically refer to the concentrations of chemical elements in environmental components that are unaffected by contamination. This reflects the inherent chemical composition characteristics of these elements in their natural state and development in the

environment [5,6]. The term "geochemical baseline" was first introduced in the International Geological Correlation Programme (IGCP) [7,8]. Different scholars have provided similar scientific definitions of this term [9,10], generally referring to the actual content of specific elements or compounds in surface environmental media at a specific point in time. This definition encompasses both natural background concentrations and contributions from diffusion concentrations caused by human activities. Geochemical background values and baseline values are important parameters for describing the geochemical characteristics of a region, aiding in the understanding and evaluation of natural element contents in a specific area. They contribute to understanding regional geological backgrounds and geological processes [6,11,12]. The concept and calculation of geochemical background in this study are primarily based on definitions and methods established in exploration geochemistry. Typically [13,14], the lower limit of anomalies is used to delineate background regions from anomalous regions [15].

Deserts represent a natural resource, with sand dunes covering over 20 million square kilometers globally, distributed across continents worldwide. Approximately 20% of arid regions and numerous coastal areas are characterized by sand dunes, which further extend to encompass gravel deserts and regions influenced by aeolian erosion, collectively affecting over 40% of the Earth's terrestrial surface subjected to aeolian processes. Due to their close relationship with human habitation environments and rich information on modern surface processes and Earth environmental evolution, deserts are considered an indispensable part of the Earth system and have been consistently studied by the international academic community [16,17]. In China, the Regional Geological Survey Project was initiated in 1979 and remains the longest-running national survey program of its kind by the Ministry of Natural Resources (formerly the Ministry of Land and Resources). While there has been extensive research on background values of inland water system sediments or soils, large areas of desert regions remain unsampled due to their vast size and difficult accessibility. Consequently, the geochemical background of desert regions in China remains largely unexplored. Given these circumstances, initiating research on background values in desert regions is crucial for subsequent desert studies and holds profound significance.

A substantial body of research [18–22] indicates that not only can geological units be classified and systematized based on their macrostructural environmental settings and evolutionary history, but they can also be geologically zoned based on micro-scale element geochemistry.

Therefore, this paper combines traditional methods with the multifractal method to determine regional geochemical background values and baseline values in desert areas. Through machine learning techniques, it measures the feature importance of different geochemical indicators comprehensively, effectively dividing desert and sandy regions into distinct geochemical zones. This approach enhances our understanding of the spatial distribution and variability of geochemical components in the study area, providing a robust basis for the exploration, assessment, and development of natural resources.

2. Study Area Overview and Sampling Analysis Testing Methods

Deserts in China cover approximately 1.73 million square kilometers, about 18% of the country's total land area [23].

This study selected the following regions in China as study areas: the Taklimakan Desert, Gurbantunggut Desert, Badain Jaran Desert, Tengger Desert, Kumtag Desert, Qaidam Desert, Hobq Desert, and Ulan Buhe Desert, Mu Us Sandy Land, Horqin Sandy Land, Hunshandak Desert, and Hulun Buir Sandy Land (Figure 1).

According to sampling instructions provided by the Institute of Geophysical and Geochemical Exploration, Chinese Academy of Geological Sciences, Langfang, China, about 30 composite samples were collected in each of these deserts and sandy lands. Each composite sample was formed by mixing several shallow (0–20 cm) aliquots of material, collected in a small area around the sampling point. Aliquots were mixed to form a 10 kg composite sample. After a mass distribution of 500 g, each subsample was sent to the

laboratory for analysis [24–26]. A total of 344 desert samples (Figure 1) were collected and analyzed for 61 indicators, as outlined in Table 1 for each indicator analysis method.

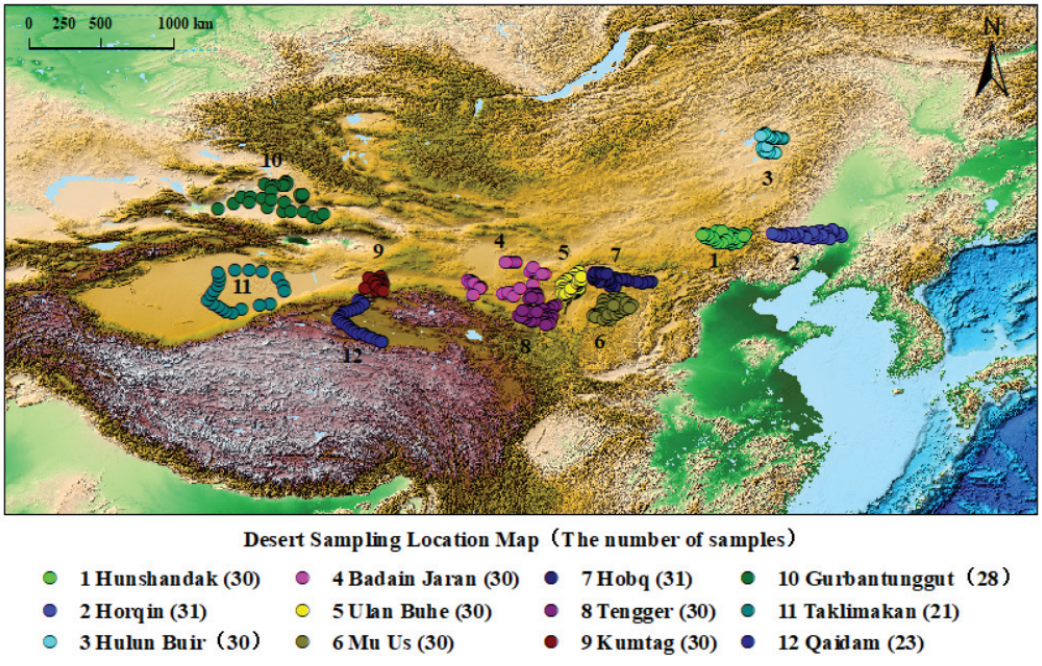

Figure 1. Desert Sampling Location Map (Data and base map sources: Institute of Geophysical and Geochemical Exploration, Chinese Academy of Geological Sciences).

Table 1. Analysis Methods and Elemental Composition (Data sources: Institute of Geophysical and Geochemical Exploration, Chinese Academy of Geological Sciences).

Analytical Methods	Target Elements
Inductively Coupled Plasma Mass Spectrometry (ICP-MS)	Ag, Bi, Cd, Ce, Co, Dy, Er, Eu, Gd, Ho, I, La, Lu, Mo, Nd, Ni, Pb, Pr, Rb, Sb, Sm, Tb, Th, Tm, Yb
X-ray Fluorescence Spectroscopy (XRF)	Al_2O_3, Ba, Br, CaO, Cl, Cr, TFe_2O_3, Ga, K_2O, MgO, Mn, Na_2O, Nb, P, S, SiO_2, Sr, Ti, Y, Zn, Zr
Inductively Coupled Plasma Atomic Emission Spectrosco (ICP-AES)	Be, Cu, Li
Atomic Fluorescence Spectroscopy (AFS)	As, Ge, Hg, Se
Graphite Furnace Atomic Absorption Spectroscopy (AAS)	Au
Alternating Current Arc-Emission Spectroscopy (AES)	B, Sn
Gas Chromatography (GC)	TC, N
Potentiometry Method (POT)	F, pH
Volumetric Method (VOL)	Corg.

3. Data Processing Methods

3.1. Calculation Methods of Geochemical Background Values and Geochemical Baseline Values

Calculation Method 1 for Geochemical Background Values: Iterative Method [27,28]. In geochemical data processing, traditional statistical parameter calculations are based on the assumption that the data follow a normal or log-normal distribution. However, in most cases, the data used for these calculations do not conform to such distributions. Therefore,

by removing values that deviate more than three times the standard deviation from the mean, the data are adjusted to approximate a normal or log-normal distribution. At this point, the similarity between the calculated mean and the original data (before removal of values exceeding three times the standard deviation) should be assessed. When they are essentially consistent or very close, it indicates satisfactory calculation results. The iterative method follows these steps: (1) Calculate the mean (X_1) and standard deviation (Sd_1) of the original data set for each element across the entire area; check if the data conform to a normal distribution. If they do, then X_1 is considered the background value. If not, proceed to step (2); (2) Remove a batch of values based on $X_1 \pm 3Sd_1$ and obtain a new data set. Then, calculate the mean (X_2) and standard deviation (Sd_2) of this new data set and check if the data conform to a normal distribution. If they do, then X_2 is considered the background value. If not, proceed to step (3); (3) Repeat step (2) until no more high-value points exist, then calculate the mean (X_n) and standard deviation (Sd_n) of the final dataset. X_n is taken as the background value C_{01}, and $n+1$ is the number of times the data conform to a normal distribution. The calculation process is carried out using Microsoft Visual Basic for Applications [15,29–32].

Calculation Method 2 for Geochemical Background Values: Frequency Distribution. Histogram Method [33,34]. For those whose histogram is unimodal and close to normal distribution, the general processing method is to connect the left top Angle S of the maximum frequency column with the left top Angle Q of the latter group of frequency columns, and the right top Angle T of the maximum frequency column with the right top Angle P of the latter group of frequency columns. The projection of the two lines intersecting on the coordinate axis is the mass value M_0, which can be used as the background value. Then, draw a horizontal line defined by 0.6 times the maximum frequency, intersecting both sides of the frequency density curve, and the length between the intersection point and the median value is the mean square error σ. In this case, the true value of the value obtained by M_0 and 2 times the mean square error σ is the lower limit of the anomaly. Then, draw a horizontal line defined by 0.6 times the maximum frequency, intersecting both sides of the frequency density curve, and the length between the intersection point and the median value is the mean square error σ. In this case, the true value of the value obtained by M_0 and 2 times the mean square error S is the lower limit of the anomaly (as shown in Figure 2a).

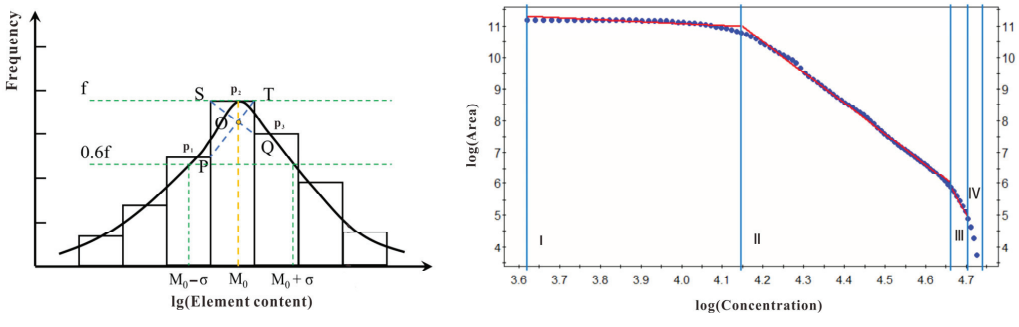

Figure 2. Schematic Diagram of Method Principles. (**a**). Schematic Diagram of Frequency Histogram Distribution; (**b**). Schematic plot of Double Logarithmic Coordinate Curve of Content-Area Method.

The mass value can be obtained mathematically:

$$M_0 = x_0 + \frac{i(p_2 - p_1)}{2p_2 - p_1 - p_3} \quad (1)$$

In Formula (1), M_0 is the crowd value, x_0 is the lower limit value of the group where the crowd value resides, i is the group distance, p_1 is the frequency of the group before the group where the crowd value resides, p_2 is the frequency of the group where the crowd value resides, and p_3 is the frequency of the group after the group where the crowd value resides. The mass value M_O is used as background C_{02}.

Calculation Method 3 for Geochemical Background Values: Concentration-Area Method (C-A method) was first proposed by Cheng et al. (1994). Later scholars also call it content-area method [34–38]. This method is based on the concentration value (that is, the frequency of the magnitude value) to separate outliers from the background; it distinguishes the background field from the abnormal field. These values can also be spatial or geometric features of geochemical indicators. The expression of the C-A model is as follows:

$$A(\rho > v) \propto \rho^{-\beta} \quad (2)$$

In Formula (2), $A(\rho)$ represents the region where the concentration is greater than or equal to the contour value; v is the threshold; β is the fractal dimension greater than zero. $A(\rho > v)$ is the area value of the element content ρ greater than A certain value v, and with the increase of the value v, $A(\rho > v)$ will decrease accordingly. The change of A with v will depend on the magnitude of the exponent β. The fractal dimension β can quantitatively describe the distribution of geochemical element content and the complexity of the variation of element content distribution in this scale-free region. This variation corresponds to different β values in the range of background values and outliers, respectively, which will determine different slopes of the line segments in the schematic plot of double Logarithmic Coordinate Curve.

In the C-A method, by the schematic plot of double Logarithmic Coordinate Curve, the area $A(\geq s)$ with a concentration value greater than s is established between the concentration value s. The power law relationship can be drawn to map the anomaly and the background region.

GeoDAS 4.0 has been used to create a double logarithmic coordinate curve for the content-area method (Figure 2b). The data do not necessarily need to follow a normal distribution. The second segment of the fitted line reflects the non-singular background information of element contents [39]. By calculating the arithmetic mean of the numbers that fall within the second segment of the fitted line, the background value C_{03} is determined.

The final geochemical background value C_0 is obtained by averaging the values calculated from the three methods.

With the Calculation Method for geochemical baseline values [6,38,40,41], the process begins with testing the desert sample data for normality using Python. If the whole dataset conforms to a normal distribution, the arithmetic mean plus or minus two standard deviations is used to denote the baseline value and its range. Alternatively, if the data adhere to a log-normal distribution, the geometric mean multiplied/split the square of geometric standard deviation represents the baseline and its range. For skewed distributions, dividing the geometric mean by the square of the geometric standard deviation is the lower limit of the baseline value, and multiplying the geometric mean by the square of the geometric standard deviation is the upper limit of the baseline value [42]. This meticulous approach ensures the accuracy and reliability of the geochemical baseline values, essential for comprehensive analysis and interpretation in geochemical research.

3.2. Methods of Geochemical Zoning

By utilizing linear regression models in machine learning [43–46], the importance of different geochemical indicators (major elements, trace elements, rare earth elements) across various desert regions was assessed. The absolute values of the regression coefficients for each feature were compared to determine their significance in the model's predictions. A feature importance stacking diagram was then created to illustrate the importance of different geochemical indicators in various desert regions, distinguishing geochemical

zones based on their relative significance. The entire calculation process was executed using Python 2.7.

Using Origin, three ternary diagrams based on the background values of major elements were plotted: SiO_2/10-Al_2O_3-CaO, (K_2O + Na_2O)-CaO-TFe_2O_3, and CaO-K_2O-Na_2O [47]. These diagrams compare the compositional components (sources) of samples from different deserts and sandy lands. Regions with similar sources or chemical compositions were grouped into the same area.

Based on the background values of trace elements, hierarchical clustering was used to construct a dendrogram to represent the nested relationships among samples. A cluster analysis heatmap was generated [48] to observe the clustering of desert regions and elements, identifying regions with similar characteristics. Additionally, using SPSS and ArcGIS, a distribution map of trace element factor weights was created [8,49]. By analyzing and comparing the different factor weights of sample points in various desert regions, each sample point displayed the factor with the highest weight. Desert regions with similar factor compositions were grouped into the same area.

4. Results and Discussion

4.1. Geochemical Background Values and Baseline Values

The results of the geochemical background values and baseline values for the desert samples in the study area are shown in Appendix A Tables A1 and A2.

The major elements that show significant differences can be categorized into three groups: SiO_2, which is related to changes in the quartz background values; CaO, which reflects changes in the carbonate background values; and MgO, whose variation is associated with changes in both carbonate and ferromagnesian silicate background values. The Hunshandak, Horqin, and Hulun Buir desert sands are characterized by high SiO_2 and low CaO, whereas the Kumtag, Gurbantunggut, Taklimakan, and Qaidam desert sands are mainly characterized by low SiO_2 and high CaO. The Badain Jaran, Ulan Buhe, Mu Us, Hobq, and Tengger desert sands have SiO_2 and CaO background values that fall between these two extremes (Appendix A Tables A1 and A2; Figure 3a).

From the analysis of the background values of trace elements (Figure 3c), it can be seen that the UCC-standardized values of trace elements in the Kumtag, Gurbantunggut, Taklimakan, and Qaidam desert sands are higher than those in other desert sands. Some trace elements (Cd, Cl, S, N) in these deserts are even higher than the upper continental crust abundance [50]. In contrast, the standardized values of most trace elements in the Hunshandake, Horqin, and Hulun Buir desert sands are lower than those in other deserts. The trace element standardized values in the Badain Jaran, Ulan Buhe, Mu Us, Hobq, and Tengger desert sands fall between these two extremes.

From the analysis of the background values of rare earth elements (Figure 3a), the UCC distribution pattern plot of rare earth element background values in the deserts show a flat trend [51–54]. This indicates that the rare earth element distribution patterns in the desert sands of the study area are similar to those of the upper continental crust (UCC), and the trend in the normalized values is almost consistent with that of the major and trace elements.

According to the ratio charts of element background values to baseline values for China's deserts (Figure 4), most of the background values for various element indicators in different desert sands are close to their baseline values, indicating that the majority of the data fall within the normal natural range. Some element indicators (such as MgO, TFe_2O_3, CaO, and TC) are relatively enriched in the Kumtag, Taklimakan, and Qaidam deserts, while they are relatively depleted in the Hunshandak, Horqin, and Hulun Buir deserts. A few elements (such as Cl and S) show significant enrichment in the Kumtag, Gurbantunggut, Taklimakan, and Qaidam deserts [4].

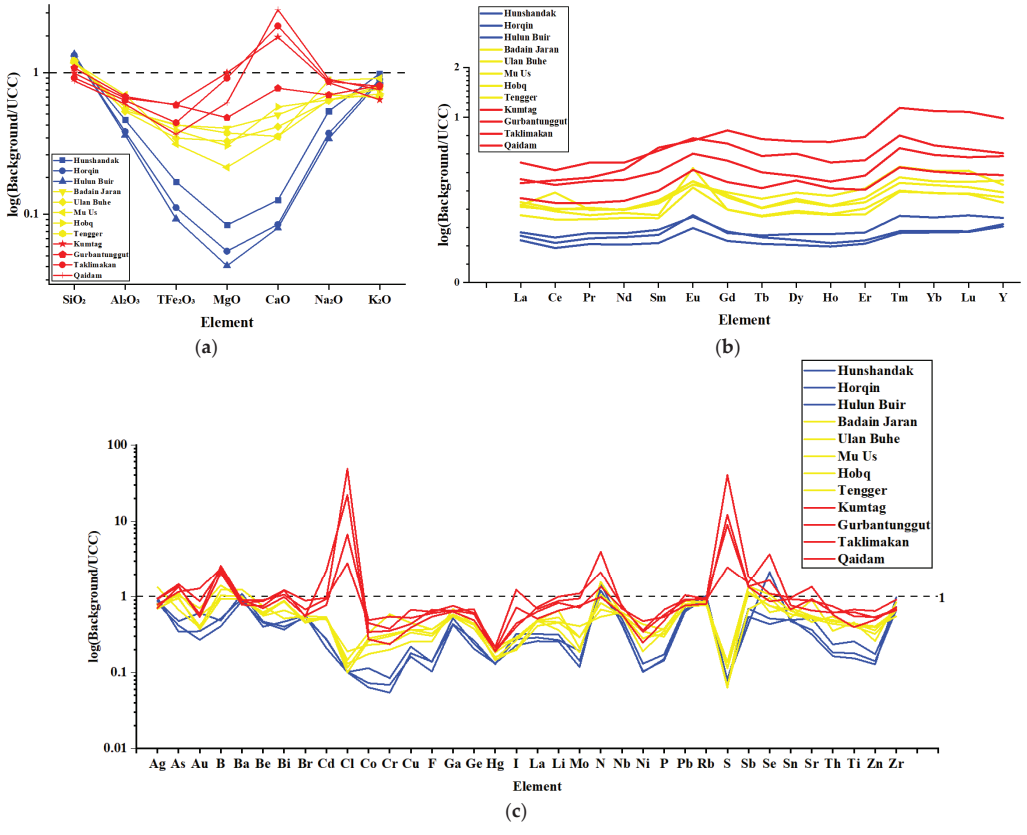

Figure 3. Element Standardized Plots. (**a**). Element Standardized Plots of Major Element; (**b**). Element Standardized Plots of Trace Element; (**c**). Element Standardized Plots of Rare Earth elements.

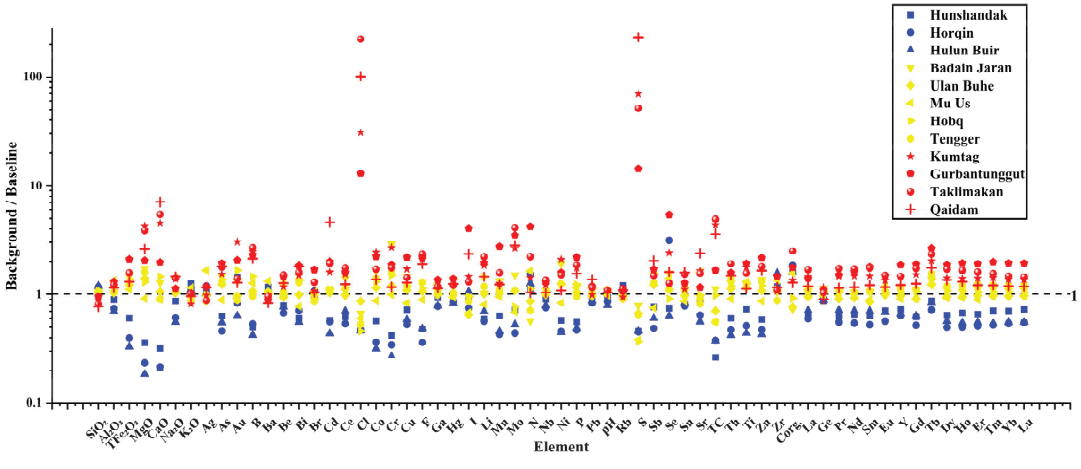

Figure 4. Ratio of Geochemical Background Values to Baseline Values in Chinese Deserts.

4.2. Geochemical Zoning

Based on the analysis of geochemical background values and baseline values, it was observed that the enrichment or depletion patterns of different elemental indicators in various deserts exhibit certain similarities (Figures 3 and 4). However, as shown in Figure 3, classifying or zoning different deserts based on enrichment or depletion alone is significantly influenced by human factors and tends to be rather coarse. Therefore, to improve the precision of geochemical zoning, it is beneficial to utilize machine learning techniques in conjunction with some geochemical indicators [55]. By applying these methods, the 12 desert areas can be divided into several geochemical zones. This approach enhances the visualization of zoning results, increases the efficiency of zoning analysis, and facilitates the evaluation and comparison of geochemical regional systems [56–59].

From the three triangular diagrams (Figure 5), it is clear that the various desert areas are divided into three distinct zones: Eastern Deserts (1. Hunshandak, 2. Horqin, 3. Hulun Buir), Central Deserts (4. Badain Jaran, 5. Ulan Buhe, 6. Mu Us, 7. Hobq, 8. Tengger), and Western Deserts (9. Kumtag, 10. Gurbantunggut, 11. Taklimakan, 12. Qaidam). The SiO_2/10-Al_2O_3-CaO triangular diagram (Figure 5a) reflects the relative proportions of quartz, carbonate, and silicate minerals. The Western Deserts, including Kumtag, Taklimakan, and Qaidam, are characterized by significantly higher carbonate mineral ratios, relatively lower quartz ratios, and intermediate silicate mineral content. The (K_2O + Na_2O)-CaO-TFe_2O_3 triangular diagram (Figure 5b) shows the relative proportions of feldspar, carbonate, and ferromagnesian silicate minerals in the samples. In the Western Deserts, Kumtag, Taklimakan, and Qaidam exhibit high carbonate mineral ratios and low ferromagnesian silicate mineral ratios. The Central Deserts, such as Badain Jaran, Ulan Buhe, Mu Us, Hobq, and Tengger, as well as Gurbantunggut in the Western Deserts, feature intermediate carbonate mineral ratios. In contrast, the Eastern Deserts, including Hunshandak, Horqin, and Hulun Buir, show high feldspar mineral ratios and low carbonate mineral ratios. The CaO-K_2O-Na_2O triangular diagram (Figure 5c) reflects the relative proportions in the content of carbonate, potassium feldspar/muscovite, and plagioclase in the samples. The Western Deserts (Kumtag, Taklimakan, and Qaidam) exhibit high carbonate mineral ratios, low potassium feldspar/muscovite, and low plagioclase content. The Central Deserts (Badain Jaran, Ulan Buhe, Mu Us, Hobq, and Tengger) and Gurbantunggut in the Western Deserts have intermediate carbonate mineral ratios, moderate plagioclase content, and high potassium feldspar/muscovite ratios. Conversely, the Eastern Deserts, including Hunshandak, Horqin, and Hulun Buir, are characterized by high plagioclase mineral ratios and low carbonate mineral ratios.

In the constant element feature importance stacked plot (Figure 6a), CaO, MgO, and TFe_2O_3 are significantly more important in the Kumtag, Gurbantunggut, Taklimakan, and Qaidam deserts compared to other deserts. The importance is somewhat lower in the Badain Jaran, Ulan Buhe, Mu Us, Hobq, and Tengger deserts, with Hunshandak, Horqin, and Hulun Buir deserts showing the lowest levels of importance.

The primary factor influencing the variation in constant elements is the composition of the source rocks. From the geochemical map of calcium oxide in China, it is evident that the Kunlun Mountains and the North Tian Shan Mountains are rich in marine carbonate rocks. These carbonate minerals are continuously supplied to the Taklimakan, Qaidam, and Kumtag deserts through river systems. The Tianshan Mountains and the Altai Mountains near Gurbantunggut also have significant carbonate rock formations, providing a certain amount of carbonate minerals to the Gurbantunggut Desert. In contrast, the Badain Jaran, Tengger, Hobq, and Mu Us deserts are surrounded by carbonate strata along the northern edge of the Qilian Mountains, the surrounding Alashan mountains, and the southern segment of the Helan Mountains, but these formations are not as extensive as those in the Kunlun Mountains [60]. Therefore, the CaO content in these deserts is lower compared to the Western Deserts. The Eastern Deserts, surrounded by areas lacking carbonate rocks [47], consequently have a lower CaO content.

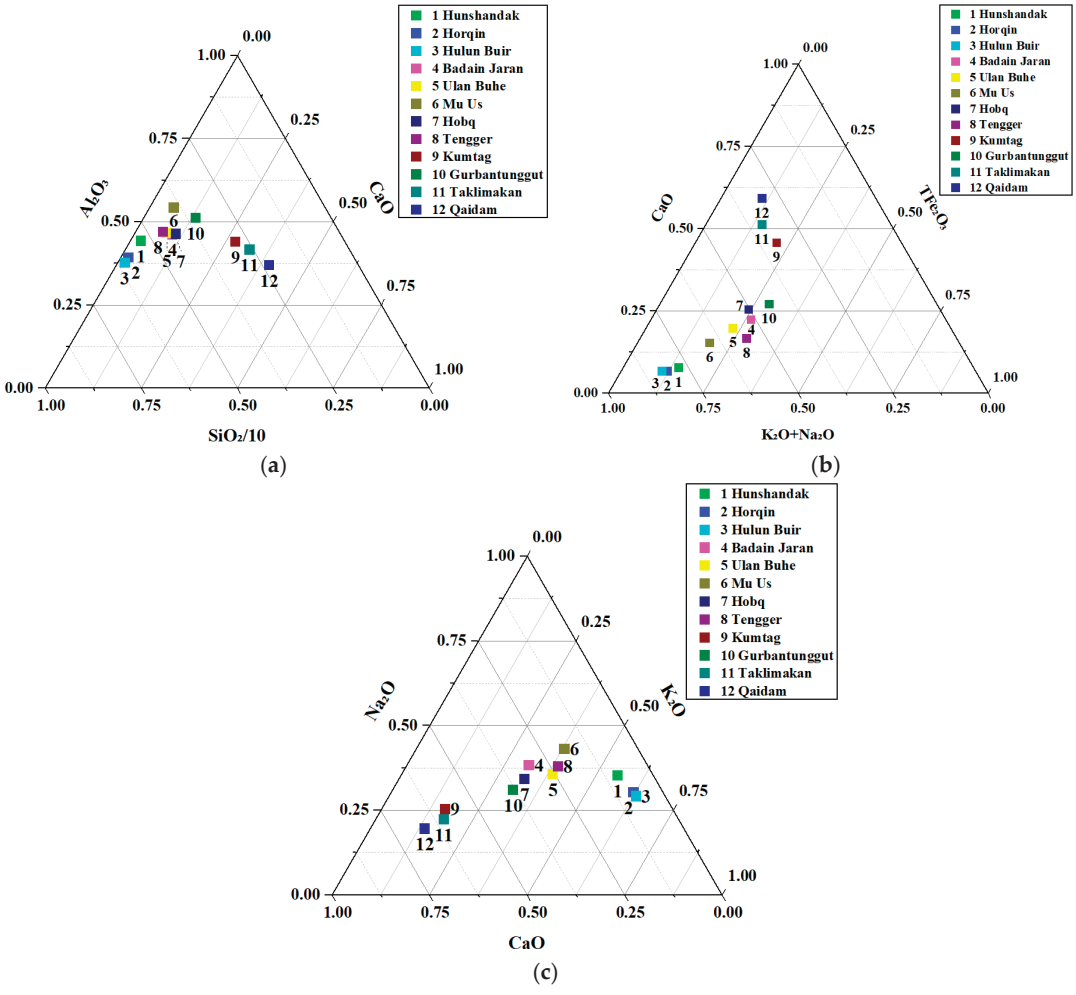

Figure 5. Triangular Diagrams of Major Elements. (**a**). $SiO_2/10$-Al_2O_3-CaO ternary diagram; (**b**). (K_2O + Na_2O)-CaO-TFe_2O_3 ternary diagram; (**c**). CaO-K_2O-Na_2O ternary diagram.

The second factor influencing the chemical composition of Chinese deserts is the supply of fresh material. This can be explored from multiple perspectives, including the erosion, weathering, transportation, and deposition of source materials. Chemical weathering leads to the dissolution of carbonate minerals and the gradual transformation of feldspars and ferromagnesian silicate minerals into secondary clay minerals. The weathering products are transported in the form of solutions or suspensions, resulting in the relative enrichment of weathering-resistant minerals like quartz in coarse fractions. Physical weathering, on the other hand, further fragments minerals like carbonates and ferromagnesian silicates, which are less resistant to physical weathering, leading to the relative enrichment of weathering-resistant minerals such as quartz in coarse fractions. From the perspective of material erosion supply and physical and chemical weathering, different deserts exhibit significant differences. In the Western Deserts, such as the Taklimakan Desert, surrounded by high mountains like the Tianshan, Pamirs, Kunlun, and Altun Mountains, with large river gradients, sparse vegetation cover, and extensive ice and snow cover on mountaintops (with more developed glaciers during the Quaternary glaciation), physical erosion is strong and

chemical weathering is relatively weak. Overall, the Western Deserts are characterized by mobile sand dunes with strong physical weathering and weak chemical weathering. In contrast, the Eastern Deserts are predominantly covered by fixed sand areas, with weaker physical weathering but stronger chemical weathering [47], resulting in the partitioning observed in the constant element importance stacking diagram (Figure 6a).

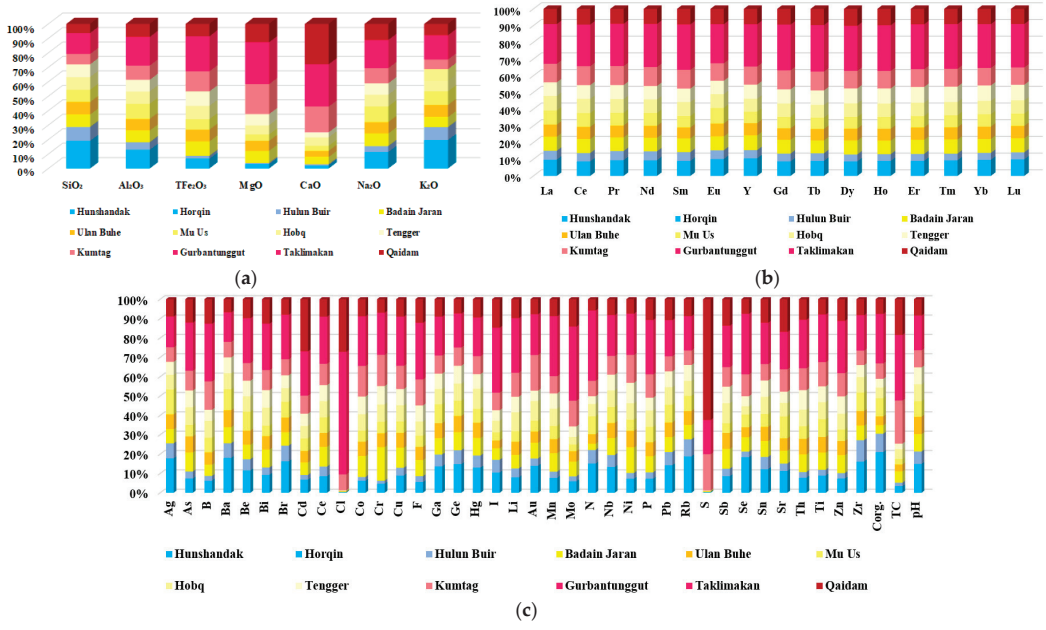

Figure 6. Feature Importance Stacked Plot. (**a**). Feature Importance Stacked Plot of Major Element; (**b**). Feature Importance Stacked Plot of Trace Element; (**c**). Feature Importance Stacked Plot of Rare Earth Element.

For the trace element importance stacking diagram (Figure 6c), it can be concluded that in desert regions such as Kumtag, Gurbantunggut, Taklimakan, and Qaidam, elements like S, Cl, and TC show significantly high importance. These elements are typically closely related to the chemical weathering processes in desert areas. Particularly under arid conditions, their accumulation may be influenced by variations in salinity and moisture. The noticeable geochemical differences in some elements are attributed to their differentiation, migration, and enrichment under varying climatic backgrounds and depositional environments. In the trace element clustering heatmap (Figure 7), the Western Deserts show a higher correlation with most trace elements. This likely reflects the geological background and depositional environment of the Western Deserts, where specific geological processes or rock compositions might lead to trace element enrichment. The Central Deserts follow in terms of correlation, while the Eastern Deserts exhibit lower trace element correlation, with only elements such as Rb and Corg. showing relatively better correlation. This may be related to the younger geological age and lower degree of chemical weathering in the Eastern Deserts. In the trace element factor weight distribution map (Figure 8), factors F1 and F2 have the highest weights in the Western Deserts, which may be related to the region's geological structure, rock composition, and chemical weathering processes. Other factors show weaker weights on the map. In the Central Deserts, besides F1 and F2, factors F3, F4, and F5 also have noticeable impacts, which may reflect the more complex geological background and chemical composition of the region. In the Eastern Deserts, the presence of factors F6 and F7 may indicate different geological features or chemical environments compared to other regions [61].

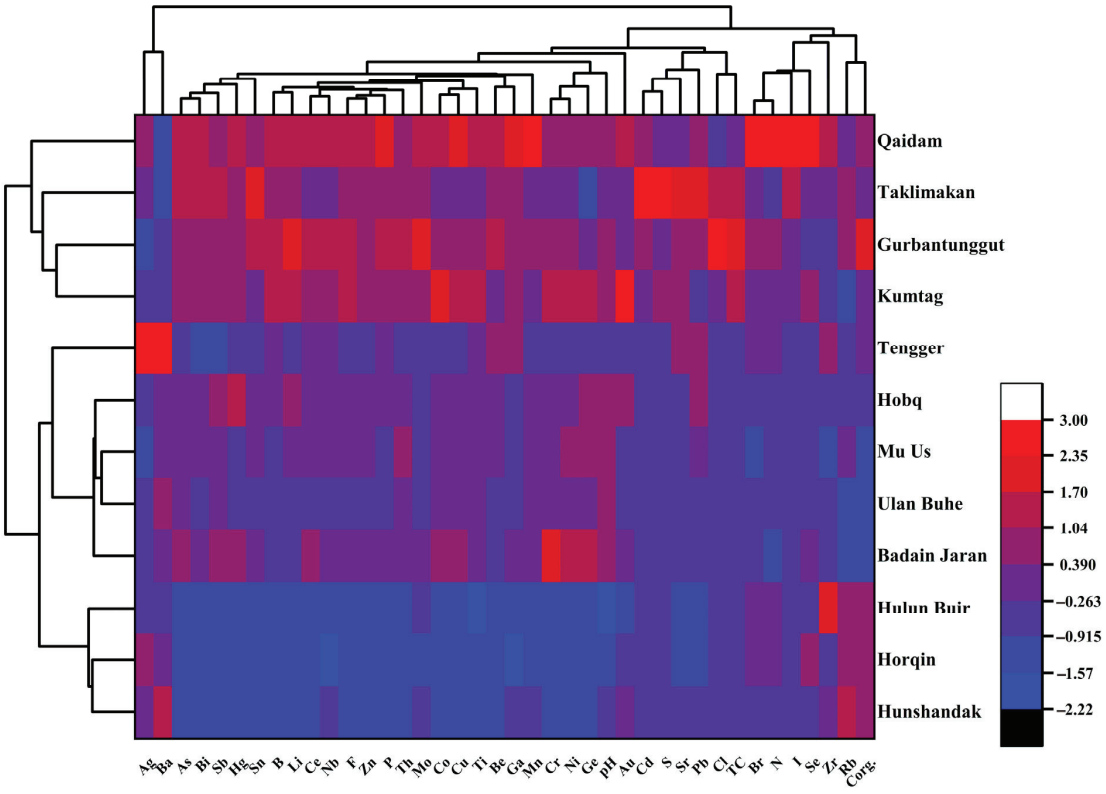

Figure 7. Trace Element Background Value Clustering Heatmap.

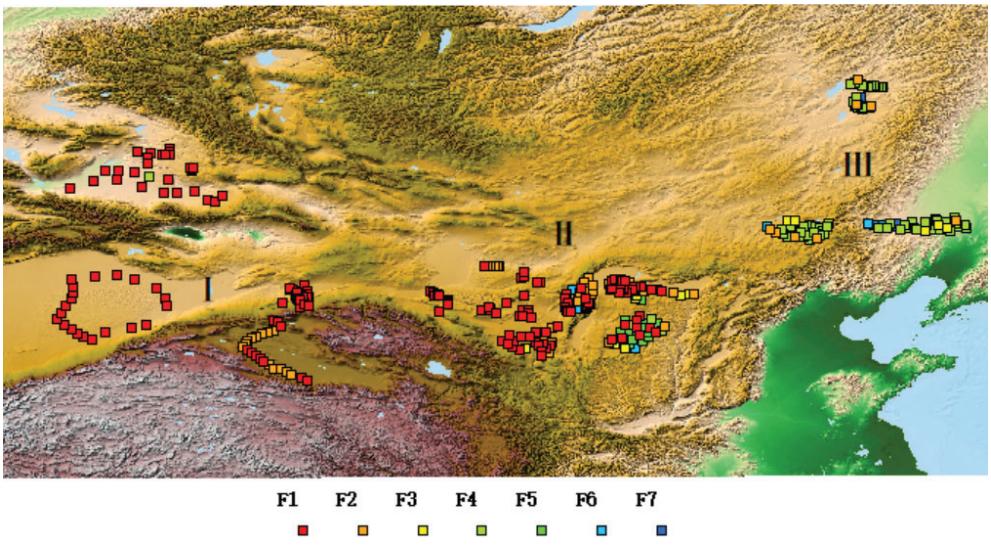

Figure 8. Trace Element Factor Weight Distribution Map.

From the rare earth element importance stacking diagram (Figure 6b), it can be concluded that the significance of rare earth elements in different desert regions follows the

order: Western > Central > Eastern. Deserts within the same large region share a common source area for their material supply. However, due to varying degrees of post-depositional weathering, the Eastern Deserts experience more intense chemical weathering, leading to a greater loss of rare earth elements [62,63].

Based on the analysis of all the geochemical indicators, the twelve desert regions can be categorized into three geochemical zones: (I) Western Desert Regions (Kumutag, Gurbantunggut, Taklimakan, Qaidam) characterized by high carbonate rock content, low quartz and feldspar content, high trace element correlation and significance, and high rare earth element significance; (II) Central Desert Regions (Badain Jaran, Ulan Buhe, Mu Us, Hobq, Tengger) with moderate carbonate rock content, moderate quartz and feldspar content, average trace element correlation, and moderate rare earth element significance; and (III) Eastern Desert Regions (Hunshandak, Hobq, Hulun Buir) showing very low carbonate rock content, high quartz and feldspar content, low trace element correlation and significance, and low rare earth element significance. This classification aligns with previous research [47], which similarly divided the deserts of China into western, central, and eastern regions based on major element analysis.

5. Conclusions

(1) In this paper, geochemical background and geochemical baseline values of 61 desert elements were calculated using various calculation methods. This provides a baseline for understanding the natural chemical composition of desert regions, which is significant for environmental change assessment and natural resource exploration and has far-reaching implications for future desert research.

(2) Combining machine learning methods, different desert areas have been grouped into three geochemical zones, which enhances our understanding of the spatial distribution and variability of geochemical components in the study area. This classification provides a solid basis for natural resources exploration and evaluation, which is useful for economic development. The zone analysis facilitates better identification and management of environmental geochemical issues in different regions.

Author Contributions: Conceptualization, W.W. and Y.Z.; methodology, W.W.; software, W.W., Y.Z. and W.Z.; validation, C.W. and Y.S.; formal analysis, W.W.; data curation, W.W. and F.Y.; writing—original draft preparation, W.W., Y.Z. and W.Z.; writing—review and editing, W.W. and S.X.; visualization, W.W.; visualization, W.W.; supervision, W.W. and S.X.; project administration, W.W. and F.Y. All authors have read and agreed to the published version of the manuscript.

Funding: This research was financed by the National Nonprofit Institute Research Grant of IGGE (Nos. AS2020Y06 and AS2020J06).

Institutional Review Board Statement: Not applicable.

Informed Consent Statement: Not applicable.

Data Availability Statement: The original contributions presented in the study are included in the article, further inquiries can be directed to the corresponding author.

Acknowledgments: We are very thankful for all the editors and reviewers who have helped us improve the manuscript.

Conflicts of Interest: The authors declare no conflicts of interest.

Appendix A

Tables A1 and A2 Statistics of Geochemical Background Values and Baseline Values for Different Deserts and Sandy Areas.

Table A1. Statistics of Geochemical Background Values and Baseline Values for Different Deserts and Sandy Areas.

Element	Hunshandak	Horqin	Hulun Buir	Badain Jaran	Ulan Buhe	Mu Us	Hobq	Tengger
SiO_2	85.409	88.249	89.740	78.647	79.286	77.744	80.539	80.889
Al_2O_3	7.135	5.902	5.579	8.286	8.196	10.693	8.732	8.272
TFe_2O_3	0.855	0.562	0.468	2.146	1.737	1.577	1.970	2.165
MgO	0.208	0.136	0.108	1.003	0.814	0.532	0.756	0.929
CaO	0.451	0.304	0.288	1.805	1.488	1.262	2.055	1.273
Na_2O	1.746	1.221	1.118	2.276	2.063	2.877	2.099	2.095
K_2O	2.751	2.504	2.437	1.866	2.254	2.547	1.978	2.151
Ag	46.496	50.535	42.935	39.934	42.391	70.371	41.749	36.652
As	2.272	1.657	1.996	5.319	4.484	3.209	4.955	4.673
Au	0.912	0.523	0.403	0.834	0.610	0.585	1.052	0.556
B	8.195	8.718	6.924	15.881	17.579	20.841	23.909	15.789
Ba	678.853	586.865	546.272	582.343	622.267	770.781	583.064	581.734
Be	0.985	0.840	0.954	1.191	1.172	1.573	1.266	1.299
Bi	0.064	0.075	0.059	0.140	0.105	0.082	0.142	0.137
Br	0.843	0.902	0.892	0.744	0.825	0.889	0.759	0.723
Cd	24.987	24.344	18.878	47.698	44.664	47.962	48.134	47.246
Cl	37.494	38.068	37.301	54.172	69.912	48.328	36.892	42.765
Co	1.975	1.256	1.099	5.728	3.990	3.032	4.512	4.872
Cr	7.760	6.330	5.001	53.544	22.156	18.373	27.613	29.409
Cu	6.126	4.526	5.022	12.586	9.387	7.138	10.194	10.204
F	76.386	57.253	77.549	206.061	169.011	142.499	181.533	205.903
Ga	9.086	7.514	7.606	10.218	9.590	11.975	9.708	9.729
Ge	0.883	0.925	0.893	1.150	1.036	0.976	1.082	1.136
Hg	6.570	6.553	6.421	9.180	8.026	7.275	10.602	7.651
I	0.385	0.319	0.453	0.400	0.276	0.289	0.405	0.370
Li	5.604	5.353	6.580	9.686	9.509	7.605	13.701	11.157
Mn	140.132	94.819	100.536	293.424	224.676	210.644	275.233	242.574
Mo	0.211	0.130	0.156	0.447	0.318	0.203	0.228	0.322
N	87.115	121.135	99.520	44.942	68.317	129.502	88.349	55.938
Nb	6.150	5.154	5.382	7.408	6.745	7.068	7.335	6.973
Ni	6.140	4.861	4.750	20.278	13.339	8.889	13.145	16.312
P	112.894	94.162	98.585	241.221	211.150	232.152	246.137	192.970
Pb	12.301	10.806	11.371	12.602	12.518	15.093	14.854	13.472
pH	7.970	7.276	6.668	9.210	9.313	8.273	8.972	8.996
Rb	86.042	80.364	79.173	65.405	64.780	69.538	68.806	73.227
S	49.556	48.581	49.307	85.168	72.074	41.134	39.514	69.862
Sb	0.277	0.176	0.217	0.546	0.443	0.271	0.558	0.458
Se	0.046	0.193	0.039	0.096	0.068	0.086	0.056	0.068
Sn	1.025	0.992	1.063	1.354	1.233	1.100	1.482	1.403
Sr	165.814	116.557	101.216	168.435	163.603	289.514	177.283	147.573
TC	0.082	0.118	0.116	0.352	0.219	0.173	0.305	0.175
Th	2.455	1.918	1.718	5.140	4.586	3.694	4.892	5.740
Ti	985.214	690.462	590.150	1673.664	1550.112	1745.705	1685.261	1555.537
Zn	11.686	9.448	8.585	27.157	21.519	17.348	23.987	26.390
Zr	140.810	128.656	187.519	126.136	127.049	161.713	133.328	105.395
Corg.	0.128	0.145	0.126	0.057	0.060	0.123	0.072	0.059
La	8.787	7.925	9.420	14.535	12.629	14.602	15.085	14.207
Ce	15.143	13.156	17.186	34.335	24.020	27.170	28.150	27.792
Pr	1.901	1.652	2.128	3.119	2.716	2.897	3.148	3.214
Nd	7.430	6.194	8.035	11.967	10.568	11.376	11.940	11.858
Sm	1.355	1.125	1.503	2.286	1.832	1.919	2.339	2.249
Eu	0.408	0.330	0.398	0.614	0.575	0.693	0.612	0.593

Table A1. *Cont.*

Element	Hunshandak	Horqin	Hulun Buir	Badain Jaran	Ulan Buhe	Mu Us	Hobq	Tengger
Y	8.216	7.121	7.414	12.963	10.845	10.185	11.472	12.429
Gd	1.199	1.007	1.236	2.123	1.770	1.766	2.065	2.183
Tb	0.200	0.164	0.192	0.317	0.283	0.280	0.315	0.355
Dy	1.148	0.885	1.007	1.977	1.694	1.652	1.919	2.123
Ho	0.244	0.181	0.199	0.386	0.344	0.340	0.383	0.435
Er	0.697	0.541	0.587	1.178	1.030	0.948	1.117	1.309
Tm	0.121	0.090	0.093	0.191	0.167	0.165	0.181	0.210
Yb	0.787	0.607	0.627	1.225	1.081	1.086	1.180	1.352
Lu	0.126	0.095	0.096	0.189	0.167	0.166	0.179	0.210

Note: Units are $\mu g \cdot g^{-1}$; Ag, Au, Cd, Hg: $ng \cdot g^{-1}$; Oxides, TC, Corg: wt%; pH is dimensionless; UCC refers to upper crustal abundances (Rudnick and Gao, 2014) [50].

Table A2. Statistics of Geochemical Background Values and Baseline Values for Different Deserts and Sandy Areas.

Element	Kumtag	Gurbantunggut	Taklimakan	Qaidam	UCC	Baseline	Baseline Range
SiO_2	65.805	71.855	61.112	58.014	66.620	75.337	49.960–113.605
Al_2O_3	10.141	10.434	9.783	9.225	15.400	7.992	4.942–12.927
TFe_2O_3	3.001	2.972	2.234	1.849	5.040	1.420	0.388–5.202
MgO	2.475	1.191	2.261	1.519	2.480	0.582	0.072–4.701
CaO	6.381	2.784	7.645	9.977	3.590	1.407	0.145–13.679
Na_2O	2.775	2.272	2.829	2.930	3.270	2.008	0.937–4.303
K_2O	1.798	2.269	2.237	2.120	2.800	2.209	1.445–2.973
Ag	41.352	49.946	37.279	49.153	53.000	42.394	24.473–73.437
As	5.546	7.003	6.408	6.555	4.800	3.614	1.198–10.904
Au	1.920	1.302	0.881	0.808	1.500	0.633	0.249–1.605
B	40.417	37.746	44.069	34.985	17.000	16.384	4.798–55.953
Ba	570.059	515.546	559.338	483.902	624.000	583.416	348.347–818.485
Be	1.467	1.820	1.887	1.579	2.100	1.247	0.705–2.206
Bi	0.158	0.194	0.169	0.192	0.160	0.106	0.040–0.281
Br	0.897	1.411	1.082	0.873	1.600	0.836	0.493–1.419
Cd	69.450	86.760	83.411	200.818	0.090	43.345	13.499–139.181
Cl	2489.497	1037.997	17,971.754	8176.649	370.000	80.713	4.050–1608.485
Co	8.439	7.732	5.901	4.729	17.300	3.462	0.845–14.182
Cr	49.974	34.632	32.502	21.687	92.000	18.510	3.386–101.195
Cu	14.640	18.733	12.196	10.941	28.000	8.568	3.316–22.138
F	334.623	349.961	373.148	302.346	557.000	159.147	45.440–557.389
Ga	11.529	13.168	11.423	11.040	17.500	9.704	6.394–14.727
Ge	1.169	1.111	1.049	0.915	1.400	1.013	0.740–1.387
Hg	9.495	10.785	9.438	9.669	0.050	7.752	4.490–13.384
I	0.621	1.721	0.558	1.002	1.400	0.426	0.160–1.132
Li	17.341	18.356	20.950	13.707	21.000	9.444	3.564–25.024
Mn	276.620	606.612	347.138	271.722	/	220.406	68.647–707.657
Mo	0.785	1.037	1.213	0.834	1.100	0.296	0.075–1.166
N	111.946	330.449	175.894	81.724	83.000	78.948	25.827–241.330
Nb	8.322	8.827	9.204	7.057	12.000	6.816	4.427–10.494
Ni	22.256	16.852	16.049	11.561	47.000	10.647	3.276–34.602
P	352.538	441.268	375.001	313.684	654.572	201.466	69.604–583.135
Pb	12.914	15.454	15.091	17.821	17.000	13.043	8.874–19.170
pH	9.168	9.233	9.174	8.720	/	8.451	6.645–10.748
Rb	67.333	76.247	81.180	78.264	84.000	71.511	52.241–97.889
S	7537.253	1537.105	5536.793	25043.051	621.000	107.837	3.733–3115.437
Sb	0.546	0.613	0.536	0.737	0.400	0.361	0.129–1.010
Se	0.148	0.331	0.078	0.099	0.090	0.062	0.023–0.163

Table A2. *Cont.*

Element	Kumtag	Gurbantunggut	Taklimakan	Qaidam	UCC	Baseline	Baseline Range
Sn	1.419	1.608	1.942	2.029	2.100	1.272	0.744–2.174
Sr	296.507	209.456	282.177	431.545	320.000	180.879	74.052–441.815
TC	1.355	0.519	1.534	1.124	/	0.312	0.129–0.756
Th	6.461	6.416	7.808	6.053	10.500	4.077	1.555–10.687
Ti	2387.824	2586.209	2104.065	1513.804	3836.795	1342.895	475.015–3796.443
Zn	35.218	43.199	35.996	33.035	67.000	19.974	6.520–61.189
Zr	127.077	175.543	131.067	139.682	193.000	119.928	59.672–241.029
Corg.	0.105	0.138	0.196	0.100	/	0.078	0.033–0.186
La	19.399	18.654	22.507	15.829	31.000	13.312	6.540–27.096
Ce	37.239	38.993	42.830	30.355	63.000	24.487	10.862–55.202
Pr	4.355	4.508	5.152	3.420	7.100	2.980	1.380–6.433
Nd	16.788	18.450	19.588	13.335	27.000	11.402	5.132–25.333
Sm	3.155	3.837	3.750	2.612	4.700	2.145	0.922–4.991
Eu	0.780	0.859	0.873	0.681	1.000	0.582	0.291–1.162
Y	16.062	20.874	16.430	13.651	21.000	11.200	5.579–22.483
Gd	2.951	3.681	3.365	2.432	4.000	1.942	0.804–4.694
Tb	0.467	0.608	0.536	0.400	0.700	0.229	0.025–2.058
Dy	2.512	3.334	3.041	2.410	3.900	1.780	0.724–4.378
Ho	0.507	0.706	0.603	0.473	0.830	0.363	0.148–0.893
Er	1.489	2.028	1.702	1.291	2.300	1.060	0.439–2.560
Tm	0.244	0.342	0.267	0.209	0.300	0.172	0.072–0.411
Yb	1.545	2.183	1.660	1.343	2.000	1.125	0.488–2.595
Lu	0.235	0.334	0.250	0.204	0.310	0.173	0.076–0.392

Note: Units are $\mu g \cdot g^{-1}$; Ag, Au, Cd, Hg: $ng \cdot g^{-1}$; Oxides, TC, Corg: wt%; pH is dimensionless; UCC refers to upper crustal abundances (Rudnick and Gao, 2014) [50].

References

1. Wu, Y.; Zhou, Y.; Yang, M.; Wang, J.; Long, T.; Yin, A.; Li, Q. Analysis of the Applies of Soil Environmental Background Value at Home and Abroad and Suggestions on Countermeasures. *J. Ecol. Rural Environ.* **2021**, *37*, 1524–1531.
2. Hawkes, H.E.; Webb, J.S. Geochemistry in mineral exploration. *Soil Sci.* **1963**, *95*, 283. [CrossRef]
3. Gałuszka, A.; Migaszewski, Z. Geochemical background-an environmental perspective. *Mineralogia* **2011**, *42*, 7–17. [CrossRef]
4. Yang, Z.; Peng, M.; Zhao, C.; Yang, K.; Liu, F.; Li, K.; Zhou, Y.; Tang, S.; Ma, H.; Zhang, Q.; et al. The study of geochemical background and baseline for 54 chemical indicators in Chinese soil. *Earth Sci. Front.* **2024**, *31*, 380–402.
5. Cheng, H.; Li, K.; Li, M.; Yang, F.; Cheng, X. Geochemical background and baseline value of chemical elements in urban soil in China. *Earth Sci. Front.* **2014**, *21*, 265–306.
6. Xi, X.; Hou, Q.; Yang, Z.; Ye, J.; Yu, T.; Xia, X.; Cheng, H.; Zhou, G.; Yao, L. Big data-based studies of the variation features of Chinese soil's background value versus reference value: A paper written on the occasion of the publication of soil geochemical parameters of China. *Geophys. Geochem. Explor.* **2021**, *45*, 1095–1108.
7. Darnley, A.G.; Bjorklund, A.; Bolviken, B.; Gustavsson, N.; Koval, P.V.; Plant, J.A.; Steenfelt, A.; Tauchid, M.; Xie, X. *A Global Geochemical Database for Environmental and Resource Management*; UNESCO: Paris, France, 1995.
8. Salminen, R.; Gregorauskien, V. Considerations regarding the definition of a geochemical baseline of elements in the surficial materials in areas differing in basic geology. *Appl. Geochem.* **2000**, *15*, 647–653. [CrossRef]
9. Jiang, H.H.; Cai, L.M.; Wen, H.H.; Luo, J. Characterizing pollution and source identification of heavy metals in soils using geochemical baseline and PMF approach. *Sci. Rep.* **2020**, *10*, 6460. [CrossRef]
10. Wang, Q.; Song, Y.; Lv, X.; Peng, M.; Zhou, Y.; Han, W.; Wang, C. Characteristics and genesis of soil geochemical baselines in Western Yunnan Province. *Geoscience* **2021**, *35*, 412.
11. Valdés Durán, A.; Aliaga, G.; Deckart, K.; Karas, C.; Cáceres, D.; Nario, A. The environmental geochemical baseline, background and sources of metal and metalloids present in urban, peri-urban and rural soils in the O'Higgins region, Chile. *Environ. Geochem. Health* **2022**, *44*, 3173–3189. [CrossRef]
12. Zhang, L.; Cheng, H.; Xie, W.; Qi, Q.; Xie, X.; Yu, W.; Wang, J. Geochemical background and baseline value of soil chemical elements in Hebei Province. *Environ. Sci.* **2023**, *44*, 2817–2828.
13. Zhang, X.; Yang, Z.; Ma, Z.; Tang, J. Geochemical background and geochemical baseline. *Geol. Bull. China* **2006**, *25*, 626–629.
14. Reimann, C.; Garrett, R.G. Geochemical background—Concept and reality. *Sci. Total Environ.* **2005**, *350*, 12–27. [CrossRef] [PubMed]
15. Ye, H.G.; Ye, H.F. Comparison of methods determining anomaly thresholds determined by means of mathematical statistics. *Gansu Geol.* **2018**, *27*, 83–92.

16. Thomas, D.S.G.; Wiggs, G.F.S. Aeolian system responses to global change: Challenges of scale, process and temporal integration. *Earth Surf. Process. Landf.* **2008**, *33*, 1396–1418. [CrossRef]
17. Liu, Z.; Wang, J.; Ding, J.; Xie, X. Analysis of spatial–temporal evolution trends and influential factors of desert-oasis thermal environment in typical arid zone: The case of Turpan–Hami region. *Ecol. Indic.* **2023**, *154*, 110747. [CrossRef]
18. Li, G.; Zhao, Z.; Wei, J.; Ulrich, T. Mineralization processes at the Daliangzi Zn-Pb deposit, Sichuan-Yunnan-Guizhou metallogenic province, SW China: Insights from sphalerite geochemistry and zoning textures. *Ore Geol. Rev.* **2023**, *161*, 105654. [CrossRef]
19. Lala, A.; Yusuf, M.; Suhendra, R.; Maulydia, N.; Dharma, D.; Saiful, S.; Idroes, R. Characterization of geochemical and isotopic profiles in the Southern Zone Geothermal Systems of Mount Seulawah Agam, Aceh Province, Indonesia. *Leuser J. Environ. Stud.* **2024**, *2*, 30–40. [CrossRef]
20. Zuo, J.; Zhao, L.; Fang, L.; Fang, Z. Soil geochemical division based on land quality geochemical survey. *J. Arid. Land. Resour. Environ.* **2021**, *35*, 133–138.
21. Wu, F.; Liu, J.; Wang, J.; Hu, P.; Cheng, X.; Li, F.; Zhao, K.; Zheng, G.; Wang, C.; Xiang, P. Division of the geochemical landscapes in Morocco. *Geophys. Geochem. Explor.* **2023**, *47*, 47–54.
22. Liu, B.; Zhong, L.; Song, Q.; Jiang, J.; Zhang, T.; Wei, X.; Jiang, H. Geochemical characteristics and zoning of soil in Pingxiang-Xinyu region, Jiangxi Province. *J. Univ. South China (Sci. Technol.)* **2022**, *36*, 20–26.
23. Zhao, H.; Zhai, X.; Li, S.; Wang, Y.; Xie, J.; Yan, C. The continuing decrease of sandy desert and sandy land in northern China in the latest 10 years. *Ecol. Indic.* **2023**, *154*, 110699. [CrossRef]
24. *DZ/T0011-2015*; Specifications for Geochemical Reconnaissance Survey (1:50,000) (DZ/T0011-2015). MLR (Ministry of Land and Resources of the People's Republic of China). Geological Publishing House: Beijing, China, 2015; pp. 1–35. (In Chinese)
25. *DZ/T0145-2017*; Code of Practice for Soil Geochemical Survey (DZ/T0145-2017). MLR (Ministry of Land and Resources of the People's Republic of China). Geological Publishing House: Beijing, China, 2015; pp. 1–38. (In Chinese)
26. *DZ/T0167-2006*; Specifications for Regional Geochemistry Exploration (DZ/T0167-2006). China Geological Survey, Ed.; Geological Publishing House: Beijing, China, 2006. (In Chinese)
27. Wang, D.; Wei, Z.; Qi, Z. The methods for estimation of soil elements background: A review. In Proceedings of the 12th National Congress of the Soil Society of China and the 9th Cross-Strait Academic Exchange Seminar on Soil and Fertilizer, Chengdu, China, 20 August 2012.
28. Zhang, J.; Huang, C.; Chen, K.; Gao, Z.; Huang, Q. The soil background values of heavy metals and ecological risk assessment based on the geo-statistical analysis. *Environ. Sci. Technol.* **2021**, *44*, 218–225.
29. Reimann, C.; Filzmoser, P. Normal and lognormal data distribution in geochemistry: Death of a myth. Consequences for the statistical treatment of geochemical and environmental data. *Environ. Geol.* **2000**, *39*, 1001–1014. [CrossRef]
30. Sinclair, A. A fundamental approach to threshold estimation in exploration geochemistry: Probability plots revisited. *J. Geochem. Explor.* **1991**, *41*, 1–22. [CrossRef]
31. Reimann, C.; Fabian, K.; Birke, M.; Filzmoser, P.; Demetriades, A.; Négrel, P.; Oorts, K.; Matschullat, J.; Caritat, D.; Albanese, S.; et al. GEMAS: Establishing geochemical background and threshold for 53 chemical elements in European agricultural soil. *Appl. Geochem.* **2018**, *88*, 302–318. [CrossRef]
32. Yang, F.; Kong, M.; Liu, H.; Yu, J.; Yang, S.; Hao, Z.; Zhang, D.; Cen, K. Discovery of Wolitu Pb-Zn deposit through geochemical prospecting under loess cover in Inner Mongolia, China. *Geosci. Front.* **2017**, *8*, 951–960. [CrossRef]
33. Wu, L.; Bo, J.; Niu, J. Statistical analysis on the distribution characteristics of topographical parameters in loess area. *Sci. Technol. Eng.* **2021**, *21*, 8797–8806.
34. Liang, X.; Yang, Y.; Luo, Q.; Yu, Z.; Lv, W.; Huang, P.; Liu, X. Application of ground gamma spectrometry in the exploration of uranium in Western Lujing Ore Field. *Uranium Geol.* **2023**, *39*, 446–459.
35. Cheng, Q.; Agterberg, F.P.; Ballantyne, S.B. The separation of geochemical anomalies from background by fractal methods. *J. Geochem. Explor.* **1994**, *51*, 109–130. [CrossRef]
36. Zadmehr, F.; Shahrokhi, S.V. Separation of geochemical anomalies by concentration-area and concentration-number methods in the Saqez 1:100,000 sheet, Kurdistan. *Iran. J. Earth Sci.* **2019**, *11*, 196–204.
37. Shafieyan, F.; Abdideh, M. Application of concentration-area fractal method in static modeling of hydrocarbon reservoirs. *J. Pet. Explor. Prod. Technol.* **2019**, *9*, 1197–1202. [CrossRef]
38. Han, D.; Gao, S.; Zheng, Y.; Chen, X.; Jiang, X.; Gu, Y.; Yan, C. A processing technique of step effect on area multifractal method. *Geophys. Geochem. Explor.* **2020**, *46*, 1420–1428.
39. Zou, L.; Peng, S.; Yang, Z.; Lai, J.; Zhang, P. Multifractal study of geochemical (anomaly) fields in the A'ercituoshan area, Qinghai. *Geol. China* **2004**, *31*, 436–441.
40. Khanna, T.; Kanakdande, P.; Bizimis, M.; Arora, K. Geochemical baselines in the Phanerozoic LIPs constrained from well-cores in the Deccan Volcanic Province, India. *Lithos* **2023**, *462*, 107403. [CrossRef]
41. Bispo, F.; de Menezes, M.; Fontana, A.; Sarkis, S.; Gonçalves, M.; de Carvalho, S.; Curi, N.; Guilherme, G. Rare earth elements (REEs): Geochemical patterns and contamination aspects in Brazilian baseline soils. *Environ. Pollut.* **2021**, *289*, 117972. [CrossRef]
42. Zhang, W.; Liu, Z.; Jia, L.; Li, T. Study on soil geochemical reference value in Shaoguan area of Guangdong Province. *Geol. Miner. Resour. South China* **2020**, *36*, 153–161.
43. Liu, K.; Hu, X.; Zhou, H.; Tong, L.; Widanage, W.; Marco, J. Feature analyses and modeling of lithium-ion battery manufacturing based on random forest classification. *IEEE/ASME Trans. Mechatron.* **2021**, *26*, 2944–2955. [CrossRef]

44. Montgomery, D.C.; Peck, E.A.; Vining, G.G. *Introduction to Linear Regression Analysis*; John Wiley & Sons: Hoboken, NJ, USA, 2021; pp. 12–500.
45. Cui, H.; Xu, S.; Zhang, L.; Welsch, R.E.; Horn, B.K.P. The key techniques and future vision of feature selection in machine learning. *J. Beijing Univ. Posts Telecommun.* **2018**, *41*, 1–12.
46. Hao, H.; Gu, Q.; Hu, X. Research advances and prospective in mineral intelligent identification based on machine learning. *Earth Sci.* **2021**, *46*, 3091–3106.
47. Zhao, W.; Liu, L.; Chen, J.; Ji, J. Geochemical characterization of major elements in desert sediments and implications for the Chinese loess source. *Sci. China Earth Sci.* **2019**, *62*, 1428–1440. [CrossRef]
48. Fahmy, H.; Pastore, F.; Bagherzadeh, M.; Briand, L. Supporting deep neural network safety analysis and retraining through heatmap-based unsupervised learning. *IEEE Trans. Reliab.* **2021**, *70*, 1641–1657. [CrossRef]
49. Zhao, M.; Yan, Q.; Liu, Z.; Wang, W.; Li, G.; Wu, Z. Analysis of temporal and spatial evolution and influencing factors of soil erosion in Ordos City. *Arid. Zone Res.* **2022**, *39*, 1819–1831.
50. Rudnick, R.L.; Gao, S. Composition of the continental crust. *Treatise Geochem.* **2013**, *3*, 659. [CrossRef]
51. He, Q.; Chen, J.; Gan, L.; Gao, M.; Zan, M.; Xiao, Y. Insight into leaching of rare earth and aluminum from ion adsorption type rare earth ore: Adsorption and desorption. *J. Rare Earths* **2023**, *41*, 1398–1407. [CrossRef]
52. Lafreniere, M.C.; Lapierre, J.F.; Ponton, D.E.; Guillemette, F.; Amyot, M. Rare earth elements (REEs) behavior in a large river across a geological and anthropogenic gradient. *Geochim. Cosmochim. Acta* **2023**, *353*, 129–141. [CrossRef]
53. Liu, C.; Deng, J.; Liu, J.; Shi, Y. Characteristics of volcanic rocks from Late Permian to Early Triassic in Ailaoshan tectono-magmatic belt and implications for tectonic settings. *Acta Petrol. Sin.* **2011**, *27*, 3590–3602.
54. An, F.; Zhu, Y. Studies on geology and geochemistry of alteration-type ore in Hatu gold deposit (western Junggar), Xinjiang, NW China. *Min. Depos.* **2007**, *26*, 621–633.
55. Wang, Y.; Gong, P.; Gong, M.; Ma, Z. Geochemical subdivisions in metallogenic belt with the 1:200,000 stream sediments and its geological significance: A case study in Gangdese Copper-Polymetallic Metallogenic Belt. *Geoscience* **2010**, *24*, 801–806.
56. Xu, C.; Fu, L.; Lin, T.; Li, W.; Ma, S. Machine learning in petrophysics: Advantages and limitations. *Artif. Intell. Geosci.* **2022**, *3*, 157–161. [CrossRef]
57. Han, W.; Zhang, X.; Wang, Y.; Wang, L.; Huang, X.; Li, J.; Wang, S.; Chen, W.; Li, X.; Feng, R.; et al. A survey of machine learning and deep learning in remote sensing of geological environment: Challenges, advances, and opportunities. *ISPRS J. Photogramm. Remote Sens.* **2023**, *202*, 87–113. [CrossRef]
58. Han, Y.; An, Z.; Qu, W. Research status of magnetotelluric time domain data processing based on machine learning. *Prog. Geophys.* **2021**, *36*, 1975–1987.
59. Shi, C.; Wei, L.; Zhang, J.; Yang, L. Reservoir prediction method based on machine learning. *Pet. Geol. Recover. Eff.* **2022**, *29*, 90–97.
60. Li, G.J.; Chen, J.; Chen, Y.; Yang, J.D.; Ji, J.F.; Liu, L.W. Dolomite as a tracer for the source regions of Asian dust. *J. Geophys. Res.* **2007**, *112*, D17201. [CrossRef]
61. Wang, P.; Dong, Q.; Gong, X.; Cheng, H.; Song, C.; Guo, J. Geochemical characteristics of soil elements in the Jingbian area of Loess Plateau-Mu Us Desert transitional zone, China during Holocene and their environmental implications. *J. Earth Sci. Environ.* **2020**, *42*, 678–687.
62. Zhang, H.; Li, J.; Ma, Y.; Cao, J.; Wang, N. A study on elemental geochemical characters of the Wuwei loess section in the south vicinity of Tengger Desert. *Acta Sedimentol. Sin.* **1997**, *15*, 152–158.
63. Yang, P.; Chi, Y.; Xie, Y.; Kuang, C.; Sun, L.; Wu, P.; Wei, Z. Characteristics of element and Sr-Nd isotope composition of the Songnen sandy land and their indications of regional dust material sources. *Chin. J. Geol.* **2024**, *59*, 549–561.

applied sciences

MDPI

Article

A Deep-Penetrating Geochemical Prospecting Experiment of Mahuagou Gold Deposit in the Core of the Huangling Anticline, Western Hubei, China

Weihang Zhou [1], Li Lei [2], Yin Gong [2], Demin Liu [1], Shuyun Xie [1,*], Zhijun Chen [3], Qinglin Xia [3], Mengqi Wang [1], Salah Fadlallah Awadelseid [4] and Oraphan Yaisamut [1,5]

[1] State Key Laboratory of Geological Processes and Mineral Resources (GPMR), Faculty of Earth Sciences, China University of Geosciences, Wuhan 430074, China; zwh15671032170@126.com (W.Z.); 5guc@163.com (D.L.); wangmq@cug.edu.cn (M.W.)
[2] Seventh Geological Brigade, Hubei Geological Bureau, Yichang 443100, China; leili854@163.com (L.L.); gongyincug@163.com (Y.G.)
[3] State Key Laboratory of Geological Processes and Mineral Resources (GPMR), Faculty of Earth Resources, China University of Geosciences, Wuhan 430074, China; zhijun.chen@cug.edu.cn (Z.C.); qlxia@cug.edu.cn (Q.X.)
[4] Department of Mineral Resources, College of Petroleum Geology and Minerals, University of Bahri, Khartoum 999129, Sudan; 95.salah@googlemail.com
[5] Department of Mineral Resources, Ministry of Natural Resources and Environment, 75/10 Rama VI Road, Ratchathewi, Bangkok 10400, Thailand
* Correspondence: tinaxie@cug.edu.cn

Abstract: The Mahuagou gold deposit is among the most important gold deposits in the core of the Huangling Anticline. However, the geochemical exploration on the surface of the mining area presents challenges due to the thin overburden. This paper focuses on the overburden soil of the Fengxiangshugou (FXS)-Mahuanggou (MHG) section as the research object. It utilizes chemical form analysis of gold, soil halogen survey, and heat-released mercury survey to determine the key deep-penetrating geochemical methods for the mining area. The results indicated that Si and Al components of samples exhibit minimal variation, suggesting that drift loads did not influence the overburden soil. Based on the systematic clustering, As, Sb, Mo, Bi, W, and Hg emerge as ore-body or ore-belt front elements of hydrothermal gold deposits. In the study area, the predominant chemical form of gold in soil is the strong organic bond. Compared to the total amount, strong organic bound gold and heat-released mercury show higher anomaly contrasts, making them crucial indicators of faults, intrusions, and hidden ore bodies. Consequently, chemical form analysis of gold and heat-released mercury surveys can enhance the anomaly contrast, proving beneficial for geochemical prospecting for weak anomalies in this area.

Keywords: overburden prospecting; deep-penetrating geochemical indicator; chemical form analysis of gold; heat-released mercury survey; Huangling Anticline

Citation: Zhou, W.; Lei, L.; Gong, Y.; Liu, D.; Xie, S.; Chen, Z.; Xia, Q.; Wang, M.; Awadelseid, S.F.; Yaisamut, O. A Deep-Penetrating Geochemical Prospecting Experiment of Mahuagou Gold Deposit in the Core of the Huangling Anticline, Western Hubei, China. *Appl. Sci.* **2023**, *13*, 12279. https://doi.org/10.3390/app132212279

Academic Editor: Oleg S. Pokrovsky

Received: 14 October 2023
Revised: 31 October 2023
Accepted: 6 November 2023
Published: 13 November 2023

1. Introduction

Mineral resource exploration is a vital aspect of contemporary society, driving economic growth and technological progress [1,2]. Gold has been highly regarded among various valuable minerals due to its rarity, enduring value, and versatile applications for centuries. However, the depletion of easily accessible reserves has made exploiting new gold deposits increasingly challenging. To address this challenge, scientists and geologists are pioneering innovative techniques, such as geochemical prospecting [3], and focusing on mineralization trials to understand subsurface permeability.

Geochemical exploration research focuses on analyzing the chemical composition of rocks, soils [4], stream sediments [5,6], and water systems [7] to target potential mineral deposits [8]. Key research methods include primary halos, secondary halos, stream

sediments, enzyme leaching [9,10], MMI (Mobile Metal Ions) [11–13], MOMEO (Leaching of Mobile Forms of Metals in Overburden) [14,15], NAMEG (Collection of Nanoscale Metals in Earthgas) [14,16], electrogeochemistry [17,18], biogeochemistry [19], Feldspar IRSL (Infrared Stimulated Luminescence), and Quartz OSL (Optically Stimulated Luminescence) [20]. In addition, the Fine-Grained Soil Prospecting Method has displayed its effectiveness in identifying hidden deposits in recent years [21–24]. These techniques enable scientists to understand the forms and enrichment patterns of ore-bearing information on the Earth's surface, identify geochemical anomaly zones, and locate concealed mineral bodies. Geochemical surveys are highly effective in delineating zones with potential gold mineralization in gold exploration. By examining the distribution of various elements and their concentration patterns, scientists can infer the geological processes responsible for gold anomalies and predict potential sources.

One of the primary challenges in exploring gold deposits is identifying and characterizing permeable conduits that govern the migration and accumulation of auriferous fluids or constituents within the surrounding lithospheric matrix [25]. These conduits, often associated with specific geotectonic features, such as faults, fractures, shear zones, and microporous domains, are intricately interconnected through various mechanistic associations [26,27]. Gold mineralization experiments provide researchers with a nuanced understanding of rock permeability and the multifaceted factors that drive the mobilization of auriferous fluids.

Gold mineralization trials involve a meticulous process, starting with carefully sampling and curating rock specimens from promising locations and proceeding with rigorous laboratory analyses. Electron microscopy [28], geochemical cartography, and stable isotopic assessment provide a comprehensive framework for elucidating the intricate interplay of mineralogical composition, chemical attributes, and alteration dynamics within gold mineralization [29]. By critically evaluating the attributes of gold-bearing minerals and their interaction with the host rock matrixes, scientific inquiry gains the capacity to unravel the underlying mechanisms driving gold enrichment phenomena, thereby facilitating the identification and delineation of potential exploration targets.

The insights derived from these experimental endeavors contribute to the discovery of novel gold reservoirs and provide invaluable data for the responsible extraction of existing reserves. A comprehensive understanding of the subsurface permeability is paramount in resource stewardship, guiding exploration initiatives while mitigating potential environmental impacts.

This paper involved the collection of samples and proceeded prospecting experiments in the Mahuagou gold deposit, Yiling District, Yichang City, and Hubei Province (Figure 1). This work analyzes major elements, trace elements, chemical forms of gold, and heat-released mercury. These deep-penetrating geochemical indicators will be identified to effectively prospect the Mahuagou gold deposit in Hubei Province, China. The research aims to unlock the potential of the Mahuagou gold deposit and contribute to the sustainable development of the mining industry.

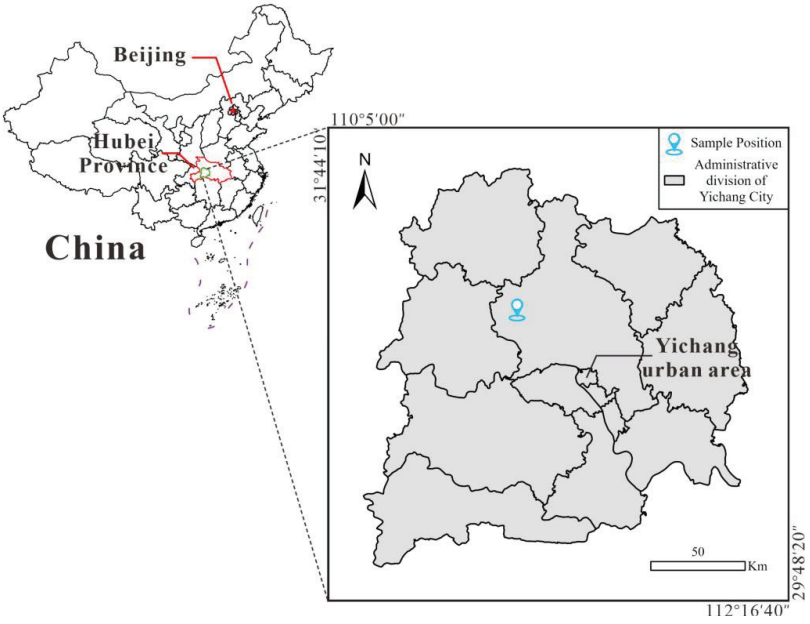

Figure 1. Geographical location of the study area (data sources: the new (2022) version of the national provinces, cities, districts, and counties administrative boundaries of the nine-dash line vector map data).

2. Geological Setting

2.1. Regional Geological Setting

The Huangling Anticline is located at the intersection of the northern margin of the Yangtze Plate and the multi-directional tectonic lines within the plate [30]. The latitude and longitude of the Huangling Anticline are 30°45′ N to 31°30′ N and 110°45′ E to 111°30′ E, respectively. Since the discovery of primary quartz vein-type gold deposits in 1966, nearly three hundred gold-bearing quartz veins have been identified in this area, accompanied by over seventy occurrences of gold mineralization. Notable deposits include Mahuagou, Baizhuping, Shuiyuesi, and Bancanghe [31]. The region predominantly showcases the Middle to Lower Ordovician metamorphic rock series. In the northern part, these rocks are classified as the "Shuiyuesi Group".

Meanwhile, in the southwestern part, they belong to the "Kongling Group", as per the West Hubei Geological Brigade reports from 1987 and 1991. Both rock units form the foundational rocks of the Huangling Anticline, and the Huangling Anticline has been intruded by subsequent granitic formations [32]. They have later been collectively termed the Kongling Group, also known as the Kongling Complex or Huangling Complex, by the Hubei Provincial Bureau of Geology and Mineral Resources. The ancient exposed basement metamorphic rocks in this region have yielded an amphibolite Sm–Nd isochron dating age of 3290 ± 170 Ma from the Kongling Complex [33]. Hence, this region is crucial for gold mineralization in Hubei Province and offers valuable insights into the ancient basement of the Yangtze Plate [34,35].

As depicted in Figure 2a, the Huangling Anticline is a nearly north–south trending dome-shaped short-axis fold, spanning roughly 73 km in the north–south direction and about 36 km in the east–west orientation. The core of the Anticline is mainly composed of the Huangling Complex and Huangling Granite. In contrast, its limbs are predominantly made up of marine carbonate and clastic rocks from the South China Series to the Triassic, all dipping away from the core [36].

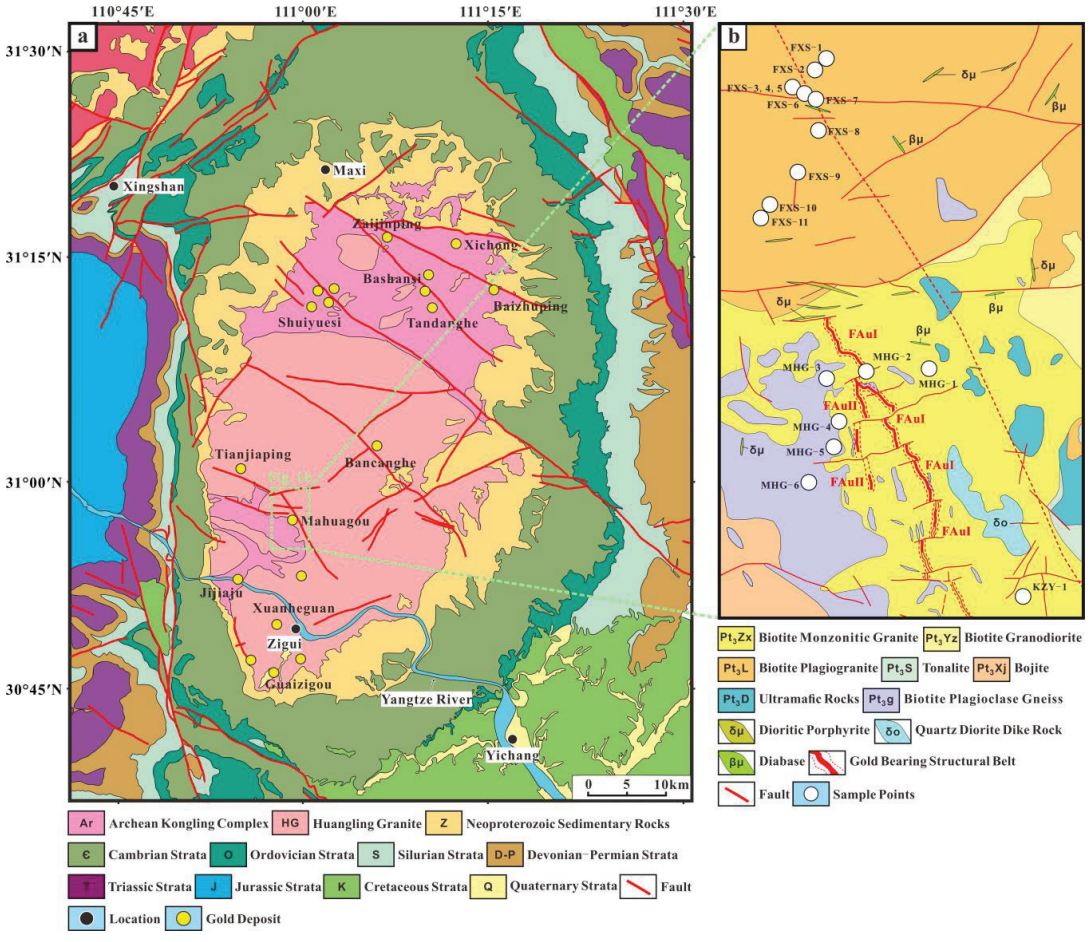

Figure 2. Geological map of the Huangling Anticline and sample point locations: (**a**) geological map of the Huangling Anticline and some gold deposit locations in the Huangling Anticline (the map was modified according to Cui et al., 2022 [35], Wang et al., 2023 [37], Institute of Geology, Chinese Academy of Geological Sciences, and Seventh Geological Brigade, Hubei Geological Bureau); (**b**) geological map of Mahuagou gold deposit and sample point locations.

The Huangling Granite primarily characterizes the magmatic rocks exposed in the Huangling Anticline area. This granite is one of the few intracontinental Neoproterozoic granitic bodies within the Yangtze Plate [38]. The Huangling Granite mainly consists of granite porphyry, trondhjemite, biotite monzogranite, tonalite, and quartz diorite. In the study "Sequence, Evolution, and Gold-bearing Properties of Precambrian Metamorphic Complexes in the Huangling Anticline", the West Hubei Geological Brigade (1996) categorized the acidic rocks in the core of the Huangling Anticline into four super units: Duanfangxi, Sandouping, Huanglingmiao, and Dalaoling, as well as the Xiaofeng composite pluton, with ages ranging from early Neoproterozoic to the middle Neoproterozoic.

2.2. Geological Setting of Mining Area

The Mahuagou gold deposit stands out as one of the most prominent gold deposits in the core area of the Huangling Anticline in Yichang, Hubei. This deposit is a medium- to low-temperature quartz vein-alteration/structural type gold deposit. It is governed by

northwest-trending brittle–ductile shear zones and stands out for small scale, high grade, and ease of beneficiation [39]. Since exploration commenced in the 1990s, two major north–northwest-trending gold-bearing structural zones have been identified and labeled as FAuI and FAuII (as illustrated in Figure 2b) [40]. At a drilling elevation of around 800 m, the No. I and No. II ore-bodies within the FAuI zone are notable for their stability, high-grade content, significant thickness, and rapid thinning out [41]. As a result, the deeper gold mineral resources within this mining region show considerable exploration potential; this makes uncovering concealed ore bodies at greater depths a pivotal challenge for future exploration breakthroughs in the Mahuagou mining district.

The geological characteristics of the Mahuagou mining area are primarily defined by the contact zone between the biotite plagioclase gneiss in the Gucunping Formation (Pt_2g) and the biotite monzonitic granite in Zongxifang Unit (γPt_3Zx). The Gucunping Formation (Pt_2g) is divided into two segments: Gucunping Formation Segment 1 (Pt_2g^1) and Gucunping Formation Segment 2 (Pt_2g^2). Both segments have similar lithology, characterized by alternating layers of biotite plagioclase gneiss and plagioclase amphibolite. Within the biotite monzonitic granite (γPt_3Zx), there are numerous lens-shaped metamorphic enclaves and bits of early plagioclase granite enclaves. Plagioclase granite enclaves often exhibit mylonitization, and the biotite monzonitic granite locally displays foliation, indicating that the rock body was emplaced under the influence of strong shearing stresses. Within the mining area, various types of veins with diverse morphologies and orientations are exposed, including granite pegmatite veins, diorite porphyrite veins ($\delta\mu$), diabase veins ($\beta\mu$), and other mafic veins. These veins have been interpreted as the filler of early faults and fracture structures, with prevalent orientations in the nearly east–west and northwest–west orientations. The Mahuagou brittle–ductile shear zone is a significant mineralized structural zone formed during the early Neoproterozoic, situated at the contact zone between biotite monzonitic granite (γPt_3Zx) and biotite plagioclase gneiss (Pt_2g). During the intrusion of the granite (γPt_3Zx), lateral compression and north–northwest orientation right lateral shearing persisted, giving rise to early compressional mineralized structures, with later tectonic activities displaying evident extensional and torsional features. Gold mineralization primarily occurs within the felsic cataclastic rock in the mineralized structural zone, with the occurrence of quartz micro veins and sulfide micro vein infillings.

3. Samples and Methods

3.1. Collection and Pretreatment of Soil and Rock Samples

Soil samples for this research were collected from the Fengxiangshugou–Mahuanggou section of the Mahuagou mining area (as shown in Figure 2b) located in Yiling District, Yichang City, Hubei Province (as shown in Figure 1). In the Fengxiangshu section, following the trend of the IP (Intensification Polarization) section, 11 bags (approximately 700 g/bag) of soil, fault gouge, and fault cataclastic rock samples were collected from the northeast to southwest. In the Mahuagou section, along exploration line No. 7 of the mining area, 6 bags (approximately 700 g/bag) of soil samples were collected from the northeast to southwest, crossing the ore body along the X206 village road. Additionally, 1 bag (approximately 700 g) of loose soil sample was taken from beside the Kaziya trench.

After returning the collected samples to the laboratory, the sealed bags were opened, and the moisture inside the bags was allowed to air dry for a day using ambient airflow naturally. After the preliminary drying, each sample was individually and evenly spread out on A4 paper. These samples were placed on a shaded, well-ventilated tabletop away from direct sunlight and areas with artificial airflow sources, such as air conditioning and frequent human activity. Subsequently, for a week, daily inspections, turning of samples, removal of small stones and plant roots, and gentle tapping of consolidated soil were conducted using small sticks; this ensured that the surface and interior of the samples dried thoroughly, preventing consolidation at the bottom. Once the drying process was completed, the samples were promptly returned to sealed bags and stored properly.

In order to accommodate the requirements of specific analytical tests, we subjected a portion of the total sample to grinding and sieving. Prior to grinding, we manually removed plant residues, stones, bricks, and non-soil components. The grinding process utilized an agate mortar and pestle while sieving employed a 200 mesh (75 μm) nylon sieve. Soil powder obtained after sieving was collected on A4 paper and labeled with corresponding numbers before being placed in paper bags, which were then sealed in plastic bags for preservation. Following the completion of grinding and sieving for each sample, all tools were rinsed with deionized water and then dried in an oven. Tabletops were cleaned, and A4 paper was replaced as needed. Throughout these procedures, stringent measures were taken to ensure the independence of each sample, preventing cross-contamination and mixing of sample components, thus ensuring the accuracy and effectiveness of subsequent experiments.

3.2. Analytical Methods

3.2.1. Mineral Composition Analysis by X-ray Diffraction (XRD)

According to the standard method, "Analysis Method for Clay Minerals and Ordinary Non-clay Minerals in Sedimentary Rocks by the X-ray Diffraction" (SY/T 5163-2018) [42], a 0.4 g sample was utilized. The sample powder was carefully placed into the groove of the sample slide, ensuring that the measured surface of the sample remained rough and maintained a flat and even alignment with the surface of the sample slide to avoid preferential crystal powder orientation. The TD-3500 diffractometer manufactured by Dandong Tongda Technology Co., LTD, Dandong, Liaoning, China, was used for detection under the following conditions: 30 kV acceleration voltage, 30 mA beam current, Cu Kα radiation, and Ni filter. The parameters for detection included a scanning range from 3.00° to 45.00° 2θ, a wide angle of 0.02°, a sampling time of 0.6 s, a scan speed of 0.033 s, and a total time (h:m:s) of 0:21:00.

The sample was detected to obtain X-ray diffraction spectra. Subsequently, the X-ray diffraction spectra were processed using the TD-3500's data processing software (MDI JADE 6.5, ICDD, Livermore, CA, USA). The software utilized the Inorganic Crystal Structure Database (ICSD) based on the sample's characteristics.

3.2.2. Soil Major Elements

According to the standard method, "Determination of Twenty-two Elements in Geological Samples by Inductively Coupled Plasma Optical Emission Spectrometry" (WSBB/004-2019) [43], an inductively coupled plasma optical emission spectrometer was used to quantify Al, Fe, Mg, Na, and S in the samples. A sample mass of 0.2500 g was weighed into a PTFE crucible and moistened with a small amount of water, followed by the addition of 6 mL of nitric acid, 10 mL of hydrofluoric acid, and 2 mL of perchloric acid. The mixture was decomposed on a 200 °C hotplate and was then evaporated. In case of incomplete decomposition, nitric acid and hydrofluoric acid were replenished before evaporation. The slightly cooled mixture was treated with 8 mL of aqua regia, heated on the hotplate until the solution volume was reduced to 3–5 mL, and the crucible walls were rinsed with approximately 10 mL of deionized water. Mild heating (5–10 min) was applied until the solution was clarified. The cooled solution was then transferred to a polyethylene tube, diluted with water, brought to a final volume of 25 mL, and thoroughly mixed. After 24 h of settling, the elemental content in the samples was determined using an ICP 7400-type plasma emission spectrometer produced by Thermo Fisher Scientific, Waltham, MA, USA. The calibration solution series medium is a 10% hydrochloric acid solution. A multi-point calibration curve is constructed using multiple calibration solutions, and the calibration curve is automatically generated by computer software. To ensure the quality of sample data, measurements of standard substances GSR-1, GSS 40, GSS 41, and GSD17a were taken during the experimental process and compared to their standard values, with errors of less than 5%. All samples were measured twice for repeatability. The Limit of Detection (LOD)

values were as follows: 0.05% for Al and Mg, 0.1% for Fe and Na, and 20 μg/g for S. It is worth noting that the standard substance/repeat sample qualification rate was 100%.

According to the standard method, "Exploration Geochemical Sample Analysis Method X-Ray Fluorescence Spectrometry for Determining Thirty-four Major and Trace Elements" (WSBB/005-2004) [44], X-ray fluorescence spectrometry was employed to quantify Si, Ca, K, Mn, P, and Ti in the samples. A dried sample mass of 4.00 g was transferred to a sample container, evenly spread within it, and pressed using a pellet press to create a homogenous sample pellet. The prepared samples were directly analyzed for each element using a ZETIUM X-ray fluorescence spectrometer produced by Malvern Panalytical, Malvern, WR14 1XZ, UK. The matrix effects between elements were corrected using the empirical coefficient method and the internal standard method for scatter correction. The LOD were as follows: 0.1% for Si, 0.05% for Ca and K, and 10 μg/g for Mn, P, and Ti. The qualification rate for standard substances/repeat samples was 100%.

3.2.3. Soil Trace Elements

According to the standard method "Exploration Geochemical Sample Analysis Method for Determining Thirty-two Trace Elements by Inductively Coupled Plasma Mass Spectrometry" (WSBB/001-2021) [45], an inductively coupled plasma mass spectrometer was utilized to quantify Ag, Bi, Cd, Co, Cu, Mo, Ni, Pb, Sb, and W in the samples. The experimental procedure was consistent with that for major soil elements. Specifically, the iCAP Qc type inductively coupled plasma mass spectrometer produced by Thermo Fisher Scientific, Waltham, MA, USA, was used to determine the elemental content in the samples. The LOD were as follows: 20 ng/g for Ag, 0.05 μg/g for Bi and Sb, 1 μg/g for Co and Cu, 30 ng/g for Cd, 0.3 μg/g for Mo, 0.4 μg/g for W, and 2 μg/g for Ni and Pb. The qualification rate for standard substances/repeat samples was 100%.

3.2.4. Soil Halogen Elements

In addition to the above analysis, the elements Br and Cl were quantified in the samples using Axios PW4400/40 X-ray fluorescence spectrometry produced by PANalytical B.V., Almelo, The Netherlands, according to the standard WSBB/005-2004, with a 1 μg/g and 20 μg/g LOD, respectively. The ion-selective electrode method determined Fluoride (F), according to the standard GB/T 14506.12-2010 [46], with 100 μg/g LOD. Iodine (I) was measured using the standard WSBB/013-2020 [47] spectrophotometric method, with a 0.5 μg/g LOD. The qualification rate for standard substances/repeat samples of halogen elements was also 100%.

3.2.5. Soil Heat-Released Mercury

According to the standard "Mercury Vapor Measurement Specification" (DZ 0003-91) [48], the XG-7Z mercury measuring instrument produced by the Institute of Geophysical and Geochemical Exploration, Chinese Academy of Geological Sciences, Langfang, Hebei Province, China, was used in this experiment. The weight method was employed to determine heat-released mercury in soils at a heat-released temperature of 200 °C (test conditions as shown in Table 1).

Table 1. Testing conditions of soil heat-released mercury instrument.

Test Conditions	Instrument Parameter
Heat-released temperature/°C	200
Heat-released time/min	2
Furnace temperature/°C	800
Carrier gas flow/(L/min)	0.6–0.8

Approximately 0.1 g of the sample was placed into a quartz boat and introduced into the central part of a thermal decomposition furnace. Upon activating the air pump, the heat-release of mercury commenced automatically. The sample was exposed to the

mercury vapor produced at this temperature, and its absorption was measured within the instrument's absorption chamber, resulting in an absorbance value (AT). The sequence of temperature for determining heat-released mercury ranged from high temperature (800 °C) to low temperature (150 °C). After the determination of heat-released mercury at one temperature, an appropriate amount of the sample was reweighed for the subsequent temperature determination, and this process continued to cover all designated temperature levels for heat-released mercury measurements.

3.2.6. Chemical Form Analysis of Gold in Soil

The determination of chemical forms of gold in soil samples refers to the analytical specifications of "Ecological Geochemistry Assessment Sample Analysis Technical Requirements (Trial)" (DD2005-03) [49]. The Tessier (1979) modified sequential extraction method [50] (seven-step procedure) is employed for the chemical forms of gold in the soil. This technique divides elements into seven forms: extraction with water for the water-soluble form; 1.0 mol/L magnesium chloride extraction for the ion-exchangeable form; 1.0 mol/L sodium acetate solution for the carbonate-bound form; 0.1 mol/L sodium pyrophosphate extraction for the weakly organic (humic acid) bound form; 0.25 mol/L hydroxylamine hydrochloride—0.25 mol/L hydrochloric acid mixed solution extraction for the iron-manganese bound form; 30% hydrogen peroxide extraction for the strongly organic bound form; and hydrofluoric acid extraction for the residual form. After quantitatively collecting samples and performing extractions with the solvents above, the gold content in each form is analyzed using the ICP-MS produced by Thermo Fisher Scientific, Waltham, MA, USA, for a full spectrum direct reading analysis.

4. Geochemical Characteristics of Overburden Soils

4.1. Overburden Soil Mineral Composition

Utilizing X-ray Diffraction (XRD) analysis, a semi-quantitative assessment of the mineral composition of representative soil samples from the Mahuagou mining area was conducted, as illustrated in Figure 3. The X-ray diffraction peak intensities are measured using integrated intensities after background subtraction. Relevant data is obtained from the X-ray diffraction spectrum of the sample and then compared to standard X-ray diffraction data for minerals to determine the mineral species. Common mineral X-ray diffraction data can be found in SY/T 5163-2018-Appendix E. Formula (1) is used to calculate the total content of clay minerals and various non-clay minerals:

$$X_i = [\frac{I_i}{K_i} / (\sum \frac{I_i}{K_i})] \times 100\%, \quad (1)$$

X_i represents the percentage content of mineral i, expressed as a percentage; I_i represents the integrated peak intensity of the selected diffraction peak of mineral i; and K_i represents the reference intensity of mineral i.

Broadly, soil samples from the FXS and MHG profiles exhibit two distinct mineral assemblages. In the FXS profile, the mineral composition of the soil is primarily comprised of clay minerals, such as illite, chlorite, and kaolinite, as well as primary minerals like quartz and sodium feldspar (e.g., FXS-5 and FXS-6). Illite is an intermediate transitional mineral between montmorillonite and mica, often formed through the alteration of potassium feldspar and mica or the replacement of montmorillonite [51–53]. Kaolinite predominantly forms during the weathering of silicate minerals like feldspar and common pyroxenes [54]. Chlorite is a secondary mineral that develops during the initial stages of soil formation, arising from the alteration of ferromagnesian minerals (e.g., biotite, hornblende, pyroxenes) in granite or other igneous rocks. Field observations indicate that the rock types exposed in the FXS profile consist mainly of moyite, monzonitic granite, granitic, and dioritic rocks, indicative of intermediate acidic intrusive rocks. Consequently, the formation of illite and kaolinite in the soil is connected to the weathering of minerals like mica and alkali feldspar

in intermediate acidic parent rocks. At the same time, the development of chlorite often results from the weathering of dark-colored minerals in the parent rock.

FXS-3 and FXS-4 exhibit a characteristic mineral composition of fault gouge. The presence of montmorillonite and a small amount of calcite in the soil leads to a notably higher Ca element content compared to other soils. The formation of this mineral assemblage is attributed to the grinding of near-surface rocks by faults under low-temperature conditions, coupled with late-stage low-temperature hydrothermal alteration and metamorphism [55,56], resulting in the mixture of unconsolidated, powdery clay minerals (illite, chlorite, and montmorillonite) with fine particles from adjacent rocks (quartz and calcite) [57].

In the MHG profile, the clay mineral composition in the soil is relatively simple, primarily consisting of montmorillonite, with minimal presence of minerals like illite and chlorite. The content of biotite and minor plagioclase is significantly higher in the soil compared to the FXS profile. Diabase dikes ($\beta\mu$) and other mafic dikes are widely exposed in MHG, which is the main factor affecting the local soil composition. Consequently, the formation of montmorillonite in the soil of MHG profile is closely related to the weathering of minerals from basic rocks in an alkaline environment [58].

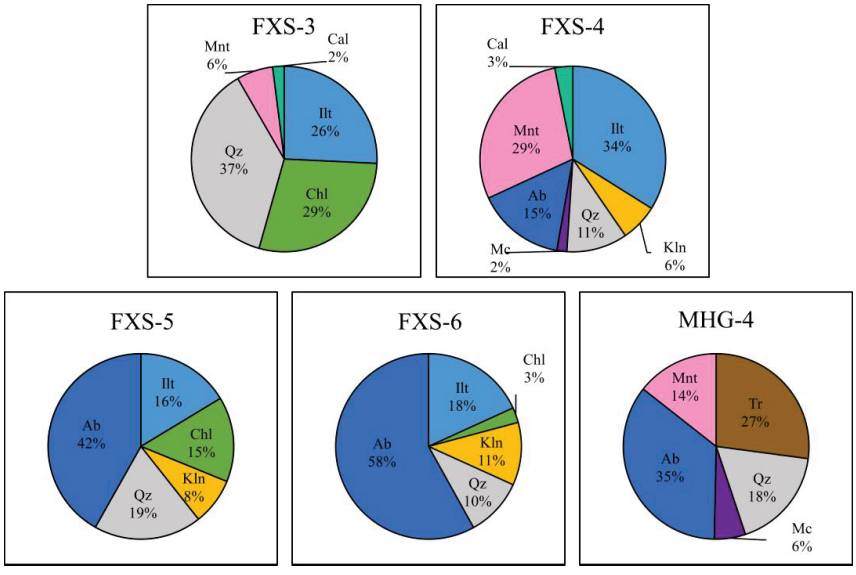

Figure 3. Mineral composition of representative soil samples from the Mahuagou mining area (Ab: albite; Cal: calcite; Chl: chlorite; Ilt: illite; Kln: kaolinite; Mc: microcline; Mnt: montmorillonite; Qz: quartz; Tr: tremolite [59]).

The soil mineral composition adjacent to the KZY trench resembles that of the FXS profile, with illite being the primary clay mineral and a relatively lower content of quartz and sodium feldspar.

Considering the mineral composition of soils in the Mahuagou mining area, it can be inferred that the soils at FXS, MHG, and KZY locations are all products of the in situ weathering of parent rock. This process facilitates the capture and preservation of in situ ore-forming information. However, due to variations in weathering and erosion conditions among different areas, the content of various soil components and their ability to preserve materials may still differ.

4.2. Overburden Soil Major Elements

The results of soil major elements testing in the Mahuagou mining area, along with descriptive statistics, are presented in Tables 2 and 3. Among the 18 samples, silicon (Si) exhibited a maximum value of 69.8%, a minimum value of 57.7%, and a mean value of 64.8%. Aluminum (Al) showed a maximum value of 19.2%, a minimum value of 12.9%, and a mean value of 15.7%. Both elements demonstrated a coefficient of variation (C_V) below 15%, indicating relatively stable content within the samples. On the other hand, calcium (Ca) and magnesium (Mg) elements displayed variation coefficients exceeding 50%, implying significant content disparities within individual samples. Notably, samples FXS-3 and FXS-4 exhibited notably distinct calcium content from other samples, possibly attributed to mineralogical associations with abundant calcium and magnesium elements in the soil.

Table 2. Test results of soil main elements in the Mahuagou mining area.

Sample Number	Element (%)							
	SiO_2	Al_2O_3	MgO	CaO	Na_2O	K_2O	MnO	TiO_2
FXS-1	57.90	18.40	2.23	1.51	1.95	2.13	0.13	0.60
FXS-2	66.60	16.30	0.45	1.60	3.42	1.94	0.05	0.24
FXS-3	59.20	16.30	1.70	4.60	0.27	2.94	0.04	0.51
FXS-4	64.20	17.10	0.67	3.74	3.13	2.90	0.03	0.28
FXS-5	65.60	15.90	0.88	0.38	3.21	2.08	0.06	0.41
FXS-6	67.20	14.70	0.29	0.11	2.49	2.59	0.03	0.26
FXS-7	65.30	15.90	0.55	1.17	4.46	1.42	0.06	0.30
FXS-8	57.70	19.20	1.03	0.93	1.81	1.81	0.07	0.49
FXS-9	64.90	15.70	0.54	0.70	2.10	1.93	0.04	0.32
FXS-10	67.50	14.30	0.52	1.14	2.50	1.94	0.04	0.33
FXS-11	60.10	16.70	1.65	1.65	2.29	1.93	0.10	0.79
KZY-1	69.80	14.60	0.77	0.14	1.42	3.05	0.06	0.27
MHG-1	66.20	15.00	2.14	1.64	2.85	2.54	0.09	0.40
MHG-2	67.80	14.70	1.79	2.14	4.71	1.06	0.04	0.41
MHG-3	65.10	14.70	1.31	0.93	2.67	2.78	0.07	0.53
MHG-4	65.90	15.10	1.66	2.14	3.50	2.42	0.07	0.50
MHG-5	65.90	15.10	1.35	0.59	1.93	2.29	0.04	0.57
MHG-6	69.70	12.90	0.65	0.91	3.72	2.90	0.05	0.35

Table 3. Descriptive statistical table of main elements in the Mahuagou mining area.

Element	Minimum	Maximum	Average	Standard Deviation	Coefficient of Variation
	%	%	μ/%	σ	C_V/%
SiO_2	57.70	69.8	64.81	3.69	5.69
Al_2O_3	12.90	19.2	15.70	1.51	9.59
MgO	0.29	2.23	1.12	0.62	55.11
CaO	0.11	4.60	1.45	1.17	80.79
Na_2O	0.27	4.71	2.69	1.08	40.22
K_2O	1.06	3.05	2.26	0.55	24.51
MnO	0.03	0.13	0.06	0.03	44.12
TiO_2	0.24	0.79	0.42	0.15	34.72

$C_V = (\sigma/\mu) \times 100\%$.

CIA (Chemical Index of Alteration) [60] and CIW (Chemical Index of Weathering) are two commonly used weathering indices. The CIA is based on the research of weathering of magmatic rocks with relatively uniform chemical composition, and its application premise is that the chemical composition of weathered parent rocks is relatively uniform [61,62]. Obviously, in this study, the parent rocks of the soil samples are not the same, and K_2O may

be active during metamorphism; biotite alteration can be affected by K_2O concentrations, which can be rich in illite and smectite clay minerals. Therefore, it is appropriate to use the CIW to evaluate its weathering. The calculation Formula (2) for CIW is provided below:

$$CIW = 100\% \times Al_2O_3/(Al_2O_3 + CaO + Na_2O) \quad (2)$$

The calculated results are depicted in Figure 4. In general, CIW values between 50% and 60% indicate that the samples are fresh and have not undergone significant chemical weathering. If the CIW value of a sample exceeds 70%, it signifies intense chemical weathering [63]. The samples from the Mahuagou mining area consistently exhibit CIW values above 70%, indicating a pronounced history of substantial weathering processes.

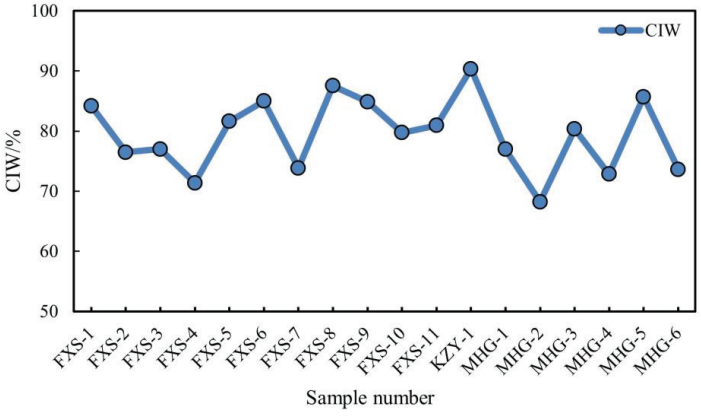

Figure 4. CIW index of soil samples in the Mahuagou mining area.

To better illustrate the compositional characteristics of major elements, the samples were categorized based on their sampling point characteristics into five sections: fault material, above the faulted structures, around the MHG ore-body, above the trench and borehole, and peripheral areas. Utilizing the (Al/Si) × 100% ratio in conjunction with Ca (%) for plotting (refer to Figure 5), it was observed that the majority of samples exhibit a relatively stable ratio of Al to Si, forming a linear distribution parallel to the *X*-axis. However, some individual samples display elevated Al/Si ratios. Fault materials (fault mud and fault cataclastic rock) exhibit higher Ca content.

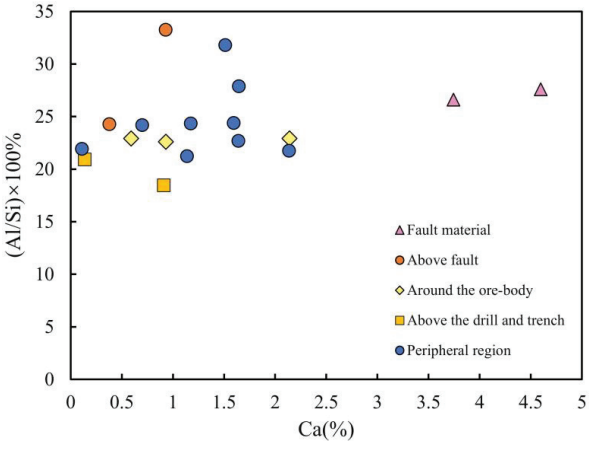

Figure 5. Al/Si–Ca relationship diagram of representative samples from different regions in the Mahuagou mining area.

The variation in major element content among soil samples reflects the heterogeneity of their compositional materials. Based on the characteristics of their composition, inferences can be drawn regarding the provenance nature of the sampled region. The relatively consistent Si and Al variations in this experiment indicate a uniform degree of weathering, unaffected by transported materials, suggesting in situ weathering from the parent rock [64]. However, significant differences in Ca and Mg composition among samples suggest mineralogical influences. These differences may be caused by minerals such as chlorite, montmorillonite, and kaolinite.

4.3. Geochemical Characteristics of Trace Elements

Geochemical prospecting has proven to be an effective approach in gold exploration work so far, and the study of epithermal gold deposits has garnered significant attention from numerous scholars [65,66]. In the field of geochemical gold exploration, the analysis of coupled elemental relationships and the determination of their significance are of particular importance [67]. Studies such as the native halo of gold deposits, trace element patterns [68], and statistical relationships between various elements [69] play a crucial role in addressing gold exploration challenges. To elucidate the distribution patterns of geochemical elements within the overlying strata of the Mahuagou mining area and establish relationships among element combinations, this study conducted content analysis on soil samples containing 17 metallic and non-metallic elements closely associated with gold mineralization, including Ag, As, Be, Bi, Cd, Co, Cr, Cu, Hg, Mo, Ni, Pb, Sb, Sn, W, Zn, and Au. A statistical analysis was subsequently performed on the collected data.

A systematic clustering analysis was conducted on the 17 metallic elements in the soil samples. It is a data analysis technique that divides objects or data points in a dataset into different groups or categories, and it finds widespread applications in many domains. Prior to analysis, the Z-score method was applied to standardize the original data, unifying data of different magnitudes onto a common scale. Calculated Z-Score values replaced the original values for analysis, ensuring data comparability. Ward's Method is used for processing sample data, and it is a systematic clustering method for dividing data points into different clusters or groups. The advantage of this method is to select, at each step, two existing clusters to merge in order to minimize the increase in their combined variance. Consequently, this method is capable of producing compact and relatively evenly-sized clusters. Employing squared Euclidean distance as the distance metric, the results of the analysis are presented in Figure 6.

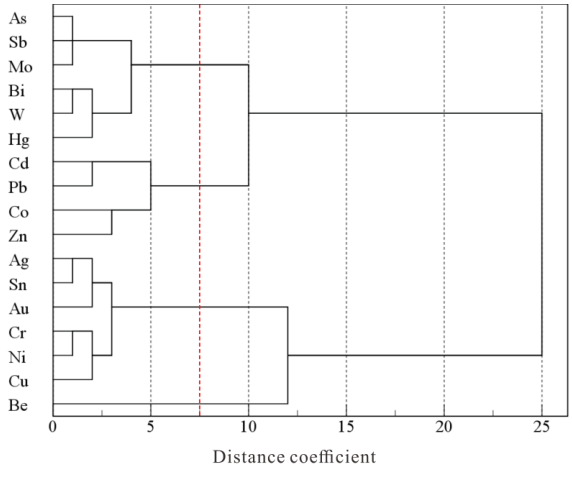

Figure 6. Phylogenetic diagram of soil elements by systematic clustering analysis.

At a similarity level of 7.5 distance coefficient, all elements can be classified into four categories: The first category includes As, Sb, Mo, Bi, W, and Hg. Among them, the cooccurrence of Mo, W, and Bi elements is often associated with alkali granite related to W–Sn mineralization, consistent with the nature of soil parent rocks [70]. The combination of Hg, As, and Sb elements is closely linked to shallow, low-temperature hydrothermal mineralization, often manifesting as elements in the halo zone of hydrothermal gold deposits, serving as significant indicators for mercury, antimony, and gold deposits. This combination not only inherits the specific characteristics of the parent rock but also retains effective indicators of deep-seated mineralization. The second category encompasses Cd, Pb, Co, and Zn, which commonly occur in polymetallic sulfide hydrothermal mineralization and are also prominent lower-level elements in gold deposits [71]. The third category comprises Ag, Sn, Au, Cr, Ni, and Cu, forming a typical assemblage in medium-temperature ore-forming zones. Be elements constitute a separate category, typically acting as late-stage anomaly indicators in gold deposits.

Even more, the cluster analysis displays the relationship between elements and rock types. The first category (As, Sb, Mo, Bi, W, and Hg) is closely associated with granite; it may indicate the crucial metallogenic significance of the biotite monzonitic granite (γPt_3Zx) in the mining area. The second category (Cd, Pb, Co, Zn, Ag, Sn, Au, Cr, Ni, and Cu) is associated with mafic rocks and ultramafic rocks, and Au has displayed an affinity for such elements; this may indicate that the mafic-ultra mafic veins have a significant influence on gold mineralization. Further analysis is conducted on the variations of the complete dataset of the first three categories of element combinations along profiles. In Figure 7, it can be observed that the anomalous elements at the front edge of the gold deposit, composed of elements such as As, Sb, and Hg (Category 1), exhibit consistent anomalies in profiles FXS and MHG.

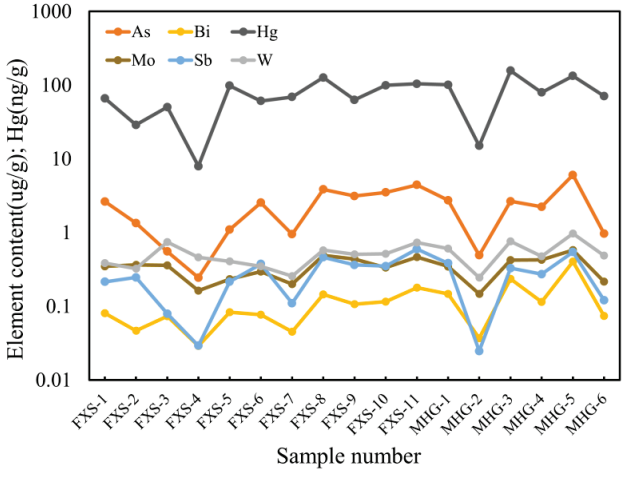

Figure 7. The content change characteristics of the first type of element combination (As, Sb, Mo, Bi, W, and Hg).

On the FXS profile (first 11 points), points FXS-5 and FXS-8 demonstrate positive anomalies in element content. These sampling locations exhibit well-developed soil profiles and are positioned directly above fault structures. At point FXS-8, multiple phases of intrusive veins are evident, with the pronounced intrusion of potassium feldspar granite veins controlled by faulting. Magmatic activity during the upward intrusion and subsequent crystallization has led to the enrichment of valuable components through filling and replacement processes facilitated by favorable structural and lithological conditions at FXS-8. The hydrothermal fluids generated during these processes, influenced by factors

like pressure gradients and temperature, have enabled the vertical migration of valuable components. These components have been preserved within the soil during their upward migration, resulting in the observed positive anomalies.

On the MHG profile (last 6 points), the elements exhibit a distinct bimodal distribution. Points MHG-3 and MHG-5 show positive anomalies, and these correspond to the mineralized segment of the MHG profile. From the results, this distribution pattern suggests a certain indicative effect of the first category of element combinations on the mineral body. However, further validation is required through subsequent unconventional exploration methods.

The content variations of the second and third categories of elements at each point along the profile are significant. Moreover, there are substantial differences in the trends of variation among elements within the same type without evident anomalous features (Figure 8). Elements like Au and Hg in soil samples beside the KZY exploration trench display much higher concentrations compared to other samples. This phenomenon may be attributed to the disturbance caused by trench excavation. This disturbance leads to the fragmentation of mineralized outcrops, allowing mineral particles to mix with the soil and subsequently be preserved. Hence, this sample is not considered for discussing the geochemical characteristics of the overlying cover in the mining area.

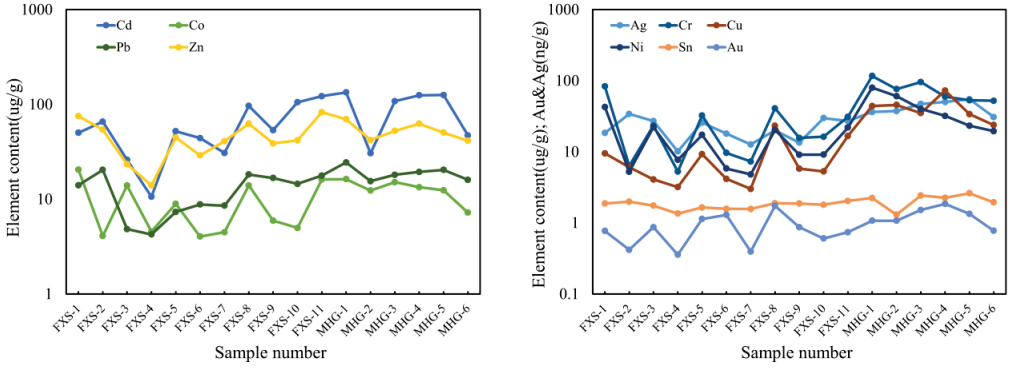

(**a**) (**b**)

Figure 8. The content change characteristics of the second combination elements and the third combination elements: (**a**) variation characteristics of Cd, Co, Pb, and Zn content; (**b**) variation characteristics of Ag, Cr, Cu, Ni, Sn, and Au content.

5. Deep-Penetrating Geochemical Result

5.1. Abnormal Characteristics of Soil Heat-Released Mercury

The soil heat-released mercury survey method involves heating the soil to release mercury that is adsorbed within the soil and is related to mineral bodies. Subsequently, the released mercury content is measured. This approach, combined with geological and mineralogical characteristics, allows for the further analysis of concealed mineral bodies or underlying structures. In this exploration study, soil heat-released mercury surveys were conducted in two locations near the Fengxiangshugou (FXS) induced IP profile and the Mahuanggou (MHG) mining area along Line 7 in the core area of the Huangling Anticline gold deposit. The results were compared with the gold content in the soil (Figure 9).

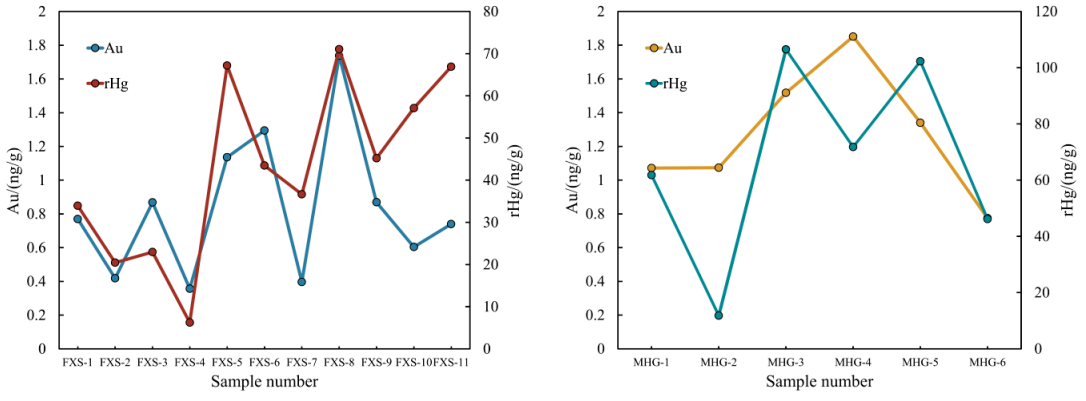

(**a**) (**b**)

Figure 9. Line chart of soil heat-released mercury anomaly: (**a**) soil heat-released mercury anomaly of Fengxiangshugou; (**b**) soil heat-released mercury anomaly of Mahuanggou.

The soil heat-released mercury anomalies along the FXS profile closely correspond to the gold content anomalies, exhibiting a bimodal distribution at points FXS-5 and FXS-8 (Figure 9a). FXS-5 is positioned directly above the fractured zone of the fault, while FXS-8 is located beneath rock masses with distinct characteristics of multiple phases of intrusive veins, notably controlled by faulting. The soil heat-released mercury results along the FXS profile demonstrate a good indication of the faulted zone and multi-phase intrusions. Furthermore, in comparison to gold content anomalies, soil heat-released mercury surveys exhibit higher anomaly contrast, thus offering a superior indication effect over gold anomalies.

In contrast, the soil heat-released mercury anomalies along the MHG profile exhibit differing characteristics from the overall gold anomalies (Figure 9b). The soil heat-released mercury anomalies align with the first category of element combinations (As, Sb, Hg, Mo, Bi, and W) identified through cluster analysis (Figure 7). These anomalies consistently appear along the MHG profile, presenting a bimodal distribution at points 3–5. On the other hand, the gold anomaly peaks at point 4 along the MHG profile, with diminishing intensities on both sides. The known mineralized segment on the MHG profile is represented by points 3–5, and both methods show anomalous indications along this profile.

5.2. Chemical Mobile Forms of Gold in Soil

In this exploratory study, the gold fractionation of 18 soil samples from three locations—Fengxiangshugou (FXS), Mahuanggou (MHG), and Kaziya (KZY)—was conducted using the seven-step sequential extraction method. The ratios of gold content in different fractions to the total mobile gold content are illustrated in Figure 10.

Residual and strongly organically bound forms of gold are predominant in the soil, while water-soluble, exchangeable, and carbonate-bound forms are in smaller proportions. With the exception of samples from KZY, the primary chemical form of gold in the remaining soil samples is the strongly organically bound form. This form involves the central heavy metal ion surrounded by organic functional groups as ligands, or it combines with sulfur ions to generate water-insoluble compounds [72]. Materials in the strongly organically bound form can undergo degradation of their contained organic molecules under oxidative conditions, leading to the leaching of some metal ions and resulting in anomalies in the soil or environmental impacts [73].

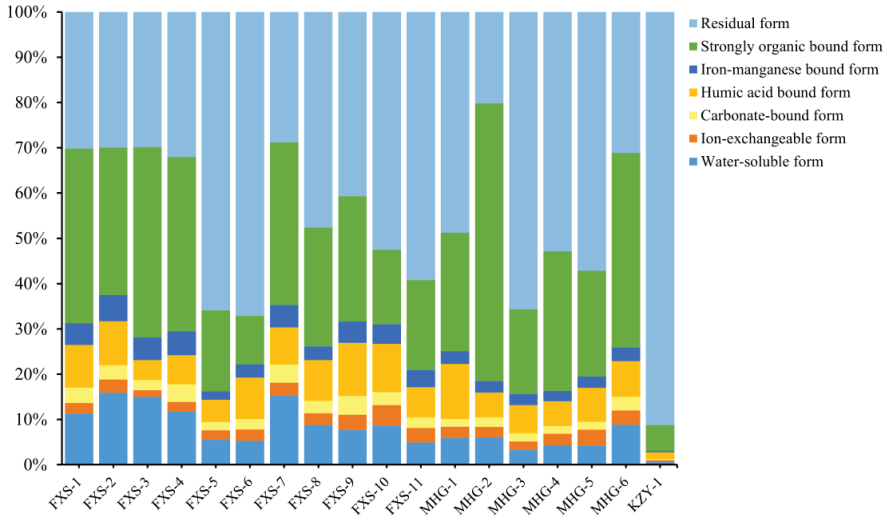

Figure 10. Chemical Mobile Forms distribution of gold in soil samples.

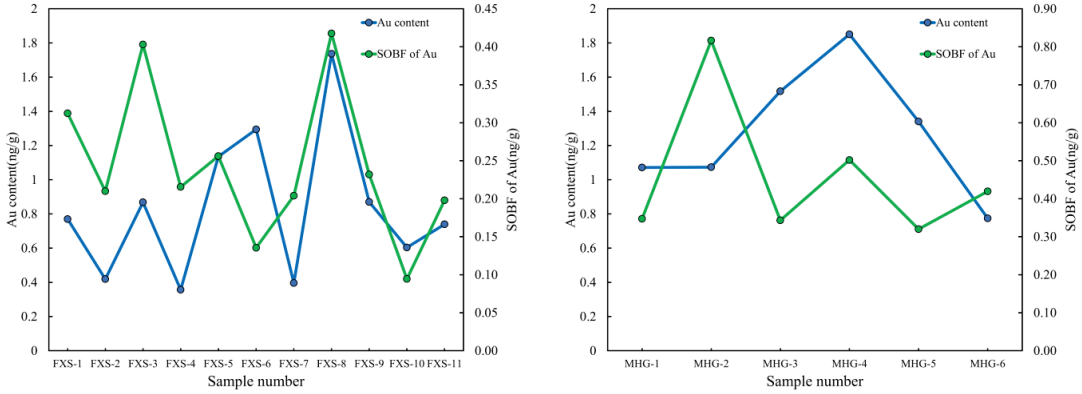

(**a**) (**b**)

Figure 11. Line chart of the strong organic bound form (SOBF) of Au and Au content in soil: (**a**) anomaly of SOBF of Au in Fengxiangshugou; (**b**) anomaly of SOBF of Au in Mahuanggou.

A comparison between the strongly organically bound form of gold and the anomalous gold content is presented in Figure 11 for this experiment. Along the FXS profile, distinct anomalies are observed in samples within the FXS-3 faulted zone and above the potassium feldspar granite intrusion at FXS-8 (Figure 11a). However, unlike the heat-released mercury anomalies, the strongly organically bound form of gold does not exhibit anomalies directly above the fault. Both methods exhibit particularly pronounced indications for the potassium feldspar granite intrusion, with anomaly contrast surpassing gold content.

The anomalies of the strongly organically bound gold along the MHG profile do not align with the heat-released mercury anomalies or the total gold anomalies, indicating a shift in peak positions (Figure 11b). It is hypothesized that the formation of this anomaly might be influenced by the vein morphology and the topography of the cover layer, both of which could lead to the displacement of mineralization-induced anomalies.

The KZY samples consist of loose soil adjacent to the exploration trench, with the primary chemical form of gold being the residual form. Residual forms of metals generally exist within primary minerals, secondary minerals, silicates, and other lattice structures. These forms are stable in nature, not easily released in surface environments, remain stable in soils, are poorly absorbed by plants, and exhibit limited migration capabilities.

5.3. Abnormal Characteristics of Soil Halogen

Halogen elements consist of four elements: F, Cl, Br, and I. These elements possess high electronegativity, strong electron-accepting capabilities, exhibit pronounced non-metallic properties, and readily form halides and halogen complexes with most metals. This property is advantageous for the migration of metallic elements in ore-forming fluids, making halogens crucial components in polymetallic mineralization processes.

The anomalous display of the four elements (F, Cl, Br, and I) along the FXS profile is relatively weak (Figure 12). Among them, F and Cl exhibit distinct enrichment and peak values in fault-related material, followed by a gradual decrease. Br and I show an overall increasing trend in content, with a single negative anomaly peak at point FXS-7. These two anomaly patterns lack correlation with geological facts and exhibit unclear indication effects.

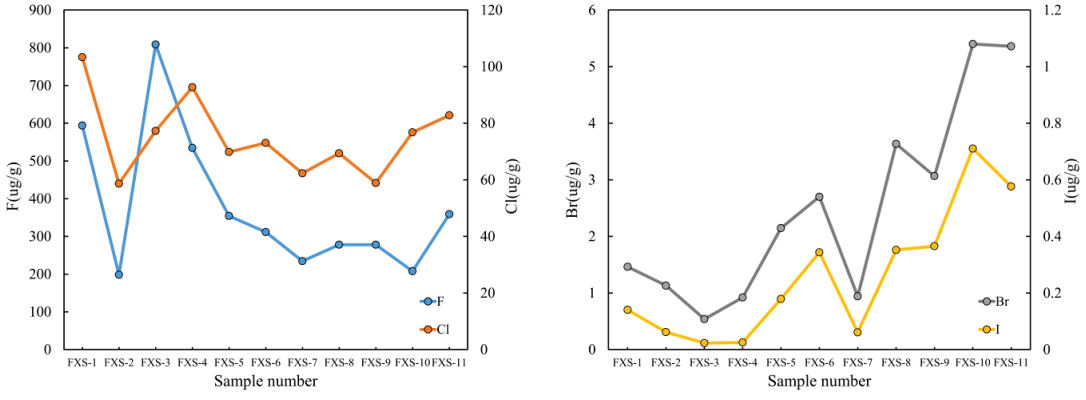

Figure 12. Halogen anomaly in the soil of FXS: (**a**) F and Cl anomaly in the soil of FXS; (**b**) Br and I anomaly in the soil of FXS.

Similarly, the F, Cl, Br, and I elements along the MHG profile display two different anomaly patterns (Figure 13). The anomalies of F and Cl resemble the overall gold anomalies, peaking at point MHG-4 with diminishing intensity on both sides. The anomalies of Br and I align with the heat-released mercury anomalies and the anomaly characteristics of the first category of element combinations identified through cluster analysis, displaying a bimodal distribution at points 3–5 along the MHG profile. Both types of anomaly patterns for the halogen elements on the MHG profile provide specific indicative effects for the underlying mineral bodies.

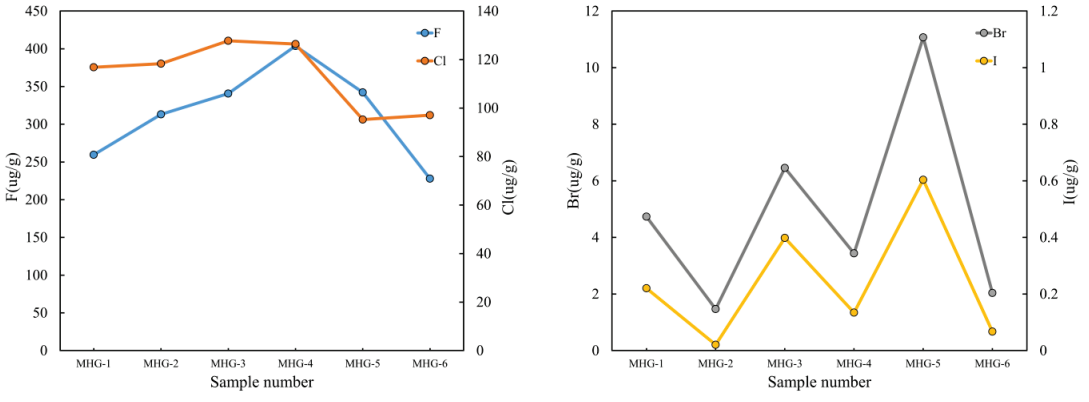

(**a**) (**b**)

Figure 13. Halogen anomaly in the soil of MHG: (**a**) F and Cl anomaly in the soil of MHG; (**b**) Br and I anomaly in the soil of MHG.

5.4. Discussion of Anomaly

Soil heat-released mercury anomalies exhibit prominent indications of concealed mineral bodies and underlying structures. Mercury possesses a significant affinity for sulfur and commonly exists in the forms of native mercury and mercury compounds within sulfides during hydrothermal stages. In surface environments, mercury-bearing metal sulfides can undergo a series of redox reactions to generate mercury oxides or chlorides. Through groundwater flow and migration in structural fractures, these mercury compounds can be adsorbed onto clay minerals, organic matter, and iron-manganese oxides in the overlying soil, thus forming soil mercury anomalies.

The lush vegetation and extensive tree-covered terrain in the Mahuagou mining area result in organic-rich and moist soils. Gold released from concealed mineral bodies and their primary halos can interact with soil organic matter through complexation, forming complexes with varying solubilities [74,75]. Therefore, the dominant chemical form of gold is the strongly organically bound form. This form of gold exhibits a similar anomaly indication effect as soil heat-released mercury surveys. It is more likely to form metal-active anomalies in locations conducive to element migration, such as near structures or above mineral bodies [75].

Soil halogen element anomalies in this area exhibit limited indication effects. On the FXS profile, the anomaly characteristics display unclear indications, whereas on the MHG profile, they provide some indication of underlying mineral bodies. This discrepancy can be attributed to the local parent rock properties. The FXS profile predominantly exposes medium -acidic intrusive rocks, while widespread basic dike intrusions characterize the MHG profile. The variation in parent rock types leads to differences in soil properties, affecting the preservation of halogen anomalies [76].

6. Conclusions

This paper comprehensively tests and analyzes major elements, mineral components, and various metallic and non-metallic elements in 18 soil samples from the Mahuagou gold deposit region. Through a comprehensive analysis of geochemical data and statistical methods, several significant indicators have been identified.

1. The element combination of As, Sb, Hg, Bi, W, and Mo holds significant indicative implications for hydrothermal gold deposits in the area. Moreover, it demonstrates a favorable coupling relationship with the unconventional exploration work conducted

in this study. In future work, attention should be given to this element combination, as it may play a crucial role in gold prospecting within the Huangling syncline region;
2. The measurement of chemical forms of gold reveals that the predominant chemical-migration form of gold in the overburden of the Mahuagou mining area is strongly organically bound. This form can indicate the faulted zone and multi-phase intrusions and exhibit higher anomaly contrast. This conclusion provides a vital theoretical foundation for the exploration of concealed ore deposits in the study area;
3. Penetration geochemical methods, such as soil heat-released mercury measurement and gold form measurement, demonstrate good applicability in the Mahuagou mining area. The experimental results indicate that in areas with relatively thin cover layers, like Mahuagou, penetration geochemical methods remain effective tools for gold prospecting. This finding offers technical support for mineral exploration efforts in the region. By prioritizing and utilizing the key indicators identified in this paper, exploration teams can enhance their efficiency and accuracy in targeting potential gold mineralization zones.

Author Contributions: Conceptualization, Q.X. and S.X.; methodology, Z.C. and Q.X.; software, W.Z.; validation, M.W.; formal analysis, S.X.; investigation, W.Z., D.L. and S.X.; resources, L.L. and Y.G.; data curation, W.Z. and M.W.; writing—original draft preparation, W.Z.; writing—review and editing, W.Z., S.X., S.F.A. and O.Y.; visualization, W.Z.; supervision, D.L. and S.X.; project administration, L.L. and Y.G.; funding acquisition, L.L. and Y.G. All authors have read and agreed to the published version of the manuscript.

Funding: This research was funded by the National Natural Science Foundation of China (41872250).

Data Availability Statement: The data presented in this study are available on request from the corresponding author. The data are not publicly available due to the confidentiality of the project.

Acknowledgments: During fieldwork, sample processing, and testing and analysis procedures, we received assistance from professors and fellow students from the Faculty of Earth Sciences and the Faculty of Earth Resources at China University of Geosciences, Wuhan, as well as guidance and support from experts of The Seventh Geological Brigade, Hubei Geological Bureau, Yichang. We express our gratitude to all for their contributions.

Conflicts of Interest: The authors declare no conflict of interest.

References

1. Zhai, M.; Hu, R.; Wang, Y.; Jiang, S.; Wang, R.; Li, J.; Chen, H.; Yang, Z.; Lü, Q.; Qi, T.; et al. Mineral Resource Science in China: Review and perspective. *Geogr. Sustain.* **2021**, *2*, 107–114. [CrossRef]
2. Hu, R.; Liu, J.; Zhai, M. *Mineral Resources Science in China: A Roadmap to 2050*; Science Press: Beijing, China, 2010; pp. 1–94.
3. Han, Z.; Liao, J.; Zhang, Y.; Zhang, B.; Wang, X. Review of deep-penetrating geochemical exploration methods. *Adv. Earth Sci.* **2017**, *32*, 828–838.
4. Wang, Y.; Yang, C.; Liang, J.; Liu, W.; Song, J. Method for Determining Lower Limit of Soil Geochemical Anomaly and Its Advantages and Disadvantages. *Environ. Resour. Ecol. J.* **2023**, *7*, 52–60.
5. Han, Z.; Lu, H.; Zhang, B.; Cheng, Z.; Fu, W.; Lao, C.; Xu, C. Delineating preliminary prospective areas of ion-adsorption rare earth deposits with stream sediments geochemical mapping in South China. *J. Asian Earth Sci.* **2023**, *243*, 105520. [CrossRef]
6. Dushyantha, N.; Ratnayake, N.; Premasiri, R.; Batapola, N.; Panagoda, H.; Jayawardena, C.; Chandrajith, R.; Ilankoon, I.; Rohitha, S.; Ratnayake, A.; et al. Geochemical exploration for prospecting new rare earth elements (REEs) sources: REE potential in lake sediments around Eppawala Phosphate Deposit, Sri Lanka. *J. Asian Earth Sci.* **2023**, *243*, 105515. [CrossRef]
7. Ayari, J.; Barbieri, M.; Boschetti, T.; Barhoumi, A.; Sellami, A.; Braham, A.; Manai, F.; Dhaha, F.; Charef, A. Major- and Trace-Element Geochemistry of Geothermal Water from the Nappe Zone, Northern Tunisia: Implications for Mineral Prospecting and Health Risk Assessment. *Environments* **2023**, *10*, 151. [CrossRef]
8. Sarala, P. Surficial Geochemical Exploration Method. In *Mineral Deposits of Finland*; Elsevier: Amsterdam, The Netherlands, 2015; pp. 711–731.
9. Clark, R.J.; Meier, A.L.; Riddle, G. Enzyme leaching of surficial geochemical samples for detecting hydromorphic trace-element anomalies associated with precious-metal mineralized bedrock buried beneath glacial overburden in northern Minnesota. In Proceedings of the Gold'90 Symposium-Gold'90, Littleton, CO, USA, 26 February–1 March 1990.
10. Wen, X. Deep-Penetrating Geochemistry: Theoretical Consideration, Methodology and Application in Desert Terrain. Ph.D. Thesis, Chang'an University, Xi'an, China, 2008.

11. Mann, A.W.; Birrell, R.D.; Mann, A.T.; Humphreys, D.B.; Perdrix, J.L. Application of the mobile metal ion technique to routine geochemical exploration. *J. Geochem. Explor.* **1998**, *61*, 87–102. [CrossRef]
12. Mann, A.; Reimann, C.; De Caritat, P.; Turner, N.; Birke, M. Mobile Metal Ion® analysis of European agricultural soils: Bioavailability, weathering, geogenic patterns and anthropogenic anomalies. *Geochem. Explor. Environ. Anal.* **2015**, *15*, 99–112. [CrossRef]
13. Sadeghi, M.; Albanese, S.; Morris, G.; Ladenberger, A.; Andersson, M.; Cannatelli, C.; Lima, A.; De Vivo, B. REE concentrations in agricultural soil in Sweden and Italy: Comparison of weak MMI® extraction with near total extraction data. *Appl. Geochem.* **2015**, *63*, 22–36. [CrossRef]
14. Wang, X.; Cheng, Z.; Lu, Y.; Xu, L.; Xie, X. Nanoscale metals in Earthgas and mobile forms of metals in overburden in wide-spaced regional exploration for giant deposits in overburden terrains. *J. Geochem. Explor.* **1997**, *58*, 63–72. [CrossRef]
15. Wang, X. Leaching of mobile forms of metals in overburden: Development and application. *J. Geochem. Explor.* **1998**, *61*, 39–55.
16. Liu, X.; Cao, J.; Li, Y.; Hu, G.; Wang, G. A study of metal-bearing nanoparticles from the Kangjiawan Pb-Zn deposit and their prospecting significance. *Ore Geol. Rev.* **2019**, *105*, 375–386. [CrossRef]
17. Sun, B.; Zhang, X.; Liu, Z.; Zhou, G.; Zhang, B.; Chen, Y. A preliminary study of the formation mechanism of the geoelectric chemistry anomaly. *Geophys. Geochem. Explor.* **2015**, *39*, 1183–1187.
18. Liu, P.; Luo, X.; Wen, M.; Zhang, J.; Gao, W.; Ouyang, F.; Duan, X. Using electrogeochemical approach to explore buried gold deposits in an alpine meadow-covered area. *Acta Geochim.* **2018**, *37*, 402–413. [CrossRef]
19. Crowther, T.W.; van den Hoogen, J.; Wan, J.; Mayes, M.A.; Keiser, A.D.; Mo, L.; Averill, C.; Maynard, D.S. The global soil community and its influence on biogeochemistry. *Science* **2019**, *365*, eaav0550. [CrossRef]
20. Zhang, Y.; Chen, Y.; Li, D.; Zhao, J.; Zhang, N.; Kang, H. Application of optically stimulated luminescence in volcanic hydrothermal uranium deposits in the Guyuan Basin, North China. *J. Geochem. Explor.* **2022**, *241*, 107054. [CrossRef]
21. Lu, Y.; Zhang, B.; Wang, X.; Liu, H.; Yan, T.; Wang, Q.; Liu, Q.; Liu, D.; Xu, Y. Application of the fine-grained soil prospecting method in a loess-covered area of central China. *Appl. Geochem.* **2022**, *143*, 105377. [CrossRef]
22. Noble, R.R.P.; Morris, P.A.; Anand, R.R.; Lau, I.C.; Pinchand, G.T. Application of ultrafine fraction soil extraction and analysis for mineral exploration. *Geochem. Explor. Environ. Anal.* **2020**, *20*, 129–154. [CrossRef]
23. Noble, R.R.P.; Lau, I.C.; Anand, R.R.; Pinchand, G.T. Refining fine fraction soil extraction methods and analysis for mineral exploration. *Geochem. Explor. Environ. Anal.* **2020**, *20*, 113–128. [CrossRef]
24. Anand, R.R.; Aspandiar, M.F.; Noble, R.R.P. A review of metal transfer mechanisms through transported cover with emphasis on the vadose zone within the Australian regolith. *Ore Geol. Rev.* **2016**, *73*, 394–416. [CrossRef]
25. Wu, Y.-F.; Evans, K.; Li, J.-W.; Fougerouse, D.; Large, R.R.; Guagliardo, P. Metal remobilization and ore-fluid perturbation during episodic replacement of auriferous pyrite from an epizonal orogenic gold deposit. *Geochim. Cosmochim. Acta* **2019**, *245*, 98–117. [CrossRef]
26. Jamtveit, B.; Yardley, B. *Fluid Flow and Transport in Rocks: Mechanisms and Effects*; Springer Science & Business Media: Berlin/Heidelberg, Germany, 1997; p. 319.
27. Kolb, J.; Rogers, A.; Meyer, F.M.; Vennemann, T.W. Development of fluid conduits in the auriferous shear zones of the Hutti Gold Mine, India: Evidence for spatially and temporally heterogeneous fluid flow. *Tectonophysics* **2004**, *378*, 65–84. [CrossRef]
28. Wang, X.; Zhang, B.; Ye, R. Nanoparticles Observed by TEM from Gold, Copper-Nickel and Silver Deposits and Implications for Mineral Exploration in Covered Terrains. *J. Nanosci. Nanotechnol.* **2017**, *17*, 6014–6025. [CrossRef]
29. Wang, X.; Zhang, B.; Lin, X.; Xu, S.; Yao, W.; Ye, R. Geochemical challenges of diverse regolith-covered terrains for mineral exploration in China. *Ore Geol. Rev.* **2016**, *73*, 417–431.
30. Deng, M. Structural Modeling of the Huangling Anticline and Its Peripheral Structural Belt. Ph.D. Thesis, China University of Geosciences, Beijing, China, 2018.
31. Xiang, M.; Hu, S.; Nie, K.; Lu, J.; Yang, P.; Zhou, Z. Geochemical Characteristics and Genesis of Gold Deposits in the Core of Huangling Anticline, Western Hubei. *Resour. Environ. Eng.* **2021**, *35*, 787–793+874.
32. Liu, S.; Yang, C.; Li, F.; Liao, Z.; Zhang, Q.; Cheng, C. Cause and Ore-bearing Characteristics of Gold Deposit in Xiangxi-Western Hubei Metallogenic Belt of Huangling Anticline. *Resour. Environ. Eng.* **2015**, *29*, 150–154.
33. Ma, D.; Li, Z.; Xiao, Z. The Constitute, Geochronology and Geologic Evolution of the Kongling Complex, Western Hubei. *Acta Geosci. Sin.* **1997**, *18*, 233–241.
34. Xiong, C.; Wei, C.; Jin, G.; Li, W.; Xiang, W. Basic characteristics and metallogenetic regularity of the gold ore deposits in the middle core of Huangling anticline, western Hubei province. *Geol. Miner. Resour. South China* **1998**, *1*, 32–40.
35. Cui, X.; Zhu, W.; Wang, X. Neoproterozoic modification of heterogeneous continental lithosphere beneath the Yangtze interior: Revealed from mafic dykes from the Huangling area, South China. *Int. J. Earth Sci.* **2022**, *111*, 27–51. [CrossRef]
36. Xiong, C.; Wei, C.; Jin, G.; Tan, W.; Li, W. Pre-Sinian Paleostructural Framework and Major Geological Events in the Huangling Anticline, Western Hubei. *J. Geomech.* **2004**, *10*, 97–112.
37. Wang, H.; Xia, Q.; Zhou, Z.; Lei, L.; Chen, C.; Yang, P.; Gong, Y.; Hua, Q.; Bao, Q. Orogenic gold mineralization in the Huangliang region and its intimate tectonic linkage to the Neoproterozoic orogeny of South China. *Precambrian Res.* **2023**, *394*, 107105. [CrossRef]
38. Guo, Y. Petrological and Geochemical Characteristics and Its Geodynamic Significance of Huangling Granite Batholith in Western Hubei Province. Master's Thesis, Chengdu University of Technology, Chengdu, China, 2019.

39. Wei, C.; Xiong, C.; Jin, G.; Li, W.; Xiang, W. Temporal-spatial pattern of the Mahuagou gold ore deposit, western Hubei, and the search for likely locations. *J. Geomech.* **2000**, *6*, 81–90.
40. Xiang, M.; Jiang, D.; Wan, X.; Wu, Q. Ore Prospecting Model and Prediction of Structural Superimposed Halo in Mahuagou Gold Deposit of Yichang City, Hubei Province. *Resour. Environ. Eng.* **2017**, *31*, 688–695.
41. Zhang, Q.; Xiang, M.; Wan, X.; Qu, Y. Discussion on Geological Characteristics and Prospecting Direction of Mahuagou Gold Deposit in Yiling District, Yichang City. *Resour. Environ. Eng.* **2015**, *29*, 383–386.
42. *SY/T 5163-2018*; Analysis Method for Clay Minerals and Ordinary Non-Clay Minerals in Sedimentary Rocks by the X-ray Diffraction. National Energy Administration: Beijing, China, 2018.
43. *WSBB/004-2019*; Determination of Twenty-Two Elements in Geological Samples by Inductively Coupled Plasma Optical Emission Spectrometry. Institute of Geophysical and Geochemical Exploration, Chinese Academy of Geological Sciences: Langfang, China, 2019.
44. *WSBB/005-2004*; Exploration Geochemical Sample Analysis Method X-ray Fluorescence Spectrometry for Determining Thirty-four Major and Trace Elements. Institute of Geophysical and Geochemical Exploration, Chinese Academy of Geological Sciences: Langfang, China, 2004.
45. *WSBB/001-2021*; Exploration Geochemical Sample Analysis Method for Determining Thirty-Two Trace Elements by Inductively Coupled Plasma Mass Spectrometry. Institute of Geophysical and Geochemical Exploration, Chinese Academy of Geological Sciences: Langfang, China, 2021.
46. *GB/T 14506.12-2010*; Methods for Chemical Analysis of Silicate Rocks-Part 12: Determination of Fluorine Content. Standards Press: Beijing, China, 2010.
47. *WSBB/013-2020*; Methods for Analysis of Exploration Geochemical Samples Catalytic Kinetic Spectrophotometry for Determination of Iodine Content. Institute of Geophysical and Geochemical Exploration, Chinese Academy of Geological Sciences: Langfang, China, 2020.
48. *DZ 0003-91*; Code of Practice for Mercury Vapor Survey. Ministry of Natural Resources of the People's Republic of China: Beijing, China, 1991.
49. *DD2005-03*; Ecological Geochemistry Assessment Sample Analysis Technical Requirements (Trial). China Geological Survey: Beijing, China, 2005.
50. Tessier, A.; Campbell, P.G.C.; Bisson, M. Sequential extraction procedure for the speciation of particulate trace metals. *Anal. Chem.* **1979**, *51*, 844–851. [CrossRef]
51. Altaner, S.P.; Ylagan, R.F. Comparison of structural models of mixed-layer illite/smectite and reaction mechanisms of smectite illitization. *Clays Clay Miner.* **1997**, *45*, 517–533. [CrossRef]
52. Mancktelow, N.; Zwingmann, H.; Mulch, A. Timing and conditions of clay fault gouge formation on the Naxos detachment (Cyclades, Greece). *Tectonics* **2016**, *35*, 2334–2344. [CrossRef]
53. Zwingmann, H.; Mancktelow, N.; Antognini, M.; Lucchini, R. Dating of shallow faults: New constraints from the AlpTransit tunnel site (Switzerland). *Geology* **2010**, *38*, 487–490. [CrossRef]
54. Yuan, J.; Yang, J.; Ma, H.; Su, S.; Chang, Q.; Kormarneni, S. Hydrothermal Synthesis of nano-kaolinite from K-feldspar. *Ceram. Int.* **2018**, *44*, 15611–15617. [CrossRef]
55. Xu, X.; Deng, F.; Wang, D.; Luo, X. Advances in composition and dating methods of fault gouge and weakening mechanisms of earthquake faults in bedrock area. *Bull. Geol. Sci. Technol.* **2022**, *41*, 122–131.
56. Argante, V.; Tanner, D.C.; Brandes, C.; von Hagke, C.; Tsukamoto, S. The Memory of a Fault Gouge: An Example from the Simplon Fault Zone (Central Alps). *Geosciences* **2022**, *12*, 268. [CrossRef]
57. Kanitpanyacharoen, W.; Chornkrathok, S.; Morley, C.K.; Wenk, H.R. Microstructural evolution and deformation mechanisms of Khao Kho Fault, Thailand. *J. Struct. Geol.* **2020**, *136*, 104055. [CrossRef]
58. Uddin, F. *Montmorillonite: An Introduction to Properties and Utilization*; IntechOpen: London, UK, 2018; pp. 1–202.
59. Warr, L.N. Recommended abbreviations for the names of clay minerals and associated phases. *Clay Miner.* **2020**, *55*, 261–264. [CrossRef]
60. Nesbitt, H.W.; Young, G.M. Early Proterozoic climates and plate motions inferred from major element chemistry of lutites. *Nature* **1982**, *299*, 715–717. [CrossRef]
61. Babechuk, M.G.; Fedo, C.M. Analysis of chemical weathering trends across three compositional dimensions: Applications to modern and ancient mafic-rock weathering profiles. *Can. J. Earth Sci.* **2023**, *60*, 839–864. [CrossRef]
62. Sergeev, N. Quantifying weathering intensity using chemical proxies: A weathering index AFB. *Aust. J. Earth Sci.* **2023**, *70*, 260–284. [CrossRef]
63. Harnois, L. The CIW index: A new chemical index of weathering. *Sediment. Geol.* **1988**, *55*, 319–322. [CrossRef]
64. Yu, S.; Xiang, W.; Li, Q.; Xie, S.; Xu, Q. Identification and interpretation of nonore-causative geochemical anomalies in arid grasslands: An example of the D2 area in the Hongennihuduge steppe, Inner Mongolia. *Geol. Explor.* **2014**, *50*, 1118–1125.
65. Cooke, D.R.; Simmons, S.F. Characteristics and genesis of epithermal gold deposits. *Rev. Econ. Geol.* **2000**, 221–244.
66. Zhu, Y.; An, F.; Tan, J. Geochemistry of hydrothermal gold deposits: A review. *Geosci. Front.* **2011**, *2*, 367–374. [CrossRef]
67. Goldfarb, R.J.; Hofstra, A.H.; Simmons, S.F. Critical elements in Carlin, epithermal, and orogenic gold deposits. In *Rare Earth and Critical Elements in Ore Deposits*; Society of Economic Geologists, Incorporated: Littleton, CO, USA, 2016.

68. Silberman, M.L.; Berger, B.R. Relationship of trace element patterns to alteration and morphology in epithermal precious-metal deposits. *Rev. Econ. Geol.* **1985**, *2*, 203–232.
69. Kadel-Harder, I.M.; Spry, P.G.; McCombs, A.L.; Zhang, H. Identifying pathfinder elements for gold in bulk-rock geochemical data from the Cripple Creek Au-Te deposit: A statistical approach. *Geochem. Explor. Environ. Anal.* **2021**, *21*, 2020–2048. [CrossRef]
70. Li, B.; Wang, X.; Tang, G.; Liu, Y.; Zou, G. S-Pb isotopes and tectono-geochemistry of the Lunong ore block, Yangla large Cu deposit, SW China: Implications for mineral exploration. *Ore Geol. Rev.* **2021**, *136*, 104249. [CrossRef]
71. Liu, C. Progress in Studies on Primary Halos of Ore Deposit. *Acta Geol. Sin.* **2006**, *80*, 1528–1538.
72. Pence, N.S.; Larsen, P.B.; Ebbs, S.D.; Lettham, D.L.D.; Lasat, M.M.; Garvin, D.F.; Eide, D.; Kochian, L.V. The molecular physiolosy of heave metal transport in the Zn/Cd hyperaccumulator. *Proc. Natl. Acad Sci. USA* **2000**, *97*, 4956–4960. [CrossRef]
73. An, Z. Reliability Assessment and Geochemical Significance of Heavy Metal Sequential Extraction in Soils and Sediments. Master's Thesis, Chinese Academy of Geological Sciences, Beijing, China, 2009.
74. Yang, F.; Xie, S.; Carranza, E.J.M.; Yao, L.; Tian, H.; Chen, Z. Vertical distribution of major ore-forming elements and the speciation in the semiarid system above the concealed Baiyinnuoer Pb-Zn deposit in inner Mongolia, China. *Geochem. Explor. Environ. Anal.* **2019**, *19*, 46–57. [CrossRef]
75. Sanyal, S.K.; Shuster, J.; Reith, F. Cycling of biogenic elements drives biogeochemical gold cycling. *Earth Sci. Rev.* **2019**, *190*, 131–147. [CrossRef]
76. Epp, T.; Marks, M.A.W.; Neidhardt, H.; Oelmann, Y.; Markl, G. Halogen (F, Cl, Br, I) contents in silt and clay fractions of a Cambisol from a temperate forest. *Am. Miner.* **2022**, *107*, 946–954. [CrossRef]

applied sciences

MDPI

Article

Removal of Heavy Metal Cd Element from Paddy Soil by Geo-Electrochemical Technology

Yao Sun, Meilan Wen *, Panfeng Liu * and Yuxiong Jiang

College of Earth Sciences, Guilin University of Technology, Guilin 541006, China; 13068035453@163.com (Y.S.); yxiongjiang@sina.com (Y.J.)

* Correspondence: mlwen@glut.edu.cn (M.W.); panfengliu@glut.edu.cn (P.L.)

Abstract: A Cd-contaminated paddy field at the Quanzhou County Institute of Agricultural Science in Guilin was selected as the research object, and geo-electrochemical technology (GT) was used to treat the Cd-contaminated paddy field in situ. The technology's effectiveness in removing the heavy metal Cd element from paddy soil and the change rule of Cd accumulation and transport in various parts of rice plants under the action of an electric field were studied. That was to provide a theoretical basis and a new technical choice for remediating paddy soil polluted by Cd. The results showed that the GT effectively removed the heavy metal Cd element from the paddy soil. When the level of soil Cd in the paddy field was 0.58 mg/kg, after in situ treatment with the GT, the soil Cd decreased to 0.39 mg/kg, which met the requirements of soil contamination risk control for agricultural land. Geo-electrochemical technology effectively reduced the content of the Cd element in various tissues and organs of rice plants, made the Cd content in brown rice lower than the requirement of the national food pollutant limit standard of 0.2 mg/kg, and achieved the production of safe rice. Geo-electrochemical technology reduced the enrichment of Cd in the tissues and organs of the rice plants, including roots, stems, leaves, and grains, and at the same time affected the process of rice roots transporting Cd.

Keywords: accumulation; Cd contamination remediation; geo-electrochemical technology; paddy soil transport

Citation: Sun, Y.; Wen, M.; Liu, P.; Jiang, Y. Removal of Heavy Metal Cd Element from Paddy Soil by Geo-Electrochemical Technology. *Appl. Sci.* **2023**, *13*, 11685. https://doi.org/10.3390/app132111685

Academic Editor: José Miguel Molina Martínez

Received: 19 September 2023
Revised: 17 October 2023
Accepted: 23 October 2023
Published: 25 October 2023

1. Introduction

Cadmium (Cd) is globally regarded as one of the most toxic heavy metals [1]. Excessive Cd in soil disrupts the normal growth of plants, especially food crops, and seriously threatens human health. A large number of studies have demonstrated that excessive intake or inhalation of Cd can cause toxicity to human immune, urinary, skeletal, nervous, circulatory, reproductive, and other systems, resulting in renal insufficiency, cardiovascular diseases, osteoporosis, and other diseases, and even carcinogenic effects [2–4]. In China, rice is the staple food for up to 60% of the population. However, the amount of Cd in paddy soil is as high as 33.2%, of which heavy polluters account for 8.6% [5]. Liu et al. [5] statistically analyzed the Cd content of surface (0−20 cm) paddy soil in China from 2000 to 2015. It was found that the concentration of Cd in that soil ranged from 0.01 to 5.50 mg/kg, with a median of 0.23 mg/kg. The provinces with the highest median Cd concentrations are Hunan (0.73 mg/kg), Guangxi (0.70 mg/kg), and Sichuan (0.46 mg/kg). Many works in the literature have indicated that mining was the main source of Cd contamination in Chinese paddy soils, and pollution incidents from mining activities were the critical driving force [5,6]. Therefore, the remediation and treatment of Cd-contaminated paddy soil are urgently needed.

Currently, remediation of heavy metal pollution in paddy soil focuses on Cd remediation, commonly with the use of agronomic control and soil amendment technologies. Agronomic control includes crop variation [7], optimized fertilization [8,9], and foliar

obstruction control [10]. Soil amendment includes chemical leaching [11], in situ passivation [12], plant enrichment [13,14], and electrokinetic remediation [15,16]. Electrokinetic remediation is an emerging in situ technology developed in recent years. It consists of inserting cathodes and anodes of an electric field into Cd-contaminated soil. The application of a direct current facilitates the directional migration of the Cd element toward electrodes due to electromigration, electro-osmotic flow, and electrophoresis in the electric field. Electromigration indicates the movement of charged ions and ionic complexes in soil solutions under the existence of an applied electric field, and it is the dominant transport mechanism for inorganic contaminants [17]. Electro-osmotic flow is the movement of the soil solution containing dissolved pollutant species through the pore system of the soil [18]. For soil heavy metal remediation, metal, or metal-containing species are usually positively charged and therefore migrate to the cathode through electromigration and electro-osmosis (electric attraction) [19]. Electrophoresis refers to the movement of charged particles or colloids under the application of an electric field. Compared with electromigration and electro-osmosis, electrophoresis has a negligible impact on inorganic matter transport in low-permeability soil systems, and thus it is not taken into account in the electrokinetic remediation process [17]. The Cd element is accumulated near the electrodes, and then the pollutants in the soil or electrolyte in the enrichment area are treated centrally to remove them [20].

The geo-electrochemical method is a low-voltage, self-powered, bipolar electrical extraction technology developed by the Hidden Ore Deposit Prediction Research Institute of the Guilin University of Technology. It is protected by independent intellectual property rights. Geo-electrochemical technology (GT) has yielded substantial results in exploring minerals for concealed ore deposits. Its working principle is also based on electrolysis, electromigration, electro-osmosis, electrophoresis, and other electric field actions to achieve directional migration and enrichment of heavy metal elements toward the cathode and anode. Therefore, it can be regarded as a kind of electrokinetic remediation technology. Geo-electrochemical technology uses lightweight and convenient equipment, is simple to use, has rapid and safe applications, and is environmentally friendly.

In this study, the paddy soil and rice plants of the Quanzhou County Institute of Agricultural Science in the north of Guilin were selected as the study subjects. The study preliminarily investigated the removal efficiency of GT on heavy metal Cd elements in paddy soil. That included the distribution rule of heavy metal Cd in the paddy soil–rice system under the influence of an electric field to provide a theoretical basis and a new technical alternative for remediating Cd-contaminated paddy soil.

2. Overview of the Study Area

Quanzhou County (25°37′ to 26°18′ N, 110°41′ to 111°14′ E), located in the northeast of Guangxi, dominates the upper reaches of the Xiang River and serves as a key point on the Hunan–Guangxi corridor. The county is in a sub-tropical humid monsoon climate zone, with a frost-free period of 298 d per year and an average annual temperature of 17.7 °C. Its primary characteristics include strong solar radiation, abundant sunlight for most of the year, an average multi-year sunshine duration of 1404.0 h, and plentiful rainfall with an average multi-year precipitation of 1565.9 mm, although it is unevenly distributed throughout the seasons. The area of Quanzhou County is approximately 4000 km^2, with karst areas accounting for more than one-third of the total land area. It is a typical karst hilly basin region, with carbonate rocks dominating the lithology of the strata [21]. Quanzhou County is a national basic farmland demonstration county and one of the national commodity grain production base counties, making it an important agricultural county in Guangxi province. However, previous investigations found that farmland soil in Quanzhou County is contaminated with heavy metals to varying degrees, with Cd showing the highest level of contamination. The farmland is considered moderately polluted [21]. The average Cd concentration of 288 air-dried farmland soil samples reaches 0.43 mg/kg, exceeding the background value of agricultural soil in the north-eastern region of Guangxi

(0.18 mg/kg) [22]. Therefore, it is urgent to implement effective technical measures to remediate and control Cd contamination of the paddy soil of Quanzhou County. The geo-electrochemical technology is expected to play a key role in the in situ treatment of Cd-contaminated paddy fields.

3. Materials and Methods

3.1. Experiment Site

The experiment site was at the Agricultural Science Institute in Quanzhou County, Guilin City, Guangxi Zhuang Autonomous Region. The experiment paddy field was consistent in fertility level and pollution degree. Before the experiment, soil sampling and related analyses were performed on the paddy soil. The soil's basic physical and chemical properties were determined: the soil type was red soil paddy field, its pH was approximately 6.4, and the total Cd content was approximately 0.58 mg/kg. The content of heavy metals in the soil is detailed in Table 1. The selected evaluation standard was the risk screening of soil contamination of agricultural land with a pH of 5.5 to $\leq$6.5 in the "Soil Environmental Quality Risk Control Standard for Soil Contamination of Agricultural Land" (GB 15618-2018) [23]. Table 1 shows that the Cd content of the experimental paddy soil exceeded the pollutant screening value for agricultural land (0.4 mg/kg for paddy fields), indicating ecological and environmental risk in that soil. Therefore, appropriate remediation should be performed to reduce the risk of Cd exceeding the limit in agricultural products. Apart from Cd, no other elements exceeded the standard, so Cd was the key element of concern for excessive heavy metals in that area.

Table 1. Heavy metal content of paddy soil in the Agricultural Science Institute experiment site.

Element:	Cr	Ni	Cu	Zn	As	Cd	Hg	Pb
Mean	53.59	19.58	31.99	85.60	20.97	0.58	0.16	63.25
Standard deviation	1.20	0.41	1.31	4.52	1.45	0.04	0.01	2.70
The legal limit for paddy fields	250	70	50	200	30	0.4	0.5	100

Note: Units are mg/kg.

3.2. Experiment Apparatus

The experiment apparatus was the "Low Voltage Bipolar Geo-Electric Extraction Device" developed by the Hidden Ore Deposit Prediction Research Institute of Guilin University of Technology. That device is small, uses a low voltage, has an independent power supply, and is easy to use [24]. The structural composition of the apparatus is shown in Figure 1. The device comprises mainly the cathode and anode extraction electrodes, power supply, and wires. The cathode and anode extraction electrodes comprise primarily cylindrical graphite carbon rods approximately 120 mm long with a 15 mm base diameter. In addition, specific adsorbent materials (high-density sponges) and filter papers (the pore size was about 20 μm) were added to form the cathode and anode extraction electrodes.

3.3. Experiment Method

The experiment started on 29 July 2021, in the paddy field at the Agricultural Science Institute in Quanzhou County. There were three treatments and two repetitions for each treatment. The experimental groups with different conditions were named T1, T2, and T3; the corresponding experimental conditions are listed in Table 2. T1 was the electrokinetic remediation experiment of the GT on paddy soil; T2 was the same experiment but on the paddy soil–rice system; and T3 was the control experiment with rice plants alone and no GT. When installing the GT device, the cathode and anode extraction electrodes were separately buried into the paddy soil, approximately 20 cm deep, with the distance between the electrodes controlled at approximately 20 cm. Figure 2 shows the mechanism related to removing the Cd element from paddy soil by the GT.

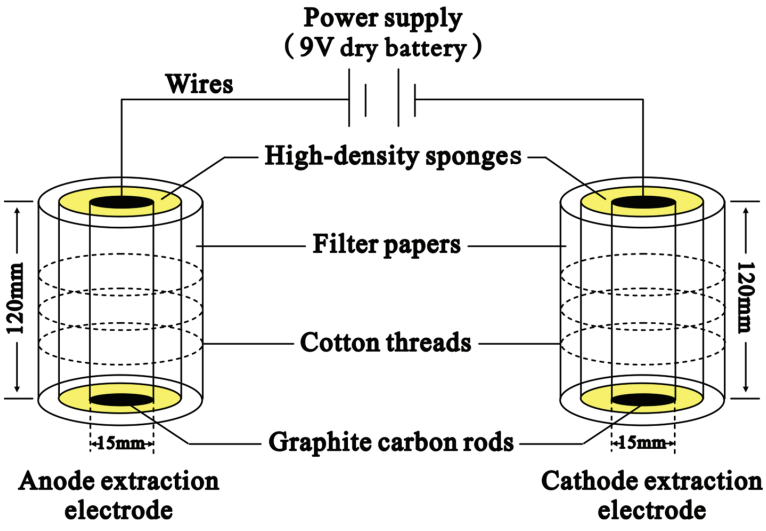

Figure 1. Schematic diagram of the geo-electrochemical technology device.

Table 2. Experimental conditions.

Experimental Group	Power-on Condition	Rice-Planting Situation	Duration of the Experiment
T1	Installation of the GT device in center (9 V direct current)	No rice planting	89 days
T2	Installation of the GT device in center (9 V direct current)	Rice planting	89 days
T3	No electricity	Rice planting	89 days

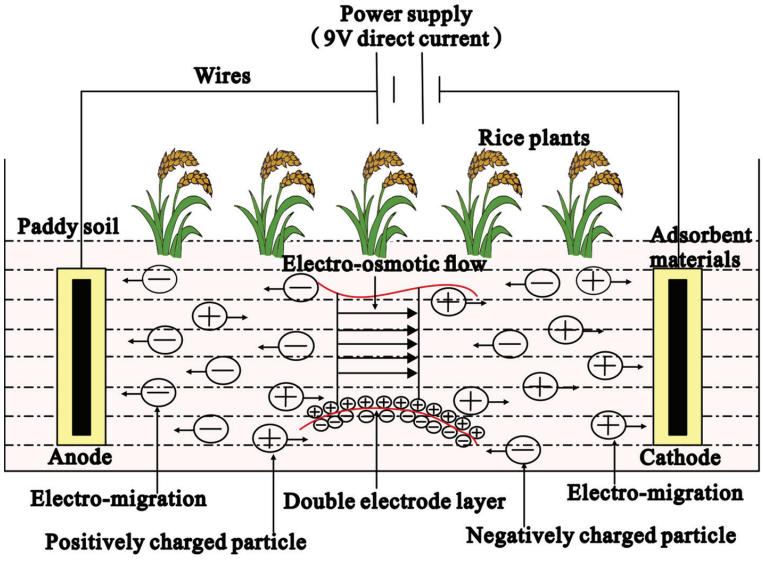

Figure 2. Schematic diagram of geo-electrochemical technology for removing Cd from paddy soil.

The paddy field area for each experimental group was 1 m^2 (1 m × 1 m), and all sides of the experimental groups were separated by polyethylene boards with a thickness

of about 1 cm and a height of about 80 cm. For T1 and T2, where GT was applied, the battery and adsorbent materials of the device were replaced every 7 days. T2 and T3 were the rice-planting experimental groups; considering local planting habits, the rice variety was uniformly Nongxiang 32, with consistent seeding and transplanting density. Manual weeding was used within the entire planting area without chemical herbicides; pest control was performed based on local pest information; and the irrigation water was tested free from Cd contamination. No high-concentration pesticides were used, and fertilization and other cultivation management techniques complied with local standards. The experiment began with the rice at the transplanting stage, and sampling was conducted on 25 October 2021, when the rice was mature, with the total duration of the experiment being 89 days.

3.4. Sample Collection and Analytical Testing

3.4.1. Sample Collection and Pretreatment

Field sampling was performed near the end of July before the experiment began and at the end of October during the rice harvest period, with soil samples collected at a depth of 0−20 cm (top tillage layer). A 5-point sampling method was used in each experimental field, with each sample comprising five subsamples mixed together, and approximately 1 kg of thoroughly mixed soil samples were placed in clean cotton bags. Rice samples, including roots, stems, leaves, and panicles, were collected using the 5-point method and were "one-to-one" with the soil samples. They were trimmed and classified on-site, then packaged in sample bags, with each panicle sample weighing more than 500 g.

Soil samples were air-dried in the laboratory, with roots and stones removed, ground with the use of an agate mortar, thoroughly sifted through a 60-mesh (0.25 mm) sieve, and mixed for pH testing. After sifting through the 60-mesh sieve, the soil samples were sifted through a 200-mesh (0.074 mm) sieve, mixed, and stored in polyethylene bags for analysis of total As, Cd, Cr, Cu, Hg, Ni, Pb, and Zn. Rice roots, stems, leaves, and panicles were initially washed in the field canal and then rinsed three times with deionized water in the laboratory. After air drying, the roots, stems, and leaves were chopped, and the panicles were threshed. All rice samples were dried to a constant weight at 60 °C and husked to produce brown rice, then 100 g of each sample was ground through a 60-mesh sieve and stored in polyethylene bags for analysis of total As, Cd, Cr, Cu, Hg, Ni, Pb, and Zn.

3.4.2. Sample Analysis Testing

The collected samples were analyzed for As, Cd, Cr, Cu, Hg, Ni, Pb, and Zn, and soil pH by the China Nonferrous Metals Guilin Geology and Mining Institute Co., Ltd. Soil samples of 10 g were weighed and sifted through a 60-mesh sieve, and the soil pH was determined in accordance with the "Soil Agricultural Chemistry Analysis Method" [25]. Soil samples of 1 g, sifted through a 200-mesh sieve, were microwave-digested and analyzed by atomic absorption for Cd, Cr, Cu, Ni, Pb, Zn and by atomic fluorescence spectrometry for As and Hg [26]. Rice root, stem, leaf, and brown-rice samples were weighed at 0.5 g each, microwave-digested, and analyzed by inductively coupled plasma mass spectrometry for As, Cd, Cr, Cu, Hg, Ni, Pb, and Zn.

3.5. Data Processing and Analysis

All data were statistically analyzed with the use of Microsoft Excel 2010 and IBM's SPSS 22.0 statistical software, with the results displayed as mean ± standard deviation. One-way ANOVA and Duncan's multiple comparison tests ($p < 0.05$) were used for differential analysis. The different letters indicate statistically significant differences. The graphs were drawn with the use of Origin 2018 (OriginLab Corp., Northampton, MA, USA).

4. Results and Discussion

4.1. Effectiveness of Cd Removal from Paddy Soil

The initial concentration of Cd in the paddy soil of the Agricultural Science Institute in Quanzhou County ranged from 0.52 to 0.64 mg/kg, with an average of 0.58 mg/kg.

Figure 3 shows the total soil Cd content changes for the three experimental groups after 89 d of experimental treatment. As shown in the figure, relative to the initial soil Cd content without experimental treatment, the total Cd content in the soil of the T1, T2, and T3 experimental groups all decreased, with a significant reduction ($p < 0.05$) in the T1 experimental group. Among the three experimental groups, the removal effectiveness of Cd in the T1 experimental group, where the GT was applied solely to the paddy soil, was the highest, reaching 36.18%. The removal effectiveness in the T2 experimental group, where the GT was applied to the paddy soil–rice system, was 10.39%. In the T3 control group, where rice was planted alone without the use of the GT, the Cd content in the soil also decreased after planting, with a reduction rate of 21.23%.

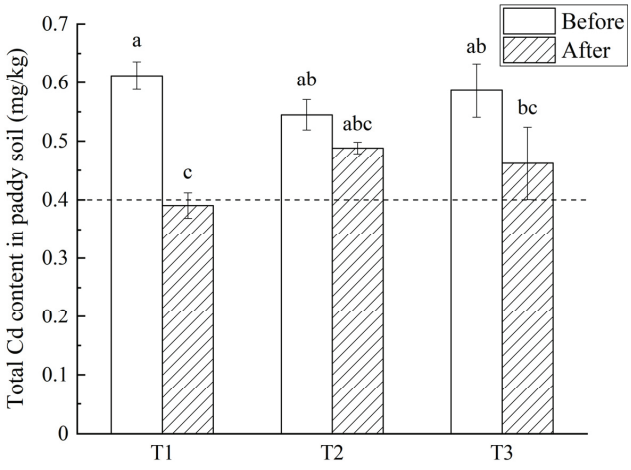

Figure 3. Variation in total Cd content in the soil of experimental groups before and after treatment (T3 was control group). Different letters above the error lines indicate significant differences ($p < 0.05$). The dashed line indicates the legal limit of Cd in the agricultural soil (0.4 mg/kg is derived from the Chinese national standard GB 15618-2018).

In accordance with GB 15618-2018 [23] and Figure 3, in the T1 experimental group, which used the GT solely on paddy soil, the total Cd content in the soil decreased to 0.39 mg/kg after the electrokinetic remediation. That is lower than the risk screening value for agricultural soil contamination (0.4 mg/kg for paddy fields), so it met the national standard. However, the T2 experimental group, which used the GT on planted rice, and the T3 control group with planted rice without the GT had total soil Cd contents of 0.49 mg/kg and 0.46 mg/kg, respectively, after the experiment. Although the total Cd content in the soil decreased in both cases, it was still higher than the risk screening value for agricultural soil contamination.

The experimental results show that the GT was effective in removing heavy metal Cd elements from paddy soil. The T1 paddy-soil-only experimental group had the best Cd-removal effect. After the remediation, the total Cd content in the paddy soil reached a safe threshold. The GT removes Cd elements from paddy soil based on the directional migration and accumulation of Cd elements toward the electrodes. It uses electrochemical effects such as electrolysis, electromigration, electro-osmosis, and electrophoresis. Then, the Cd element in the soil was collected with the use of specific adsorbent materials, thereby achieving the goal of reducing the content of the Cd element in the soil. The decrease in the soil Cd content in the T3 control group planted with rice alone was due to the absorption of Cd in the soil by rice plants. The less effective Cd removal in the T2 soil–rice system group might be related to the rice plants' absorption mechanism of Cd from the soil. According to the literature, Cd is a non-essential element of plants and enters into their roots through the absorption channels of Ca, Fe, Mn, Zn, and other essential elements [27]. For Cd-

contaminated soil, the toxic effects of Cd on crops can be alleviated to a certain extent by applying a certain amount of exogenous substances (such as Ca, Fe, Zn, Mn, Mg, and other elements) to the contaminated soil [28–30]. Because the above elements and Cd have similar ionic radii and chemical properties, they can share many transport proteins, ion transport channels, and binding sites in crop roots, thereby inhibiting the accumulation and transport of Cd in crops [30]. Therefore, it can be preliminarily speculated that under the application of GT, the migration and enrichment of Ca, Fe, Mn, Zn, and other metal elements in the soil inhibited the absorption of Cd by rice plants (especially in the roots), which resulted in the insignificant reduction of soil Cd content in the T2 experiment group. However, the actual mechanism is still unclear, and further research is undoubtedly required.

4.2. Variation in Cd Content in Various Parts of Rice

For the T2 and T3 experimental groups, after 89 d of experimental treatment, the changes in Cd content in various tissues and organs of the rice in both groups were recorded. Figure 4 shows a reduction in Cd content in various tissues and organs of rice in the T3 control group, which did not use the GT, and in the T2 planted-rice experimental group, which used the GT. In both groups, the Cd content in rice plants from high to low was in the order of rice roots > rice stems > rice leaves > rice grains (brown rice). That was basically consistent with the research of Zhou et al. [31], Zhao et al. [32], and others, i.e., the Cd content in organs storing nutrients (rice grains) is lower than that in organs with vigorous metabolisms (rice roots, rice stems, and rice leaves).

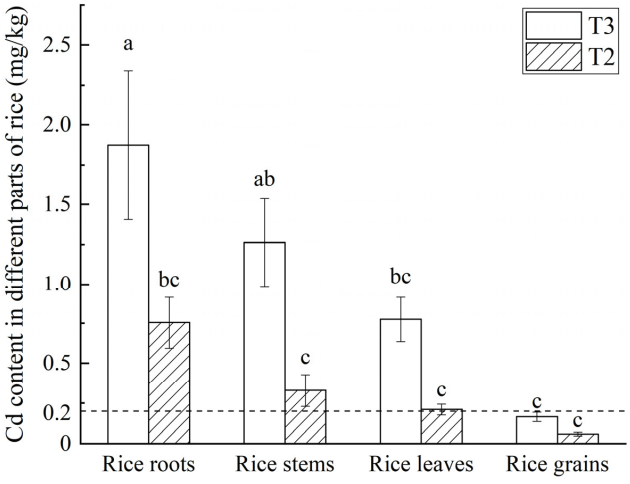

Figure 4. Variations in Cd contents in various tissues and organs of rice. The T3 group was the control group, and the T2 group used the geo-electrochemical technology. Different letters above the error lines indicate significant differences ($p < 0.05$). The dashed line indicates the legal limit of Cd in brown rice (0.2 mg/kg is derived from the Chinese national standard GB 2762-2022).

According to Figure 4, relative to the T3 control group without the technology, the Cd content in various parts of rice in the T2 experimental group decreased significantly, especially in the roots and stems of rice, where there was a significant difference ($p < 0.05$) compared with the T3 control group. Relative to the T3 control group, the Cd content in the roots, stems, leaves, and grains of the T2 experimental group decreased by 59.78%, 73.95%, 72.76%, and 64.56%, respectively. That shows that the GT effectively reduced the Cd element content in the tissues and organs of the rice plants. The Cd content in brown rice samples from the T2 and T3 experimental groups was evaluated in accordance with the "National Standard for Food Safety: Maximum Residue Limits for Pollutants in Food" (GB 2762-2022) [33] to determine whether it exceeded the limited standard of 0.2 mg/kg. It

was found that neither group's brown rice exceeded the limit of heavy metal Cd, indicating good food safety.

That shows that although the initial total soil Cd content of the T2 and T3 experimental groups exceeded the risk screening value for agricultural soil contamination, indicating that there might be ecological and environmental risks in that soil, brown rice had no above-standard Cd content after actual rice planting. In addition to the GT's reduction of the Cd content of the entire paddy soil–rice system, it also shows that the Cd content of rice grains did not have a strong positive correlation with soil Cd content. That is consistent with the views of Wang et al. [34], Wang et al. [35], and others; i.e., at the regional scale, the correlation between rice Cd content and soil Cd content is usually low, with a correlation coefficient R^2 of typically less than 0.2. The Cd content of rice is related to the Cd content in the soil but also to rice variety, soil pH, soil organic matter content, and soil moisture content. Huang et al. [36] found that low-accumulation rice varieties can still guarantee the safety of rice consumption when grown in paddy fields where the Cd content exceeds the risk screening value for agricultural soil contamination. Through research, Liu et al. [37] found that the soil pH value has an important effect on the Cd content of rice. As the soil pH value rises from 5.5 to 7.5, the safe critical value of soil Cd content to ensure that the Cd content in rice does not exceed the standard rises from 0.27 mg/kg to 0.8 mg/kg. Xue et al. [38] studied the effect of organic fertilizer on the Cd content in double-season rice. They found that the organic carbon components in organic fertilizer can reduce the availability of Cd in the soil and ultimately reduce the Cd content in rice. Chen et al. [39] found that over 90% of the Cd in rice is directly absorbed from the soil by the rice root system during the grain-filling period and transported to the grains. The higher the soil moisture content during the rice grain-filling period, the lower the activity of Cd in the soil and the lower the Cd content in the rice. Conversely, in the mid-to-late stage of rice grain filling, the lower the soil moisture content due to the dry climate or early drainage of the paddy field, the higher the activity of Cd in the soil and the higher the Cd content in the rice.

4.3. Variation in Cd Accumulation and Transport Capacity in Various Parts of Rice

The capacity of heavy metals to accumulate and be transported to different parts of rice can be reflected by the bioconcentration factor (BCF) and the translocation factor (TF) [40]. The BCF is the ratio of the heavy metal element content in various rice organs to the heavy metal element content in the soil. It can be used to characterize the difficulty of heavy metal element migration in the soil–rice system. The larger the coefficient, the stronger the ability of heavy metals to migrate from the soil to the plant. The BCF of Cd in various tissues and organs of rice in the T2 and T3 experimental groups is shown in Figure 5. According to Figure 5, there was a certain difference in the Cd BCF in various tissues and organs of rice in the T3 control group, which did not use the GT, and the T2 experimental group, which used the GT. In both experimental groups, the Cd BCF in rice plants from high to low was in the order of rice roots > rice stems > rice leaves > rice grains (brown rice), which is consistent with the change characteristics of Cd content in various parts of rice discussed in Section 4.2. At the same time, according to Figure 5, relative to the T3 control group, the Cd BCF in various parts of rice in the T2 experimental group decreased, among which the decrease in the root BCF was the most significant ($p < 0.05$). That shows that the GT had an influence on the accumulation capacity of Cd in the paddy soil in various tissues and organs of rice.

The TF refers to the ratio of the heavy metal content in the subsequent parts of rice (stem, leaf, and brown rice) to that in the antecedent parts (root, stem, and leaf) [41]. The TF is used to evaluate the transport capacity of heavy metals between different parts of the plant. The larger the TF, the stronger the transport capacity of that part for heavy metals [42]. Figure 6 shows the translocation factors of Cd from root to stem, stem to leaf, and leaf to brown rice in the T3 control group with no GT and the T2 experimental group with the GT. According to Figure 6, the translocation factors of Cd in rice plants in the T3 control

group from high to low were in the order of $TF_{stem/root} > TF_{leaf/stem} > TF_{brown\ rice/leaf}$. That indicates that the roots and stems of rice had a strong transport capacity for Cd, whereas the leaves had a relatively weak capacity. Relative to the T3 control group, the $TF_{stem/root}$ of the T2 group that used the GT significantly decreased ($p < 0.05$), but the $TF_{leaf/stem}$ and $TF_{brown\ rice/leaf}$ increased. This result indicates that the GT affects the process of rice stems and leaves to transport Cd, but the most crucial aspect is that it affects the process of rice roots to transport Cd. That reduced the accumulation of Cd in the aboveground parts of rice plants from the source, ultimately reducing the Cd content in brown rice. The combined effect of the BCF and the TF made the Cd content in the rice grains of the T2 experimental group that used the GT the lowest, meeting the national food safety standard.

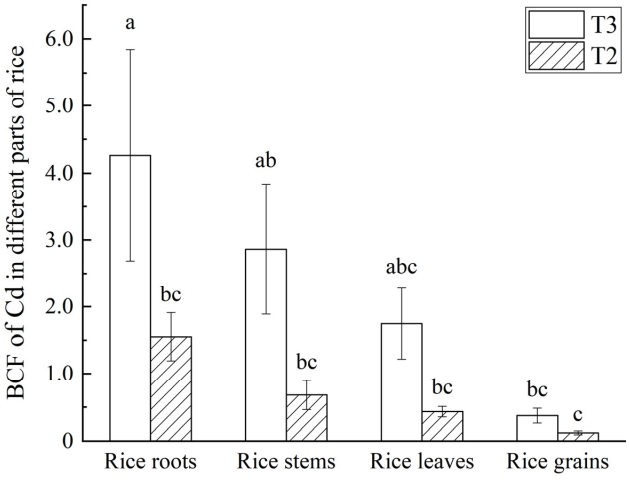

Figure 5. Variation in Cd bioconcentration factor in various tissues and organs of rice. The T3 group was the control group, and the T2 group used the geo-electrochemical technology. Different letters above the error lines indicate significant differences ($p < 0.05$).

4.4. Variation in the Content of the Seven Remaining Heavy Metal Elements of Paddy Soil

Before the experiment, soil sampling and related analyses were performed on the paddy soil. The results showed no exceedances for all seven elements except Cd. The content of the remaining seven heavy metal elements in the three experimental groups is detailed in Table 3. As presented in the table, relative to the initial content of heavy metal elements in soil without experimental treatment, the contents of Cr, Ni, Cu, Zn, As, Hg, and Pb in the soil of the T1, T2, and T3 experimental groups all decreased, with a significant reduction ($p < 0.05$) of Cr, Ni, and Cu. In accordance with GB 15618-2018 [23], it can be argued that after the experimental treatment, the content of seven heavy metal elements in the soil of each experimental group also meets the national standard.

The experimental results clearly indicate that the content of other heavy metal elements in the soil will decrease correspondingly when the GT is selected for the remediation of Cd-contaminated paddy field. Based on the above-mentioned results, it can be preliminarily speculated that under the action of a direct current electric field, some heavy metal elements in the paddy soil will also have directional migration and accumulation along with Cd, and then will be collected through the adsorbent materials around the electrodes, thus reducing the content of heavy metal elements in the soil. Therefore, the GT is anticipated to show a certain potential in the remediation and treatment of composite-contaminated soils with multiple heavy metal elements.

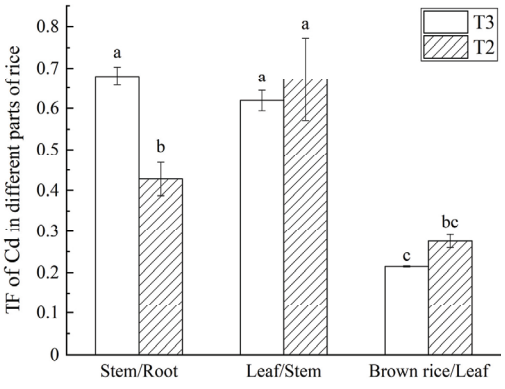

Figure 6. Variation in Cd translocation factor in various tissues and organs of rice. The T3 group was the control group, and the T2 group used the geo-electrochemical technology. Different letters above the error lines indicate significant differences ($p < 0.05$).

Table 3. The content of the remaining seven heavy metal elements of paddy soil in the Agricultural Science Institute experiment site.

Element	Cr	Ni	Cu	Zn	As	Hg	Pb
Initial value	53.59 ± 1.20 a	19.58 ± 0.41 a	31.99 ± 1.31 a	85.60 ± 4.52 a	20.97 ± 1.45 a	0.16 ± 0.01 a	63.25 ± 2.70 a
T1	47.37 ± 0.23 b	18.44 ± 0.26 b	25.35 ± 2.09 c	77.37 ± 2.57 a	17.45 ± 1.44 a	0.16 ± 0.01 a	57.75 ± 3.22 a
T2	45.78 ± 0.85 bc	18.49 ± 0.26 b	29.14 ± 1.13 ab	81.59 ± 1.76 a	20.46 ± 1.70 a	0.14 ± 0.00 a	60.97 ± 2.27 a
T3	44.45 ± 0.71 c	18.32 ± 0.29 b	27.72 ± 0.37 bc	79.86 ± 1.46 a	20.44 ± 0.38 a	0.15 ± 0.00 a	61.03 ± 2.52 a
Legal limit	250	70	50	200	30	0.5	100

Note: Units are mg/kg. The results are displayed as mean ± standard deviation. Different letters after the value indicate significant differences ($p < 0.05$). The legal limits are derived from Chinese national standards (GB 15618-2018).

5. Conclusions

(1) The experiment findings were that the GT was effective in removing the Cd element from paddy soil, particularly when it was applied directly to the soil. Therefore, it is suggested that in situ treatment of Cd-contaminated paddy fields should be carried out by the GT during the rice fallow period so as to ensure the safe use of the paddy fields.

(2) The GT effectively reduced the Cd element content in various parts of the rice plants by reducing the accumulation of Cd in soil by various tissues and organs such as rice roots, stems, leaves, and grains. Furthermore, the implementation of the GT affected the process of the rice plants to transport Cd from the underground parts to the aboveground parts; specifically, it affected the process of the rice root system to transport Cd, thereby ensuring the safe production of the rice.

(3) The results showed a good application prospect for the GT to reduce the content of the Cd element in the paddy soil. At the same time, the GT is also expected to show a certain potential in the remediation and treatment of composite-contaminated soils with multiple heavy metal elements.

Author Contributions: Conceptualization, Y.S. and M.W.; methodology, Y.S., M.W. and P.L.; investigation, Y.S., M.W. and Y.J.; data curation, Y.S., M.W. and Y.J.; writing—original draft preparation, Y.S. and M.W.; writing—review and editing, Y.S., M.W. and P.L.; visualization, Y.S. and M.W. All authors have read and agreed to the published version of the manuscript.

Funding: This research was funded by the Guangxi Science and Technology Planning Project (Grant No. 2021JJA150037) and the National Natural Science Foundation of China (Grant No. 42163004).

Institutional Review Board Statement: Not applicable.

Informed Consent Statement: Not applicable.

Data Availability Statement: Not applicable.

Acknowledgments: We would like to express our heartfelt gratitude to the Quanzhou County Institute of Agricultural Science in Guilin for providing the experimental base and conditions for this research. We also sincerely thank Binyan Chen, Quanhui Yan, and Xiaohong Deng for their help in this study.

Conflicts of Interest: The authors declare no conflict of interest.

References

1. Rai, P.K.; Lee, S.S.; Zhang, M.; Tsang, Y.F.; Kim, K.H. Heavy metals in food crops: Health risks, fate, mechanisms, and management. *Environ. Int.* **2019**, *125*, 365–385. [CrossRef]
2. Jarup, L.; Akesson, A. Current status of cadmium as an environmental health problem. *Toxicol. Appl. Pharmacol.* **2009**, *238*, 201–208. [CrossRef]
3. Nawrot, T.S.; Staessen, J.A.; Roels, H.A.; Munters, E.; Cuypers, A.; Richart, T.; Ruttens, A.; Smeets, K.; Clijsters, H.; Vangronsveld, J. Cadmium exposure in the population: From health risks to strategies of prevention. *Biometals* **2010**, *23*, 769–782. [CrossRef] [PubMed]
4. Satarug, S.; Moore, M.R. Adverse health effects of chronic exposure to low-level cadmium in foodstuffs and cigarette smoke. *Environ. Health Perspect.* **2004**, *112*, 1099–1103. [CrossRef] [PubMed]
5. Liu, X.; Tian, G.; Jiang, D.; Zhang, C.; Kong, L. Cadmium (Cd) distribution and contamination in Chinese paddy soils on national scale. *Environ. Sci. Pollut. Res.* **2016**, *23*, 17941–17952. [CrossRef] [PubMed]
6. Zhang, X.; Chen, D.; Zhong, T.; Zhang, X.; Cheng, M.; Li, X. Assessment of cadmium (Cd) concentration in arable soil in China. *Environ. Sci. Pollut. Res.* **2015**, *22*, 4932–4941. [CrossRef]
7. Fu, X.Q.; Liu, Y.B.; Yang, H.J.; Xu, Y.H.; Jin, H.Y.; Zhou, Z.M.; Dai, J.P. Effects and evaluation of rice cultivars combined with other remediation methods on heavy metal contents in cultivated land and rice. *Jiangsu Agric. Sci.* **2019**, *47*, 307–315. (In Chinese) [CrossRef]
8. Li, S.J.; Li, P.; Li, X.R.; Zhao, L.P.; Ma, M.T.; Zhao, T.K. The influence of concentration of Chromium, Cadmium in soil-crop system under different fertilizers and fertilization amount. *J. Agric. Resour. Environ.* **2015**, *32*, 235–241, (In Chinese with English Abstract). [CrossRef]
9. Yang, Z.; Guo, W.; Cheng, Z.; Wang, G.; Xian, J.; Yang, Y.; Liu, L.; Xu, X. Possibility of using combined compost-attapulgite for remediation of Cd contaminated soil. *J. Clean. Prod.* **2022**, *368*, 133216. [CrossRef]
10. Zhang, Y.P.; Tan, X.X.; Chen, X.Y.; Liang, J.H.; Ma, C.J.; Guo, Y.J.; Zhou, J.B. Effects of inorganic Silicon foliar fertilizer and soil conditioner on Plumbum and Cadmium absorption in rice. *Ecol. Environ. Sci.* **2020**, *29*, 388–393, (In Chinese with English Abstract). [CrossRef]
11. Kedziorek, M.A.M.; Bourg, A.C.M. Solubilization of lead and cadmium during the percolation of EDTA through a soil polluted by smelting activities. *J. Contam. Hydrol.* **2000**, *40*, 381–392. [CrossRef]
12. Zhang, Q.M.; Wang, H.M.; Lin, X.B.; Liu, H.; Wang, J.; Guo, N.J.; Yu, Y.; Zhang, H.Y.; Liu, Y.X.; Wu, H.L.; et al. Remediation effects of different passivators on Cadmium passivation in polluted farmland. *Acta Agric. Univ. Jiangxiensis* **2021**, *43*, 703–710, (In Chinese with English Abstract). [CrossRef]
13. Song, B.; Zhang, Y.X.; Tian, M.L.; Yang, Z.J.; Wang, F.P.; Chen, T.B. Potential for Cadmium contaminated farmland remediation with *Amaranthus hypochondriacus* L. *Chin. J. Environ. Eng.* **2019**, *13*, 1711–1719, (In Chinese with English Abstract).
14. Yu, C.L. Study on the Plant Growth Regulator Enhancing Remediation Effieiency of *Solanum nigrum* L. on Contaminated Soil by Cadmium. Ph.D. Thesis, Harbin University of Science and Technology, Harbin, China, 2011. (In Chinese with English Abstract).
15. Luan, Y.; Xu, J.; Zhou, J.; Wang, H.; Han, F.; Wang, K.; Lv, Y. Migration and removal of labile Cadmium contaminants in paddy soils by electrokinetic remediation without changing soil pH. *Int. J. Environ. Res. Public Health* **2022**, *19*, 3812. [CrossRef]
16. Xiao, H.P.; Tu, Q.Y.; Wu, L.H.; Le, S.; Hou, J.T. Influence of several typical soils on removal of Cadmium contaminants during electrokinetic remediation. *Chin. J. Environ. Eng.* **2017**, *11*, 1205–1210, (In Chinese with English Abstract).
17. Wen, D.; Fu, R.; Li, Q. Removal of inorganic contaminants in soil by electrokinetic remediation technologies: A review. *J. Hazard. Mater.* **2021**, *401*, 123345. [CrossRef]
18. Vocciante, M.; Caretta, A.; Bua, L.; Bagatin, R.; Ferro, S. Enhancements in ElectroKinetic Remediation Technology: Environmental assessment in comparison with other configurations and consolidated solutions. *Chem. Eng. J.* **2016**, *289*, 123–134. [CrossRef]
19. Cai, Z.; Sun, Y.; Deng, Y.; Zheng, X.; Sun, S.; Romantschuk, M.; Sinkkonen, A. In situ electrokinetic (EK) remediation of the total and plant available cadmium (Cd) in paddy agricultural soil using low voltage gradients at pilot and full scales. *Sci. Total Environ.* **2021**, *785*, 147277. [CrossRef]
20. Liu, W.Q.; Zhu, F.; Ma, S.Y. Research progress on the electrokinetic remediation of soil polluted by heavy metal. *Saf. Environ. Eng.* **2015**, *22*, 55–60, (In Chinese with English Abstract). [CrossRef]
21. Liu, P.; Wu, Z.; Luo, X.; Wen, M.; Huang, L.; Chen, B.; Zheng, C.; Zhu, C.; Liang, R. Pollution assessment and source analysis of heavy metals in acidic farmland of the karst region in southern China-A case study of Quanzhou County. *Appl. Geochem.* **2020**, *123*, 104764. [CrossRef]
22. Zheng, W. Investigation of background values of some heavy metal elements in agricultural soil environment in the north-eastern region of Guangxi, China. *J. Ecol. Rural Environ.* **1993**, *04*, 39–42+63–64. (In Chinese)

23. *GB 15618-2018*; Soil Environmental Quality Risk Control Standard for Soil Contamination of Agricultural Land. China Environment Publishing Group: Beijing, China, 2018.
24. Luo, X.R.; Ouyang, F.; Hu, Y.H.; Wen, M.L.; Wang, B.H. Low Voltage Bipolar Geo-Electric Extraction Device. Patent CN201096644, 6 August 2008.
25. Lu, R.S. *Soil Agricultural Chemistry Analysis Method*; China Agricultural Science and Technology Press: Beijing, China, 2000; pp. 147–211. (In Chinese)
26. *HJ 832-2017*; Soil and Sediment. Digestion of Total Metal Elements. Microwave Assisted Acid Digestion Method. China Environment Publishing Group: Beijing, China, 2017.
27. Clemens, S. Toxic metal accumulation, responses to exposure and mechanisms of tolerance in plants. *Biochimie* **2006**, *88*, 1707–1719. [CrossRef]
28. Cai, Y.; Xu, W.; Wang, M.; Chen, W.; Li, X.; Li, Y.; Cai, Y. Mechanisms and uncertainties of Zn supply on regulating rice Cd uptake. *Environ. Pollut.* **2019**, *253*, 959–965. [CrossRef] [PubMed]
29. Liu, H.; Zhang, C.; Wang, J.; Zhou, C.; Feng, H.; Mahajan, M.D.; Han, X. Influence and interaction of iron and cadmium on photosynthesis and antioxidative enzymes in two rice cultivars. *Chemosphere* **2017**, *171*, 240–247. [CrossRef] [PubMed]
30. Li, H.Y. Effects of Calcium on Chemical Speciation of Cadmium in the Soil and Cadmium Absorbed by Rice. Master's Thesis, Guizhou Normal University, Guizhou, China, 2022. (In Chinese with English Abstract). [CrossRef]
31. Zhou, J.; Yang, Y.; Meng, G.Y.; Ma, G.H.; Chen, Y.Y. Cadmium accumulation and translocation efficiency of rice under different Cadmium-polluted soils. *Chin. J. Ecol.* **2018**, *37*, 89–94, (In Chinese with English Abstract). [CrossRef]
32. Zhao, X.; Li, F.Y.; Zhang, D.M.; Qi, Z.P. Relationship between paddy soils Cadmium pollution and Cadmium content in rice. *J. Agro-Environ. Sci.* **2009**, *28*, 2236–2240, (In Chinese with English Abstract).
33. *GB 2762-2022*; National Standard for Food Safety: Maximum Residue Limits for Pollutants in Food. Standards Press of China: Beijing, China, 2022.
34. Wang, P.; Chen, H.; Kopittke, P.M.; Zhao, F.J. Cadmium contamination in agricultural soils of China and the impact on food safety. *Environ. Pollut.* **2019**, *249*, 1038–1048. [CrossRef]
35. Wang, J.; Wang, P.M.; Gu, Y.; Kopittke, P.M.; Zhao, F.J.; Wang, P. Iron-Manganese (Oxyhydro) oxides, rather than Oxidation of Sulfides, determine mobilization of Cd during soil drainage in paddy soil systems. *Environ. Sci. Technol.* **2019**, *53*, 2500–2508. [CrossRef]
36. Huang, J.L.; Lin, H.; Lai, Y.H.; Zhang, Q.L.; Chen, L.F. Anti-Cadmium accumulation ability of different rice varieties. *J. Chin. Cereals Oils* **2020**, *35*, 6–10, (In Chinese with English Abstract).
37. Liu, Y.P.; Kan, Z.Z.; Jin, L.X.; Li, Z.H. The study of Cadmium assignment in soil-large amount crop and its environmental significance. *Geosciences* **2009**, *23*, 372–377, (In Chinese with English Abstract).
38. Xue, Y.; Yin, Z.R.; Sheng, H.; Ma, H.L.; Zhou, Q.; Song, D.Q.; Zhang, Y.Z. Reduction of soil Cadmium activity and rice Cadmium content by 4-year-consecutive application of organic fertilizer. *Environ. Sci.* **2020**, *41*, 1880–1887, (In Chinese with English Abstract). [CrossRef]
39. Chen, H.; Wang, P.; Gu, Y.; Kretzschmar, R.; Kopittke, P.M.; Zhao, F.J. The within-field spatial variation in rice grain Cd concentration is determined by soil redox status and pH during grain filling. *Environ. Pollut.* **2020**, *261*, 114151. [CrossRef] [PubMed]
40. Zhu, C.; Wen, M.L.; Liu, P.F.; Chen, B.Y.; Bao, H.Y.; Zhao, Y.Q.; Chen, H.; Yang, Y.B. Distribution characteristics and pollution evaluation of heavy metals in typical organic rice in Lingchuan county, Guilin city. *Geosciences* **2021**, *35*, 1433–1440, (In Chinese with English Abstract). [CrossRef]
41. Gu, J.F.; Zhou, H.; Jia, R.Y.; Wang, Q.Q.; Li, H.C.; Zhang, P.; Peng, P.Q.; Liao, B.H. Effects of a tribasic amendment on Cadmium and Arsenic accumulation and translocation in rice in a field experiment. *Environ. Sci.* **2018**, *39*, 1910–1917, (In Chinese with English Abstract). [CrossRef]
42. Liu, J.; Ma, X.; Wang, M.; Sun, X. Genotypic differences among rice cultivars in lead accumulation and translocation and the relation with grain Pb levels. *Ecotoxicol. Environ. Saf.* **2013**, *90*, 35–40. [CrossRef] [PubMed]

applied sciences

MDPI

Article

Characterization and Source Analysis of Heavy Metal(loid)s Pollution in Soil of an Industrial Park in Kunming, China

Wenping Luo [1,2], Pingtang Wei [3,*], Yan Zhang [1,2,*] and Chengshuai Sun [1,2]

[1] Faculty of Land Resources Engineering, Kunming University of Science and Technology, Kunming 650093, China; luowen9967@163.com (W.L.); 15667635897@163.com (C.S.)
[2] South-West Institute of Geological Survey, Geological Survey Center for Nonferrous Metals Resources, Kunming 650093, China
[3] Kunming Geological Exploration Institute of China Metallurgical Geology Bureau, Kunming 650024, China
* Correspondence: weipingtang@163.com (P.W.); m15925201825@163.com (Y.Z.)

Abstract: This study investigated the characteristics and sources of heavy metal(loid) pollution in the soil of a key industrial park in Kunming, China. In total, 60 soil samples (40 from agricultural land and 20 from construction land) were collected from and around the park. The soil pH and contents of Arsenic (As), lead (Pb), copper (Cu), zinc (Zn), cadmium (Cd), mercury (Hg), nickel (Ni), and chromium (Cr) were measured. The contents of the eight heavy metal(loid)s were analyzed using the background values of heavy metal(loid)s in the Kunming soil. The pollution load, geoaccumulation, and Nemero Comprehensive Pollution Indices were used for environmental risk evaluation. Cluster and principal component analyses were used to resolve heavy metal(loid) sources. Cd was enriched in construction and agricultural soils. As, Hg, Cd, Pb, Cu, and Zn exhibited large spatial differentiation and were significantly affected by the external environment. A regional pollution load index of 3.02 indicated overall heavy pollution. The pollution load index for each heavy metal(loid) indicated light pollution. The geoaccumulation index indicated relatively severe As, Cd, Cu, Pb, and Zn pollution. The Nemero Composite Pollution Index value showed that the study area was heavily polluted, with construction land being mildly polluted by Cd, and agricultural land being moderately polluted. The results of the spatial distribution show that there were high levels of contamination in the center. Correlation and principal component analyses showed that the pollution sources of the eight heavy metal(loid)s varied. Hg, Cd, and Pb originate primarily from industrial and agricultural pollution. Traffic sources significantly impacted Cu, Pb, Cd, and Cr. Natural sources are the main sources of Cr, Ni, and Cd. Ni is also affected by industrial sources, whereas Zn and Cu are affected by agricultural pollution. The influences of As, Cd, and Pb on the surface soil in the study area were more serious. Cd is more widely polluted and should be a priority in controlling soil heavy metal(loid)s.

Keywords: different site; pollution assessment; source analysis; Atomic fluorescence method; inductively coupled plasma mass spectrometry

Citation: Luo, W.; Wei, P.; Zhang, Y.; Sun, C. Characterization and Source Analysis of Heavy Metal(loid)s Pollution in Soil of an Industrial Park in Kunming, China. *Appl. Sci.* **2024**, *14*, 6547. https://doi.org/10.3390/app14156547

Academic Editor: Mauro Marini

Received: 4 June 2024
Revised: 24 July 2024
Accepted: 24 July 2024
Published: 26 July 2024

1. Introduction

Heavy metal(loid)s are characterized by their accumulation, persistence, and toxicity. Heavy metal(loid)s are easily absorbed by humans and animals through the food chain, jeopardizing the ecology and human health [1]. The sources of heavy metal(loid)s in soil are relatively complex and mainly comprise anthropogenic and natural sources [2]. Anthropogenic sources include mining, smelting, wastewater, exhaust, fertilizers, and pesticides. Natural sources include rock weathering during soil and volcanic eruptions [3]. Qualitative identification of soil heavy metal(loid) pollution and source analysis are important for controlling soil heavy metal(loid) pollution. Timely determination of soil heavy metal(loid) levels and their source pathways is particularly important for preventing and controlling soil heavy metal(loid) pollution.

Identification of pollution sources is a scientific prerequisite to carry out pollution prevention and control work, and previous researchers have used stable isotope techniques (Pb) [4,5], new geochemical tracers (Cd) [6], and multivariate statistical analyses (PCA and CA) [7] to qualitatively analyze the sources of heavy metals, whereas the chemical mass balance (CMB) model [8], the absolute principal component score-multivariate linear regression (APCS-MLR) model [9], UNMIX model [10], and Positive Matrix Factorization (PMF) [11] were used for quantitative analysis, and the accuracy of their results can be significantly affected by the number of samples. T-NSE [12], which has higher accuracy and flexibility, uses neural networks to derive t-SNE hyperparameter combinations. Semi-supervised learning, which has the advantages of both supervised and unsupervised learning, can be used mainly for datasets with mainly unlabeled data, and few labeled data and automatic clustering of unlabeled data [13] improves the machine learning prediction performance to a great extent.

With industrialization and urbanization, soil heavy metal(loid) pollution from industrial parks has become increasingly significant. Different concentrations of Cd, Zn, Pb, and Hg pollution have been reported in various industrial parks [14]. The highly contaminated samples were mainly distributed in enterprise-intensive areas [15].

The important mineral resource regions in China include Sichuan, Yunnan, and Guizhou. The development of these regional economies has driven heavy metal(loid) pollution by Cd, Zn, Pb, As, and other heavy metal(loid)s [16,17]. Heavy metal(loid) pollution of soils is more serious in the Yunnan Province, especially in industrial parks where polluting enterprises are concentrated, owing to the early non-standardized treatment of pollutants, lack of a functional layout, and other reasons. This could result from the extensive accumulation of heavy metal(loid)s in the surrounding soil. However, little is known about heavy metal(loid) pollution in the soil of industrial parks. Furthermore, the unknown characteristics of soil heavy metal(loid) pollution, unclear spatial distribution patterns, and unknown sources make it difficult to provide a basis for controlling soil pollution sources and remediating contaminated land in the area.

This study was conducted in an industrial park in Kunming, Yunnan Province, China. Heavy metal(loid)s in the surface soil (0 to an approximate depth of 20 cm) were studied; evaluation of soil contamination in different land use types using the pollution load index, geoaccumulation index, and Nemero composite index methods; and analysis of heavy metal(loid) sources, which provide theoretical support for the prevention and control of heavy metal(loid) pollution of soil in Kunming City, will inform efforts to enhance regional environmental quality.

2. Materials and Methods

2.1. Overview of the Study Area

The study area is a key industrial park in the northernmost area of Kunming City, Yunnan Province, covering a total area of 1858.79 km^2. The study area is divided into two groups. Block 1 is mainly used in chemical industries involving heavy metal(loid) Cu and phosphorus (P). This area focuses on the comprehensive utilization of resources, the processing of ferrous, rare, and precious metals, and the extension and development of new building materials. Block 2 contains advanced manufacturing industries that focus mainly on foodstuffs, light industry, and machinery.

At the end of 2018, there were ferrous metal enterprises, such as the production of ferroalloys, manganese (Mn), Cr, silicon (Si), furnace charge, and steelmaking deoxidizers; nonferrous and rare metal enterprises, such as Cu smelting and sulfuric acid production; P-related chemical enterprises, such as production of feed additives, hazardous chemicals, fertilizer, and other products; machinery manufacturing industries; food and drug processing industries, including pharmaceutical manufacturing, food processing, and others; building materials enterprises, including production of cement, gypsum, mechanized sand, and other products; battery car manufacture; and processing of plastic and other products [18].

2.2. Sample Collection and Analyses

Based on the sewage discharge of enterprises in the industrial park, the distribution of sensitive points within a certain range in the surrounding area, the original use function of the land parcels, the characteristics of contamination, the soil monitoring network in the industrial park, and the surrounding area were constructed. One hundred samples of differently utilized land surface soil (0–20 cm) were collected; 60 samples were from construction land and 40 from agricultural land. To accurately determine whether the soil was polluted, the pollutant type, and the degree of pollution, sampling points were designed by combining professional judgment and systematic random distribution (Figure 1).

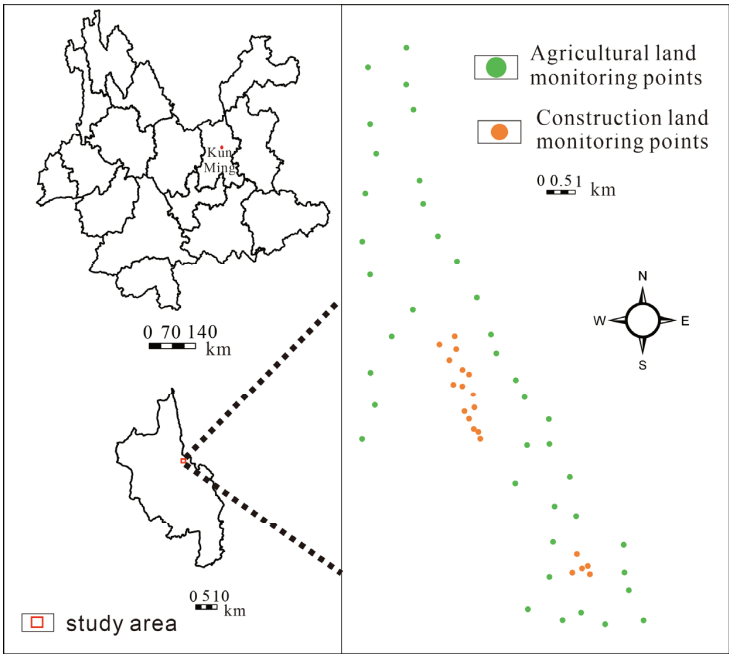

Figure 1. Map of the distribution of soil sample collection points in an industrial park in Kunming.

Soil samples were collected in strict accordance with the China Soil Environmental Quality Risk Control Standards for Soil Pollution of Agricultural Land (GB15618-2018) [19], Soil Environmental Quality Risk Control Standards for Soil Pollution of Construction Land (GB36600-2018) [20], Technical Specification for Soil Environmental Monitoring (HJ/T166-2004) [21], Determination of eight Effective State Elements in Soil (HJ804-2016) [22], and other relevant technical specifications. The samples were prepared using non-metallic tools and utensils to remove impurities such as plant roots and gravel (at least 2 kg per portion), packed in cloth bags, dried naturally, crushed with a wooden stick, passed through a 2 mm aperture sieve, mixed and weighed, and then sent to the laboratory for analysis. Sample testing was performed at the Testing Center of the China Inspection Body and Laboratory Mandatory Approved by the qualified Kunming Geological Survey Institute of the General Administration of Metallurgical Geology of China. The sample testing process adopted national-level standard substances (GBW series) for quality control. Each batch of the analytical process involved quality control measurements of parallel double samples. Eight elements (As, Pb, Cu, Zn, Cd, Hg, Ni, and Cr) were detected. The Cr content was determined using flame atomic absorption spectroscopy. The As and Hg contents were determined using atomic fluorescence spectrometry. Cd, Pb, Ni, and Cu contents were determined by inductively coupled plasma mass spectrometry. Zn content was determined

using inductively coupled plasma emission spectrometry. Finally, pH was determined using a potentiometric method.

2.3. Pollution Load Index (PLI)

The PLI evaluates the integrated pollution levels of multiple heavy metal(loid)s in the soil, visualizes the contribution of pollutants to the polluted area, and determines the spatial and temporal trends of heavy metal(loid)s a site [23]. The PLI can be used to determine whether pollutants are under the integrated control of natural and anthropogenic sources [24,25]. The formulae used are as follows:

$$PLI = \sqrt[n]{CF_1 \times CF_2 \times \ldots \times CF_n} \quad (1)$$

$$CF_i = C_i / C0_i \quad (2)$$

where PLI is the pollution load index of a point in the study area, n is the number of polluted heavy metal(loid) elements, CF_i is the pollution coefficient of heavy metal(loid) i in the soil, C_i is the measured content of heavy metal(loid) i in the soil (mg/kg), and $C0_i$ is the evaluation standard of heavy metal(loid) i. The background value of the heavy metal(loid)s in the soil of Kunming was chosen as the standard evaluation value (mg/kg).

The PLI for a given region is calculated as follows.

$$P_{zone} = \sqrt[m]{PLI_1 \times PLI_2 \times \ldots \times PLI_m} \quad (3)$$

where P_{zone} is the regional PLI, n is the number of metal elements, and m is the number of sampling points. The evaluation levels are presented in Table 1.

Table 1. Evaluation and classification of soil heavy metal(loid) pollution.

Geological Cumulative Index	Degree of Contamination	Nemero Combined Pollution Index	Degree of Contamination	Pollution Load Index	Degree of Contamination
Igeo $\leq$ 0	Uncontaminated	$P_N \leq 0.7$	Uncontaminated	PLI < 1	Uncontaminated
0 < Igeo $\leq$ 1	Low pollution	0.7 < $P_N \leq$ 1	Warning Level of Caution	1 $\leq$ PLI < 2	Low pollution
1 < Igeo $\leq$ 2	Medium pollution	1 < $P_N \leq$ 2	Low pollution	2 $\leq$ PLI < 3	Moderate pollution
2 < Igeo $\leq$ 3	Medium-strong pollution	2 < $P_N \leq$ 3	Moderate pollution	PLI > 3	High pollution
3 < Igeo $\leq$ 4	Strong pollution	P_N > 3	High pollution		
4 < Igeo $\leq$ 5	Strong-extreme pollution				
Igeo > 5	extreme pollution				

2.4. Geoaccumulation Index (I_{geo})

This index integrates the effects of anthropogenic factors and soil matrices on the distribution of heavy metal(loid) contents. I_{geo} is widely used to study soil heavy metal(loid) pollution caused by anthropogenic activities [26]. The formula is as follows.

$$I_{geo} = \log_2[C_n / 1.5 \times B_n] \quad (4)$$

where I_{geo} is the geoaccumulation index, C_n is the measured value of elements in soil (mg/kg), B_n is the background value of heavy metal(loid)s in the soil (mg/kg), and 1.5 reflects the fluctuation of the background value in different areas due to differences in soil matrices. The evaluation levels are listed in Table 1.

2.5. Nemero Combined Pollution Index

Based on a single factor index, this index synthesizes the pollution level of each heavy metal(loid) and highlights the environmental damage caused by heavy metal(loid)s [27,28]. The formula is as follows.

$$PN = \sqrt{\frac{p_{iave}^2 + p_{imax}^2}{2}} \quad (5)$$

$$P_i = C_i / S_i \quad (6)$$

where P_N is the soil heavy metal(loid) Nemero Comprehensive Pollution Index, P_{iave} is the average value of n heavy metal(loid) single factor pollution index; P_{imax} is the maximum value of n heavy metal(loid) single factor pollution index; C_i is the measured value of soil heavy metal(loid) i content (mg/kg), and S_i is the evaluation standard for heavy metal(loid) i pollution in soil. Soil Environmental Quality Construction Land Soil Pollution Risk Control Standards (GB15618-2018) and Soil Environmental Quality Agricultural Land Soil Pollution Risk Control Standards (GB36600-2018) [19,20] were selected as the heavy metal(loid) control standard values. The evaluation levels are listed in Table 1.

3. Results

3.1. Statistical Characterization of the Meta-Content of the Selected Heavy Metal(loid)s in Soil Samples

The mean soil pH was 7.8 and 9.02 for construction and agricultural lands, respectively (Table 2). The average heavy metal(loid) content in the surface soil was in the order of Pb > Zn > Cu > As > Cd > Ni > Hg > Cr for construction land and Zn > Cu > Cr > Pb > Ni > As > Cd > Hg for agricultural land.

Table 2. Heavy metal(loid) contents and soil statistical characteristics.

Land Use Patterns		pH	As	Hg	Cd	Pb	Ni	Cu	Zn	Cr
construction land	Max.		9.11	1912.00	18.40	1208.00	6484.00	93.40	3429.00	7455.00	1.40
	Min.		5.23	14.70	0.06	0.61	43.30	19.40	48.20	63.70	0.50
	Avg.		7.80	423.72	3.23	92.15	1153.11	60.21	692.78	1136.99	0.87
	SD		0.90	555.37	4.86	259.33	1561.01	18.48	909.51	1664.64	0.27
	CV		0.12	1.31	1.51	2.81	1.35	0.31	1.31	1.46	0.31
agricultural land	Max.		9.46	38.40	0.50	7.85	298.00	74.40	249.00	388.00	129.00
	Min.		6.05	11.20	0.05	0.69	35.60	22.40	43.20	111.00	51.10
	Avg.		8.02	23.08	0.16	2.29	76.61	45.40	141.10	206.38	80.57
	SD		0.54	7.11	0.10	1.45	43.01	13.96	64.23	65.96	15.08
	CV		0.07	0.31	0.63	0.63	0.56	0.31	0.46	0.32	0.19
Upper Crustal Mean (UCC)				4.80	0.05	0.09	17.00	47.00	28.00	67.00	92.00
Enrichment Factor (EF)	construction land			88.28	64.60	1023.89	67.83	1.28	24.72	16.97	0.01
	agricultural land			4.81	3.20	25.44	4.51	0.97	5.04	3.08	0.86
screening value	construction land			60	38	65	800	900	18,000	-	5.7
	agricultural land	$5.5 \leq pH \leq 6.5$		30	0.5	0.3	90	70	50	200	150
		$6.5 < pH \leq 7.5$		25	0.6	0.3	120	100	100	250	200
		$pH > 7.5$		20	1	0.6	170	190	100	300	250

The coefficients of variation (Cv) [29] of As, Hg, Cd, Pb, Cu, and Zn in construction land were all >1, which is an anomalously strong variation, indicating that they are greatly influenced by human activities. Cd content was significantly higher than the background

value in Kunming [30]. The Cv values of the contents of Hg, Cd, and Pb contents in the agricultural soils were >0.5, which also indicated strong variation. Relative to the background values in Kunming and the contents of the upper crust [31], the study area was significantly enriched in Cd (1023.89 times). All elements exceeded the background values in the agricultural land in Kunming, except for Cr (the data were logarithmically (In) treated to observe subtle changes in heavy metal(loid) content data in a more subtle manner considering that the data differed too much) (Figure 2).

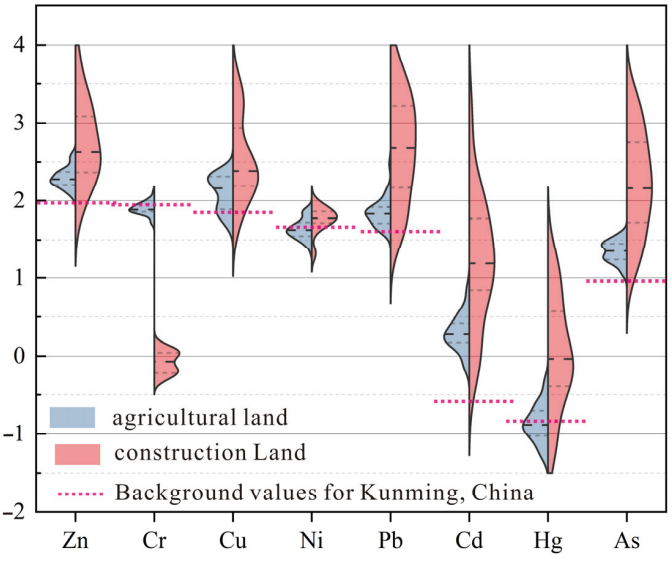

Figure 2. The content of soil sampling points in construction land and agricultural land was compared with the background value of Kunming City.

A comparison of the screening values (Table 2) revealed certain points in the soil samples where different heavy metal(loid) concentrations were exceeded. In the 20 sample points of the construction land soil, the contents of As, Cd, and Pb exceeded the standards in 14 (70%), five (25%), and eight (40%) samples, respectively. The concentrations of Cd, As, and Cu in the 40 soil sample points on the agricultural land exceeded the standards in 40 (100%), 22 (55%), and 25 (62.5%) samples, respectively. In these soil samples, Zn and Pb exceeded the relevant standards in only 15% and 2.5%, respectively. None of the remaining heavy metal(loid)s exceeded the relevant standards.

3.2. Characterization of Spatial Distribution and Pollution Evaluation

3.2.1. PLI

The PLI was used to evaluate and analyze the pollution characteristics of soil heavy metal(loid)s in the study area. The zone of soil heavy metal(loid)s in the study area was 3.02, indicating heavy soil pollution. The PLI values for each sampling point (Table 3) showed that the proportions of non-polluted, lightly polluted, moderately polluted, and heavily polluted samples were 1.7, 53.3, 15, and 30%, respectively, with light pollution being predominant. The statistical results of the soil contamination levels of different land use types in the study area showed that the percentage of contaminated sample points on construction land (100%) was higher than that on agricultural land (97.5%).

Table 3. Statistical characteristics of pollution levels in soil samples of different land use types.

Pollution Load Index	Agricultural Land	Construction Land	Total	Proportions (%)
Uncontaminated	1	0	1	1.7
Low pollution	28	4	32	53.3
Moderate pollution	9	0	9	15
High pollution	2	16	18	30
Total (number of sampling points)	40	20	60	100
Proportion of pollution (%)	97.5	100	98.3	

Note: The number of statistics is the number of sampling points.

3.2.2. Geoaccumulation and Nemero Composite Pollution Indices

The I_{geo} results revealed slight contamination with all heavy metal(loid)s, except for Cr (Figure 3). The contaminated samples, relative to the total number of samples, were in the following order Cd > As > Zn > Cu = Pb > Hg > Ni > Cr.

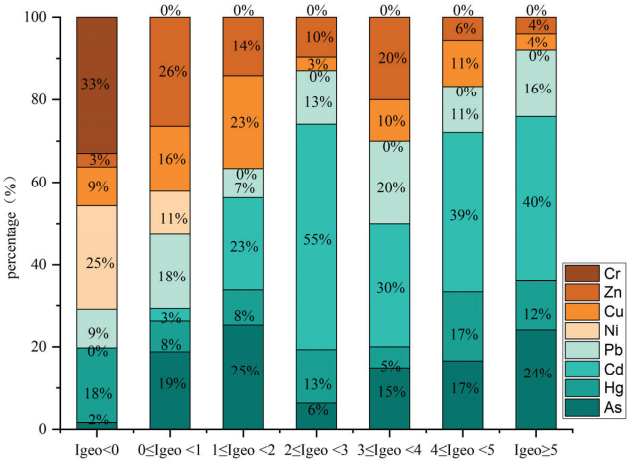

Figure 3. Proportion of geo-accumulation index contaminated samples.

The degree of soil heavy metal(loid) pollution is shown in Table 4. All samples showed heavy pollution (P_N > 3). However, the Nemero Composite Pollution Index of the construction land was higher than that of agricultural land. Construction land was contaminated with As and Pb to a greater extent than agricultural land. Agricultural land was heavily contaminated with As, mildly contaminated with Cd and Pb, and moderately contaminated with Cd.

Table 4. Degree of soil heavy metal(loid) pollution.

Item	P_i								P_N
Heavy Metal(loid)	**As**	**Hg**	**Cd**	**Pb**	**Ni**	**Cu**	**Zn**	**Cr**	
Construction land	7.06	0.08	1.42	1.44	0.07	0.04	-	0.15	35.51
Agricultural land	0.31	0.09	2.22	0.17	0.1	0.62	0.2	0.06	7.38

Note: '-' means that there is no such reference value in the Soil Pollution Risk Control Standard for Construction Land (GB36600-2018).

3.3. Source Analysis of Heavy Metal(loid)s

3.3.1. Spatial Distribution Characteristics

Using the inverse distance-weighted interpolation method in the statistical module of ArcGIS 10.8 software (10.8.12790), the contents of 60 surface soil sample points were

interpolated and analyzed to obtain the spatial distribution of the contents of the eight heavy metal(loid)s (Figure 4) and different distribution characteristics in the region. The soil As content was high in the center of the area and symmetrically distributed in the northwest and southeast. The Ni content is high in the central and southeastern regions. The content distributions of Hg and Pb were very similar, with two highly polluted areas in the center of the area. Areas were highly polluted with Cd and Zn. The Cu content was distributed as an island with a high center and low circumference, and its content gradually decreased along circumference. The distribution pattern of Cr was completely different from that of other heavy metal(loid)s, with the presence of two highly polluted areas in the southeast. In general, the distribution characteristics of the other seven elements are similar. The high pollution content in the center of the area was primarily due to it being an industrial area dominated by heavy metal(loid) smelting, P-related chemical industries, and other relevant industries. It was initially inferred that some heavy metal(loid)s in the study area originated from industrial parks.

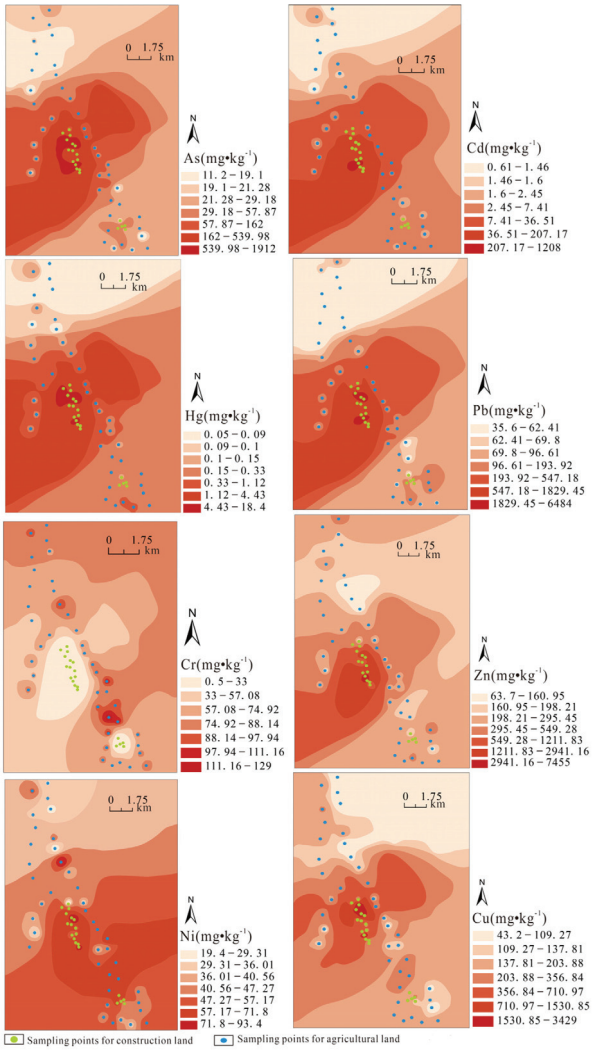

Figure 4. Spatial distribution map of heavy metal(loid) contents in soil.

3.3.2. Heavy Metal(loid) Correlation Analysis

To investigate the geochemical characterization of heavy metal(loid)s in the soils of construction and agricultural lands in the study area, Pearson correlation was performed for analysis of the contents of heavy metal(loid)s (Table 5). In the construction land (A), at the $p < 0.01$ and $p < 0.05$ levels, all the elements, except for Cr, showed highly significant positive correlations between the two elements. Excess As, Cd, and Pb showed highly significant positive correlations with other elements. In the Pearson correlation coefficient table of heavy metal(loid)s in agricultural land soil (B), at $p < 0.01$ level, Cr was the only element showing highly significant positive correlation with Ni. At $p < 0.05$, Ni was the only element that showed a highly significant positive correlation with Cd, indicating that a portion of the heavy metal(loid)s in the soil (Cr, Ni, and Cd) had other sources. Cd, which exceeded the standard, showed a highly significant positive correlation with the other elements, with the exception of Cr.

Table 5. Pearson correlation coefficients of different elements in construction land and agricultural land.

Item		As	Hg	Cd	Pb	Ni	Cu	Cr	Zn
Construction land (A)	As	1							
	Hg	0.950 **	1						
	Cd	0.954 **	0.906 **	1					
	Pb	0.925 **	0.816 **	0.918 **	1				
	Ni	0.541 *	0.456 *	0.640 **	0.616 **	1			
	Cu	0.795 **	0.769 **	0.764 **	0.777 **	0.631 **	1		
	Cr	0.266	0.157	0.380	0.281	0.278	0.154	1	
	Zn	0.874 **	0.756 **	0.920 **	0.898 **	0.608 **	0.701 **	0.408	1
Agricultural land (B)	As	1							
	Hg	0.583 **	1						
	Cd	0.680 **	0.817 **	1					
	Pb	0.515 **	0.620 **	0.517 **	1				
	Ni	0.199	0.294	0.346 *	0.256	1			
	Cu	−0.017	0.361 *	0.411 **	0.061	0.586 **	1		
	Cr	0.250	0.168	0.197	0.163	0.721 **	0.286	1	
	Zn	0.203	0.397 *	0.325 *	0.404 **	0.093	0.293	−0.012	1

Note: * indicates that the correlation is significant at the $p < 0.05$ level (two-sided); ** indicates that the correlation is significant at the $p < 0.01$ level (two-sided).

3.3.3. Principal Component Analysis of Heavy Metal(loid) Elements

To further analyze the heavy metal(loid) pollution characteristics of construction and agricultural lands, the variables were subjected to principal component analysis. This analysis is one of the most important means for determining the sources of heavy metal(loid)s [32] (Table 6A). The three principal component factors obtained by rotational solving contributed approximately 92.39%, and the first principal component factor (PC1) contributed 58.60% of the variance. Six elements (As, Hg, Cd, Pb, Cu, and Zn) exhibited high loadings, indicating similar origins. The second principal component factor (PC2) contributed 18.99%, with high loadings of Ni and Cu. The contribution of the third principal component (PC3) was approximately 14.81%, and Cr had a high loading. Figure 5A depicts that the elemental components with higher scores in PC1 and PC2 were identical, indicating similar origins. Pearson's correlation analysis indicates a highly significant correlation between these elements.

The three principal component factors of the rotation solving soil samples from the agricultural land (Table 6B) contributed approximately 78.43%, whereas PC1 contributed approximately 35.34%, with As, Hg, Cd, and Pb having the highest scores. Ni and Cr had the highest PC2 scores (with approximately 24.75%). PC3 had the highest scores for Cu and Zn, explaining approximately 18.34% of the overall variation. The results of the Pearson correlation analysis are shown in Figure 5B. Therefore, heavy metal(loid)s have similar sources in construction and agricultural soils.

Table 6. Principal component analysis results of soil heavy metal(loid) elements in construction land and agricultural land.

Item	Construction Land (A)			Agricultural Land (B)		
	Principal Component Factors (Maximum Variance Rotated Solution)					
	PC1	PC2	PC3	PC1	PC2	PC3
As	0.956	0.223	0.124	0.877	0.128	−0.166
Hg	0.951	0.137	0.002	0.805	0.130	0380
Cd	0.893	0.324	0.254	0.798	0.214	0.323
Pb	0.869	0.352	0.159	0.781	0.038	0.147
Ni	0.319	0.920	0.156	0.155	0.898	0.222
Cu	0.739	0.505	−0.050	−0.020	0.533	0.756
Cr	0.125	0.104	0.974	0.157	0.884	−0.128
Zn	0.813	0.332	0.325	0.338	−0.166	0.729
eigenvalue	4.696	1.519	1.185	2.827	1.980	1.467
variance (%)	58.596	18.985	14.813	35.340	24.752	18.336

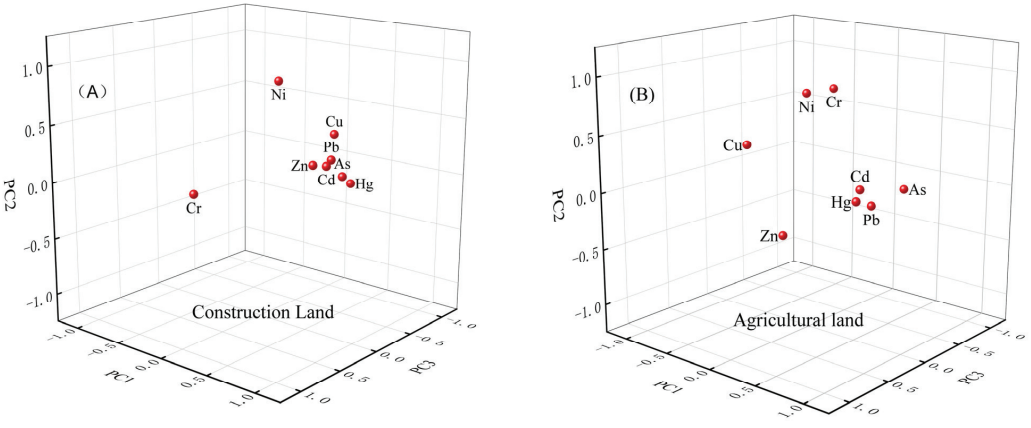

Figure 5. Spatial distribution of principal components of heavy metal(loid)s in soil of construction land (**A**) and agricultural land (**B**).

4. Discussion

4.1. Heavy Metal(loid) Pollution and Risk Assessment

Three evaluation methods were selected to accurately assess the status of soil heavy metal(loid) pollution in the industrial parks, understand the contribution of heavy metal(loid) pollutants to the soil environment in the study area, and perform risk evaluation. The results differed owing to the different evaluation methods used. The three evaluation methods revealed that As, Cd, and Pb pollution in the study area was concerning. In particular, Cd contamination sites were more extensive, consistent with a previous study [33]. Varying degrees of As (which has a high risk of carcinogenicity), Pb, and, most seriously, Cd contamination were evident in all areas of Yunnan [34–37].

4.2. Source Analysis of Heavy Metal(loid) Pollution

Accurate identification of pollution sources is vital for the prevention and control of soil heavy metal(loid) pollution [38,39]. Pearson and principal component analyses were used to broadly classify the sources of the eight heavy metal(loid)s contaminating construction land into three categories. During the first stage (As, Cd, Hg, Pb, and Zn), the mean values of these elements significantly exceeded the soil background values in Kunming (Figure 2). The Cv values of As, Hg, Cd, Pb, and Zn were high, indicating that they were subjected to large anthropogenic factors. Industrial pollution significantly affects

As and Hg are greatly affected by industrial pollution [40,41]. There are more vehicles in industrial parks, and these enterprises include automobile recycling and dismantling. Cd and Pb may originate from automobile exhaust emissions and tire wear, whereas Pb and Zn may originate from engine wear, braking, or other sources [42]. Metal smelting is the primary cause of Cd and Pb pollution [43,44].

The second category (Ni and Cu) includes elements that occur in metal smelting wastes [45,46]. The third category comprises only Cr and is strongly influenced by motor vehicle exhaust [47], although Cr is released in varying degrees from various parts of the cement production process [48].

The eight heavy metal(loid)s in the agricultural land were divided into three categories. In the first stage (As, Hg, Cd, and Pb), the average values of the four elements were higher than the background values of the soil in Kunming. The spatial variability of Hg, Cd, and Pb was more obvious. Irrational use of fertilizers and pesticides has led to increased concentrations of As, Cd, and Pb in soil [49–51]. Hg contamination is caused by industrial and agricultural pollutants (the latter involves the long-term use of chemical pesticides) [52,53]. Cd can reflect a high Cd geological background and transportation source [54,55].

The second category (Ni and Cr) is less affected by anthropogenic factors. Ni and Cr are closely related to soil matrix formation [56,57]. The third category comprises Cu and Zn, which originate from chicken and pig manure applied during cultivation. Fertilizers containing P or other chemicals can also produce Zn when applied [58].

4.3. Prevention and Control Measures for Heavy Metal(loid) Pollution

This study identified As, Cd, and Pb as the main heavy metal(loid) pollutants found in industrial parks. Their main sources are industries, such as preparing raw materials for the smelting of Cu and Fe and the smelting process, in which the energy mainly comes from coal combustion [59–61]. Second, Pb and Cd originate from transportation and natural sources, respectively. Additionally, exhaust emissions, discharge or leakage of heavy metal(loid)-containing wastewater, storage or improper disposal of waste residues, and steel processing and stacking may result in Cd infiltration into site soil [62,63]. Industrial activities, such as hazardous chemical production, pharmaceutical manufacturing, and fertilizer production, can also produce As and Pb pollution [64,65]. Pb pollution also results from automobile exhaust, oil leakage, and wear and tear of concrete pavements, rubber tires, brake pads, etc. [66,67].

At the national level, regular updates on online environmental pollution monitoring information and data sharing should be jointly promoted. Local governments should properly manage and dispose of waste in accordance with local environmental protection laws, actively promote the upgrading of processes and industries, determine diversified evaluation standards and systems, strictly implement the requirements of air pollutant emission limits, formulate scientifically sound regional soil heavy metal(loid) pollution management, soil utilization and remediation, and balanced governance programs for other ecological elements [68,69].

Comprehensive management of industrial parks is performed at the park level, with management projects planned in non-polluted areas to control the generation of new pollutants and a permanent protection system established to ensure park safety. In places affected by heavy metal(loid) pollution, strict control, research, and development of new technologies for heavy metal(loid) pollution remediation should be implemented, such as the study of soil heavy metal(loid) pollution management systems and mechanisms and improved soil heavy metal(loid) pollution management capacity and level. The aim is to achieve sustainable development of the soil environment. Furthermore, enterprises in the affected industrial parks should be supervised to strictly enforce national pollutant emission standards and eliminate the "three industrial wastes." Relevant companies must formulate technical specifications for the prevention and control of heavy metal(loid)s to enable their supervision and management of heavy metal(loid) emissions. Industrial parks need to establish centralized collection, treatment, and disposal facilities for solid and hazardous

wastes and improve measures to prevent seepage, loss, and dispersal of heavy metal(loid) contaminated soil. For the copper smelting industry, strict implementation of measures to curb the emissions of particulate matter and key heavy metal(loid) pollutants is required. The development of clean energy should be encouraged through the development of environmentally friendly raw materials, and the filtration of automobile exhaust pollutants, purification, and prevention capabilities should be strengthened.

As, Cd, Pb, and other heavy metal(loid)s cannot be naturally degraded and are easily enriched in all chains. Acid-based degradation and other methods must also be considered when discharging exhaust gases and treating wastewater [70,71].

5. Conclusions

The present findings revealed significant enrichment of As, Hg, Cd, Pb, Ni, Cu, and Zn in construction land soil in Kunming City. The surrounding agricultural land was significantly enriched in As, Hg, Cd, Pb, Cu, and Zn. Cd was the most enriched element in construction and agricultural lands. In the construction land, seven of the heavy metal(loid)s were higher than the background value of Kunming City, except for Cr, and the contents of As, Cd, and Pb in the construction and agricultural land soil samples were all higher than the soil risk screening values of construction and agricultural lands in China.

The PLI results indicated that the study area was heavily polluted. The I_{geo} values indicated slight pollution by all eight heavy metal(loid)s, with relatively more serious pollution by As, Cd, Cu, Pb, and Zn. The Nemero Integrated Pollution Index showed that the P_N for construction and agricultural land exceeded 3. Construction land was more polluted by As and Pb than agricultural land. The As pollution of the construction land was heavy, the Cd and Pb pollution of the construction land was mild, and the Cd pollution of the agricultural land was moderate.

The results of the spatial distribution show that, except for Cr, the distribution characteristics of the other seven elements were relatively similar, and there were noticeably high levels of pollution in the center. Correlation and principal component analyses showed that the sources of pollution were different in general. Arsenic, mercury, cadmium, and lead were primarily derived from industrial and agricultural sources. Traffic sources had a greater impact on Zn, Cd, Pb, and Cr, whereas natural sources were the primary sources of Cr, Ni, Cd, and Ni were also affected by industrial sources. Zn and Cu concentrations were also affected by agricultural sources.

In summary, the surface soil of the study area is severely polluted by As, Cd, and Pb. Cd is a widespread pollutant and should be a priority for the management of soil heavy metal (loid) pollution.

Author Contributions: Conceptualization, Y.Z. and W.L.; methodology, Y.Z. and W.L.; software, W.L.; validation, Y.Z.; formal analysis, W.L. and Y.Z.; investigation, P.W., W.L. and C.S.; resources, Y.Z. and P.W.; data curation, P.W., W.L. and C.S.; writing—original draft preparation, W.L.; writing—review and editing, Y.Z. and W.L.; visualization, W.L.; supervision, Y.Z. and P.W.; project administration, Y.Z. and P.W.; funding acquisition, Y.Z. All authors have read and agreed to the published version of the manuscript.

Funding: This research was funded by the Ten Thousand Talent Program of Yunnan Province (grant no. YNWR-QNBJ-2019-157), the projects of the YM Lab (2011), and the Innovation Team of the Yunnan Province (2008 and 2012).

Data Availability Statement: The dataset used in this study is not publicly available because of data privacy agreements with the Kunming Geological Exploration Institute of the China Metallurgical Geology Bureau. This information can be obtained from the corresponding author upon request.

Conflicts of Interest: The authors declare no conflicts of interest.

References

1. Fang, B.; Xiao, T.W.; Su, N.N.; Xia, Y.; Shen, Z.G.; Cui, J. Research progress on cadmium uptake and its transport and accumulation among organs in rice. *Chin. J. Rice Sci.* **2021**, *35*, 225–237.
2. Sun, L.; Guo, D.K.; Liu, K.; Meng, H.; Zheng, Y.J.; Yuan, F.Q.; Zhu, G.H. Levels, sources, and spatial distribution of heavy metals in soils from a typical coal industrial city of Tangshan, China. *Catena* **2019**, *175*, 101–109. [CrossRef]
3. Bao, L.R.; Deng, H.; Jia, Z.M.; Li, Y.; Huang, J.X.; Yan, S.M.; Zhang, F.L. Ecological health risk assessment of heavy metals in farmland soils in northwest Xiushan, Chongqing. *Geol. China* **2020**, *47*, 1625–1636.
4. Komárek, M.; Ratié, G.; Vaňková, Z.; Šípková, A.; Chrastný, V. Metal isotope complexation with environmentally relevant surfaces: Opening the isotope fractionation black box. *Crit. Rev. Env. Sci. Technol.* **2022**, *52*, 3573–3603. [CrossRef]
5. Wang, P.; Hu, J.; Liu, T.Y.; Liu, J.K.; Ma, S.R.; Ma, W.M.; Li, J.; Zheng, H.Y.; Lu, R. Advances in the application of metallic isotopes to the identification of contaminant sources in environmental geochemistry. *J. Hazard. Mater.* **2023**, *458*, 131913. [CrossRef]
6. Wiggenhauser, M.; Bigalke, M.; Imseng, M.; Keller, A.; Rehkämper, M.; Wilcke, W.; Frossard, E. Using isotopes to trace freshly applied cadmium through mineral phosphorus fertilization in soil-fertilizer-plant systems. *Sci. Total Environ.* **2019**, *648*, 779–786. [CrossRef]
7. Zhang, Y.X.; Li, T.S.; Guo, Z.H.; Xie, H.M.; Hu, Z.H.; Ran, H.Z.; Li, C.Z.; Jiang, Z.C. Spatial heterogeneity and source apportionment of soil metal(loid)s in an abandoned lead/zinc smelter. *J. Environ. Sci.* **2023**, *127*, 519–529. [CrossRef]
8. Cui, M.; Chen, Y.J.; Yan, C.Q.; Li, J.; Zhang, G. Refined source apportionment of residential and industrial fuel combustion in the Beijing based on real-world source profiles. *Sci. Total Environ.* **2022**, *826*, 154101. [CrossRef] [PubMed]
9. Xie, D.; Li, X.; Zhou, T.T.; Feng, Y.Q. Estimating the contribution of environmental variables to water quality in the postrestoration littoral zones of Taihu Lake using the APCS-MLR model. *Sci. Total Environ.* **2022**, *857*, 159678. [CrossRef]
10. Chen, Z.F.; Ding, Y.F.; Jiang, X.Y.; Duan, H.J.; Ruan, X.L.; Li, Z.H.; Li, Y.P. Combination of UNMIX, PMF model and Pb-Zn-Cu isotopic compositions for quantitative source apportionment of heavy metals in suburban agricultural soils. *Ecotox. Environ. Saf.* **2022**, *234*, 113369. [CrossRef]
11. Anaman, R.; Peng, C.; Jiang, Z.C.; Liu, X.; Zhou, Z.R.; Guo, Z.H.; Xiao, X.Y. Identifying sources and transport routes of heavy metals in soil with different land uses around a smelting site by GIS based PCA and PMF. *Sci. Total Environ.* **2022**, *823*, 153759. [CrossRef] [PubMed]
12. Gove, R.; Cadalzo, L.; Leiby, N.; Singer, J.M.; Zaitzeff, A. New guidance for using t-SNE: Alternative defaults, hyperparameter selection automation, and comparative evaluation. *Vis. Inform.* **2022**, *6*, 87–97. [CrossRef]
13. Kwon, H.; Ali, Z.A.; Wong, B.W. Harnessing Semi-Supervised Machine Learning to Automatically Predict Bioactivities of Per- and Polyfluoroalkyl Substances (PFASs). *Environ. Sci. Technol. Let.* **2023**, *10*, 1017–1022. [CrossRef] [PubMed]
14. Yin, C.J. Inversion of Soil Heavy Metal Pollution in Ganhe Industrial Park, Huangzhong District, Qinghai Province. Master's Thesis, Chang'an University, Xi'an, China, 2022.
15. Zhuang, S.K. Environmental Risks and Sources of Heavy Metals and Polycyclic Aromatic Hydrocarbons in Dust of Coal-Related Comprehensive Industrial Park. Master's Thesis, Shaanxi Normal University, Xi'an, China, 2021.
16. Chen, Y.L.; Weng, L.P.; Ma, J.; Wu, X.J.; Li, Y.T. Research progress of heavy metal pollution sources in soils in China in recent 10 years. *J. Agro-Environ. Sci.* **2019**, *38*, 2219–2238.
17. Liu, Y.; He, Z.H.; Niu, X.K.; Zhang, D.; Pan, B. Health risk assessment of soil heavy metals in a small watershed of a mining area in Yunnan Province. *Environ. Sci.* **2022**, *43*, 936–945.
18. Dongchuan District People's Government of Kunming. *14th Five-Year Plan" Industrial High-Quality Development Plan (2021–2025) [EB/OL]*; Dongchuan District People's Government of Kunming: Kunming, China, 2022.
19. *GB15618-2018*; Soil Environmental Quality Construction land Soil Pollution Risk Control Standard. Ministry of Ecology and Environment: Beijing, China, 2018.
20. *GB36600-2018*; Soil Environmental quality Agricultural Land Soil Pollution Risk Control Standard. Ministry of Ecology and Environment: Beijing, China, 2018.
21. *HJ/T166-2004*; The Technical Specification for Soil Environmental Monitoring. General Administration of Environmental Protection of the People's Republic of China: Beijing, China, 2004.
22. *HJ804-2016*; Soil-Determination of Bioavailable form of Eight Elements. Ministry of Environmental Protection of the People's Republic of China: Beijing, China, 2016.
23. He, R.H.; Xue, Z.J.; Liu, N.; Li, Q.S.; Hu, H.X. Characteristics and evaluation of soil heavy metal pollution under two land use modes. *Resour. Environ. Yangtze Basin* **2020**, *29*, 1858–1864.
24. Rahmanian, M.; Safari, Y. Contamination factor and pollution load index to estimate source apportionment of selected heavy metals in soils around a cement factory, SW Iran. *Arch. Agron. Soil Sci.* **2022**, *68*, 903–913. [CrossRef]
25. Fei, X.F.; Lou, Z.H.; Xiao, R.; Ren, Z.Q.; Lv, X.N. Source analysis and source-oriented risk assessment of heavy metal polution in aricultural soils of diferent cultivated land qualities. *J. Clean Prod.* **2022**, *341*, 1786–1879. [CrossRef]
26. Liu, X.S.; Wang, Y.S.; Yin, D.C.; Wang, X.Q. Distribution characteristics and pollution evaluation of heavy metals in soil of different land use types in Baiyangdian Lake. *Chin. J. Soil Sci.* **2022**, *53*, 710–717.
27. Xiang, M.T.; Li, Y.; Yang, J.Y.; Li, Y.; Li, F.; Hu, B.F.; Cao, Y. Assessment of Heavy Metal Pollution in Soil and Classification of Pollution Risk Management and Control Zones in the Industrial Developed City. *Env. Manag.* **2020**, *66*, 1105–1119. [CrossRef]
28. Chai, L.; Wang, Y.L.; Wang, X.; Ma, L.; Cheng, Z.X.; Su, L.M. Polution characteristics, spatial distributions, and source apportionment of heavy metals in cultivated soil in Lanzho China. *Ecol. Indic.* **2021**, *125*, 107507. [CrossRef]

29. Karimi, N.; Mohammad, T.; Tabatabaii, S.M.; Gholami, A. Geochemical assessment of steel smelter-impacted urban soils, Ahvaz, Iran. *J. Geochem. Explor.* **2015**, *152*, 91–109. [CrossRef]
30. Cheng, H.X.; Li, K.; Li, M.; Yang, K.; Liu, F.; Cheng, X.M. Background and reference values of urban soil chemical elements in China. *Earth Sci. Front.* **2014**, *21*, 265–306.
31. Rudnick, R.L.; Gao, S.L. Composition of the continental trust. In *Treatise on Geochemistry*; Elsevier: Amsterdam, NY, USA, 2003; Volume 3, pp. 1–64.
32. Facchinelli, A.; Sacchi, E.; Mallen, L. Multivariate statistical and GIS-based approach to identify heavy metal sources in soils. *Environ. Pollut.* **2001**, *114*, 313–324. [CrossRef]
33. Tang, J.L.; Zhao, K.; Hu, R.X.; Xu, T.; Wang, Y.X.; Yang, Y.; Zhou, B.H. Characteristics, source analysis and pollution assessment of heavy metals in surface soil of Chuzhou. *Environ. Sci.* **2023**, *44*, 3562–3572.
34. Liu, X.Y.; Chen, M.B.; Li, L.Z.; Hu, G.C.; Huang, J.H.; Liu, S.; Zhang, L.J.; Yu, Y.J. Soil heavy metal pollution characteristics and health risk assessment around Huize lead-zinc smelter in Yunnan Province. *J. Agric. Resour. Environ.* **2016**, *33*, 221–229.
35. Ran, J.W.; Ning, P.; Sun, X.; Liang, D.L. Characteristics and potential risks of heavy metal pollution in Gejiu soil crops in Yunnan Province. *Environ. Monit. China* **2019**, *35*, 62–68.
36. Huang, J.X.; Xu, S.C.; Gong, Q.J.; Chen, Z.W.; Huang, Z. Environmental pollution assessment of heavy metals in northeast Huize, Yunnan Province. *Acta Geol. Sin.* **2022**, *43*, 93–100.
37. Liu, Y.; Liu, M.Q.; Wang, L.; Yin, A.J.; Huang, Z.L.; Yao, D.D.; Dai, W.; Wang, N.; Wang, H. Evaluation of heavy metal pollution in farmland around an abandoned silicon plant in Yunnan. *J. Agro-Environ. Sci.* **2022**, *41*, 785–793.
38. Wang, Q.; Xie, Z.Y.; Li, F.B. Using ensemble models to identify and apportion heavy metal pollution sources in agricultural soils on a local scale. *Environ. Pollut.* **2015**, *206*, 227–235. [CrossRef]
39. Zhang, Y.X.; Song, B.; Zhou, Z.Y. Pollution assessment and source apportionment of heavy metals in soil from lead: Zinc mining areas of south China. *J. Environ. Chem. Eng.* **2023**, *11*, 109320. [CrossRef]
40. Wang, H.Z.; Cai, L.M.; Wang, Q.S.; Hu, G.C.; Chen, L.G. A comprehensive exploration of risk assessment and source quantification of potentially toxic elements in road dust: A case study from a large Cu smelter in central China. *Catena* **2021**, *196*, 104930. [CrossRef]
41. Huang, J.L.; Wu, Y.Y.; Sun, J.X.; Li, X.; Geng, X.L.; Zhao, M.L.; Sun, T.; Fan, Z.Q. Health risk assessment of heavy metal(loid)s in park soils of the largest megacity in China by using Monte Carlo simulation coupled with Positive matrix factorization model. *J. Hazard. Mater.* **2021**, *415*, 125629. [CrossRef] [PubMed]
42. Du, X.L.; Zhu, Y.J.; Han, Q.; Yu, Z.Y. The influence of traffic density on heavy metals distribution in urban road runoff in Beijing, China. *Environ. Sci. Pollut. Res.* **2019**, *26*, 886–895. [CrossRef]
43. Liu, L.L.; Liu, Q.Y.; MA, J.; Wu, H.W.; Qu, Y.J.; Gong, Y.W.; Yang, S.H.; An, Y.F.; Zhou, Y.Z. Heavy metal(loid)s in the topsoil of urban parks in Beijing, China: Concentrations, potential sources, and risk assessment. *Environ. Pollut.* **2020**, *260*, 114083. [CrossRef] [PubMed]
44. Qiao, B.W.; Liu, Z.R.; Hu, B.; Liu, J.Y.; Pang, N.N.; Wu, F.K.; Xu, Z.J.; Wang, Y.S. Concentration and source analysis of metal elements in PM2.5 in winter in Beijing. *Environ. Sci.* **2017**, *38*, 876–883.
45. Li, Y.Q.; Zhao, B.W.; Niu, W.J.; Dong, B.; Cai, J.X. Special heavy metal pollution features in atmospheric dust-fall and top soil in main urban districts of Lanzhou. *J. Saf. Environ.* **2020**, *20*, 1440–1448.
46. Shi, X.L.; Zong, Z.; Peng, H.; Zhang, X.J.; Sun, R.; Wang, X.P.; Tian, C.G. Changes of health risks and pollution sources of heavy metals in background atmospheric $PM_{2.5}$ in North China in recent 10 years. *Environ. Sci.* **2012**, *44*, 5335–5343.
47. Di, Y.A.; Zhou, R.; Yu, Y.; Yan, Y.; Liu, Y.; Ma, Z.Q.; Yang, Y.J. Characteristics and sources of chromium hexavalent in atmospheric particulate matter in urban area of Beijing. *Environ. Chem.* **2014**, *33*, 2117–2122.
48. Zhu, H.P.; Fang, F.M.; Lin, Y.S.; Yao, Y.R.; Wu, M.H. Analysis on the content, sources and potential ecological risks of heavy metals in different media around a cement factory in Digang Town. *Environ. Chem.* **2017**, *36*, 2711–2718.
49. Fei, X.F.; Lou, Z.H.; Xiao, R.; Ren, Z.Q.; Lv, X.N. Contamination assessment and source apportionment of heavy metals in agricultural soil through the synthesis of PMF and GeogDetector models. *Sci. Total Environ.* **2020**, *747*, 141293. [CrossRef] [PubMed]
50. Zhang, X.W.; Wei, S.; Sun, Q.Q.; Wadood, S.A.; Guo, B.L. Source identification and spatial distribution of arsenic and heavy metals in agricultural soil around Hunan industrial estate by positive matrix factorization model, principle components analysis and geo statistical analysis. *Ecotox. Environ. Saf.* **2018**, *159*, 354–362. [CrossRef]
51. Huang, H.W.; Xiao, H.; Wang, D.Q.; Xi, B.D.; Sun, X.J.; Li, J.Y.; Li, X.K. Pollution Characteristics and Health Risk Assessment of Heavy Metals in the Water of Lijiang River Basin. *Environ. Sci.* **2021**, *42*, 1714–1723.
52. Zhang, L.; Zhang, N.M.; Bao, L.; Li, Y.; Zhang, M.; Yang, H.Y.; Lu, H.B. Distribution characteristics and pollution risk assessment of heavy metals in farmland soil in southeast Yunnan. *Chin. J. Soil Sci.* **2020**, *51*, 473–480.
53. Zhang, Y.X.; Wang, M.; Huang, B.; Akhtar, M.S.; Hu, W.Y.; Xie, E.Z. Soil mercury accumulation, spatial distribution and its source identification in an industrial area of the Yangtze Delta, China. *Ecotox. Environ. Saf.* **2018**, *163*, 230–237. [CrossRef]
54. Li, Q.H.; Li, X.X.; Bu, C.J.; Wu, P. Distribution, risk assessment, and source apportionment of heavy metal pollution in cultivated soil of typical mining area in Southwest, China. *Environ. Toxicol. Chem.* **2023**, *42*, 888–900. [CrossRef]
55. Wang, X.K.; Zhang, Y.X.; Huang, B.; Xie, E.Z.; Fan, Y.N.; Hu, W.Y.; Zhao, Y.C.; Qiu, Y.G. Accumulation characteristics and sources of heavy metals in typical urban farmland soils in the Yangtze River Delta. *Acta Pedol. Sin.* **2021**, *58*, 82–91.
56. Jin, Y.L.; O'conno, D.; Ok, Y.S.; Tsang, D.C.W.; Liu, A.; Hou, D.Y. Assessment of sources of heavy metals in soil and dust at children's playgrounds in Beijing using GIS and multivariate statistical analysis. *Environ. Int.* **2019**, *124*, 320–328. [CrossRef]

57. Jiang, H.H.; Cai, L.M.; Wen, H.H.; Luo, J. Characterizing pollution and source identification of heavy metals in soils using geochemical baseline and PMF approach. *Sci. Rep.* **2020**, *10*, 6460. [CrossRef]
58. Liu, R.L.; Li, S.T.; Wang, X.B.; Wang, M. Status and analysis of heavy metal content in commercial organic fertilizer and organic waste in China. *J. Agro-Environ. Sci.* **2005**, *24*, 392–397.
59. Zhao, D.J.; Wang, X.Q. Heavy metal content, sources and potential ecological risk in floodplain soil of Yunnan, Guizhou and Guangxi. *China Environ. Sci.* **2020**, *40*, 1609–1619.
60. Yang, Y.; Guo, T.T.; Liu, X.L.; Tie, B.Q. Spatial distribution characteristics and pollution assessment of heavy metals in cultivated soil of agricultural small watershed in typical mining areas in Southern China. *Environ. Sci.* **2023**, *44*, 1602–1610.
61. Zeng, J.Q.; Gao, W.Y.; Li, X.; Li, C.X.; Tang, L.; Ke, W.S.; Luo, X.H.; Xue, S.G. Research progress on pollution characteristics and remediation of heavy metals in non-ferrous smelting sites. *Chin. J. Non-Ferrous Met.* **2023**, *33*, 3440–3461.
62. Li, Q.; Cao, Y.; He, L.S.; Wang, Y.F.; Gong, C.; He, S.H. Spatial distribution characteristics and sources of heavy metals in soil of typical smelting industry sites. *Environ. Sci.* **2021**, *42*, 5930–5937.
63. Chen, M.Y.; Zhu, H.H.; She, W.D.; Yin, G.C.; Huang, Z.Z.; Yang, Q.L. Human health risk assessment and source analysis of heavy metals in soil of a legacy shipyard site in the Pearl River Delta. *Ecol. Environ. Sci.* **2023**, *32*, 794–804.
64. Chai, L.; Wang, X.; Ma, L.; Cheng, Z.X.; Su, L.M.; Wang, Y.H. Sources of heavy metals in cultivated soil in Lanzhou based on PMF model. *China Environ. Sci.* **2020**, *40*, 3919–3929.
65. Lu, Y.; Li, Q.; Zhang, Y.; Wang, J.; Yang, L.T.; Ding, Z.Y.; Xu, N.C. Pollution and sources of heavy metals in soil of phosphating plant and surrounding farmland. *Environ. Pollut. Control.* **2022**, *44*, 1514–1518+1525.
66. Dietrich, M.; Huling, J.; Krekeler, M.P.S. Metal pollution investigation of Goldman Park, Middletown Ohio: Evidence for steel and coal pollution in a high child use setting. *Sci. Total Environ.* **2018**, *618*, 1350–1362. [CrossRef]
67. Men, C.; Liu, R.M.; Xu, L.B.; Wang, Q.R.; Guo, L.J.; Miao, Y.X.; Shen, Z.Y. Source-specific ecological risk analysis and critical source identification of heavy metals in road dust in Beijing, China. *J. Hazard. Mater.* **2020**, *388*, 121763. [CrossRef]
68. Ministry of Ecology and Environment of the People's Republic of China. *Opinions on Further Strengthening the Prevention and Control of Heavy Metal Pollution [EB/OL]*; Ministry of Ecology and Environment of the People's Republic of China: Beijing, China, 2022.
69. Cai, A.Z. Source Analysis and Pollution Assessment of Heavy Metals in Soil Surrounding Industrial Area of Handan City. Master's Thesis, Hebei University of Engineering, Handan, China, 2022.
70. Qi, W.Q.; You, Y.; Lin, Y.C.; Li, T.; Feng, Y.L.; Qiu, L.L. Acceptance monitoring of heavy metal pollution. *Labor Prax.* **2012**, 20–22.
71. Gan, T.T.; Zhao, N.J.; Yin, G.F.; Ma, M.J.; Meng, D.S.; Fang, L.; Yang, R.F.; Liu, W.Q. Status of heavy metal pollution in agricultural soil in Yangtze River Delta and its prevention and control. *Strateg. Study CAE* **2021**, *23*, 174–184.

applied sciences

MDPI

Article

Environmental Pollution Assessment of Heavy Metals in Soils and Crops in Xinping Area of Yunnan Province, China

Shengchao Xu [1,2,3], Zhao Huang [1,2,3,*], Jiaxin Huang [4], Song Wu [1,2,3], Yan Dao [1,2,3], Zheng Chen [1,2,3], Baichun Yang [2,5], Yongqiang Xu [1,2,3], Ningqiang Liu [4] and Qingjie Gong [4,*]

1 Yunnan Institute of Geological Survey, Kunming 650216, China; ynwhts@126.com (S.X.); 18213864164@163.com (S.W.); daoyan_1120@126.com (Y.D.); chenzheng3442@163.com (Z.C.); 13648859445@163.com (Y.X.)
2 Key Laboratory of Sanjiang Metallogeny and Resources Exploration and Utilization, MNR, Kunming 650051, China; 13700659259@139.com
3 Yunnan Key Laboratory of Sanjiang Metallogeny and Resources Exploration and Utilization, Kunming 650051, China
4 School of Earth Sciences and Resources, China University of Geosciences, Beijing 100083, China; 3001220024@email.cugb.edu.cn (J.H.); lnqcug@cugb.edu.cn (N.L.)
5 Yunnan Geological Survey, Kunming 650051, China
* Correspondence: huangzhao0505@163.com (Z.H.); qjiegong@cugb.edu.cn (Q.G.)

Abstract: With the development of the economy and society, the environmental problems caused by heavy metals have always been the focus of attention. Strong concern has been recently shown for the heavy metal pollution of soils in southwestern China. The heavy metals of surface soils in the Xinping area of Yunnan province, China are surveyed along with some crop samples. There are 3312 surface soils and 95 crop samples collected in about 370 square kilometers. Heavy metals including As, Cd, Cr, Hg, and Pb and pH are analyzed. New single and integrated pollution indices of heavy metals for soils (PI and PI_n) and crops (PI^c and PI_n^c) based on Chinese criteria (GB15618-2018 and GB2762-2022) are described and presented here and used to assess the pollution status of heavy metals. The results indicate that the background level of surface soils is about 62.1%, the screening level is about 33.4%, and the intervention level is about 4.5%, which is mainly a result from Cr and spatially coincides with the peridotite rock, indicating a geogenic pollution source. Most crop samples are not contaminated with heavy metals. Comparing the results of the two integrated pollution indices between soils and crops, two inconsistent assessments are observed. One is that some contaminated crops are growing in unpolluted areas (or Type I) and the other is that some uncontaminated crops are growing in polluted areas (or Type II). This indicates a new challenge between the assessment criteria on soils and crops.

Keywords: heavy metals; surface soil; crops; pollution index; Xinping area

Citation: Xu, S.; Huang, Z.; Huang, J.; Wu, S.; Dao, Y.; Chen, Z.; Yang, B.; Xu, Y.; Liu, N.; Gong, Q. Environmental Pollution Assessment of Heavy Metals in Soils and Crops in Xinping Area of Yunnan Province, China. *Appl. Sci.* **2023**, *13*, 10810. https://doi.org/10.3390/app131910810

Academic Editor: Yuebing Sun

Received: 13 September 2023
Revised: 25 September 2023
Accepted: 26 September 2023
Published: 28 September 2023

1. Introduction

Generally, heavy metals refer to metals whose densities are greater than 5 g/cm^3, such as cadmium (Cd), chromium (Cr), mercury (Hg), lead (Pb), iron (Fe), manganese (Mn), and cobalt (Co), while the metalloid arsenic (As) is usually classified as a heavy metal due to similarities in chemical properties and environmental behavior [1–3]. Concerns over heavy metals are due to their high toxicity, long durability, persistent bioavailability, stability, and profusion [4–6]. Heavy metal pollution not only degrades the quality of the soil, crops, atmosphere, and water bodies, but also threatens human health through the food chain [7–9]. Soils are important sinks for heavy metals discharged into the environment [10–12]. Therefore, heavy metal pollution in soils has become a serious issue that has attracted much attention worldwide [13–15].

Since the 1980s, the economy of China has developed rapidly with the acceleration of industrialization and urbanization, while heavy metal pollution in soil has become

increasingly concerning due to competing pressures between the population, resources, and environment [16–18]. Due to the high geochemical backgrounds and activities of mining and smelting in southwest China, the study of heavy metals of soils has been a hotspot of environmental evaluation [19,20].

The assessment methods commonly used for heavy metal pollution can be grouped into two types. One is on heavy metals with established criteria such as Cd, Cr, Hg, Pb, and As with the criterion GB15618-2018 for soil of agricultural land in China [21–24]. The other is on heavy metals without specific criteria such as Fe, Mn, and Co in which the evaluation can be conducted through pollution indices such as single indices and integrated indices [25–28].

In this paper, the heavy metals of surface soils in the Xinping area of Yunnan Province, China are first surveyed on a scale of 1:50,000 along with some crop samples. Then, new single and integrated pollution indices are described and proposed to assess the pollution status of soils and crops on Chinese criteria of GB15618-2018 [21] and GB2762-2022 [29], respectively. Finally, the assessment results between soils and crops are compared and discussed.

2. Materials and Methods

2.1. Geological Settings

The study area was located in the Xinping area of Yunnan province, China (Figure 1a), with an area of about 370 km^2 ranging from E 101°29′ to 101°44′ and N 23°39′ to 23°51′ with grid lines at an interval of 3′ (Figure 1b). According to the public network data, the Xinping area is situated in a temperate zone with humid climate, with an average precipitation of about 900 mm and topography characterized by mountains, and the temperature ranges from 1.3 to 32.8 °C with a mean of about 18 °C. The soil type is mainly lateritic red soil, dry red soil, red soil, yellow brown soil, paddy soil, and purple soil, and the land-use type is dominated by forest land and dry land, followed by paddy field and meadow [30]. The main crops include rice, maize, beans, and buckwheat, and the economic crops are composed of walnuts, sugarcane, citrus, tea, and tropical fruits [31].

The strata in the study area belong to Neoproterozoic, Palaeozoic, Devonian, Carboniferous, Permian, Triassic, and Jurassic, of which petrological descriptions are illustrated briefly in Figure 1b as notes [32–34]. Faults are very common in the study area, trending NW-SE and NNW-SSE [35,36]. Three magmatic intrusions, composed of potassium-feldspathic granite, granite, and peridotite, are known in the area with a trend of NNW-SSE, which is almost parallel to the faults [31,37–39].

2.2. Materials

Based on the sampling grids (8 samples each square kilometer) and the land use types, the surface soil samples were collected vertically from top to bottom along the pit wall within a depth of about 0–20 cm, removing the grass roots, gravel, and fertilizer clumps. Each soil sample was composed of 3–5 sub samples near the sampling point with a weight of about 1 kg. A total of 3312 surface soil samples were collected in the study area with an actual average sampling density of 8.95 samples in each square kilometer.

Maize and rice as bulk grain crops and walnut as an economic crop were collected in the study area on harvest season and sunny days, while avoiding special plants with pests and diseases. Each crop sample was collected from multiple points and mixed evenly to form a composite sample with a weight of about 500 g. A total of 95 crop samples were collected in the study area including 40 maize, 40 walnut, and 15 rice samples.

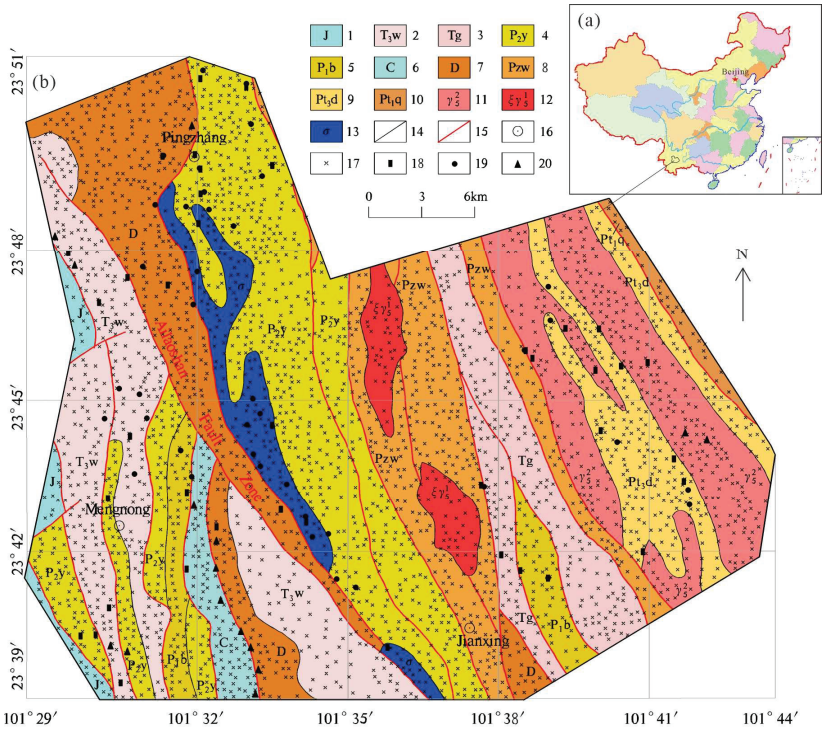

Figure 1. Location of the study area in China (**a**) and its geological map modified after Huang et al. [30] with sample locations of surface soils and crops (**b**). Notes in (**b**): 1—Jurassic sandstone; 2—Upper-Triassic Waigucun Formation sandstone, conglomerate, limestone, and marl; 3—Triassic Ganbatang Formation metamorphic conglomerate, sandstone, and phyllite; 4—Middle-Permian Yangbazhai Formation mudstone, sandstone, and siltstone; 5—Lower-Permian Baliu Formation limestone, siltstone, fine-grained sandstone, mudstone, and siliceous rock; 6—Carboniferous slate, phyllite, fused breccia, and tuff; 7—Devonian sandstone, siltstone, mudstone, limestone, and siliceous rock; 8—Palaeozoic Waimaidi Formation metamorphic sandstone, siltstone, and phyllite; 9—Neoproterozoic Dahebian Formation quartz schist, and phyllite intercalated with leptynite; 10—Paleoproterozoic Qingshuihe Formation of Ailaoshan Group schist, leptynite, and marble; 11—granite; 12—potassium-feldspathic granite; 13—peridotite; 14—petrological boundary; 15—fault; 16—main residential place; 17—locations of surface soil samples; 18—locations of maize samples; 19—locations of walnut samples; and 20—locations of rice samples.

2.3. Analytical Methods

The collected surface soil samples were first naturally air-dried. Then, the soil samples were sieved through a nylon sieve of 10 mesh. Finally, the soil samples were crushed to less than 200 mesh ($\leq$0.074 mm) using a pollution-free planetary ball mill before chemical analysis. The collected crop samples (maize, walnut, and rice) were preprocessed through dehulling or peeling, and rinsed with clean water and then deionized water three times. They were dried naturally and then crushed to pass through nylon sieves of 40–60 mesh in an agate mortar before elemental analysis. And they were digested into sample solution with nitric acid and hydrogen peroxide in a dedicated microwave digester at high temperature and pressure. Then, the contents of heavy metals were determined using an inductively coupled plasma spectrometer, which can scan the plasma with masses ranging between 5 u and 250 u, with the minimum resolution at a peak height of 5% and a peak

width of 1 u; and an atomic fluorescence spectrometer, which is equipped with a special mercury lamp.

All chemical analyses were performed at the Center of Laboratory in Yunnan Exploration and Development Bureau of Geology and Mineral Resources (Kunming Testing and Quality Supervision Center for Geological and Mineral Products in the Ministry of Natural Resources, Yunnan Province). The analysis of soil and crop samples was strictly carried out in accordance with the requirements of the Specification of Land Quality Geochemical Assessment (DZ/T 0295-2016) [40]. The data of six items (As, Cd, Cr, Hg, Pb, and pH) were analyzed in this study.

The analytical methods and detection limits of soil samples were as follows. The pH was determined using the ion selective electrode (ISE) with a detection limit of 0.01. The contents of As and Hg were analyzed using the atomic fluorescence spectroscopy (AFS) method with detection limits of 0.05 μg/g and 0.4 ng/g, respectively. Cadmium, Cr, and Pb were determined using inductively coupled plasma–mass spectrometry (ICP-MS) with detection limits of 10 ng/g, 0.82 μg/g, and 0.96 μg/g, respectively. With respect to the crop samples, Cd, As, Cr, and Pb were determined through ICP-MS with detection limits of 10 ng/g, 0.1 μg/g, 0.05 μg/g, and 0.02 μg/g, respectively. Mercury was determined using AFS with a detection limit of 1 ng/g.

The analytical methods, detection limits, accuracy, and precision all met the requirements in Specification of Land Quality Geochemical Assessment (DZ/T 0295-2016) [40]. The analytical qualification rates, controlled by the first-grade standard samples and spiked recovery, were larger than 99.6% for soil samples and 99.4% for crop samples.

3. Results

3.1. Heavy Metal Contents

3.1.1. Soil Samples

The statistical parameters of heavy metal contents and pH in 3312 surface soil samples from the Xinping area are listed in Table 1, and the histograms and their box plots are shown in Figure 2.

Table 1. Statistical parameters of analytical values of surface soil samples in the Xinping area.

Analysis Items	Min.	Q_1	Q_2	Q_3	Max.	n1	Mean1	Mean*	n2	Mean2	Mean**
As	0.05	8.0	15.2	25.4	480	3312	12.9	10.6	3282	13.3	9.1
Cd	10	73	110	180	6130	3312	120	254	3251	116	211
Cr	4.78	79	107	139	4619	3312	112	95	3045	104	87
Hg	8	57	111	179	10200	3312	101	65	3298	100	58
Pb	2.11	25.2	30.9	37.7	855	3312	30.9	41	3190	31.0	36
pH	3.89	4.69	4.93	5.26	8.12	3312	5.02	-	3204	4.96	-

Notes: The units of As, Cr, and Pb are μg/g except Cd and Hg, which are in ng/g. Q_1, Q_2, and Q_3 are first, second, and third quartiles of heavy metal contents and pH values, respectively. Mean1 and Mean2 are the geometric mean contents of surface soil samples from the Xinping area. Mean1 was calculated from all samples, while Mean2 was calculated by repeatedly culling data outliers using the threshold of avg. ±3 SD geometrically. Mean* and Mean** are the geometric mean contents of surface soil (0–20 cm) in Yunnan province after Hou et al. [41]. Mean* was obtained from all samples, while Mean** was calculated by culling data outliers.

The pH values of the surface soil samples vary from 3.89 to 8.12, which can be divided into four parts, pH $\leq$ 5.5 for 2803 samples, 5.5 < pH $\leq$ 6.5 for 418 samples, 6.5 < pH $\leq$ 7.5 for 82 samples, and pH > 7.5 for 9 samples according to the soil criterion (GB15618-2018). The samples with pH values lower than 6.5 are about 97.3%, which indicates that the surface soil in the Xinping area is generally acidic.

Compared to the geometric mean contents of surface soils in Yunnan province [41], it can be seen from Table 1 that the geometric mean contents of As, Cr, and Hg in Xinping area are greater than those in Yunnan Province, while the geometric mean contents of Cd and Pb are lower.

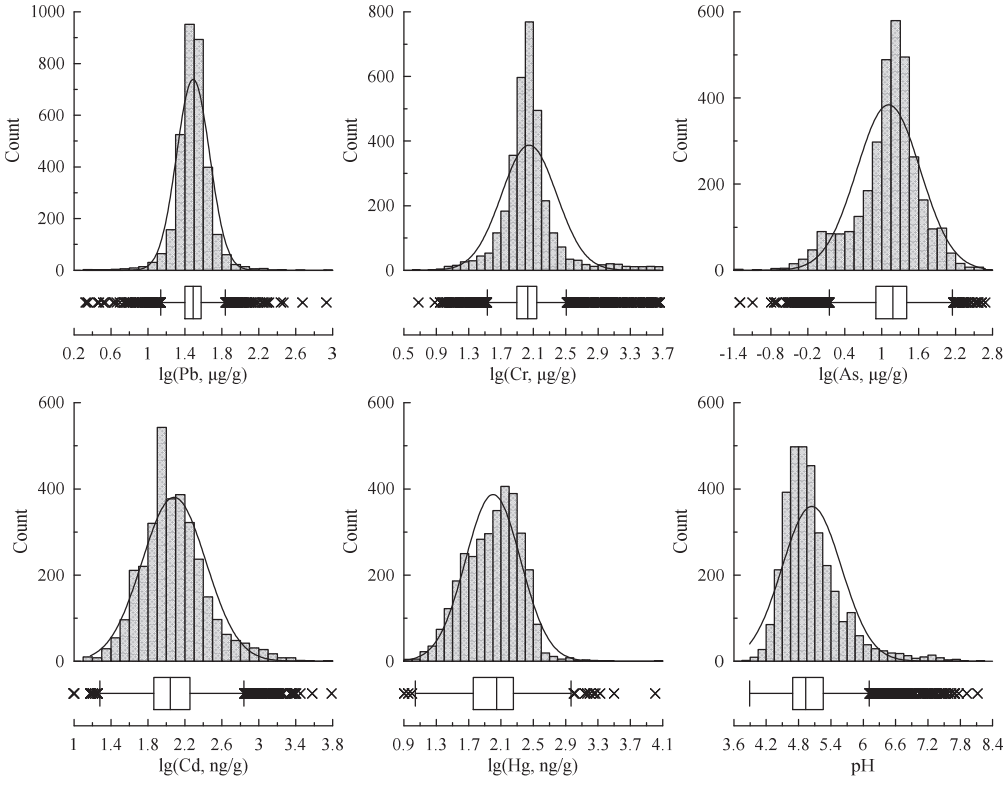

Figure 2. Histograms with box plots of heavy metal contents and pH of surface soil samples from the Xinping area.

3.1.2. Crop Samples

The statistical parameters of heavy metal contents in 95 crop samples from the Xinping area are listed in Table 2.

Table 2. Statistical parameters of analytical values of crop samples in the Xinping area.

Crops Samples	Maize			Walnut			Rice		
Statistical Parameters	Min.	Median	Max.	Min.	Median	Max.	Min.	Median	Max.
As	<0.1	<0.1	<0.1	<0.1	<0.1	0.13	<0.1	0.11	0.20
Cd	<10	<10	26	<10	<10	14.13	<10	33.5	560
Cr	0.10	0.15	0.26	0.51	0.70	0.85	0.24	0.32	1.36
Hg	<1	1.1	1.35	<1	<1	<1	2.7	3.3	4
Pb	0.04	0.07	0.13	0.03	0.08	0.19	0.06	0.09	0.16

Notes: The units of As, Cr, and Pb are μg/g except Cd and Hg, which are in ng/g.

The contents of five heavy metals in maize, walnut, and rice samples are described, respectively, as follows.

Among 40 maize samples, the contents of As are all lower than the detection limit of 0.1 μg/g. The Cd contents in 35 samples are lower than the detection limit of 10 ng/g. The contents of Cr vary between 0.10 and 0.26 μg/g. The Hg contents range from the detection limit of 1 ng/g (in nine samples) to 1.35 ng/g. The contents of Pb vary between 0.04 and 0.13 μg/g.

Among 40 walnut samples, the contents of As in 39 samples are lower than the detection limit of 0.1 μg/g. The contents of Cd range from the detection limit of 10 ng/g (in 38 samples) to 14.13 ng/g. The Cr contents vary between 0.51 and 0.85 μg/g. The contents of Hg are all lower than its detection limit of 1 ng/g. The Pb contents vary between 0.03 and 0.19 μg/g.

Among 15 rice samples, the contents of As range from the detection limit of 0.1 μg/g (in six samples) to 0.20 μg/g. The Cd contents vary from the detection limit of 10 ng/g (in four samples) to 560 ng/g. The contents of Cr range from 0.24 to 1.36 μg/g. The contents of Hg vary between 2.7 and 4 ng/g. The contents of Pb vary from 0.06 to 0.16 μg/g.

3.2. Single Pollution Index

On the basis of the risk screening and intervention values in GB15618-2018, the pollution risk of heavy metal in soil of agricultural land can be divided into three levels and classified as ① the background level, which means that the pollution risk can be ignored if the contents of heavy metals are lower than their risk screening values; ② the screening level, which means the pollution risk is moderate if the contents of heavy metals are equal to or greater than their risk screening values but lower than risk intervention values; ③ the intervention level, which means the pollution risk is high if the contents of heavy metals are equal to or greater than their risk intervention values. Then, the single pollution index of heavy metals for soil of agricultural land was proposed by Huang et al. [42] to qualitatively describe the pollution risk level of heavy metal in soils.

3.2.1. Single Pollution Index for Soils

The single pollution index (*PI*) to describe the contamination risk of heavy metals for soil of agricultural land proposed by Huang et al. [42] is

$$PI = \begin{cases} 0 & C < C_{RS} \\ 1 & C_{RS} \le C < C_{RI} \\ 10 & C_{RI} \le C \end{cases} \quad (1)$$

where C are the contents of heavy metals in soil samples, and C_{RS} and C_{RI} are their risk screening and intervention values for soil of agricultural land in GB15618-2018, respectively (Table A1).

According to Equation (1), the *PI* values of Hg, Pb, Cd, As, and Cr in 3312 surface soil samples in this study are calculated to draw geochemical maps of the single pollution index of heavy metals in the Xinping area (Figure 3). The geochemical maps of *PI* can not only intuitively visualize the spatial distribution of heavy metal pollution in the area through different color scales [43], but also identify the pollution source for each heavy metal like multivariate statistical analysis and a new geochemical gene technique [44–46].

For Hg, there are 3 samples with *PI* values of 10 that belong to the intervention level, 3 samples with *PI* values of 1 that belong to the screening level, and 3306 samples with *PI* values of 0 that belong to the background level. For Pb, there are 2 samples with *PI* values of 10 that belong to the intervention level, 83 samples with *PI* values of 1 that belong to the screening level, and 3227 samples with *PI* values of 0 that belong to the background level. For Cd, there are 6 samples with *PI* values of 10 that belong to the intervention level, 384 samples with *PI* values of 1 that belong to the screening level, and 2922 samples with *PI* values of 0 that belong to the background level. These results indicate that most areas are classified as the background level except sporadic areas as the screening and intervention level of Hg, Pb, and Cd.

For As, there are 30 samples with *PI* values of 10 that belong to the intervention level, 399 samples with *PI* values of 1 that belong to the screening level, and 2883 samples with *PI* values of 0 that belong to the background level. The result indicates that most areas belong to the background level except small areas belonging to the screening level and sporadic areas belonging to the intervention level.

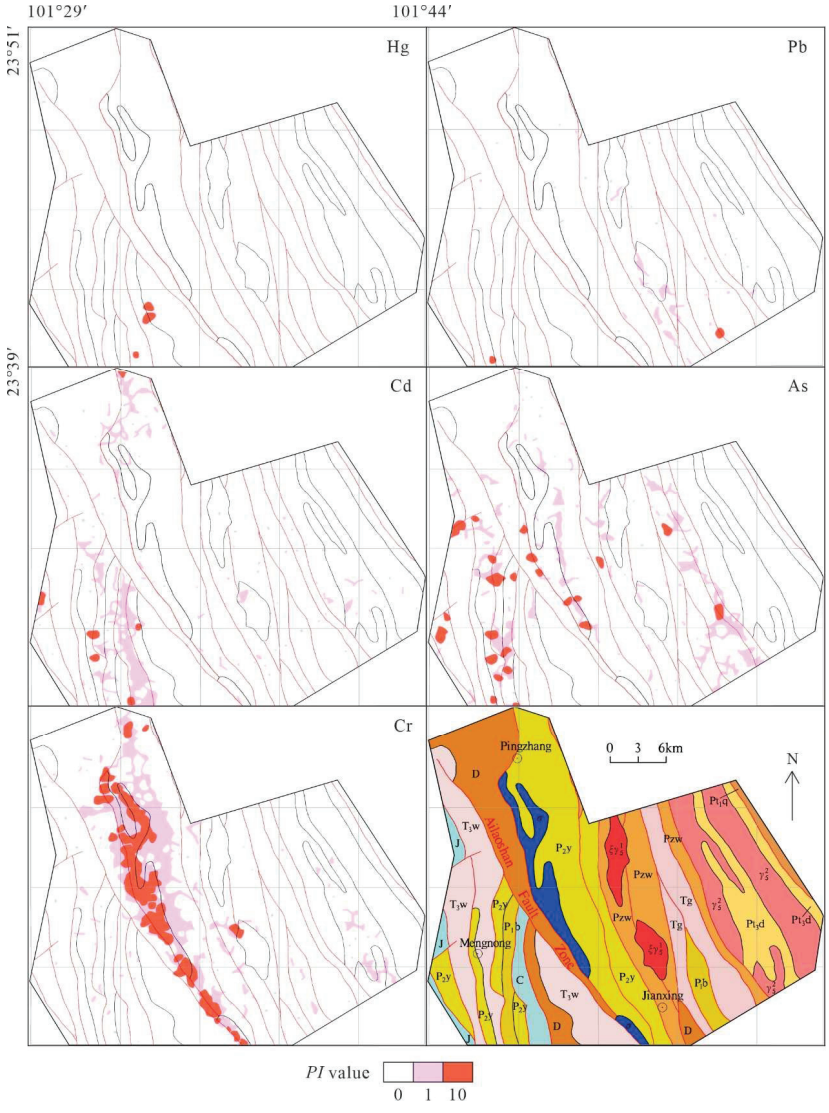

Figure 3. Geochemical maps of the single pollution index of heavy metals in surface soil samples from the Xinping area along with its geological map.

For Cr, there are 112 samples with *PI* values of 10 that belong to the intervention level, 577 samples with *PI* values of 1 that belong to the screening level, and 2623 samples with *PI* values of 0 that belong to the background level. The result indicates that most areas belong to the background level, while some areas belonging to the intervention level are mainly distributed in a planar shape within the area where the peridotite rock is located, and the areas belonging to the screening level are also mainly distributed within the peridotite rock and its surrounding areas in a planar shape. This indicates that the Cr pollution must result from the parent rock.

3.2.2. Single Pollution Index for Crops

Based on the single pollution index (*PI*) of heavy metal for soil of agricultural land proposed by Huang et al. [42], a single pollution index (PI^c) to describe the contamination degree of crops as food is proposed as

$$PI^c = \begin{cases} 0 \; C < C_{MCC} \\ 1 \; C \geq C_{MCC} \end{cases} \quad (2)$$

where *C* are the contents of heavy metals in crop samples, and C_{MCC} are their maximum contents of contaminants allowed in food referring to GB2762-2022.

The maximum contents of contaminants allowed in food (Table A2) in GB2762-2022 are adopted in this study. Because the maximum contents allowed in walnut on As, Cr, and Hg are not given in GB2762-2022, the values for As, Cr, and Hg of 0.5 μg/g, 1.0 μg/g, and 20 ng/g, respectively, in grain from GB2762-2022 are used to assess the walnut.

According to Equation (2), the PI^c values of five heavy metals in 95 crop samples from the Xinping area are calculated. For Cd, there are only two samples with PI^c values of 1 that belong to contaminated crops. For Cr, there is only one sample with a PI^c value of 1. For As, Hg, and Pb, all values in 95 samples are 0, indicating unpolluted status.

3.3. Integrated Pollution Index

3.3.1. Integrated Pollution Index for Soils

On the basis of the single pollution index (*PI*) mentioned above, the integrated pollution index (PI_n) to describe the pollution risk of heavy metals for soil of agricultural land is proposed by Huang et al. [42] as

$$PI_n = \Sigma PI \quad (3)$$

where *PI* are the single pollution indices of heavy metals mentioned above, and *n* is the count of heavy metals.

According to Equations (1) and (3), the theoretical values of integrated pollution index (PI_5) for five heavy metals of Hg, Pb, Cd, As, and Cr include 0, 1–5, 10–14, 20–23, 30–32, 40–41, and 50. When PI_5 values are 0, it means that these samples belong to the background level with the contents of the five heavy metals being lower than risk screening values in GB15618-2018. When PI_5 values range from 1 to 5, it means that these samples belong to the screening level with the contents of the five heavy metals being lower than risk intervention values, while there is at least one heavy metal with contents greater than risk screening values. When PI_5 values range from 10 to 50, the tens digit (n) of the PI_5 values indicate the number of heavy metals with contents equal to or greater than risk intervention values.

The actual PI_5 values in 3312 surface soil samples from the study area range from 0 to 21. There are 2057 samples with PI_5 values of 0 belonging to the background level, which is about 62.1% in total; 1107 samples with PI_5 values varying between 1 and 5 belonging to the screening level, which is about 33.4%; 143 samples with PI_5 values ranging from 10 to 14; and 5 samples with PI_5 values varying between 20 and 21, which is about 4.5% in all soil samples. The geochemical map of PI_5 in the Xinping area is shown in Figure 4, which can visualize the spatial distribution of heavy metals to trace integrated anomalies like the mineralization similarity of metallogenes presented recently [47–49].

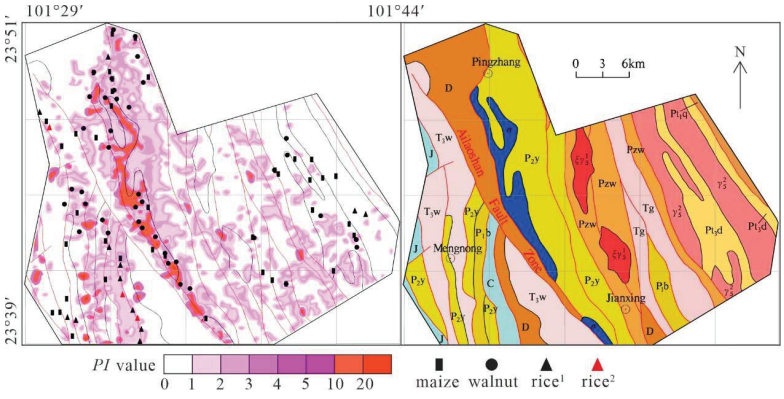

Figure 4. Geochemical map of the PI_5 of heavy metals in surface soils from the Xinping area along with its geological map. Notes: the triangle symbol in black (rice[1]) represents the uncontaminated rice samples, while that in red (rice[2]) represents contaminated rice samples.

3.3.2. Integrated Pollution Index for Crops

Based on the single pollution index (PI^c), the integrated pollution index (PI_n^c) to describe the contamination degree of crops as food is proposed as

$$PI_n^c = \Sigma PI^c \quad (4)$$

where PI^c are the single pollution indices for crops as food, and n is the count of heavy metals.

According to Equations (2) and (4), the theoretical values of PI_5^c range from 0 to 5. When PI_5^c values are 0, it indicates that these samples are uncontaminated crops with the contents of the five heavy metals being lower than the maximum contents of contaminants allowed in food from GB2762-2022. When PI_5^c values range from 1 to 5, it indicates that these samples are contaminated crops in which there is at least one heavy metal with contents equal to or greater than the maximum content of contaminants allowed in food.

The actual PI_5^c values in the 95 crop samples from the Xinping area range from 0 to 1. There are only three rice samples with PI_5^c values of 1.

4. Discussion

In order to test the consistency of pollution status between crops and soils in the Xinping area, 95 crop samples along with 95 corresponding soil samples are abstracted from Figures 3 and 4. Then, the pollution indices of heavy metals between crop and soil samples are compared.

4.1. Between PI in Soil and Contents in Crops

The *PI* values of heavy metals in soils and their contents in crops in the 95 corresponding samples in the Xinping area are illustrated in Figure 5.

For Hg and Pb, all crops are unpolluted and grew in the soils with background-level pollution. For As, Cd, and Cr, most crops are unpolluted and grew in the risk-free-level soils with percentages of about 93.7%, 82.1%, and 77.8%, respectively, in the 95 crop samples. Meanwhile, two polluted crops grew in the screening-level soils (accounting for about 2.1%) for Cd. Therefore, the consistency of pollution status between crops and soils for Hg, Pb, As, Cd, and Cr in the Xinping area are 100%, 100%, 93.7%, 84.2%, and 77.8%, respectively.

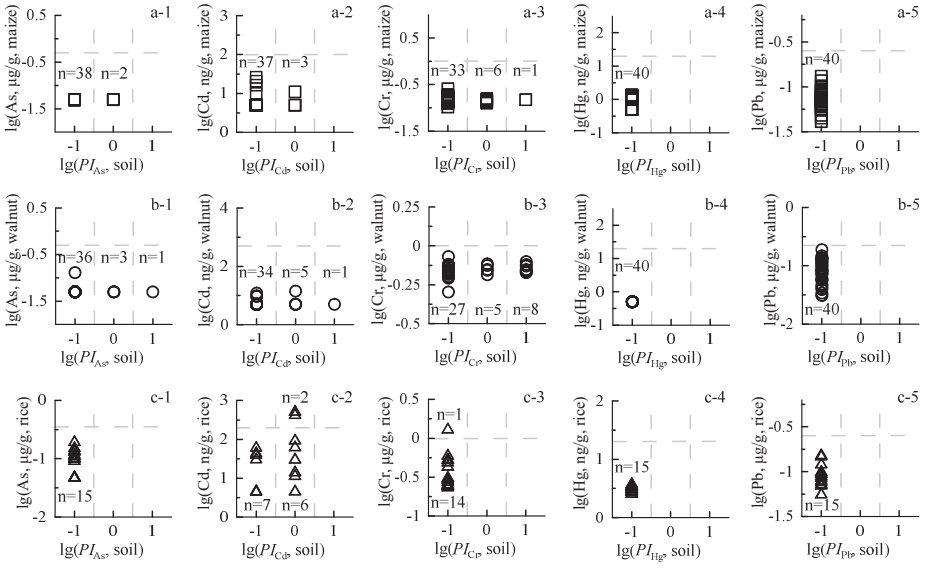

Figure 5. Scatter plots of PI values of heavy metals in soils and their contents in crops in the Xinping area. Notes: (**a-1**–**a-5**) for maize, (**b-1**–**b-5**) for walnut, and (**c-1**–**c-5**) for rice. For a better illustration, the lg(*PI*) is set to −1 when the *PI* values are 0. When the contents of heavy metals are lower than their detection limits, the values of half of the detection limits are used. The values of the dashed lines, perpendicular to the vertical axis, are the logarithmic values of the maximum contents of contaminants allowed in food for heavy metals in GB2762-2022.

However, one polluted crop grew in the background-level soils (accounting for about 1.1%) for Cr. This inconsistency in pollution status between crop and soil is called Type I inconsistency here, while a few unpolluted crops grew in the screening- and intervention-level soils for As (about 5.3% and 1.0%, respectively), Cd (about 14.7% and 1.1%, respectively), and Cr (about 11.6% and 9.5%, respectively). This inconsistency in pollution status between crop and soil is called Type II inconsistency here. These inconsistencies are new challenges between criteria of crops and soils.

4.2. Between PI_5 and $PI_5{}^c$

The pollution status of PI_5 and $PI_5{}^c$ in the Xinping area is illustrated in Table 3 and Figure 6.

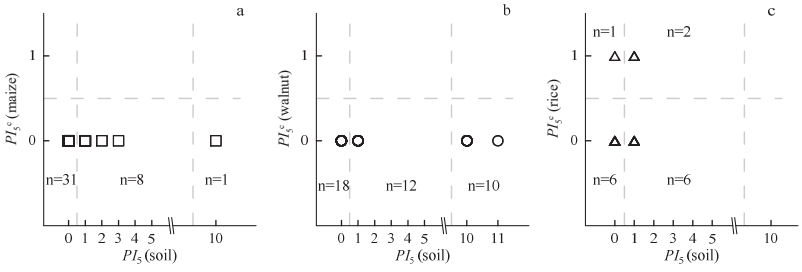

Figure 6. Pollution status between PI_5 and $PI_5{}^c$ in the Xinping area. Notes: (**a**) for maize, (**b**) for walnut, and (**c**) for rice.

Table 3. The pollution status of PI_5 and $PI_5{}^c$ in the Xinping area.

Crops		Soils		Consistency	
Pollution Status	**n1**	**Pollution Status**	**n2**	**Status**	**Percent**
uncontaminated	92	the background level	55	Yes	59.8
		the screening level	26	Type II	28.3
		the intervention level	11	Type II	11.9
contaminated	3	the background level	1	Type I	33.3
		the screening level	2	Yes	66.7
		the intervention level	-	-	-

Notes: n1 represents the number of crop samples and n2 represents the number of soil samples.

There are 55 corresponding samples with $PI_5{}^c = 0$ and $PI_5 = 0$, which means that the uncontaminated crops grew in the background-level soils or the consistency in pollution status. There are two samples with $PI_5{}^c = 1$ and $1 \leq PI_5 \leq 5$, which also means the consistency in pollution status. Therefore, the consistency percent of pollution status is 60% between crops and soils according to the national criteria in the Xinping area.

There is one sample with $PI_5{}^c = 1$ and $PI_5 = 0$, which means that the contaminated crop grew in the background-level soil. This is the type I insistency of pollution status. However, there are 11 samples with $PI_5{}^c = 0$ and $PI_5 = 10$ and 26 other samples with $PI_5{}^c = 0$ and $1 \leq PI_5 \leq 5$. This means the uncontaminated crops grew in the screening-level or intervention-level soils or the type II insistency of pollution status.

Among the aforementioned results on $PI_5{}^c$ and PI_5, two types of inconsistency of pollution status appear according to the criterion GB15618-2018 for soil of agricultural land and criterion GB2762-2022 for food on heavy metal assessments. These inconsistencies are new challenges between the criteria of crops and soils, which needs to be solved urgently in research in the near-future.

5. Conclusions

(1) New single and integrated pollution indices for soils and crops based on Chinese criteria (GB15618-2018 and GB2762-2022) are described and proposed, respectively, to evaluate the degree of heavy metal pollution.

(2) The pollution status of heavy metals in soils and crops in the Xinping area of Yunnan province, China is evaluated using the new pollution indices. The areas polluted by Cr strongly coincide with the peridotite rock in a spatial manner, which indicates a geogenic pollution source.

(3) The results of the pollution indices between crops and their soils show two inconsistent assessments. Some contaminated crops are collected from unpolluted areas and some uncontaminated crops are collected from polluted areas, which indicates a new challenge between the criteria on soils and crops.

Author Contributions: S.X.: conceptualization, data curation, writing—original draft. Z.H.: data curation, writing—review and editing. J.H.: conceptualization, data curation. S.W.: data curation, formal analysis. Y.D.: data curation, formal analysis. Z.C.: data curation. B.Y.: formal analysis. Y.X.: data curation. N.L.: conceptualization, formal analysis. Q.G.: conceptualization, methodology, writing—review and editing. All authors have read and agreed to the published version of the manuscript.

Funding: This work was supported by the Yunnan Provincial Financial Fund project "1:50,000 Geochemical Survey and Evaluation of Land Quality in Zhelong-Gasa Area, Xinping County, Yunnan Province" (D201710).

Institutional Review Board Statement: Not applicable.

Informed Consent Statement: Not applicable.

Data Availability Statement: Not applicable.

Acknowledgments: We greatly appreciate the comments from the anonymous reviewers and editors for their valuable suggestions to improve the quality of this manuscript.

Conflicts of Interest: The authors declare that they have no known competing financial interests or personal relationships that could have appeared to influence the work reported in this paper.

Appendix A

Table A1. The risk control standard of heavy metals for soil contamination of agricultural land extracted from GB15618-2018 of China [21].

Element	Risk Value	pH ≤ 5.5	5.5 < pH ≤ 6.5	6.5 < pH ≤ 7.5	pH > 7.5
Cd	Risk Screening value	300	300	300	600
	Risk Intervention value	1500	2000	3000	4000
Hg	Risk Screening value	1300	1800	2400	3400
	Risk Intervention value	2000	2500	4000	6000
As	Risk Screening value	40	40	30	25
	Risk Intervention value	200	150	120	100
Pb	Risk Screening value	70	90	120	170
	Risk Intervention value	400	500	700	1000
Cr	Risk Screening value	150	150	200	250
	Risk Intervention value	800	850	1000	1300

Notes: The units of As, Pb, and Cr are μg/g except Cd and Hg, which are in ng/g. The type of agricultural land is "others".

Table A2. The maximum contents of heavy metals allowed in food extracted from GB2762-2022 of China [29].

Crops	As	Cd	Cr	Hg	Pb
Maize	0.5	100	1.0	20	0.2
Walnut	0.5 *	500	1.0 *	20 *	0.2
Rice	0.35	200	1.0	20	0.2

Notes: The units of As, Cr, and Pb are μg/g except Cd and Hg, which are in ng/g. *—values in walnut adopted from grain.

References

1. Yang, Q.Q.; Li, Z.Y.; Lu, X.N.; Duan, Q.N.; Huang, L.; Bi, J. A review of soil heavy metal pollution from industrial and agricultural regions in China: Pollution and risk assessment. *Sci. Total Environ.* **2018**, *642*, 690–700. [CrossRef] [PubMed]
2. Zeng, L.; Wang, Y.H.; Jing, L.H.; Cheng, Q.M. Quantitative determination of auxiliary information for mapping soil heavy metals and soil contamination risk assessment. *Appl. Geochem.* **2021**, *130*, 104964. [CrossRef]
3. Zhang, J.; Liu, Y.; Hong, S.; Wen, M.; Zheng, C.; Liu, P. Speciation analysis and pollution assessment of heavy metals in farmland soil of a typical mining area: A case study of Dachang tin polymetallic ore, Guangxi. *Appl. Sci.* **2023**, *13*, 708. [CrossRef]
4. Hu, B.F.; Shao, S.; Ni, H.; Fu, Z.Y.; Hu, L.S.; Zhou, Y.; Min, X.X.; She, S.F.; Chen, S.C.; Huang, M.X.; et al. Current status, spatial features, health risks, and potential driving factors of soil heavy metal pollution in China at province level. *Environ. Pollut.* **2020**, *266*, 114961. [CrossRef]
5. Khorshidi, N.; Parsa, M.; Lentz, D.R.; Sobhanverdi, J. Identification of heavy metal pollution sources and its associated risk assessment in an industrial town using the K-means clustering technique. *Appl. Geochem.* **2021**, *135*, 105113. [CrossRef]
6. Merola, C.; Bisegna, A.; Angelozzi, G.; Conte, A.; Abete, M.C.; Stella, C.; Pederiva, S.; Faggio, C.; Riganelli, N.; Perugini, M. Study of heavy metals pollution and vitellogenin levels in brown trout (*Salmo trutta trutta*) wild fish populations. *Appl. Sci.* **2021**, *11*, 4965. [CrossRef]
7. Li, Z.Y.; Ma, Z.W.; Van Der Kuijp, T.J.; Yuan, Z.W.; Huang, L. A review of soil heavy metal pollution from mines in China: Pollution and health risk assessment. *Sci. Total Environ.* **2014**, *468*, 843–853. [CrossRef]
8. Kumar, S.; Prasad, S.; Yadav, K.K.; Shrivastava, M.; Gupta, N.; Nagar, S.; Bach, Q.V.; Kamyab, H.; Khan, S.A.; Yadav, S.; et al. Hazardous heavy metals contamination of vegetables and food chain: Role of sustainable remediation approaches-A review. *Environ. Res.* **2019**, *179*, 108792. [CrossRef]
9. Xu, L.; Dai, H.P.; Skuza, L.; Wei, S.H. Comprehensive exploration of heavy metal contamination and risk assessment at two common smelter sites. *Chemosphere* **2021**, *285*, 131350. [CrossRef]

10. Wu, S.; Peng, S.Q.; Zhang, X.X.; Wu, D.L.; Luo, W.; Zhang, T.B.; Zhou, S.G.; Yang, G.Y.; Wan, H.F.; Wu, L.Q. Levels and health risk assessments of heavy metals in urban soils in Dongguan, China. *J. Geochem. Explor.* **2015**, *148*, 71–78. [CrossRef]
11. Nazir, A.; Shafiq, M.; Bareen, F. Fungal biostimulant-driven phytoextraction of heavy metals from tannery solid waste contaminated soils. *Int. J. Phytorem.* **2022**, *24*, 47–58. [CrossRef] [PubMed]
12. Laila, U.; Nazir, A.; Bareen, F.; Shafiq, M. Role of composted tannery solid waste and its autochthonous microbes in enhancing phytoextraction of toxic metals and stress abatement in sunflower. *Int. J. Phytorem.* **2023**, *25*, 229–239. [CrossRef] [PubMed]
13. Du, P.; Xie, Y.F.; Wang, S.J.; Zhao, H.H.; Zhang, Z.; Wu, B.; Li, F.S. Potential sources of and ecological risks from heavy metals in agricultural soils, Daye City, China. *Environ. Sci. Pollut. Res.* **2015**, *22*, 3498–3507. [CrossRef] [PubMed]
14. Tang, J.Y.; Zhang, J.C.; Ren, L.H.; Zhou, Y.Y.; Gao, J.; Luo, L.; Yang, Y.; Peng, Q.H.; Huang, H.L.; Chen, A.W. Diagnosis of soil contamination using microbiological indices: A review on heavy metal pollution. *J. Environ. Manag.* **2019**, *242*, 121–130. [CrossRef] [PubMed]
15. Sarim, M.; Jan, T.; Khattak, S.A.; Mihoub, A.; Jamal, A.; Saeed, M.F.; Soltani-Gerdefaramarzi, S.; Tariq, S.R.; Fernández, M.P.; Mancinelli, R.; et al. Assessment of the Ecological and Health Risks of Potentially Toxic Metals in Agricultural Soils from the Drosh-Shishi Valley, Pakistan. *Land* **2022**, *11*, 1663. [CrossRef]
16. Li, M.; Xi, X.H.; Xiao, G.Y.; Cheng, H.X.; Yang, Z.F.; Zhou, G.H.; Ye, J.Y.; Li, Z.H. National multi-purpose regional geochemical survey in China. *J. Geochem. Explor.* **2014**, *139*, 21–30. [CrossRef]
17. Yang, L.Y.; Li, Y.; Peng, K.; Wu, S.T. Nutrients and heavy metals in urban soils under different green space types in Anji, China. *Catena* **2014**, *115*, 39–46. [CrossRef]
18. Wen, J.W.; Wu, C.; Bi, X.Y.; Zhang, S.L.; Ouyang, H.; Ye, J.X.; Ohnuki, T.; Yu, Q.Q. Soil pH change induced by smelting activities affects secondary carbonate production and long-term Cd activity in subsoils. *Appl. Geochem.* **2023**, *152*, 105663. [CrossRef]
19. Chen, H.Y.; Teng, Y.G.; Lu, S.J.; Wang, Y.Y.; Wang, J.S. Contamination features and health risk of soil heavy metals in China. *Sci. Total Environ.* **2015**, *512*, 143–153. [CrossRef]
20. Zhou, H.M.; Ouyang, T.P.; Guo, Y.; Peng, S.S.; He, C.J.; Zhu, Z.Y. Assessment of soil heavy metal pollution and its ecological risk for city parks, vicinity of a landfill, and an industrial area within Guangzhou, South China. *Appl. Sci.* **2022**, *12*, 9345. [CrossRef]
21. *GB15618-2018*; Soil Environmental Quality, Risk Control Standard for Soil Contamination of Agricultural Land. SEPA, Ministry of Ecology and Environment of the People's Republic of China: Beijing, China, 2018.
22. Zhang, H.S.; Yang, Z.F.; Yu, T.; Xia, X.Q.; Yang, Q.; Xu, D.X.; Yang, S.F. A preliminary discussion on a framework for health geological survey and evaluation. *Appl. Geochem.* **2023**, *155*, 105738. [CrossRef]
23. Shi, T.R.; Zhang, Y.Y.; Gong, Y.W.; Ma, J.; Wei, H.Y.; Wu, X.; Zhao, L.; Hou, H. Status of cadmium accumulation in agricultural soils across China (1975–2016): From temporal and spatial variations to risk assessment. *Chemosphere* **2019**, *230*, 136–143. [CrossRef] [PubMed]
24. Li, Y.H.; Zhu, Q.; Tang, X.J.; Wang, C.P.; Zhai, S. Ecological and health risk assessment of heavy metals in farmland in the South of Zhangbei County, Hebei Province, China. *Appl. Sci.* **2022**, *12*, 12425. [CrossRef]
25. Gong, Q.J.; Deng, J.; Xiang, Y.C.; Wang, Q.F.; Yang, L.Q. Calculating pollution indices by heavy metals in ecological geochemistry assessment and a case study in parks of Beijing. *J. China Univ. Geosci.* **2008**, *19*, 230–241.
26. O'Connor, K.F.; Al-Abed, S.R.; Pinto, P.X.; Potter, P.M. Zinc transport and partitioning of a mine-impacted watershed: An evaluation of water and sediment quality. *Appl. Geochem.* **2022**, *142*, 105333. [CrossRef]
27. Jia, L.; Liang, H.L.; Fan, M.; Wang, Z.; Guo, S.S.; Chen, S. Spatial distribution characteristics and source appointment of heavy metals in soil in the areas affected by non-ferrous metal slag field in the dry-hot valley. *Appl. Sci.* **2022**, *12*, 9475. [CrossRef]
28. Zhao, H.D.; Wu, Y.; Lan, X.P.; Yang, Y.H.; Wu, X.N.; Du, L.Y. Comprehensive assessment of harmful heavy metals in contaminated soil in order to score pollution level. *Sci. Rep.* **2022**, *12*, 3552. [CrossRef]
29. *GB2762-2022*; National Food Safety Standard: Maximum Levels of Contaminants in Food. National Health Commission, State Administration for Market Regulation of the People's Republic of China: Beijing, China, 2022.
30. Huang, Z.; Chen, Z.; Xue, C.D.; Dao, Y.; Xu, S.C.; Dai, D.L.; Wu, S. Study on the genesis and influencing factors of Selenium-enriched soil in the Ailaoshan Area, Xinping County, Yunnan Province. *Geoscience* **2020**, *34*, 609–617, (In Chinese with English Abstract).
31. Wu, S.; Chen, Z.; Li, Y.B.; Huang, Z.; Zhang, L.; Xu, S.C.; Wang, K.G. Cr, and Ni geochemistry and some suggestions on soil pollution risk prevention control in the Zhelong-Gasa area, Yunnan Province. *Geophys. Geochem. Explor.* **2021**, *45*, 517–527, (In Chinese with English Abstract).
32. Fan, W.M.; Wang, Y.J.; Zhang, A.M.; Zhang, F.F.; Zhang, Y.Z. Permian arc-back-arc basin development along the Ailaoshan tectonic zone: Geochemical, isotopic and geochronological evidence from the Mojiang volcanic rocks, Southwest China. *Lithos* **2010**, *119*, 553–568. [CrossRef]
33. Wang, Q.F.; Deng, J.; Li, C.S.; Li, G.J.; Yu, L.; Qiao, L. The boundary between the Simao and Yangtze blocks and their locations in Gondwana and Rodinia: Constraints from detrital and inherited zircons. *Gondwana Res.* **2014**, *26*, 438–448. [CrossRef]
34. Faure, M.; Lin, W.; Chu, Y.; Lepvrier, C. Triassic tectonics of the Ailaoshan belt (SW China): Early Triassic collision between the South China and Indochina blocks, and Middle Triassic intracontinental shearing. *Tectonophysics* **2016**, *683*, 27–42. [CrossRef]
35. Yang, L.Q.; Liu, J.T.; Zhang, C.; Wang, Q.F.; Ge, L.S.; Wang, Z.L.; Zhang, J.; Gong, Q.J. Superimposed orogenesis and metallogenesis: An example from the orogenic gold deposits in Ailaoshan gold belt, Southwest China. *Acta Petrol. Sin.* **2010**, *26*, 1723–1739, (In Chinese with English Abstract).

36. Wang, Q.F.; Groves, D.I.; Deng, J.; Li, H.J.; Yang, L.; Dong, C.Y. Evolution of the Miocene Ailaoshan orogenic gold deposits, southeastern Tibet, during a complex tectonic history of lithosphere-crust interaction. *Miner. Depos.* **2020**, *55*, 1085–1104. [CrossRef]
37. Jian, P.; Liu, D.Y.; Kröner, A.; Zhang, Q.; Wang, Y.Z.; Sun, X.M.; Zhang, W. Devonian to Permian plate tectonic cycle of the Paleo-Tethys Orogen in southwest China (I): Geochemistry of ophiolites, arc/back-arc assemblages and within-plate igneous rocks. *Lithos* **2009**, *113*, 748–766. [CrossRef]
38. Lai, C.K.; Meffre, S.; Crawford, A.J.; Zaw, K.; Xue, C.D.; Halpin, J.A. The Western Ailaoshan Volcanic Belts and their SE Asia connection: A new tectonic model for the Eastern Indochina Block. *Gondwana Res.* **2014**, *26*, 52–74. [CrossRef]
39. Lai, C.K.; Meffre, S.; Crawford, A.J.; Zaw, K.; Halpin, J.A.; Xue, C.D.; Salam, A. The Central Ailaoshan ophiolite and modern analogs. *Gondwana Res.* **2014**, *26*, 75–88. [CrossRef]
40. *DZ/T 0295-2016*; Specification of Land Quality Geochemical Assessment. Ministry of Land and Resources of the People's Republic of China: Beijing, China, 2016.
41. Hou, Q.Y.; Yang, Z.F.; Yu, T.; Xia, X.Q.; Cheng, H.X.; Zhou, G.H. *Soil Geochemical Parameters in China*; Geological Publishing House: Beijing, China, 2020; pp. 1–3172. (In Chinese)
42. Huang, J.X.; Xu, S.C.; Gong, Q.J.; Chen, Z.W.; Huang, Z. Environmental assessment of heavy metal contamination in the northeast of Huize County, Yunnan Province. *Acta Geosci. Sin.* **2022**, *43*, 93–100, (In Chinese with English Abstract).
43. An, Y.L.; Yan, T.T.; Gong, Q.J.; Wang, X.Q.; Huang, Y.; Zhang, B.M.; Yin, Z.Q.; Zhao, X.F.; Liu, N.Q. Chromium (Cr) geochemical mapping based on fixed-values' method: Case studies in China. *Appl. Geochem.* **2022**, *136*, 105168. [CrossRef]
44. Wu, Y.; Li, X.L.; Gong, Q.J.; Wu, X.; Yao, N.; Peng, C.; Chao, Y.D.; Wang, X.Y.; Pu, X.L. Test and application of the geochemical lithogene on weathering profiles developed over granitic and basaltic rocks in China. *Appl. Geochem.* **2021**, *128*, 104958. [CrossRef]
45. Wu, Y.; Gong, Q.J.; Liu, N.Q.; Wu, X.; Yan, T.T.; Xu, S.C.; Li, W.J. Classification of geological materials on geochemical lithogenes: Illustration on a case study in Gejiu area of Yunnan Province, China. *Appl. Geochem.* **2022**, *146*, 105460. [CrossRef]
46. An, Y.L.; Yin, X.L.; Gong, Q.J.; Li, X.L.; Liu, N.Q. Classification and Provenance on Geochemical Lithogenes: A Case Study on Rock–Soil–Sediment System in Wanquan Area of Zhangjiakou, North China. *Appl. Sci.* **2023**, *13*, 1008. [CrossRef]
47. Gong, Q.J.; Liu, N.Q.; Wu, X.; Yan, T.T.; Fan, T.Q.; Li, X.L.; Liu, M.X.; Li, R.K.; Albanese, S. Using regional geochemical survey data to trace anomalous samples through geochemical genes: The Tieshanlong tungsten deposit area (Southeastern China) case study. *J. Geochem. Explor.* **2020**, *219*, 106637. [CrossRef]
48. Gong, Q.J.; Yan, T.T.; Wu, X.; Li, R.K.; Wang, X.Q.; Liu, N.Q.; Li, X.L.; Wu, Y.; Li, J. Geochemical gene: A promising concept in discrimination and traceability of geological materials. *Appl. Geochem.* **2022**, *136*, 105133. [CrossRef]
49. Li, J.; Gong, Q.J.; Zhang, B.M.; Liu, N.Q.; Wu, X.; Yan, T.T.; Li, X.L.; Wu, Y. Construction, test and application of a Tungsten metallogene named MGW11: Case studies in China. *Appl. Sci.* **2023**, *13*, 606. [CrossRef]

applied sciences

MDPI

Article

The Distribution and Health Risk Assessment of Potential Toxic Elements in Atmospheric Deposition from Ion-Adsorption Rare Earth Mining Areas in the Ganzhou City of Southeast China

Jixin Wei [1], Siwen Liu [2,3,*], Tianshu Chu [2], Guoli Yuan [1], Manman Xie [2,3], Yuanying Huang [2], Qing Sun [2,3], Chenge Ma [2] and Qiang Xue [4,*]

[1] School of Earth Sciences and Resources, China University of Geosciences (Beijing), Beijing 100083, China; jixinwei@email.cugb.edu.cn (J.W.); yuangl@cugb.edu.cn (G.Y.)
[2] National Research Center for Geoanalysis, Beijing 100037, China; 18210631191@163.com (T.C.); xiemm827@163.com (M.X.); yuanyinghuang304@163.com (Y.H.); sunqing1616@yahoo.com (Q.S.); machenge23@mails.ucas.ac.cn (C.M.)
[3] Key Laboratory of Eco-Geochemistry, Ministry of Natural Resources, Beijing 100037, China
[4] MOE Key Laboratory of Groundwater Circulation and Environmental Evolution, School of Water Resources and Environment, China University of Geosciences (Beijing), Beijing 100083, China
* Correspondence: siwenzliu@126.com (S.L.); xueqiang@cugb.edu.cn (Q.X.)

Abstract: Potential toxic elements (PTEs), including Pb, Cr, Cd, Ni, Cu, As, and Mo, are common pollutants in ion-adsorption rare earth mines (IAREEMs), and atmospheric deposition is an important method of PTE migration. However, the level of PTE atmospheric deposition in and around IAREEMs remains unknown. We established 25 stations at typical sites in the Ganzhou city of southeast China. An exposure assessment model was used to evaluate the health risks for adults and children. The results show that the concentration and fluxes of atmospheric deposition of PTEs follow the order of Pb > Cu > Cr > Ni > As > Mo > Cd, and most PTEs present no human health risk. However, due to the high toxicty of As, it poses both carcinogenic and non-carcinogenic risks to children as indicated by the analysis of an exposure assessment model of heavy rare earth minerals in Longnan county, Ganzhou city. The As concentration in atmospheric deposition ranged from 3.18 to 251.87 mg kg^{-1}, and the As atmospheric fluxes in atmospheric deposition ranged from 0.11 to 39.4 mg m^{-2} y^{-1}. This is because As-rich materials (e.g., arsenic-adsorbing clay zones and chernovite-(Y) (Y[AsO_4])) are exposed in fully weathered layers, and the formed suspended particulate matter is transported into the atmosphere at Longnan county. Consequently, restoring vegetation to reduce particulate matter transport is an important method for controlling the spread of pollutants. These results provide significant insights into pollution characteristics and prevention in and around mining areas under the influence of atmospheric deposition.

Keywords: atmospheric deposition; potential toxic elements; health risk assessment; ion-adsorption rare earth mining; Ganzhou city of southeast China

Citation: Wei, J.; Liu, S.; Chu, T.; Yuan, G.; Xie, M.; Huang, Y.; Sun, Q.; Ma, C.; Xue, Q. The Distribution and Health Risk Assessment of Potential Toxic Elements in Atmospheric Deposition from Ion-Adsorption Rare Earth Mining Areas in the Ganzhou City of Southeast China. *Appl. Sci.* **2024**, *14*, 3585. https://doi.org/10.3390/app14093585

Academic Editor: Dibyendu Sarkar

Received: 16 March 2024
Revised: 18 April 2024
Accepted: 20 April 2024
Published: 24 April 2024

1. Introduction

Ion-adsorption rare earth element mines (IAREEMs) are widely distributed in Jiangxi, Guangdong, and Fujian in southern China [1], with the first discovery and mining in Ganzhou taking place in 1969 [2]. The use of heap leaching and in-situ leaching in these areas has led to significant ecological and environmental issues, including vegetation destruction, delayed vegetation recovery, and pollution from potentially toxic elements (PTEs) [3,4]. Particulate matter from mining operations, such as mining, beneficiation, smelting, and waste, plays a crucial role in migration of pollutants, impacting nearby areas [5,6]. Atmospheric pollution, distinct from soil and water pollution, disperses rapidly over longer distances [7,8], and atmospheric deposition is a key route for pollutants to enter

soil, biological, and other media [9,10]. However, current studies are mainly focused on soil and water pollution, and researches on atmospheric deposition are limited [4,11].

Mine atmospheric deposition contains various PTEs, including metals and metalloids (e.g., As, Cd, Cr, Cu, Mo, Ni, and Pb). These elements are concerning due to their persistence, toxicity, and potential for bioaccumulation [12–14]. Usually, human activities contribute significantly to the atmospheric deposition of PTEs in mining areas [15]. For IAREEM areas, the distribution of PTEs through atmospheric deposition remains unknown.

Given the bioaccumulation of PTEs [16,17], human exposure near IAREEM areas could pose substantial health risks. This study employs the exposure assessment model developed by the United States Environmental Protection Agency (USEPA) to evaluate these risks [18]. The model is widely used and is an effective tool for assessing human health risks, and the results of the assessment can provide a reference and basis for environmental governance policies [19–21]. Our analysis focuses on the spatial distribution and pollution levels of PTEs in atmospheric deposition around IAREEM areas. We also assess the human health risks associated with PTE exposure and provide insights for environmental management in IAREEM regions. In this study, we first investigate PTEs of atmospheric deposition in IAREEM areas, offering valuable information for managing atmospheric deposition pollution in these regions.

2. Materials and Methods

2.1. Study Area

The study area is located in Ganzhou city of Jiangxi Province (Southeast China), having a subtropical monsoon climate (Figure 1e). Large-scale mining in Ganzhou city began in the late 20th century. The IAREEMs in Ganzhou city, known as the first discovered and mined IAREEM region in the world, are categorized into two types: the heavy rare earth (Gd, Tb, Dy, Ho, Er, Tm, Yb, Lu, Y, HREE) type in Longnan county and the light rare earth (La, Ce, Pr, Nd, Pm, Sm, Eu) type in Xunwu county [11,22,23]. Currently, most IAREEMs have been abandoned and wind erosion of the mine's surface soil poses a risk of spreading PTEs [4,11].

2.2. Sample Collection

Eight major IAREEM areas in Ganzhou city were selected for atmospheric deposition sampling. Based on prevailing wind directions (N-W), each mining area was equipped with three atmospheric deposition stations (Figure 1a,b). The atmospheric deposition was successively collected using a self-designed collector from sampling stations at 25 sites in the study area (Figure 1a). Samples of atmospheric deposition were collected over the course of a year from August 2019 to August 2020 and sampled at the end. Collected samples were stored in PVC plastic bottles (Figure 1d), which were cleaned with Milli-Q water and 1:1 HNO_3 before use. The collection bottles were placed and fixed in an open area, such as on a roof or a broad balcony. The collected atmospheric deposition samples (including wet and dry deposition) were transferred into a clean tank. Sparse collectors due to evaporation were replenished with pure water, ensuring complete sample transfer. Additionally, a typical regolith sample was collected at a depth of 50 cm below the surface to minimize anthropogenic influence in fully weathered layers (Figure 1a,b). Since the surface layer is potentially subject to disturbances from exogenous substances and exhibits high variability, soil sampling at a depth of 50 cm can better represent the basic conditions of the surface soil in this region [24].

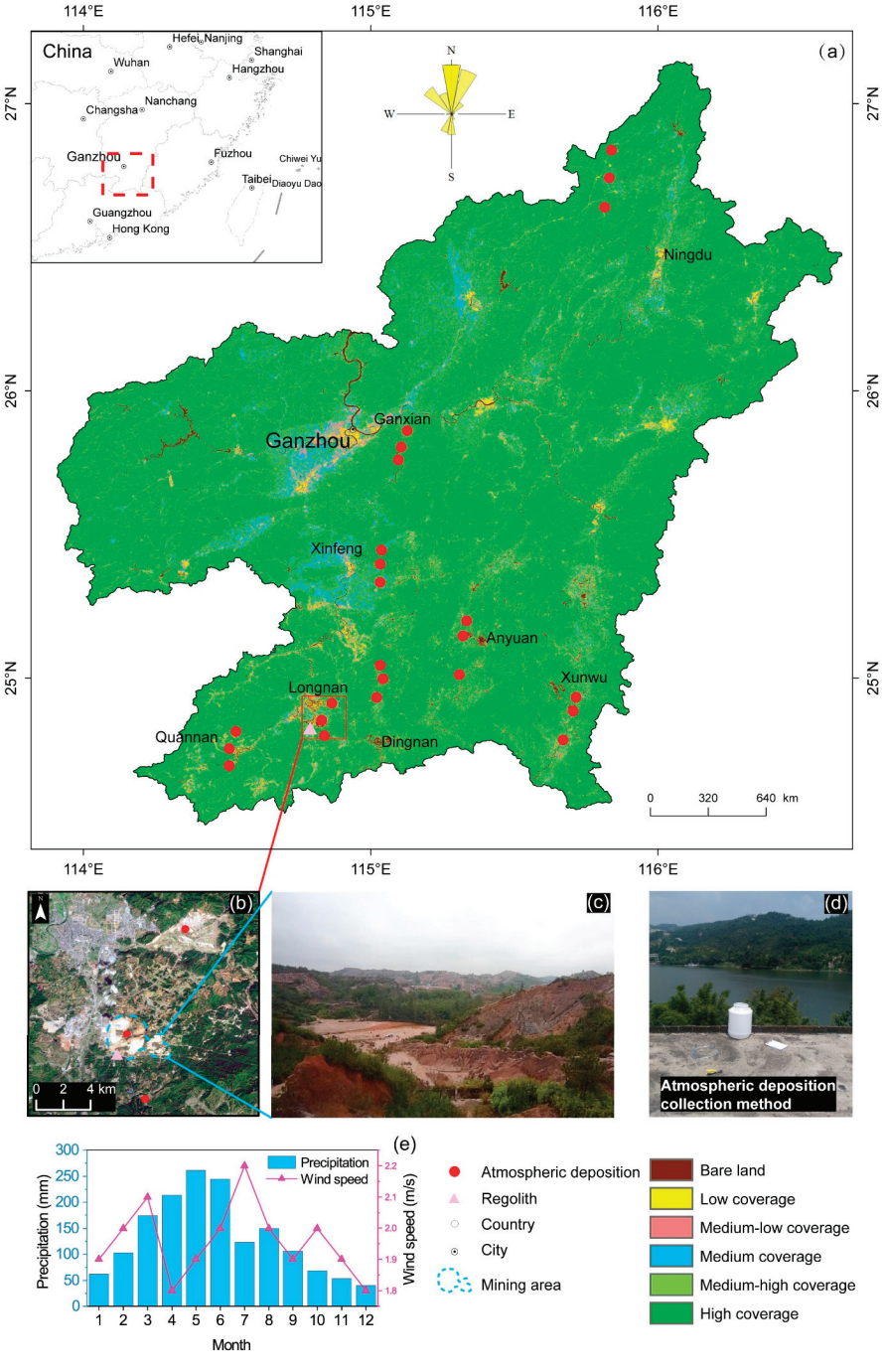

Figure 1. (**a**) Overview of the study area (Ganzhou city, China) including sampling location, Fractional Vegetation Cover (FVC), and wind rose diagram. (**b**) Shows the places of atmospheric deposition samples in typical IAREEMs. (**c**) Shows the landform and vegetation of ionic rare earth mines. (**d**) Shows the collection methods of atmospheric deposition. (**e**) Shows precipitation and wind speed.

2.3. Sample Treatment and Analysis

The wet and dry samples were collected and transferred to the laboratory within 72 h. They were filtered through a 0.45 μm quartz fiber membrane, which was pre-measured and recorded. The filtrates (wet deposition) were acidified with 1:1 HNO_3 in a 30 mL aliquot and ready for analysis. Both the membrane and its precipitate were dried below 65 °C until the mass difference between the two measurements was under 0.5 mg. The dried precipitates (dry deposition) could then be used for analysis.

Samples were analyzed for Pb, Cr, Cd, Ni, Cu, and Mo. About 50 mg of each sample was digested in a mixture of HCl, HNO_3, HF, and $HClO_4$ [12], and analyzed using Inductively Coupled Plasma Mass Spectrometry (ICP-MS, NexION 300Q, PerkinElmer, Waltham, MA, USA) and Atomic Fluorescence Spectrometry (AFS, AFS-8330, Titan Instruments, Beijing, China) for As concentration.

Quality assurance and control involved standard reference substances (soil, GSS21–GSS26) from the National Institute of Metrology, China. Table 1 shows the detection limits of the wet and dry depositions. The sample recoveries ranged from 90% to 110%, and the analyses were performed in triplicate, ensuring levels of accuracy and precision that meet the quality requirements [25].

Table 1. Detection limits of dry and wet deposition of atmosphere.

Element	Type	Unit	Pb	Cr	Cd	Ni	Cu	Mo	As
Limit	Dry	mg kg^{-1}	0.1	1	0.01	1	0.2	0.01	0.02
	Wet	mg/L	0.01	0.004	0.05	0.03	0.05	0.001	0.05

The Mineral Liberation Analyzer (MLA) is a process mineralogy automatic analysis and testing equipment developed by the University of Queensland, Australia. Equipped with an energy spectrometer, we can achieve automatic scanning and energy spectrum analysis, accurately identify mineral types, and determine content. Regolith sample observations were made with the aid of an MLA in the Institute of Resource Utilization and Rare Earth Development, Guangdong Academy of Sciences in China. The MLA 650 system consisted of an FEI Quanta 650 scanning electron microscope, Bruker Quanta 200 dual probe electric refrigeration energy spectrometer, and MLA software version 3.1. The working conditions were an acceleration voltage of 20 kV, a working distance of 10 mm, and high vacuum mode.

2.4. Data Analysis

2.4.1. Concentrations and Flux of Trace Elements

The concentrations of PTEs in the atmospheric deposition samples were calculated using Equation (1):

$$C_{ij} = \frac{V_i \times p_{ij} + M_i \times w_{ij}}{M_i} \quad (1)$$

where C_{ij} (mg kg^{-1}) is the concentration of the j-th PTE of the i-th atmospheric deposition sample; V_i (L) is the volume of the filtrate of the i-th sample; p_{ij} (mg/L) is the concentration of the j-th PTE of the filtrate of the i-th sample; M_i (kg) is the mass of the i-th sample deposition; w_{ij} (mg kg^{-1}) is the concentration of the j-th PTE of the i-th sample deposition.

The annual deposition flux of PTEs from the atmospheric deposition samples was calculated using Equation (2):

$$f_{ij} = \frac{C_{ij} \times M_i}{Sa} \quad (2)$$

where f_{ij} (mg m^{-2} y^{-1}) is the deposition flux of the j-th trace element of the i-th atmospheric deposition sample; S (m^2) is the collection area of the atmospheric deposition collection device; a (y) is the collection time of the atmospheric deposition sample.

2.4.2. Fractional Vegetation Cover

Utilizing Landsat 8 data (refer to Table 2), the fractional vegetation cover (FVC) was calculated using the normalized difference vegetation index (NDVI) in conjunction with the image dichotomy method [26]. The calculations involved the following Equations (3) and (4):

$$NDVI = (NIR - R)/(NIR + R) \tag{3}$$

$$FVC = (NDVI - NDVI_{soil})/(NDVI_{veg} - NDVI_{soil}) \tag{4}$$

where NDVI is the normalized vegetation index of a mixed image element; NIR is the near-infrared band reflectance; R is the red band reflectance. $NDVI_{soil}$ and $NDVI_{veg}$ represent a pure soil and pure vegetation image element value, respectively [26,27]. $NDVI_{soil}$ and $NDVI_{veg}$ vary in time and space due to different environmental backgrounds, photographic conditions, and image quality. In the actual calculation process, 5% and 95% confidence levels were used to select the maximum and minimum thresholds for NDVI data for the corresponding periods [27–29].

Table 2. The information of Landsat 8 remote sensing images.

Sensor	Date	Path/Raw	Resolution (m)
Landsat OLI	22 October 2019	121/41	30
Landsat OLI	22 October 2019	121/42	30
Landsat OLI	20 September 2019	121/43	30
Landsat OLI	14 November 2019	122/42	30
Landsat OLI	18 February 2020	122/43	30

2.4.3. Human Health Risk Assessment

Human health risks from exposure to PTEs in atmospheric deposition, as identified by the United States Environmental Protection Agency (USEPA), are categorized into non-carcinogenic and carcinogenic risks [18]. These risk assessments are conducive to quantifying exposure to PTEs [14,20]. Exposure routes include unintentional oral ingestion and inhalation. We conducted a human health risk assessment of PTEs in atmospheric deposition from IAREEs for two demographic groups (adults and children). The primary exposure routes to PTEs in atmospheric deposition are ingestion and inhalation [18]. This assessment evaluates both carcinogenic and non-carcinogenic risks from atmospheric deposition of PTEs at mine sites. Carcinogenicity assessments were conducted for ingestion (As, Cr, Pb) and inhalation (As, Cd, Cr, Ni) pathways due to the unavailability of carcinogenic slope factors for other PTEs [19,20].

The non-carcinogenic risk (HQ) of PTEs to the human via the ingestion and inhalation routes was calculated using the following Equations (5) and (6) [30]:

$$HQ_{\text{ingestion}} = C_i \cdot \frac{IR \cdot RBA \cdot EF \cdot ED}{BW \cdot AT \cdot RfD_0 \cdot 10^6} \tag{5}$$

$$HQ_{\text{inhalation}} = C_i \cdot \frac{InhR \cdot EF \cdot ED \cdot PM_{10}}{AT \cdot RfC} \tag{6}$$

The carcinogenic risk (CR) of PTEs to the population via the ingestion and inhalation routes was calculated using the following Equations (7) and (8) [30]:

$$CR_{\text{ingestion}} = C_i \cdot \frac{IR \cdot RBA \cdot EF \cdot ED \cdot CSF}{BW \cdot AT \cdot 10^6} \tag{7}$$

$$CR_{inhalation} = C_i \frac{InhR \cdot EF \cdot ED \cdot IUR \cdot PM_{10} \cdot 1000}{AT} \tag{8}$$

The total non-carcinogenic risk (HI) of PTEs to the population was calculated [30] using the following Equation (9):

$$HI = HQ_{\text{ingestion}} + HQ_{\text{inhalation}} \quad (9)$$

The total carcinogenic risk (TCR) of PTEs to the population was calculated [30] using the following Equation (10):

$$TCR = CR_{ingestion} + CR_{inhalation} \quad (10)$$

The relevant calculation parameters for human health risk assessment are shown in Tables 3 and 4.

Table 3. Relative bioavailability factor, oral reference dose, oral slope factor, inhalation reference concentration, and inhalation unit risk values for each potential toxic element.

Element	As	Cd	Cr	Cu	Mo	Ni	Pb	Reference
Relative bioavailability factor (RBA) (unitless)	0.6	1	1	1	1	1	1	[31]
Oral reference dose (RfD_o) (mg kg^{-1} day^{-1})	0.0003	0.001	0.003	0.04	0.005	0.02	0.0014	[32]
Inhalation reference concentration (RFC) (mg m^{-3})	0.000015	0.00001	0.0001	0.04	0.002	0.00009	0.035	[32]
Oral slope factor (CSF_o) (mg kg^{-1} day^{-1})$^{-1}$	1.5		0.5				0.0085	[32]
Inhalation unit risk (IUR) (μg m^{-3})$^{-1}$	0.0043	0.0018	0.084			0.0003		[32]

Table 4. Variables with their descriptions and reference values used for health risk assessment of PTEs in atmospheric deposition.

Parameters	Description	Units	Values		Reference
			Adult (>18 Years Old)	Child (1~6 Years Old)	
C_i	Concentration of PTE	mg/kg			Site-specific
IR	Intake ratio	mg/day	100	200	USDOE (2011)
EF	Exposure frequency	day/year	180	180	[33]
ED	Exposure duration	year	24	6	[31]
BW	Body weight	kg	70	15	[31]
AT	Average time	day	365 × ED (non-carcinogen)//365 × 70 (carcinogen)		[31]
InhR	Inhalation rate	m^3/day	20	7.5	[29]
PM_{10}	Inhalable particulate matter	kg/m^3	3.525×10^{-8}	3.525×10^{-8}	[34]

If the values of HQ and HI are below 1, it is assumed that no non-carcinogenic risk will occur. If the values are higher than 1, there is a potential health risk to human health [20,29]. Besides, no greater carcinogenic risk is expected if the carcinogenic risk value does not exceed 10^{-4} [20,29].

3. Results and Discussion

3.1. Spatial Distribution Characteristics of PTEs

The statistical analysis of PTEs in atmospheric deposition is summarized in Table 4. All skewness coefficients for PTEs exceed 1, indicating a right-skewed distribution, where median concentrations are lower than mean concentrations. Due to the presence of concentrations skewed towards lower values, the median provides a more reliable measure than the mean for PTEs in atmospheric deposition in and around IAREEM areas [35,36]. The median concentrations of PTEs followed the order of Pb > Cu > Cr > Ni > As > Mo > Cd. It is clear that spatial variability in PTE concentrations for atmospheric deposition near IAREEM areas is minimal (shown in Table 5). This is probably because elements dominated by natural sources typically exhibit low coefficients of variation, while those influenced by anthropogenic sources have higher coefficients [37,38]. In this study area, most atmospherically deposited PTEs show low spatial variability. Notably, the coefficients of variation

for As and Pb are greater than 1, with higher concentrations at mining regions containing heavy rare earth elements in Longnan county (Figure 2), suggesting mining influences concentration of these elements.

Table 5. Statistical analysis of trace element concentration of atmospheric deposition.

Element *	Mean	Min	Max	Median	Std [1]	Skew	CV [2]	Reference [3]
As	23.64	3.18	251.87	8.15	52.39	3.94	2.22	70.00
Cd	2.85	0.45	13.30	2.35	2.46	3.36	0.86	0.13
Cr	58.24	10.31	303.11	45.03	55.84	3.82	0.96	78.00
Cu	76.68	26.08	319.85	60.54	71.44	2.75	0.93	26.00
Mo	5.67	1.09	18.96	4.53	4.47	1.99	0.79	0.73
Ni	26.43	5.37	143.39	20.69	26.58	3.90	1.01	33.00
Pb	121.04	32.40	654.10	73.88	136.23	3.27	1.13	26.00

* Units are mg kg^{-1}. [1] Standard deviation, [2] coefficient of variation, [3] the data in references [39].

Compared to open-pit coal mining areas [40], atmospheric deposition of PTE concentrations of As are significantly higher in IAREEM areas. However, compared to the average level of PTEs in urban areas in China and the world [41,42], the concentration of PTEs in IAREEM areas is at a relatively low level. In addition, the PTE concentrations of Pb, Cr, Cd, Ni, Cu, and As in the IAREEM areas are slightly lower compared to those in the rural areas of Shanghai and the Taihu Lake forest region in the Yangtze River Delta Economic Zone [14,43]. IAREEMs have a relatively low impact on the concentration levels of atmospheric-deposited PTEs (Table 6), and we found that they had the characteristics of atmospheric PTE deposition in other rural regions of China.

Table 6. Comparison of atmospheric deposition (mg kg^{-1}) of metals for concentration between the REE and other regions.

Location	Period	Landuse	As	Cd	Cr	Cu	Mo	Ni	Pb	Reference
Ganzhou, China	2019~2020	Rare earth mine	23.64	2.85	58.24	76.68	5.67	26.43	121.04	This study
Wuhai, China	2018~2019	Coal mine	408.78	1.97	45.97	27.40		25.41	38.93	[40]
Shanghai, China	2011~2012	Rural region	47.60	1.53					150.60	[43]
Taihu lake, China	2016~2018	Woodland		9.42	71.60	139.60		45.98	223.60	[14]
Yinchuang, China	2019~2020	Urban	28.00	0.74	82.60	46.50	2.72	35.10	48.80	[41]
Kandy, Sri Lanka	2017~2018	Urban	10.12	68.60	103.00	123.60		87.60	234.40	[42]

3.2. Human Health Risks Assessment

The assessment of Hazard Quotients (HQ), Hazard Indexes (HI), and Total Hazard Indexes (THI) for adults revealed all values are below 1 (Figure 3a–c). This indicates no significant non-carcinogenic health risk from PTEs absorbed via ingestion and inhalation routes in atmospheric deposition in and around IAREEM areas. The ranking of elements by non-carcinogenic risk is Pb > As > Cr > Cd > Cu > Ni > Mo for adults. However, $HQ_{ingestion}$ values for Pb and As exceed 1 for children in mining regions containing heavy rare earth elements (Figure 3e), suggesting potential adverse health effects from exposure to atmospheric deposition containing Pb and As.

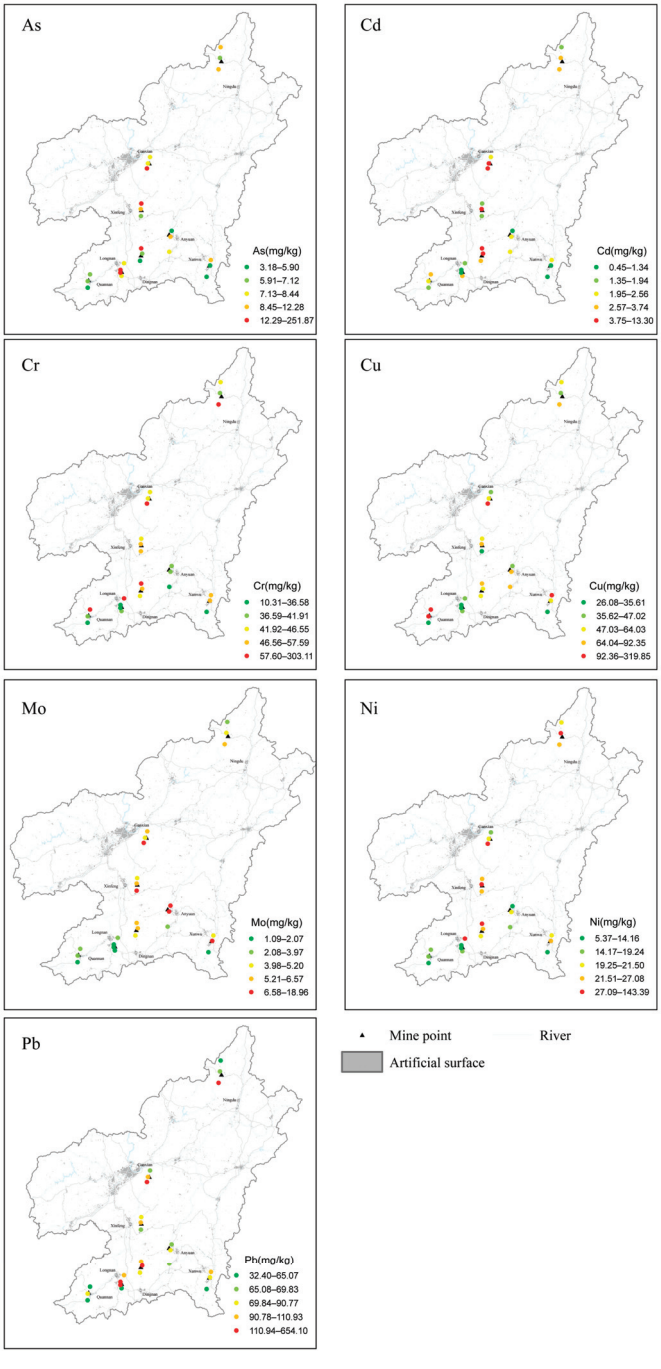

Figure 2. The regional distribution of seven potentially toxic elements (PTEs) in atmospheric deposition. Each dot in the legend symbolizes a sampling site. The color of each dot categorizes PTE concentrations into five distinct groups, based on quartile divisions.

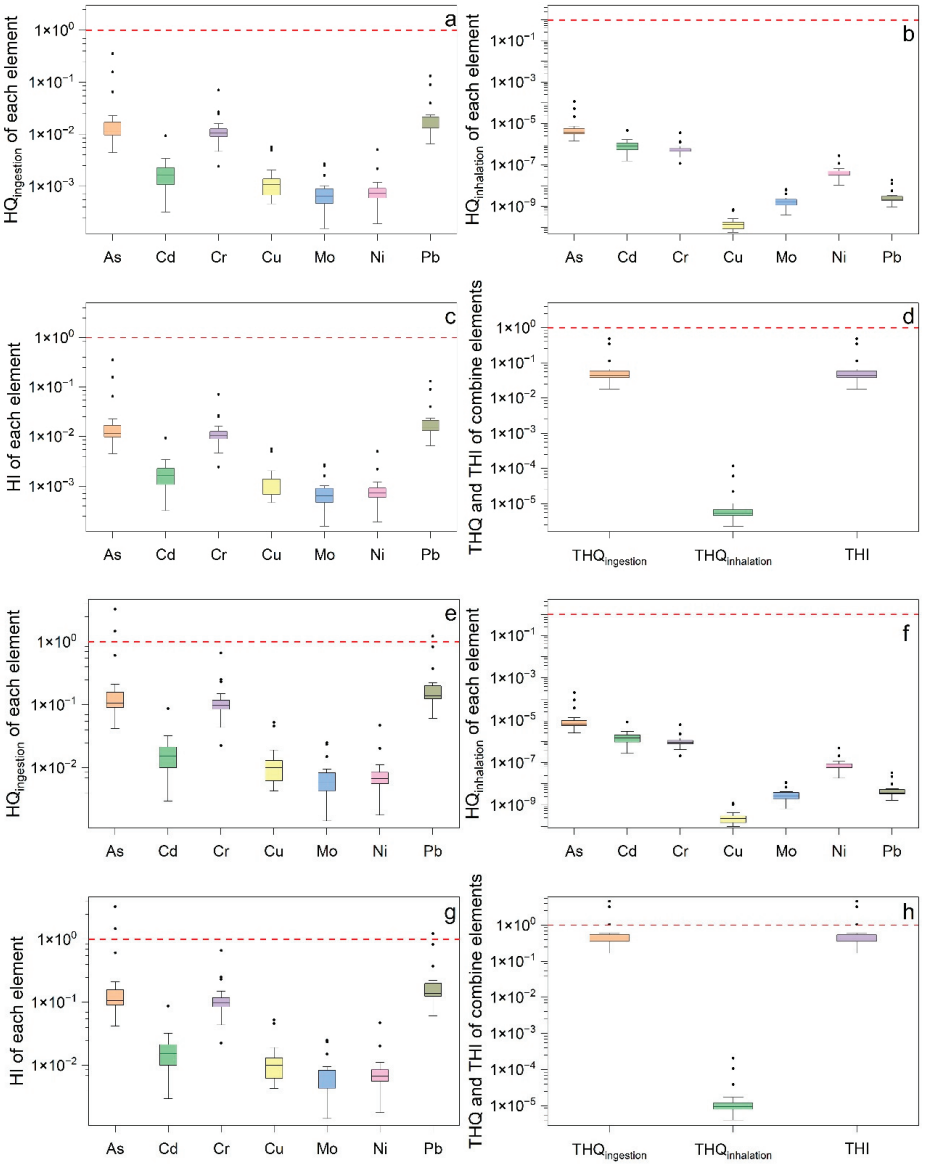

Figure 3. Non-cancer Hazard Quotients (HQ) and Hazard Indexes (HI) of PTEs via ingestion and inhalation exposure pathways calculated for adults (**a**–**d**) and for children (**e**–**h**). In detail: (**a**) HQ of each element through ingestion; (**b**) HQ of each element through inhalation; (**c**) HI of each element through ingestion and inhalation; (**d**) HQ and HI of combined elements through ingestion and inhalation. Figure 3e–h is similar to Figure 3a–d. The red dotted line reflects the safety threshold for potential non-carcinogenic risks. Dark solid circles represent outliers.

In terms of carcinogenic risk, the values for $CR_{ingestion}$, $CR_{inhalation}$, and combined exposure were all below 1×10^{-4}, indicating that the carcinogenic risk for adults from PTEs in atmospheric deposition is within acceptable limits. Regarding carcinogenic risk, the values for $CR_{ingestion}$, $CR_{inhalation}$, and CR were less than 1×10^{-4} (Figure 4a–d). The ranking of elements by non-carcinogenic risk followed the order of Pb > As > Cr > Cd > Cu > Ni > Mo

(Figure 4c,g). Carcinogenic risk to children from single exposure routes also falls within an acceptable range (Figure 4e,h). Only As poses a significant risk in certain areas for children.

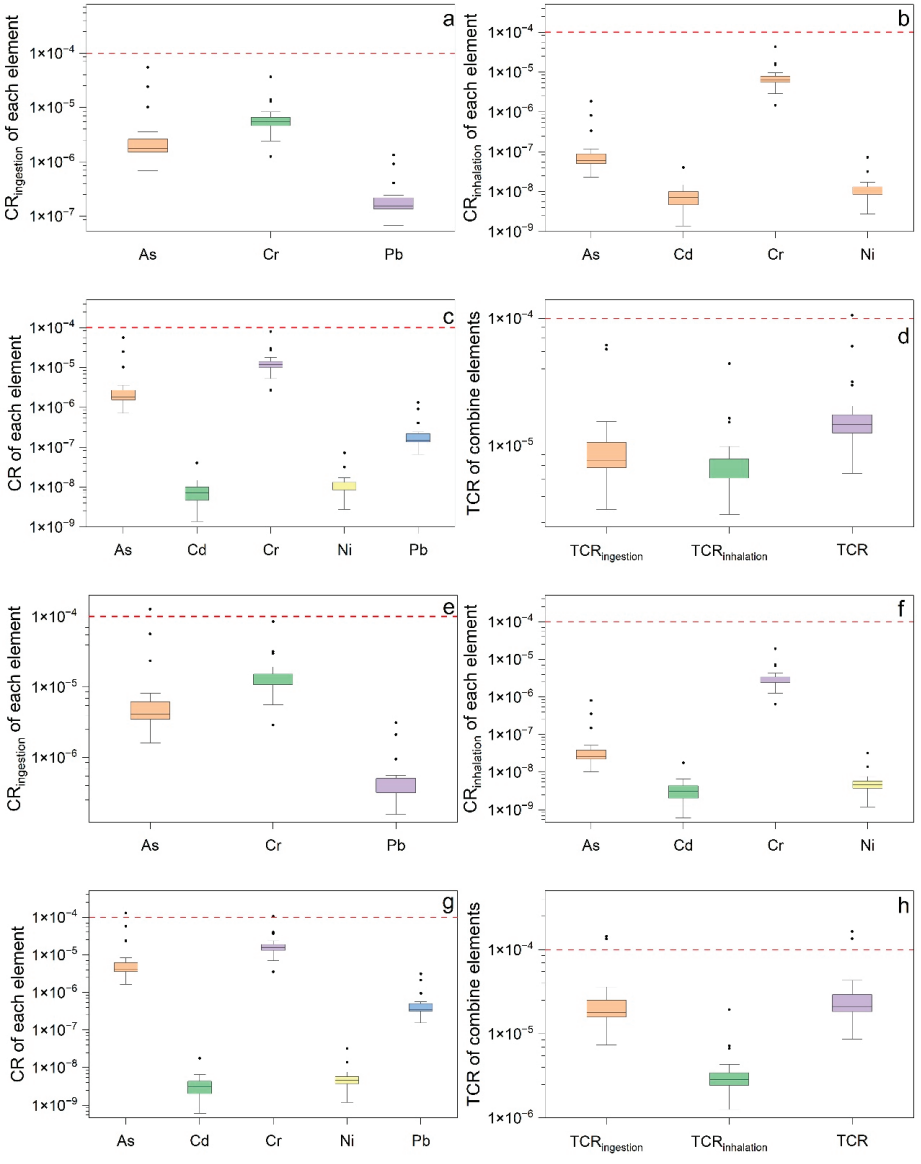

Figure 4. Carcinogenic Risk (CR) of PTEs via ingestion and inhalation exposure pathways calculated for adults (**a**–**d**) and for children (**e**–**h**). In detail: (**a**) CR of each element through ingestion; (**b**) CR of each element through inhalation; (**c**) CR of each element through ingestion and inhalation; (**d**) TCR of combined elements through ingestion and inhalation. Figure 4e–h is similar to Figure 4a–d. The red dotted line reflects the safety threshold for carcinogenic risk. Dark solid circles represent outliers.

Regarding different exposure routes, the human health risks of ingestion is higher than that of inhalation (Figures 3d,h and 4d,h), and ingestion is the primary exposure route. Non-carcinogenic risks are higher in children compared with adults (Figure 3d,h), and

this trend is similar for carcinogenic risks (Figure 4d,h). Children are potentially more susceptible to health risks and are more sensitive to PTEs than adults, and this is consistent with the findings of other researchers [20]. Due to the low oral reference dose and high oral slope factor of As (Table 3), As has high toxicity characteristics. The high concentration areas of As are mainly distributed in Longnan county (Figure 2), posing both carcinogenic and non-carcinogenic risks.

3.3. Source of As

Overall, based on human health risk assessment, As in the atmospheric deposition of this study area poses the greatest risk to humans and is mainly distributed in HREE mines and surrounding areas. Therefore, it was necessary to analyze the sources of As in these atmospheric depositions.

3.3.1. Correlation Analysis and Cluster Analysis

A correlation analysis of elements offers insights into their origins and migration pathways. Strong positive correlations indicate similar sources [15,44]. Following Jacob's correlation grading [45], strong correlations were observed among Cd, Cr, Ni, Mo, and Cu (Figure 5a, $r > 0.71$, $p \leq 0.05$), suggesting a common origin. They may have the exact same origin. Pb and As also showed a significant positive correlation (Figure 5a, $r = 0.97$, $p \leq 0.05$). Cluster analysis further classifies trace elements based on their similarity in concentration and assesses the correlation between elements by constructing a tree diagram to help determine the source of the elements [37,38]. The Pearson clustering method clusters the elements; the results are shown in Figure 3b. The distance indicates the degree of correlation between elements. The lower the value on the distance cluster, the more significant the correlation. According to the cluster analysis diagram, the seven elements can be classified into two categories (Figure 5b) Pb and As forming a distinct cluster at a distance of approximately 0.02; and Cd, Cr, Ni, Mo and Cu forming a distinct cluster at a distance of approximately 0.25. Most importantly, As and Pb may have a common source. Meanwhile, many studies have reported that IAREEMs may be a significant source of Pb contamination in the surrounding areas [4,11]. Based on previous findings, As is predominantly distributed around mines containing heavy rare earth elements in Longnan county (Figure 2), suggesting that these mines may be the principal source of As in atmospheric deposition in the area.

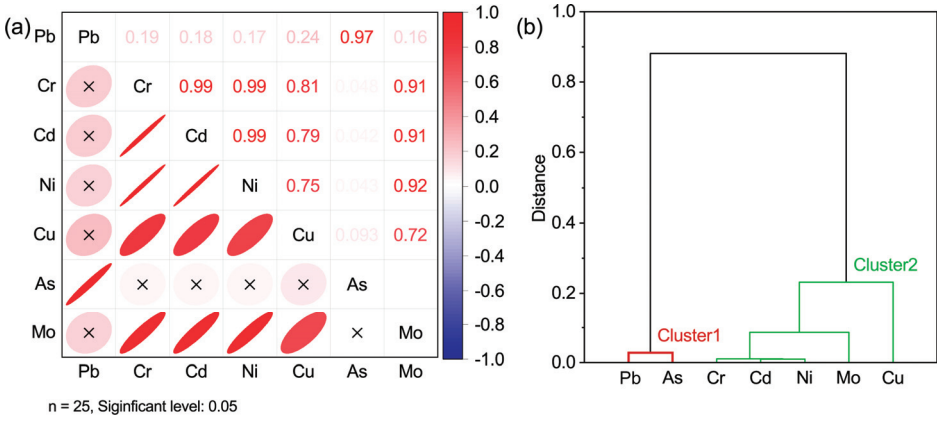

Figure 5. (**a**) Correlation for the concentration of PTEs in atmospheric deposition ($n = 25$). × indicates no significant correlation. (**b**) Cluster for the concentration of PTEs in atmospheric deposition ($n = 25$). Distance reflects the degree of correlation between different elements.

3.3.2. Transport of Arsenic

The median annual deposition fluxes of PTEs at IAREEMs followed the order of Pb > Cu > Cr > Ni > As > Mo > Cd (Figure 6a). The deposition flux of Pb was the highest (7.60 mg m^{-2} y^{-1}), and that of Cd was the lowest (0.11 mg m^{-2} y^{-1}). Mining in IAREEMs resulted in land exposure and vegetation destruction, posing a risk of PTE migration through atmospheric deposition [3]. High atmospheric deposition fluxes of Pb and As around IAREEM areas are shown in Figure 7. In areas with low vegetation coverage near an IAREEM, significant quantities of suspended particulates have been collected from atmospheric deposition (Figure 6b). The transport and deposition of PTEs in the atmospheric deposition of mining areas are controlled by the PTE concentrations in the surrounding soil particulates and vegetation [46,47]. The scarcity of vegetation may facilitate the resuspension of soil particles into the atmosphere, resulting in an increase in arsenic deposition in the IAREEM area.

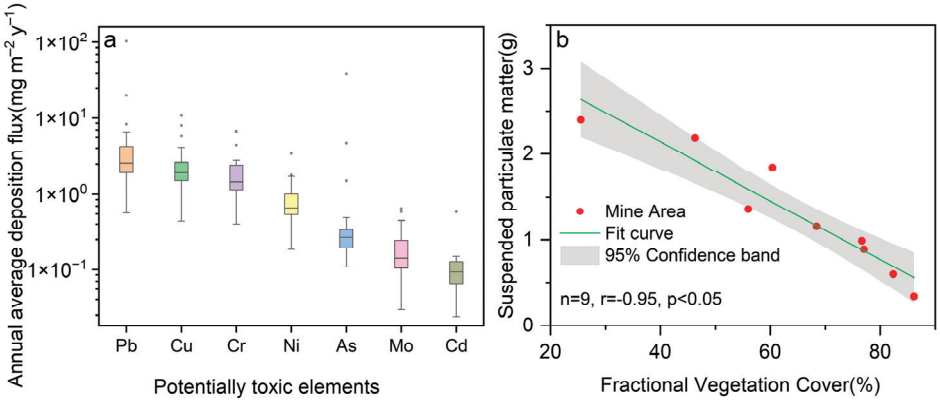

Figure 6. (**a**) Boxplot of atmospheric deposition fluxes for PTEs. The box reflects the 25th and 75th quantiles. Whiskers are the maximum and minimum values within 1.5 times the interquartile range. The dark line inside the box represents the median. Dark solid circles outside the whisker are outliers. (**b**) The correlation of Fractional Vegetation Cover with suspended particulate matter collected from atmospheric deposition. The remote sensing images used for the FVC calculations and the calculation process are shown in Table 1.

3.3.3. Mineralogy of the Regolith

In Ganzhou city, IAREEMs are divided into heavy and light rare earth types, with significant As content in the semi-differentiated layer of the heavy rare earth deposit in Longnan county, exceeding China's agricultural land soil safety standards [22,25]. The minerals in the regolith are listed in Table 7. The main minerals in the regolith are kaolinite\illite (46.00%) and quartz (45.89%). Among them, is a type of As-containing mineral called chernovite-(Y) occuring as micron-sized pseudocubic crystals in the regolith (Figure 8a). The chemical composition of chernovite-(Y) is shown in Figure 8b. It is clear that there is a high content (over 25%) of As in chernovite-(Y) of semi-weathered regolith samples. This results in a high background value of As in the heavy rare earth deposit. Under the ongoing surface fluid–mineral interaction, As and REEs precipitate to generate chernovite-(Y) [22,48]. Additionally, the fully weathered layer of IAREEM contains 46% kaolinite and other clay minerals. Studies have shown As being readily adsorbed by clay minerals such as kaolinite [22,49]. Therefore, the As in atmospheric deposition in Longnan county and surrounding areas is highly likely to come from heavy rare earth minerals. Rare earth mining activities have led to vegetation destruction and soil erosion [3,4,11], exposing weathered layers beneath the soil humus and resulting in wind-borne transport of fine-

grained arsenic-adsorbing clay minerals and chernovite-(Y), thereby increasing the risk of As exposure.

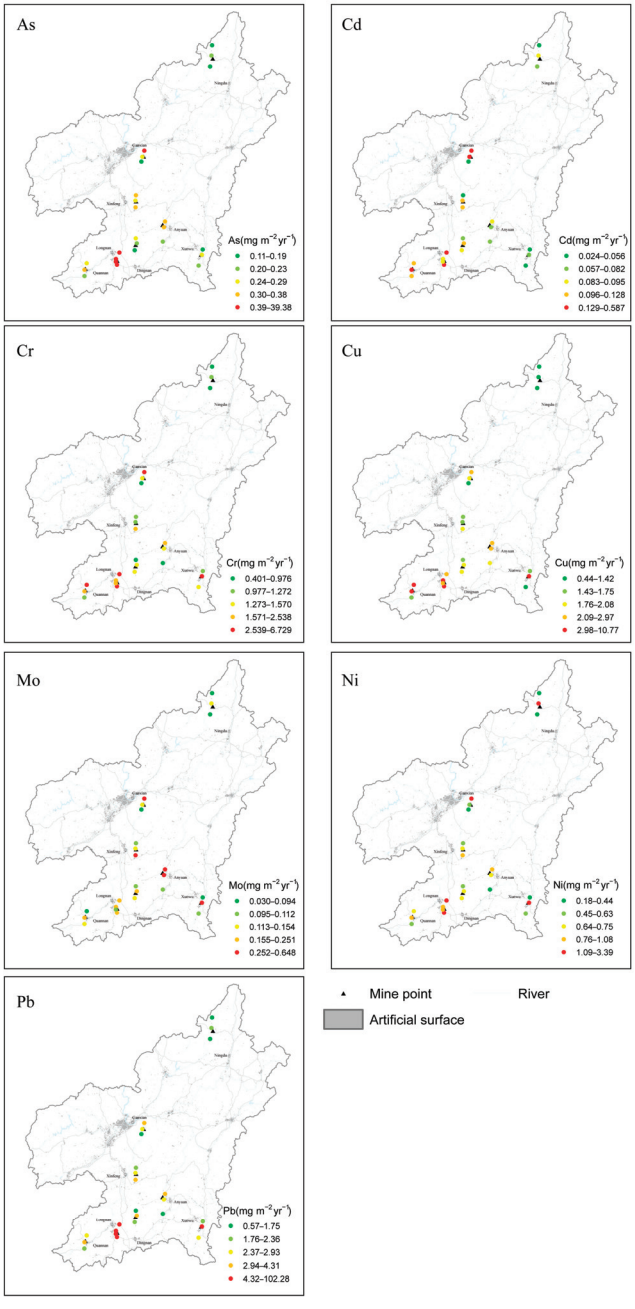

Figure 7. This figure depicts the regional distribution of seven potentially toxic elements (PTEs) in atmospheric deposition. The dots in the legend indicate the locations of sampling sites. The color coding of each dot corresponds to PTE fluxes, which are classified into five tiers based on quartile analysis.

Table 7. Minerals in the regolith.

Mineral Name	Chemical Formula	wt%
Kaolinite/Illite	$Al_4[Si_4O_{10}](OH)_8/KAl_2[(SiAl)_4O_{10}]\cdot(OH)_2\cdot nH_2O$	46.0072
Quartz	SiO_2	45.8911
K-feldspar	$K[AlSi_3O_8]$	5.0466
Muscovite	$Al_2K_2O_6Si$	2.4201
Limonite	$Fe_2O_3\cdot nH_2O$	0.4462
Albite	$NaAlSi_3O_8$	0.0559
Montmorillonite	$Al_2Si_2O_5\cdot(OH)_4$	0.0221
Zircon	$ZrSiO_4$	0.0196
Chernovite-(Y)	$Y[AsO_4]$	0.0159
Ilmenite	$FeTiO_3$	0.0092
Xenotime-(Y)	YPO_4	0.0030
Chlorite	$(Mg,Fe,Al)_6(Si,Al)_4O_{10}(OH)_8$	0.0026
Euxenite-group mineral	$(Y,Ca)(Nb,Ta,Ti,Fe)_2O_6$	0.0023
Calcite	$CaCO_3$	0.0022
Fergusonite-group mineral	$YNbO_4$	0.0013
Coronadite	$Pb(Mn^{4+},Mn^{2+})_8O_{16}$	0.0013
Dolomite	$CaMg(CO_3)_2$	0.0013
Thorite	$Th[SiO_4]$	0.0006
Monazite	$CePO_4$	0.0003
Total		99.9486

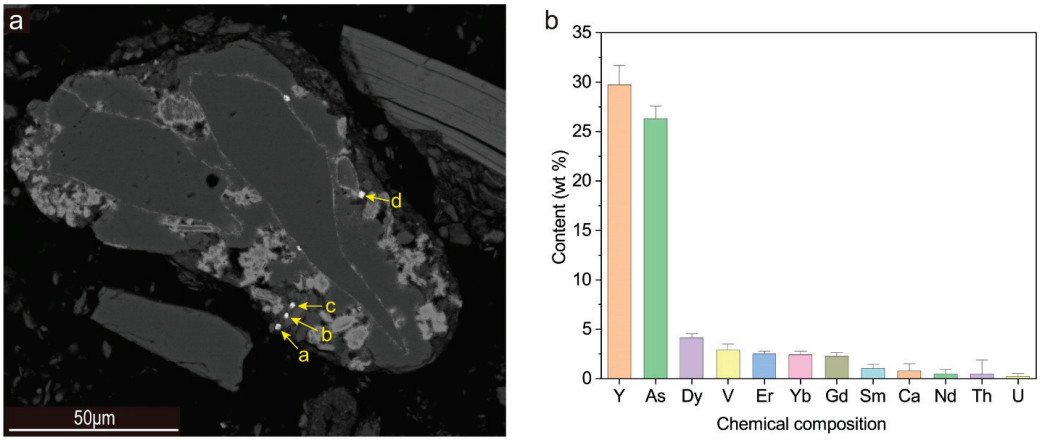

Figure 8. (**a**) Backscattered electron images of HREE minerals in the regolith. Yellow arrows indicate chernovite-(Y). (**b**) Chemical composite of chernovite-(Y) of four points in Figure 8a (yellow arrow). The bar chart represents the mean. Whiskers outside the bar chart are the maximum and minimum values within 1.5 times the interquartile range.

Therefore, it is necessary to carry out ecological restoration and restore vegetation in mining areas, which can inhibit the migration of pollutants in mining areas, and reduce the risk to children, especially those exposed to As.

4. Conclusions

In this study, we investigated atmospheric deposition of PTEs from typical IAREEMs in Ganzhou city, China. The study reveals the distribution and human health risks associated with PTEs from atmospheric deposition in IAREEM areas. The results show that As concentrations in atmospheric deposition ranged from 3.18 to 251.87 mg kg^{-1}, and As atmospheric fluxes varied from 0.11 to 39.4 mg m^{-2} y^{-1}. The concentration and fluxes of atmospheric deposition of PTEs in Ganzhou and its surrounding areas followed the order

of Pb > Cu > Cr > Ni > As > Mo > Cd. Human health risk assessments for ingestion and inhalation routes indicate that ingestion is the primary exposure route posing health risks. There are no significant non-carcinogenic or unacceptable carcinogenic risks to adults from atmospheric deposition of PTEs in IAREEM areas. However, children are more vulnerable to PTEs than adults, suffering from potential non-carcinogenic and greater carcinogenic risks at mines containing heavy rare earth elements in Longnan county. Pb and As are the primary contributors to non-carcinogenic risks, and As is the main contributor to carcinogenic risks because of its low oral reference dose and high oral slope factor. Because As-rich materials (e.g., arsenic-adsorbing clay zones and chernovite-(Y)) are exposed in fully weathered layers, and the formed suspended particulate matter is transported into the atmosphere at heavy rare earth mineral sites in Longnan county, As poses both carcinogenic and non-carcinogenic risks to children. PTEs are primarily transmitted to surrounding areas through fine particulate matter. Vegetation recovery plays a crucial role in controlling the migration of suspended particulate matter and inhibiting the outward movement of PTEs from mines through atmospheric transmission. Therefore, it is necessary to carry out ecological restoration and restore vegetation in mining areas, for inhibiting the migration of pollutants in mining areas, and reducing the risk to children, especially those exposed to As. Our results provide a deep understanding of the pollution in and around mining areas under the influence of atmospheric deposition, and provide support for pollution prevention.

Author Contributions: J.W.: conceptualization, methodology, data curation, writing—original draft; S.L.: conceptualization, writing—review and editing, supervision, project administration, funding acquisition; T.C.: formal analysis; G.Y.: supervision; M.X.: investigation, resources; Y.H.: investigation, formal analysis; Q.S.: supervision; C.M.: data curation, visualization; Q.X.: conceptualization, writing—review and editing, supervision. All authors have read and agreed to the published version of the manuscript.

Funding: This research was funded by the project of China Geological Survey Study on National Comprehensive Survey and Evaluation of Mining Geological Environment, grant number DD20190703, the project of China Geological Survey Study on Typical Regional Health Geological Survey, grant number DD20230118, and the National Natural Science Foundation of China, grant number 42177061.

Institutional Review Board Statement: Not applicable.

Informed Consent Statement: Not applicable.

Data Availability Statement: The data that support the findings of this study are available on request from the corresponding author S. Liu. The data are not publicly available due to them containing information that could compromise rese arch participant privacy.

Acknowledgments: The authors greatly appreciates the helpful suggestions provided by the editors and reviewers, which have greatly improved the quality of the manuscript.

Conflicts of Interest: The authors declare that they have no conflicts of interest.

References

1. Bao, Z.; Zhao, Z. Geochemistry of mineralization with exchangeable REY in the weathering crusts of granitic rocks in South China. *Ore Geol. Rev.* **2008**, *33*, 519–535. [CrossRef]
2. Feng, W.; Guo, Z.; Peng, C.; Xiao, X.; Shi, L.; Zeng, P.; Ran, H.; Xue, Q. Atmospheric bulk deposition of heavy metal(loid)s in central south China: Fluxes, influencing factors and implication for paddy soils. *J. Hazard. Mater.* **2019**, *371*, 634–642. [CrossRef] [PubMed]
3. Li, H.; Xu, F.; Li, Q. Remote sensing monitoring of land damage and restoration in rare earth mining areas in 6 counties in southern Jiangxi based on multisource sequential images. *J. Environ. Manag.* **2020**, *267*, 110653.
4. Liu, J.H.; Chen, L.K.; Liu, C.Y.; Qiu, L.R.; He, S. Pb speciation in rare earth minerals and use of entropy and fuzzy clustering methods to assess the migration capacity of Pb during mining activities. *Ecotox. Environ. Saf.* **2018**, *165*, 334–342. [CrossRef]
5. Guo, G.; Zhang, D.; Wang, Y. Characteristics of heavy metals in size-fractionated atmospheric particulate matters and associated health risk assessment based on the respiratory deposition. *Environ. Geochem. Health* **2021**, *43*, 285–299. [CrossRef]

6. Castillo, S.; de la Rosa, J.D.; Sánchez De La Campa, A.M.; González-Castanedo, Y.; Fernández-Caliani, J.C.; Gonzalez, I.; Romero, A. Contribution of mine wastes to atmospheric metal deposition in the surrounding area of an abandoned heavily polluted mining district (Rio Tinto mines, Spain). *Sci. Total Environ.* **2013**, *449*, 363–372. [CrossRef] [PubMed]
7. Zhang, Y.; Zhang, S.; Zhu, F.; Wang, A.; Dai, H.; Cheng, S.; Wang, J.; Tang, L. Atmospheric heavy metal deposition in agro-ecosystems in China. *Environ. Sci. Pollut. Res.* **2018**, *25*, 5822–5831. [CrossRef]
8. Braune, B.M.; Outridge, P.M.; Fisk, A.T.; Muir, D.C.G.; Helm, P.A.; Hobbs, K.; Hoekstra, P.F.; Kuzyk, Z.A.; Kwan, M.; Letcher, R.J.; et al. Persistent organic pollutants and mercury in marine biota of the Canadian Arctic: An overview of spatial and temporal trends. *Sci. Total Environ.* **2005**, *351–352*, 4–56. [CrossRef] [PubMed]
9. Wang, J.; Zhang, X.; Yang, Q.; Zhang, K.; Zheng, Y.; Zhou, G. Pollution characteristics of atmospheric dustfall and heavy metals in a typical inland heavy industry city in China. *J. Environ. Sci.-China* **2018**, *71*, 283–291. [CrossRef]
10. Wong, C.S.C.; Li, X.D.; Zhang, G.; Qi, S.H.; Peng, X.Z. Atmospheric deposition of heavy metals in the Pearl River Delta, China. *Atmos. Environ.* **2003**, *37*, 767–776. [CrossRef]
11. Qiao, J.; Tang, J.; Xue, Q. Study on Pb release by several new lixiviants in weathered crust elution-deposited rare earth ore leaching process: Behavior and mechanism. *Ecotox. Environ. Saf.* **2020**, *190*, 110138. [CrossRef] [PubMed]
12. Siddiqui, A.U.; Jain, M.K.; Masto, R.E. Distribution of some potentially toxic elements in the soils of the Jharia Coalfield: A probabilistic approach for source identification and risk assessment. *Land Degrad. Dev.* **2022**, *33*, 333–345. [CrossRef]
13. Li, L.; Zhang, B.; Jiang, B.; Zhao, Y.; Qian, G.; Hu, X. Potentially toxic elements in weathered waste-rocks of Fushun western opencast mine: Distribution, source identification, and contamination assessment. *Environ. Geochem. Health* **2021**, *44*, 1813–1826. [CrossRef] [PubMed]
14. Chen, L.; Zhou, S.; Wu, S.; Wang, C.; He, D. Concentration, fluxes, risks, and sources of heavy metals in atmospheric deposition in the Lihe River watershed, Taihu region, eastern China. *Environ. Pollut.* **2019**, *255*, 113301. [CrossRef] [PubMed]
15. Tian, S.; Liang, T.; Li, K.; Wang, L. Source and path identification of metals pollution in a mining area by PMF and rare earth element patterns in road dust. *Sci. Total Environ.* **2018**, *633*, 958–966. [CrossRef]
16. Haghnazar, H.; Belmont, P.; Johannesson, K.H.; Aghayani, E.; Mehraein, M. Human-induced pollution and toxicity of river sediment by potentially toxic elements (PTEs) and accumulation in a paddy soil-rice system: A comprehensive watershed-scale assessment. *Chemosphere* **2023**, *311*, 136842. [CrossRef]
17. Li, Y.; Chen, H.; Song, L.; Wu, J.; Sun, W.; Teng, Y. Effects on microbiomes and resistomes and the source-specific ecological risks of heavy metals in the sediments of an urban river. *J. Hazard. Mater.* **2021**, *409*, 124472. [CrossRef]
18. *Exposure Assessment Tools by Media–Soil and Dust*; Office of Solid Waste and Emergency Response: Washington, DC, USA, 2022.
19. Guo, G.; Wang, Y.; Zhang, D.; Li, K.; Lei, M. Human health risk apportionment from potential sources of heavy metals in agricultural soils and associated uncertainty analysis. *Environ. Geochem. Health* **2023**, *45*, 881–897. [CrossRef]
20. Ivaneev, A.I.; Brzhezinskiy, A.S.; Karandashev, V.K.; Ermolin, M.S.; Fedotov, P.S. Assessment of sources, environmental, ecological, and health risks of potentially toxic elements in urban dust of Moscow megacity, Russia. *Chemosphere* **2023**, *321*, 138142. [CrossRef]
21. Xu, J.; Gui, H.; Chen, J.; Li, C.; Li, Y.; Zhao, C.; Guo, Y. A combined model to quantitatively assess human health risk from different sources of heavy metals in soils around coal waste pile. *Hum. Ecol. Risk Assess. Int. J.* **2021**, *27*, 2235–2253. [CrossRef]
22. Li, M.Y.H.; Zhou, M.; Williams-Jones, A.E. The Genesis of Regolith-Hosted Heavy Rare Earth Element Deposits: Insights from the World-Class Zudong Deposit in Jiangxi Province, South China. *Econ. Geol.* **2019**, *114*, 541–568. [CrossRef]
23. Tian, J.; Tang, X.; Yin, J.; Chen, J.; Luo, X.; Rao, G. Enhanced Leachability of a Lean Weathered Crust Elution-Deposited Rare-Earth Ore: Effects of Sesbania Gum Filter-Aid Reagent. *Metall. Mater. Trans. B* **2013**, *44*, 1070–1077. [CrossRef]
24. Bockheim, J.G. Classification and development of shallow soils (<50 cm) in the USA. *Geoderma Reg.* **2015**, *6*, 31–39.
25. *DZ/T 0295-2016*; Specification of Land Quality Geochemical Assessment. Ministry of Land and Resources of the People's Republic of China: Beijing, China, 2016.
26. Gutman, G.; Ignatov, A. The derivation of the green vegetation fraction from NOAA/AVHRR data for use in numerical weather prediction models. *Int. J. Remote Sens.* **1998**, *19*, 1533–1543. [CrossRef]
27. Sun, X.; Liu, S.; Jiang, J.; Bai, X.; Chen, Y.; Zhu, C.; Guo, W. Coordination inversion methods for vegetation cover of winter wheat by multi-source satellite images. *Trans. Chin. Soc. Agric. Eng. (Trans. CSAE)* **2017**, *33*, 161–167.
28. Yan, Y.; Liu, H.; Bai, X.; Zhang, W.; Wang, S.; Luo, J.; Cao, Y. Exploring and attributing change to fractional vegetation coverage in the middle and lower reaches of Hanjiang River Basin, China. *Environ. Monit. Assess.* **2022**, *195*, 131. [CrossRef] [PubMed]
29. Yan, L.; Franco, A.; Elio, P. Health risk assessment via ingestion and inhalation of soil PTE of an urban area. *Chemosphere* **2021**, *281*, 130964. [CrossRef] [PubMed]
30. *Regional Screening Levels (RSLs)—Equations*; Office of Solid Waste and Emergency Response: Washington, DC, USA, 2022.
31. *Regional Screening Levels (RSLs)—User's Guide*; Office of Solid Waste and Emergency Response: Washington, DC, USA, 2022.
32. *Regional Screening Level (RSL) Summary Table*; Office of Solid Waste and Emergency Response: Washington, DC, USA, 2022.
33. Lu, X.; Wu, X.; Wang, Y.; Chen, H.; Gao, P.; Fu, Y. Risk assessment of toxic metals in street dust from a medium-sized industrial city of China. *Ecotox. Environ. Saf.* **2014**, *106*, 154–163. [CrossRef]
34. Annual Average Value of the Concentration of Six Pollutants by County (City, District) in Jiangxi Province in 2020, 2021. Available online: http://sthjt.jiangxi.gov.cn/art/2021/3/12/art_42079_3315206.html (accessed on 1 March 2024).

35. Zhong, C.; Yang, Z.; Jiang, W.; Hu, B.; Hou, Q.; Yu, T.; Li, J. Ecological geochemical assessment and source identification of trace elements in atmospheric deposition of an emerging industrial area: Beibu Gulf economic zone. *Sci. Total Environ.* **2016**, *573*, 1519–1526. [CrossRef]
36. Xia, X.; Chen, X.; Liu, R.; Liu, H. Heavy metals in urban soils with various types of land use in Beijing, China. *J. Hazard. Mater.* **2011**, *186*, 2043–2050. [CrossRef]
37. Yuan, G.L.; Sun, T.H.; Han, P.; Li, J.; Lang, X.X. Source identification and ecological risk assessment of heavy metals in topsoil using environmental geochemical mapping: Typical urban renewal area in Beijing, China. *J. Geochem. Explor.* **2014**, *136*, 40–47. [CrossRef]
38. Huang, S.; Tu, J.; Liu, H.; Hua, M.; Liao, Q.; Feng, J.; Weng, Z.; Huang, G. Multivariate analysis of trace element concentrations in atmospheric deposition in the Yangtze River Delta, East China. *Atmos. Environ.* **2009**, *43*, 5781–5790. [CrossRef]
39. Xi, X.; Hou, Q.; Yang, Z.; Ye, J.; Yu, T.; Xia, X.; Cheng, H.; Zhou, G.; Yao, L. Big data based studies of the variation features of Chinese soil' s background value versus reference value: A paper written on the occasion of Soil Geochemical Parameters of China' s publication. *Geophys. Geochem. Explor.* **2020**, *45*, 1095–1108.
40. Wu, H.; Shi, C.; Zhang, Y.; Zhao, T.; Hu, P.; Liu, Y.; Chen, T. Characteristics and Source Apportionment of Dustfall Pollution in the Coal Mine Area and Surrounding Areas of Wuhai City in Spring. *Environ. Sci.* **2020**, *41*, 1167–1175.
41. Kai, J.; Wang, C.; Niu, Y.; Li, C.; Zuo, Z. Distribution characteristics and source analysis of atmospheric fallout elements in Yinchuan City. *Environ. Sci. Technol.* **2020**, *43*, 96–103.
42. Weerasundara, L.; Magana-Arachchi, D.N.; Ziyath, A.M.; Goonetilleke, A.; Vithanage, M. Health risk assessment of heavy metals in atmospheric deposition in a congested city environment in a developing country: Kandy City, Sri Lanka. *J. Environ. Manag.* **2018**, *220*, 198–206. [CrossRef] [PubMed]
43. Shi, G.; Chen, Z.; Teng, J.; Bi, C.; Zhou, D.; Sun, C.; Li, Y.; Xu, S. Fluxes, variability and sources of cadmium, lead, arsenic and mercury in dry atmospheric depositions in urban, suburban and rural areas. *Environ. Res.* **2012**, *113*, 28–32. [CrossRef] [PubMed]
44. Li, W.; Zuo, Y.; Wang, L.; Wan, X.; Yang, J.; Liang, T.; Song, H.; Weihrauch, C.; Rinklebe, J. Abundance, spatial variation, and sources of rare earth elements in soils around ion-adsorbed rare earth mining areas. *Environ. Pollut.* **2022**, *313*, 120099. [CrossRef] [PubMed]
45. Jacob, C. *Statistical Power Analysis for the Behavioral Sciences*; Lawrence Erlbaum Associates: Mahwah, NJ, USA, 1988.
46. Corona Sánchez, J.E.; González Chávez, M.D.C.A.; Carrillo González, R.; Scheckel, K.; Tapia Maruri, D.; García Cue, J.L. Metal(loid) bioaccessibility of atmospheric particulate matter from mine tailings at Zimapan, Mexico. *Environ. Sci. Pollut. Res.* **2021**, *28*, 19458–19472. [CrossRef]
47. Ao, M.; Qiu, G.; Zhang, C.; Xu, X.; Zhao, L.; Feng, X.; Qin, S.; Meng, B. Atmospheric deposition of antimony in a typical mercury-antimony mining area, Shaanxi Province, Southwest China. *Environ. Pollut.* **2019**, *245*, 173–182. [CrossRef]
48. Smedley, P.L.; Kinniburgh, D.G. A review of the source, behaviour and distribution of arsenic in natural waters. *Appl. Geochem.* **2002**, *17*, 517–568. [CrossRef]
49. Borst, A.M.; Smith, M.P.; Finch, A.A.; Estrade, G.; Villanova-De-Benavent, C.; Nason, P.; Marquis, E.; Horsburgh, N.J.; Goodenough, K.M.; Xu, C.; et al. Adsorption of rare earth elements in regolith-hosted clay deposits. *Nat. Commun.* **2020**, *11*, 4386. [CrossRef] [PubMed]

applied sciences

MDPI

Article

Arsenic in a Karstic Paddy Soil with a High Geochemical Background in Guangxi, China: Its Bioavailability and Controlling Factors

Xuezhen Li [1], Xudong Ma [1], Qingye Hou [1], Xueqi Xia [1], Bo Li [1], Kun Lin [1], Xu Liu [2], Zhiliang Wu [1], Wenbing Ji [3], Lei Wang [4], Tao Yu [5,6,*] and Zhongfang Yang [1,6,*]

[1] School of Earth Sciences and Resources, China University of Geosciences, Beijing 100083, China
[2] Ministry Environmental Protection Key Laboratory of Eco-Industry, Chinese Research Academy of Environmental Sciences, Beijing 100012, China
[3] Nanjing Institute of Environmental Sciences, Ministry of Ecology and Environment, Nanjing 210042, China
[4] Guangxi Bureau of Geology and Mineral Prospecting and Exploitation, Nanning 530023, China
[5] School of Science, China University of Geosciences, Beijing 100083, China
[6] Key Laboratory of Ecological Geochemistry, Ministry of Natural Resources, Beijing 100037, China
* Correspondence: yutao@cugb.edu.cn (T.Y.); yangzf@cugb.edu.cn (Z.Y.)

Abstract: Arsenic (As) is of widespread concern, as its elevated contents in soil and water have a serious impact on the ecological environment and human health. Soils in karst regions are characterized by a high geochemical background of As. However, the bioavailability of As in paddy soils and the potential risk of As transfer from the soil to rice remain unclear. In this study, 305 paired soil–rice samples were collected from karst regions in Guangxi, China, in order to examine the controlling variables and As bioavailability in the soil–rice system. According to this study, the karst region's paddy soil had higher As concentrations than the non-karst region's paddy soil. The As concentration in the rice grains was low, with only 0.62% of the rice samples exceeding the permissible value of inorganic As (0.2 mg/kg). Arsenic in the karstic paddy soils existed mainly in the residual fraction, while the water-soluble and exchangeable fractions, which are readily absorbed by rice, accounted for a relatively small proportion. The high content but low bioavailability of As in the karstic paddy soil was mostly attributed to the abundant Fe–Mn nodules, which contributed 64.45% of the As content in the soil. Within the Fe–Mn nodules, As was primarily bound to Fe-(oxyhydr)oxides, which could be released into the paddy soil under certain reduction conditions via the reductive dissolution of Fe-(oxyhydr)oxides. Under the natural pH conditions of the karstic paddy soil (pH 4.9–8.38), the leaching of As was almost negligible, and As could be steadily retained within the Fe–Mn nodules. However, extremely acidic or alkaline conditions promoted the release of As from the Fe–Mn nodules.

Keywords: arsenic; paddy soil; bioavailability; Fe–Mn nodules; karst regions

Citation: Li, X.; Ma, X.; Hou, Q.; Xia, X.; Li, B.; Lin, K.; Liu, X.; Wu, Z.; Ji, W.; Wang, L.; et al. Arsenic in a Karstic Paddy Soil with a High Geochemical Background in Guangxi, China: Its Bioavailability and Controlling Factors. *Appl. Sci.* **2024**, *14*, 1400. https://doi.org/10.3390/app14041400

Academic Editor: Mauro Marini

Received: 30 December 2023
Revised: 29 January 2024
Accepted: 5 February 2024
Published: 8 February 2024

1. Introduction

Arsenic (As), a potentially toxic element to humans, is bioaccumulative and non-biodegradable in the natural environment [1–3]. Karst terrains occupy about 7–10% of the planet [4]. China has approximately 2 million square kilometers of karst landforms, distributed in various provinces and regions, with the majority located in the southern part of the country, particularly widespread in Guangxi, Guizhou, Yunnan, and Chongqing. Because of the high average background values of karstic landscape-formed soils, they are frequently enriched in As [5,6]. Since As can enter the food chain and endanger human health [7–9], its excess in karst soils has drawn considerable attention from the public in an effort to protect the environment, the ecology, and public health in karst regions [10–12].

The natural presence of As in soils is primarily influenced by the composition of geological parent materials [13,14]. It has been shown that there is a strong correlation

between As in soils in northwest Greece and geological parent materials and anthropogenic sources of pollution [4]. In karst areas, the heredity of a parent rock with a high heavy metal content (e.g., black shale, sulfide deposits, and coal measure strata) and secondary enrichment caused by the leaching and weathering of a parent rock with a low heavy metal content (e.g., carbonate rocks) during soil development may lead to an As content that is higher than the normal background [15]. This natural process may result in wide areas of soil exceeding the environmental quality standards for As [16]. Consequently, a certain proportion of cultivated fields in karst regions may fall under strict supervision and be unsuitable for agricultural production, leading to significant public concern and constraining the local agricultural economy [5,17].

The physico-chemical characteristics and chemical forms of heavy metals largely determine the potential mobility and bioavailability of As [18,19]. In comparison with the total content of As, the bioavailability of As is more closely related to plant absorption [20,21]. The primary reasons for soil heavy metal elements in karst regions are pedogenic processes, which cause the high geological background values in the area [22,23]. In their natural state, the reactivity of most heavy metals is relatively low. Nonetheless, there have been notable alterations in the physico-chemical characteristics of soils as a result of frequent human production activities, for example, in northwestern Greece [4], southern China [22], and southwestern China [23]. As a result, the amount of certain heavy metals that are readily available has increased, which poses a major risk to the safety of agricultural products [24]. To date, the majority of relevant studies concerning As bioavailability and transfer in the soil–plant system have primarily focused on localized areas or limited regions with anthropogenic contamination [25,26]. However, the bioavailability of soil As and the potential high transfer risk of As from the soil to rice remain unclear, particularly in regions with a naturally high As background.

Guangxi, a region of China with one of the most extensive distributions of karst regions and with a significant carbonate rock development [27], faces significant environmental concerns related to the heavy metal contamination of soil. Recent studies have verified that the combination of secondary enrichment and parental rock inheritance is responsible for the high accumulation of As in Guangxi's karstic soil [6]. Fe–Mn nodules are present in many agricultural soils in the karst areas of Guangxi, China [28,29]. Fe–Mn nodules share a common origin with the surrounding soils and are formed in situ by the cementation of Fe-(oxyhydr)oxides to the soil matrix components. It has been proven that soil Fe–Mn nodules, which are mainly composed of Fe-(oxyhydr)oxides, also have a strong adsorption capacity for heavy metal elements and control the migration, adsorption, and precipitation of heavy metal pollutants in the soil, thus affecting the bioavailability of heavy metals [28–30].

In this study, a total of 305 paired soil–rice samples were gathered from Guangxi's karst regions, spanning a sizable geographic area, in order to obtain a thorough understanding of the environmental chemical behavior of As in rice–soil systems. Various extraction reagents and experimental conditions were employed to obtain more information about the bioavailability of soil As. Therefore, the objectives of this study were to (1) identify the As concentrations in the soil and rice in karst regions in Guangxi; (2) determine the bioavailability of As in the soils; and (3) investigate the controlling factors of As bioavailability and its potential environmental implications.

2. Materials and Methods

2.1. Study Area and Sample Collection

The Guangxi Zhuang Autonomous Region is located in the southern part of China (104°26′–112°04′ E, 20°54′–26°24′ N) (Figure 1). It has high temperatures and an abundance of rain due to its subtropical monsoon climate. Carbonate rocks make up the majority of the study area, that is, about 42% of the total land area, and they are mostly found in Guangxi's middle and western regions [31].

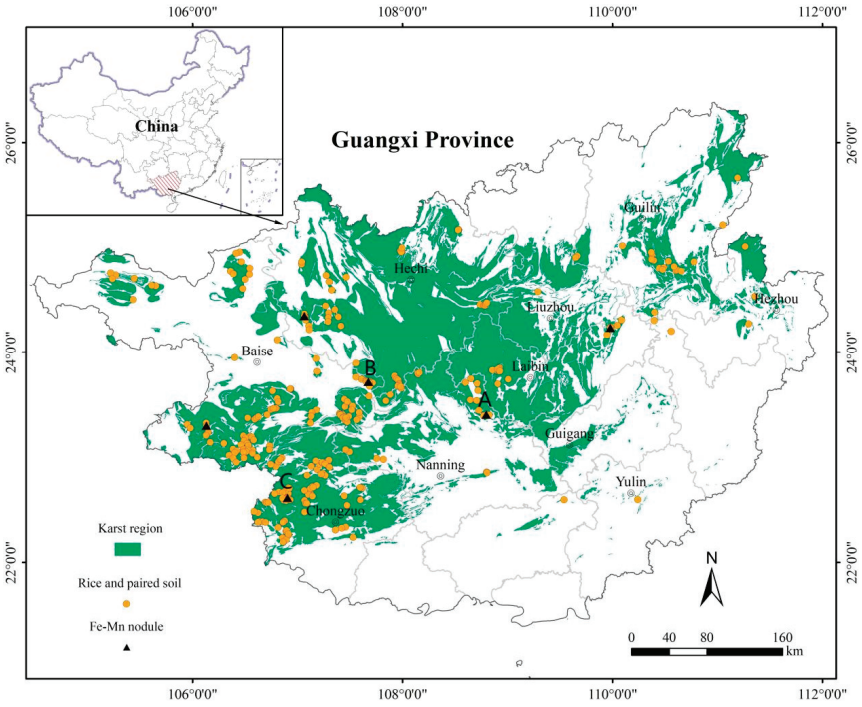

Figure 1. Sampling sites (yellow circles) from the karst region in Guangxi, China. (A, C): Mn nodules; (B): Fe nodules, the specific shapes of Fe-Mn nodules are shown in Figure 2.

In total, 305 paired soil–rice samples were obtained from the karst region in the study area in cooperation with the Guangxi Bureau of Geological and Mineral Exploration (Figure 1), and the samples were pre-processed in compliance with the Specification of Land Quality Geochemical Assessment [32]. Each rice sample consisted of an equal amount of rice grains from 3 sub-sampling points. The collected rice grains were placed in a mesh bag, hung in a cool place, air-dried, and then sent to the laboratory after threshing. Alongside the rice grain collection, the corresponding rhizosphere soil was also collected. After uprooting the rice roots, the soil adhering to the roots was shaken off. The depth of the rhizosphere soil collection depended on the depth of the rice roots. After uniformly mixing the soil shaken off from all sub-sampling points, the Four-Quarter Method was used to select a 1000 to 2000 g sample, which was then placed in a clean cloth bag and taken back to the base for air drying and processing. To minimize anthropogenic pollution inputs, the sampling locations were purposefully selected far from towns, highways, and mining regions.

Previous studies have shown that the enrichment of soil As in karst areas is closely related to the extensive development of Fe–Mn nodules in the soil [29,33]; therefore, six typical karst areas enriched with rooted soil As and where Fe–Mn nodules had extensively developed were selected in the study area (Figure 2), and the screening of the samples of Fe–Mn nodules with different diameters was carried out (Figure 1).

2.2. Sample Pretreatment and Chemical Analysis

Soil samples were first air-dried in a shady place and then passed through a 10-mesh (2 mm) nylon sieve to eliminate non-soil material (e.g., debris and plant residues). After being taken out of the husks, the rice grain samples were repeatedly rinsed in distilled water. After air drying at 25 °C, they were threshed, hulled, and crushed using a 60-mesh nylon sieve (0.25 mm).

Figure 2. The Fe–Mn nodules in the soil in the study area. (**A**,**C**): Mn nodules; (**B**): Fe nodules, the exact positional distribution of which is labelled in Figure 1.

For the soil samples passed through the 10-mesh nylon sieve, the Fe–Mn nodules with diameters > 2 mm were removed, and only those with diameters $\leq$ 2 mm were retained as a soil component. Fe–Mn nodules with a diameter of more than 2 mm were eliminated from the samples that were sieved through a 10-mesh nylon sieve. Consequently, the Fe–Mn nodules with diameters lower than 2 mm were subjected to analysis. In consideration of previous studies and the presence of Fe–Mn nodules in the study area [34,35], we categorized the nodules into three groups based on the varying diameters: Group A (0.3–0.5 mm), Group B (0.5–1 mm), and Group C (1–2 mm). Each of the six samples underwent sieving through 10-mesh (2 mm), 18-mesh (1 mm), 35-mesh (0.5 mm), and 60-mesh (0.3 mm) nylon sieves to isolate the three groups of Fe–Mn nodules with different diameters. The quantity of each sample was documented for the three groups.

The concentrations of As in the soil samples were determined via atomic fluorescence spectrometry (AFS, AFS-9700, Kechuang Haiguang Instrument Co., Ltd., Beijing, China). TFe_2O_3 (total iron oxides), SiO_2, Al_2O_3, and K_2O were analyzed using X-ray fluorescence spectrometry (XRF, PW2440, Philips Co., Eindhoven, Netherlands). MgO, CaO, and Mn were analyzed via inductively coupled plasma–optical emission spectrometry (ICP-OES, iCAP 7400 Radial, Thermo Fisher Scientific Co., Cambridge, MA, USA). The sample was decomposed with HNO_3, $HClO_4$, and HF; dissolved with aqua regia (1 + 1); fixed in 25 mL polytetrafluoroethylene tubes and shaken well; and left to stand overnight. Soil organic carbon (SOC) was assessed using the potassium dichromate volumetric method [32,36]. The pH was assessed using ion-selective electrode methods [32,36]. The mineralogical compositions were determined using X-ray diffraction (XRD, BRUKER-D2 PHASER, Bruker Co., Karlsruhe, Germany) with the following parameters: target material: Cu; scanning speed: 2°/min; receiving gap: 0.03 mm; scanning surface range: 5–55°; step length: 0.02°; accelerating voltage: 40 kV; and current: 200 mA. The chemical analysis method used for the Fe–Mn concretion samples, after grinding into powder, was the same as that used for the soil samples. The levels of As in the rice grains were measured using inductively coupled plasma–mass spectrometry (ICP-MS, iCAP Q, Thermo Fisher Scientific Co., Waltham, MA, USA): Weigh 0.2000 g of the dry specimen in a microwave digestion jar, add HNO_2 and MOS-grade H_2O_2, tighten the lid, put the jar into a microwave digestion instrument for digestion, take out the digestion jar at the end of the reaction, put it on an acid catcher, evaporate it to a small volume, cool it and then transfer it to a 10 mL colorimetric tube, condense it with ultrapure water, and shake it well. As was measured using ICP-MS. Using reference standards, the analytical methods' accuracy was confirmed (GSS17, GSS19, GSS24, GSS28, GSB1, GSB4, GSB5, and GSB7) [32].

2.3. Sequential Extraction of As in the Soil

The seven-step sequential extraction procedures (SEP, amended Tessier Sequential Extraction) formulated by the China geological survey [37] were employed to investigate the fractions of As in the soil. This method divided As into seven fractions (F1–F7) [38]. The details of the fractionation and the SEP process are outlined in Table 1.

Table 1. Fractionation and seven-step sequential extraction procedures.

	Fraction	Process
F1	water-soluble	2.5 g of sample and 25 mL of distilled water were mixed, shaken well, shaken for 30 min, centrifuged for 20 min, and filtered *
F2	exchangeable	25 mL $MgCl_2$ was added to the residue, shaken well, shaken for 30 min, and centrifuged for 20 min
F3	bound to carbonates	25 mL NaOAc was added to the residue, shaken well, shaken for 1 h, and centrifuged for 20 min
F4	weakly bound to organic matter	50 mL Na_4PO_7 was added to the residue, shaken well, shaken for 40 min, left for 2 h, and centrifuged for 20 min
F5	Fe/Mn oxide-bound	50 mL 0.25 M NH_2OH-HCI mixture was added to the residue, shaken well, shaken for 1 h, and centrifuged for 20 min
F6	strongly bound to organic matter	3 mL HNO_3 and 5 mL H_2O_2 were heated for 1.5 h at 85 °C + 3 mL of H_2O_2 + 2.5 mL NH_4OAc-HNO_3, diluted to 25 mL, left for 10 h, and centrifuged for 20 min
F7	residual	the residues were dried, ground, and weighed; 2.0 g of the residue was digested with the 5 mL HCI-HNO_3-$HClO_4$ mixture + 5 mL HF

* Centrifuge: Centrifugation for 20 min, 4000 rpm. Filter: The clear solution was filtered with a 0.45 μm filter membrane aperture, and the filtrate was used in a 25 mL colorimetric tube. Cleaning: Add about 100 mL of water to the residue, centrifuge for 10 min, discard the water phase, and retain the residue.

The recovery of SEP was based on a comparison of the sum of the seven fractions with the total content of As: Weigh 0.25 g of the sample accurate to 0.0001 g, place the sample in a 50 mL stoppered test tube, add a small amount of water to moisten it, add 10 mL (1 + 1) of aqua regia, cover with a stopper, and shake well. Add boiling water to the sample and leave it for 1 h, shake 2 times in the middle, take it out and cool it, fix the volume to 25 mL, shake well, and let it stand overnight. Dispense 5 mL of the clear solution in a small beaker, add 2.5 mL 1 g/L iron salt solution and 2.5 mL thiourea–ascorbic acid mixed solution, shake well, leave for 30 min, and use a KBH_4 solution as the reducing agent. As was determined using AFS, and it is expressed using the following equation (Equation (1)) [37,38]:

$$Recovery = \frac{F1 + F2 + F3 + F4 + F5 + F6 + F7}{Total} \times 100\% \quad (1)$$

The accuracy of the SEP analysis method was determined by conducting a full analysis of the elements in the soil as a standard and comparing the results with the sum of the fractions. The relative deviation (RE) was required to be $\leq$40% [37]. The pass rate for the single-element single-morphology analysis data was $\geq$85%.

$$\mathrm{RE}\% = \frac{C_1 - C_0}{C_1} \times 100\% \quad (2)$$

where C_1 is the full amount of the element; and C_0 is the form of the element's total amount. The recovery ranged from 80.55% to 101.14%, and our study's RE values obtained following seven steps were lower than 10%; thus, these findings meet the requirements of standard DD2005-03 [37].

2.4. Selective Extractions and pH-Dependent Leaching Test

Selective extractions and pH-dependent leaching tests were conducted to identify whether these Fe–Mn nodules could be potential "Arsenic main sources" in soil [39,40]. Three extractants were utilized for the selective extractions of soil As, namely, acidified hydrogen peroxide (H_2O_2–HNO_3), hydroxylamine hydrochloride (NH_2OH–HCl), and citrate–bicarbonate–dithionite (CBD), aiming to elucidate the association of As with the Fe, Mn, and Al (oxyhydr) oxides in the Fe–Mn nodules [41,42]. Additionally, a control experiment was conducted using 0.5 mol/L HNO_3, which may dissolve some Al-containing minerals [35]. Hydroxylamine hydrochloride, known for its aggressive extraction properties,

targets As associated with easily reducible Fe and Mn oxides [43]. Acidified hydrogen peroxide extraction primarily involves dissolved Mn oxides [35]. CBD demonstrates a strong extraction capability for As bound to both amorphous and crystalline iron oxides [44].

The pH-dependent leaching test was adapted from the CEN/TS 14997 methodology [45]. A pH ranging from 2 to 11 was chosen for the experiment to analyze how As is released under different pH conditions. A total of 1 gram of the sample was placed in a 50 mL centrifuge PP tube, and 9.6 mL of deionized water was added to keep the ratio of liquid to solid (L/S) at 9.6, reaching a final value of roughly 10 when the acid and base were added. Ten pH values—2, 3, 4, 5, 6, 7, 8, 9, 10, and 11—were tested, including an extreme pH higher than that of typical soil. The pH levels were adjusted using HNO_3 (1 mol/L or 0.1 mol/L) and NaOH (2 mol/L or 1 mol/L). In every instance, a control experiment was carried out. For 48 h, the reactors were agitated. ICP-MS was then used to measure the leachate filtrate (Millipore® 0.45 μm) [28,35,39]. Table 2 describes the selective extraction procedure. Every extraction was carried out twice, using procedural blanks. The extracts underwent analysis for Fe, Al, Mn, and As using inductively coupled plasma–optical emission spectrometry (ICP-OES, iCAP 6500, Thermo Fisher Scientific Co., Taufkirchen, Germany), after being filtered through a 0.45 μm membrane filter.

Table 2. Detailed steps of the selective extraction procedure [35,41,42].

Extractant	Process
Control (HNO_3)	The sample (100 mg) was placed in a container and mixed with 100 mL of 0.5 mol/L HNO_3. The container was placed at room temperature, stirring for 30 min.
Hydroxylamine hydrochloride (NH_2OH–HCl)	The soil (100 mg) was placed in a container and mixed with 200 mL of 0.1 mol/L NH_2OH–HCl (non-acidified, pH 3.6). The container was placed at room temperature, stirring for 2 h.
Acidified hydrogen peroxide (H_2O_2–HNO_3)	The soil (100 mg) was placed in a container and mixed with 50 mL 30% of H_2O_2 and 50 mL 1 mol/L HNO_3. The container was placed at room temperature, stirring for 30 min.
Citrate–bicarbonate–dithionite (CBD)	The soil (100 mg) was placed in a container and mixed with a solution containing 40 mL 0.3 mol/L sodium citrate ($Na_3C_6H_5O_7{\cdot}2H_2O$), 5 mL 1 mol/L sodium bicarbonate (Na_2CO_3), and 1g sodium dithionite ($Na_2S_2SO_3$). The container was placed in a 80 °C water bath and shaken for 1 h.

2.5. Data Analysis

Maps with geographic information were drawn using ArcGIS 10.8. Basic statistical analyses were carried out using SPSS 24.0 and Microsoft Excel 2021. The X-ray diffraction (XRD) pattern was analyzed with Jade 6.0. Other graphics were drawn using the OriginLab Origin v.2021.

The bioconcentration factor (BCF) is an important index to quantitatively calculate the accumulation of As in plant tissues from the environment [46,47]. The BCF is calculated as follows:

$$BCF = C_{rice}/C_{soil} \quad (3)$$

where C_{rice} is the As content in the rice (mg/kg); and C_{soil} is the whole As content in the soil (mg/kg).

The effect of nodules on soil heavy metal elements is manifested in two ways: the content of the element in the nodules of each grain size and the mass fraction of the element in the nodules of each grain size (i.e., the ratio of the mass of the element in the nodules of each grain size to the total mass of the element in the soil containing the nodules). To investigate the contribution of the nodules to the soil chemical composition and trace

element content, the parameter PQ (percentage of quality, %) was introduced and calculated as follows [48]:

$$PQ = \frac{\sum_{j=1}^{j} C_i \times M_j}{C_0 \times M_0 + \sum_{j=1}^{j} C_i \times M_j} \times 100 \quad (4)$$

where M is the mass of the nodule of particle size j, expressed in g; M_0 is the mass of the soil with the smallest particle size, expressed in g; C_i is the content of element i in the nodule of particle size j, expressed in mg/kg; and C_0 is the content of element i in the soil with the smallest particle size, expressed in mg/kg. The greater the value of PQ, the greater the proportion of the element present in the nodule and the greater the nodule's contribution of the element to the soil; the converse trend is observed with the smaller the value of PQ.

3. Results and Discussion

3.1. Soil Properties and As Concentrations

The average As concentration in the paddy soil (Table 3) was 23.49 mg/kg, higher than that in the non-karst area of Guangxi (12.01 mg/kg) [49]. The concentrations ranged from 2.36 to 162.92 mg/kg. Arsenic had a high degree of variability, as evidenced by its coefficient of variation (CV % = (standard deviation/mean) × 100%) of 98.32% (>35%) [27]. The paddy soil's As content was greater than the background values of Guangxi (8.0 mg/kg) and the rest of the country (9.0 mg/kg) [50]. Moreover, compared with the published data on the As content in other regions and countries, the mean value of the paddy soil's As content in our study area was higher (Table 4). The median value of As in the study area was close to that in Hunan Province, China, and lower than that in French soils. However, the minimum values of As in Shanghai and Fujian, China, were greater than those in the study area (Table 4). Overall, the paddy soils formed by carbonate rocks had a high level of As enrichment, resulting in a higher geochemical background. Akun et al. [51] confirmed that Pleistocene carbonate-rich terrace deposits, pouri, are the cause of the elevated As concentrations.

Table 3. Descriptive statistic summary of the paddy soil properties (N = 305).

Statistics	Min	Max	Median	Mean	CV	Background Value of the Topsoil in Guangxi, China [a]	Background Value of the Topsoil in China [a]
As (mg/kg)	2.36	162.92	15.60	23.49	98.32	8.0	9.1
TFe_2O_3 (%)	1.16	25.18	5.59	6.26	50.50	3.63	4.35
Mn (mg/kg)	29.9	2804.0	353.0	523.3	92.46	159	552
Al_2O_3 (%)	5.04	28.27	14.01	14.57	28.69	13.07	12.96
CaO (%)	0.16	31.50	0.81	4.45	151.36	0.17	2.79
pH	4.97	8.38	7.18	7.04	13.83	5.15	7.15
SiO_2 (%)	17.07	85.57	62.00	57.82	27.56	73.67	64.96
SOC (%)	1.16	6.30	2.60	2.80	35.69	1.29	1.15

[a] The background value of the topsoil was obtained from Hou et al. [50].

Table 4. Arsenic concentration in the topsoil and rice from other regions/countries.

	Region/Country	N	Min	Max	Mean	Median	References
Topsoil (mg/kg)	Hunan, China	18,773	0.1	2670.1	19.5	13.0	[50]
	Jiangxi, China	15,547	0.4	19.2	8.4	8.0	[52,53]
	Jilin, China	23,465	0.4	15.9	8.0	7.9	
	Shanghai, China	1744	4.6	11.4	7.9	7.9	
	Fujian, China	14,682	4.7	3.9	0.1	13.5	
	France	2017	0.39	412.00	12.20	17.93	
	Italy	201	1.8	60	20	\	
	Cyprus	260	0.2	22.5	11.0	10.87	[51,54]

Table 4. *Cont.*

	Region/Country	*N*	Min	Max	Mean	Median	References
Rice (mg/kg)	Hunan, China	43	0.05	0.25	0.13	\	[55]
	Jiangxi, China	30	0.07	0.25	0.15	0.15	
	Guangxi, China	45	0.11	0.37	0.23	\	
	Jilin, China	4	0.09	0.16	0.13	0.13	
	Shanghai, China	34	0.01	0.16	0.11	0.11	
	Fujian, China	36	0.04	0.20	0.12	\	
	U.S.	163	0.03	0.66	0.25	0.25	[56–58]
	France	33	0.09	0.56	0.28	0.23	
	Bangladesh	144	0.02	0.33	0.13	0.13	
	Italy	38	0.07	0.33	0.15	0.13	
	Japan	26	0.07	0.42	0.19	0.18	
	Egypt	110	0.01	0.58	0.05	0.04	

The paddy soil was primarily neutral with a median pH of 7.04, varying from 4.97 to 8.38. Notably, the median CaO content in the paddy soil was 0.81%, which was significantly higher than that in clastic and quaternary regions [38]. Research has revealed that elevated levels of Ca^{2+} ions in the soil are a principal cause of an increased soil pH [59]. An acidic environment could increase the soluble As content in the soil; however, the desorption of As from Fe (oxyhydr)oxides in alkaline environments might result in As(III) and As(V) mobility in the soil solution, which, in turn, increases As accumulation in rice [60]. Additionally, the TFe_2O_3, Mn, and Al_2O_3 contents in the paddy soil were 6.62%, 523.30 mg/kg, and 14.57%, respectively, which were higher than the background values of Guangxi and the rest of the country; however, the SiO_2 content (57.82%) exhibited the opposite trend. This indicates the desilicification–allitization of paddy soils in karst areas. The soil organic carbon content ranged from 1.16% to 6.30%, with a mean value of 2.80%, regulating the solubility of As in the soil and thus affecting the bioavailability of As in rice [61,62].

3.2. Accumulation of As in Rice Grains

The land quality directly affects the quality and safety of crops, which, in turn, affect the health of those who rely on them. The As concentration in the rice grains ranged from 0.03 to 0.25 mg/kg, with a mean value of 0.11 mg/kg (Table 5), which was lower than that reported in many regions/countries (Table 4). Meharg et al. [58,63] reported that the average As content in rice was 0.14 mg/kg in China, and 81.64% of the rice samples containing As in our study area had As contents lower than this value. The BCF_{As} of the rice was 0.0084, which was considerably below that of other heavy metals, such as Cd, Zn, and Cu [11]. In summary, the As content in the rice grains remained low in the karst area.

Table 5. Arsenic concentration and BCF_{As} in rice grains (N = 305).

Statistics	Total As (mg/kg)	BCF_{As}	Inorganic As (mg/kg)
Min	0.03	0.0004	0.08
Max	0.25	0.0530	0.20
Median	0.10	0.0058	\
Mean	0.11	0.0084	\
REF [a]	\	\	0.62 [b]

[a] REF (%) means the rate of exceeding the national food safety standard (GB2762-2017) [64]. [b] Seven rice grain samples with a total As concentration greater than 0.2 mg/kg were selected for the determination of inorganic As concentration, and the results show that the samples of inorganic As concentrations exceeded the standard.

Extensive studies on As speciation have demonstrated the coexistence of inorganic and organic As in rice [65,66]. Considering the greater levels of toxicity and carcinogenicity of inorganic As [67–69], the Ministry of Health of China states that the maximum permissible

content of inorganic As is 0.2 mg/kg (GB2762-2017) [64]. Remarkably, just 0.62% of the rice samples had inorganic As contents above the recommended level, a far lower percentage than the 4.0% in Guangxi's non-karst region [49]; however, the proportions of soil samples that exceeded the As risk screening values and risk intervention values were 31.46% and 1.31%, respectively (GB 15618-2018) (Figure 3) [16]. The As concentrations of most of the rice grains in the paddy soil with an above-standard As content were within the safety range. A high As content but low bioavailability in rice soils in the Guangxi karst region resulted in a low As accumulation in rice. If the existing standards are strictly enforced, the use of paddy soils with an As content exceeding the standards will be restricted in agricultural production, and this is wrong and unscientific. Therefore, it is imperative to explore the causes of the low bioavailability of soil As and provide scientific support for the management of agricultural soil quality.

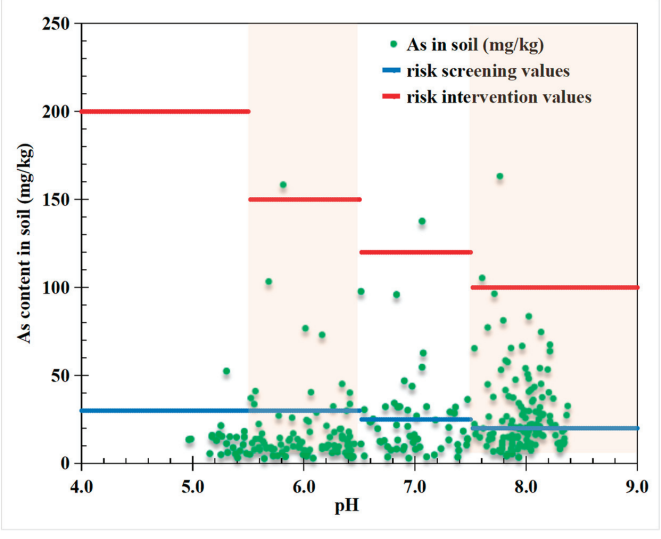

Figure 3. Arsenic content in the root soil under different pH values [16].

3.3. Arsenic Bioavailability in Paddy Soils Determined Using the Sequential Extraction Procedure

The bioavailability and mobility of As are closely related to its geochemical speciation, which is indicated by the extractable fraction [70,71]. Each As fraction is diverse in mobility and bioavailability [72]. In this study, the first two fractions (F1 and F2) were mobile and unstable and thus considered the bioavailable fractions for rice [70,73].

As shown in Table 6, As in the paddy soil existed mostly as the residual fraction (F7) in the karst area, accounting for 76.96%. F7 is considered stable in mineral crystal lattices and is unavailable for plants [73]. The proportions of other fractions (F3, F4, F5, and F6) were F4 (11.73%) > F5 (8.07%) > F6 (1.19%) > F3 (0.97%) > F1 (0.56%) > F2 (0.51%). The water-soluble and exchangeable fractions of As were the least abundant of the seven fractions. By comparing the bioavailable fractions of As with those of another enriched heavy metal, cadmium, in karst areas, it was found that the proportion of bioavailable fractions of As was lower than that of cadmium [38]. Furthermore, dendrograms were drawn using a hierarchical cluster analysis to determine the similarities between the different As fractions and rice grains (Figure 4). F1 and F2 were amalgamated as one fraction (F1, F2), owing to their low concentrations. The results indicate a statistical similarity between F1, F2 and the As content in the rice grains. Conversely, no significant similarity was observed between the As content in the rice grains and other fractions, including the total soil As. This implies that the bioavailable fraction (F1, F2) of As in paddy soils is readily absorbed by rice, while

massive residual As in paddy soils is hardly absorbed by rice, which causes a low As content in rice grains and a high As content in paddy soils in karst areas.

Table 6. The proportion of As in each fraction by the sequential extraction procedure (N = 305).

Fraction	Proportion (%) [a]			
	Min	Max	Median	Mean
Water-soluble (F1)	0.02	7.80	0.38	0.56
Exchangeable (F2)	0.01	3.34	0.37	0.51
Bound to carbonates (F3)	0.03	5.76	0.75	0.97
Weakly bound to organic matter (F4)	0.48	45.03	10.21	11.73
Fe/Mn oxide-bound (F5)	1.11	22.49	7.35	8.07
Strongly bound to organic matter (F6)	0.03	7.10	0.79	1.19
Residual (F7)	37.06	94.56	78.74	76.96

[a] Proportion (%): Proportion of each fraction to the sum of the seven fractions.

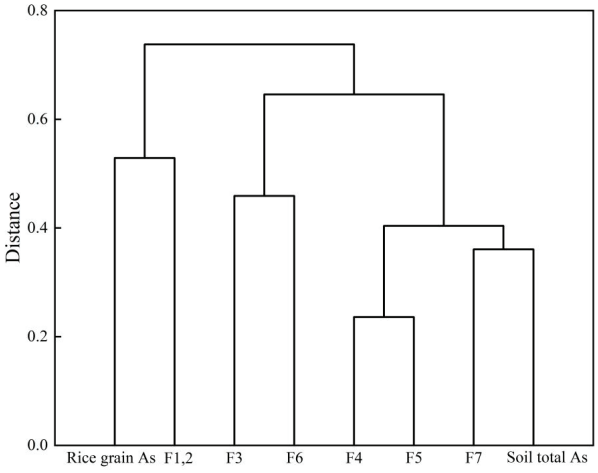

Figure 4. Dendrograms of As in soils and rice grains. F1, F2: water-soluble and exchangeable; F3: bound to carbonates, F4: weakly bound to organic matter, F5: Fe/Mn oxide-bound, F6: strongly bound to organic matter, F7: residual.

3.4. Genesis of Low As Bioavailability in Paddy Soils in Karst Areas

The computed Pearson's correlation values among the soil properties, residual As (F7), and the total soil As are shown in Table 7. Both the total soil As and F7 showed positive correlations with TFe_2O_3, Mn, and Al_2O_3, and they showed negative correlations with SiO_2. Notably, previous research employing field-emission scanning electron microscopy reported that the basic elements in Fe–Mn nodules were Fe, Mn, Al, and Si [28,35].

Table 7. Pearson's correlation coefficients between the soil properties and residual As (F7) (N = 305).

	TFe_2O_3	Mn	Al_2O_3	SiO_2	CaO	SOC
Total As	0.664 **	0.579 **	0.449 **	−0.393 **	−0.003	0.051
F7	0.712 **	0.605 **	0.464 **	−0.424 **	0.032	0.067

** at 99% confidence level ($p < 0.01$).

Guangxi encompasses the largest and most distinctive karst landform worldwide [74]. Temperature and rainfall intensify the pedogenesis of carbonate rocks, which includes two stages: leaching accumulation and weathering [27]. The bulk of alkali metals and alkaline earth metals, such as Ca, Mg, and K, leaches from carbonate rocks, whereas Fe, Mn, and

Al are retained in and form into (oxyhydr)oxides and minerals, which strongly adsorb As and trace metals, resulting in their comparative enrichment [6,34,71]. These hydrous oxides and some clay minerals gradually dissolve and are repeatedly deposited with alternating oxidation and reduction, ultimately forming Fe–Mn nodules [75,76]. During later pedogenesis, Fe–Mn nodules are progressively exposed to the ground, along with the strengthening of weathering [38]. The research findings indicate that Fe–Mn nodules accounted for 26.21% of the total amount of soil, and those with diameters lower than 2 mm accounted for 14.18% of the total soil mass in karst areas in Guangxi [28]. As detailed in Table 8, the mean As contents in the Fe–Mn nodules with different diameters were 151.33 mg/kg (0.3–0.5 mm), 188.50 mg/kg (0.5–1 mm), and 201.50 mg/kg (1–2 mm) in the study area, which shows that the As content in Fe–Mn nodules increases rapidly with the particle size. Furthermore, we calculated the contribution of the As, TFe_2O_3, Mn, Al_2O_3, and SiO_2 contents in the Fe–Mn nodules (0.3 mm $\leq$ diameter $\leq$ 2 mm) to the host soil, and the results are depicted in Figure 5. The average contribution of As reached 64.45%, with the highest contribution being 82.48%. Additionally, the average contributions of TFe_2O_3, Mn, Al_2O_3, and SiO_2 were 44.38%, 40.17%, 21.57%, and 7.77%, respectively. These results indicate that, as a part of the soil, Fe–Mn nodules play a significant role in the enrichment of As in karst areas.

Table 8. The contents of As, TFe_2O_3, Mn, Al_2O_3, and SiO_2 in the three groups of the Fe–Mn nodules (N = 6).

Groups	Diameter (mm)	Statistics	As (mg/kg)	TFe_2O_3 (%)	Mn (mg/kg)	Al_2O_3 (%)	SiO_2 (%)
A	0.3–0.5	Min	128.00	25.78	764.00	18.48	14.14
		Max	187.00	30.01	11,640.00	22.04	27.92
		Mid	143.50	26.69	3830.00	20.47	22.00
		Mean	151.33	27.10	5108.00	20.35	21.04
B	0.5–1	Min	158.00	27.67	832.00	18.34	11.55
		Max	253.00	32.55	15,451.00	20.28	20.01
		Mid	175.50	30.03	3296.50	19.23	15.86
		Mean	188.50	30.09	5458.67	19.37	15.81
C	1–2	Min	153.00	27.96	803.00	17.62	10.63
		Max	288.00	32.33	26,331.00	20.51	20.88
		Mid	196.00	31.27	5194.00	19.35	14.77
		Mean	201.50	30.54	9512.00	19.20	15.24

The XRD analysis showed that the Fe–Mn nodules primarily consisted of quartz, goethite, hematite, lithiophorite, birnessite, and phyllosilicates (kaolinite, illite, and clinochlore) (Figure 6). Previous studies have demonstrated that Mn oxide minerals play a primary role in oxidizing As(III) to As(V), which is typically accompanied by the reduction of Mn(IV) to Mn(III) and Mn(II) [77,78]. It was found that the released Mn(II) was easily re-adsorbed at the vacancy sites of Mn oxides until they were completely occupied, which led to the surface passivation of Mn oxides, thereby reducing As adsorption [79]. Iron oxide minerals are recognized as effective adsorbents of As, exhibiting a notably stronger adsorption capacity for As than Mn oxide minerals under isothermal conditions [80]. The X-ray absorption spectroscopy results of the partial environment of As in goethite show that, in addition to the usual bidentate binuclear complex, there is a bidentate mononuclear complex in the absorption, which suggests that As is adsorbed onto the surface of the particles or blocked in the voids and pores [81]. Giménez et al. [82] observed a stronger As(III) adsorption on hematite than on goethite over a broad pH range from 0 to 14. Furthermore, a similar adsorption of As was observed in clay minerals. Lin and Puls [83] investigated six clay minerals, demonstrating that As adsorbed onto clay surfaces can likely infiltrate into the inner pores of clay aggregates, and the dehydration of As residing on clay surfaces could enhance the adherence of As to clays.

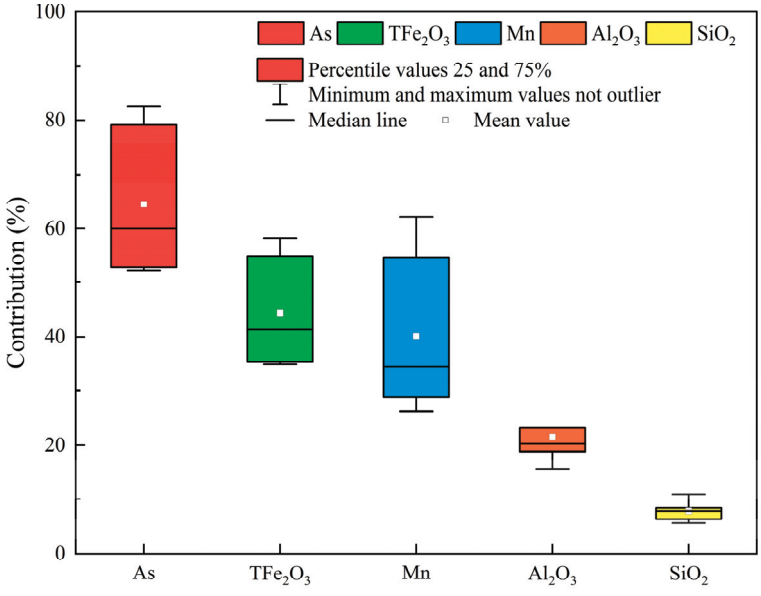

Figure 5. The contributions of As, TFe_2O_3, Mn, Al_2O_3, and SiO_2 in the Fe–Mn nodules (0.3 mm $\leq$ diameter $\leq$ 2 mm) to the host soils.

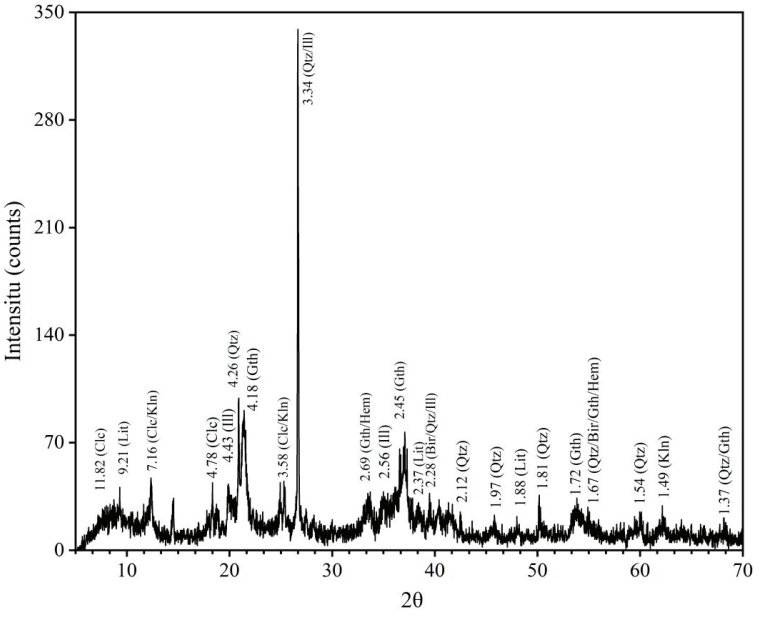

Figure 6. X-ray diffraction patterns of Fe–Mn nodules. Bir, Birnessite; Clc, Clinochlore; Hem, Hematite; Ill, Illite; Gth, Goethite; Kln, Kaolinite; Lit, Lithiophorite; and Qtz, Quartz. Numbers represent the d-values in Å.

To further understand the bioavailability of As in Fe–Mn nodules, the bioavailable As (F1,2) was extracted via the first two steps of SEP. As anticipated, the bioavailable As in the Fe–Mn nodules of three different diameters was negligible, and the extractability was lower

than 0.01%. This suggests that, in karst areas, generous As, tightly adsorbed into Fe–Mn nodules, is barely bioavailable, making it difficult for rice to assimilate it, which may be the ultimate cause of the high content but low bioavailability of As in the paddy soil.

3.5. Stability of Fe–Mn Nodules in the Soil

Selective extraction methods can facilitate the analysis of As distribution within the distinct phases of Fe–Mn nodules. As depicted in Figure 7, HNO_3 dissolved a minor fraction of As (0.78%), Fe (2.35%), Mn (3.63%), and Al (4.16%). NH_2OH-HCl, H_2O_2-HNO_3, and CBD exhibited a strong affinity for Mn, extracting Mn within the range of 64.22–87.01%. However, the extractable As did not show a substantial increase when Mn was significantly dissolved in NH_2OH-HCl. The order of extractability for As and Fe remained consistent: CBD > H_2O_2-HNO_3 > NH_2OH-HCl. Notably, the dissolution of Fe (21.69–67.05%) resulted in a marked increase in As extractability (22.62–51.40%) during CBD extraction. These findings indicate that As within Fe–Mn nodules is predominantly sequestered within Fe-(oxyhydr)oxides, such as goethite and hematite, which exhibit recalcitrance and remain undissolved. Arsenic associated with amorphous iron oxides can undergo dissolution through acid-enhanced, reductive, and chelant-enhanced mechanisms [43,44], while As bound to crystalline iron oxides can only be dissolved via reductive processes [84]. CBD, functioning as a potent reducing agent, triggers the reductive dissolution of crystalline iron oxides [44]. In essence, under strongly reducing conditions in the soil (i.e., hypoxia), the reductive dissolution of Fe-(oxyhydr)oxides within Fe–Mn nodules can release As into the soil solution, potentially enhancing the uptake of As by rice [85,86].

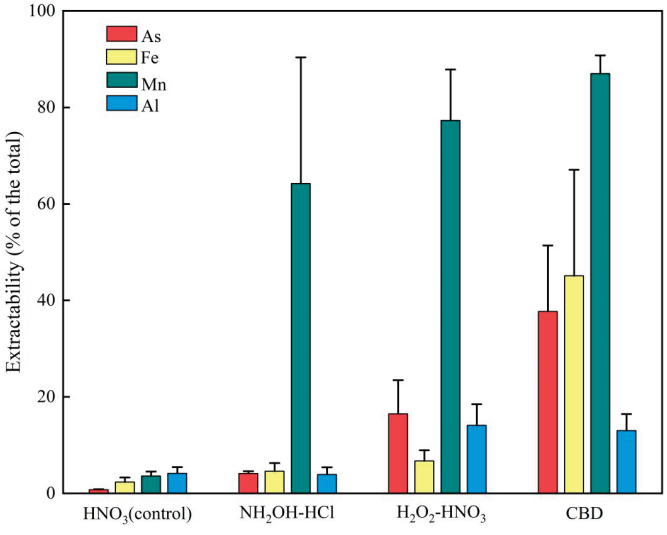

Figure 7. Dissolution of As, Fe, Mn, and Al from Fe–Mn nodules using different selective extractions.

The findings of the pH-dependent leaching assessments are depicted in Figure 8. Across a pH range from 2 to 11, the overall leaching of As remained notably low. At pH 2, the leached concentration of As was 0.05 mg/kg, constituting a mere 0.02% of the total concentrations within the Fe–Mn nodules. Similarly, at pH 11, the leached As concentration was 0.03 mg/kg, accounting for 0.01%. The dissolved As concentrations at other pH levels (3–10) were all less than 0.01% of the total concentrations in the Fe–Mn nodules, rendering them nearly negligible. Moreover, the trend of As variation mirrored that of Fe, underscoring the close association between As and Fe within the Fe–Mn nodules. In essence, the results suggest that Fe–Mn nodules exhibit a robust stability in storing As, with extremely acidic or alkaline conditions promoting the potential release of As from the

nodules due to the desorption or dissolution of the Fe-(oxyhydr)oxides. The pH range of the karstic paddy soil (4.97–8.38) provides favorable conditions for the preservation of As within the Fe–Mn nodules.

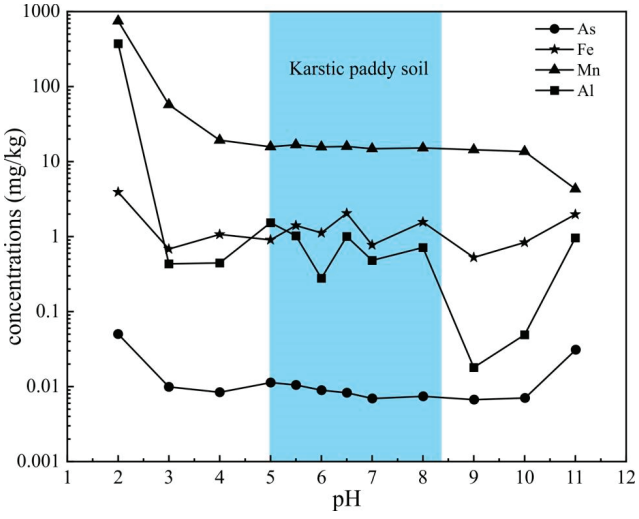

Figure 8. The pH-dependent leaching of As, Fe, Mn, and Al from Fe–Mn nodules. The blue area is the portion with a pH of 4.97–8.38.

4. Conclusions

The paddy soil in karst areas exhibited a higher geochemical background of As, with the concentration significantly surpassing that found in non-karst regions. However, the As concentration in the rice grains within the karst area remained low, with only 0.62% of the rice samples exceeding the permissible value for inorganic As (0.2 mg/kg). The SEP results show that As in the karstic paddy soil is present mostly in the residual fraction, and the water-soluble and exchangeable fractions of As, readily absorbed by rice, are extremely rare. The high As content but low bioavailability of As in the karstic paddy soil can be primarily attributed to the abundant Fe–Mn nodules, which adsorbed and immobilized a significant portion of As, contributing to 64.45% of the As content in the host soil. The bioavailable fraction of As was found to be less than 0.01% of the total As in the Fe–Mn nodules. Selective extractions revealed that As was primarily sequestered within Fe-(oxyhydr)oxides, which could release As into the soil under certain reduction conditions through the reductive dissolution of Fe-(oxyhydr)oxides. pH-dependent leaching tests showed that only under extremely acidic (pH = 2) and alkaline (pH = 11) conditions was there a trend of As leaching from the Fe–Mn nodules. In the natural pH range of the karstic paddy soil (pH 4.97–8.38), As remained steadily adhered to the Fe–Mn nodules. Therefore, agricultural soil quality management in karst areas should not only be based on the total As content in the soil but should also consider the bioavailability of As, thereby tailoring adaptations to fully utilize arable land.

Author Contributions: X.L. (Xuezhen Li): Conceptualization, Methodology, Formal analysis, Writing original—draft, Writing—review and editing, and Visualization. X.M.: Methodology, Formal analysis, and Visualization. Q.H.: Writing—review and editing, and Supervision. X.X.: Supervision. B.L.: Investigation and Resources. K.L.: Investigation and Resources. X.L. (Xu Liu): Investigation and Resources. Z.W.: Investigation and Resources. W.J.: Data curation. L.W.: Resources. T.Y.: Conceptualization, Writing—review and editing, Supervision, Project administration, and Funding acquisition. Z.Y.: Conceptualization, Writing—review and editing, Supervision, and Funding acquisition. All authors have read and agreed to the published version of the manuscript.

Funding: This work was financially supported by the Geological Survey Project of China (Grant No. DD20211414) and the National Natural Science Foundation of China (42330703).

Data Availability Statement: The data presented in this study are available upon request from the corresponding author. The data are not publicly available due to the confidentiality of the project.

Acknowledgments: The authors appreciate the helpful and useful suggestions of the editors and reviewers.

Conflicts of Interest: The authors declare no conflicts of interest.

References

1. Wei, B.G.; Yang, L.S. A review of heavy metal contaminations in urban soils, urban road dusts and agricultural soils from China. *Microchem. J.* **2010**, *94*, 99–107. [CrossRef]
2. Li, C.J.; Wang, J.H.; Yan, B.; Miao, A.J.; Zhong, H.; Zhang, W.; Ma, L.Q. Progresses and emerging trends of arsenic research in the past 120 years. *Crit. Rev. Environ. Sci. Technol.* **2021**, *51*, 1306–1353. [CrossRef]
3. Bundschuh, J.; Armienta, M.A.; Morales-Simfors, N.; Alam, M.A.; López, D.L.; Quezada, V.D.; Dietrich, S.; Schneider, J.; Tapia, J.; Sracek, O.; et al. Arsenic in Latin America: New findings on source, mobilization and mobility in human environments in 20 countries based on decadal research 2010–2020. *Crit. Rev. Environ. Sci. Technol.* **2021**, *51*, 1727–1865. [CrossRef]
4. Alexakis, D.E.; Bathrellos, G.D.; Skilodimou, H.D.; Gamvroula, D.E. Spatial Distribution and Evaluation of Arsenic and Zinc Content in the Soil of a Karst Landscape. *Sustainability* **2021**, *13*, 6976. [CrossRef]
5. Zhao, F.J.; Ma, Y.B.; Zhu, Y.G.; Tang, Z.; McGrath, S.P. Soil Contamination in China: Current Status and Mitigation Strategies. *Environ. Sci. Technol.* **2015**, *49*, 750–759. [CrossRef]
6. Yang, Q.; Yang, Z.F.; Filippelli, G.M.; Ji, J.F.; Ji, W.B.; Liu, X.; Wang, L.; Yu, T.; Wu, T.S.; Zhuo, X.X.; et al. Distribution and secondary enrichment of heavy metal elements in karstic soils with high geochemical background in Guangxi, China. *Chem. Geol.* **2021**, *567*, 120081. [CrossRef]
7. Mombo, S.; Foucault, Y.; Deola, F.; Gaillard, I.; Goix, S.; Shahid, M.; Schreck, E.; Pierart, A.; Dumat, C. Management of human health risk in the context of kitchen gardens polluted by lead and cadmium near a lead recycling company. *J. Soil Sediment* **2016**, *16*, 1214–1224. [CrossRef]
8. Chen, J.; Garbinski, L.D.; Rosen, B.; Zhang, J.; Xiang, P.; Ma, L.Q. Organoarsenical compounds: Occurrence, toxicology and biotransformation. *Crit. Rev. Environ. Sci. Technol.* **2020**, *50*, 217–243. [CrossRef]
9. Li, H.B.; Li, M.Y.; Zhao, D.; Li, J.; Li, S.W.; Xiang, P.; Juhsaz, A.L.; Ma, L.N.Q. Arsenic, lead, and cadmium bioaccessibility in contaminated soils: Measurements and validations. *Crit. Rev. Environ. Sci. Technol.* **2020**, *50*, 1303–1338. [CrossRef]
10. Chen, H.Y.; Teng, Y.G.; Lu, S.J.; Wang, Y.Y.; Wang, J.S. Contamination features and health risk of soil heavy metals in China. *Sci. Total Environ.* **2015**, *512*, 143–153. [CrossRef]
11. Gu, Q.B.; Yang, Z.F.; Yu, T.; Ji, J.F.; Hou, Q.Y.; Zhang, Q.Z. Application of ecogeochemical prediction model to safely exploit seleniferous soil. *Ecotoxicol. Environ. Safe* **2019**, *177*, 133–139. [CrossRef]
12. Xiao, J.; Chen, W.; Wang, L.; Zhang, X.K.; Wen, Y.B.; Bostick, B.C.; Wen, Y.L.; He, X.H.; Zhang, L.Y.; Zhuo, X.X.; et al. New strategy for exploring the accumulation of heavy metals in soils derived from different parent materials in the karst region of southwestern China. *Geoderma* **2022**, *417*, 115806. [CrossRef]
13. Lu, A.X.; Wang, J.H.; Qin, X.Y.; Wang, K.Y.; Han, P.; Zhang, S.Z. Multivariate and geostatistical analyses of the spatial distribution and origin of heavy metals in the agricultural soils in Shunyi, Beijing, China. *Sci. Total Environ.* **2012**, *425*, 66–74. [CrossRef]
14. Yamasaki, S.; Takeda, A.; Nunohara, K.; Tsuchiya, N. Red soils derived from limestone contain higher amounts of trace elements than those derived from various other parent materials. *Soil Sci. Plant Nutr.* **2013**, *59*, 692–699. [CrossRef]
15. Yang, Q.; Yang, Z.F.; Zhang, Q.Z.; Ji, W.B.; Guan, D.X.; Liu, X.; Yu, T.; Wang, L.; Zhuo, X.X.; Ji, J.F. Transferability of heavy metal(loid)s from karstic soils with high geochemical background to peanut seeds. *Environ. Pollut.* **2022**, *299*, 118819. [CrossRef] [PubMed]
16. *GB 15618-2018*; Soil Environmental Quality—Risk Control Standards for Soil Contamination of Agricultural Land. MEEC (Ministry of Ecology and Environment of the People's Republic of China): Beijing, China, 2018.
17. Xia, X.Q.; Ji, J.F.; Zhang, C.S.; Yang, Z.F.; Shi, H.D. Carbonate bedrock control of soil Cd background in Southwestern China: Its extent and influencing factors based on spatial analysis. *Chemosphere* **2022**, *290*, 133390. [CrossRef] [PubMed]
18. Peijnenburg, W.; Baerselman, R.; de Groot, A.; Jager, T.; Leenders, D.; Posthuma, L.; Van Veen, R. Quantification of metal bioavailability for lettuce (*Lactuca sativa* L.) in field soils. *Arch. Environ. Contam. Toxicol.* **2000**, *39*, 420–430. [CrossRef] [PubMed]
19. Wenzel, W.W.; Kirchbaumer, N.; Prohaska, T.; Stingeder, G.; Lombi, E.; Adriano, D.C. Arsenic fractionation in soils using an improved sequential extraction procedure. *Anal. Chim. Acta.* **2001**, *436*, 309–323. [CrossRef]
20. Adamo, P.; Iavazzo, P.; Albanese, S.; Agrelli, D.; De Vivo, B.; Lima, A. Bioavailability and soil-to-plant transfer factors as indicators of potentially toxic element contamination in agricultural soils. *Sci. Total Environ* **2014**, *500*, 11–22. [CrossRef] [PubMed]
21. Zhang, J.R.; Li, H.Z.; Zhou, Y.Z.; Dou, L.; Cai, L.M.; Mo, L.P.; You, J. Bioavailability and soil-to-crop transfer of heavy metals in farmland soils: A case study in the Pearl River Delta, South China. *Environ. Pollut.* **2018**, *235*, 710–719. [CrossRef] [PubMed]

22. Luo, H.; Liu, X.M.; Wang, S.J.; Liu, F.; Li, Y. Pollution characteristics and sources of cadmium in soils of the karstarea in South China. *Chin. J. Ecol.* **2018**, *37*, 1538–1544. [CrossRef]
23. Zhang, F.G.; Peng, M.; Wan, H.Y.; Ma, H.H.; Xu, R.T.; Cheng, X.M.; Hou, Z.L.; Chen, Z.F.; Li, K.; Cheng, H.X. Ecological risk assessment of heavy metals at township scale in the high background of heavy metals, southwestern China. *Environ. Sci.* **2020**, *41*, 4197–4209. [CrossRef]
24. Tu, C.L.; He, T.B.; Liu, C.Q.; Lu, X.H. Effects of Land Use and Parent Materials on Trace Elements Accumulation in Topsoil. *J. Environ. Qual.* **2013**, *42*, 103–110. [CrossRef] [PubMed]
25. Chang, C.; Li, F.; Wang, Q.; Hu, M.; Du, Y.; Zhang, X.; Zhang, X.; Chen, C.; Yu, H.-Y. Bioavailability of antimony and arsenic in a flowering cabbage–soil system: Controlling factors and interactive effect. *Sci. Total Environ.* **2022**, *815*, 152920. [CrossRef]
26. Kwon, J.C.; Nejad, Z.D.; Jung, M.C. Arsenic and heavy metals in paddy soil and polished rice contaminated by mining activities in Korea. *Catena* **2017**, *148*, 92–100. [CrossRef]
27. Wang, Y.Z.; Yu, T.; Yang, Z.F.; Bo, H.Z.; Lin, Y.; Yang, Q.; Liu, X.; Zhang, Q.Z.; Zhuo, X.X.; Wu, T.S. Zinc concentration prediction in rice grain using back-propagation neural network based on soil properties and safe utilization of paddy soil: A large-scale field study in Guangxi, China. *Sci. Total Environ.* **2021**, *798*, 149270. [CrossRef] [PubMed]
28. Ji, W.B.; Yang, Z.F.; Yu, T.; Yang, Q.; Wen, Y.B.; Wu, T.S. Potential Ecological Risk Assessment of Heavy Metals in the Fe-Mn Nodules in the Karst Area of Guangxi, Southwest China. *Bull. Environ. Contam. Toxicol.* **2021**, *106*, 51–56. [CrossRef]
29. Feng, Y.F.; Liao, Q.L.; Ji, W.B.; Ren, J.L.; Ji, J.F.; Yang, Z.F. Geochemical Characteristics of Heavy Metal Enrichment in Soil Fe-Mn Nodules in the Karst Area of Guangxi. *Geol. J. China Univ.* **2022**, *28*, 787–798. [CrossRef]
30. Gasparatos, D. *Fe–Mn Concretions and Nodules to Sequester Heavy Metals in Soils*; Springer: Houten, The Netherlands, 2012. [CrossRef]
31. Li, Y.L.; Li, P.Y.; Liu, L.N. Source Identification and Potential Ecological Risk Assessment of Heavy Metals in the Topsoil of the Weining Plain (Northwest China). *Expos. Health* **2022**, *14*, 281–294. [CrossRef]
32. MNR (Ministry of Land and Resources of the People's Republic of China). *Regional Geochemical Sample Analysis Method—Part 27: Potassium Dichromate Capacity Method. DZ/T 0279.27-2016.0. and Part 34: Determination of pH Values Ion Selection Electrode Method DZ/T 0279.34-2016.0*; China University of Geosciences Press: Beijing, China, 2016.
33. Ji, W.; Ying, R.; Yang, Z.; Hu, Z.; Yang, Q.; Liu, X.; Yu, T.; Wang, L.; Qin, J.; Wu, T. Arsenic Concentration, Fraction, and Environmental Implication in Fe–Mn Nodules in the Karst Area of Guangxi. *Water* **2022**, *14*, 3021. [CrossRef]
34. Yu, X.L.; Fu, Y.N.; Brookes, P.C.; Lu, S.G. Insights into the Formation Process and Environmental Fingerprints of Iron-Manganese Nodules in Subtropical Soils of China. *Soil Sci. Soc. Am. J.* **2015**, *79*, 1101–1114. [CrossRef]
35. Ettler, V.; Chren, M.; Mihaljevič, M.; Drahota, P.; Kříbek, B.; Veselovský, F.; Sracek, O.; Vaněk, A.; Penížek, V.; Komárek, M.; et al. Characterization of Fe-Mn concentric nodules from Luvisol irrigated by mine water in a semi-arid agricultural area. *Geoderma* **2017**, *299*, 32–42. [CrossRef]
36. Li, X.Z.; Hou, Q.Y.; Duan, Y.R.; Li, Y.C.; Lin, K.; Li, B.; Sheng, W.K.; Wang, Y.L.; Su, R.; Gu, Z.L.; et al. Soil selenium enrichment in the Loess Plateau of China: Geogenic evidence, spatial distribution, and it's influence factors. *Chemosphere* **2023**, *340*, 139746. [CrossRef]
37. CGS (China Geological Survey). *China Geological Survey Bureau Geological Survey Technical Standard—The Technical Requirements for Eco-Geochemical Analysis of Sample (DD2005-03)*; CGS (China Geological Survey): Beijing, China, 2005.
38. Li, C.; Yang, Z.F.; Yu, T.; Hou, Q.Y.; Liu, X.; Wang, J.; Zhang, Q.Z.; Wu, T.S. Study on safe usage of agricultural land in karst and non -karst areas based on soil Cd and prediction of Cd in rice: A case study of Heng County, Guangxi. *Ecotoxicol. Environ. Saf.* **2021**, *208*, 111505. [CrossRef]
39. Houben, D.; Evrard, L.; Sonnet, P. Mobility, bioavailability and pH-dependent leaching of cadmium, zinc and lead in a contaminated soil amended with biochar. *Chemosphere* **2013**, *92*, 1450–1457. [CrossRef]
40. Stigliani, W.M.; Doelman, P.; Salomons, W.; Schulin, R.; Smidt, G.R.B.; Vanderzee, S.E.A.T.M. Chemical Time Bombs—Predicting the Unpredictable. *Environment* **1991**, *33*, 4. [CrossRef]
41. Neaman, A.; Mouélé, F.; Trolard, F.; Bourrié, G. Improved methods for selective dissolution of Mn oxides:: Applications for studying trace element associations. *Appl. Geochem.* **2004**, *19*, 973–979. [CrossRef]
42. Neaman, A.; Waller, B.; Mouélé, F.; Trolard, F.; Bourrié, G. Improved methods for selective dissolution of manganese oxides from soils and rocks. *Eur. J. Soil Sci.* **2004**, *55*, 47–54. [CrossRef]
43. Zhang, X.; Dayton, E.A.; Basta, N.T. Predicting the modifying effect of soils on arsenic phytotoxicity and phytoaccumulation using soil properties or soil extraction methods. *Environ. Pollut.* **2020**, *263*, 114501. [CrossRef] [PubMed]
44. Lee, M.E.; Jeon, E.K.; Tsang, D.C.W.; Baek, K. Simultaneous application of oxalic acid and dithionite for enhanced extraction of arsenic bound to amorphous and crystalline iron oxides. *J. Hazard. Mater.* **2018**, *354*, 91–98. [CrossRef] [PubMed]
45. *CEN/TS 14997*; Characterization of Waste-Leaching Behaviour Tests—Influence of pH on Leaching with Continuous pH-Control. CEN: Brussels, Belgium, 2006.
46. Chopra, A.K.; Pathak, C. *Accumulation of Heavy Metals in the Vegetables Grown in Wastewater Irrigated Areas of Dehradun, India with Reference to Human Health Risk*; Department of Zoology and Environmental Science, Gurukula Kangri University: Haridwar, India, 2015; Volume 187, pp. 1–16. [CrossRef]
47. Torralba-Sanchez, T.; Kuo, D.; Allen, H.; Di Toro, D. Bioconcentration factors and plant–water partition coefficients of munitions compounds in barley. *Chemosphere* **2017**, *189*, 538–546. [CrossRef]

48. Yang, Q.; Yang, Z.F.; Ji, J.F.; Liu, X.; Ji, W.B.; Wang, J.; Wu, T.S.; Wang, L. Characteristics of Mineralogy and Heavy Metal Geochemistry in Ferromanganese Nodule Rich Soils with High Geochemical Background from Guigang, Guangxi. *Geoscience* **2021**, *35*, 1450–1458. [CrossRef]
49. Yang, Q.; Yang, Z.F.; Zhang, Q.Z.; Liu, X.; Zhuo, X.X.; Wu, T.S.; Wang, L.; Wei, X.J.; Ji, J.F. Ecological risk assessment of Cd and other heavy metals in soil-rice system in the karst areas with high geochemical background of Guangxi, China. *Sci. China Earth Sci.* **2021**, *64*, 1126–1139. [CrossRef]
50. Hou, Q.Y.; Yang, Z.F.; Yu, T.; Xia, X.Q.; Cheng, H.X.; Zhou, G.H. *Soil Geochemical Dataset of China*; Geological Publishing House: Beijing, China, 2020; pp. 2656–2668.
51. Akun, M.E.; Yamacı, R.F.; Charalambous, C.; Lechtvich, S.; Djamgoz, M. The distribution of carcinogenic heavy metals in cyprus soil. In *Environmental Earth Sciences-Series*; Springer: Berlin/Heidelberg, Germany, 2010; pp. 353–359. [CrossRef]
52. Marchant, B.P.; Saby, N.P.A.; Arrouays, D. A survey of topsoil arsenic and mercury concentrations across France. *Chemosphere* **2017**, *181*, 635–644. [CrossRef]
53. Ungaro, F.; Ragazzi, F.; Cappellin, R.; Giandon, P. Arsenic concentration in the soils of the Brenta Plain (Northern Italy): Mapping the probability of exceeding contamination thresholds. *J. Geochem. Explor.* **2008**, *96*, 117–131. [CrossRef]
54. Golfinopoulos, S.K.; Varnavas, S.P.; Alexakis, D.E. The Status of Arsenic Pollution in the Greek and Cyprus Environment: An Overview. *Water* **2021**, *13*, 224. [CrossRef]
55. Ma, L.; Wang, L.; Jia, Y.; Yang, Z. Arsenic speciation in locally grown rice grains from Hunan Province, China: Spatial distribution and potential health risk. *Sci. Total Environ.* **2016**, *557–558*, 438–444. [CrossRef] [PubMed]
56. Fu, Y.; Chen, M.; Bi, X.; He, Y.; Ren, L.; Xiang, W.; Qiao, S.; Yan, S.; Li, Z.; Ma, Z. Occurrence of arsenic in brown rice and its relationship to soil properties from Hainan Island, China. *Environ. Pollut.* **2011**, *159*, 1757–1762. [CrossRef] [PubMed]
57. Huang, R.; Gao, S.; Wang, W.; Staunton, S.; Wang, G. Soil arsenic availability and the transfer of soil arsenic to crops in suburban areas in Fujian Province, southeast China. *Sci. Total Environ.* **2006**, *368*, 531–541. [CrossRef] [PubMed]
58. Meharg, A.A.; Williams, P.N.; Adomako, E.; Lawgali, Y.Y.; Deacon, C.; Villada, A.; Cambell, R.C.J.; Sun, G.; Zhu, Y.G.; Feldmann, J.; et al. Geographical Variation in Total and Inorganic Arsenic Content of Polished (White) Rice. *Environ. Sci. Technol.* **2009**, *43*, 1612–1617. [CrossRef]
59. Mahar, A.; Wang, P.; Ali, A.; Guo, Z.Y.; Awasthi, M.K.; Lahori, A.H.; Wang, Q.; Shen, F.; Zhang, Z.Q. Impact of CaO, fly ash, sulfur and Na_2S on the (im)mobilization and phytoavailability of Cd, Cu and Pb in contaminated soil. *Ecotoxicol. Environ. Saf.* **2016**, *134*, 116–123. [CrossRef] [PubMed]
60. Khan, I.; Awan, S.A.; Rizwan, M.; Ali, S.; Zhang, X.Q.; Huang, L.K. Arsenic behavior in soil-plant system and its detoxification mechanisms in plants: A review. *Environ. Pollut.* **2021**, *286*, 117389. [CrossRef] [PubMed]
61. Williams, P.N.; Zhang, H.; Davison, W.; Meharg, A.A.; Hossain, M.; Norton, G.J.; Brammer, H.; Islam, M.R. Organic Matter-Solid Phase Interactions Are Critical for Predicting Arsenic Release and Plant Uptake in Bangladesh Paddy Soils. *Environ. Sci. Technol.* **2011**, *45*, 6080–6087. [CrossRef] [PubMed]
62. Yan, M.M.; Zeng, X.B.; Wang, J.; Meharg, A.A.; Meharg, C.; Tang, X.J.; Zhang, L.L.; Bai, L.Y.; Zhang, J.Z.; Su, S.M. Dissolved organic matter differentially influences arsenic methylation and volatilization in paddy soils. *J. Hazard. Mater.* **2020**, *388*, 121795. [CrossRef] [PubMed]
63. Meharg, A.A.; Meharg, C.; Carey, M.; Williams, P.; Shi, Z.Y.; Campbell, K.; Elliott, C.; Marwa, E.; Xiao, J.J.; Farias, J.G.; et al. Global Geographical Variation in Elemental and Arsenic Species Concentration in Paddy Rice Grain Identifies a Close Association of Essential Elements Copper, Selenium and Molybdenum with Cadmium. *Expos. Health* **2022**, *15*, 505–518. [CrossRef]
64. *GB2762-2017*; Maximum Level of Contaminants in Food. MHC (Ministry of Health of the People's Republic of China) Chinese National Standard Agency: Beijing, China, 2017.
65. Williams, P.N.; Price, A.H.; Raab, A.; Hossain, S.A.; Feldmann, J.; Meharg, A.A. Variation in arsenic speciation and concentration in paddy rice related to dietary exposure. *Environ. Sci. Technol.* **2005**, *39*, 5531–5540. [CrossRef]
66. Zhao, F.; Zhu, Y.; Meharg, A. Methylated Arsenic Species in Rice: Geographical Variation, Origin, and Uptake Mechanisms. *Environ. Sci. Technol.* **2013**, *47*, 3957–3966. [CrossRef]
67. Armendariz, A.L.; Talano, M.A.; Travaglia, C. Arsenic toxicity in soybean seedlings and their attenuation mechanisms. *Plant Physiol. Biochem.* **2016**, *98*, 119–127. [CrossRef]
68. Siddiqui, M.H.; Alamri, S.; Khan, M.N.; Corpas, F.J.; Al-Amri, A.A.; Alsubaie, Q.D.; Ali, H.M.; Kalaji, H.M.; Ahmad, P. Melatonin and calcium function synergistically to promote the resilience through ROS metabolism under arsenic-induced stress. *J. Hazard. Mater.* **2020**, *398*, 122882. [CrossRef]
69. Xue, X.M.; Xiong, C.; Yoshinaga, M.; Rosen, B.; Zhu, Y.G. The enigma of environmental organoarsenicals. *Crit. Rev. Environ. Sci. Technol.* **2021**, 1–28.
70. Du, X.; Gao, L.; Xun, Y.; Feng, L. Comparison of different sequential extraction procedures to identify and estimate bioavailability of arsenic fractions in soil. *J. Soil Sediments* **2020**, *20*, 3656–3668. [CrossRef]
71. Yamaguchi, N.; Nakamura, T.; Dong, D.; Takahashi, Y.; Amachi, S.; Makino, T. Arsenic release from flooded paddy soils is influenced by speciation, Eh, pH, and iron dissolution. *Chemosphere* **2011**, *83*, 925–932. [CrossRef]
72. Srithongkul, C.; Wongsaipun, S.; Krongchai, C.; Santasup, C.; Kittiwachana, S. Investigation of mobility and bioavailability of arsenic in agricultural soil after treatment by various soil amendments using sequential extraction procedure and multivariate analysis. *Catena* **2019**, *181*, 104084. [CrossRef]

73. Malandrino, M.; Abollino, O.; Buoso, S.; Giacomino, A.; La Gioia, C.; Mentasti, E. Accumulation of heavy metals from contaminated soil to plants and evaluation of soil remediation by vermiculite. *Chemosphere* **2011**, *82*, 169–178. [CrossRef]
74. Jia, Z.Y.; Wang, J.X.; Zhou, X.D.; Zhou, Y.J.; Li, Y.; Li, B.J.; Zhou, S.L. Identification of the sources and influencing factors of potentially toxic elements accumulation in the soil from a typical karst region in Guangxi, Southwest China. *Environ. Pollut.* **2020**, *256*, 113505. [CrossRef]
75. Gao, T.; Ke, S.; Wang, S.; Li, F.; Liu, C.; Lei, J.; Liao, C.; Wu, F. Contrasting Mg isotopic compositions between Fe-Mn nodules and surrounding soils: Accumulation of light Mg isotopes by Mg-depleted clay minerals and Fe oxides. *Geochim. Cosmochim Acta* **2018**, *237*, 205–222. [CrossRef]
76. Wei, X.; Ji, H.B.; Wang, S.J.; Chu, H.S.; Song, C.S. The formation of representative lateritic weathering covers in south-central Guangxi (southern China). *Catena* **2014**, *118*, 55–72. [CrossRef]
77. Suda, A.; Makino, T. Functional effects of manganese and iron oxides on the dynamics of trace elements in soils with a special focus on arsenic and cadmium: A review. *Geoderma* **2016**, *270*, 68–75. [CrossRef]
78. Zhang, G.S.; Qu, J.H.; Liu, H.J.; Liu, R.P.; Li, G.T. Removal mechanism of As(III) by a novel Fe-Mn binary oxide adsorbent: Oxidation and sorption. *Environ. Sci. Technol.* **2007**, *41*, 4613–4619. [CrossRef]
79. Rady, O.; Liu, L.H.; Yang, X.; Tang, X.J.; Tan, W.F.; Qiu, G.H. Adsorption and catalytic oxidation of arsenite on Fe-Mn nodules in the presence of oxygen. *Chemosphere* **2020**, *259*, 127503. [CrossRef] [PubMed]
80. Violante, A.; Pigna, M. Competitive sorption of arsenate and phosphate on different clay minerals and soils. *Soil Sci. Soc. Am. J.* **2002**, *66*, 1788–1796. [CrossRef]
81. Jerzykowska, I.; Majzlan, J.; Michalik, M.; Göttlicher, J.; Steininger, R.; Błachowski, A.; Ruebenbauer, K. Mineralogy and speciation of Zn and As in Fe-oxide-clay aggregates in the mining waste at the MVT Zn–Pb deposits near Olkusz, Poland. *Geochemistry* **2014**, *74*, 393–406. [CrossRef]
82. Giménez, J.; Martínez, M.; Depablo, J.; Rovira, M.; Duro, L. Arsenic sorption onto natural hematite, magnetite, and goethite. *J. Hazard. Mater.* **2007**, *141*, 575–580. [CrossRef] [PubMed]
83. Lin, Z.; Puls, R.W. Adsorption, desorption and oxidation of arsenic affected by clay minerals and aging process. *Environ. Geol.* **2000**, *39*, 753–759. [CrossRef]
84. Anschutz, A.J.; Penn, R.L. Reduction of crystalline iron(III) oxyhydroxides using hydroquinone: Influence of phase and particle size. *Geochem. Trans.* **2005**, *6*, 60–66. [CrossRef]
85. Kocar, B.D.; Borch, T.; Fendorf, S. Arsenic repartitioning during biogenic sulfidization and transformation of ferrihydrite. *Geochim. Cosmochim. Acta* **2010**, *74*, 980–994. [CrossRef]
86. Smedley, P.L.; Kinniburgh, D.G. A review of the source, behaviour and distribution of arsenic in natural waters. *Appl. Geochem.* **2002**, *17*, 517–568. [CrossRef]

applied sciences

MDPI

Article

Predicting the Zinc Content in Rice from Farmland Using Machine Learning Models: Insights from Universal Geochemical Parameters

Wenda Geng [1], Tingting Li [2], Xin Zhu [2], Lei Dou [2], Zijia Liu [3,4], Kun Qian [1], Guiqi Ye [1], Kun Lin [1], Bo Li [1], Xudong Ma [1], Qingye Hou [1,5], Tao Yu [5,6] and Zhongfang Yang [1,5,*]

[1] School of Earth Sciences and Resources, China University of Geosciences, Beijing 100083, China; gengwd0911@163.com (W.G.); shiqiankun515@126.com (K.Q.); yegq77@163.com (G.Y.); 3001200073@cugb.edu.cn (K.L.); bobo_lee0425@126.com (B.L.); maxudongcugb@126.com (X.M.); qingyehou@cugb.edu.cn (Q.H.)
[2] Guangdong Institute of Geological Survey, Guangzhou 510080, China; tingtingliscsio@126.com (T.L.); ddystar@163.com (X.Z.); ggsdl@163.com (L.D.)
[3] Research Center of Geochemical Survey and Assessment on Land Quality, Institute of Geophysical and Geochemical Exploration, Chinese Academy of Geological Sciences, Langfang 065000, China; zijialiu@outlook.com
[4] Key Laboratory of Geochemical Cycling of Carbon and Mercury in the Earth's Critical Zone, Institute of Geophysical and Geochemical Exploration, Chinese Academy of Geological Sciences, Langfang 065000, China
[5] Key Laboratory of Ecological Geochemistry, Ministry of Natural Resources, Beijing 100037, China; yutao@cugb.edu.cn
[6] School of Science, China University of Geosciences, Beijing 100083, China
* Correspondence: yangzf@cugb.edu.cn

Abstract: Zinc (Zn) is an essential nutrient for the human body and is prone to deficiency. Supplementing Zn through zinc-enriched cereals is of great significance in addressing the widespread issue of zinc deficiency. However, there is no simple linear correlation between the soil zinc content and rice grain zinc content, which poses challenges for zoning zinc-enriched rice cultivation based on the soil Zn content. Therefore, accurately predicting the zinc content in rice grains is of great importance. To verify the robustness of the prediction model and expand its applicability, this study established a prediction model using 371 sets of previously collected and tested rice grain and root zone soil samples from the Pearl River Delta and Heyuan regions in Guangdong. The model was validated using the data from 65 sets of rice and root zone soil samples collected and analyzed in Zijin and Dongyuan counties, Heyuan, in 2023. The results show that zinc absorption by rice grains is controlled by multiple factors, primarily related to the soil S, P, CaO, Mn, TFe_2O_3, TOC, and SiO_2/Al_2O_3 ratio. Both the artificial neural network model and random forest model demonstrated a good predictive performance across large regions. However, in the Heyuan region, the random forest model outperformed the artificial neural network model, with an R^2 of 0.79 and an RMSE of 0.05 when the predicted data were compared against the measured BAF_{Zn} of the rice. This suggests that predicting the zinc content in rice grains based on the soil macro-elements (including oxides) and TOC is feasible, and, within certain regional boundaries, the prediction model is robust and widely applicable. This study provides valuable insights into the rational development of zinc-enriched rice in the Heyuan region and offers a useful reference for establishing prediction models of the beneficial element content in rice grains in areas with limited data.

Keywords: Zinc; soil; artificial neural network model; random forest model; Guangdong

Academic Editor: Roberto Romaniello

Received: 27 November 2024
Revised: 16 January 2025
Accepted: 21 January 2025
Published: 26 January 2025

Citation: Geng, W.; Li, T.; Zhu, X.; Dou, L.; Liu, Z.; Qian, K.; Ye, G.; Lin, K.; Li, B.; Ma, X.; et al. Predicting the Zinc Content in Rice from Farmland Using Machine Learning Models: Insights from Universal Geochemical Parameters. *Appl. Sci.* **2025**, *15*, 1273. https://doi.org/10.3390/app15031273

1. Introduction

Zinc (Zn) is an essential trace element for the human body, playing a crucial role in physiological processes such as growth, reproduction, immunity, and endocrine functions [1]. Zinc deficiency can lead to weakened immunity and impaired digestive function, and, in children, it may cause stunted growth or, in severe cases, dwarfism. Studies have shown that approximately 40% of the global population faces health issues related to zinc deficiency [2]. Most people obtain zinc primarily from food, and insufficient zinc intake is considered one of the major causes of zinc deficiency [3]. Rice, a staple food for over 3.5 billion people worldwide, is closely linked to dietary zinc intake, especially in Asia [4]. However, in many regions, the zinc content in rice is very low [5,6], insufficient to meet human nutritional needs [7]. Therefore, the development of natural zinc-enriched rice from zinc-rich soils is of great importance for addressing the widespread issue of zinc deficiency.

Rice's absorption of trace elements is influenced not only by the total amount of these elements in the soil but also by factors such as their bioavailability, the forms in which the elements occur in the soil, soil physicochemical properties, and the interactions between elements [8]. Previous research has shown that a high soil zinc content does not necessarily correlate with a high zinc content in rice grains. In most cases, there is no significant correlation between the two [9], making it difficult to classify zinc-rich soils based solely on the soil zinc content. Therefore, understanding the characteristics of rice's zinc absorption and constructing predictive models for the zinc content in rice grains is crucial for the development of zinc-rich land resources.

In recent years, several studies have established models for predicting the absorption of heavy metals by rice [10,11], and machine learning methods have been widely used in the construction of these models, achieving good predictive results. Artificial neural networks (ANNs) and random forest (RF) are two of the most commonly applied machine learning methods and have shown excellent performance in predicting the heavy metal content in crops [12,13]. However, due to the high costs of field data collection and the intensive labor, equipment, and financial support required, as well as the complexity and variability of the soil environments in agricultural regions [14,15], predicting the heavy metal content in soil–rice systems using machine learning remains challenging in different research areas [9].

Wang et al. [9] selected soil pH, TOC (total organic carbon), Mn, and Zn as the input variables and used an artificial neural network model to predict the bioaccumulation factor of zinc (BAF_{Zn}) in rice in farmland in central and eastern Guangxi, achieving a strong predictive effect with an R^2 of 0.93. Ma et al. [16] used Fe_2O_3, Mn, and SiO_2/Al_2O_3 as the input variables for a maize prediction model and Fe_2O_3, SiO_2/Al_2O_3, and P for a rice prediction model. They applied a backpropagation neural network model to predict the BAF_{Zn} in maize and rice in Guang'an county, Sichuan Province, achieving good predictive results. Similarly, Liu et al. [17] used a neural network algorithm and selected soil Zn, SiO_2/Al_2O_3, Fe_2O_3, and K_2O as the input variables to construct a predictive model for the wheat grain zinc content in the Weining Plain of Ningxia, with a good model fitting. Several scholars' studies have shown that, despite the differences in input variables and machine learning methods across different research regions, predicting the crop zinc content based on the major soil elements (including oxides) and TOC is feasible. However, in these studies, both the training and validation datasets were collected from the same research region. Whether the training and validation datasets from different regions can be used in machine learning to predict the crop grain zinc content and whether the model's robustness and generalization ability can meet the requirements remains a key issue explored in this paper.

The zinc content in rice grains in Guangdong Province is higher than the national average, indicating a great potential for the development of zinc-enriched rice. Although

there is no linear correlation between the zinc content in rice grains and in the soil, there have been numerous cases where machine learning has been used to predict the elemental content of rice grains [9,11,14,18]. This study focuses on the Pearl River Delta and Heyuan areas in Guangdong Province, using 371 datasets collected from these regions for the model training and 65 datasets from Heyuan for the validation. The aim is to address the robustness and generalizability of the machine learning models for predicting the zinc content in rice grains and provide a scientific basis for delineating zinc-rich rice cultivation zones in the study area.

Against this background, the objectives of this study are as follows: (1) to investigate the impact of soil properties on the absorption of zinc in rice grains; (2) to explore whether machine learning models for predicting the zinc content in rice grains, based on the major soil elements and the TOC content, exhibit robustness and generalizability across a defined geographical area; (3) to provide useful references for the rational development of zinc-rich rice in Heyuan and for constructing models to predict the beneficial element content in rice grains when data availability is limited in the study area.

2. Materials and Methods

2.1. Study Area

The study area is located in the central and southern regions of Guangdong Province, including the Pearl River Delta and Heyuan city (Figure 1). Geographically, it spans from 111°22′ E to 115°36′ E and 21°28′ N to 24°47′ N, covering an area of 71,022 km^2. The area lies in the South Asian subtropical zone, characterized by a South Asian monsoon climate with abundant rainfall, ample heat, and a simultaneous rainy and hot season. The annual sunshine duration is 2000 h, and the seasonal distribution is relatively uniform. The average annual temperature ranges from 21.4 to 22.4 °C, and the annual precipitation is between 1600 and 2300 mm, with most rainfall occurring between April and September due to the monsoon influence. The study area has a total rice planting area of 1,030,440 hectares, mainly distributed across the cities of Zhaoqing, Jiangmen, Heyuan, and Huizhou, with two harvests per year and a total annual yield of 3.9191 million tons.

The Pearl River Delta is a complex delta formed by the deposition of sediments from the Xijiang, Beijiang, and Dongjiang rivers and their tributaries. Approximately one-fifth of the area consists of hills, terraces, and residual hills, with the overall landscape being a plain formed by Quaternary sediments. The Heyuan area, on the other hand, is a mountainous and hilly region, with the Dongjiang and Xinfengjiang rivers running through the area. The landscape is characterized by alternating mountain ranges and basins, with granite as the primary parent material for soil formation.

2.2. Sample Collection

According to the standards for the multi-target regional geochemical surveys (DZ/T 0258-2014) and land quality geochemical evaluations (DZ/T 0295-2016) [19,20], a total of 371 rice grain and root soil samples were collected from the study area (Figure 2). Of these, 306 samples were collected from the Pearl River Delta region during 2016 and 2017, and 65 samples were collected from the Heyuan region in 2023. The samples were taken at the rice maturity stage, with multiple points sampled within each plot, and the samples were mixed in equal amounts to form a composite sample. Simultaneously, the corresponding root soil samples were collected by uprooting the rice plants and gently shaking off the soil from the roots.

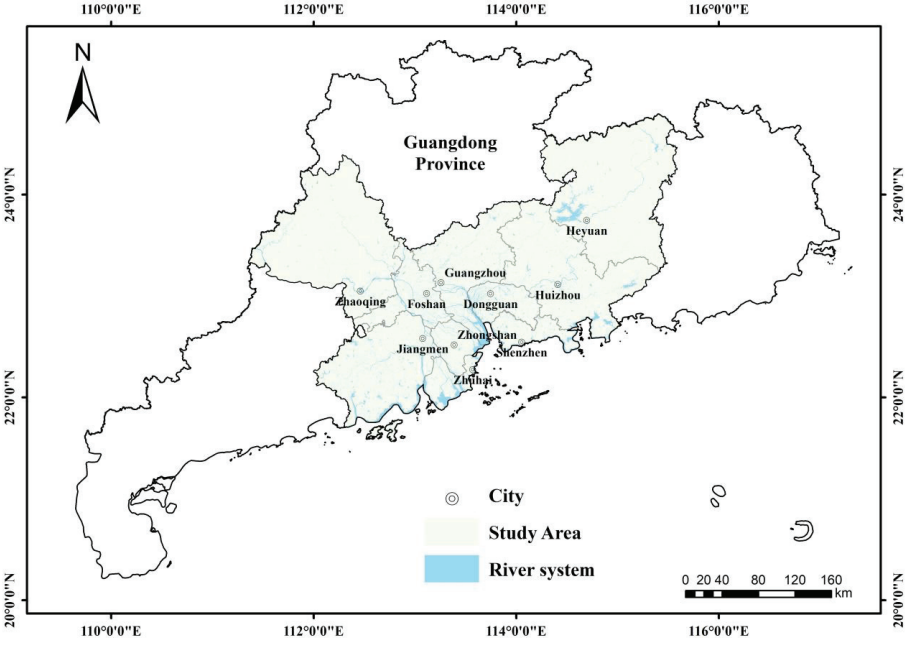

Figure 1. Geographical location of study area.

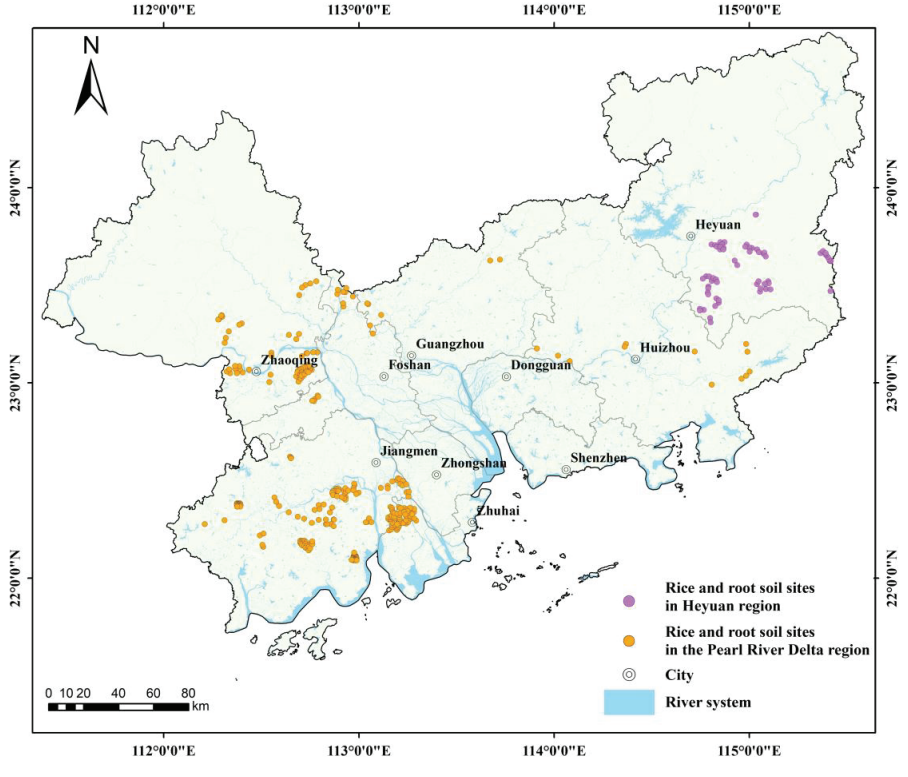

Figure 2. Distribution of sampling sites in study area.

After collection, the rice grain and root soil samples were placed in a cool, ventilated area to air-dry. Once the rice grains were dried, they were threshed, weighed, and prepared for testing. During the drying process of the soil samples, the samples were periodically tapped with a rubber mallet to prevent clumping. After drying, the samples were sieved through a nylon sieve (with a 2 mm mesh size) using a shaking motion and stored in clean polyethylene bags for analysis.

2.3. Chemical Analysis

The rice grain and root soil samples were analyzed at the Anhui Geological Laboratory. The laboratory sample treatment and analytical process were as follows: After threshing the rice grains, they were rinsed with clean water, placed on a clean tray, and dried at temperatures below 65 °C, followed by dehulling. The dried and dehulled samples were then ground using a ceramic mortar and pestle until they passed through a 40-mesh (425 μm) to 60-mesh (250 μm) nylon sieve and were thoroughly mixed before testing. The root soil samples were ground in a ceramic mortar, sieved through a 200-mesh nylon sieve, and evenly mixed before testing.

The analysis followed the methods outlined in the DZ/T 0279-2016 "Regional Geochemical Sample Analysis Methods" and the GB5009.268-2016 "National Food Safety Standard for Multi-Element Determination in Foods" [21,22]. The specific analysis methods and detection limits are shown in Table 1. National primary standard materials and duplicate samples were used for quality control during the testing process. The accuracy of the methods was verified by calculating the logarithmic deviation (ΔlgC) or relative error (RE%) between the measured and standard values. The precision was evaluated by calculating the relative standard deviation (RSD%) between the measured and standard values [23]. All the detection limits, reporting rates, accuracy, and precision for the full element analysis methods met the monitoring limits specified, ensuring data reliability.

Table 1. Sample analysis method scheme and detection limit.

Samples	Item	Method	Detecting Limit
Soil	SiO_2	X-ray Fluorescent Spectroscopy (XRF)	0.05 *
	TFe_2O_3		0.02 *
	Al_2O_3		0.03 *
	CaO		0.02 *
	Mn		10
	P		10
	S		50
	Zn		4
	TOC	Volumetric method (VOL)	0.1 *
	pH	Ion-selective electrode (ISE)	0.08 **
Rice	Zn	Inductively coupled plasma mass spectrometry (ICP-MS)	0.05

The unit of measurement for "*" is %, "**" is dimensionless, and other elements are in mg/kg.

2.4. Models' Development

The bioaccumulation factor (BAF) is used to measure the accumulation of zinc (Zn) in rice grains, and, based on the soil properties, relevant predictive models, and corresponding theoretical framework, a predictive model for the BAF_{Zn} of rice grains is established [24].

The bioaccumulation factor of Zn is calculated using the following formula:

$$BAF_{Zn} = \frac{C_{Rice\ Zn}}{C_{Soil\ Zn}} \quad (1)$$

where BAF_{Zn} is the bioaccumulation factor for Zn, $C_{Rice\ Zn}$ is the zinc content in the rice grains, and $C_{Soil\ Zn}$ is the zinc content in the corresponding root soil.

Before constructing the model, the input features are logarithmically transformed and normalized. This preprocessing step is aimed at making the data have similar scales and an approximately normal distribution, which accelerates the convergence of the machine learning algorithms and improves the prediction accuracy [12].

2.4.1. Artificial Neural Network (ANN)

Artificial neural networks (ANNs) are powerful data modeling tools consisting of an input layer, hidden layers, and an output layer [25]. The nodes in the input layer receive the input information, which is processed by activation functions and passed to the nodes in the hidden layers. The information from the hidden layers is then sent to the output layer. Each node is connected to the others through corresponding weights and thresholds [26]. If the output of any individual node is above the specified threshold, then that node is activated and the data are sent to the next layer of the network. Otherwise, no data are passed on to the next layer of the network [27]. Many factors can affect the stability of an ANN model, including the model used, the modeling process, and the simulated training data. The optimal combination of neurons could not be determined in advance; therefore, the optimal structure of the network was determined by testing multiple models using correlation coefficient and root mean square error (RMSE) guidelines [28]. Artificial neural networks are widely applied in various research fields due to their strong learning ability and good predictive performance [29–32]. In the field of ecology, Li et al. [14] used an artificial neural network model to predict the cadmium content in rice, and the prediction results were optimistic.

In this study, the elastic backpropagation algorithm (RPROP) was used to train the ANN model, where the maximum step size of the neural network training was set to 100,000, and the partial derivative of the error function was specified as a stopping criterion threshold of 0.01. As a variant of backpropagation, the RPROP eliminates the influence of derivative changes on the weight step size and only considers the sign of the derivative, which enhances the efficiency and stability of the algorithm [33]. The ANN prediction model in this study was built using the neuralnet package in R Studio.

2.4.2. Random Forest (RF)

Random forest (RF) is a widely used ensemble learning method that combines multiple decision trees to cluster data based on similar patterns [34]. It is an extension of decision trees. The algorithm divides the feature space using hierarchical rules and builds each decision tree using a random subset of the predictor variables [35]. Each decision tree is built using bootstrap sampling, where random subsets of the training data are selected with replacements. Additionally, at each split in a tree, a random subset of features is considered, introducing further randomness that helps reduce the correlation between individual trees and enhances the overall performance of the models [36]. The final prediction is obtained by averaging the regression results of all the decision trees in the ensemble [37,38].

Random forest reduces model variance by combining multiple decision trees, which effectively lowers the risk of overfitting. It also provides feature importance, which helps in understanding the model and the data [39]. This method is particularly suitable for handling high-dimensional data, making it applicable across various fields. Zhao et al. [40] used the random forest model to predict heavy metal pollution in soil, and Ma et al. [11] used the random forest model to predict the cadmium content in paddy rice, both achieving good predictive results. The RF prediction model in this study was built using the random forest package in R Studio.

2.5. Models' Evaluation

To assess the accuracy of the predictive models, the rice grain and root soil samples were divided into a training set and a test set at an 8:2 ratio. The model was trained using the training set and evaluated using the test set to verify its accuracy. The accuracy of the predictive models was validated using the regression coefficient of determination (R^2), normalized mean error (NME), mean relative error (MRE), and root mean square error (RMSE) [41]. The formulas are as follows:

$$R^2 = 1 - \frac{\sum_{i=1}^{N}(o_i - e_i)^2}{\sum_{i=1}^{N}(o_i - \overline{o})^2} \quad (2)$$

$$NME = \frac{\overline{e} - \overline{o}}{\overline{o}} \quad (3)$$

$$MRE = \frac{\sum_{i=1}^{N} \frac{|e_i - o_i|}{o_i}}{N} \times 100\% \quad (4)$$

$$RMSE = \sqrt{\frac{\sum_{i=1}^{N}(e_i - o_i)^2}{N}} \quad (5)$$

where e_i and o_i represent the predicted and observed values for each sample, respectively; $\overline{e}$ and $\overline{o}$ are the average predicted and observed values; and N is the total number of samples.

The model is considered more accurate when R^2 approaches 1. A negative NME indicates that the BAF is underestimated, while a positive value indicates overestimation. The smaller the MRE and RMSE, the more accurate the model is.

3. Results and Discussion

3.1. Zn Content Characteristics in the Soil–Rice Ecosystem

Table 2 summarizes the Zn content and bioaccumulation factor (BAF_{Zn}) characteristics of the rice grains and root soil in the study area, including both the Heyuan and Pearl River Delta regions. In the Heyuan region, the Zn content in the root soil ranged from 32.00 to 156.70 mg/kg, with an average content of 72.30 mg/kg. According to the GB15618-2018 Soil Environmental Quality Risk Control Standards for Agricultural Land [42], the screening value for Zn is set at 200 mg/kg, meaning that the Zn content in all the root soil samples from the Heyuan region was below the screening value. The Zn content in the rice grains from the Heyuan region ranged from 13.60 to 25.40 mg/kg, with an average content of 18.47 mg/kg. Referring to the Chinese Food Composition Table Standard Edition 6, the national average Zn content in rice grains is 15.40 mg/kg. The proportion of samples from the Heyuan region with a Zn content higher than the national average was 84.6%, indicating substantial potential for developing Zn-enriched rice. The bioaccumulation factor (BAF_{Zn}) of the soil–rice system in the Heyuan region ranged from 0.10 to 0.67, with an average value of 0.28.

In the Pearl River Delta region, the Zn content in the root soil ranged from 16.90 to 253.30 mg/kg, with an average of 79.78 mg/kg. Only one sample exceeded the screening value of 200 mg/kg. The Zn content in the rice grains from the Pearl River Delta region ranged from 11.33 to 30.37 mg/kg, with an average of 18.10 mg/kg, and 83.33% of the samples had a Zn content higher than the national average, indicating substantial potential for Zn development in rice. The BAFZn in the soil–rice system of the Pearl River Delta region ranged from 0.06 to 1.19, with an average value of 0.31.

Table 2. Zn content and BAF_{Zn} of rice grains and root soil in study area.

Sample Distribution Area	Sample Size	Type	Min Value (mg/kg)	Max Value (mg/kg)	Mean Value (mg/kg)	Median Value (mg/kg)	Coefficient of Variation
Heyuan Region	65	Root Soil	32.00	156.70	72.30	68.40	0.32
		Rice Grains	13.60	25.40	18.47	18.40	0.15
		BAF_{Zn}	0.10	0.67	0.28	0.25	0.35
Pearl River Delta	306	Root Soil	16.90	253.30	79.78	71.32	0.49
		Rice Grains	11.33	30.37	18.10	17.73	0.16
		BAF_{Zn}	0.06	1.19	0.31	0.26	0.64

Compared to Heyuan, the Pearl River Delta region showed a broader range of Zn content in both rice grains and root soil, as well as a wider range of BAF_{Zn}. However, the average and median values of the Zn content and BAF_{Zn} in both regions were quite similar. As shown in Figure 3, the distribution characteristics of the Zn content in both regions are similar. This suggests that, across the entire study area, there may be a similar relationship between the soil Zn content and rice grain Zn content.

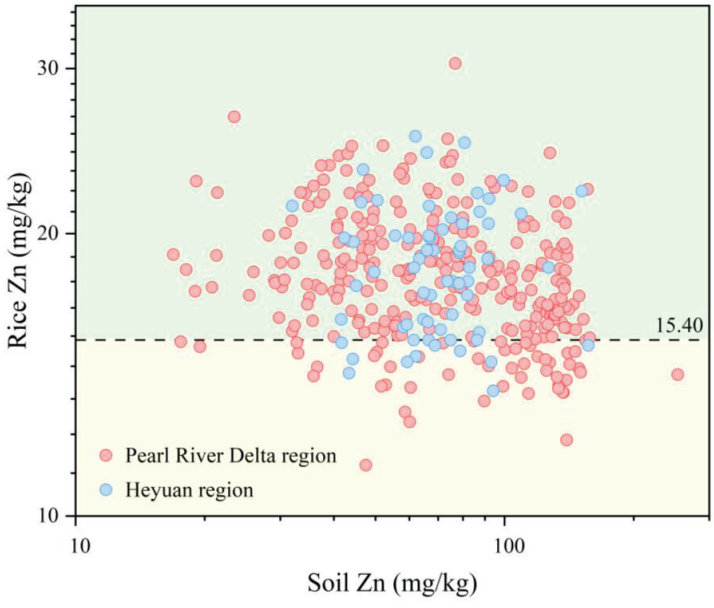

Figure 3. The relationship between soil Zn and rice Zn in different regions.

Figure 3 shows that there is no correlation between the soil Zn content and rice grain Zn content in the study area. Based on the Zn content in the soil, it is not possible to predict the Zn content in rice grains. Therefore, accurately predicting the Zn content in rice and identifying the Zn-enriched rice regions are crucial for the efficient and precise production of Zn-enriched rice.

3.2. Influence of Soil Properties on Zn Absorption by Rice Grains

The Zn content in rice grains is influenced by various factors. As shown in Figure 3, there is no significant correlation between the Zn content in the rice grains and the Zn

content in the root soil, indicating that the Zn content in the rice grains is not simply determined by the Zn content in the soil. Instead, it is closely related to the bioavailable form of Zn in the soil [43] and other physicochemical properties of the soil.

The relationship between the soil properties and the bioaccumulation factor of Zn (BAF_{Zn}) in the rice was evaluated using Pearson's correlation coefficient (Figure 4). The data were log-transformed to approximate a normal distribution. The results show that the BAF_{Zn} is negatively correlated with sulfur (S) ($r = -0.45$), phosphorus (P) ($r = -0.53$), calcium oxide (CaO) ($r = -0.75$), manganese (Mn) ($r = -0.72$), total iron (TFe_2O_3) ($r = -0.78$), and total organic carbon (TOC) ($r = -0.65$) and positively correlated with SiO_2/Al_2O_3 ($r = 0.69$). BAF_{Zn} has a strong correlation with CaO, Mn, and TFe_2O_3 and a moderate correlation with P, TOC, and SiO_2/Al_2O_3.

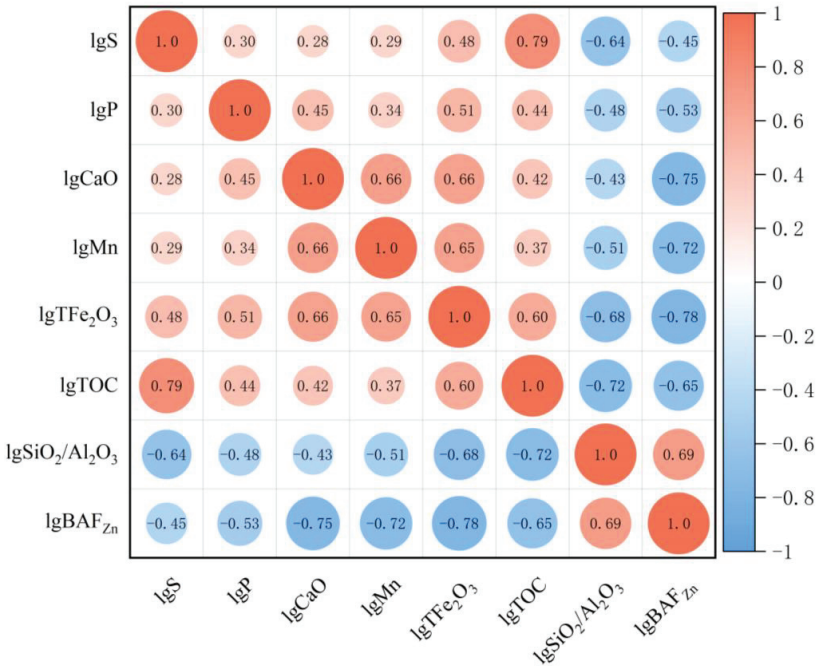

Figure 4. Correlation heatmap between soil properties and BAF_{Zn}.

Sulfur (S) can form insoluble zinc sulfide (ZnS), reducing the bioavailability of Zn in the soil [44,45]. In flooded paddy soils, the redox potential is low, and sulfur is often reduced to S^{2-}, which reacts with Zn^{2+} to form ZnS precipitates, reducing the mobility of Zn in the soil [46,47]. In addition to the above redox reactions, sulfur-containing organic compounds in the soil can form covalent bonds with heavy metals, playing a significant role in the activation and fixation of heavy metals.

The TOC content is used as an indicator of the soil organic matter content [48]. In general, the mobility and bioavailability of heavy metals increase as the organic matter content decreases [49]. Organic matter in the soil contains a variety of components, including abundant ligands or functional groups such as carboxyl (-COOH), hydroxyl (-OH), and phenolic hydroxyl groups (aromatic ring-OH), which can form complexes with metal ions and affect the migration and transformation of heavy metals [50].

Calcium oxide (CaO) is an effective buffering agent in soil. Increasing soil CaO raises soil pH [51], promoting the formation of the carbonate and hydroxide precipitates of heavy

metals, thereby reducing the bioavailability of heavy metals like Zn and Cd and inhibiting their absorption by plants.

Iron (Fe) and manganese (Mn) readily form iron and manganese oxide minerals in surface environments [52]. Zn and other heavy metals may be incorporated into the crystal lattice of these minerals [53], reducing their bioavailability. Additionally, iron and manganese hydroxide colloids have a significant effect on the adsorption of Zn^{2+} [54].

SiO_2/Al_2O_3 represents the degree of silicon depletion and aluminum enrichment in the soil. A higher SiO_2 content indicates a higher sand fraction in the soil and fewer clay minerals and organic matter, which reduces the soil's ability to adsorb Zn [55,56].

Phosphorus (P), as a nutrient element, shows a high negative correlation with the bioaccumulation factor of Zn in rice grains. Many studies suggest that P and Zn exhibit antagonistic effects [57,58]. Studies has found that high concentrations of P significantly reduced the Zn content and bioavailability in rice grains. Su et al. [59] observed that applying phosphorus fertilizer reduced the Zn content in wheat grains by 17% to 56%.

3.3. Development of Prediction Models

Based on the findings in Section 3.2, the soil properties, including S, P, CaO, Mn, TFe_2O_3, TOC, and SiO_2/Al_2O_3, were selected as the input variables and the BAF_{Zn} as the output variable for the model development. The dataset of 371 rice grain and root soil samples from the study area was divided into 80% for the training set and 20% for the validation set to build two models: the artificial neural network (ANN) and random forest (RF).

The ANN model structure is illustrated in Figure 5, with two hidden layers containing six and four neurons, respectively. The larger first layer and smaller second layer allow for the extraction of low-order features in the first layer, which are then used to extract higher order features in the second layer, potentially improving the ANN performance. The RF model had 800 trees (ntree = 800) and three features considered at each split (mtry = 3). The feature importance for the RF model is shown in Figure 6, where mtry plays a more significant role in optimizing the model compared to ntree.

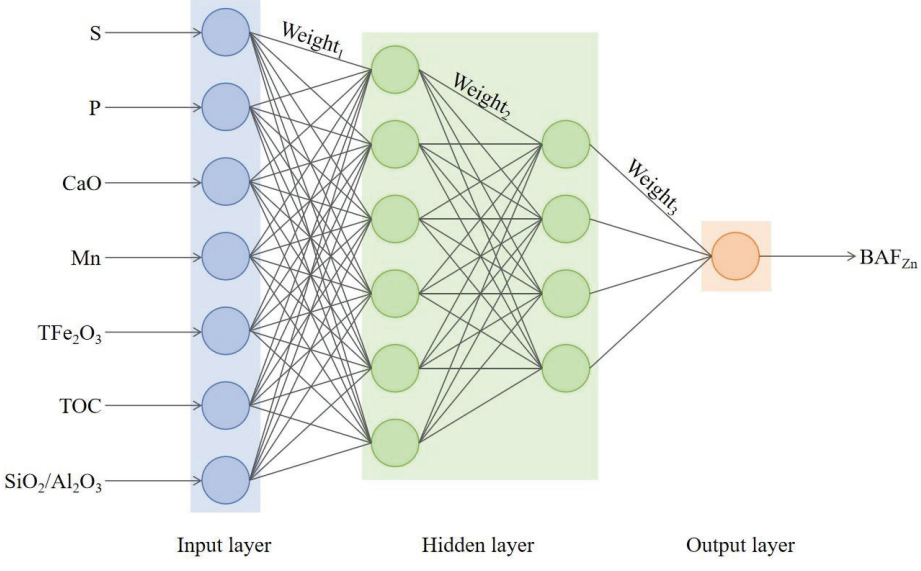

Figure 5. ANN model.

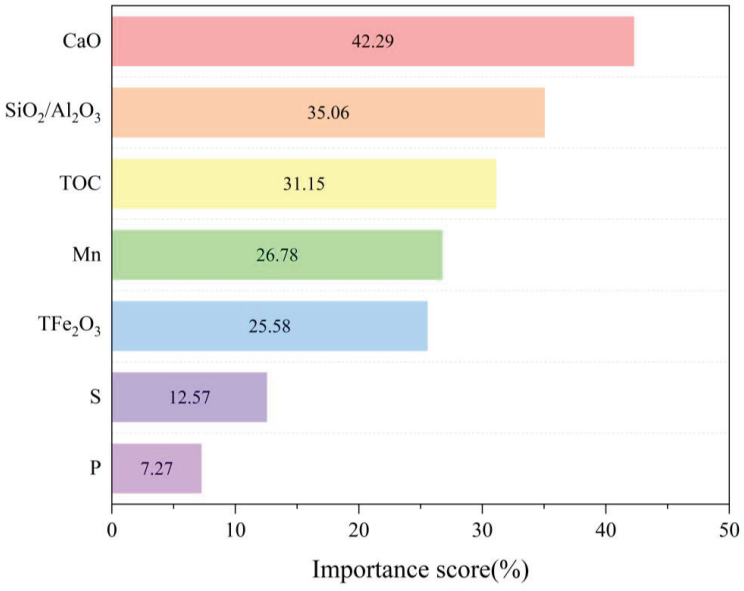

Figure 6. Importance score in random forest model.

The models' accuracies were assessed using R^2, the NME, the MRE, and the RMSE, and the results are summarized in Table 3. Both the ANN and RF models had an NME of 0.01, indicating that both models slightly overestimated the BAF_{Zn} values. The ANN model had MRE and RMSE values closer to zero than the RF model, although the difference was small. The predicted BAF_{Zn} values from both models were highly correlated with the measured values, and the predicted-to-observed ratio was nearly 1:1 (Figure 7). The R^2 value for the ANN model was slightly higher than for the RF model, indicating that both models are robust and provide reliable predictions.

Table 3. Accuracy of various models.

Model	Validation Sample Size	R^2	NME	MRE (%)	RMSE
Artificial Neural Network	75	0.88	0.01	11.02	0.06
Random Forest	77	0.85	0.01	15.09	0.07

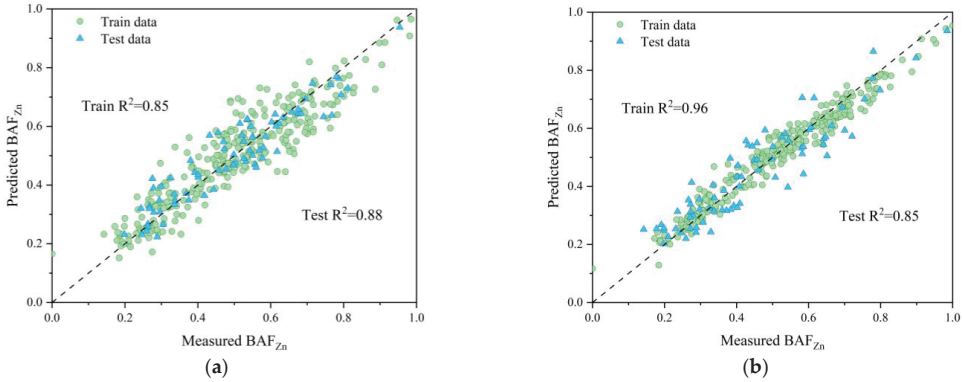

Figure 7. Predicted BAF_{Zn} and measured BAF_{Zn} by (**a**) ANN and (**b**) RF.

3.4. Model Validation

To further validate whether the prediction models could be broadly applied to any small region within the study area, 65 rice grain and root soil samples from Heyuan, collected in 2023, were used as a validation set. The models' accuracies were again assessed using R^2, the NME, the MRE, and the RMSE, with the results summarized in Table 4.

Table 4. Accuracy of the model for Heyuan.

Model	Validation Sample Size	R^2	NME	MRE (%)	RMSE
Artificial Neural Network	65	0.58	0.02	11.93	0.07
Random Forest	65	0.79	0.04	8.28	0.05

Both the ANN and RF models had NME values of 0.02 and 0.04, respectively, indicating that both models overestimated the BAF_{Zn} values in Heyuan. The RF model performed better than the ANN model, with MRE and RMSE values closer to zero. The R^2 value for the RF model was higher, and the predicted values were closer to the 1:1 ratio (Figure 8). Overall, the RF model showed a better performance than the ANN model for Heyuan, demonstrating the broader applicability and robustness of the prediction models.

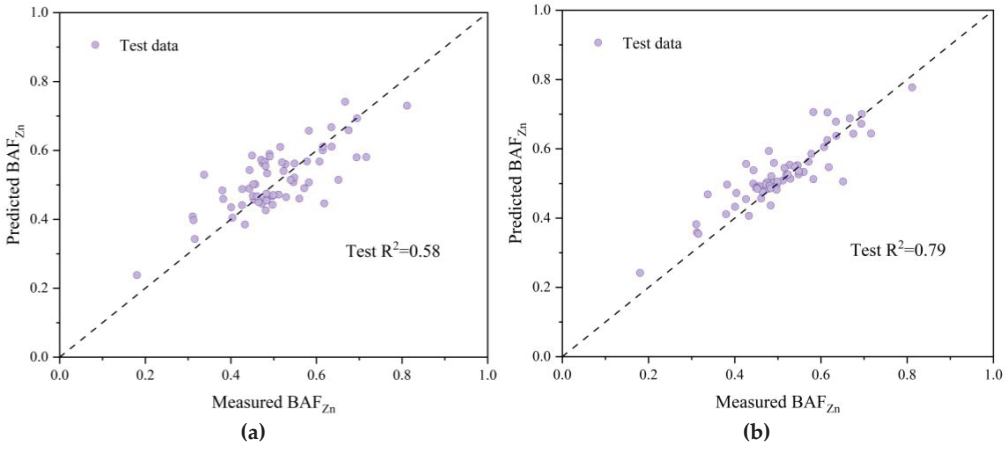

Figure 8. Predicted BAF_{Zn} and measured BAF_{Zn} for (**a**) ANN and (**b**) RF in Heyuan.

3.5. Model Robustness and Generalization

Previous studies often develop prediction models using the data from a single region for both the training and validation, which limits their applicability to other regions. This study aimed to assess the robustness and generalizability of the prediction models across regions. The models were developed using 65 samples from Heyuan and 306 samples from the Pearl River Delta. When applied to the Heyuan data, the models performed poorly, while the models for the Pearl River Delta performed well (Table 5, Figure 9).

Table 5. Predicting accuracy comparison for Heyuan and Pearl River Delta areas.

Region	Model	Validation Sample Size	R^2	NME	MRE (%)	RMSE
Heyuan	Artificial Neural Network	13	0.34	−0.03	18.47	0.13
	Random Forest	13	0.55	−0.07	16.30	0.11
Pearl River Delta	Artificial Neural Network	63	0.84	−0.003	15.09	0.07
	Random Forest	64	0.86	0.003	13.25	0.07

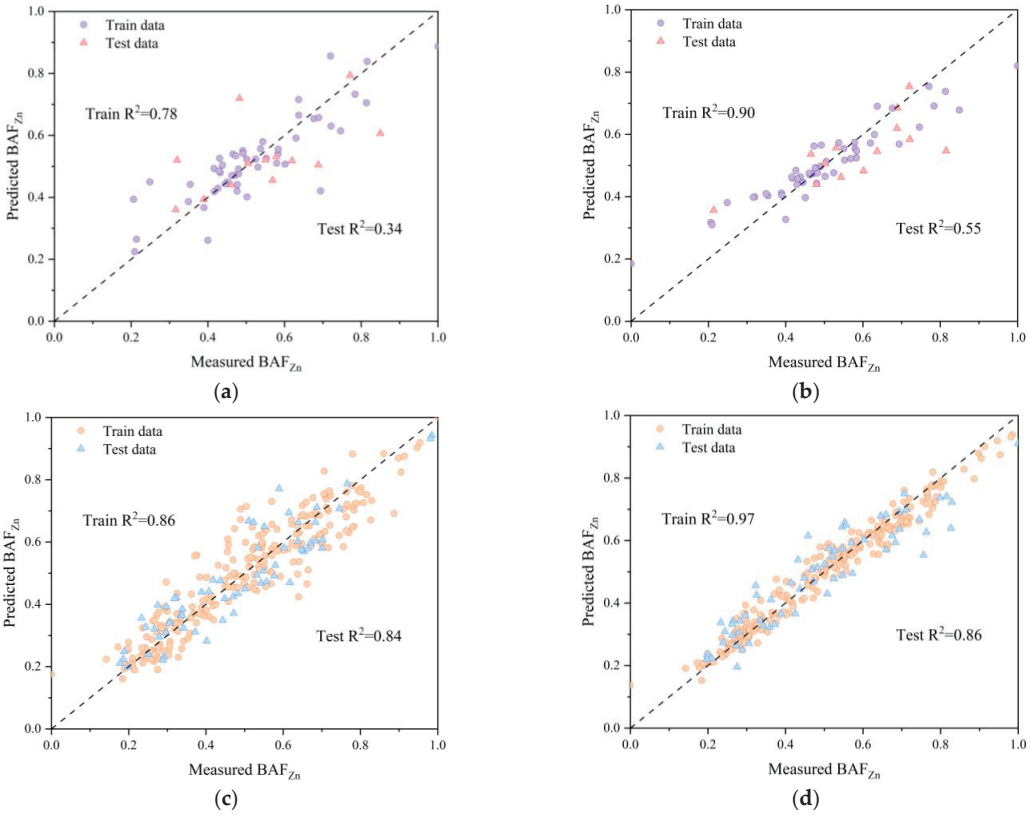

Figure 9. Predicted BAF_{Zn} and measured BAF_{Zn} for (**a**,**b**) Heyuan and (**c**,**d**) Pearl River Delta.

The sample-to-feature ratio (SFR) for Heyuan was 7.43, which is less than the ideal threshold of 10, leading to a weaker model performance. In contrast, the SFR for the Pearl River Delta was 34.71, ensuring better model stability. Combining the data from both regions improved the SFR and allowed the model to perform well across the study area, demonstrating its robustness and generalizability.

Finally, to further validate the models' generalization ability, the models were tested on 65 samples from Zhaoqing, collected in 2016. The results showed that the models performed

well, with the RF model slightly outperforming the ANN model (Table 6, Figure 10). This indicates that the prediction models have good generalizability within the study area, although further research is needed to refine the prediction methods for different regions.

Table 6. Accuracy of the model for Zhaoqing.

Model	Validation Sample Size	R^2	NME	MRE (%)	RMSE
Artificial Neural Network	65	0.80	0.02	13.18	0.08
Random Forest	65	0.90	−0.003	9.50	0.06

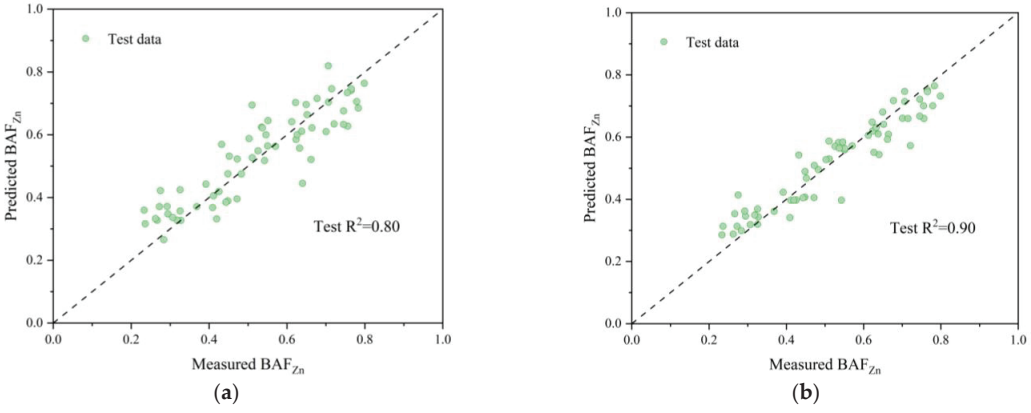

Figure 10. Predicted BAF_{Zn} and measured BAF_{Zn} for (**a**) ANN and (**b**) RF in Zhaoqing.

4. Summary and Conclusions

The rice grains in the study area are rich in zinc content, indicating a great potential for the development of zinc-enriched rice. However, the zinc content in the rice grains does not have a linear correlation with the zinc content in the soil. Research has found that the uptake of zinc by rice grains is controlled by multiple factors, mainly related to soil S, P, CaO, Mn, TFe_2O_3, TOC, and SiO_2/Al_2O_3. To accurately predict the zinc content in the rice grains in the study area, this study employed machine learning methods to establish a predictive model using 371 sets of data collected from rice grains and rhizosphere soil samples in the Pearl River Delta and Heyuan areas of Guangdong. The robustness and generalizability of the predictive model were further verified, and the model showed a good predictive performance across the entire study area.

This study provides valuable references for the rational development of zinc-enriched rice in the Heyuan area, as well as for establishing predictive models of rice grain elemental content in small areas with limited data. This paper focuses solely on the zinc content in rice grains in Guangdong, but similar properties are expected in other regions or for other elements. Therefore, it is anticipated that more research will be conducted in the future to precisely predict the content of beneficial or harmful elements in rice grains across more regions. At the same time, with the rapid development of machine learning in recent years, the interpretability and prediction accuracy of the predictive models will be further improved.

Author Contributions: Conceptualization, W.G., Z.Y. and T.Y.; methodology, W.G., K.L. and B.L.; validation, K.Q. and G.Y.; formal analysis, X.M.; investigation, W.G., K.Q. and G.Y.; resources, T.L.; data curation, Q.H.; writing—original draft preparation, W.G., Z.Y. and T.Y.; writing—review and editing, Q.H.; visualization, W.G. and Z.L.; supervision, K.L., B.L. and X.M.; project administration, T.L., X.Z., L.D. and Z.L.; and funding acquisition, X.Z. and L.D. All authors have read and agreed to the published version of the manuscript.

Funding: The research was supported by the Geological Exploration and Urban Geological Survey Project of Guangdong Province, China (2024-16, 2023-25), and the National Nonprofit Institute Research Grant of IGGE (NO. AS2023P01).

Institutional Review Board Statement: Not applicable.

Informed Consent Statement: Not applicable.

Data Availability Statement: The data presented in this study are available upon request from the corresponding author. The data are not publicly available due to the confidentiality of the project.

Acknowledgments: The authors are grateful for the assistance of the editors and reviewers.

Conflicts of Interest: The authors declare no conflicts of interest.

References

1. Sturikova, H.; Krystofova, O.; Huska, D.; Adam, V. Zinc, Zinc Nanoparticles and Plants. *J. Hazard. Mater.* **2018**, *349*, 101–110. [CrossRef]
2. Zhang, Y.; Huang, Y.; Yang, P.; Chen, J.; Zhu, L.; Zhao, Y.; Guo, J. Characteristics of zinc absorption and distribution after silking in the different maize inbred lines. *J. Hebei Agric. Univ.* **2018**, *41*, 14–20. [CrossRef]
3. Gupta, S.; Brazier, A.K.M.; Lowe, N.M. Zinc Deficiency in Low- and Middle-income Countries: Prevalence and Approaches for Mitigation. *J. Hum. Nutr. Diet.* **2020**, *33*, 624–643. [CrossRef]
4. Singh, A.P.; Johari, D. *Hymenophyllum javanicum* Spreng: An Addition to the Pteridophytic Flora of Central India. *Proc. Natl. Acad. Sci. India Sect. B Biol. Sci.* **2018**, *88*, 531–537. [CrossRef]
5. Prom-U-Thai, C.; Rashid, A.; Ram, H.; Zou, C.; Guilherme, L.R.G.; Corguinha, A.P.B.; Guo, S.; Kaur, C.; Naeem, A.; Yamuangmorn, S.; et al. Simultaneous Biofortification of Rice with Zinc, Iodine, Iron and Selenium Through Foliar Treatment of a Micronutrient Cocktail in Five Countries. *Front. Plant Sci.* **2020**, *11*, 589835. [CrossRef] [PubMed]
6. Utasee, S.; Jamjod, S.; Lordkaew, S.; Prom-U-Thai, C. Improve Anthocyanin and Zinc Concentration in Purple Rice by Nitrogen and Zinc Fertilizer Application. *Rice Sci.* **2022**, *29*, 435–450. [CrossRef]
7. Cakmak, I.; Kutman, U.B. Agronomic Biofortification of Cereals with Zinc: A Review. *Eur. J. Soil Sci.* **2018**, *69*, 172–180. [CrossRef]
8. Lin, Q.; Zhu, W.; Chen, Z.; Peng, X.; Zhao, S. Progress in Species and Bioavailability of Heavy Metals in Soil. *J. Guangdong Univ. Technol.* **2013**, *30*, 113–118.
9. Wang, Y.; Yu, T.; Yang, Z.; Bo, H.; Lin, Y.; Yang, Q.; Liu, X.; Zhang, Q.; Zhuo, X.; Wu, T. Zinc Concentration Prediction in Rice Grain Using Back-Propagation Neural Network Based on Soil Properties and Safe Utilization of Paddy Soil: A Large-Scale Field Study in Guangxi, China. *Sci. Total Environ.* **2021**, *798*, 149270. [CrossRef]
10. Gu, Q.; Yu, T.; Yang, Z.; Ji, J.; Hou, Q.; Wang, L.; Wei, X.; Zhang, Q. Prediction and Risk Assessment of Five Heavy Metals in Maize and Peanut: A Case Study of Guangxi, China. *Environ. Toxicol. Pharmacol.* **2019**, *70*, 103199. [CrossRef] [PubMed]
11. Ma, X.; Yu, T.; Guan, D.-X.; Li, C.; Li, B.; Liu, X.; Lin, K.; Li, X.; Wang, L.; Yang, Z. Prediction of Cadmium Contents in Rice Grains from Quaternary Sediment-Distributed Farmland Using Field Investigations and Machine Learning. *Sci. Total Environ.* **2023**, *898*, 165482. [CrossRef]
12. Hu, B.; Xue, J.; Zhou, Y.; Shao, S.; Fu, Z.; Li, Y.; Chen, S.; Qi, L.; Shi, Z. Modelling Bioaccumulation of Heavy Metals in Soil-Crop Ecosystems and Identifying Its Controlling Factors Using Machine Learning. *Environ. Pollut.* **2020**, *262*, 114308. [CrossRef]
13. Pyo, J.; Hong, S.M.; Kwon, Y.S.; Kim, M.S.; Cho, K.H. Estimation of Heavy Metals Using Deep Neural Network with Visible and Infrared Spectroscopy of Soil. *Sci. Total Environ.* **2020**, *741*, 140162. [CrossRef]
14. Li, C.; Zhang, C.; Yu, T.; Liu, X.; Yang, Y.; Hou, Q.; Yang, Z.; Ma, X.; Wang, L. Use of Artificial Neural Network to Evaluate Cadmium Contamination in Farmland Soils in a Karst Area with Naturally High Background Values. *Environ. Pollut.* **2022**, *304*, 119234. [CrossRef] [PubMed]
15. Zhao, B.; Zhu, W.; Hao, S.; Hua, M.; Liao, Q.; Jing, Y.; Liu, L.; Gu, X. Prediction Heavy Metals Accumulation Risk in Rice Using Machine Learning and Mapping Pollution Risk. *J. Hazard. Mater.* **2023**, *448*, 130879. [CrossRef] [PubMed]
16. Ma, X.; Yu, T.; Yang, Z.; Zhang, H.; Wu, Z.; Wang, J.; Li, M.; Lei, F. Geochemical characteristics of zinc in soil and prediction of zinc content in maize and rice grains in Linshui County, Sichuan Province. *Geol. China* **2022**, *49*, 324–335.

17. Liu, Z.; Zhang, X.; Dong, Y.; Qing, C.; Cheng, X.; Zhao, W.; Li, X.; Sang, L.; Hai, L. Geochemical characteristics of zinc in soil and prediction of Zn-rich wheat cultivating areas in Weining Plain, Northwest China. *Geol. China* **2024**, *51*, 1319–1330.
18. Guo, R.; Ren, R.; Wang, L.; Zhi, Q.; Yu, T.; Hou, Q.; Yang, Z. Using Machine Learning to Predict Selenium and Cadmium Contents in Rice Grains from Black Shale-Distributed Farmland Area. *Sci. Total Environ.* **2024**, *912*, 168802. [CrossRef] [PubMed]
19. *DZ/T 0258-2014*; Specification of Multi-Purpose Regional Geochemical Survey (1:250 000). MNR (Ministry of Land and Resources of the People's Republic of China): Beijing, China, 2014.
20. *DZ/T 0295-2016*; Specification of Land Quality Geochemical Assessment. MNR (Ministry of Land and Resources of the People's Republic of China): Beijing, China, 2016.
21. *GB5009.268-2016*; National Food Safety Standard for Multi-Element Determination in Foods. National Health and Family Planning Commission of the People's Republic of China: Beijing, China, 2016.
22. *DZ/T 0279-2016*; Regional Geochemical Sample Analysis Methods. MNR (Ministry of Land and Resources of the People's Republic of China): Beijing, China, 2016.
23. Li, M.; Xi, X.; Xiao, G.; Cheng, H.; Yang, Z.; Zhou, G.; Ye, J.; Li, Z. National Multi-Purpose Regional Geochemical Survey in China. *J. Geochem. Explor.* **2014**, *139*, 21–30. [CrossRef]
24. Yang, Y.; Li, C.; Yang, Z.; Yu, T.; Jiang, H.; Han, M.; Liu, X.; Wang, J.; Zhang, Q. Application of Cadmium Prediction Models for Rice and Maize in the Safe Utilization of Farmland Associated with Tin Mining in Hezhou, Guangxi, China. *Environ. Pollut.* **2021**, *285*, 117202. [CrossRef] [PubMed]
25. Li, P.; Hao, H.; Zhang, Z.; Mao, X.; Xu, J.; Lv, Y.; Chen, W.; Ge, D. A Field Study to Estimate Heavy Metal Concentrations in a Soil-Rice System: Application of Graph Neural Networks. *Sci. Total Environ.* **2022**, *832*, 155099. [CrossRef]
26. Yang, G.R.; Wang, X.-J. Artificial Neural Networks for Neuroscientists: A Primer. *Neuron* **2020**, *107*, 1048–1070. [CrossRef]
27. Georgevici, A.I.; Terblanche, M. Neural Networks and Deep Learning: A Brief Introduction. *Intensive Care Med.* **2019**, *45*, 712–714. [CrossRef] [PubMed]
28. Ebrahimi, M.; Sarikhani, M.R.; Safari Sinegani, A.A.; Ahmadi, A.; Keesstra, S. Estimating the Soil Respiration Under Different Land Uses Using Artificial Neural Network and Linear Regression Models. *Catena* **2019**, *174*, 371–382. [CrossRef]
29. Shao, W.; Guan, Q.; Tan, Z.; Luo, H.; Li, H.; Sun, Y.; Ma, Y. Application of BP—ANN Model in Evaluation of Soil Quality in the Arid Area, Northwest China. *Soil Tillage Res.* **2021**, *208*, 104907. [CrossRef]
30. Zhu, J.-J.; Yang, M.; Ren, Z.J. Machine Learning in Environmental Research: Common Pitfalls and Best Practices. *Environ. Sci. Technol.* **2023**, *57*, 17671–17689. [CrossRef] [PubMed]
31. Zhao, B.; Song, J.; Xie, L.; Ma, H.; Li, H.; Ren, J.; Sun, W. Multiaxial Fatigue Life Prediction Method Based on the Back-Propagation Neural Network. *Int. J. Fatigue* **2023**, *166*, 107274. [CrossRef]
32. Wang, X.; Liu, L.; Zhang, W.; Ma, X. Prediction of Plant Uptake and Translocation of Engineered Metallic Nanoparticles by Machine Learning. *Environ. Sci. Technol.* **2021**, *55*, 7491–7500. [CrossRef]
33. Santra, A.K.; Chakraborty, N.; Sen, S. Prediction of Heat Transfer Due to Presence of Copper–Water Nanofluid Using Resilient-Propagation Neural Network. *Int. J. Therm. Sci.* **2009**, *48*, 1311–1318. [CrossRef]
34. Guio Blanco, C.M.; Brito Gomez, V.M.; Crespo, P.; Ließ, M. Spatial Prediction of Soil Water Retention in a Páramo Landscape: Methodological Insight into Machine Learning Using Random Forest. *Geoderma* **2018**, *316*, 100–114. [CrossRef]
35. Carranza, C.; Nolet, C.; Pezij, M.; van der Ploeg, M. Root Zone Soil Moisture Estimation with Random Forest. *J. Hydrol.* **2021**, *593*, 125840. [CrossRef]
36. Chen, W.; Li, Y.; Xue, W.; Shahabi, H.; Li, S.; Hong, H.; Wang, X.; Bian, H.; Zhang, S.; Pradhan, B.; et al. Modeling Flood Susceptibility Using Data-Driven Approaches of Naïve Bayes Tree, Alternating Decision Tree, and Random Forest Methods. *Sci. Total Environ.* **2020**, *701*, 134979. [CrossRef] [PubMed]
37. Chagas, C.D.S.; De Carvalho Junior, W.; Bhering, S.B.; Calderano Filho, B. Spatial Prediction of Soil Surface Texture in a Semiarid Region Using Random Forest and Multiple Linear Regressions. *Catena* **2016**, *139*, 232–240. [CrossRef]
38. Zhu, X.; Wang, X.; Ok, Y.S. The Application of Machine Learning Methods for Prediction of Metal Sorption onto Biochars. *J. Hazard. Mater.* **2019**, *378*, 120727. [CrossRef]
39. Bhagat, S.K.; Paramasivan, M.; Al-Mukhtar, M.; Tiyasha, T.; Pyrgaki, K.; Tung, T.M.; Yaseen, Z.M. Prediction of Lead (Pb) Adsorption on Attapulgite Clay Using the Feasibility of Data Intelligence Models. *Environ. Sci. Pollut. Res.* **2021**, *28*, 31670–31688. [CrossRef] [PubMed]
40. Zhao, W.; Ma, J.; Liu, Q.; Dou, L.; Qu, Y.; Shi, H.; Sun, Y.; Chen, H.; Tian, Y.; Wu, F. Accurate Prediction of Soil Heavy Metal Pollution Using an Improved Machine Learning Method: A Case Study in the Pearl River Delta, China. *Environ. Sci. Technol.* **2023**, *57*, 17751–17761. [CrossRef] [PubMed]
41. Pouladi, N.; Møller, A.B.; Tabatabai, S.; Greve, M.H. Mapping Soil Organic Matter Contents at Field Level with Cubist, Random Forest and Kriging. *Geoderma* **2019**, *342*, 85–92. [CrossRef]
42. *GB 15618-2018*; Soil Environment Quality—Risk Control Standard for Soil Contamination of Agriculture Land. Ministry of Ecology and Environment of the People's Republic of China: Beijing, China, 2018.

43. Grant, C.A.; Clarke, J.M.; Duguid, S.; Chaney, R.L. Selection and Breeding of Plant Cultivars to Minimize Cadmium Accumulation. *Sci. Total Environ.* **2008**, *390*, 301–310. [CrossRef]
44. Bunquin, M.A.B.; Tandy, S.; Beebout, S.J.; Schulin, R. Influence of Soil Properties on Zinc Solubility Dynamics Under Different Redox Conditions in Non–Calcareous Soils. *Pedosphere* **2017**, *27*, 96–105. [CrossRef]
45. Khampuang, K. Effect of Sulfur Fertilization on Productivity and Grain Zinc Yield of Rice Grown Under Low and Adequate Soil Zinc Applications. *Rice Sci.* **2023**, *30*, 632–640. [CrossRef]
46. Du Laing, G.; Vanthuyne, D.R.J.; Vandecasteele, B.; Tack, F.M.G.; Verloo, M.G. Influence of Hydrological Regime on Pore Water Metal Concentrations in a Contaminated Sediment-Derived Soil. *Environ. Pollut.* **2007**, *147*, 615–625. [CrossRef] [PubMed]
47. De Livera, J.; McLaughlin, M.J.; Hettiarachchi, G.M.; Kirby, J.K.; Beak, D.G. Cadmium Solubility in Paddy Soils: Effects of Soil Oxidation, Metal Sulfides and Competitive Ions. *Sci. Total Environ.* **2011**, *409*, 1489–1497. [CrossRef] [PubMed]
48. Enya, O.; Heaney, N.; Iniama, G.; Lin, C. Effects of Heavy Metals on Organic Matter Decomposition in Inundated Soils: Microcosm Experiment and Field Examination. *Sci. Total Environ.* **2020**, *724*, 138223. [CrossRef]
49. Stefanowicz, A.M.; Kapusta, P.; Zubek, S.; Stanek, M.; Woch, M.W. Soil Organic Matter Prevails over Heavy Metal Pollution and Vegetation as a Factor Shaping Soil Microbial Communities at Historical Zn–Pb Mining Sites. *Chemosphere* **2020**, *240*, 124922. [CrossRef]
50. Li, R.; Tan, W.; Wang, G.; Zhao, X.; Dang, Q.; Yu, H.; Xi, B. Nitrogen Addition Promotes the Transformation of Heavy Metal Speciation from Bioavailable to Organic Bound by Increasing the Turnover Time of Organic Matter: An Analysis on Soil Aggregate Level. *Environ. Pollut.* **2019**, *255*, 113170. [CrossRef]
51. Ruehlmann, J.; Bönecke, E.; Meyer, S. Predicting the Lime Demand of Arable Soils from pH Value, Soil Texture and Soil Organic Matter Content. *Agronomy* **2021**, *11*, 785. [CrossRef]
52. Yan, D.; Li, J.; Hu, M.; Lang, Y. Characteristics and Genesis of Supergene Manganese Ores in Xialei, Guangxi. *Geol. Sci. Technol. Inf.* **2006**, *25*, 61–67.
53. Tang, J. Enrichment Characteristics and Poison Research to Crops of Heavy Metals in Fe-Mn Nodules Soil in Karst Area of Guangxi Central. Ph.D. Thesis, China University of Geosciences, Beijing, China, 2011.
54. Wang, K.; Xu, S.; Yang, Y.; Lin, Q. Study on Zn and Cd Colloid-affected Adsorption in Three Different Soils. *Soils* **2011**, *43*, 239–246. [CrossRef]
55. Li, Y.; Gao, Q.; Li, H.; Wang, X.; Wang, T.; Wang, Y. Study of Cu and Zn adsorption on the clay and its main components in surficial sediments. *J. North China Electr. Power Univ.* **2009**, *36*, 89–93.
56. Qiu, Z.; Ma, W.; Zhang, M. Formation Characteristics of Soils Developed from Metamorphic Rocks in the Hilly and Mountain Areas of Southwest Zhejiang Province. *Chin. J. Soil Sci.* **2020**, *51*, 1009–1015. [CrossRef]
57. Rose, T.; Kretzschmar, T.; Liu, L.; Lancaster, G.; Wissuwa, M. Phosphorus Deficiency Alters Nutrient Accumulation Patterns and Grain Nutritional Quality in Rice. *Agronomy* **2016**, *6*, 52. [CrossRef]
58. Zhang, W.; Liu, D.; Liu, Y.; Chen, X.; Zou, C. Overuse of Phosphorus Fertilizer Reduces the Grain and Flour Protein Contents and Zinc Bioavailability of Winter Wheat (*Triticum aestivum* L.). *J. Agric. Food Chem.* **2017**, *65*, 1473–1482. [CrossRef] [PubMed]
59. Su, D.; Wu, L.; Søren, K.R.; Zhou, L.; Pan, G.; Cheng, F. Influence of phosphorus on rice (*Oryza sativa* L.) grain zinc bioavailability and its relation to inositol phosphate profiles concentration. *Acta Agron. Sin.* **2020**, *46*, 228–237. [CrossRef]

applied sciences

MDPI

Article

The Geochemistry, Petrogenesis, and Rare-Metal Mineralization of the Peralkaline Granites and Related Pegmatites in the Arabian Shield: A Case Study of the Jabal Sayid and Dayheen Ring Complexes, Central Saudi Arabia

Hamdy H. Abd El-Naby [1,*] and Yehia H. Dawood [2]

[1] Faculty of Earth Sciences, King Abdulaziz University, P.O. Box 80206, Jeddah 21589, Saudi Arabia
[2] Department of Geology, Faculty of Science, Ain Shams University, Cairo 11566, Egypt; yhdawood@yahoo.com
* Correspondence: hyuosef@kau.edu.sa; Tel.: +966-549569066; Fax: +966-12-6952441

Abstract: The Neoproterozoic period in the Jabal Sayid and Dayheen areas is characterized by three distinct magmatic phases: an early magmatic phase of granodiorite–diorite association, a transitional magmatic phase of monzogranites, and a highly evolved magmatic phase of peralkaline granites and associated pegmatites. The presence of various accessory minerals in the peralkaline granites and pegmatites, such as synchysite, bastnaesite, xenotime, monazite, allanite, pyrochlore, samarskite, and zircon, plays an important role as contributors of REEs, Zr, Y, Nb, Th, and U. The geochemical characteristics indicate that the concentration of these elements occurred primarily during the crystallization and differentiation of the parent magma, with no significant contributions from post-magmatic hydrothermal processes. The obtained geochemical data shed light on the changing nature of magmas during the orogenic cycle, transitioning from subduction-related granodiorite–diorite compositions to collision-related monzogranites and post-collisional peralkaline suites. The granodiorite–diorite association is thought to be derived from the partial melting of predominantly metabasaltic sources, whereas the monzogranites are derived from metatonalite and metagraywacke sources. The peralkaline granites and associated pegmatites are thought to originate from the continental crust. It is assumed that these rocks are formed by the partial melting of metapelitic rocks that are enriched with rare metals. The final peralkaline phase of magmatic evolution is characterized by the enrichment of the residual melt with alkalis (such as sodium and potassium), silica, water, and fluorine. The presence of liquid-saturated melt plays a decisive role in the formation of pegmatites.

Keywords: whole-rock geochemistry; petrogenesis; Jabal Sayid and Dayheen; rare-metal mineralization; Jeddah terrane; Arabian Shield

Citation: Abd El-Naby, H.H.; Dawood, Y.H. The Geochemistry, Petrogenesis, and Rare-Metal Mineralization of the Peralkaline Granites and Related Pegmatites in the Arabian Shield: A Case Study of the Jabal Sayid and Dayheen Ring Complexes, Central Saudi Arabia. *Appl. Sci.* **2024**, *14*, 2814. https://doi.org/10.3390/app14072814

Academic Editors: Zeming Shi and Qingjie Gong

Received: 5 March 2024
Revised: 22 March 2024
Accepted: 23 March 2024
Published: 27 March 2024

1. Introduction

Many peralkaline granites are considered specialized granites due to their distinct geochemical properties, including high concentrations of rare earth elements (REEs) and other elements such as Nb, Ta, Zr, Y, U, and Th [1,2]. The composition of the parental magma is a crucial factor for the subsequent enrichment of rare metals in peralkaline granites and related pegmatites. In addition, the degree and type of magmatic differentiation and the transition from magmatic to hydrothermal processes can significantly influence the final enrichment of rare metals in the resulting magma. The study of alkaline/peralkaline granites and related pegmatites with rare metals is important because it provides valuable insights into the behavior of rare metals during late magmatic processes. These studies help scientists to understand the processes that control the concentration and dispersion of rare metals in igneous rocks.

The origin and formation of the rare-metal alkaline and peralkaline granites in the Arabian Shield (AS) have been the subject of investigation in several studies [2–10]. Al-Ghurayyah, Jabal Hamara, Umm Al-Birak, Jabal Tawlah, Jabal Sayid, and the Hadb Ad

Dayheen ring complex (referred to herein as the Dayheen intrusion) are indeed significant occurrences of rare metals in the AS (Figure 1). Both Jabal Sayid and Dayheen plutons were described earlier as A-type peralkaline granite that was produced in a within-plate tectonic setting [7,8].

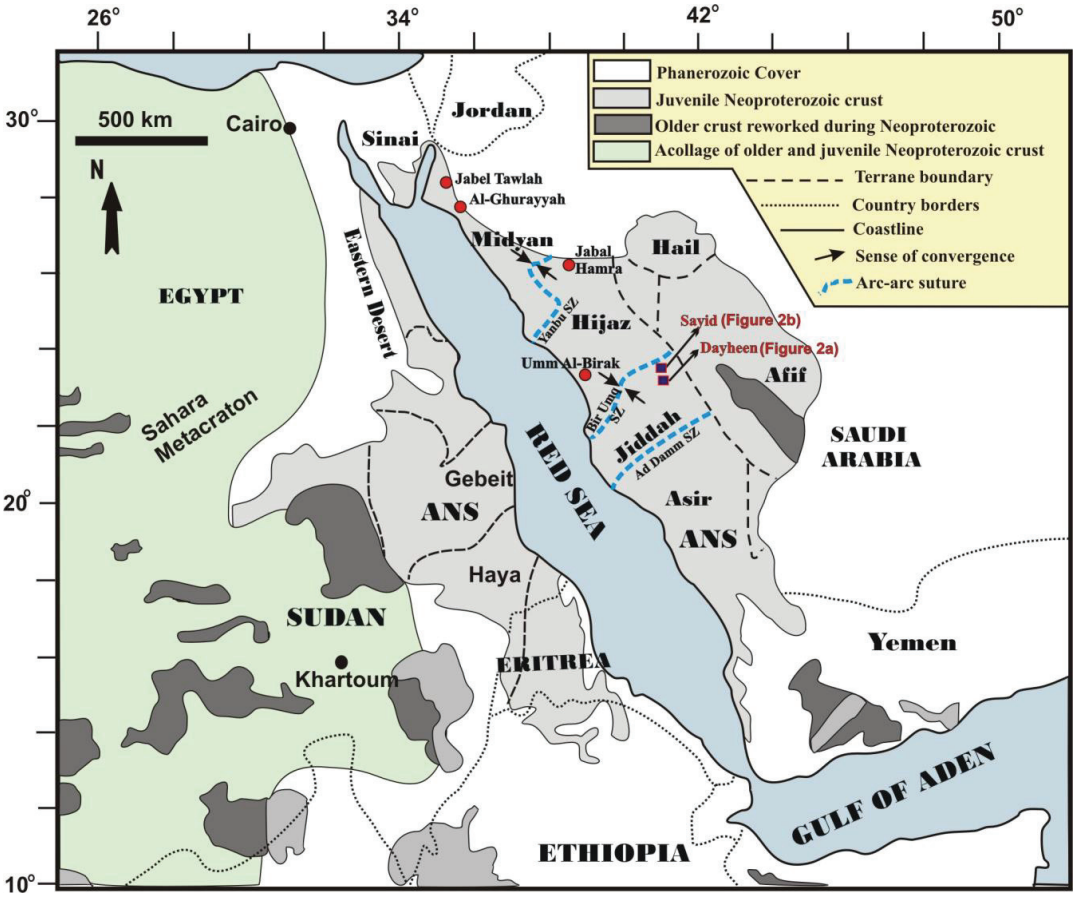

Figure 1. A simplified geological map of the ANS (modified after [11–13]) with the sites of the study areas and other rare-metal alkaline granites in the AS (red circles).

The granitic rocks and related pegmatites in Jabal Sayid and the Dayheen areas are characterized by the high content of certain elements, including Zr, Nb, U, Th, and REEs. In both areas, the final stages of magmatic evolution played an important role in the concentration of rare metals. The study by [4] proposes that the Dayheen peralkaline granite was formed through the partial melting of the juvenile lower crust. This melting event is thought to have occurred after the collision between the East and West Gondwana supercontinents during the final stages of the AS evolution. Ref. [6] discussed the U-Pb zircon dating and Nd-Hf-O isotopic analyses of the Dayheen ring complex. These findings suggest that the complex was primarily derived from juvenile crust formed during the Neoproterozoic period. Ref. [8] concluded that the variations in rare-metal mineralization between Jabal Sayid and Dayheen primarily occur from a magmatic to a hydrothermal stage, suggesting the influence of hydrothermal processes on mineralization. Similarly, ref. [9] concluded that both magmatic and hydrothermal processes contributed to the

formation of mineralization in the Dayheen complex. The study by [10] suggests that part of the Dayheen granitic rocks developed during an extension stage.

Overall, these previous studies propose that the tectonic evolution of post-collision alkaline and peralkaline granites is closely linked to the assembly of the Arabian-Nubian Shield (ANS). The specific tectonic setting and processes that led to the emplacement of these granites are still subjects of ongoing study and debate among geologists and researchers in the field. To contribute to the understanding of the origin of rare-metal granites and pegmatites, the present authors conducted investigations on the Jabal Sayid and Dayheen plutons in the Jeddah terrane (Figure 1). These plutons are known to host the significant mineralization of Nb, Zr, REEs, U, and Th. This article aims to address several fundamental questions concerning the evolution of rare-metal granite–pegmatite systems based on petrological and geochemical data. Here are the key questions that could be presented:

(1) What are the specific mechanisms involved in the petrogenesis of the peralkaline granites and related pegmatites in the Jabal Sayid and Dayheen areas?
(2) What are the geochemical similarities or differences among the peralkaline granites and related pegmatites in the Jabal Sayid and Dayheen areas?
(3) What is the significance of the rare metal data in terms of the granitic evolution in both the Jabal Sayid and Dayheen areas? The researchers aim to understand how rare metals, including REEs, Zr, Y, Nb, U, and Th, are concentrated and fractionated during the late-stage magmatic processes that have influenced the evolution of the granitic systems in these areas.
(4) What is the role of crystallization, partial melting, and the nature of the source protolith in shaping the rare-metal granitic systems in the Jabal Sayid and Dayheen areas?

2. Geological Settings

2.1. Dayheen Ring Complex

The Dayheen ring complex is situated approximately 30 km south of the Jabal Sayid rare-metal granites (Figure 1). The rocks found in the Dayheen complex exhibit a distinct variety of granite rocks. In the central part of the complex, there are monzogranites, which represent a remnant of the original block and have undergone significant weathering processes, resulting in low topography. These rocks are then followed by hornblende–biotite granites as one moves outward. At the outermost part of the Dayheen complex, there are aegirine–riebeckite granites (Figure 2a). These granites intrude into older rocks, specifically the granodiorite–diorite association. The granites within the Dayheen complex demonstrate notable variations in composition, color, and texture. This suggests that different processes and conditions have influenced the formation and evolution of these rocks. The grain size of the monzogranite ranges from medium- to coarse-grained. In terms of color, it exhibits a transition from pink to pinkish gray. The hornblende–biotite granite as well as the aegirine–riebeckite granite constitutes the primary rock units within the circular complex. In some areas, these main rock units are intruded by fine-grained granites.

During field observations, distinct and well-defined boundaries were observed between the aegirine–riebeckite granite and the other granite types within the complex. These contacts between different granitic units exhibit clear and sharp transitions (Figure 3a). Within the aegirine–riebeckite granites, dykes of pegmatite and quartz veins are commonly observed. These pegmatite dykes display irregular topography, varying in both width and length (Figure 3b). Their dimensions can range from a few centimeters to one meter in width and length, and in some cases, they can extend beyond 30 m. The concentration of pegmatite dykes is particularly notable in the southern part of the Dayheen area.

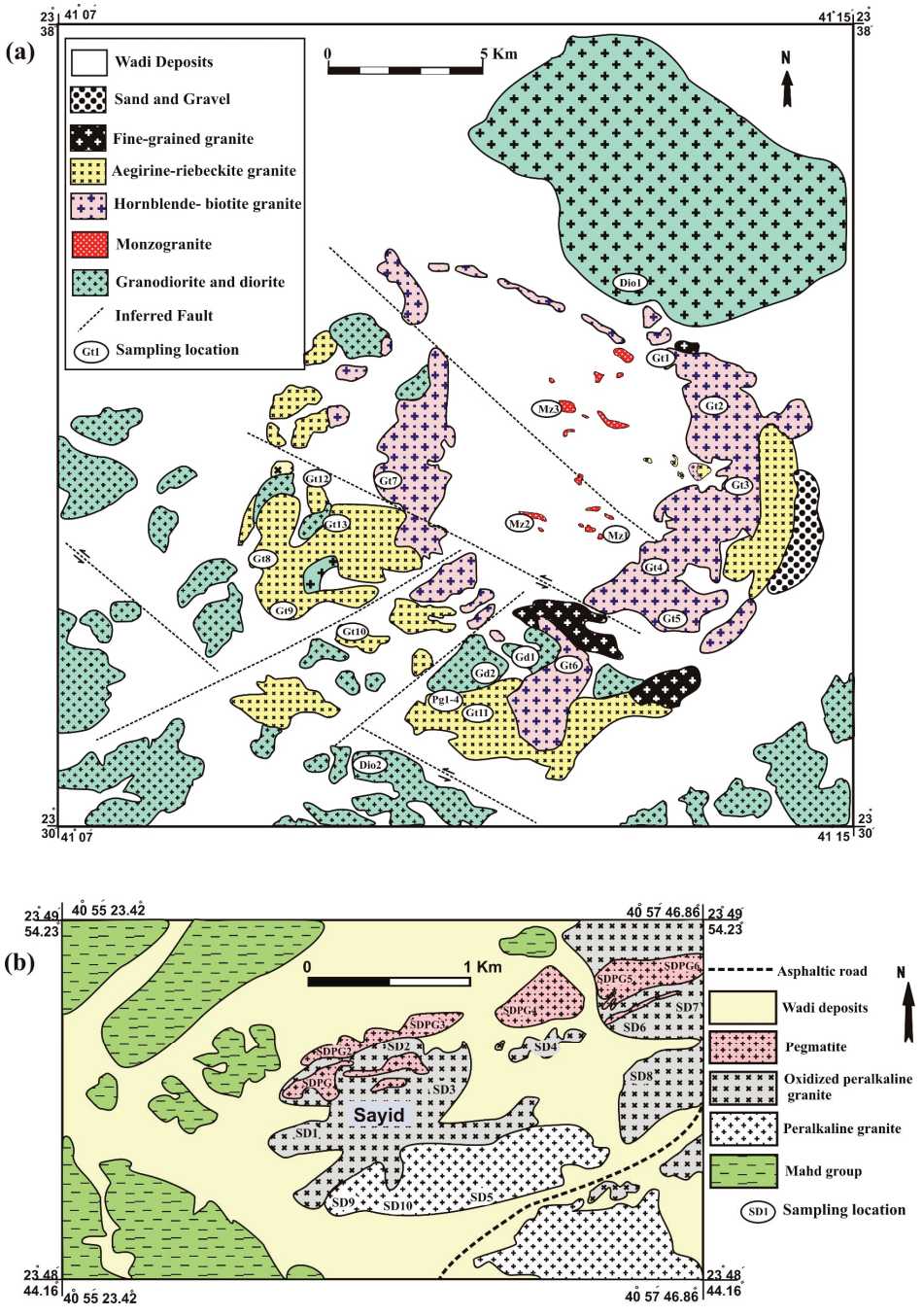

Figure 2. A geological map of (**a**) the Dayheen area (modified after [14]) and (**b**) the Jabal Sayed area (modified after [15]). Sample locations are also shown.

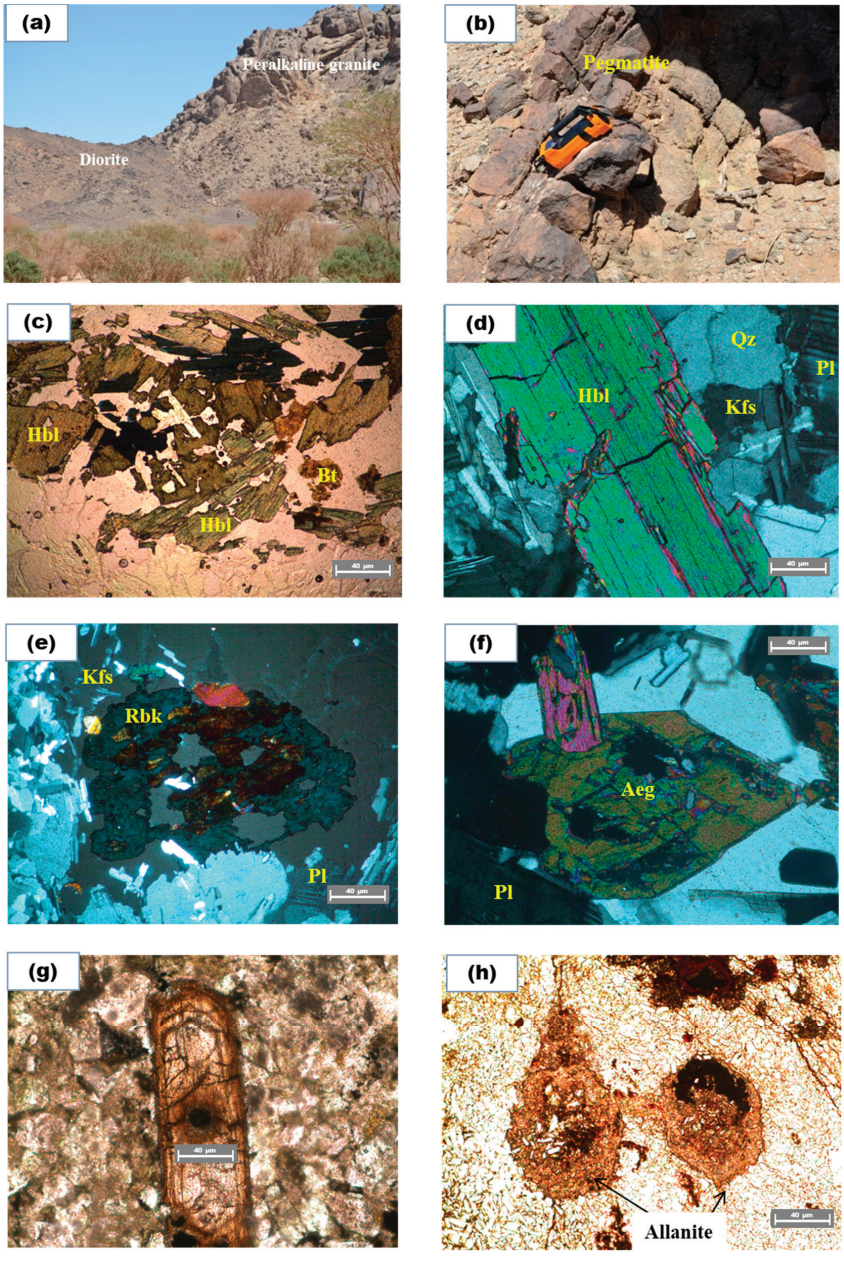

Figure 3. (**a**) Sharp intrusive contact between diorite and peralkaline granite in the Dayheen area. (**b**) A pegmatite dyke within the Dayheen peralkaline granite. (**c**,**d**) Photomicrographs showing the major minerals in the Dayheen hornblende–biotite granite. (**e**) A photomicrograph showing a blue subhedral crystal of riebeckite within the Dayheen aegirine–riebeckite granite. (**f**) A photomicrograph showing the slender prismatic shape of aegirine within the Dayheen aegirine–riebeckite granite. (**g**) A prismatic crystal of zircon within the Dayheen pegmatite. (**h**) Zoned allanite crystals within the Dayheen pegmatite. Mineral abbreviations according [16].

2.2. Jabal Sayid

The Jabal Sayid mineralization is recognized as a significant rare-metal deposit within the AS, primarily owing to its economic importance. The Jabal Sayid area falls within the Jeddah terrane and is situated near the Bir Umq suture zone (Figure 1). The Bir Umq suture zone represents a boundary or contact zone between two distinct terranes, namely the Hijaz and Jeddah terranes. The Jeddah terrane is geographically situated in the western part of the AS. It is bounded by several other tectonic units: the Hijaz terrane to the north, the Afif terrane to the east, the Asir terrane to the south, and the Red Sea coastal plain to the west. The Jabal Sayid peralkaline granite is a component of the larger Jabal Sayid complex, which is primarily covered by volcano-sedimentary rocks belonging to the Mahd Group (Figure 2b). The Mahd Group is a geological formation composed of volcano-sedimentary rocks. These rocks typically include volcanic types such as basalt, andesite, dacite, rhyolite, and pyroclastic rocks. Additionally, sedimentary rocks such as sandstone, siltstone, and conglomerate are included. Insignificant limestone is also present within the Mahd Group.

The Jabal Sayid peralkaline granites have been dated using different isotopic dating methods, yielding slightly different ages. According to [17], the Rb/Sr age of the Jabal Sayid peralkaline granites is reported as 584 ± 26 Ma. On the other hand, ref. [7] conducted zircon U-Pb isotopic dating on peralkaline granites and reported an age of 593 Ma. The similarity of the Ediacaran age of the peralkaline granites in the Jabal Sayid pluton to other alkaline granites found in the ANS suggests a regional geodynamic event or tectonic process that influenced the formation of these granites. This similarity in age implies a broader geologic event that affected a larger region rather than being isolated to a specific locality. According to [8], the mineralization in the peralkaline granite of Jabel Sayid occurred in two distinct stages, namely a magmatic stage and a hydrothermal stage. During the magmatic stage, several minerals crystallized within the peralkaline granite. These minerals include zircon-1, quartz, hematite, and fresh aegirine. The crystallization of these minerals during the magmatic stage suggests that they formed directly from the cooling and solidification of the magma that gave rise to the peralkaline granite. In the hydrothermal stage, further mineralization occurred due to hydrothermal fluids interacting with the existing rock.

According to [18], the Jabal Sayid pegmatite is described as a sheet-like body with a width ranging from approximately 5 to 13 m. It extends for a significant strike length of about 2 km. The northern margin of the Jabal Sayid complex, where the pegmatite is situated, likely represents an area of interest for exploration and mining activities targeting the rare-metal mineralization associated with the pegmatite. The internal structure of the pegmatite is layered, and its composition exhibits variation [15]. The layers within the pegmatite are reported to be 0.3 to 5.0 m thick. These layers include coarse pegmatite, which contains crystals that can reach up to 3 cm in length. Additionally, micropegmatite and aplite are present within the layers. According to [15], there is a sharp contact between the peralkaline granite and the pegmatite (Figure 4a). Below this contact, dykes and veins are observed intruding joints and fractures that are parallel to the contact. This observation suggests that the emplacement of the pegmatite occurred at a later stage. The rocks within the pegmatite exhibit different colors, which can vary based on their iron oxide content. The color variations range from pink to brown varieties. Additionally, there are a few occurrences of black-colored rocks within the pegmatite.

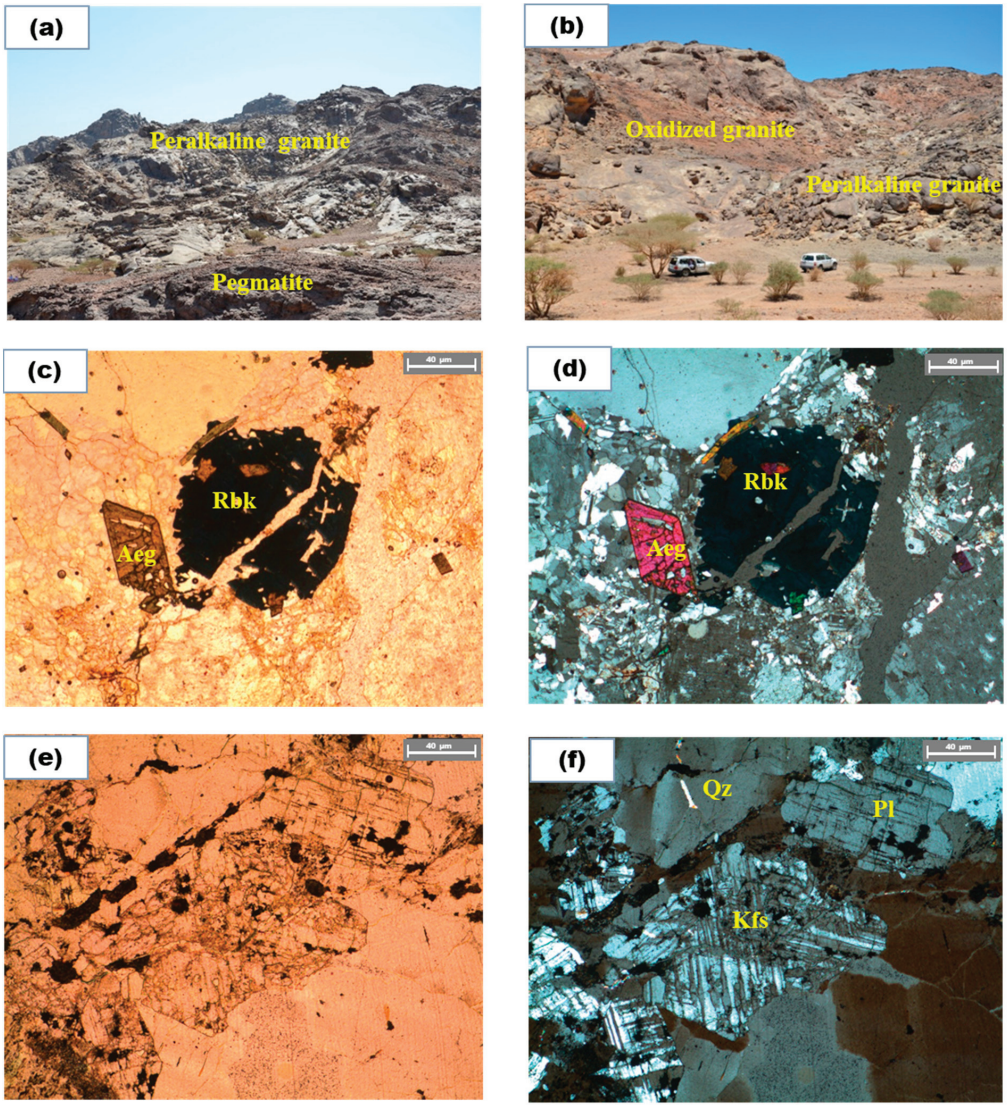

Figure 4. (**a**) A photo of the pegmatite sheets showing the contact with the Jabal Sayid peralkaline granite. (**b**) A photo of the oxidized granite within the Jabal Sayid peralkaline granite. (**c**,**d**) Photomicrographs showing the deep-blue crystal of riebeckite and the euhedral crystal of aegirine within the Jabal Sayid peralkaline granite. (**e**,**f**) Photomicrographs showing major mineral constituents of the Jabal Sayid pegmatite. Mineral abbreviations according to [16].

Uranyl mineralization has been discovered within the pegmatite of Jabel Sayid through radiological surveys conducted by [19]. Following the discovery, several test wells were drilled by [20] to further identify and characterize uranyl mineralization in the area. This mineralization is related to the high content of Nb and REEs, as reported by [21]. Fluorite is a common mineral throughout the pegmatite, but it becomes particularly abundant in the alteration zones. Kasolite, which is a secondary uranium mineral, occurs mainly as cavity fillings and encrustations on quartz veins and along their contacts with the pegmatite [22].

To the south of the pegmatite sheets in the Jabal Sayid area, there is an oxidized peralkaline granite (Figure 4b). This granite has undergone varying degrees of hematization.

3. Analytical Techniques

The collection of 40 samples from various locations within the Dayheen and Jabal Sayid areas provides a representative dataset for studying the spatial variability of the granitic rocks in the region. These samples were prepared for petrographic examination in the "Laboratory for Rock and Thin Section Preparation" at King Abdulaziz University. To prepare the samples for petrographic examination, a flat face of rock was glued to a microscope slide and polished to achieve the desired thickness to be examined under a microscope. This thin section allows for a detailed examination of the rock's mineral composition, texture, and other petrographic features under a petrographic microscope. The selected samples were prepared for major, trace, and rare earth element analyses at the ACME Analytical Laboratories in Vancouver, Canada. The major oxides were measured by X-ray Fluorescence (XRF), with an accuracy of $\pm$0.01 wt.%. In addition, the number of volatiles in the form of Loss On Ignition (LOI) was measured with an accuracy of 0.01%. Trace and REEs were measured by the inductively coupled plasma mass spectrometer (ICP-MS) method, with an accuracy of 0.01 ppm to 1 ppm.

4. Petrography

4.1. Dayheen Ring Complex

4.1.1. Peralkaline Granites

Petrographically, the peralkaline granites in the Dayheen complex can be classified into two main types: hornblende–biotite granite and aegirine–riebeckite granite. The hornblende–biotite granite is primarily composed of quartz (28–35%), alkali feldspar (32–38%), plagioclase (20–30%), and 5–10% hornblende and biotite (Figure 3c,d). It exhibits a dark-gray to reddish-brown color and has a porphyritic texture. Poikilitic inclusions are common within granite and consist of plagioclase laths and hornblende. In some areas, quartz forms a myrmekitic texture with K-feldspar. Perthite and minor microcline represent the main K-feldspar minerals. Locally, perthite may be partially replaced by sericite. Plagioclase occurs as tabular crystals and exhibits simple albite twinning. It occasionally contains irregular fluorite crystals. Locally, plagioclase may undergo alteration to sericite and epidote. Subhedral prismatic crystals of dark blueish-green hornblende are present (Figure 3d). It shows pleochroism and contains inclusions of magnetite and titanite. The biotite crystals have a pale reddish-brown color and weak pleochroism. The granite contains several accessory minerals, including apatite, zircon, allanite, magnetite, and titanite.

The aegirine–riebeckite granite within the Dayheen complex is primarily composed of quartz (35–40%), K-feldspars (20–30%), albite (25–30%), and 7 to 10% aegirine and amphibole. It exhibits a porphyritic texture, where the phenocrysts consist of microcline, quartz, riebeckite, aegirine, and biotite. In the groundmass, the major minerals present are quartz and plagioclase. Quartz occurs as large, anhedral rounded grains within the rock. These quartz grains contain numerous inclusions of fine laths of albite, aegirine, and riebeckite. Albite is present as subhedral crystals in the groundmass of the rock. The K-feldspar crystals are primarily microclines and occur as microphenocrysts. Occasionally, the microcline crystals may have a rim of lath-shaped albite. In some instances, subhedral crystals of riebeckite can also be observed. They are characterized by their deep-blue color and exhibit varying degrees of pleochroism (Figure 3e). Aegirine is present as subhedral to euhedral prismatic crystals (Figure 3f). The color of the aegirine ranges from deep-green to pale olive-green. The accessory minerals mainly include apatite, zircon, fluorite, allanite, pyrochlore, samarskite, and hematite.

4.1.2. Monzogranite

The monzogranite in the Dayheen complex exhibits a grayish-white color, and in some instances, it displays a porphyritic texture. Monzogranite is primarily composed

of several minerals, including plagioclase, quartz, K-feldspar, and biotite. In addition to the main minerals, zircon, titanite, magnetite, apatite, allanite, and fluorite are present as accessory minerals. In certain areas of the monzogranite, chlorite alteration can be identified. Plagioclase is the dominant mineral, accounting for approximately 30–35% of the rock's volume. Its crystals are euhedral to subhedral and typically display tabular morphology. They often exhibit zoning, which is characterized by distinct compositional variations within individual crystals. The plagioclase crystals may also show signs of corrosion or resorption, indicating partial dissolution and reprecipitation during the rock's formation. In certain areas, plagioclase is altered into secondary minerals such as sericite and epidote. Quartz crystals (25–30%) are typically anhedral to subhedral. They occupy the spaces between the feldspar crystals or form intergrowths with K-feldspar known as graphic and myrmekitic textures. K-feldspar, constituting approximately 20–25% of the rock's volume, occurs as large anhedral crystals of microcline. It commonly displays Carlsbad twinning. Biotite forms subhedral flakes and elongated aggregates within the rock. It exhibits strong pleochroism from straw yellow to deep brown.

4.1.3. Pegmatite

The pegmatite within the Dayheen complex consists of large grains of quartz and K-feldspar minerals and minor mafic minerals. Pegmatitic rocks show a high content of radiation because they contain minerals rich in uranium and thorium, such as monazite, zircon (Figure 3g), allanite (Figure 3h), fluorite, pyrochlore, and thorite. Orthoclase and microcline are the two types of K-feldspars present. Microcline is characterized by a cross-hatched pattern and is occasionally intergrown with albite, forming patchy perthite. Riebeckite, which is the dominant mafic mineral, is blue in color. Aegirine occurs as needle-like crystals, and some are partially altered to hematite.

4.2. Jabal Sayed

4.2.1. Peralkaline Granite

The peralkaline granite in the Jabel Sayid area exhibits a porphyritic texture, characterized by the presence of large crystals embedded in a finer-grained groundmass. The major mineral constituents are quartz, which comprises approximately 35–40% of the rock, and K-feldspars, which make up about 30–40%. Albite, plagioclase is present in smaller amounts, around 8–10%. The mafic minerals, aegirine and riebeckite, account for 5 to 10% of the rock's composition (Figure 4c,d). The rare-metal minerals identified in the peralkaline granite include zircon, bastnaesite, monazite, and xenotime. These minerals are valuable due to their content of REEs and other economically significant metals. In addition to the primary minerals, secondary minerals such as hematite and fluorite are also present (Figure 5a). Quartz presents as anhedral crystals that fill the spaces between other mineral grains and is intergrown with K-feldspars, forming a graphic texture. The alkali feldspars, orthoclase and microcline, form subhedral to anhedral tabular to equant crystals. Some albite crystals are present in the groundmass, but they are rare and occur as fine-grained laths surrounding perthite and microcline grains. Aegirine occurs as subhedral to euhedral prismatic or needle-like crystals (Figure 4c). It exhibits pleochroism ranging from grass- or gray-green to brownish green. Riebeckite occurs as subhedral grains, less than 3 mm in size (Figure 4d). It is found interstitially between perthite and quartz grains.

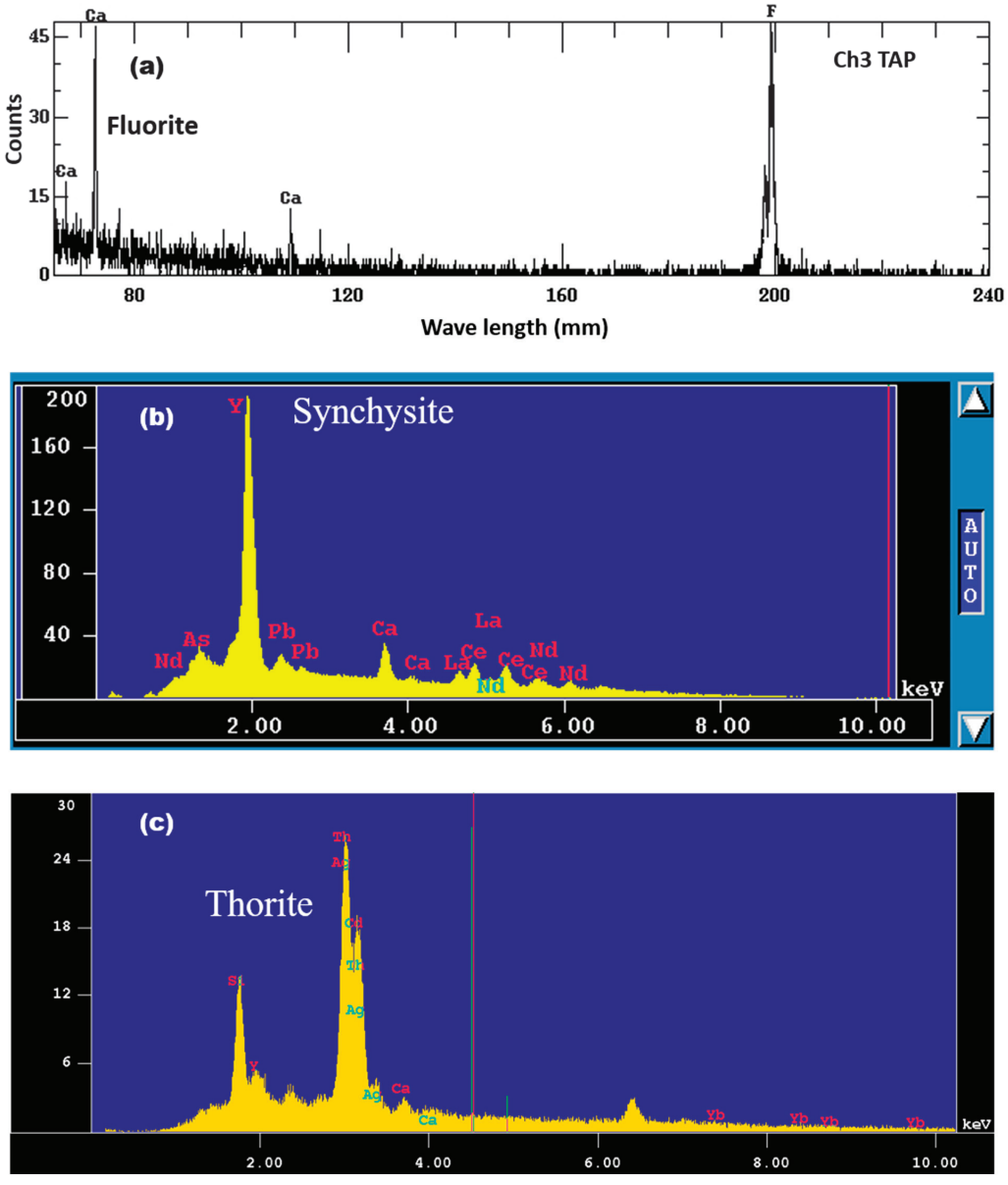

Figure 5. (**a**) Wavelength-dispersion spectral scans of fluorite from Jabel Sayid peralkaline granite. (**b**) Energy-dispersive X-ray spectrum of synchysite from Jabel Sayid pegmatite. (**c**) Energy-dispersive X-ray spectrum of thorite from Jabel Sayid pegmatite.

4.2.2. Pegmatite

The pegmatite in the Jabel Sayid area is characterized by its coarse-grained nature and pink to pinkish-white coloration. The major mineral constituents of the pegmatite are K-feldspar and quartz, with minor amounts of plagioclase (Figure 4e,f). Additionally, minor biotite is present in the pegmatite. Accessory minerals include zircon, bastnasite, pyrochlore, xenotime, synchysite, and thorite (Figure 5b,c). These minerals are of interest due to their potential content of rare earth elements and other valuable metals. Quartz is

the dominant mineral in the pegmatite and shows undulose extinction. The alkali feldspars are orthoclase and microcline. Orthoclase exhibits Carlsbad twinning, while microcline is characterized by cross-hatched patterns. Microcline commonly appears intergrown with albite, forming patchy perthite textures. Plagioclase laths display perfect lamellae twinning. Biotite occurs as flaky or tabular brown crystals and exhibits pleochroism from pale brown to dark brown. Chlorite is present as a secondary mineral in pegmatite.

From above, the accessory minerals found in the Jabal Sayid and Dayheen peralkaline granites and related pegmatites can be grouped into four main compositional categories: (a) the REEs-Ti-Zr association, which includes minerals such as synchysite, bastnaesite, titanite, and zircon in Jabal Sayid and zircon and titanite in Dayheen; (b) the REEs-Ca-P association, which includes minerals like xenotime and monazite in Jabal Sayid and apatite, allanite, and monazite in Dayheen; (c) the REEs-Y-Nb association, which is represented by minerals such as pyrochlore in Jabal Sayid and pyrochlore and samarskite in Dayheen; and (d) the Th-U-Pb association, which includes minerals like thorite and kasolite in Jabal Sayid and thorite in the Dayheen area. These mineral associations are enriched with incompatible elements, such as Light Rare Earth elements (LREEs), Zr, Y, Nb, Th, and U (Table 1).

Table 1. The names and generalized chemical formulae of REEs, Zr Y, Nb, Th, and U-bearing minerals known in the Dayheen and Jabal Sayid peralkaline intrusion and related pegmatites.

Accessory Mineral Group	Dayheen		Jabal Sayid	
	Mineral Name	Formula	Mineral Name	Formula
REEs-Ti-Zr association	Zircon Titanite	$ZrSiO_4$ $CaTiSiO_5$	Synchysite Bastnaesite Titanite Zircon	(Ca, $Ce(CO_3)_2F$ (Ca, La)$(CO_3)F$ $CaTiSiO_5$ $ZrSiO_4$
REEs-Ca-P association	Apatite Allanite Monazite	$Ca_5(PO4)_3(OH,F,Cl)$ $(Ce,Ca)_2(Al, Fe^{3+})_3(SiO_3)_3(OH)$ $(La,Ce,Nd,Th)PO_4$	Xenotime Monazite	(Y, Yb)(PO_4) $(La,Ce,Nd,Th)PO_4$
REEs-Y-Nb association	Pyrochlore Samarskite	$(Na,Ca)_2Nb_2O_6$ (OH,F) (Y-Yb) $Fe^{3+}Nb_2O_8$	Pyrochlore	$(Na,Ca)_2Nb_2O_6$ (OH,F)
Th-U-Pb minerals	thorite	$ThSiO_4$	Thorite Kasolite	$ThSiO_4$ $Pb(UO_2)(SiO_4)\cdot H_2O$

5. Geochemistry

5.1. Major and Trace Element Characteristics

Granitoids are classified into different types based on various criteria such as mineral assemblages, field and petrographical features, and chemical and isotopic characteristics [23]. Major, trace, and REE analyses of the granites and related pegmatites from the Jabal Sayid and Dayheen areas are listed in Tables 2 and 3. In harmony with the field and petrographic studies, most of the peralkaline granites in Jabal Sayid and Dayheen are classified as peralkaline granites based on the R1-R2 geochemical diagram of [24]. The samples that are petrographically assigned to the Dayheen monzogranite plot as expected in the monzogranite field, whereas the granodiorite–diorite samples plot in the granodiorite and diorite fields (Figure 6).

Table 2. Major (wt%), trace (ppm), and rare earth elements (ppm) of selected granitoids and related pegmatites from the Dayheen area, Jeddah Terrane, Saudi Arabia.

Rock Type	DL *	Peralkaline Granites													Pegmatites				Monzogranites			Granodiorites		Diorites	
		Aegirine–Riebeckite Granite						Hornblende–Biotite Granite																	
Sample		GT1	GT2	GT3	GT4	GT5	GT6	GT7	GT8	GT9	GT10	GT11	GT12	GT13	PG1	PG2	PG3	PG4	MZ1	MZ2	MZ3	GD1	GD2	Dio1	Dio2
Major elements (wt%)																									
SiO_2	0.1	73.2	71.5	71.8	73.0	71.3	72.5	75.9	70.5	72.5	74.1	74.2	71.8	72.1	69.7	66.3	72.6	71.9	73.6	73.0	72.7	69.9	62.5	56.9	58.8
TiO_2	0.01	0.1	0.1	0.1	0.1	0.1	0.1	0.2	0.1	0.1	0.1	0.1	0.1	0.1	0.8	0.9	0.2	0.5	0.2	0.2	0.2	0.4	0.5	0.6	1.0
Al_2O_3	0.01	11.6	14.2	12.9	12.5	12.8	11.6	9.6	11.0	12.3	11.2	11.3	12.7	10.6	7.8	9.6	10.5	10.0	12.6	13.0	14.0	14.7	15.7	16.3	16.8
Fe_2O_3 **	0.01	4.2	3.1	3.1	3.8	3.8	4.5	5.3	5.0	3.4	4.1	3.7	4.5	5.0	9.4	7.7	6.0	5.4	2.0	1.6	1.5	3.3	5.5	5.9	6.4
MnO	0.01	0.02	0.02	0.04	0.04	0.04	0.05	0.04	0.07	0.04	0.05	0.04	0.02	0.06	0.09	0.06	0.09	0.06	0.05	0.04	0.04	0.07	0.10	0.10	0.12
MgO	0.01	0.01	0.01	0.02	0.03	0.02	0.02	0.01	0.04	0.01	0.05	0.03	0.01	0.04	0.24	0.22	0.19	0.15	0.29	0.49	0.55	1.02	2.60	2.76	2.03
CaO	0.01	0.3	0.3	0.2	0.3	0.3	0.1	0.1	1.7	0.7	0.1	0.5	0.2	1.0	0.7	1.1	0.7	0.8	2.1	1.8	1.5	2.8	5.6	8.3	6.1
Na_2O	0.01	5.5	6.7	5.8	6.2	6.5	6.0	4.9	5.0	5.5	5.5	5.8	4.6	5.4	3.9	9.0	4.3	3.8	4.3	4.4	4.7	4.5	3.8	4.4	4.5
K_2O	0.01	4.2	3.5	4.7	4.3	4.0	3.9	3.5	4.1	4.4	3.9	3.6	4.9	4.4	0.8	0.6	2.2	2.7	3.2	3.6	3.4	2.6	1.9	0.7	0.9
P_2O_5	0.01	0.01	0.01	0.01	0.01	0.06	0.05	0.02	0.01	0.01	0.01	0.01	0.01	0.03	0.05	0.05	3.00	0.05	0.02	0.03	0.10	0.12	0.15	0.31	0.01
Cr_2O_3	0.01	0.01	0.01	0.01	0.01	0.01	0.01	0.01	0.01	0.01	0.01	0.01	0.01	0.01	0.01	0.01	0.01	0.01	0.01	0.01	0.01	0.01	0.02	0.01	0.01
LOI	−5.11	0.2	0.2	0.3	0.3	0.3	0.2	0.4	1.7	0.7	0.1	0.4	0.2	0.9	1.3	0.9	0.7	1.0	1.8	1.1	1.3	1.0	1.7	4.2	2.8
SUM		99.4	99.7	99.0	100.6	99.2	99.0	100.0	99.2	99.7	99.2	99.7	99.1	99.6	94.8	96.4	100.5	96.4	100.2	99.3	100.0	100.4	100.1	100.5	99.5
REEs (ppm)																									
La	0.1	82.4	27.7	161	106	62.3	120	360	108	94.2	89.2	38.9	204	109	907.6	759.0	361.0	337	22.2	25.5	18.9	36.8	11.6	10.8	15.7
Ce	0.1	187	59.0	358	227	146	273	870	191	195	196	93.4	385	247	2316	1731	848.7	779	46.2	34.5	50.2	70.2	26.4	20.8	34.6
Pr	0.02	24.1	7.9	48.2	29.8	20.1	37.6	99.2	21.7	25.7	26.0	12.1	48.5	30.5	300.5	219.0	110.5	101	6.0	5.7	5.0	7.9	3.6	2.5	4.7
Nd	0.3	101	32.6	206	126	87.2	154	334	89.3	109	111	49.3	194	119	1215	719.0	430.1	416	23.9	24.5	27.9	30.4	16.3	11.1	21.2
Sm	0.05	24.0	6.8	45.9	25.9	20.7	38.4	91.4	20.6	20.8	22.2	12.1	38.9	27.2	345.7	172.0	120.1	101	6.2	5.2	5.1	5.0	3.8	2.7	5.6
Eu	0.02	1.1	0.3	1.9	1.1	1.0	1.9	4.5	1.2	0.9	0.9	0.6	1.7	1.3	17.2	8.8	6.8	4.9	0.6	0.6	0.6	0.9	0.8	0.7	1.3
Gd	0.05	23.5	5.9	40.2	21.0	19.3	39.4	96.1	27.3	16.2	19.1	11.7	31.9	28.3	372.5	166.9	139.1	131	6.8	4.3	4.0	4.3	3.7	3.6	5.4
Tb	0.01	3.1	0.7	5.3	2.3	2.7	6.3	17.9	5.6	2.0	2.7	1.9	4.0	5.3	64.7	37.9	29.0	26.0	1.3	1.0	0.9	0.7	0.6	0.7	1.2
Dy	0.05	15.5	3.3	25.9	9.7	15.0	36.9	107	43.4	9.8	14.4	10.4	17.9	35.0	378.5	302.9	191.0	163	9.3	3.6	4.5	4.2	3.7	4.9	7.1
Ho	0.02	2.9	0.5	4.2	1.3	2.9	7.4	22.5	11.8	1.9	2.7	2.1	2.7	8.2	79.6	81.9	38.6	36.1	2.1	0.9	1.9	0.8	0.7	1.1	1.6
Er	0.03	6.7	1.1	9.3	2.4	7.8	19.5	57.6	39.5	4.6	7.2	5.3	5.3	24.6	209.6	278.9	112.0	106	6.5	2.7	3.9	2.5	1.9	2.8	4.3
Tm	0.01	0.9	0.2	1.4	0.3	1.2	2.8	7.4	7.0	0.7	1.2	0.8	0.7	3.9	31.2	46.9	16.3	15.0	1.2	0.3	0.2	0.4	0.3	0.4	0.6
Yb	0.05	5.4	1.1	7.9	1.7	8.3	15.2	36.5	49.0	4.6	7.5	4.3	3.5	23.6	196.2	313.9	118.3	103	7.7	2.2	1.9	2.3	1.9	2.0	3.5
Lu	0.01	0.7	0.2	1.2	0.3	1.3	2.2	4.7	8.1	0.7	1.3	0.7	0.4	3.9	29.5	47.0	19.8	17.0	1.2	0.4	0.2	0.4	0.3	0.3	0.5

Table 2. *Cont.*

Rock Type	DL *	Peralkaline Granites													Pegmatites				Monzogranites			Granodiorites		Diorites	
		Aegirine–Riebeckite Granite							Hornblende–Biotite Granite																
Sample		GT1	GT2	GT3	GT4	GT5	GT6	GT7	GT8	GT9	GT10	GT11	GT12	GT13	PG1	PG2	PG3	PG4	MZ1	MZ2	MZ3	GD1	GD2	Dio1	Dio2
Trace elements (ppm)																									
Y	0.1	73.6	18.5	103	33.6	76.5	192	640	314	55.8	68.2	59.4	79.2	223	185.7	2399	1461	974	66.3	45.3	29.2	23.2	19.5	27.5	42.5
Hf	0.1	19.5	5.5	30.4	3.7	23.5	44.5	41.7	258	11.7	31.6	8.9	3.6	80.6	617.7	531.0	360.0	131	6.1	5.5	4.3	4.0	3.1	2.1	4.8
Nb	0.1	64.0	9.4	58.0	32.3	121	115	579	141	42.6	40.7	60.5	360	136	2129	659.0	1639	1351	16.9	14.0	21.0	6.2	2.4	4.7	6.6
Ta	0.1	5.3	1.1	4.0	2.5	8.5	8.9	28.8	13.1	3.1	3.0	4.1	40.7	11.6	163.8	81.6	96.6	94.7	2.0	1.5	2.1	0.9	0.5	0.4	0.6
Th	0.2	7.4	2.1	18.0	1.2	4.5	13.1	91.7	21.3	3.1	10.5	7.2	267	22.2	263.8	2201	601.2	222	7.4	6.0	6.2	9.5	2.5	5.3	5.8
Zn	1	86.0	32.0	17.0	20.0	38.0	65.0	630	26.0	13.0	20.0	14.0	62.0	69.0	1653	255	381.8	503	42.0	61.0	52.0	51.0	43.0	53.0	63.0
Co	0.2	4.4	4.7	39.9	4.8	4.5	5.7	7.7	3.5	4.8	5.2	2.4	2.3	22.3	13.0	6.0	5.0	9.1	5.2	5.0	4.0	7.4	16.6	16.9	15.9
Ni	0.1	1.7	2.6	3.2	2.5	1.2	3.0	3.7	3.1	2.8	2.1	1.4	2.3	6.2	6.8	4.0	8.0	5.1	4.5	8.0	5.0	6.6	10.6	28.7	13.9
Ba	0.01	4.0	12.0	14.0	9.0	10.0	16.0	12.0	11.0	6.0	5.0	7.0	12.0	16.0	155.0	61.0	229.9	137	256	193	189	565	727	171	178
V	8	8.0	10.0	9.0	8.0	8.0	8.0	8.0	8.0	8.0	8.0	8.0	8.0	8.0	53.0	13.0	19.0	18.0	9.0	8.0	3.0	36.0	145	158	156
Cu	0.1	2.9	1.9	3.3	2.5	2.6	2.7	15.2	6.1	3.2	1.3	3.1	4.3	6.8	9.0	8.5	17.9	17.0	3.4	3.3	2.8	21.8	89.3	60.8	73.8
Sr	0.5	13.5	8.6	5.7	5.9	8.2	12.0	20.3	21.5	21.2	3.6	6.8	16.7	13.2	53.7	59.0	56.0	12.0	92.6	120	290	331	531	440	615
Zr	0.1	642	175	1115	101	918	1622	1563	9295	409	1157	311	102	2936	24,596	20,950	15,020	2392	149	180	156	152	121	73	149
Rb	0.1	441	349	444	438	429	385	390	530	372	314.1	329.8	599.2	540.4	96.6	11.0	373.0	373	77.9	125	144	43.7	32.0	13.6	16.0
As	0.5	0.6	1.8	0.6	0.9	1.6	0.2	3.8	1.4	0.8	0.6	5.0	5.4	4.9	0.4	0.2	0.2	0.5	0.9	0.6	0.5	1.3	1.2	5.6	2.6
Be	1	6.0	7.0	13.0	13.0	11.0	6.0	11.0	12.0	3.0	5.0	2.0	9.0	11.0	108.0	92.0	88.2	95.2	5.0	6.0	3.0	4.0	1.0	<1	5.0
Sb	0.1	0.2	0.1	0.1	0.1	0.3	<0.1	0.6	0.1	0.1	0.1	0.3	0.9	0.2	0.5	0.4	0.1	0.6	0.1	0.1	0.1	0.1	0.1	0.1	0.1
Sn	1	20.0	14.0	15.0	16.0	18.0	25.0	39.0	35.0	8.0	13.0	14.0	25.0	34.0	202.0	269.0	130.2	124	8.0	4.0	2.0	4.0	1.0	<1	<1
U	0.1	8.0	1.0	6.6	3.4	7.4	9.4	68.2	28.5	4.3	4.8	4.8	12.1	15.8	287.8	251.0	139.7	101	2.6	2.0	1.9	1.6	0.9	1.4	1.3
W	0.5	48.1	38.2	408	43.4	47.6	54.5	88.5	38.0	48.1	50.5	21.9	21.0	228.7	103.7	97.1	92.3	67.0	35.0	40.1	38.0	17.6	20.8	11.4	23.8
Cd	0.1	0.2	0.1	0.1	0.1	0.1	0.2	0.2	0.1	0.1	0.1	0.1	<0.1	0.2	1.6	1.0	1.0	1.2	0.1	0.1	0.1	0.1	0.1	0.1	0.1
Cs	0.1	1.3	0.9	1.2	1.9	1.9	1.5	1.9	1.4	1.4	1.0	2.1	2.0	1.9	1.0	1.1	10.9	11.1	1.6	3.5	5.7	1.9	1.1	0.4	0.2
Ga	0.5	51.7	64.6	56.4	55.8	59.5	51.4	39.3	48.2	52.0	47.2	46.7	58.8	48.0	45.5	57.2	29.2	38.5	16.1	24.0	28.0	13.8	15.5	15.7	15.0
Mo	0.1	0.5	1.6	0.5	1.0	0.6	1.5	1.1	0.7	0.5	1.2	0.4	1.4	1.0	0.8	0.8	1.1	98.2	0.7	0.5	0.7	0.7	0.9	0.6	0.8
Pb	0.1	30.0	11.1	34.8	10.4	29.6	74.7	258	147	11.6	15.6	25.1	37.0	19.5	414	101	261.5	243	5.2	7.0	4.0	6.3	2.7	1.8	2.5
Au	0.3	0.4	0.4	0.4	0.4	0.4	0.4	0.4	0.4	0.4	0.4	0.4	0.4	0.4	0.4	0.3	0.3	0.3	0.4	0.4	0.4	0.4	9.7	0.9	0.4
Bi	0.1	3.4	1.3	2.4	1.4	3.2	2.7	0.5	0.6	2.0	1.3	0.8	2.0	1.1	1.3	1.0	1.2	1.1	0.1	0.1	0.1	0.1	0.1	0.1	0.1
Se	0.2	0.4	0.4	0.7	1.1	0.3	1.4	2.9	0.3	0.2	0.2	0.4	0.6	0.4	11.9	7.7	8.2	10.5	0.4	0.2	0.3	0.4	0.4	0.4	0.4

Table 2. *Cont.*

Rock Type	DL *	Peralkaline Granites													Pegmatites				Monzogranites			Granodiorites		Diorites	
		Aegirine–Riebeckite Granite							Hornblende–Biotite Granite																
Sample		GT1	GT2	GT3	GT4	GT5	GT6	GT7	GT8	GT9	GT10	GT11	GT12	GT13	PG1	PG2	PG3	PG4	MZ1	MZ2	MZ3	GD1	GD2	Dio1	Dio2
Eu/Eu *		0.14	0.16	0.14	0.14	0.15	0.15	0.15	0.16	0.15	0.14	0.14	0.14	0.14	0.15	0.16	0.16	0.13	0.29	0.36	0.41	0.58	0.66	0.64	0.72
$(La/Yb)_N$		14.34	23.06	19.07	57.27	7.06	7.40	9.49	2.07	19.12	11.16	8.45	54.96	4.34	4.36	2.28	2.87	3.09	2.70	11.02	9.32	15.19	5.64	5.04	4.26
Y/Nb		1.15	1.97	1.78	1.04	0.63	1.67	1.11	2.23	1.31	1.68	0.98	0.22	1.64	0.09	3.64	0.89	0.72	3.92	3.24	1.39	3.74	8.13	5.85	6.44
Nb/Ta		12.08	8.55	14.50	12.92	14.21	12.93	20.11	10.78	13.74	13.57	14.76	8.85	11.76	13.00	8.08	16.97	14.27	8.45	9.33	10.00	6.89	4.80	11.75	11.00
Rb/Sr		32.6	40.6	77.9	74.3	52.3	32.1	19.2	24.6	17.5	87.3	48.5	35.9	40.9	1.8	0.186	6.659	31.05	0.8	1.042	0.497	0.1	0.1	0.031	0.026

* ACME laboratory detection limits. ** Total iron is calculated as Fe_2O_3.

Table 3. Major (wt%), trace (ppm), and rare earth elements (ppm) of selected granitoids and related pegmatites from the Jabal Sayid area, Jeddah Terrane, Saudi Arabia.

Rock Type	DL *	Peralkaline Granites										Pegmatites					
Sample		SD1	SD2	SD3	SD4	SD5	SD6	SD7	SD8	SD9	SD10	SDPG1	SDPG2	SDPG3	SDPG4	SDPG5	SDPG6
Major elements (wt%)																	
SiO_2	0.1	73.9	74.8	74.3	74.0	74.9	74.2	75.3	74.9	75.0	74.8	74.6	73.7	71.8	73.8	70.0	71.6
TiO_2	0.01	11.03	11.01	11.22	10.89	10.92	11.09	10.44	10.40	10.88	11.20	9.28	7.25	7.53	7.37	6.65	6.14
Al_2O_3	0.01	0.10	0.16	0.07	0.10	0.07	0.20	0.21	0.17	0.05	0.18	0.40	1.75	1.33	0.62	0.88	0.45
Fe_2O_3 **	0.01	3.97	3.55	3.71	3.98	3.97	4.01	4.74	3.33	3.10	3.21	4.15	4.09	2.93	5.01	4.84	7.22
MnO	0.01	0.03	0.06	0.05	0.05	0.04	0.15	0.12	0.15	0.07	0.05	0.50	<0.01	<0.01	0.11	<0.01	0.34
MgO	0.01	0.21	0.03	0.09	0.11	0.02	0.13	0.12	0.03	0.07	0.04	0.44	0.44	0.28	0.14	0.08	0.17
CaO	0.01	0.91	0.71	0.50	0.66	0.19	0.32	0.25	0.28	1.12	0.19	1.06	1.20	2.82	0.81	4.21	1.91
Na_2O	0.01	4.66	4.86	5.56	5.51	4.96	5.30	4.13	5.11	4.58	5.51	4.19	0.61	0.54	0.32	0.26	0.37
K_2O	0.01	3.99	3.97	3.39	3.88	3.94	4.02	3.98	4.34	3.82	3.98	3.34	5.26	5.09	5.07	4.41	4.53
P_2O_5	0.01	<0.01	0.01	<0.01	0.01	0.03	<0.01	<0.01	<0.01	<0.01	<0.01	<0.01	<0.01	0.31	<0.01	0.12	0.13
Cr_2O_3	0.01	0.018	0.022	0.017	0.010	0.019	0.112	0.123	0.107	0.005	0.003	0.320	0.420	0.239	0.142	0.027	0.161
LOI	−5.11	0.78	0.57	0.78	0.76	0.41	0.38	0.50	0.44	0.99	0.21	1.28	1.83	3.58	1.86	4.02	2.60
SUM		99.60	99.75	99.69	99.95	99.47	99.91	99.91	99.26	99.69	99.38	99.56	96.55	96.45	95.25	95.50	95.65

Table 3. *Cont.*

Rock Type	DL *	Peralkaline Granites										Pegmatites					
Sample		**SD1**	**SD2**	**SD3**	**SD4**	**SD5**	**SD6**	**SD7**	**SD8**	**SD9**	**SD10**	**SDPG1**	**SDPG2**	**SDPG3**	**SDPG4**	**SDPG5**	**SDPG6**
REEs (ppm)																	
La	0.1	65.1	110.0	79.2	54.6	72.80	93.6	135.4	63.9	61.3	85.7	334.6	745.4	2008.6	415.4	1775.6	1241.2
Ce	0.1	144.9	271.1	185.0	131.0	181.70	224.9	323.0	156.8	150.3	181.6	828.3	1731.9	2881.0	971.2	2742.2	2580.5
Pr	0.02	19.02	35.00	22.00	15.82	19.84	29.03	40.76	21.13	18.86	22.70	103.03	230.28	269.47	121.73	288.12	339.20
Nd	0.3	83.0	134.1	82.0	63.9	82.30	116.3	167.9	86.4	78.6	89.7	409.4	927.0	852.1	470.8	1024.1	1530.1
Sm	0.05	22.00	45.00	22.10	16.03	22.32	31.98	41.18	25.90	18.99	19.34	131.72	310.82	282.40	180.75	409.61	700.37
Eu	0.02	1.00	2.08	1.06	0.80	0.29	1.45	2.15	1.80	1.14	0.90	7.33	18.20	18.29	11.94	28.26	42.57
Gd	0.05	23.93	57.11	25.01	16.79	26.29	30.96	43.62	31.70	18.55	19.95	179.61	432.22	500.88	299.01	736.33	1138.77
Tb	0.01	3.83	11.04	4.80	2.69	4.67	4.40	8.01	6.27	3.42	3.47	39.64	99.02	130.52	79.94	176.13	241.11
Dy	0.05	22.97	76.00	29.01	14.49	35.43	23.57	46.38	37.09	19.13	19.70	244.81	661.31	945.39	612.56	1223.14	1496.99
Ho	0.02	3.67	15.92	5.47	2.90	7.49	4.73	8.78	8.77	4.71	4.15	52.80	154.65	238.82	155.56	284.26	324.01
Er	0.03	12.99	44.81	12.99	7.19	22.74	11.95	21.86	26.49	13.21	11.04	135.24	424.68	695.71	473.31	767.08	774.31
Tm	0.01	1.80	7.74	1.67	0.98	2.63	1.89	3.31	4.59	2.24	1.79	18.16	55.61	97.60	77.07	109.79	90.12
Yb	0.05	11.10	31.04	7.99	5.22	18.88	11.47	19.83	27.42	12.15	10.43	87.79	303.28	549.87	470.88	609.28	399.70
Lu	0.01	1.95	3.79	0.99	0.84	2.08	1.76	3.39	4.92	2.44	1.79	10.45	46.08	78.33	66.31	77.77	46.67
Trace elements (ppm)																	
Y	0.1	1229.7	443.9	149.0	76.1	210.20	123.5	223.9	229.2	121.3	107.1	1322.5	3626.7	5764.3	3445.5	7049.0	7905.0
Hf	0.1	29.9	48.0	23.0	23.0	15.50	28.5	57.7	68.6	28.8	32.1	45.2	414.3	271.7	369.7	278.0	111.6
Nb	0.1	87.3	167.1	55.0	119.0	113.70	123.6	219.0	121.0	104.5	63.7	912.7	1107.7	928.0	1480.5	618.6	1386.2
Ta	0.1	6.0	12.6	3.4	23.9	8.60	8.1	14.7	10.8	8.0	5.0	67.2	92.0	107.3	131.8	61.4	94.0
Th	0.2	25.1	56.0	45.5	11.7	79.60	34.2	86.1	5.1	27.9	31.9	236.1	163.0	2224.7	1628.0	1886.8	2617.1
Zn	1	81	277	42	25	84.10	25	249	36	93	50	1583	181	171	424	509	3873
Co	0.2	9.7	7.0	4.9	6.1	5.30	6.0	7.2	7.8	6.4	50.2	5.1	6.6	4.7	5.4	5.3	4.0
Ni	0.1	12.8	6.0	5.9	4.7	3.60	2.3	6.6	2.9	4.6	3.9	3.7	6.5	6.5	6.2	5.0	4.5
Ba	0.01	21	25	14	19	9.10	14	16	6	15	9	76	26	80	41	28	47
V	8	35	<8	8	<8	<8	<8	<8	<8	<8	15	23	16	14	12	13	11
Cu	0.1	10.5	6.6	47.0	8.3	3.10	2.9	7.8	3.0	3.7	2.1	17.3	29.7	24.9	30.3	9.8	43.0
Sr	0.5	26.0	18.1	14.6	13.0	5.90	17.1	6.9	13.5	12.0	6.7	35.7	27.6	55.7	27.6	622.8	317.5

Table 3. *Cont.*

Rock Type	DL *	Peralkaline Granites										Pegmatites					
Sample		**SD1**	**SD2**	**SD3**	**SD4**	**SD5**	**SD6**	**SD7**	**SD8**	**SD9**	**SD10**	**SDPG1**	**SDPG2**	**SDPG3**	**SDPG4**	**SDPG5**	**SDPG6**
Zr	0.1	11,310	2015	769	788	731.6	1120	2261	2712	1079	1064	2342	19,962	14,577	19,914	15,867	5846
Rb	0.1	243.0	323.2	221.1	225.0	248.30	345.7	320.0	309.3	242.0	214.6	227.6	650.4	748.7	598.4	622.3	696.8
As	0.5	6.1	1.0	2.1	1.0	4.40	21.1	1.1	5.8	4.5	6.2	<0.5	<0.5	1.8	0.5	10.2	12.2
Be	1	5	8	19	6	14.10	10	4	17	11	14	9	25	25	14	10	18
Sb	0.1	0.7	0.2	0.4	0.2	0.40	0.3	0.7	0.8	0.7	0.5	0.1	1.3	1.3	1.5	0.3	0.6
Sn	1	12	20	13	12	13.10	17	38	15	10	12	63	180	132	154	77	182
U	0.1	9.0	19.9	11.9	12.0	16.20	9.4	25.1	13.5	11.4	11.7	87.8	139.6	357.6	319.6	252.1	552.8
W	0.5	67.4	61.0	55.6	51.0	60.30	55.4	60.8	77.8	56.8	550.7	37.6	69.3	40.8	49.7	38.4	32.7
Cd	0.1	<0.1	0.4	0.1	<0.1	<0.1	<0.1	0.7	0.5	0.4	0.2	2.2	0.4	2.3	1.3	2.9	5.5
Cs	0.1	2.1	1.5	1.4	1.6	1.00	2.8	1.0	2.3	1.9	2.3	1.0	4.2	4.6	4.0	3.9	4.6
Ga	0.5	37.9	40.0	41.2	36.2	36.60	42.8	40.8	38.8	39.1	35.8	39.6	31.9	32.1	40.1	34.2	32.1
Mo	0.1	2.5	1.2	0.9	1.2	0.00	0.7	1.9	0.9	1.0	0.6	1.0	3.0	1.7	2.2	1.5	2.1
Pb	0.1	27.3	38.3	37.6	9.0	48.30	29.7	112.9	29.3	14.2	20.3	63.9	146.4	320.5	847.5	139.9	284.9
Au	0.3	1.3	2.1	<0.5	<0.5	<0.5	<0.5	2.1	<0.5	<0.5	<0.5	<0.5	<0.5	31.2	<0.5	<0.5	<0.5
Bi	0.1	0.5	<0.1	0.5	0.2	0.50	0.6	0.5	0.8	0.6	0.3	0.1	0.1	<0.1	0.4	<0.1	0.3
Se	0.2	<0.5	<0.5	<0.5	<0.5	<0.5	<0.5	<0.5	<0.5	<0.5	0.7	<0.5	<0.5	<0.5	<0.5	<0.5	<0.5
Eu/Eu*		0.13	0.13	0.14	0.15	0.04	0.14	0.16	0.19	0.19	0.14	0.15	0.15	0.15	0.16	0.16	0.15
$(La/Yb)_N$		5.53	3.34	9.34	9.86	3.63	7.69	6.43	2.20	4.75	7.74	3.59	2.32	3.44	0.83	2.75	2.93
Y/Nb		14.09	2.66	2.71	0.64	1.85	1.00	1.02	1.89	1.16	1.68	1.45	3.27	6.21	2.33	11.40	5.70
Nb/Ta		14.55	13.26	16.18	4.98	13.22	15.26	14.90	11.20	13.06	12.74	13.58	12.04	8.65	11.23	10.07	14.74
Rb/Sr		9.3	17.9	15.1	17.3	42.08	20.2	46.4	22.9	20.2	32.0	6.4	23.6	13.4	21.7	1.0	2.2

* ACME laboratory detection limits. ** Total iron is calculated as Fe_2O_3.

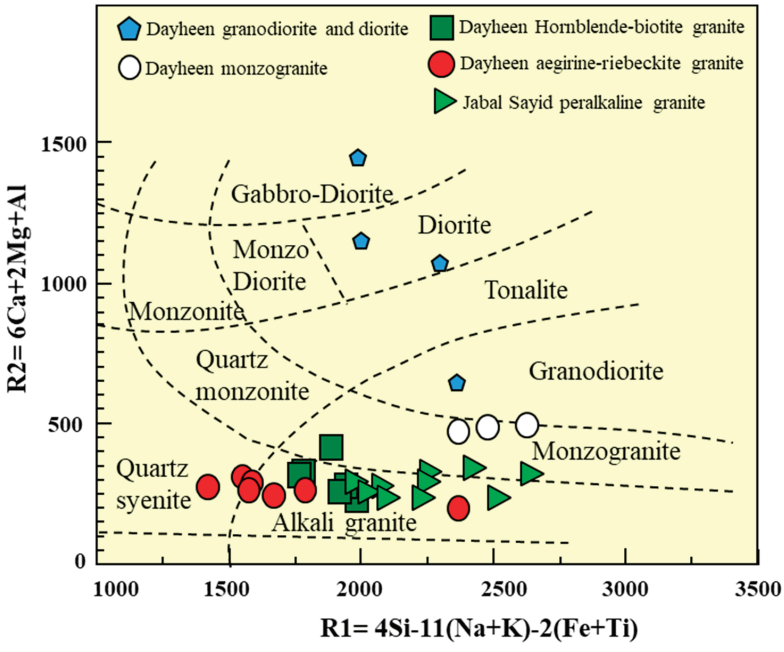

Figure 6. The classification of the studied granitic samples according to the R1-R2 diagram [24].

In the classification based on the ACNK versus ANK diagram [25], the peralkaline granites from Jabal Sayid and Dayheen are classified as peralkaline granites (Figure 7a). Conversely, monzogranite and granodiorite–diorite samples fall within a metaluminous field. The plotting of the studied granites on the alkalinity ratio (AR) against the SiO_2 diagram of [26] indicates that the peralkaline granite samples from Jabal Sayid and Dayheen are plotted within the alkaline and peralkaline fields (Figure 7b), while the Dayheen monzogranites fall within the alkaline field. This suggests that they have a slightly lower alkali content compared to the peralkaline granites, but they still exhibit alkaline characteristics. The alkaline/peralkaline character of the Jabal Sayid and Dayheen peralkaline granites is in agreement with the presence of aegirine and riebeckite as deduced from a petrographical study (Figures 3e,f and 4c,d). On the other hand, the Dayheen granodiorite–diorite samples are placed in the calc-alkaline field (Figure 7b). This indicates that these rocks have a different geochemical composition compared to the peralkaline granites and monzogranites. The change in alkalinity observed from calc-alkaline through alkaline to peralkaline in these rocks suggests a variation in the source of the magma and the tectonic setting in which they formed.

In the K_2O vs. SiO_2 diagram of [27], the peralkaline granite samples from Jabal Sayid and Dayheen, as well as the monzogranite samples from Dayheen, are plotted within the fields of the high-K calc-alkaline and shoshonite series (Figure 7c). However, it is also mentioned that granodiorite–diorite samples fall within the medium-K calc-alkaline. The change in magma composition from medium-K calc-alkaline to high-K calc-alkaline and shoshonite series indicates a progressive evolution of the magmas. This evolution can involve fractional crystallization, the assimilation of crustal rocks, or mixing between different magma sources. These processes can modify the chemical composition of the magma and result in observed variations in potassium content.

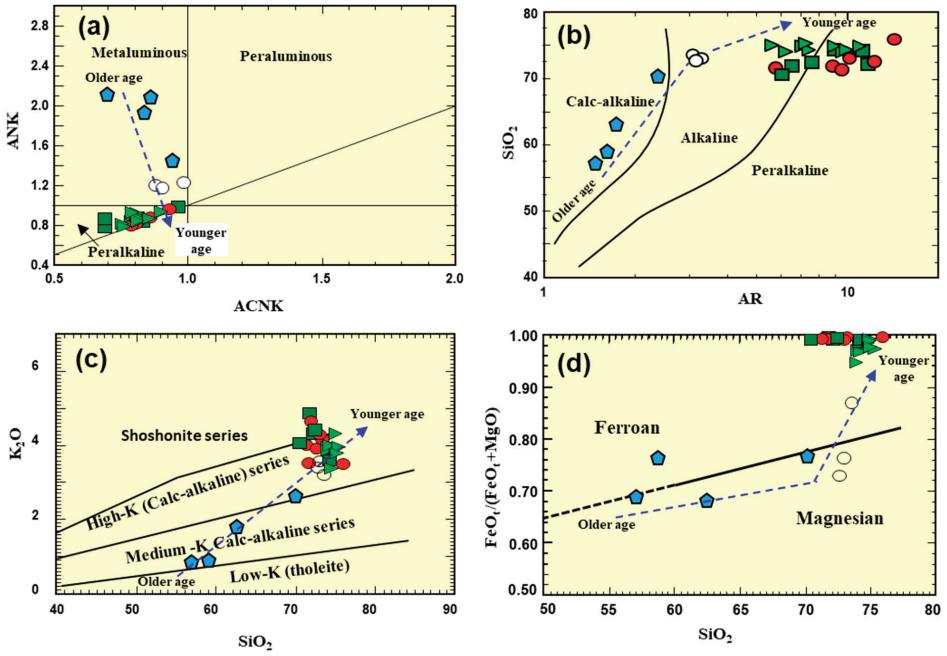

Figure 7. Magma-type diagrams of Jabal Sayid and Dayheen granites. (**a**) A/CNK vs. A/NK diagram [25], (**b**) AR vs. SiO_2 diagram [26], AR (Alkalinity Ratio) = $[Al_2O_3 + CaO + (Na_2O + K_2O)]/[Al_2O_3 + CaO-(Na_2O + K_2O)]$, (**c**) K_2O vs. SiO_2 diagram [27], and (**d**) $FeO_t/(FeO_t + MgO)$ vs. SiO_2 diagram of [28]. Symbols as in Figure 6.

The $FeO_t/(FeO_t + MgO)$ versus SiO_2 diagram of [28] provides insights into the composition and characteristics of the studied granitoids (Figure 7d). Samples of the peralkaline granites from Jabal Sayid and Dayheen fall within the ferroan field, whereas the monzogranite and granodiorite–diorite samples fall within the magnesian field. The ferroan nature of the peralkaline granites, similar to most of the rare-metal A-type granite in the ANS, suggests a higher iron content compared to magnesium. On the other hand, the positioning of the monzogranite and granodiorite–diorite samples within the magnesian field may be indicative of different source materials or differentiation processes that favor the incorporation of magnesium-rich minerals. The change from the magnesian field to the ferroan field can indicate a transition in the source rocks or the conditions under which these granitoids formed.

The trace element profiles of the peralkaline granites and their related pegmatites from Jabal Sayid and Dayheen exhibit similar patterns, as normalized to the ocean ridge granite (ORG, [29]). In general, these rocks are enriched in most trace elements (Figure 8a,b), except for Ba, which is depleted and exhibits values lower than one, specifically in the peralkaline granites. However, there are a few samples where the concentrations of Zr, Sm, Y, and Yb are lower than one. The enrichment of most trace elements suggests a significant contribution from crustal materials to the composition of these granites and related pegmatites. Figure 8c illustrates that the trace elements in monzogranites can be divided into two distinct groups based on their concentrations. The first group includes elements such as K, Rb, Ba, Th, Ta, Nb, Sr, and Ce, which are enriched relative to the values of ORG. The second group comprises elements like Zr, Sm, Y, and Yb, which have concentrations lower than one. The trace element patterns observed in the monzogranites align with those typically found in monzogranites associated with island or continental arc settings in the ANS context. In Figure 8d, a typical saw-tooth pattern of magma related to

subduction is observed in the granodiorite–diorite association, where elements such as K, Rb, Ba, and Th are enriched in these rocks compared to the values of ORG. On the other hand, elements like Ta, Nb, Sr, Ce, Zr, Sm, Y, and Yb show depletion.

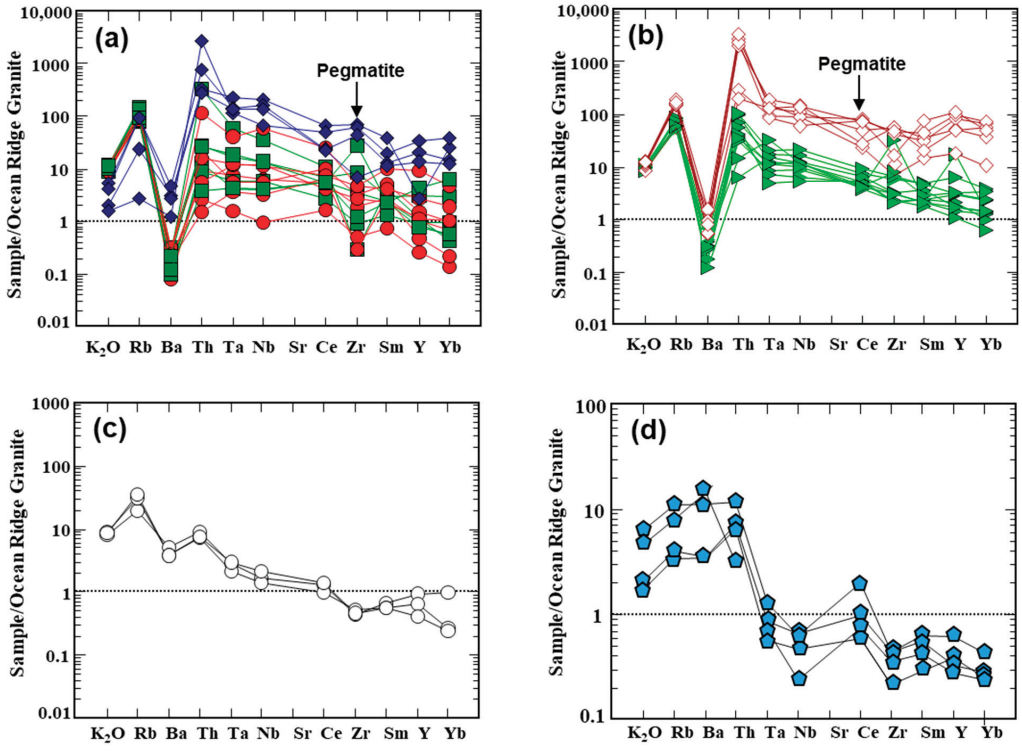

Figure 8. The ocean ridge granite normalized spider diagram of trace elements [29] for (**a**) the Dayheen peralkaline granites and pegmatites; (**b**) the Jabal Sayid peralkaline granites and pegmatites; (**c**) the Dayheen monzogranites; and (**d**) the Dayheen granodiorite–diorite association. Symbols as in Figure 6.

5.2. REEs Characteristics

The Dayheen granodiorite–diorite association has the lowest total REE contents (103 ppm, on average, Table 2), followed by monzogranites with slightly higher total REE contents (126 ppm, on average). The Jabal Sayid and Dayheen pegmatites show the highest total REE contents (4056 and 7313 ppm, on average, respectively, Tables 2 and 3). The Jabal Sayid and Dayheen peralkaline granites have lower total REE contents (541 and 678 ppm, on average, respectively) compared to the related pegmatites. Chondrite-normalized REE patterns (using the chondrite values of [30]) are presented in Figure 9. The REE profiles of the peralkaline granites and their related pegmatites from Jabal Sayid and Dayheen exhibit a close similarity in shape. Both profiles display a gentle sloping LREE subprofile and a relatively flat Heavy Rare Earth element (HREE) subprofile (Figure 9a,b). This suggests that the peralkaline granites and their related pegmatites share a common geochemical signature, characterized by a consistent distribution pattern of REEs. Another prominent feature in the REE profiles of both the peralkaline granite and pegmatites is the presence of a negative Eu anomaly. The presence of this anomaly and the strong overall REE enrichment in pegmatites further support the notion of distinct mineralogical and chemical processes that differentiate pegmatites from the parental peralkaline granites. In Dayheen peralkaline granites and related pegmatites, REE compositions are highly vari-

able, with $(La/Yb)_N$ ratios ranging from 2.07 to 57.27 and negative Eu anomalies (Eu/Eu*) from 0.13 to 0.16 (Table 2). Meanwhile, in the Jabal Sayid peralkaline granites and related pegmatites, REE compositions are less variable, with $(La/Yb)_N$ ratios ranging from 0.83 to 9.86 and comparable negative Eu anomalies (Eu/Eu*) from 0.13 to 0.19. Chondrite-normalized REE patterns of the monzogranite and granodiorite–diorite association are also shown in Figure 9c,d. They are distinguished by LREE enrichment and small negative Eu anomalies (Eu/Eu* = 0.29–0.41 for monzogranite, and 0.58–0.72 for the granodiorite–diorite association) with variable La/Yb ratios (2.7–11.02 for monzogranite, and 4.26–15.9 for the granodiorite–diorite association).

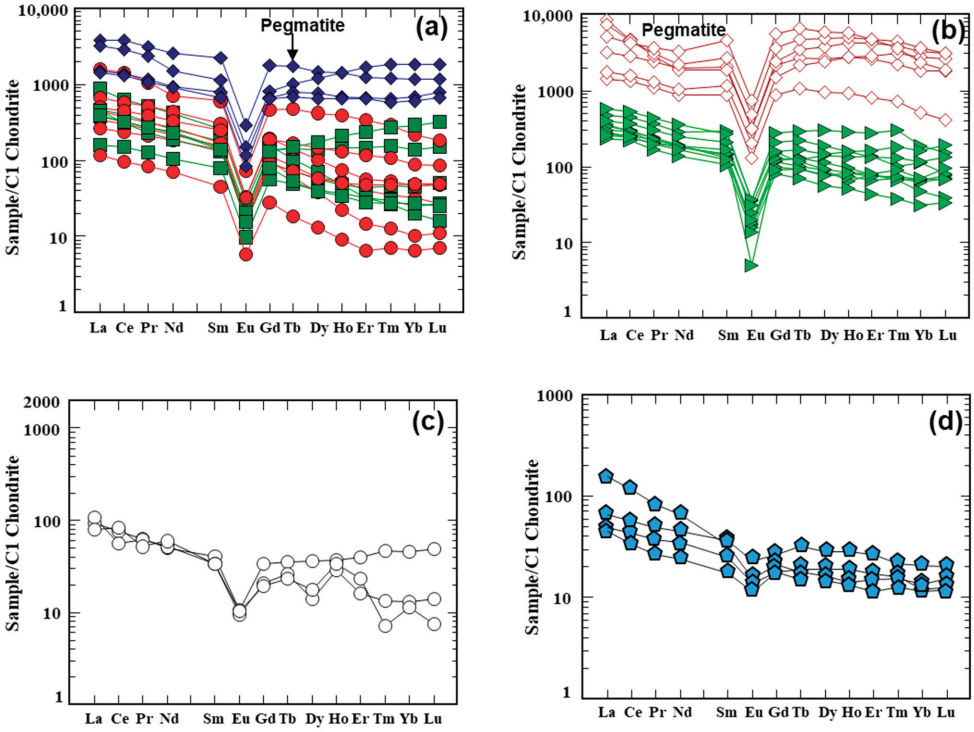

Figure 9. Chondrite-normalized REE patterns [30] for (**a**) the Dayheen peralkaline granites and pegmatites; (**b**) the Jabal Sayid peralkaline granites and pegmatites; (**c**) the Dayheen monzogranites; and (**d**) the Dayheen granodiorite–diorite association. Symbols as in Figure 6.

5.3. Rare Metal Contents

The comparison between Jabal Sayid and Dayheen in terms of their rare metal contents, as shown in Figure 10, reveals some distinct variations in the composition of their pegmatites and peralkaline granites. Jabal Sayid pegmatites show the highest average contents of LREEs (4494 ppm), HRREs (2819 ppm), Y (4852 ppm), Th (1459 ppm), U (285 ppm), and Zn (1124 ppm) compared to Dayheen pegmatites. Dayheen pegmatites show the highest average contents of Zr (15,937 ppm), Nb (1445 ppm), and Ta (109 ppm). Furthermore, the Dayheen peralkaline granites have a higher average content of LREEs (581 ppm) and Nb (135 ppm) and lower contents of HREEs (98 ppm), Zr (1565 ppm), and Y (149 ppm) compared to the Jabal Sayid peralkaline granites. Th, U, Ta, and Zn contents are comparable between the peralkaline granites of both locations. The enrichment of these elements in the peralkaline granites and related pegmatites can be attributed to the presence of various mineral associations, as shown in Table 1.

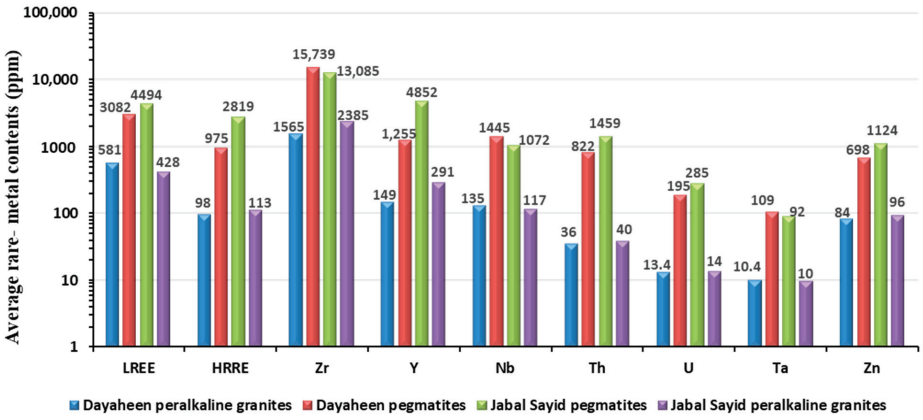

Figure 10. The histogram shows a comparison between Jabal Sayid and Dayheen in terms of their rare metal contents.

6. Discussion

6.1. Tectonic Setting

The R1-R2 tectonic setting discrimination diagram developed by [24] and the tectonic setting fields based on [31] can be used to classify different types of granitoids based on their geochemical signatures and relate them to specific tectonic environments (Figure 11a): (1) Subduction-related granitoids that are represented by the granodiorite–diorite association. These granitoids are typically related to an early stage in the orogenic cycle, characterized by subduction or pre-plate collision magmatism; (2) collision-related granitoids that are represented by monzogranites. The presence of monzogranites in the studied granitoids indicates a transitional stage in the orogenic cycle, where the tectonic collision has occurred, leading to the generation of collision-related magmas; (3) post-orogenic/Anorogenic granitoids that are represented by peralkaline granites. The presence of these rocks suggests a late stage in the orogenic cycle, characterized by post-orogenic or anorogenic magmatism. These observations support the idea that the granitoids in the Jabal Sayid and Dayheen areas may represent different stages within a single orogenic cycle, reflecting the evolving tectonic processes that occurred during their formation (blue dashed lines with arrows in Figure 11a).

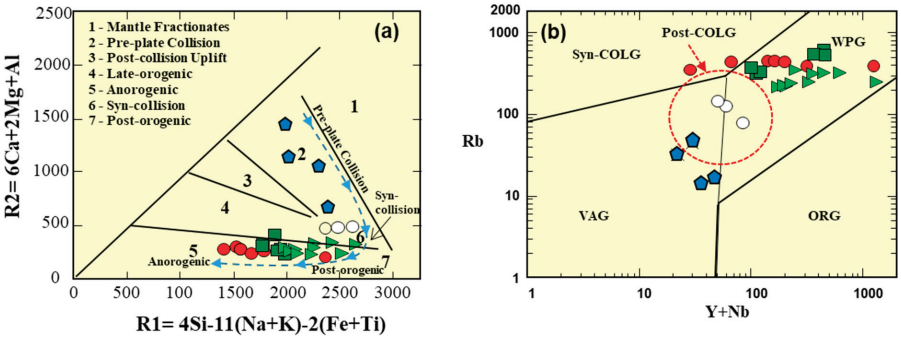

Figure 11. (**a**) The R1-R2 tectonic setting discrimination diagram of [24], with tectonic setting fields based on [31]. The blue dashed line with arrows reflects different stages within a single orogenic cycle. (**b**) Y + Nb vs. Rb discrimination diagram [29], post-collisional field (red dashed circle) after Pearce (1996). VAG = volcanic arc granite, SYN-COLG = syn-collision granite, ORG = ocean ridge granite, and WPG = within-plate granite. Symbols as in Figure 6.

In the Y + Nb vs. Rb discrimination diagram ([29]; Figure 11b), the Jabal Sayid and Dayheen peralkaline granite samples fall within the within-plate field. This indicates that these samples have geochemical characteristics consistent with an intraplate tectonic setting. In contrast, the Dayheen granodiorite–diorite samples fall within the volcanic-arc granite field. This suggests that these samples have geochemical characteristics similar to those of subduction-related granitoids. Furthermore, the Dayheen monzogranite samples fall within the post-collisional field as defined [32]. This indicates that these samples have geochemical characteristics consistent with collision-related granitoids.

The chemical characteristics described for the Jabal Sayid and Dayheen peralkaline granites suggest a within-plate tectonic setting. These characteristics include significant depletions in CaO, MgO, Sr, and transition metals, along with high alkali contents and notable enrichments in High-Field-Strength Elements (HFSEs) such as Zr, Nb, Ta, and rare earth elements (REEs). The pronounced negative Eu anomalies in the REE patterns of the granites (Figure 9a,b) indicate the involvement of plagioclase feldspar fractionation in their petrogenesis, where the preferential removal of Eu^{2+} from the melt leads to the relative depletion of Eu compared to the other REEs. Overall, the described geochemical features are consistent with the within-plate tectonic setting of the Jabal Sayid and Dayheen peralkaline granites, indicating their formation in an intraplate environment away from plate boundaries [33–35].

6.2. The Petrogenesis of the Jabal Sayid and Dayheen Granitoids

6.2.1. Subduction-Related Granitoids

During an orogenic cycle, which encompasses the development of a mountain belt, the character of magmas can change as different tectonic processes occur. Regionally, this cycle is characterized by a transition in the nature of magmatism. It starts with typical subduction-related calc-alkaline compositions, followed by late-orogenic calc-alkaline rocks, and finally culminates in post-collisional peralkaline suites. As mentioned above, the Dayheen granodiorite–diorite association exhibits characteristics consistent with I-type granitoids. These characteristics include the following: high LREE/HREE ratios (7.47, on average) with nearly flat patterns for HREEs; small negative Eu anomalies; HFSE (Nb, Ta, and Ti) depletion; and Sr and Ba enrichment. This implies that these rocks were possibly derived from the partial melting of a subducted oceanic crust, with subsequent interaction with fluids and/or melts from the subduction zone. Geochemically, these granites yield lower Rb/Zr than that of S-type granitoids (Figure 12a, [36]). Moreover, they have lower $(Na_2O + K_2O)/CaO$ and Zr + Nb + Ce + Y than A-type granitoids (Figure 12b, [35]). The positioning of the Dayheen granodiorite–diorite rocks in the low-K mafic rocks field (Figure 12d) further supports their classification as I-type granitoids (Figure 12c, [37]). The Dayheen granodiorite–diorite association, as indicated by Figure 12e, is characterized by being Sr- and Ba-rich and Rb-poor. This implies that the generation of these magmas occurred in a subduction-like setting [38]. Additionally, the $CaO/(MgO + FeO_{total})$ vs. $Al_2O_3/(MgO + FeO_{total})$ diagram (Figure 12f) provides insights into the probable magma sources for the considered granitoids. The diagram suggests that most of the granodiorite–diorite association was developed by the melting of a mainly metabasaltic source. The composition of the lower crust in the AS, where the study areas are located, is consistent with the nature of this source.

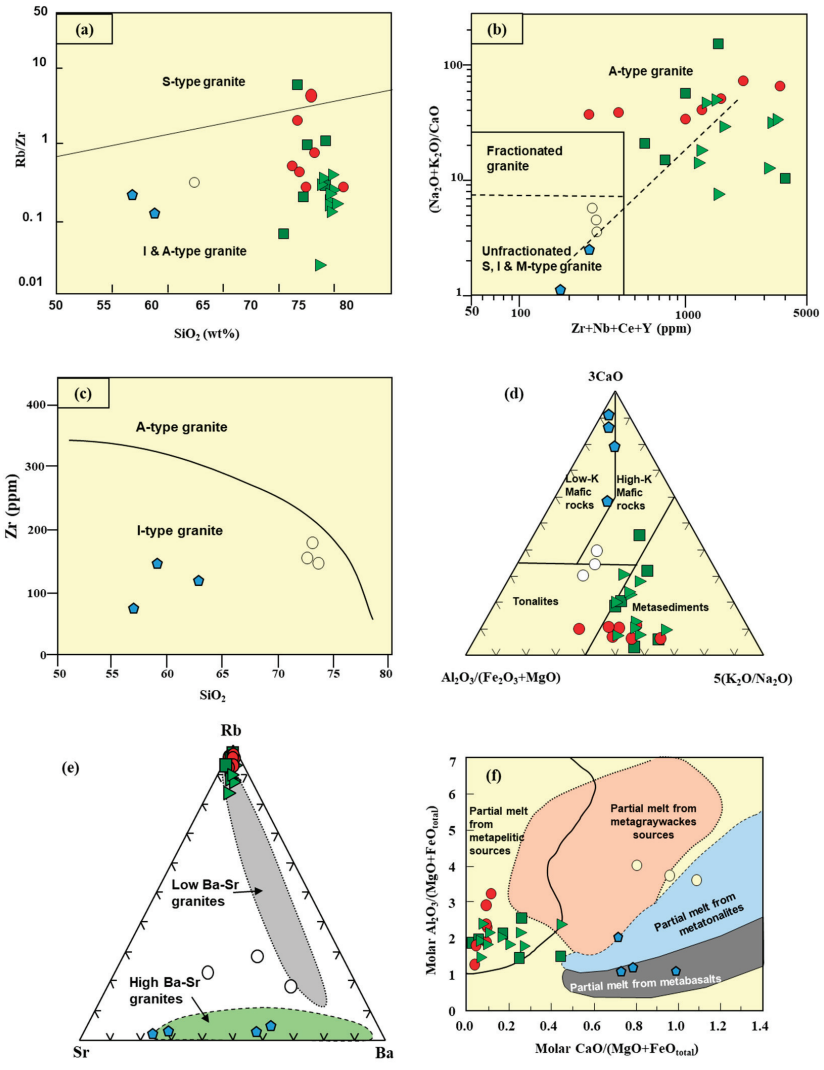

Figure 12. (**a**) Rb/Zr vs. SiO_2 (after [36]). (**b**) Zr + Nb + Ce + Y (ppm) vs. $(Na_2O + K_2O)/CaO$ (after [35]). (**c**) The Zr vs. SiO_2 discrimination diagram for I- and A-type granitoid rocks [37]. (**d**) The ternary diagram of $Al_2O_3/(Fe_2O_3 + MgO)$-3CaO-$5(K_2O/Na_2O)$ (after [38]). The different fields represent the compositions of melts derived from a range of potential sources (tonalites, metasediments, and low- and high-K mafic rocks), determined by major element compositions of partial melts in experimental studies. (**e**) The Sr–Rb–Ba ternary plot for the studied granites (modified after [39]). (**f**) Molar $CaO/(MgO + FeO_{total})$ vs. $Al_2O_3/(MgO + FeO_{total})$ (after [40]). Symbols as in Figure 6.

6.2.2. Collision-Related Granitoids

In the discrimination diagram by [35] (Figure 12b), the Dayheen monzogranites plot as unfractionated S-, I-, and M-type granite. Furthermore, in the Zr vs. SiO_2 discrimination diagram of [37], the high-K calc-alkaline Dayheen monzogranites fall within the I-type field (Figure 12c). This observation aligns with the idea that the monzogranites have an intrusion-related origin, as I-type granites, and are typically related to magmatic arcs and subduction zones. However, the presence of a sedimentary component in the magma

sources of the monzogranites is indicated in Figure 12f, where the samples fall within the overlapping partial melts of metatonalites and metagraywackes. This sedimentary component could have been derived from the descending slab during subduction and collision processes. Additionally, Figure 12d proposes that the monzogranite samples plot in the field of the melting of high-K mafic rocks to tonalitic rocks. This further supports the interpretation that the Dayheen monzogranites have a complex origin involving the melting of mafic rocks, potentially related to subduction processes. It is worth noting that the lower (Na_2O + K_2O)/CaO values observed in the Dayheen monzogranites indicate a relatively lower alkali content compared to the calcium content. This can be indicative of a more calc-alkaline nature, which is commonly related to S-type granites that form during collision events. The presence of S-type characteristics in the monzogranites could be related to specific geological conditions and processes occurring during their formation.

The composition of the Dayheen monzogranites suggests a mixing or hybridization process involving different source materials or a combination of magmas derived from different sources. After a collision event and crustal thickening, melting occurs in the mantle wedge due to the fractionation of an amphibole-dominated phase [41]. These melts then intrude on the base of the already hot and thickened crust, which promotes the further melting of the thickened lower crust [42]. As the magmas ascend towards the surface, they interact with the overlying continental crust, which is composed of older and more felsic rocks. This interaction leads to the assimilation of continental crustal material into the ascending magmas. The findings of [43] provide an alternative explanation for the formation of I-type granitoids, highlighting the importance of sedimentary materials in the process, i.e., how the interaction between mantle-derived magmas and sedimentary materials can lead to the formation of I-type granitoids. This suggests that the composition of the monzogranites may be influenced by the addition of sedimentary components during their formation. Collision-related magmas, such as the Dayheen monzogranites, are often characterized by their intermediate-to-felsic compositions. This composition reflects the complex processes of crustal thickening, mantle melting, and interaction with the continental crust, resulting in the generation of hybridized magmas with intermediate compositions.

6.2.3. Post-Orogenic or Anorogenic Granitoids

After a collision, significant amounts of high-K calc-alkaline granitoids are often emplaced, primarily as batholiths [44]. The isotopic ratios of Nd are often used as tracers to identify the sources of magmatic rocks. However, in the case of the ANS, the possible crustal materials for post-orogenic or anorogenic magmatism were themselves relatively young and had not undergone enough geological processes to develop distinctively crustal Nd isotope signatures, making it difficult to apply Nd isotope ratios as a reliable tracer in this context [45,46]. In that case, we can go to other evidence to identify the source of the Jabal Sayid and Dayheen parental peralkaline magmas. The Nb/Ta ratio and Y/Nb ratio are geochemical signatures that can provide valuable information about the source of magmas. These ratios are particularly useful in differentiating between mantle-derived and crustal-derived magmas. The Nb/Ta ratios in the Jabal Sayid and Dayheen peralkaline granites and pegmatites propose that these rocks crystallized from magmas derived from crustal sources rather than mantle-derived sources. The average Nb/Ta ratios are 12.94 for peralkaline granites and 11.72 for pegmatites in the case of Jabal Sayid and 12.98 for peralkaline granites and 13.08 for pegmatites in the case of Dayheen (Tables 2 and 3). These values fall within the range typically observed for crustal materials, which is generally lower than the Nb/Ta ratios observed in mantle-derived rocks. The typical Nb/Ta ratios for the continental crust range from 8 to 14, as reported by Stepanov and Hermann (2013). In contrast, the chondritic ratio, which represents the composition of the Earth's primitive mantle, is approximately 19.9 $\pm$ 0.6 [47]. Moreover, the Nb/Ta ratios in ocean island basalts typically fall around 15.9 $\pm$ 0.6 [48].

The Y/Nb ratio is another geochemical parameter commonly used to distinguish between different sources of magma. The average Y/Nb ratios reported for the peralkaline granites and pegmatites of Jabal Sayid (2.87 and 5.06, respectively, Table 3) and the peralkaline granites and pegmatites of Dayheen (1.34 and 1.33, respectively, Table 2) are higher than the typical Y/Nb ratios observed in mantle-derived sources, which are often less than 1.2 [33]. In terms of Rb/Sr ratios, mantle-derived materials typically have low Rb/Sr ratios, ranging from 0.1 to 0.01 [49], whereas lower and middle continental crust tends to be enriched in Rb relative to Sr [50]. Based on the Rb/Sr ratios observed in the studied granitoids, it is reasonable to conclude that the granodiorite–diorite association was formed from mantle material where lower Rb/Sr ratios between 0.03 and 0.1 were observed (Figure 13a). However, the higher Rb/Sr ratios in the monzogranites and peralkaline granites compared to typical mantle values suggest a significant contribution from sources other than the mantle, such as crustal materials.

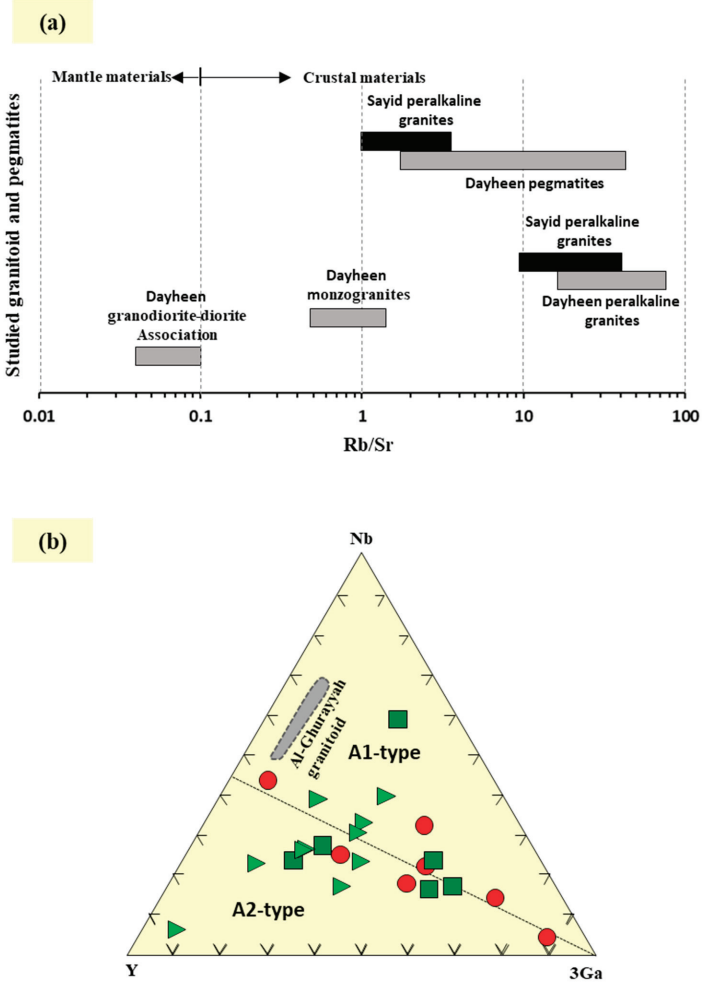

Figure 13. (**a**) Rb/Sr ranges of the studied granitoid and associated pegmatites. (**b**) The Nb-Y-3Ga ternary diagram of [33]. Symbols as in Figure 6.

The use of the ternary discrimination diagram developed by [38] provides further evidence supporting the conclusion that the Jabal Sayid and Dayheen peralkaline granites

have a metasedimentary source (Figure 12d). Similarly, most of the Jabal Sayid and Dayheen peralkaline granites are plotted in the metapelitic source field, indicating a continental crustal source (Figure 12f). This further supports the idea that the peralkaline granitoids in the study area have a continental crustal source and are consistent with the broader geological context of the ANS. This is in agreement with the highest rubidium values and the lowest strontium and barium contents of the Jabal Sayid and Dayheen peralkaline granites (Figure 12e). The petrographical study indicating that the Jabal Sayid and Dayheen peralkaline granites are high in K-feldspar content is consistent with the observed variations in the Sr, Ba, and Rb contents in these rocks.

In the Zr + Nb + Ce + Y vs. $(Na_2O + K_2O)/CaO$ diagram of [35], the Jabal Sayid and Dayheen peralkaline granites fall within the A-type field (Figure 12b). When plotted on the discrimination diagram of [33], the Jabal Sayid and Dayheen granitoid samples overlap the boundary between the A1 and A2 subgroups (Figure 13b). The A1 subgroup is associated with rare-metal-bearing granitoids, similar to the Al-Ghurayyah granitoids in Saudi Arabia. On the other hand, the A2 subgroup aligns with the overall assumption of peralkaline granites in the ANS, where many peralkaline granites of crustal origin have been recognized, such as Al-Hamra granites, Saudi Arabia [51]; Feinan granites, Jordan [52]; and Um Taghir granites, Egypt [53].

6.3. Genesis of Rare Metals

The pie charts presented in Figure 14 provide information on the relative proportions of different rare metals in the Jabal Sayid and Dayheen peralkaline granites as well as in the related pegmatites from these locations. Based on the charts, the following observations can be made: (1) Jabal Sayid peralkaline granites have higher proportions of Zr and Y and lower proportions of LREEs, HREEs, and Nb compared to Dayheen peralkaline granites; (2) the Dayheen pegmatites have higher proportions of Zr and Nb and lower proportions of LREEs, HREEs, and Y compared to Jabal Sayid pegmatites. The variations in rare metal proportions in peralkaline granites and related pegmatites in Jabal Sayid and Dayheen can be related to different geological processes, such as the following: (1) different sources of magmatic material that contributed to the formation of these rocks; (2) fractional crystallization process, where different minerals can selectively incorporate or exclude certain elements, leading to variations in rare metal proportions; (3) late-stage hydrothermal alteration processes that can significantly affect the rare metal contents in these rocks; and (4) surficial weathering processes that can lead to the alteration and breakdown of rocks and minerals, resulting in the release, redistribution, and concentration of elements, including rare metals. Based on the present petrological and geochemical data, the investigation of these alternatives will be covered in the following sections.

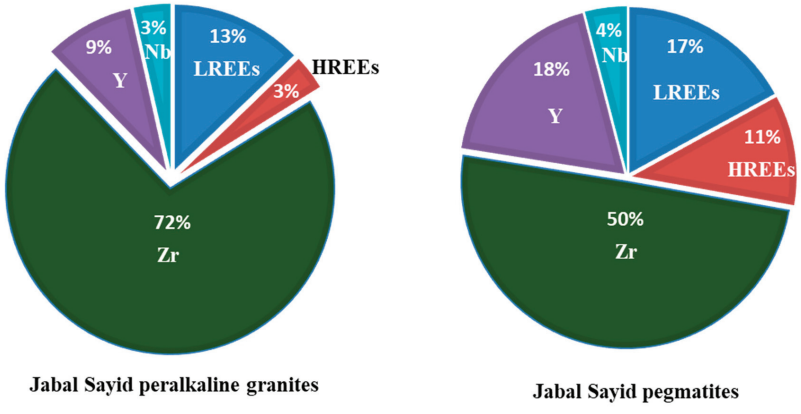

Figure 14. *Cont.*

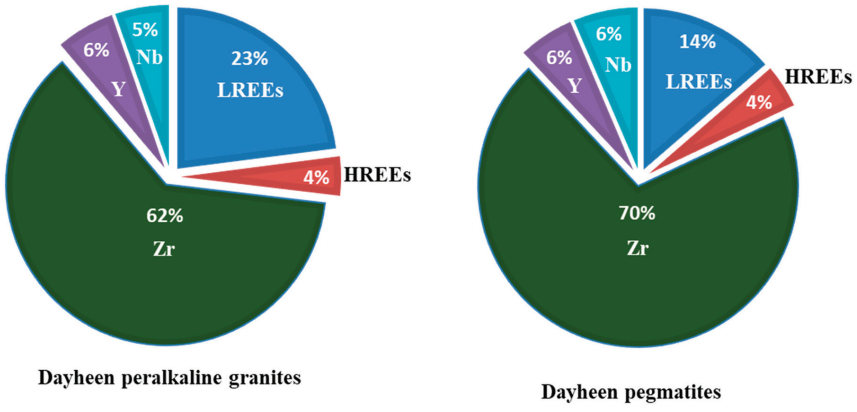

Figure 14. Pie charts illustrating the proportions of HREEs (Gd to Lu), LREEs (La to Sm), Zr, Y, and Nb in rare-metal peralkaline granites and related pegmatite in the Jabal Sayid and Dayheen areas.

The remarkably similar chondrite-normalized REE patterns (Figure 9a,b), as well as the trace element profiles (Figure 8a,b) of the peralkaline granites and related pegmatites from Jabal Sayid and Dayheen, support the idea of a common origin. This indicates that the variations in rare metal proportions are less likely to be attributed to differences in the source material. Instead, it suggests that the source material for these rocks had a consistent composition, contributing to the similar rare metal signatures observed in both areas. The correlations between the contents of rare metals (Zr, Y, Ta, U, Th, Pb, Hf, LREEs, and HREEs) and Nb as a measure of magma fractionation, as shown in Figure 15, offer meaningful information about the processes involved in the formation of rare-metal granitic and pegmatitic rocks. The choice of these elements, which are progressively increased in the residual melt of fractionating magma regardless of its composition, allows for a better understanding of the enrichment mechanisms that control the formation of these rare-metal-bearing rocks.

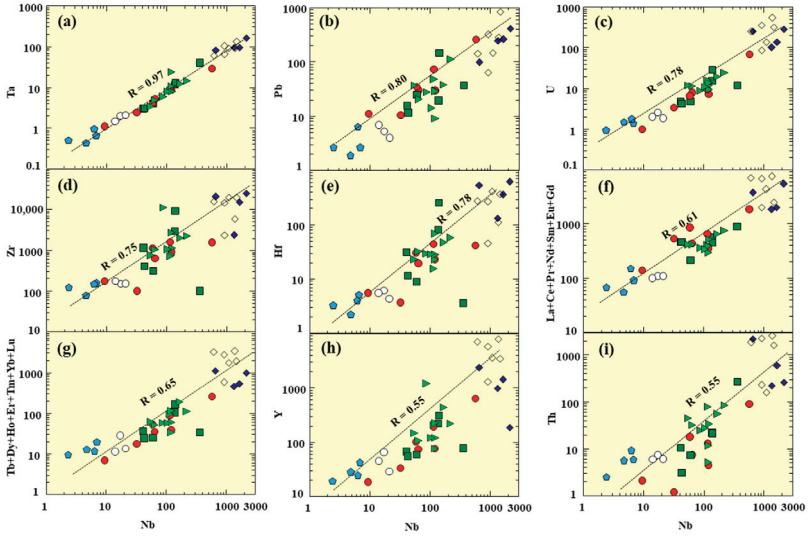

Figure 15. Correlations between the contents of rare metals and Nb as an indicator of magma fractionation. The open diamond symbols represent the Dayheen pegmatites, closed diamond symbols represent the Jabal Sayid pegmatites, and other symbols as in Figure 6.

The strong positive correlation coefficients (>0.9) between Nb and Ta in granitic rocks and related pegmatites from Jabal Sayid and Dayheen indicate their genetic links and derivation from common sources. The fact that Nb and Ta have a tendency to be higher in peralkaline granites and related pegmatites compared to monzogranites, granodiorites, and diorites (as shown in Figure 15a) is consistent with their behavior as incompatible elements during magmatic differentiation.

The elements Pb, U, Zr, and Hf exhibit moderate to strong correlations with Nb ($R > 0.7$) in the studied magmatic systems. This correlation suggests a common genetic origin and shared processes influencing their behavior. In the early magmatic phases, such as the granodiorite–diorite association, the concentrations of Pb, Zr, and Hf tend to be relatively low. This could be attributed to the fact that these elements are not significantly enriched during the initial stages of magmatic differentiation. The early magmatic phases may have undergone more extensive fractionation, resulting in the preferential loss or limited incorporation of Pb, Zr, and Hf. On the other hand, in the late magmatic phases, such as peralkaline granites and related pegmatites, the concentrations of Pb, U, Zr, and Hf are generally higher. This indicates that these elements become more enriched as the magmatic system evolves. The late-stage magmas may have experienced different processes, such as fractional crystallization or magma mixing, that promote the concentration and incorporation of Pb, U, Zr, and Hf. The correlation coefficients (R) between Nb and LREEs (La to Eu), HREEs (Gd to Lu), Y, and Th are generally weak and range from 0.55 to 0.65. Although these values can still be statistically significant and provide valuable insights, other factors or variables, such as magma mixing or late-stage hydrothermal alteration, may influence the relationship between Nb and LREEs, HREEs, Y, and Th.

The low values of the chemical index of alteration (CIA), chemical index of weathering (CIW), and plagioclase index of alteration (PIA) in the Jabal Sayed peralkaline granites and related pegmatites indicate that these rocks have experienced limited weathering and alteration [54]. This means that the chemical composition of these rocks has been relatively stable and has not undergone significant changes due to surficial weathering processes.

From above, it is suggested that the Jabal Sayid and Hadb Adh Dayheen peralkaline granites, along with their associated pegmatites, share a common parental magma and have formed primarily through fractional crystallization processes. The rare metal signature present in these rocks is believed to have been preserved during their formation. The previous age dating from Dayheen supports the idea that the rare-metal-bearing rocks in this region developed in a post-orogenic setting. Additionally, assessments of the published Sm-Nd isotopes for Jabal Sayid and Dayheen indicate that they have the same source [6–8,55]. This suggests that these granites and pegmatites share a common origin and were derived from a melt that underwent magmatic processes. The extreme levels of evolution that the melt experienced during its magmatic evolution likely contributed to the concentration of rare metals in the Jabal Sayid and Hadb Adh Dayheen peralkaline granites. This extreme evolution could have involved processes such as fractional crystallization, where certain minerals and elements become concentrated in the residual melt as it cools and solidifies. The higher concentrations of rare metals observed in the pegmatites can be interpreted by the influence of fractional crystallization. If the pegmatites formed from residual magma batches derived from the precursor granites, the concentrations of rare metals in the pegmatites could have been influenced by the fractionation process that occurred in the precursor granites. This process could have resulted in the enrichment of rare metals in the residual magmas that eventually formed the pegmatites. The presence of various accessory minerals in the Jabal Sayid and Dayheen peralkaline granites and related pegmatites, as listed in Table 1, is significant in controlling the behavior of rare metals in these rocks. The minerals synchysite, bastnaesite, xenotime, monazite, allanite, pyrochlore, samarskite, and zircon are recognized petrographically as important contributors of REEs, Y, Nb, and Zr in these rocks. Additionally, other minerals such as titanite, thorite, kasolite, apatite, and fluorite have been identified from petrographic studies. These minerals are typically enriched in elements such as Ti, Th, U, Pb, and F. Their presence further expands

the mineralogical inventory of the Jabal Sayid and Dayheen intrusions and suggests the potential involvement of these minerals in controlling the behavior of these specific elements. Fluids, such as aqueous solutions or volatile-rich gases, can play a crucial role in the formation of highly fractionated pegmatites with high concentrations of the rare metals Zr, Y, Nb, REEs, U, and Th and result in the formation of economically significant mineral deposits.

6.4. Genetic Model

Overall, the evolution of the ANS during the Pan-African period was marked by intense tectonic activity, magmatic intrusions, metamorphism, and the formation of various geological structures. These processes played a crucial role in shaping the distinctive geological features observed in the AS today and contributed to the formation of mineralized granitic rocks that exhibit significant enrichments of rare metals.

The geodynamic transition observed in the Jabal Sayid and Dayheen areas, from subduction-related granodiorite–diorite association to collision-related monzogranite and finally to post-collision or anorogenic peralkaline granites and related pegmatites, can be successfully modeled by considering three distinct magmatic stages:

(a) Subduction-related magmatism: During this stage, the early mafic magma produced subduction-related granodiorite–diorite in the early stage of underplating. This mafic magma, likely derived from the subducting oceanic lithosphere, interacted with the overlying continental crust. The interaction resulted in the production of subduction-related granodiorite–diorite (Figure 16A). This stage represents the initial phase of magmatic activity related to subduction. Slab breakoff can lead to a change in subduction dynamics and the cessation of subduction-related magmatism. Subduction initiation and the formation of arc terranes occurred between 870 and 620 Ma [10].

(b) Collision-related magmatism: As the tectonic processes continued, crustal thickening occurred in the region, and consequently the subducted oceanic slab broke off (Figure 16B). The deeper portions of the overlying crust, composed of metatonalites and graywackes, were subjected to increased pressure and temperature conditions. These conditions brought these rocks above their solidus temperatures, leading to partial melting. The resulting melt contributed to the early mafic magma, giving rise to a new generation of intermediate magma that produced monzogranites. Ref. [6] reported zircon U-Pb ages of 625 $\pm$ 11 Ma for the hornblende–biotite granite and 613 $\pm$ 4 Ma for the monzogranite in the core of the Dayheen ring complex. These ages suggest that the monzogranite is younger than the rimmed hornblende–biotite granite. This age relationship contradicts the interpretation based on the present geochemical results, which suggest that the monzogranite is related to the collision stage, while the hornblende–biotite granite formed later in a post-collision stage. This implies that the monzogranite in the core of the ring complex is indeed older than the peralkaline rocks in the rim, consistent with the geological fact that the monzogranite was emplaced earlier than the rimmed granitic rocks, as stated by [56].

(c) Post-collision magmatism: The geochemistry and previous geochronology show that the Dayheen and Jabal Sayid rare-metal-bearing peralkaline granites and related pegmatites were probably generated in a post-collision extensional setting. During this stage, anatexis, or partial melting, took place in the crustal material, leading to the generation of a new magma, which produced peralkaline granites and related pegmatites (Figure 16C). The magma composition was likely influenced by progressive chemical fractionation processes, which caused the development of peralkaline A-type granites and related pegmatites. The development of the Najd fault system is believed to have facilitated the ascent of magmas and the formation of peralkaline granitoids within the AS [9,57–61]. This fault system provided pathways for the upward migration of magmas from deeper levels to shallower crustal levels, where they eventually crystallized and formed peralkaline granitoids. The extensive crystal-

lization and differentiation processes that occur during the emplacement and cooling of post-collision granite magma can lead to the enrichment of rare metals and other related elements in the Jabal Sayid and Dayheen areas.

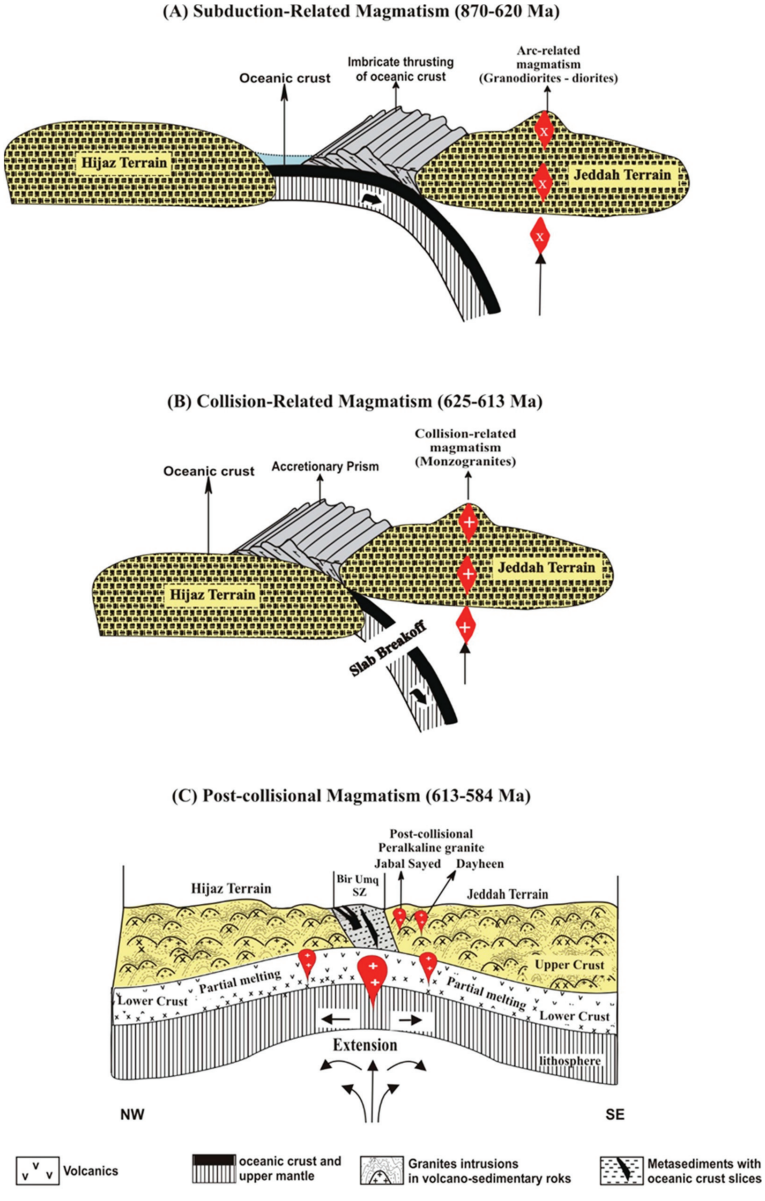

Figure 16. A simplified model for the tectonomagmatic evolution of the juvenile crust in the Jabal Sayid and Dayheen areas, the western AS of Saudi Arabia. (**A**) The subduction of the oceanic crust, ophiolite detachment, and thrusting along the Bir Umq suture zone with the arc volcanism and arc-related plutonism of the granodiorite–diorite association. (**B**) The collisional phase, crustal anatexis, and monzogranite intrusions. (**C**) The partial melting of the crustal material leads to the generation of peralkaline granites and related pegmatites in post-collisional extension settings. The crust and mantle thickness are not to scale.

The reported ages of the peralkaline granites in Jabal Sayid and Dayheen are in agreement with the broader post-orogenic or anorogenic plutonic activity that occurred in the Arabian-Nubian Shield (AS) between 680 and 550 Ma, as documented by [62]. Ref. [63] reported a whole-rock Rb-Sr isochron age of 584 ± 26 Ma for the Dayheen ring complex, indicating the timing of granite emplacement in that area. This age aligns with the estimated age of zircon from the alkali granite at Jabal Sayid, which is reported as 593 ± 2.4 Ma, according to [7]. Furthermore, ref. [10] reported zircon U-Pb ages for various granitic rocks in the Dayheen area, including the hornblende–biotite granite, microgranite, and aegirine–riebeckite granites. These ages range from 613.3 ± 8.1 Ma to 596 ± 5.6 Ma. The ages reported by [7,10] are in close agreement, indicating that the emplacement of peralkaline granites in the Dayheen and Jabal Sayid areas occurred between 613 and 584 Ma.

The εNd values of the Jabal Sayid and Dayheen plutons are positive and relatively uniform, demonstrating similarity to the Jabal Sayid and Dayheen plutons in the Jeddah Terrane. The initial εNd for the alkaline granite in Jabal Sayid is +4.9 to 5.3 [7], while that of the Dayheen monzogranite, hornblende–biotite granite, and aegirine granite is +4.1 to 5.3 [6]. The observed similarity in isotopic composition between the Jabal Sayid and Dayheen peralkaline granites suggests a homogeneous isotopic signature in the source region. This similarity implies that these granites and their associated pegmatites were likely derived from the partial melting of the lower part of the juvenile AS crust. It is possible that the melting process involved the lower crust with or without direct contributions from upper mantle materials. This interpretation aligns with the findings of [10], who concluded that the granitic rocks in the Dayheen ring complex primarily originated from the juvenile crust, although there may have been some involvement of mantle-derived materials. Ref. [64] concluded that the S-type two-mica granitoids in the Bafoussam area of western Cameroon had heterogeneous isotopic signatures, which they attributed to anatectic melts of the upper continental crust with variable contributions from the lower continental crust or mantle melts. It is worth mentioning that the present geochemical data do not support a hybridized source for the formation of the Jabal Sayid and Dayheen peralkaline granites. If hybridization had occurred, it would likely result in scattered isotope signatures of Sm-Nd. However, the restricted εNd values observed in Jabal Sayid and Dayheen suggest a more homogeneous source without significant hybridization.

7. Conclusions

The Jabal Sayid and Dayheen ring complexes provide valuable insights into the geological processes that govern the enrichment and segregation of rare metals, particularly in highly evolved peralkaline granites and associated pegmatites. In the Dayheen ring complex, the central part of the complex consists predominantly of monzogranites. Towards the outermost part of the complex, there is a transition to hornblende–biotite granites, followed by aegirine–riebeckite granite. This zonation of granitic rock types indicates variations in the chemical composition and evolution of the magmatic system within the complex. The Jabal Sayid granites, on the other hand, intrude into the Late Proterozoic volcano-sedimentary unit of the Mahd Group. The granites in this area are primarily peralkaline and are accompanied by a sheet-like pegmatite body.

The evolution from an early granodiorite–diorite association to intermediate monzogranites and peralkaline granites with associated pegmatites can be successfully explained by the involvement of three different magma generations. During the early phase of underplating, which took place between 870 and 620 Ma, the first mafic magma was generated. This mafic magma led to the formation of the granodiorite–diorite association. This stage represents the first phase of magmatic activity associated with subduction. As tectonic processes continued, crustal thickening occurred, and the subducted oceanic plate broke away, leading to collisional magmatism (625–613 Ma). The deep parts of the overlying crust partially melted, and monzogranites were formed. During the post-collisional phase, which took place between 613 and 584 Ma, the crustal material underwent anatexis, i.e., the partial melting of the pre-existing rocks due to increased heat and pressure. This anatexis led to

the formation of magmas that produced peralkaline granites and associated pegmatites through progressive chemical fractionation. This process can result in the enrichment of certain elements, including rare metals such as Zr, Y, Nb, REEs, U, and Th, in the residual melt. As the peralkaline granitic magmas underwent progressive chemical fractionation, they became increasingly enriched in these rare metals. The ascent of these magmas from deeper levels to shallower depths was likely facilitated by the Najd fault system. The interaction of the ascending magmas with surrounding rocks and fluids further influenced their composition and mineralogy. Fluids, such as aqueous solutions or volatile-rich gases, can contribute to the formation of highly fractionated pegmatites. These fluids can interact with the evolving magmas, causing further chemical differentiation and promoting the crystallization of rare-metal-bearing minerals within the pegmatites. The enrichment of rare metals within the Jabal Sayid and Dayheen peralkaline granites and related pegmatites can lead to the development of economically significant mineral deposits, making them of interest for mineral exploration and extraction.

Author Contributions: Methodology, H.H.A.E.-N. and Y.H.D.; formal analysis, H.H.A.E.-N. and Y.H.D.; investigation, H.H.A.E.-N. and Y.H.D.; resources, H.H.A.E.-N.; data curation, Y.H.D.; writing—original draft, H.H.A.E.-N.; writing—review and editing, H.H.A.E.-N. and Y.H.D.; visualization, H.H.A.E.-N. and Y.H.D.; supervision, Y.H.D.; project administration, H.H.A.E.-N.; funding acquisition, H.H.A.E.-N. All authors have read and agreed to the published version of the manuscript.

Funding: This research work was funded by Institutional Fund Projects under grant no. (IFPIP-1441-145-1443).

Institutional Review Board Statement: Not applicable.

Informed Consent Statement: Not applicable.

Data Availability Statement: The data presented in this study are contained within the article.

Acknowledgments: The authors gratefully acknowledge technical and financial support from the Ministry of Education and King Abdulaziz University, Jeddah, Saudi Arabia. We would like to express our gratitude to the reviewers for their valuable comments and suggestions, which have greatly contributed to improving the quality of this manuscript.

Conflicts of Interest: The authors declare no conflict of interest.

References

1. Drysdall, A.R.; Douch, C.J. Nb–Th–Zr mineralization in microgranite—Microsyenite at Jabal Tawlah, Midyan region, Kingdom of Saudi Arabia. *J. Afr. Earth Sci.* **1986**, *4*, 275–288.
2. Küster, D. Granitoid-hosted Ta mineralization in the Arabian-Nubian Shield: Ore deposit types, tectono-metallogenetic setting and petrogenetic framework. *Ore Geol. Rev.* **2009**, *35*, 68–86. [CrossRef]
3. Johnson, P.R.; Andresen, A.; Collins, A.S.; Fowler, A.R.; Fritz, H.; Ghebreab, W.; Kusky, T.; Stern, R.J. Late Cryogenian-Ediacaran history of the Arabian-Nubian Shield: A review of depositional, plutonic, structural, and tectonic events in the closing stages of the northern East African Orogen. *J. Afr. Earth Sci.* **2011**, *61*, 167–232. [CrossRef]
4. Moghazi, A.M.; Harbi, H.M.; Ali, K.A. Geochemistry of the Late Neoproterozoic Hadb adh Dayheen ring complex, Central Arabian Shield: Implications for the origin of rare-metal-bearing post-orogenic A-type granites. *J. Asian Earth Sci.* **2011**, *42*, 1324–1340. [CrossRef]
5. Bakhsh, R.A.M. Granites from the Midyan Terrain, NW Saudi Arabia: Petrology, Geochemistry and Geochronology. Ph.D. Thesis, Royal Holloway, University of London, Egham, UK, 2013; 250p.
6. Ali, K.A.; Jeon, H.; Andresen, A.; Li, S.Q.; Harbi, H.M.; Hegner, E. U-Pb zircon geochronology and Nd-Hf-O isotopic systematics of the Neoproterozoic Hadb adh Dayheen ring complex, Central Arabian Shield, Saudi Arabia. *Lithos* **2014**, *206–207*, 348–360. [CrossRef]
7. Moghazi, A.K.M.; Iaccheri, L.M.; Bakhsh, R.A.; Kotov, A.B.; Ali, K.A. Sources of rare-metal-bearing A-type granites from Jabel Sayed complex, northern Arabian shield, Saudi Arabia. *J. Asian Earth Sci.* **2015**, *107*, 244–258. [CrossRef]
8. Aseri, A.A. Rare-Metal Alkaline Granite from the Arabian Shield, Saudi Arabia. Electronic Thesis and Dissertation Repository. 6822. 2020. Available online: https://ir.lib.uwo.ca/etd/6822 (accessed on 1 March 2020).
9. Abuamarah, B.A.; Azer, M.K.; Asimow, P.D.; Shi, Q. Petrogenesis of the post-collisional rare-metal-bearing Ad-Dayheen granite intrusion, Central Arabian Shield. *Lithos* **2021**, *384–385*, 105956. [CrossRef]

10. Tong, Q.; Li, Z.; Fan, H.; Jahdali, N.; Al-Nahdi, M.M. Petrogenesis and Tectonic Implications of the Jabal Hadb Ad Dayheen Granitic Complex, Central Arabian Shield. *J. Earth Sci.* **2023**, *34*, 20–36. [CrossRef]
11. Worku, H.; Schandelmeier, H. Tectonic evolution of the Neoproterozoic Adola Belt of southern Ethiopia: Evidence for a Wilson Cycle process and implications for oblique plate collision. *Precambrian Res.* **1996**, *77*, 179–210. [CrossRef]
12. Fritz, H.; Abdelsalam, M.; Ali, K.A.; Bingen, B.; Collins, A.S.; Fowler, A.R.; Ghebreab, W.; Hauzenberger, C.A.; Johnson, P.R.; Kusky, T.M.; et al. Orogen styles in the East African Orogen: A review of the Neoproterozoic to Cambrian tectonic evolution. *J. Afr. Earth Sci.* **2013**, *86*, 65–106. [CrossRef]
13. Blades, M.L.; Collins, A.S.; Foden, J.; Payne, J.L.; Xu, X.; Alemu, T.; Woldetinsae, G.; Clark, C.; Taylor, R.J.M. Age and hafnium isotopic evolution of the Didesa and Kemashi Domains, western Ethiopia. *Precambrian Res.* **2015**, *270*, 267–284. [CrossRef]
14. Radain, A.A.M.; Kerrich, R. Peralkaline granite in the western part of the Arabian Shield. *Bull. Fac. Earth Sci. King Abdulaziz Univ.* **1980**, *3*, 117–130.
15. Hackett, D. Mineralized aplite-pegmatite at Jabel Sayid, Hijaz region, Kingdom of Saudi Arabia. *J. Afr. Earth Sci.* **1986**, *4*, 257–267.
16. Kretz, R. Symbols of rock-forming minerals. *Am. Mineral.* **1983**, *68*, 277–279.
17. Calvez, J.-Y.; Alsac, C.; Delfour, J.; Kemp, J.; Pellaton, C. *Geologic Evolution of Western, Central and Eastern Parts of the Northern Precambrian Shield*; Saudi Arabian Deputy Ministry for Mineral Resources Open-File Report BRGM-OF-03-17; Ministry of Petroleum and Mineral Resources; Deputy Ministry for Mineral Resources: Jiddah, Saudi Arabia, 1983; 57p.
18. Turkistany, A.R.A. Radioactive Pegmatite and Its Host Granites of Jabal Sayid, Saudi Arabia. Master's Thesis (unpublished), King Abdulaziz University, Jiddah, Saudi Arabia, 1979.
19. Ahmed, M.I. *Report on the Reconnaissance Survey in Saudi Arabia*; Saudi Arabian Directorate General of Mineral Resources Open-File Report DGMR-69; Directorate General of Mineral Resources: Jiddah, Saudi Arabia, 1957.
20. Schaffner, D.F. *Preliminary Report on Investigation of Radioactivity at Jebel Sayid*; Saudi Arabian Directorate General Mineral Resources Open-File Report DGMR-74; Directorate General of Mineral Resources: Jiddah, Saudi Arabia, 1957.
21. Turkistany, A.R.; Ramsay, C.R. Mineralized apogranite associated with alkali granite at Jabal Sa'id, Kingdom of Saudi Arabia. *Deputy Minstry Miner. Resour.* **1982**, *PP-1*, 78–88.
22. Dawood, H.Y.; Harbi, H.M.; Abd El-Naby, H.H. Genesis of kasolite associated with aplite-pegmatite at Jabel Sayid, Hijaz region, Kingdom of Saudi Arabia. *J. Asian Earth Sci.* **2010**, *37*, 1–9. [CrossRef]
23. Bernard, B. A review of the relationships between granitoid types, their origins and their geodynamic environments. *Lithos* **1999**, *46*, 605–626. [CrossRef]
24. De La Roche, H.; Leterrier, J.; Grandelaude, P.; Marchal, M. A classification of volcanic and plutonic rocks using R1R2-diagram and major-element analyses—Its relationships with current nomenclature. *Chem. Geol.* **1980**, *29*, 183–210. [CrossRef]
25. Maniar, P.D.; Piccoli, P.M. Tectonic discrimination of granites. *Geol. Soc. Am. Bull.* **1989**, *101*, 635–643. [CrossRef]
26. Wright, J.B. A simple alkalinity ratio and its application to questions of non-orogenic granite genesis. *Geol. Mag.* **1969**, *106*, 370–384. [CrossRef]
27. Peccerillo, A.; Taylor, S.R. Geochemistry of Eocene calcalkaline volcanic rocks from the Kastamonu area, northern Turkey. *Contrib. Miner. Petrol.* **1976**, *58*, 63–81. [CrossRef]
28. Frost, B.R.; Barnes, C.G.; Collins, W.J.; Arculus, R.J.; Ellis, D.J.; Frost, C.D. A geochemical classification for granitic rocks. *J. Petrol.* **2001**, *42*, 2033–2048. [CrossRef]
29. Pearce, J.A.; Harris, N.B.W.; Tindle, A.G. Trace Element Discrimination Diagrams for the Tectonic Interpretation of Granitic Rocks. *J. Petrol.* **1984**, *25*, 956–983. [CrossRef]
30. McDonough, W.F.; Sun, S. The composition of the Earth. *Chem. Geol.* **1995**, *120*, 223–253. [CrossRef]
31. Batchelor, R.A.; Bowden, P. Petrogenetic Interpretation of Granitoid Rock Series Using Multicationic Parameters. *Chem. Geol.* **1985**, *48*, 43–55. [CrossRef]
32. Pearce, J.A. Sources and settings of granitic rocks. *Episode* **1996**, *19*, 120–125. [CrossRef]
33. Eby, G.N. Chemical subdivision of the A-type granites: Petrogenetic and tectonic implications. *Geology* **1992**, *20*, 641–644. [CrossRef]
34. Eby, G.N. The A-type granitoids: A review of their occurrence and chemical characteristics and speculations on their petrogenesis. *Lithos* **1990**, *26*, 115–134. [CrossRef]
35. Whalen, J.B.; Currie, K.L.; Chappell, B.W. A-type granites: Geochemical characteristics, discrimination and petrogenesis. *Contrib. Mineral. Petrol.* **1987**, *95*, 407–419. [CrossRef]
36. Harris, N.B.W.; Pearce, J.A.; Tendle, A.G. Geochemical Characteristics of Collision-Zone Magmatism. In *Collision Tectonics*; Coward, M.P., Ries, A.C., Eds.; Geological Society, London, Special Publications: Bath, UK, 1986; Volume 19, pp. 67–81.
37. Collins, W.J.; Beams, S.D.; White, A.J.R.; Chappell, B.W. Nature and origin of A-type granites with particular reference to southeastern Australia. *Contrib. Mineral. Petrol.* **1982**, *80*, 189–200. [CrossRef]
38. Laurent, O.; Martin, H.; Moyen, J.; Doucelance, R. The Diversity and Evolution of Late-Archean Granitoids: Evidence for the Onset of "Modern-Style" Plate Tectonics between 3.0 and 2.5 Ga. *Lithos* **2014**, *205*, 208–235. [CrossRef]
39. Tarney, J.; Jones, C.E. Trace element geochemistry of orogenic igneous rocks and crustal growth models. *J. Geol. Soc. Lond.* **1994**, *151*, 855–868. [CrossRef]
40. Gerdes, A.; Montero, P.; Bea, F.; Fershater, G. Peraluminous granites frequently with mantle-like isotope compositions: The continental-type Murzinka and Dzhabyk batholiths of the eastern Urals. *Int. J. Earth Sci.* **2002**, *91*, 3–19. [CrossRef]

41. Crawford, M.B.; Windley, B.F. Leucogranites Himalaya/Karakoram: Implications for magmatic evolution within collisional belts and the study of collision related leucogranite petrogenesis. *J. Volcanol. Geothermal. Res.* **1990**, *44*, 1–19. [CrossRef]
42. Liégeois, J.P.; Bertrand, J.M.; Black, R. The subduction and collision-related Pan-African composite batholith of the Adrar des Iforas (Mali): A review. *Geol. J.* **1987**, *22*, 185–211. [CrossRef]
43. Kemp, A.I.S.; Hawkesworth, C.J.; Foster, J.L.; Paterson, B.A.; Woodhead, J.D.; Hergt, J.M.; Gray, C.M.; Whitehouse, M.J. Magmatic and crustal differentiation history of granitic rocks from Hf-O isotopes in zircon. *Science* **2007**, *315*, 980–983. [CrossRef] [PubMed]
44. Liégeois, J.P.; Navez, J.; Hertogen, J.; Black, R. Contrasting origin of post-collisional high-K calc-alkaline and shoshonitic versus alkaline and peralkaline granitoids: The use of sliding normalization. *Lithos* **1998**, *45*, 1–28. [CrossRef]
45. Eyal, M.; Litvinovsky, B.; Jahn, B.M.; Zanvilevich, A.; Katzir, Y. Origin and evolution of post-collisional magmatism: Coeval Neoproterozoic calc-alkaline and alkaline suites of the Sinai Peninsula. *Chem. Geol.* **2010**, *269*, 153–179. [CrossRef]
46. Gahlan, H.A.; Azer, M.K.; Asimow, P.D.; Al-Hashim, M.H. Geochemistry, Petrogenesis and Alteration of Rare-Metal-Bearing Granitoids and Mineralized Silexite of the Al-Ghurayyah Stock, Arabian Shield, Saudi Arabia. *J. Earth Sci.* **2023**, *34*, 1488–1510. [CrossRef]
47. Münker, C.; Pfänder, J.A.; Weyer, S.; Büchl, A.; Kleine, T.; Mezger, K. Evolution of planetary cores and the Earth–Moon system from Nb/Ta systematics. *Science* **2003**, *301*, 84–87. [CrossRef]
48. Pfänder, J.A.; Münker, C.; Stracke, A.; Mezger, K. Nb/Ta and Zr/Hf in Ocean Island Basalts—Implications for Crust-Mantle Differentiation and the Fate of Niobium. *Earth Planet. Sci. Lett.* **2007**, *254*, 158–172. [CrossRef]
49. Hofmann, A.W. Chemical differentiation of the Earth: The relationship between mantle, continental crust, and oceanic crust. *Earth Planet. Sci. Lett.* **1988**, *90*, 297–314. [CrossRef]
50. Wedepohl, K.H. The Composition of the Continental-Crust. *Geochim. Cosmochim. Acta* **1995**, *59*, 1217–1232. [CrossRef]
51. Qadhi, T.M. Origin and hydrothermal alteration of rare-metal granites in the Al-Hamra area, northeastern Arabian Shield, Saudi Arabia. *Cent. Eur. Geol.* **2007**, *50*, 259–282. [CrossRef]
52. Jarrar, G.H.; Mantonb, W.I.; Stern, R.J.; Zachmann, D. Late Neoproterozoic A-type granites in the northernmost Arabian-Nubian Shield formed by fractionation of basaltic melts. *Geochemistry* **2008**, *68*, 295–312. [CrossRef]
53. Awad, A.A.; Abu El-Leil, A.; Nastavkin, A.V.; Tolba, A.; Kamel, M.; El-Wardany, R.M.; Rabie, A.; Ene, A.; Tekin, H.O.; Issa, S.A.M.; et al. Statistical analysis on the radiological assessment and geochemical studies of granite rocks in the north of Um Taghir area, Eastern Desert, Egypt. *Open Chem.* **2022**, *20*, 254–266. [CrossRef]
54. Abd El-Naby, H.H.; Dawood, Y.H.; Sabtan, A.; Al Yamani, M. Significance of radioelements distribution in the Precambrian rocks of Jabel Sayid, western Saudi Arabia, using spectrometric and geochemical data. *Resour. Geol.* **2020**, *71*, 105–122. [CrossRef]
55. Moghazi, A.M.; Ali, K.A.; Wilde, S.A.; Zhou, Q.; Andersen, T.; Andresen, A.; El-enen, M.M.A.; Stern, R.J. Geochemistry, geochronology, and Sr–Nd isotopes of the Late Neoproterozoic Wadi Kid volcano-sedimentary rocks, Southern Sinai, Egypt: Implications for tectonic setting and crustal evolution. *Lithos* **2012**, *154*, 147–165. [CrossRef]
56. Radain, A.A. Petrogenesis of Some Peralkaline and Non-Peralkaline Post-Tectonic Granites in the Arabian Shield, Kingdom of Saudi Arabia. Ph.D. Thesis, University of Western Ontario, London, ON, Canada, 1978.
57. Brown, G.B. *Tectonic Map of the Arabian Peninsula. Saudi Arabian Directorate General of Mineral Resources Map, Scale 1:4,000,000*; USGS: Reston, VA, USA, 1972.
58. Greenwood, W.R.; Hadley, D.G.; Anderson, R.E.; Fleck, R.J.; Schmidt, D.L. Late Proterozoic cratonization in southwestern Saudi Arabia. *Philos. Transact. R. Soc. Lond. Ser. A* **1976**, *280*, 517–527.
59. Greenwood, W.R.; Anderson, R.E.; Fleck, R.J.; Robert, R.J. Precambrian geologic history and plate tectonic evolution of the Arabian Shield. *Saudi Arab. Dir. Miner. Resour. Bull.* **1980**, *24*, 35.
60. Stoeser, D.B.; Jackson, N.J.; Ramsay, C.R.; Drysdall, A.R.; Du Bray, E.A.; Douch, C.J. *Map of Plutonic Rocks in the Arabian Shield, Kingdom of Saudi Arabia (Northern Sheet)*; Saudi Arabian Deputy Ministry for Mineral Resources Technical Record USGS-TR-04-5; USGS: Reston, VA, USA, 1985.
61. Abdallah, S.E.; Azer, M.K.; Al Shammari, A.S. The Petrological and Geochemical Evolution of Ediacaran Rare-Metal Bearing A-Type Granites from the Jabal Aja Complex, Northern Arabian Shield, Saudi Arabia. *Acta Geol. Sin.* **2020**, *94*, 743–762. [CrossRef]
62. Nehlig, P.; Genna, A.; Asfirane, F. A review of the Pan-African evolution of the Arabian shield. *GeoArabia* **2002**, *7*, 103–124. [CrossRef]
63. Calvez, J.Y.; Kemp, J. *Geochronological Investigations in the Mahd Ahd Dhahab Quadrangle, Central Arabian Shield: Saudi Arabian Deputy Ministry for Mineral Resources*; Technical Report BRGM-TR-02-5; USGS: Reston, VA, USA, 1982.
64. Djouka-Fonkwe, M.L.; Schulz, B.; Schüssler, U.; Tchouankoue, J.-P.; Nzolang, C. Geochemistry of the Bafoussam Pan-African I- and S-type granitoids in western Cameroon. *J. Afr. Earth Sci.* **2008**, *50*, 148–167. [CrossRef]

applied sciences

MDPI

Article

Genesis of Cu-Sn Mineralization in the Shuangjianzishan Super-Large Silver Deposit, Inner Mongolia: Trace Element Constraints from Chalcopyrite and Cassiterite

Yu Liu [1], Biao Jiang [1,*], Yuchuan Chen [1], Liwen Wu [2], Yushan Zuo [2] and Zhao Liu [2]

[1] MNR Key Laboratory of Metallogeny and Mineral Assessment, Institute of Mineral Resources, Chinese Academy of Geological Sciences, Beijing 100037, China; liuyu201801050205@163.com (Y.L.)
[2] Inner Mongolia Autonomous Region Geological Survey Institute, Huhhot 010020, China
* Correspondence: jiangbiao334223@163.com

Abstract: The Shuangjianzishan silver polymetallic deposit is located in the copper–tin–lead–zinc–silver polymetallic metallogenic belt in the Southern Great Xing'an Range, with silver resources of more than 18,000 t, which is the largest silver polymetallic deposit in Asia. Early studies concluded that the Shuangjianzishan deposit is typically an epithermal Ag-Pb-Zn deposit that lacks a high-temperature mineralization stage. In recent years, with the deepening of research, a large amount of Cu-Sn mineralization has been found in the deep part of the Shuangjianzishan deposit, but it is less studied. The laser-ablation inductively coupled mass spectroscopy (LA-ICP-MS) technique is used to investigate the distribution and substitution of trace elements in chalcopyrite and cassiterite. In this paper, the trace element study of chalcopyrite and cassiterite from the Shuangjianzishan deposit reveals that Sn, In, As, Se, Sb, and Tl mainly exist in chalcopyrite in isomorphic form, while Pb, Bi, and Ni mainly exist in chalcopyrite in the form of mineral inclusions. The enrichment of the high-temperature elements Sn and Se in chalcopyrite, and the deficit of the middle- and low-temperature elements Ga, Sb, etc., reflect that the chalcopyrite in the Shuangjianzishan deposit was formed in a middle- and high-temperature environment, and it also indicates that the early ore-forming hydrothermal solution may be rich in Sn. Fe, In, Co, and Ni mainly exist in cassiterite in isomorphic form, and the content of W in cassiterite is high. There are two main forms, one is isomorphic and the other is wolframite inclusion. Cassiterite has Fe-rich and W-U-poor characteristics, indicating that cassiterite from the Shuangjianzishan deposit was formed under relatively oxidized conditions, and the relative enrichment of elements such as Fe, W, Zr, and Hf indicates that the temperature of cassiterite formation was high. The elemental content and inter-ionic coupling relationships suggest that the cassiterite from the Shuangjianzishan deposit may have an elemental replacement mechanism of $W^{6+} + Fe^{2+} \leftrightarrow 2Sn^{4+}$ or $Fe^{3+} + OH^{-} \leftrightarrow Sn^{4+} + O^{2-}$. The trace elements in cassiterite of the Shuangjianzishan deposit are rich in Fe and Mn and depleted in Nb and Ta, according to the Fe-W diagram, and the tin mineralization of the Shuangjianzishan deposit belongs to cassiterite–sulfide-type tin mineralization. Chalcopyrite Co/Ni ratios >1 are consistent with the characteristics of chalcopyrite genesis in hydrothermal deposits.

Keywords: the Shuangjianzishan deposit; tin mineralization; deposit genesis; trace element

Citation: Liu, Y.; Jiang, B.; Chen, Y.; Wu, L.; Zuo, Y.; Liu, Z. Genesis of Cu-Sn Mineralization in the Shuangjianzishan Super-Large Silver Deposit, Inner Mongolia: Trace Element Constraints from Chalcopyrite and Cassiterite. *Appl. Sci.* **2024**, *14*, 3822. https://doi.org/10.3390/app14093822

Academic Editor: Mauro Marini

Received: 17 March 2024
Revised: 4 April 2024
Accepted: 4 April 2024
Published: 30 April 2024

1. Introduction

The Great Xing'an Range is in a region where two global tectonic mineralization domains, the Paleozoic Paleo-Asian Ocean Tectonic Mineralization Domain and the Mesozoic Paleo-Pacific Ocean Tectonic Mineralization Domain, are strongly superimposed. On the basis of the ancient basement tectonics and the Late Paleozoic orogenic belt, the Mesozoic volcanic–magmatic activities were intense, and the polymetallic metallogenetic belts of Cu-Sn-Mo-Pb-Zn-Ag were formed. As an important Pb-Zn-Ag polymetallic ore-concentrated area in China, the southern section of the Great Xing'an Range has more than 30 Ag-Pb-Zn

deposits in the area, with a total Ag resource of more than 57,000 t, making it the largest silver-metallogenic province in China [1]. Important Ag-Pb-Zn hydrothermal deposits include the Shuangjianzishan, Bianjiadanyuan, Weilasituo, and Bairendaba deposits. With the deepening of theoretical research and geological work, a number of tin polymetallic deposits have been discovered in the district, such as the Huanggang, Maodeng, Baiyinnuoer, Baiyinchagan, Weilasituo, and Bianjiadayuan. These hydrothermal tin polymetallic mineralizations are closely related to vein Pb-Zn-Ag polymetallic mineralization, showing good prospects for finding tin polymetallic resources [2]. Overall, the Sn-Cu-Pb-Zn-Ag polymetallic system has a similar vertical zonation, with Sn-Cu(-W) mineralization developed at depth and associated with highly fractionated granite bodies, while Ag-Pb-Zn is close to the shallow surface and fracture-controlled [3]. The intrinsic genesis relationship between medium- and high-temperature tin mineralization and medium- and low-temperature Cu-Pb-Zn-Ag mineralization has long been debated. The debate centers on the spatial distance, and the age difference between the Pb-Zn-Ag mineralization and the rock mass makes it difficult to establish a genesis link between the mineralization and the rock mass [4], restricting the exploration of the mineral sources of Pb-Zn and Cu-Sn mineralization [5]. A previous study held that the Shuangjianzishan deposit is typically an epithermal Ag-Pb-Zn deposit that lacks a high-temperature mineralization stage [6–9]. In recent years, some scholars found abundant Cu-Sn mineralization in the ore and drill holes of the Shuangjianzishan deposit and concluded that the Shuangjianzishan deposit has great potential for Cu-Sn mineralization [10,11]. As the discovery of copper–tin mineralization in the Shuangjianzishan deposit is still recent, less work has been carried out on the metallogenic chronology and mineralogy of chalcopyrite and cassiterite. Chalcopyrite and cassiterite, as important ore minerals in the copper–tin mineralization stage, often contain a variety of trace elements [12,13] and contain rich metallogenic information, which is an important indication of the formation process and genesis type of the deposit [14,15]. At present, there are more studies on pyrite [16], sphalerite, and galena, but the trace element characteristics of chalcopyrite and cassiterite are seldom reported. In this paper, we carry out detailed mineralogical and LA-ICP-MS trace element studies on chalcopyrite and cassiterite from the Shuangjianzishan deposit to reveal the trace element characteristics of chalcopyrite and cassiterite and their relationship with the genesis of the deposit.

2. Regional Geology

The Shuangjianzishan silver–polymetallic deposit in Inner Mongolia is located in the southern section of the Great Xing'an Range's silver–lead–zinc–tin–rare metal metallogenic belt. The geotectonic location belongs to the eastern part of the Xing'an–Mongolia orogenic belt, in the geosynclinal fold system of Middle Inner Mongolia, surrounded by the Siberian Plate and the North China Plate; bounded by the Xilamulun Fault Zone, Erenhot–Hegenshan fault belt, and Nenjiang fault belt; and connected with the North China Craton, Xing'an Block, and Songliao Basin, respectively (Figure 1a). Since the Paleozoic, the study area was successively affected by the subduction collision and splicing system due to the development and demise of the Paleo-Asian Ocean, the continuous subduction of the Mongolia–Okhotsk Plate on the Siberian Plate, and the subduction tectonic system of the Pacific Rim, which realized the obvious transformation from the compressional tectonic system to the extensional tectonic system in the late Mesozoic [17–19]. Under the complex tectonic background, the deep fractures and secondary fracture structures in the region are extremely developed, showing a lattice fracture system based on two northeast-trending deep fractures, namely, the Xar Moron Fault Zone and the Hegenshan–Nenjiang Fault Zone, and the extensive development of NW-, NNE-, and near-EW-trending secondary fractures, which provide transportation channels and metallogenic space. Under such favorable mineralization conditions, there are a series of large-scale and super-large Ag-Pb-Zn polymetallic deposits and Sn polymetallic deposits, such as the Baiyinnuoer large Pb-Zn deposit, Huaaobaote large Ag polymetallic deposit, Bairendaba super-large Ag polymetallic deposit, Haobugao large Pb-Zn polymetal-

lic deposit, Huangganglianq super-large Fe-Sn polymetallic deposit, and Weilasituo Sn polymetallic deposit, owing considerable prospecting potential (Figure 1b). The district is dominated by Late Paleozoic strata and Mesozoic volcanic complex rock mass, except for some small-scale exposures of Early Proterozoic Xilingol metamorphic assemblages in some areas. The area is mainly dominated by emerging Permian strata, the Carboniferous System exposes a set of marine clastic rocks of the Middle Carboniferous Benbatu Formation and the Upper Carboniferous Amushan Formation, and the Permian System from the oldest to the newest exposes the Lower Permian Shoushangou Formation, the Lower Permian Dashizhai Formation, the Middle Permian Zhesi Formation, the Upper Permian Huangganglianq Formation, and the Upper Permian Linxi Formation. Most of the deposits in the southern section of the Great Xing'an Range are hosted in Permian strata [20], and in particular, the volcanic-sedimentary construction of the Dashizhai Formation is an important ore-holding stratum for silver, lead, and zinc polymetallic deposits in the region. The Mesozoic mainly exposed a set of Jurassic–Cretaceous volcaniclastic rock, which are the Xinmin Formation, Manketouebo Formation, Manitou Formation, Baiyingaolao Formation, and Meilertu Formation from bottom to top. There are frequent magmatic activities in the area, and the intrusions of the Hercynian, Indo-Chinese, and Yanshanian period are all developed, which are mainly controlled by the NE-trending fault structure. The Mesozoic magmatic rocks are most widely distributed, and the lithology is mainly granite porphyry, dioritic porphyrite, and quartz syenite, which are closely related to mineralization.

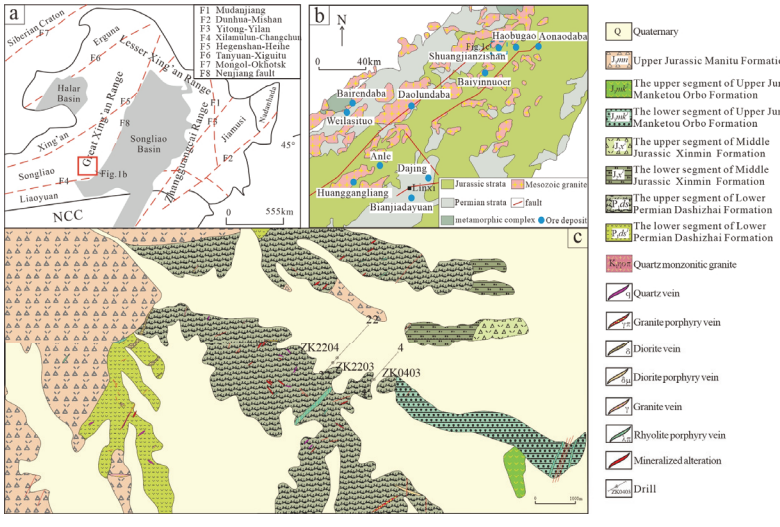

Figure 1. (**a**) Tectonic sketch of NE China (modified after [8]. The red box indicates the approximate scope of (**b**). (**b**) Regional geological map of the southern section of Great Xing'an Range (modified after [9]). (**c**) Geological sketch map of Xinglongshan ore section in the Shuangjianzishan deposit.

3. Deposit Geology

The Shuangjianzishan deposit is geographically located in the Fuhe Town, Balin Left Banner, Inner Mongolia. The geographic coordinates of the center of the mine are 119°07′ E and 44°30′ N. There are two ore sections in the mine, the eastern Xinglongshan section and the western Shuangjianzishan section, both of which are 4.7 km apart. The mineralization of the Shuangjianzishan section is weaker and the working degree is lower, while the ore body of the Xinglongshan section is larger and the exploration degree is higher. In the mine area, mainly the Lower Permian Dashizhai Formation (P_1d) slate and volcanic-sedimentary rocks, Middle Jurassic Xinmin Formation (J_2x) volcaniclastic and volcaniclastic sedimentary rocks, Upper Jurassic Manketouebo Formation (J_3m) acidic volcanic lava, clastic rocks and volcaniclastic sedimentary rocks, and Quaternary Holocene (Qh) alluvion are exposed

(Figure 1c). The ore body is mainly hosted in the stratum of the Dashizhai Formation, and locally extends to the stratum of the Xinmin Formation. Only dioritic porphyrite, granite, granite porphyry, rhyolite porphyry, quartz veins, and other vein rocks are exposed in the area, and the intrusive rocks are mainly granitic rocks, which are not exposed on the surface. Fold tectonics in the mine is relatively simple, the mine is located in the northwest wing of the Linxi-Zhesi anticlinorium, and the Dashizhai Formation strata is generally monoclinic tectonics, NW-trending, with a dip angle of 55°~60°. The fracture structure is very developed in the mining area, controlling the output of the ore body. There are mainly NW-trending, NNE-trending, and near-NS-trending fracture structures, of which the NW-trending ductile shear zone is the most important ore-controlling fracture zone, controlling the output of the NW-trending Ag polymetallic vein group. The ore bodies, in order of mineralization, are the NW-trending Ag polymetallic vein group, the NE-trending ore body, and the near-NS-trending ore body (Figure 2a). The ore bodies are generally lenticular, vein-like, and stratiform-like (Figure 2b). The alteration of the wall rocks near the mine mainly includes silicification, chloritization, pyritization, and carbonatation, followed by sericitization and kaolinization. Among them, silicification and pyritization are closely related to silver, lead, and zinc mineralization. The ore structure is mainly of subhedral–euhedral texture, followed by metasomatic texture, emulsion texture, poikilitic texture, lamellar texture, etc. The ore structures are of brecciated structure, mesh vein structure, banded structure, disseminated structure, dense block structure, and so on. The main metallic minerals are pyrite, galena, sphalerite, chalcopyrite, cassiterite, pyrrhotite, arsenopyrite, canfieldite, kustelite, polybasite, aguilarite, acanthite, stephanite, pyrargyrite, freibergite, native silver, argentite, etc. Gangue minerals include quartz, calcite, chlorite, epidote, and so on.

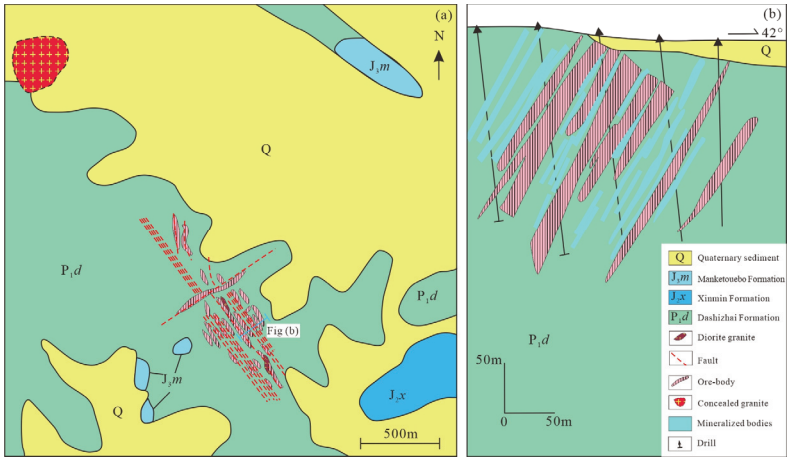

Figure 2. Geological plan of Xinglongshan ore section in the Shuangjianzishan deposit (**a**); typical profile (**b**) (modified after [21]).

4. Characteristics of Copper–Tin Mineralization

The newly revealed copper–tin mineralization mainly appears in the Xinglongshan ore section. Wu [10] found a large amount of tin mineralization in the NW-trending ore body and drill core at level 625 of the Xinglongshan ore section. The massive lead–zinc ore at level 625 contains copper (5.67%) and tin (2.35%), and the Cu and Sn grades in the Cu-rich ore in the drilling hole are 12.98% and 4.75%, respectively. There is a lack of Cu-Sn mineralization in the NE-trending ore body. Wu [22] further divided the NW-trending silver polymetallic vein group into silver–copper polymetallic ore bodies developed on the hanging wall of the ductile shear zone and silver–lead–zinc polymetallic ore bodies on the footwall, with the silver–copper polymetallic ore bodies being the main tin-bearing ore

bodies. Tin mineralization is marked by the occurrence of large quantities of canfieldite and cassiterite, accompanied by assemblages of medium- and high-temperature minerals such as chalcopyrite, arsenopyrite, and wolframite. The selenite-rich canfieldite is coeval with sphalerite and galena, and cassiterite is mainly produced in fine grains or fine columns, often parceled by sphalerite, galena, and chalcopyrite (Figure 3d), or may be produced in cassiterite–quartz veins. Ma [11] pointed out that copper mineralization developed sporadically around −300 m and developed on a large scale at a depth of −700 m, and the spatial pattern of change in the vertical direction is as follows: −400 m to the surface is dominated by fine-veined, low-dipping Py-Pb-Zn veins; between −400 and −900 m is characterized by thicker veins, high-dipping, or near-erect Pb-Zn veins; and there are lead–zinc–copper ore bodies below −900 m. From west to east on the plane: At the same elevation, relatively high-temperature Cu-Sn assemblages are more developed in the western part of the mine than in the eastern part of the drill core. Copper ores are produced in massive (Figure 3a), disseminated (Figure 3b), brecciated (Figure 3c), and vein structures. The metallic minerals are mainly chalcopyrite, sphalerite, galena, pyrite, and arsenopyrite. Chalcopyrite in hand specimens is often coeval with quartz, chlorite, and calcite. Microscopic chalcopyrite is often metasomatized for by galena, sphalerite, etc. (Figure 3f), or chalcopyrite is distributed in sphalerite as an emulsion texture (Figure 3e), but it is not the focus of this study.

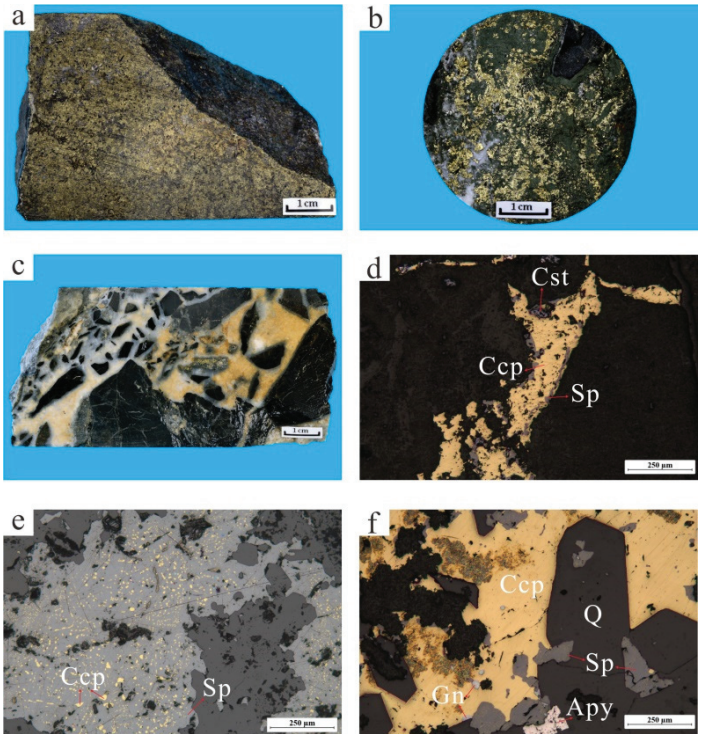

Figure 3. Copper–tin mineralized hand specimen and microscopic characteristics of the Shuangjianzishan silver polymetallic deposit. (**a**) Massive structure; (**b**) dense disseminated structure; (**c**) brecciated structure; (**d**) chalcopyrite is replaced by sphalerite and cassiterite is parceled by chalcopyrite; (**e**) chalcopyrite is distributed in sphalerite as emulsion texture; (**f**) chalcopyrite and arsenopyrite are replaced by galena and sphalerite. Apy—arsenopyrite; Ccp—chalcopyrite; Sp—sphalerite; Gn—galena; Cst—cassiterite; Q—quartz.

5. Sampling and Analytical Methods

The chalcopyrite and cassiterite samples used in this study were taken from fresh rock cores and ores in drills ZK0403 and ZK2204 and tunnels. The collected samples were ground into optically thin sections for mineralogical observation, and representative points were selected to carry out electron microprobe analysis (EMPA) and finally LA-ICP-MS in situ trace element analysis.

On the basis of detailed microscopic observation, the major and trace element fractions of cassiterite were determined. The electron microprobe analysis (EMPA) of cassiterite was completed at the Key Laboratory of Mineralization and Resource Evaluation, Institute of Mineral Resources, Chinese Academy of Geological Sciences, and the testing instrument was a JEOL JXA-iHP200F field emission electron microprobe (Figure 4). The accelerating voltage was 15 kV, the beam current was 20 nA, the electron beam spot diameter was 5 μm, and the tested elements included F, Si, Mg, Zr, Ca, Fe, Hf, Sn, Sr, and Th, using natural minerals or the national standards of synthetic metal oxides as the standard sets. The data were uniformly corrected by ZAF.

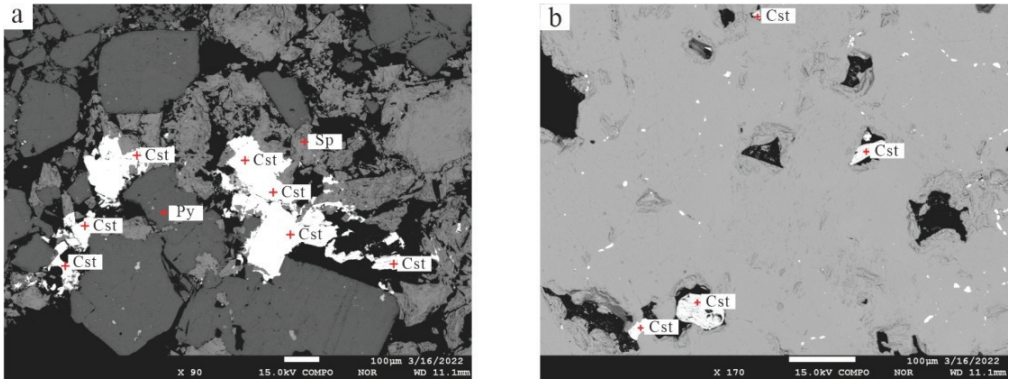

Figure 4. Electron probe BES of minerals in the Shuangjianzishan silver polymetallic deposit, Inner Mongolia. (**a**) Cassiterite is parceled by sphalerite and pyrite; (**b**) cassiterite is associated with quartz. Cst—cassiterite; Sp—sphalerite; Py—pyrite.

Based on the results of the electron microprobe analysis (EMPA), LA-ICP-MS in situ trace element analysis was carried out on chalcopyrite and cassiterite. A total of 5 samples were collected in this work, including 2 samples of cassiterite with 32 points tested and 13 samples of chalcopyrite with 21 points tested. The specific sampling location and mineral combination characteristics are shown in Table 1. In this paper, we focus on testing early chalcopyrite and cassiterite connected with gangue minerals. As far as possible, samples with clean surfaces and free of fissures and inclusions were selected for testing and analysis. The in situ LA-ICP-MS analysis of chalcopyrite and cassiterite was carried out at the National Research Center for Geoanalysis (CAGS), using a Thermo Element II single-receiver, high-resolution magnetic sector ICP-MS connected to a New Wave UP 213. The denuded material was transported by helium. The operating conditions were a 40 μm wide spot beam, 10 Hz frequency, and a laser flow of 10–30 J/cm^2 with an energy of 0.176 mJ. In the analysis process, first, 15 s of background values was collected, followed by 45 s of sample stripping, and finally 15 s of cleaning the system. The specific analysis process and technique refer to [23]. The calibration of trace elements was carried out using MASS1, NIST610, and NIST612 as the joint external standards and KL2G was used as a monitoring standard sample; the analytical precision was 0.1×10^{-6}. GJ-1 and AY-4 were used as standard samples for cassiterite trace element correction. Compared with the electron microprobe analysis, the LA-ICP-MS analysis was characterized by a lower detection limit and higher accuracy.

Table 1. Sampling locations and sample characteristics of chalcopyrite and cassiterite in the Shuangjianzishan deposit.

Sample No.	Mineral	Sampling Location	Description
ZK0403-61	Ccp	ZK0403 at 171 m depth	Quartz–sphalerite veins with chalcopyrite dotted among them
ZK2203-19	Ccp	ZK2203 at 396 m depth	Vein chalcopyrite ore, gangue minerals are mainly quartz
ZK2203-20	Ccp	ZK2203 at 445 m depth	Vein chalcopyrite ore
ZK2203-21	Ccp	ZK2203 at 498 m depth	Vein-like sphalerite ore with chalcopyrite is sparsely disseminated in it
ZK2203-23	Ccp	ZK2203 at 594 m depth	Chlorite-dense disseminated chalcopyrite ore
ZK2203-29	Ccp	ZK2203 at 993 m depth	Quartz–chalcopyrite–sphalerite veins
ZK2203-33	Ccp	ZK2203 at 1172 m depth	The vented galena ore and chalcopyrite are distributed in disseminated form
ZK2204-7	Ccp	ZK2204 at 280 m depth	Striped galena–sphalerite ore with chalcopyrite dots in it
ZK2204-9	Ccp	ZK2204 at 298 m depth	Chalcopyrite ore with quartz and calcite veins
ZK2204-10	Ccp	ZK2204 at 308 m depth	Vein sphalerite ore, chalcopyrite sporadic distribution
ZK2204-12	Ccp	ZK2204 at 389 m depth	Chalcopyrite ore with quartz vein
ZK2204-14	Ccp	ZK2204 at 462 m depth	Quartz vein chalcopyrite ore
ZK2204-17	Ccp	ZK2204 at 625 m depth	Breccia chalcopyrite–sphalerite ore
ZD5-02	Cst	Level 5 elevation 625 m, vein 75	Dense disseminated chalcopyrite ore with cassiterite
ZK2204-B3	Cst	ZK2204 at 1386 m depth	Vein sphalerite ore with cassiterite

6. Result

6.1. Geochemical Characteristics of Trace Elements in Chalcopyrite

The results of chalcopyrite trace elements (see Table S1, Figure 5) show that chalcopyrite is generally enriched in Ni, Sn, Pb, Se, and Ag; relatively enriched in Cr, Cu, As, Rb, Sr, Cd, and In; contains a small amount of Co, Sb, Ge, Mn, and B; and poor in Cs, Hf, Ta, W, Tl, Ga, Nb, Mo, and Bi elements. The specific characteristics are as follows:

(1) Rich in Sn, Se, Ni, Pb, and Ag. Sn content ranged from 20.61×10^{-6} to $14{,}363.11 \times 10^{-6}$, average 2710.5×10^{-6}. Se content ranged from 0×10^{-6} to 4257.89×10^{-6}, average 665.83×10^{-6}. Ni content ranged between 0×10^{-6} and 2776.85×10^{-6}, average 530.23×10^{-6}. Pb content ranged between 3.17×10^{-6} and 3728.26×10^{-6}, average 366.78×10^{-6}. Ag content ranged between 6.15×10^{-6} and 703.47×10^{-6}, average 193.33×10^{-6}.

(2) Less rich in Cr, Cu, As, Rb, Sr, Cd, and In. Cr content ranged between 0×10^{-6} and 101.01×10^{-6}, average 26.34×10^{-6}. Cu content ranged between 5.52×10^{-6} and 46.61×10^{-6}, average 20.56×10^{-6}. As content ranged between 0×10^{-6} and 59.73×10^{-6}, average 14.53×10^{-6}. Rb content ranged between 0×10^{-6} and 82.66×10^{-6}, average 15.09×10^{-6}. Sr content ranged between 1×10^{-6} and 59.49×10^{-6}, average 20.32×10^{-6}. Cd content ranged between 0×10^{-6} and 394.91×10^{-6}, average 63.24×10^{-6}. In content ranged between 2.39×10^{-6} and 263.41×10^{-6}, average 71.34×10^{-6}.

(3) Contains small amounts of Co, Sb, Ge, Mn, and Ba. Co content ranged between 0×10^{-6} and 7.66×10^{-6}, average 1.85×10^{-6}. Ge content ranged between 0×10^{-6} and 22.94×10^{-6}, average 4.27×10^{-6}. Sb content ranged between 0.22×10^{-6} and 6.94×10^{-6}, average 1.93×10^{-6}. Ge content ranged between 0×10^{-6} and 22.94×10^{-6}, average 4.27×10^{-6}. Mn content ranged between 0×10^{-6} and 47.72×10^{-6}, average 9.52×10^{-6}. Ba content ranged between 0.1×10^{-6} and 67.53×10^{-6}, average 10.88×10^{-6}.

(4) Poor in Zn, Cs, Hf, Ta, W, Tl, Ga, Nb, Mo, and Bi. Zn content ranged between 0×10^{-6} and 3.36×10^{-6}, average 0.6×10^{-6}. Cs content ranged between 0×10^{-6} and 1.02×10^{-6}, average 0.15×10^{-6}. Hf content ranged between 0.08×10^{-6} and 0.63×10^{-6}, average 0.25×10^{-6}. Ta content ranged between 0×10^{-6} and 0.14×10^{-6},

average 0.01 × 10^{-6}. W content ranged between 0 × 10^{-6} and 3.21 × 10^{-6}, average 0.27 × 10^{-6}. Tl content ranged between 0 × 10^{-6} and 0.3 × 10^{-6}, average 0.09 × 10^{-6}. Ga content ranged between 0 × 10^{-6} and 4.78 × 10^{-6}, average 0.85 × 10^{-6}. Nb content ranged between 0 × 10^{-6} and 4.2 × 10^{-6}, average 0.85 × 10^{-6}. Mo content ranged between 0 × 10^{-6} and 2.63 × 10^{-6}, average 0.54 × 10^{-6}. Bi content ranged between 0 × 10^{-6} and 10.66 × 10^{-6}, average 0.74 × 10^{-6}.

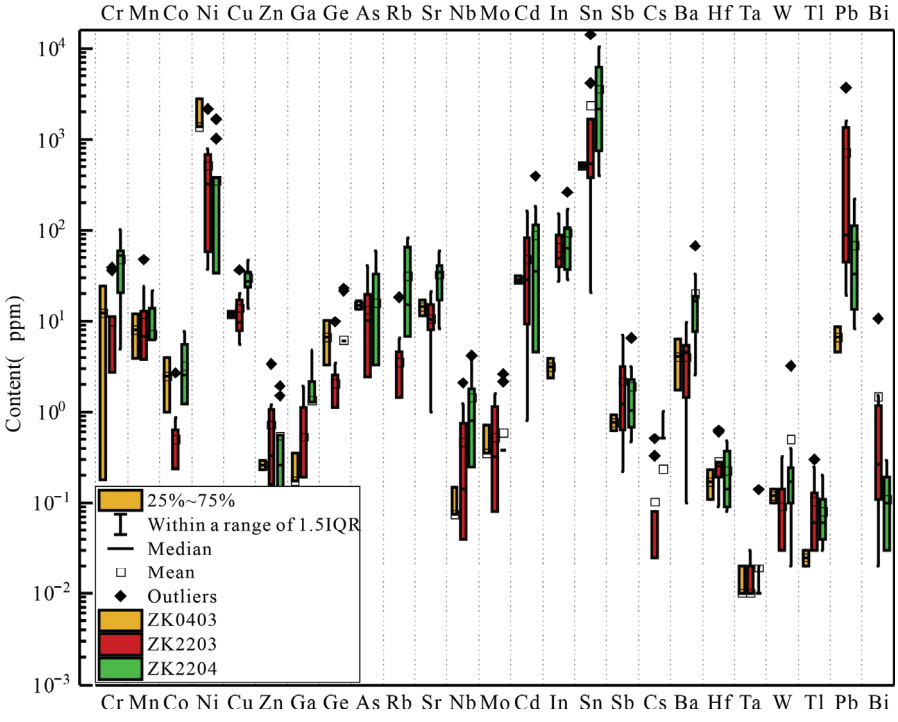

Figure 5. Boxand-whisker plots for different generations of chalcopyrite in situ trace elements from the Shuangjianzishan ore area.

6.2. Geochemical Characteristics of Trace Elements in Cassiterite

Cassiterite is one of the main tin-bearing minerals in the Shuangjianzishan deposit. Containing 78.6% tin, cassiterite is the most common tin mineral and the most important ore mineral of tin. Its chemical component is SnO_2, which is a rutile tetragonal crystal system oxide mineral. The results of cassiterite trace elements (see Table S2, Figure 6) show that the trace element contents of the two cassiterite samples extracted from the tunnel and the drill, respectively, are similar, generally enriched in Fe, Co, Ni, Cd, In, Sb, and W; relatively enriched in Mn, Zn, and Pb; with a small amount of Cu, Ga, Ge, Sr, Nb, and Ba; and poor in Cr, As, Rb, Mo, Cs, Hf, Ta, Tl, and Bi. Some element contents are even below the detection limit, and the elemental content of tunnel samples is generally higher than that of drill holes. The specific characteristics are as follows:

(1) Rich in Fe, Cd, Ni, In, Co, and W. Fe content ranged between 1272.46 × 10^{-6} and 36,766.47 × 10^{-6}, average 7405.76 × 10^{-6}. Cd content ranged between 28,522.69 × 10^{-6} and 31,034.52 × 10^{-6}, average 29,820.29 × 10^{-6}. Ni content ranged between 6944.71 × 10^{-6} and 7731.47 × 10^{-6}, average 7337.13 × 10^{-6}. In content ranged between 2475.65 × 10^{-6} and 2536.9 × 10^{-6}, average 2651.89 × 10^{-6}. Co content ranged between 1153.17 × 10^{-6} and 1274.97 × 10^{-6}, average 1205.67 × 10^{-6}. W content ranged between 0 × 10^{-6} and 9952.13 × 10^{-6}, average 1193.93 × 10^{-6}.

(2) Less rich in Mn, Zn, Pb, and Sb. Sb content ranged between 0×10^{-6} and 802.1×10^{-6}, average 73.89×10^{-6}. Mn content ranged between 0×10^{-6} and 185.46×10^{-6}, average 18.42×10^{-6}. Pb content ranged between 0×10^{-6} and 225.18×10^{-6}, average 9.08×10^{-6}. Zn content ranged between 0×10^{-6} and 117.03×10^{-6}, average 7.43×10^{-6}.

(3) Contains small amounts of Cu, Ga, Ge, Sr, Nb, Ba, and As. Cu content ranged between 0×10^{-6} and 2.49×10^{-6}, average 0.2×10^{-6}. Ga content ranged between 0×10^{-6} and 36.61×10^{-6}, average 7.08×10^{-6}. Ge content ranged between 0×10^{-6} and 3.59×10^{-6}, average 0.56×10^{-6}. Sr content ranged between 0×10^{-6} and 28.83×10^{-6}, average 2.18×10^{-6}. Nb content ranged between 0×10^{-6} and 5.64×10^{-6}, average 1.02×10^{-6}. Ba content ranged between 0×10^{-6} and 17.25×10^{-6}, average 1.01×10^{-6}. As content ranged between 0×10^{-6} and 51.73×10^{-6}, average 4.46×10^{-6}.

(4) Poor in Cr, Rb, Mo, Cs, Hf, Ta, Tl, and Bi. The contents of Cr, Rb and Cs in all cassiterite samples were lower than the detection limit, and the contents were very low. Mo content ranged between 0×10^{-6} and 2.89×10^{-6}, average 0.31×10^{-6}. Hf content ranged between 0×10^{-6} and 2.22×10^{-6}, average 0.21×10^{-6}. Ta content ranged between 0×10^{-6} and 0.11×10^{-6}, average 0.02×10^{-6}. Tl content ranged between 0×10^{-6} and 0.06×10^{-6}, average 0.01×10^{-6}. Bi content ranged between 0×10^{-6} and 0.08×10^{-6}, average 0.01×10^{-6}.

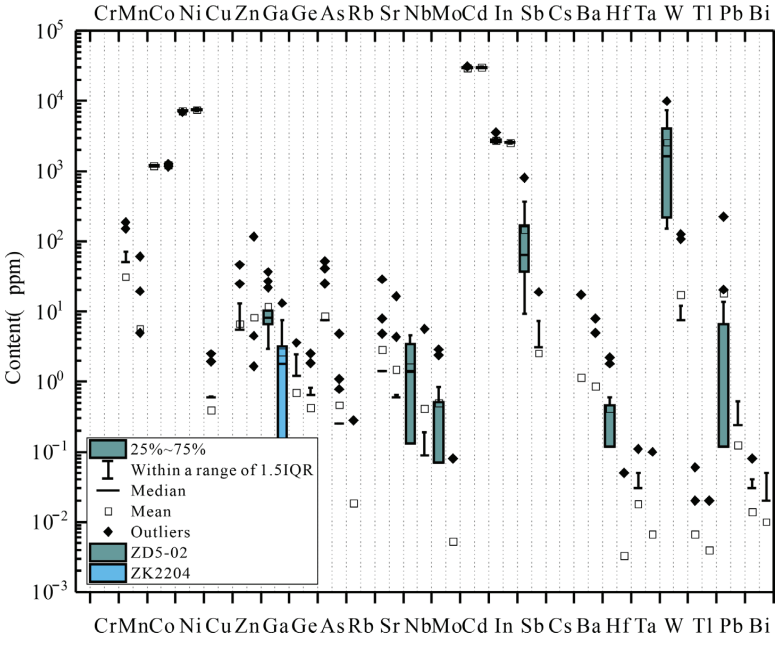

Figure 6. Box-and-whisker plots for different generations of cassiterite in situ trace elements from the Shuangjianzishan ore area.

6.3. Cassiterite Electron Microprobe Analysis Results

The results of cassiterite electron microprobe analysis (Table 2) show that cassiterite from the Shuangjianzishan deposit is enriched in Si, Fe, Mg, and Ca. The elemental content of Si ranges from 0.57% to 2.69% (average 1.33%), the Fe elemental content from 0.39% to 4.16% (average 1.73%), the Mg elemental content from 0.08% to 0.42% (average 0.18%), and the Ca elemental content ranges from 0.38% to 0.61% (average 0.51%). The contents of F, Zr, Hf, Sr, and Th are very small.

Table 2. Electron microprobe analysis results of cassiterite in the Shuangjianzishan silver polymetallic deposit.

	F	SiO_2	MgO	ZrO_2	CaO	FeO	HfO_2	SnO_2	SrO	ThO_2	Total
ZK2204-17-01	0	1.098	0.227	0.033	0.506	1.564	0	96.252	0	0.038	99.718
ZK2204-17-02	0.131	1.769	0.166	0	0.527	1.706	0	95.086	0	0.022	99.407
ZK2204-17-03	0.058	1.271	0.15	0.056	0.548	2.188	0.15	95.853	0.032	0.019	100.325
ZK2204-17-04	0	1.207	0.152	0	0.384	1.332	0.156	96.38	0.024	0	99.635
ZK2204-17-05	0	2.693	0.42	0	0.498	4.158	0	91.456	0.071	0	99.296
ZK2204-17-06	0	1.844	0.216	0	0.488	3.093	0.388	94.169	0	0	100.198
ZK2204-17-07	0.101	0.993	0.122	0.098	0.407	1.629	0.058	96.288	0	0	99.696
KZ0001-05-01	0	0.571	0.076	0.033	0.535	0.393	0	98.272	0.008	0.008	99.896
KZ0001-05-02	0	0.641	0.115	0.056	0.484	1.111	0	96.667	0.031	0	99.105
KZ0001-05-03	0	1.605	0.162	0.089	0.61	0.99	0	96.381	0.013	0	99.85
KZ0001-05-04	0	0.989	0.157	0.005	0.565	0.904	0.063	97.805	0	0	100.488

7. Discussion

7.1. Occurrence State of Trace Elements in Chalcopyrite and Its Indicating Significance

Chalcopyrite is the main carrier of Cu in the Shuangjianzishan deposit. Its ideal chemical formula is $CuFeS_2$, and the tetragonal variant is the most common in nature. Pauling and Brockway [24] thought that there was a strong covalent bond between Cu and Fe, and the valence states of Cu and Fe fluctuated between monovalent–divalent and divalent–trivalent, respectively. Compared with base metal sulfides such as galena and sphalerite, the situation of trace elements entering the chalcopyrite structure is often more complicated [25], and because of the existence of covalent bonds in chalcopyrite, it means that the GoldSchmidt rule [26] cannot be used to predict the distribution trend of elements just like pure ionic structure minerals, but it still has certain reference significance. The content of trace elements in chalcopyrite is controlled by many factors, such as the chalcopyrite crystal structure, element partition with co-crystallization minerals, and magma/fluid composition [25,27]. The content of Sn is highest in chalcopyrite in this test. Sn, Cu, and Fe have similar ionic radius, so Sn can enter chalcopyrite through isomorphism. Eugster [28] thought that the migration and enrichment of high-concentration Sn were mainly formed under high-temperature and reduction conditions. George et al. [25,27] pointed out that chalcopyrite is not the "first preferred host" of trace elements when there are co-crystallization sulfides such as sphalerite, but it is also beneficial to enrich trace elements in minerals if the ore-forming fluid is rich, so the early hydrothermal solution of the Shuangjianzishan deposit may be rich in Sn, which makes the Sn content in chalcopyrite higher. In the -CPS signal diagram (Figure 7), some In and Sn signals are consistent. The ionic radii of In and Sn are similar, and there is a good positive correlation (Figure 8b). It is speculated that In and Sn enter chalcopyrite in the form of coupling instead of Fe at high temperature [29], forming $CuInS_2$ and Cu_2FeSnS_4 solid solutions with the same structure as chalcopyrite. Although In and Zn also show a weak positive correlation (Figure 8c), the synchronous change in Zn and In is not observed in the signal diagram, which further proves that there may be a coupling substitution relationship between In and Sn. The positive correlation between Zn and Mn (Figure 8d) shows that Zn mainly exists in chalcopyrite in the form of inclusions. There is a positive correlation between Pb and Bi in chalcopyrite (Figure 8f), but Pb and Bi cannot exist in chalcopyrite in the form of solid solution, but mostly exist in chalcopyrite in the form of inclusions, due to the large difference between the ionic radius of Cu and Fe ions. The content of As is high, which may replace the S element in chalcopyrite. Butler et al. [30] think that As can promote the entry of Au and Ag. There is a weak correlation between As and Sb (Figure 8e), and there may be As-rich inclusions. The content of Se in chalcopyrite is high (the average is 665.83 ppm), and the S element is primarily substituted by other elements through isomorphic replacement, which implies that the formation temperature of chalcopyrite is relatively high [31]. The low content of medium- and low-temperature elements such as Ga and Sb

in chalcopyrite reflects that chalcopyrite was formed in a medium- and high-temperature environment. There is a positive correlation between Sb and Tl (Figure 8a), which indicates that Sb and Tl may enter chalcopyrite through coupling substitution. Chalcopyrite in the Shuangjianzishan deposit has a high content of Ni (with an average of 530.23 ppm), but George et al. [25] think that Ni is not obviously enriched in chalcopyrite, but exists in pyrite, so Ni may mainly exist in chalcopyrite as pyrite or pyrrhotite inclusions, instead of replacing Fe in chalcopyrite by isomorphism.

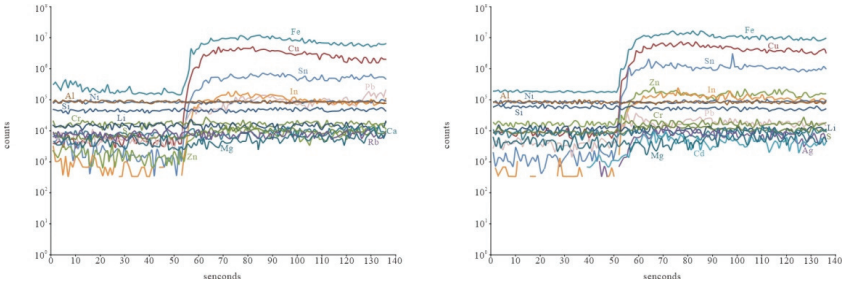

Figure 7. Typical LA-ICP-MS–time -CPS signal spectrum of chalcopyrite in the Shuangjianzishan deposit.

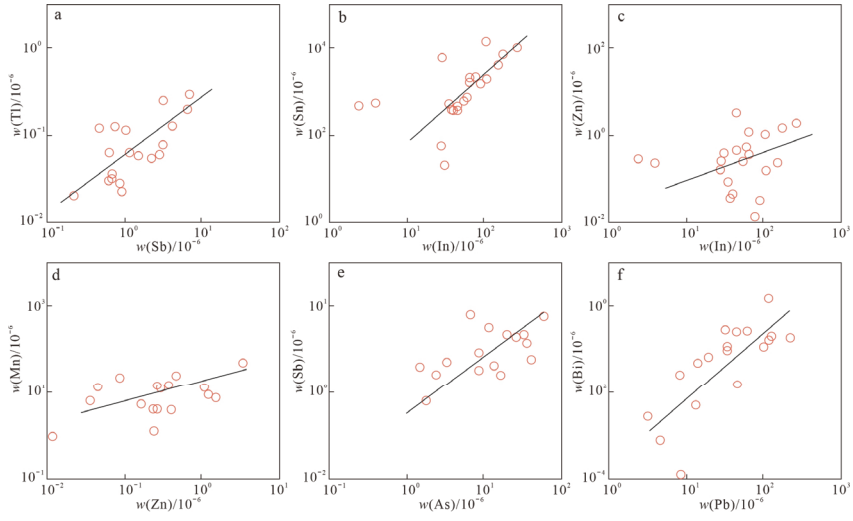

Figure 8. Binary diagrams of trace elements content in chalcopyrite in the Shuangjianzishan deposit. (**a**) Sb versus Tl; (**b**) In versus Sn; (**c**) In versus Zn; (**d**) Zn versus Mn; (**e**) As versus Sb; (**f**) Pb versus Bi.

7.2. Occurrence State of Trace Elements in Cassiterite and Its Indicating Significance

Cassiterite has strong weathering and erosion resistance and is not easily influenced by hydrothermal alteration in the later period. It often contains siderophile elements such as Ti, V, Cr, Mn, Fe, Co, and Ni; chalcophile elements such as Cu, Pb, and Ag; and some rare elements [32]. The research results in this paper show that cassiterite has relatively high Fe (average 7405.76 ppm) and W (average 1193.93 ppm), and relatively low Sb (average 73.89 ppm) and U (average 1.64 ppm), and W-U has a positive correlation (Figure 9c). Predecessors thought that high temperature was beneficial to the replacement of Sn in cassiterite by Fe [33], and Huang et al. [34] further concluded that the FeO content in cassiterite was positively correlated with the crystallization temperature of cassiterite. The electron microprobe analysis data in this paper show that the FeO content of cassiterite is basically greater than 1%, and it is considered that the crystallization temperature

of cassiterite in the Shuangjianzishan deposit is higher, but Tan et al. [35] think that the universality of this conclusion is still controversial, so this paper only takes it as a secondary reference condition. Generally speaking, the W content in cassiterite is not high, and it is elevated only when it coexists with wolframite or scheelite [36]. In this paper, cassiterite has a higher W content, and there is a certain correlation between Fe and W (Figure 10), which indicates that cassiterite in the Shuangjianzishan deposit may have an element replacement mechanism of $W^{6+} + Fe^{2+} \leftrightarrow 2Sn^{4+}$; it is suggested that the cassiterite formation temperature is higher. At the same time, it also reflects the characteristics that magmatic hydrothermal fluid is rich in W. But at the same time, Wu [37] found wolframite inclusions in cassiterite, and the W content in cassiterite has a large range (0×10^{-6}~9952.13×10^{-6}), indicating that W may not enter cassiterite mainly in isomorphic form, but in the form of wolframite micro-inclusions. Previous studies have shown that the primary cassiterite rich in W-U(Sb) and poor in Fe was formed under the condition of relative reduction, and Sn^{2+} can migrate in acidic fluid, while the cassiterite rich in Fe and poor in W-U was formed under the metasomatism of late oxidizing hydrothermal fluid [38]. The cassiterite in the Shuangjianzishan deposit is characterized by being rich in Fe and poor in U and Sb, so it is speculated that it was formed under the condition of relative oxidation. The content of Fe-Ga is high in the relative oxidation environment (Figure 9e).

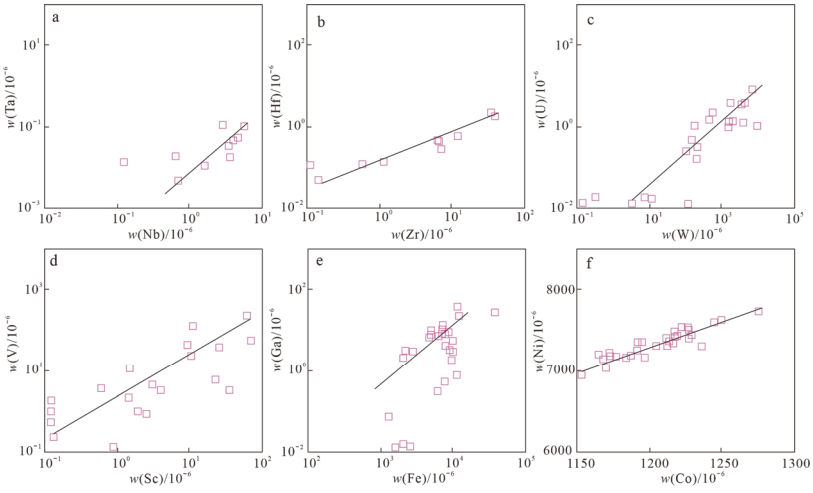

Figure 9. Binary diagrams of trace element content in cassiterite in the Shuangjianzishan deposit. (**a**) Nb versus Ta; (**b**) Zr versus Hf; (**c**) W versus U; (**d**) Sc versus V; (**e**) Fe versus Ga; (**f**) Co versus Ni.

The results of this test show that the content of In in cassiterite is relatively high (with an average of 2651.89 ppm). Pavlova et al. [39] think that the content of In in cassiterite has a certain corresponding relationship with the depth of mineralization, and the content of In in quartz-vein-type tin ore with deep formation is relatively low (<160 ppm), while that in sulfide tin ore with a shallow formation is usually relatively high. At the same time, the hydrothermal fluid is rich in volatiles such as F and Li, which is also beneficial to the enrichment of In and the replacement of Sn in cassiterite. Therefore, the high content of In in cassiterite is not necessarily due to the decrease in temperature and pressure during the formation of cassiterite, but may also be due to the further enrichment of In in cassiterite due to the volatile substances such as F and Li contained in the ore-forming hydrothermal solution [35]. Zhu et al. [40] pointed out that Sn plays an important role in the enrichment process of In. Tin and indium are co-enriched and migrated in ore-forming fluids and separated in the mineralization and precipitation stage. It is especially obvious in skarn deposits and epithermal deposits related to granite (hydrothermal vein type) [41].

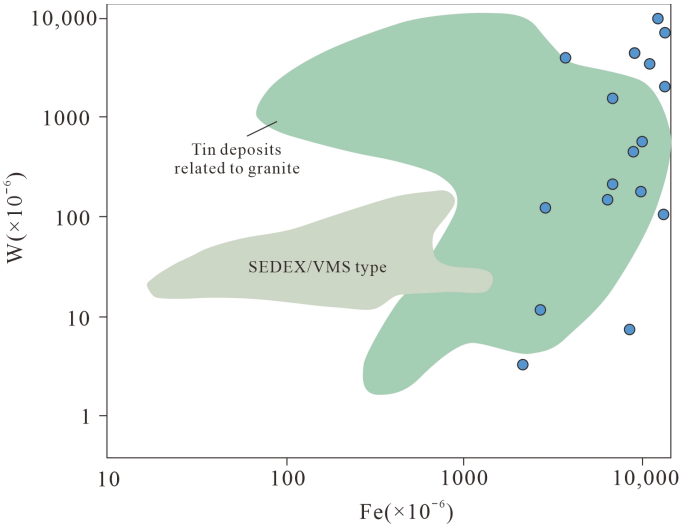

Figure 10. W-Fe diagram of cassiterite in the Shuangjianzishan deposit (After [39]).

Nb-Ta and Fe-Mn usually appear in pairs and enter the cassiterite crystal lattice together. Cassiterite often replaces $Sn^{4+} \leftrightarrow Fe^{2+} + Mn^{2+} + Nb^{5+} + Ta^{5+}$ in pegmatite and high-temperature quartz veins, while $Fe^{3+} + Nb^{5+} + Ta^{5+} \leftrightarrow Sn^{4+}$ is replaced in middle–low-temperature quartz veins [42]. However, cassiterite in the Shuangjianzishan deposit is rich in Fe and poor in Nb and Ta. It is speculated that Fe may enter the cassiterite lattice through $Fe^{3+} + OH^{-} \leftrightarrow Sn^{4+} + O^{2-}$ instead of the above two replacement reactions, which also explains the reason why cassiterite is poor in Nb and Ta. Chen et al. [43] thought that cassiterite of hydrothermal origin was generally poor in Nb and Ta, especially cassiterite in quartz veins, and $(Nb, Ta)_2O_5$ was generally less than 1%. Nb^{5+} and Ta^{5+} have similar ionic charge and ionic radius, and ZrO_2, HfO_2, and SnO_2 have the same structure, so the contents of Nb, Ta, Zr, and Hf and the ratio of Nb/Ta and Zr/Hf have a clear indication for the genesis of cassiterite, and Nb-Ta and Zr-Hf in cassiterite show obvious positive correlation characteristics (Figure 9a,b). The mass fraction of Zr and Hf in cassiterite of high-temperature hydrothermal origin is high. The (Fe + Mn)/(Nb + Ta) indices of cassiterite in the Shuangjianzishan deposit are all less than 2, indicating that it has the characteristics of cassiterite in hydrothermal deposits [44]. The Nb/Ta ratio of cassiterite in the Shuangjianzishan deposit ranges from 9.17 to 201.66, with an average value of 81.51, suggesting that it is related to magmatic hydrothermal solution (Nb/Ta ratio > 1), suggesting that ore-forming materials may mainly come from magma. There is a positive correlation between Sc-V and Co-Ni (Figure 9d,f), indicating the existence of isomorphic substitution reactions between Sc-V, Co-Ni, and Sn.

7.3. Genesis of Cu-Sn Mineralization

A cassiterite–chalcopyrite–quartz–arsenopyrite high-temperature mineral assemblage appears in the deep ore of the Shuangjianzishan mining area, which contradicts the previous understanding that the Shuangjianzishan deposit only has a medium–low-temperature mineralization stage [9]. Previous studies have shown that magmatic cassiterite is rich in Nb and Ta, but relatively poor in Fe and Mn, while hydrothermal cassiterite is the opposite [44]. In this study, cassiterite is richer in Fe and Mn, but relatively poor in Nb and Ta, indicating that it was formed in a relatively high-temperature hydrothermal environment, and tin mineralization belongs to the cassiterite–sulfide type. Most tin mineralization in the world is considered related to hydrothermal processes related to highly differentiated and relatively reduced granite bodies [45,46]. Cassiterite related to granite is rich in Nb and Ta, and the

Nb + Ta content is generally higher than 1%, while cassiterite related to sedimentary or metamorphic hydrothermal solution has a low content of high-field elements [44]. The cassiterite in the Shuangjianzishan deposit in this study has a low content of high-field-strength elements (Nb is 1.02×10^{-6}, Ta is 0.02×10^{-6}). It is rich in Fe (7405.76×10^{-6}) and W (1193.93×10^{-6}), which is different from typical magmatic hydrothermal deposits and SEDEX/VHMS-type deposits. This shows that the enrichment degree of W, Nb, Ta, Zr, Hf, and other elements in cassiterite is not only related to the source, but also influenced by many factors such as temperature, pH, pressure, and oxygen fugacity, and the source cannot be simply judged by the content of trace elements [32]. Chen [47] thinks that the Co/Ni ratio of chalcopyrite in Cu-Ni sulfide deposits is less than 1, while the Co/Ni ratio of chalcopyrite in porphyry, skarn, and epithermal deposits in hydrothermal deposits is more than 1. Because chalcopyrite contains Ni-rich micro-inclusion minerals in this test, the Ni content is not representative, but according to the data of trace elements of chalcopyrite in the Shuangjianzishan deposit [37], it conforms to the characteristics of chalcopyrite in hydrothermal deposits. The enrichment of high-temperature elements such as Sn, Se, and W in cassiterite and chalcopyrite indicates that the Shuangjianzishan deposit has a high-temperature metallogenic stage of Sn-Cu, which is not a simple medium–low-temperature magmatic hydrothermal deposit.

7.4. Discussion of the Relationship between Tin and Silver Mineralization

Sn is typically a high-temperature element, and a high-temperature environment is more conducive to the migration and enrichment of Sn. A large amount of early tin mineralization was found in the Shuangjianzishan deposit. From the mineralogical characteristics, chalcopyrite and sphalerite grew around the early cassiterite (Figure 4), or early tin-bearing mineral inclusions were found in sphalerite and chalcopyrite. Chalcopyrite and cassiterite coexisted with gangue minerals such as quartz (Figure 3f), and were later metasomatized by galena and sphalerite, indicating that chalcopyrite and cassiterite were formed earlier than sphalerite and galena. From the geochemistry of mineral trace elements, cassiterite is rich in high-temperature elements such as W and In, while the contents of Cu, Pb, Zn, and Ag are all low, indicating that its formation temperature is high, but it is not rich in concentrated low-temperature ore-forming elements. Chalcopyrite is rich in high-temperature elements such as Sn and Se, suggesting that early ore-forming fluids may be rich in Sn, and copper–tin mineralization is closely related. Therefore, according to the observed macroscopic and microscopic characteristics, it is concluded that the metallogenic sequence of the Shuangjianzishan deposit is Sn→Cu→Pb-Zn-Ag. Wei [48] speculated that the ore-forming age of cassiterite is about 129 Ma, which is basically consistent with the isochron age of sphalerite of 133 ± 4 Ma [6]. From the perspective of ore-forming age, it is considered that there may be a certain relationship between Cu-Sn mineralization and Pb-Zn-Ag mineralization, but the source of ore-forming materials, evolution of ore-forming fluids, and spatial zonation of high-temperature Sn mineralization and medium–low-temperature Cu-Pb-Zn-Ag mineralization are still unclear. Therefore, it is uncertain whether the tin polymetallic mineralization and silver–lead–zinc mineralization in the Shuangjianzishan deposit are similar to the same metallogenic systems as those in the Weilasituo deposit [49] or the spatial superposition of multi-center mineralization like the Dajing deposit [50,51].

8. Conclusions

1. Chalcopyrite is rich in medium–high-temperature elements such as Sn, In, and Se, but poor in low-temperature elements such as Ga and Sb, which indicates that chalcopyrite has a high formation temperature, and the early ore-forming fluid is rich in Sn, while Pb, Bi, Ni, and other elements mostly exist in chalcopyrite as inclusions.
2. Cassiterite is rich in Fe, W, and In but poor in U and Sb, indicating that cassiterite was formed in a medium–high-temperature oxidation environment, and the early ore-forming fluid was rich in W. Because there are wolframite inclusions in cassiterite, and the W content changes greatly, it is considered that the cassiterite in the

Shuangjianzishan deposit mainly has the element replacement mechanism of Fe^{3+} + $OH^- \leftrightarrow Sn^{4+}$ + O^{2-}, followed by W^{6+} + $Fe^{2+} \leftrightarrow 2Sn^{4+}$.

3. Cassiterite is rich in Fe and Mn, but relatively poor in Nb and Ta, indicating that it was formed in a relatively high-temperature hydrothermal environment, and tin mineralization belongs to the cassiterite–sulfide type.
4. The metallogenic sequence of the Shuangjianzishan deposit is Sn→Cu→Pb-Zn-Ag, and the copper–tin mineralization is closely related.

Supplementary Materials: The following supporting information can be downloaded at: https://www.mdpi.com/article/10.3390/app14093822/s1, Table S1: The laser ablation ICP-MS spot analyses of chalcopyrite from the Shuangjianzishan deposit (ppm), Table S2: The laser ablation ICP-MS spot analyses of cassiterite from the Shuangjianzishan deposit (ppm).

Author Contributions: Y.L.: Conceptualization, Data Acquisition, Investigation, Methodology, Writing—Original Draft Preparation, Writing—Review and Editing. B.J. and Y.C.: Funding Acquisition, Project Administration, Supervision, Resources, Writing—Review and Editing. L.W.: Methodology, Software, Visualization, Writing—Original Draft Preparation. Y.Z.: Visualization, Software, Editing. Z.L.: Funding Acquisition, Project Administration, Supervision, Resources, Writing—Review and Editing. All authors have read and agreed to the published version of the manuscript.

Funding: This research was funded by Geology of mineral resources in China, grant number DD20221695, DD20190379, DD20160346; the Fundamental Research Funds of the Central Public Welfare Scientific Research Institutes, grant number JKYZD202313; the Inner Mongolia Geological Exploration Fund Project, grant number 2020-YS03.

Institutional Review Board Statement: Not applicable.

Informed Consent Statement: Not applicable.

Data Availability Statement: Data is contained within the article or Supplementary Material.

Acknowledgments: We would like to extend our heartfelt gratitude to Tianming Zhang, Yanbin Liu, Zhanwen Yin, and Hongjun Sun from Chifeng Yubang Mining Co., Ltd., for their invaluable assistance during our fieldwork and in the publication of our paper.

Conflicts of Interest: The authors declare that they have no known competing financial interests or personal relationships that could have appeared to influence the work reported in this paper.

References

1. Zhai, D.; Liu, J.; Zhang, A.; Sun, Y. U-Pb, Re-Os and 40Ar/39Ar Geochronology of porphyry Sn ± Cu ± Mo and polymetallic (Ag-Pb-Zn-Cu) vein mineralization at Bianjiadayuan, Inner Mongolia, NE China: Implications for discrete mineralization events. *Econ. Geol.* **2017**, *112*, 2041–2059. [CrossRef]
2. Wang, C.N.; Wang, Q.M.; Yu, X.F. Metallognetic characteristics of tin and ore-search prospect in the southern part of Da Hinggan Mountains. *Geol. Explor.* **2016**, *52*, 220–227.
3. Sillitoe, R.H. Porphyry copper systems. *Econ. Geol.* **2010**, *105*, 3–41. [CrossRef]
4. Criss, R.E.; Eaton, G.F. Evidence for proterozoic and late cretaceous-early tertiary ore-forming events in the Coeur d'Alene district, Idaho and Montana-a discussion. *Econ. Geol.* **1998**, *93*, 1103–1109. [CrossRef]
5. Zhu, J.; Duan, H.; Yang, L.; Chen, Q.; Liu, L.; Shi, K.; Qian, J.; Li, Q.; Hu, R. Genesis of the Baiyangping Cu–Co and Pb–Zn Mineralizations in Lanping Basin, SW China. *Appl. Sci.* **2022**, *12*, 2129. [CrossRef]
6. Wu, G.B.; Liu, J.M.; Zeng, Q.D.; Sun, H.S.; Liu, M.H. Metallogenic Age of Shuangjianzishan Pb-Zn-Ag Deposit in Daxinganling, Inner Mongolia. *Acta Mineral. Sin.* **2013**, *33*, 619.
7. Kuang, Y.S.; Zheng, G.R.; Lu, M.J.; Liu, Y.L.; Zhang, S.J.; Li, Y.; Cheng, W.J. Basic characteristics of Shuangjianzishan sliver polymetallic deposit in Chifeng City, Inner Mongolia. *Miner. Depos.* **2014**, *33*, 847–856.
8. Ouyang, H.G.; Li, R.H.; Zhou, Z.H. The Jurassic Mineralization of the Shuangjianzisha Ag polymetallic Deposit and its Significance in Prospecting: Evidence from Geochronology. *Acta Geol. Sin.* **2016**, *90*, 1835–1845.
9. Jiang, B.; Wu, G.; Chen, Y.C.; Zhang, T.; Liu, W.Y.; Zhang, T.; Li, X.J. Constraint on the Genesis of the Shuangjianzishan Silver Polymetallic Deposit, Balinzuo Qi, Inner Mongolia: Evidence from Trace and Rare Earth Elements. *Acta Geol. Sin.* **2018**, *92*, 769–786.
10. Wu, X.L.; Zhao, J.F.; Liu, W.Y.; Wu, G.; Jiang, B.; Li, Z.Y.; Sun, H.J. New discovery of tin mineralization in Shuangjianzishan A g polymetallic deposit, Inner Mongolia and its significance. *Miner. Depos.* **2021**, *40*, 631–635.

11. Ma, W.W.; Jiang, B.; Chen, Y.C.; Gong, Q.J.; Yin, Z.W.; Sun, H.J.; Li, Z.Y.; Wu, L.W.; Zuo, Y.S.; Li, Z. Discovery and Significance of Large-scale Copper Mineralization in Shuangjianzishan Silver-polymetallic Deposit, Inner Mongolia. *Acta Geosci. Sin.* **2022**, *43*, 521–526.
12. Ahmad, A.; Hafeez, M.; Abbasi, S.A.; Khan, T.M.; Faruque, M.R.I.; Khandaker, M.U.; Ahmad, P.; Rafique, M.; Haleem, N. Compositional Analysis of Chalcopyrite Using Calibration-Free Laser-Induced Breakdown Spectroscopy. *Appl. Sci.* **2020**, *10*, 6848. [CrossRef]
13. Stergiou, C.L.; Melfos, V.; Voudouris, P.; Papadopoulou, L.; Spry, P.G.; Peytcheva, I.; Dimitrova, D.; Stefanova, E. A Fluid Inclusion and Critical/Rare Metal Study of Epithermal Quartz-Stibnite Veins Associated with the Gerakario Porphyry Deposit, Northern Greece. *Appl. Sci.* **2022**, *12*, 909. [CrossRef]
14. Bi, R.; Wang, F.; Zhang, W. Whole Rock, Mineral Chemistry during Skarn Mineralization-Case Study from Tongshan Cu-Mo Skarn Profile. *Appl. Sci.* **2023**, *13*, 8118. [CrossRef]
15. Czapowski, G.; Tomassi-Morawiec, H.; Handke, B.; Wachowiak, J.; Peryt, T.M. Trace Elements and Mineralogy of Upper Permian (Zechstein) Potash Deposits in Poland. *Appl. Sci.* **2022**, *12*, 7183. [CrossRef]
16. Stergiou, C.L.; Melfos, V.; Voudouris, P.; Spry, P.G.; Papadopoulou, L.; Chatzipetros, A.; Giouri, K.; Mavrogonatos, C.; Filippidis, A. The Geology, Geochemistry, and Origin of the Porphyry Cu-Au-(Mo) System at Vathi, Serbo-Macedonian Massif, Greece. *Appl. Sci.* **2021**, *11*, 479. [CrossRef]
17. Robinson, P.T.; Zhou, M.F.; Hu, X.F.; Reynolds, P.; Bai, W.J.; Yang, J.S. Geochemical constraints on the origin of the Hegenshan Ophiolite, Inner Mongolia, China. *J. Asian Earth Sci.* **1999**, *17*, 423–442. [CrossRef]
18. Xiao, W.J.; Windley, B.F.; Hao, J.; Zhai, M.G. Accretion leading to collision and the Permian Solonker suture, Inner Mongolia, China: Termination of the central Asian orogenic belt. *Tectonics* **2003**, *22*, 1069. [CrossRef]
19. Windley, B.F.; Alexeiev, D.; Xiao, W.J.; Kroner, A.; Badarch, G. Tectonic models for accretion of the Central Asian Orogenic Belt. *J. Geol. Soc.* **2007**, *164*, 31–47. [CrossRef]
20. Jiang, B.; Zhang, T.; Chen, Y.C.; Huang, F.; Wu, G.; Sun, H.J.; Li, Z.Y.; Li, X.J.; Yan, J. The source of ore forming fluid and mechanism of metal precipitation in the Shuangjianzishan Ag polymetallic deposit in Chifeng, Inner Mongolia. *Acta Geol. Sin.* **2019**, *93*, 3166–3182.
21. Sun, K.W.; Yang, S.S.; Liu, Y.L. *Exploration Report of Silver-Lead Ore in Shuangjianzishan Mining Area, Balinzuoqi, Inner Mongolia Autonomous Region (Mine Exploration Report)*; Chifeng Tiantong Geological Exploration Co., LTD.: Beijing, China, 2013; pp. 1–96.
22. Wu, X.; Zhao, J.; Liu, W.; Xie, G.; Ye, Z.; Li, Z.; Sun, H. Tin mineralization in the giant Shuangjianzishan Ag-Pb-Zn deposit, Inner Mongolia. *Ore Geol. Rev.* **2023**, *152*, 105241. [CrossRef]
23. Yuan, J.H.; Zhan, X.C.; Hu, M.Y.; Zhao, L.H.; Sun, D.Y. Characterization of Matrix Effects in Microanalysis of Sulfide Minerals by Laser Ablation Inductively Coupled Plasma-Mass Spectrometry Based on An Element Pair Method. *Spectrosc. Spectr. Anal.* **2015**, *35*, 512–518.
24. Pauling, L.; Brockway, L.O. The crystal structure of chalcopyrite $CuFeS_2$. *Z. Krist. Cryst. Mater.* **1932**, *82*, 188–194. [CrossRef]
25. George, L.L.; Cook, N.J.; Crowe, B.B.; Ciobanu, C.L. Trace Elem Hydrothermal Chalcopyrite. *Mineral. Mag.* **2018**, *82*, 59–88. [CrossRef]
26. Goldschmidt, V.M. Geochemistry. *Soil Sci.* **1954**, *78*, 156. [CrossRef]
27. George, L.L.; Cook, N.J.; Ciobanu, C.L. Partitioning of trace elements in co-crystallized sphalerite–galena–chalcopyrite hydrothermal ores. *Ore Geol. Rev.* **2016**, *77*, 97–116. [CrossRef]
28. Eugster, H.P. Minerals in hot water. *Am. Mineral.* **1986**, *71*, 655–673.
29. Wang, Q.L.; Zhang, J.Y.; Yan, D.T.; Min, H.; Liu, S.; Li, C. Genesis type of ore deposits indicated by trace elements of chalcopyrite. *Bull. Geol. Sci. Technol.* **2023**, *42*, 126–143.
30. Butler, I.B.; Nesbitt, R.W. Trace element distributions in the chalcopyrite wall of ablack smoker chimney:Insights from laser ablation inductively coupled plasma mass spectrometry (LA-ICP-MS). *Earth Planet. Sci. Lett.* **1999**, *167*, 335–345. [CrossRef]
31. Bethke, P.M.; Barton, P.B. Distribution of some minor elements between coexisting sulphide minerals. *Econ. Geol.* **1971**, *66*, 140–163. [CrossRef]
32. Taylor, R.G. *Geology of Tin Deposits*; Elsevier Scientific Publishing Company: Amsterdam, The Netherlands, 1979.
33. Wang, P.; Pan, Z.L.; Weng, L.B. *Systematic Mineralogy*; Geological Publishing House: Beijing, China, 1982; pp. 541–544.
34. Huang, P.Y.; Wang, X.; Chen, J.; Ren, M.H.; Lai, G.B. Morphological and Geochemical Studies of the Cassiterite in Taoxikeng Tin Deposit, Southern Jiangxi, China. *Geol. Rev.* **2012**, *58*, 987–1000.
35. Tan, S.C.; Guo, X.Y.; He, X.H.; Xie, Z.P.; Zhang, Y.H.; Li, H.M.; Hao, S. Mineral Chemical Characteristics and Genesis of Cassiterite in Gejiu Tin-Polymetallic Deposit, Y unnan Province. *J. Jilin Univ. Earth Sci. Ed.* **2018**, *48*, 736–753.
36. Möller, P.; Dulski, P.; Szacki, W.; Malow, G.; Riedel, E. Substitution of tin in cassiterite by tantalum, niobium, tungsten, iron and manganese. *Geochim. Cosmochim. Acta* **1988**, *52*, 1497–1503. [CrossRef]
37. Wu, X.L. *Mineralogical Constraints on the Ag-Sn Mineralization Relationship of Shuangjianzishan Ag-Polymetallic Deposit, Inner Mongolia*; Fuzhou University: Fuzhou, China, 2023.
38. Cheng, Y.; Spandler, C.; Kemp, A.; Mao, J.; Rusk, B.; Hu, Y.; Blake, K. Controls on cassiterite (SnO_2) crystallization: Evidence from cathodoluminescence, trace-element chemistry, and geochronology at the Gejiu Tin District. *Am. Mineral.* **2019**, *104*, 118–129. [CrossRef]

39. Pavlova, G.G.; Palessky, S.V.; Borisenko, A.S.; Vladimirov, A.G.; Seifert, T.; Phan, L.A. Indium in cassiterite and ores of tin deposits. *Ore Geol. Rev.* **2015**, *66*, 99–113. [CrossRef]
40. Zhu, X.Q.; Zhang, Q.; He, Y.L.; Zhu, C.H. Relationships between indium and tin, zinc and lead in ore-forming fluid from the indium-rich and -poor deposits in China. *Geochimica* **2006**, *35*, 6–12.
41. Xu, J.; Li, X.F. Spatial and temporal distributions, metallogenic backgrounds and processes of indium deposits. *Acta Petrol. Sin.* **2018**, *34*, 3611–3626.
42. Murciego, A.; Sanchez, A.G.; Dusausoy, Y.; Pozas, J.M.; Ruck, R. Geochemistry and EPR of cassiterites from the Iberian Hercynian Massif. *Mineral. Mag.* **1997**, *61*, 357–365. [CrossRef]
43. Chen, J.; Wang, R.C.; Zhou, J.P. *Geochemistry of Tin*; Nanjing University Press: Nanjing, China, 1990.
44. Tindle, A.G.; Breaks, F.W. Oxide minerals of the Separation Rapids rare-element granitic pegmatite group, northwestern Ontario. *Can. Mineral.* **1998**, *36*, 609–635.
45. Lehmann, B. *Metallogeny of Tin*; Springer: Berlin/Heidelberg, Germany, 1990.
46. Heinrich, C.A. The chemistry of tin (-tungsten) ore deposition. *Econ. Geol.* **1990**, *85*, 529–550. [CrossRef]
47. Chen, D.F. Characteristics of Main Meta llic Minerals in Some Copper-Nickel Sulfide Deposits of China. *Acta Petrol. Mineral.* **1995**, *14*, 345–354.
48. Wei, W. *Genetic Mineralogy and Metallogenesis of Shuangjianzishan Ag Pb-Zn Polymetallic Deposit, Inner Mongolia*; China University of Geosciences: Beijing, China, 2021.
49. Sun, Y.L.; Xu, H.; Zhu, X.Y.; Liu, X.; Jiang, B.B. Characteristics of fluid inclusion and its geological significance in the Weilasituo tin polymetallic deposit, Inner Mongolia. *Miner. Explor.* **2017**, *8*, 1044–1053.
50. Wang, J.B.; Wang, Y.W.; Wang, L.J. Tin-polymetallic metallogenic series in the southern part of Da Hinggan Mountains, China. *Geol. Explor.* **2005**, *6*, 18–23.
51. Wang, L.J.; Wang, J.B.; Wang, Y.W. Metallogenic mechanism of fluid and prospecting forecast of Dajing Sn-Cu polymetallic deposit, Inner Mongolia. *Acta Petrol. Sin.* **2015**, *31*, 991–1001.

applied sciences

MDPI

Article

A Complex Meso–Cenozoic History of Far-Field Extension and Compression: Evidence from Fission Track Analysis in the Helanshan Mountain Tectonic Belt, NW China

Cheng Wu *, Yu Wang, Wanming Yuan and Liyun Zhou

Institute of Earth Sciences, China University of Geosciences, Beijing 100083, China
* Correspondence: hugh_pocket@126.com; Tel.: +86-10-82321028

Abstract: The Helanshan Mountain tectonic belt (HTB) is an intraplate deformation belt along the northwestern border of the Ordos Block in the North China Craton. When and why this intracontinental tectonic belt formed, its subsequent uplift and erosion, and the relationships between ranges and adjacent basins remain unclear. To better assess the connections between the temporal and structural activity in HTB, apatite fission-track (AFT) and zircon fission-track (ZFT) analyses were conducted in this study. The lack of adequate FT data from the HTB is a source of contention and dispute. This paper collected samples for AFT and ZFT techniques from the central and southern HTB, trying to improve the research. The ZFT and AFT ages could be divided into the following 7 groups: 279 Ma, 222–213 Ma, 193–169 Ma, 151–147 Ma, 130–109 Ma, 92–77 Ma, and 65–50 Ma. The inverse modeling results of AFT indicate 4 fast cooling episodes of 170–120 Ma, 120–95 Ma, 66–60 Ma, and ~10–8 Ma to the present. Combining the results of FT analysis with radial plot and inverse modeling of AFT, the following eight age groups are believed to reveal the distinct tectonic activities in HTB: the first age group of 279 Ma mainly represented the back-arc extension of the southern HTB; the age group of 222–213 Ma was bounded with NNE-SSE trending contraction between the South China block and North China Craton; the event of 193–169 Ma responded to the post-orogenic collapse followed after the second event; the 151–147 Ma group was interpreted as the eastward extrusion induced by the subduction between Qiangtang and Lhasa blocks; the Early Cretaceous (130–109 Ma) group was not only affected by the rollback of the Pacific Plate, but also denoted the collapse of the thickened lithosphere formed in the Late Jurassic; the Late Cretaceous (92–77 Ma) group was attributed to long-distance impact from the subduction of the Pacific Plate beneath the Eurasian Plate; the event during 65–50 Ma was a correspondence to far-field effect of the onset collision between the Eurasian and Indian Plates; and from 10–8 Ma to the present, the progressive collision of the Indian and Eurasian Plates have a significant impact on the HTB and the northeastern Tibetan Plateau.

Keywords: thermal evolution; tectonic events; rapid uplift; apatite fission-track; zircon fission-track; Helanshan tectonic belt

Citation: Wu, C.; Wang, Y.; Yuan, W.; Zhou, L. A Complex Meso–Cenozoic History of Far-Field Extension and Compression: Evidence from Fission Track Analysis in the Helanshan Mountain Tectonic Belt, NW China. *Appl. Sci.* **2024**, *14*, 3559. https://doi.org/10.3390/app14093559

Academic Editor: Andrea L. Rizzo

Received: 11 March 2024
Revised: 19 April 2024
Accepted: 19 April 2024
Published: 23 April 2024

1. Introduction

The HTB is situated between the Alxa Plate and the Ordos Block in the northwest of the North China Craton (NCC), the Langshan and Liupanshan Mountains, and the Qinling Orogenic Belt to the north and south, respectively (Figure 1). As an important N–S trending tectonic belt, geologists pay more attention [1–9] and find that the HTB experienced complicated intracontinental deformation during the Mesozoic and Cenozoic. In addition, the HTB is near the northeastern Tibetan Plateau (TP) and its neighboring region, which are the hot spots for investigating Meso–Cenozoic denudation history [10–14] and the far-field effects from the subduction between the Eurasian and Indian Plates during the Cenozoic. However, the specific Meso–Cenozoic deformation ages, mechanisms, and dynamics still need to be addressed due to insufficient thermochronology evidence of uplift, exhumation, and deformation in the past for the HTB.

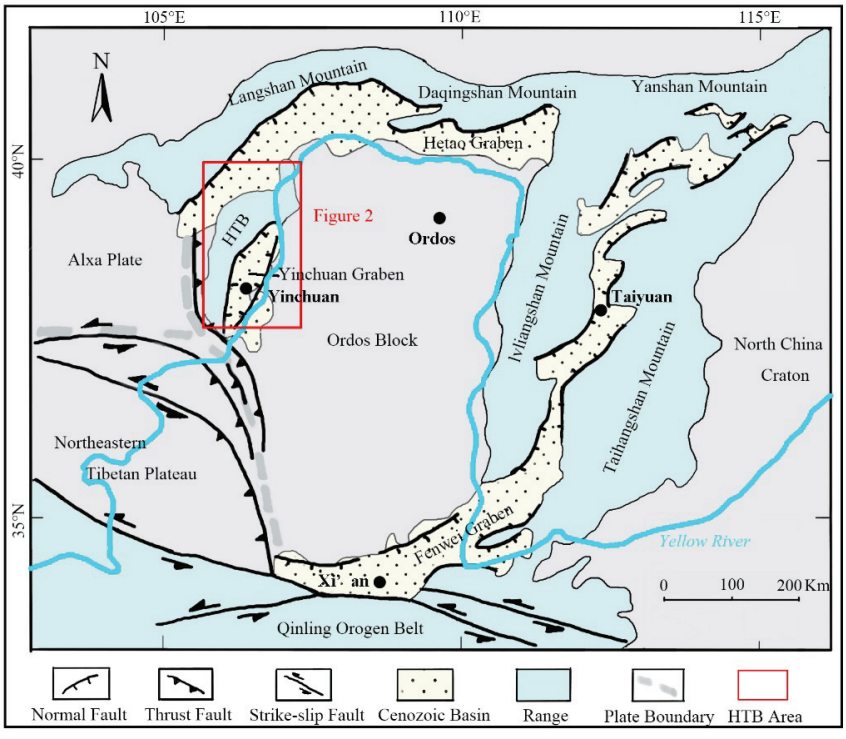

Figure 1. Tectonic map of the HTB modified from Darby and Ritts (2002) [1].

The HTB occurred along the western margin of the Ordos Block, and their geological processes were interconnected according to basin–range theory. Prior research suggests that the HTB and Ordos Block experienced the subsequent phases: (1) the N–S to NNE–SSW trending extension in the Early Jurassic [8,15], which was induced by the post-collapse after the Triassic collision between the North China Craton with the South China Block [16]; (2) the multi-directional compression in the Late Jurassic (mainly in the E–W direction [1,6,17]), which was effected by the subduction of the Pacific Plate in the east, the growth of the Qiangtang-Lhasa Block in the southwest and Siberian Block in the north; (3) a WNW-trending extension in the Early Cretaceous [3,8,15], correlated to the roll-back of subduction of the east Pacific Plate; (4) the NW–SE trending compression in the Late Cretaceous [4,8], transmitted from the growing subduction boundary of the Pacific Plate; and (5) the NE-trending compression in the Late Miocene [3,18,19], resulting from the uplift and NE-directed growth of the TP.

Some important AFT data were used by Zhao et al. (2007) [20] and Liu et al. (2010) [5]. However, their samples were limited to the northern and central HTB (Figure 2) and the ZFT data were insufficient. Therefore, the main objective of this study is to examine the exhumation history of the southern and central HTB using a combination of AFT and ZFT thermochronology, and the existing FT data obtained from previous studies were designed to be complemented. These newly acquired FT data will be utilized to enhance comprehension of the far-field impact resulting from the subduction of the Pacific Plate in the eastern region, as well as the collision between the Indian Plate and the Eurasian Plate.

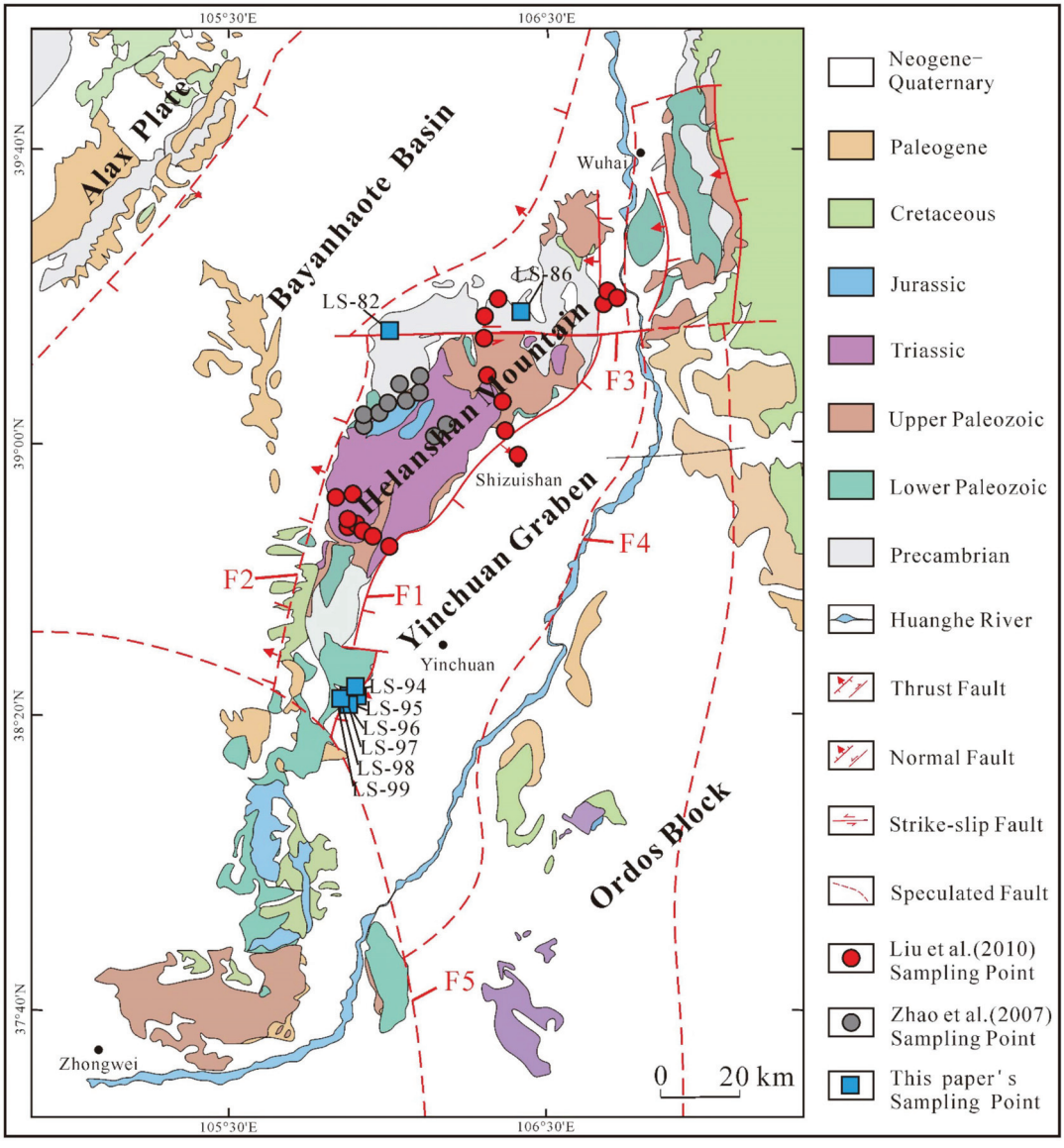

Figure 2. Geological map of HTB modified from Yang et al. (2018) [3]. F1—East Piedmont Fault, F2—West Piedmont Fault, F3—Xiaosongshan thrust fault, F4—Huanghe fault, F5—Sanguankou fault [5,20].

2. Geological Setting

The Helanshan Mountain tectonic belt (HTB), an important tectonic boundary between East and West China with an abrupt geophysical field, trends NNE and forms the northwestern margin of the Ordos Block. The eastern Yinchuan Block is a Cenozoic rift basin with over 7000 m of Cenozoic deposits.

The Neoarchean–Paleoproterozoic metamorphic basement rocks and the Meso–Neoproterozoic strata consist of sandstone and dolostone and are mainly exposed in the northern HTB. The Cambrian rocks include phosphorus sandstone, limestone with

mudstone, and dolomitic limestone. The Ordovician rocks consist of dolomite, sandstone, limestone, and conglomerate. They mainly occur in the southern HTB and the central HTB and have experienced multiple tectonic deformations from the Paleozoic to the Cenozoic [21,22]. The Permian rocks mainly involve quartz sandstones, shales, and siltstone interbedded with coal layers in the central and the northern HTB [23].

The Triassic succession is characterized by quartz sandstones interlayered with shales in the central HTB, and angular unconformity is found between the Late Triassic shale rocks and the Middle Jurassic sandstone and conglomerate. The Jurassic rocks are fluvial-lacustrine deposits, which comprise predominantly sandstones, siltstones, and mudstones with coal beds. The Late Jurassic Fengfang River Formation consists of conglomerate and sandstone, which is scarcely distributed in the north of the HTB. The Early Cretaceous coarse-grained conglomerates and sandstones are unconformably overlying the previous strata in the central HTB and southern HTB.

The Cenozoic sedimentary section has three primary groups: the Qingshuiying Group, the Hongliugou Group, and the Ganhegou Group [23]. The Oligocene Qingshuiying Group is composed of mudstone and sandstone and belongs to fluvial-lacustrine deposits. The Miocene Hongliugou Group comprises mudstone and clay. Moreover, the Pliocene Ganhegou Group consists of sandstone, siltstone, and mudstone. In addition, the Miocene strata developed several parallel unconformity sections with the lower Oligocene in Dingjia from Tongxin Country and in Hongliugou from Zhongning Country.

The East Piedmont Fault of the HTB is located on the east edge of the range belt and is a significant boundary between the uplifted HTB and the rifted Yinchuan Block. In the Late Jurassic and Early Cretaceous, a WNW–ESE horizontal shortening [6] developed, causing west- or east-directed folds and thrusts [1]. During the Late Jurassic, the Upper Jurassic comprising sandstone and mudstone was overlapped by the Early Paleozoic formation due to the compression and movement of the Xiaosongshan thrust nappe. The West Piedmont Fault of the HTB dipped to WNW and the East Piedmont Fault of the HTB dipped to SE, both of which are normal boundary faults from the NNE-trending HTB. Meanwhile, the West Piedmont Fault and the East Piedmont Fault controlled the Cretaceous sedimentation in the Bayinhaote Basin and Yinchuan Basin (Figure 2), respectively [3]. Moreover, the East Piedmont Fault of the HTB has developed different lithologic strata in the corresponding wall since Cenozoic. While the upper (east) wall has fluvial and lacustrine facies deposits, a piedmont deposit exists in the lower (west) wall. During the Cenozoic, the NE–SW extension along the HTB formed the arc-shaped Hetao graben and the NNE–SSW trending Yinchuan Block [2]. The above geology and structure suggest that the HTB underwent intense extensional deformation and exhumation during the Cenozoic.

Since the Phanerozoic, the HTB has exhibited little magmatic activity. In the Rujigou region, only a few Late Triassic–Early Jurassic basaltic beds developed [3,24,25].

3. Sampling and Analyses

3.1. Sampling

This study collected eight samples for zircon and apatite fission-track analysis from the southern and central HTB (Figure 2). The sample information is displayed in Table 1. Sample LS–82 is from an Archean gneiss, which is composed of migmatitic granite and K-feldspar granite. Sample LS–86 is attributed to an Archean granitic gneiss, characterized by a red color and composed of K-feldspar granite. The samples LS–82 and LS–86 were collected from the central HTB (Figure 2), while samples LS–94, LS–95, LS–96, LS–97, LS–98, and LS–99 were collected in the southern HTB from the Ordovician conglomerates (Figure 3), characterized by breccia structure and gray color, among which the gravels mainly comprise limestones and dolomites.

Table 1. Description of samples and samples' host rock.

Samples	Strata	Lat (N) Lon (E)	Elevation (m)	Lithology
LS–82	Archean	39°15′23″ 106°01′53″	1541	Gneiss
LS–86	Archean	39°17′42″ 106°17′16″	1548	Granitic Gneiss
LS–94	O_2	38°21′28″ 105°52′30″	1422	Conglomerate
LS–95	O_2	38°21′28″ 105°52′30″	1432	Conglomerate
LS–96	O_2	38°21′28″ 105°52′30″	1433	Conglomerate
LS–97	O_2	38°21′29″ 105°52′31″	1435	Conglomerate
LS–98	O_2	38°21′29″ 105°52′31″	1442	Conglomerate
LS–99	O_2	38°21′29″ 105°52′31	1451	Conglomerate

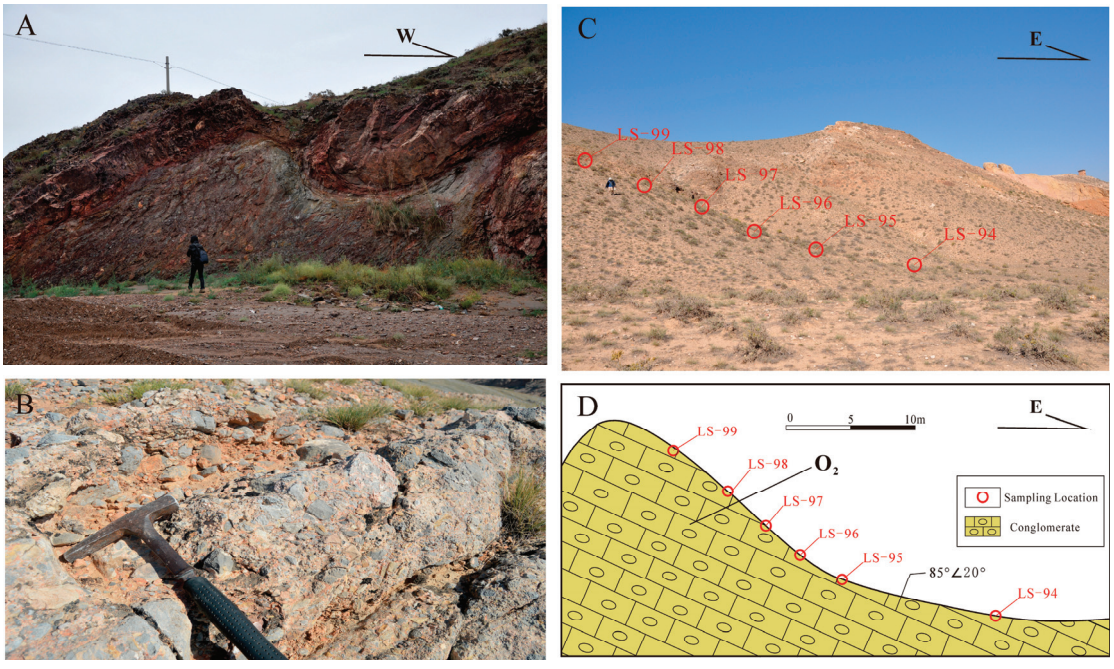

Figure 3. The field photos and section plot in central and southern HTB. (**A**) The field photo of the gneiss from the central HTB. (**B**) The field photo of the conglomerate from the southern HTB. (**C**) The field photo of the sampling location from the southern HTB. (**D**) Section plot of sampling location from the southern HTB.

3.2. FT Analysis

AFT and ZFT methods were used to analyze samples. The fission track analyses were conducted at the Beijing Anputaide Technology Co. Ltd., Beijing, China. Apatite and zircon grains were obtained from crushed rock samples using standard magnetic and heavy liquids separation techniques. Zircon was mounted in FEP Teflon wafers on glass slides, polished, and etched to reveal the spontaneous tracks in a eutectic (1:1) mixture of KOH and

NaOH at 220 °C for about 22 h. Apatite grains were mounted in epoxy resin on glass slides, and polished to expose grain surfaces to etching in 5% HNO_3 for 20 s at 21 °C [26]. This study employed the external detector method for zircon and apatite fission-track analysis. The muscovite flake was then irradiated with thermal neutrons in the well-thermalized (Cd value for Au > 100) hot neutron nuclear reactor at the Beijing Institute of High Energy Physics, Chinese Academy of Sciences. After irradiation, the muscovite grains were etched in 40% HF for 20 min at 25 °C to reveal the induced fission tracks. Using a 100× dry objective and a magnification of 1500, the density of spontaneous and induced fission track populations was determined. The lengths of horizontally confined fission tracks in apatite grains were determined using methods like those employed for age determinations [27]. Neutron fluence was monitored using CN_2 and CN_5 uranium dosimeter glasses for the zircon and apatite samples, respectively.

The Zeta calibration method [28–30] was applied to calculate the fission-track central ages. Green's (1981) [31] error calculation approach was used, and the χ^2 test of Galbraith (1981) [28] was applied to judge whether or not all the grains are attributed to a single population. The $P(\chi^2) < 5\%$ represents that the single-grain ages of the sample are homogeneous, which means they experienced a single thermal event. The $P(\chi^2) < 5\%$ denotes that the single-grain ages differ and should be decomposed into several groups.

4. Results and Interpretation

4.1. AFT Age Data

The central ages, mean track lengths, and mean Dpars of the apatite fission track are listed in Table 2. The seven samples (LS–82, LS–86, LS–94, LS–95, LS–96, LS–97, and LS–98) have been dated with the AFT methods. The mean track lengths vary from 11.8 ± 1.8 μm to 12.8 ± 1.8 μm, and the central ages of the AFT are between 52 and 118 Ma. The standard deviation (SD) ranges between 1.5 and 1.8 μm for the AFT track lengths. The mean Dpar values of the AFT range from 1.25 to 1.49 μm.

All AFT ages in this paper are younger than their strata ages, indicating that all single-grain ages have been reset after deposition (Figure 4A). Most of the samples experienced multiple annealing processes because the χ^2 value is <5%, except sample LS–82, for which the χ^2 value of apatite is >5%. Apatite fission track age was decomposed by using Radial Plotter [32] with the automatic mixture model (Figure 5), and then divided into 4 age groups (Figures 4A and 5): 147 Ma, 120–109 Ma, 92–77 Ma, and 65–50 Ma.

According to Gleadow's collection and conclusion [33], we could divide the apatite tracks into three types with different dispersions of the track lengths and standard deviations: (i) the freshly induced tracks in all apatites with a narrow and symmetrical length distribution of 16.3 μm track length and 0.9 μm SD; (ii) the track lengths in apatite from undisturbed 'volcanic' rocks with track lengths ranging from 14 to 16 μm and SD ranging from 0.7 to 1.3 μm; and (iii) the track lengths in apatite from crystalline basement rocks with track lengths ranging from 12.2 to 13.9 μm and SD ranging from 1 to 1.6 μm. For type (ii), if the mean length is <13 μm and SD > 2 μm, a bimodal distribution will exist. Therefore, the tracks in this study belong to type (iii) with <14 μm track length and 1.8~1 μm SD, indicating that the southern HTB has crystalline basement rocks.

Table 2. Fission-track data of apatite and zircon from the central and south HTB.

Samples/ Mineral	N	Spontaneous ρ_s (10^5/cm^2) (Ns)	Induced ρ_i (10^5/cm^2) (Ni)	Dosimeter ρ_d (10^5/cm^2) (Nd)	P(χ^2) (%)	Central Age (Ma) ($\pm$ 1σ)	Pooled Age (Ma) ($\pm$ 1σ)	Mean Track Length (μm) (N)	Mean Dpar (μm)
LS–82–Ap	35	3.207 (1491)	11.291 (5250)	9.107 (6788)	69.9	52 ± 3	53 ± 3	12.8 ± 1.8 (102)	1.37
LS–86–Ap	35	2.275 (1773)	7.558 (5889)	9.524 (6788)	0	59 ± 4	59 ± 3	12.2 ± 1.7 (107)	1.30
LS–94–Ap	37	6.182 (1808)	13.565 (3967)	9.93 (6788)	0.3	93 ± 6	92 ± 5	12.2 ± 1.5 (101)	1.25
LS–95–Ap	35	8.222 (1774)	17.848 (3851)	10.36 (6788)	0	90 ± 8	97 ± 5	12.7 ± 1.5 (108)	1.24
LS–96–Ap	35	15.856 (4266)	52.177 (14,038)	10.714 (6788)	0	61 ± 4	66 ± 3	12.2 ± 1.6 (112)	1.32
LS–97–Ap	35	8.585 (2049)	12.343 (2946)	8.573 (6788)	0	118 ± 8	121 ± 6	11.8 ± 1.8 (112)	1.49
LS–98–Ap	35	6.371 (1719)	11.648 (3143)	8.923 (6788)	0.7	99 ± 6	99 ± 5	11.9 ± 1.5 (110)	1.28
LS–94–Zr	36	146.74 (7645)	61.537 (3206)	12.792 (8055)	0	133 ± 7	137 ± 5	-	-
LS–95–Zr	24	177.869 (4511)	66.518 (1687)	13.282 (8055)	0	160 ± 10	159 ± 7	-	-
LS–96–Zr	20	169.687 (2869)	65.0 (1099)	13.773 (8055)	0	171 ± 13	161 ± 8	-	-
LS–97–Zr	35	127.275 (5067)	56.667 (2256)	14.263 (8055)	0	143 ± 9	144 ± 6	-	-
LS–98–Zr	34	176.761 (10,130)	71.525 (4099)	14.875 (8055)	0	166 ± 8	165 ± 6	-	-
LS–99–Zr	35	156.345 (4918)	66.188 (2082)	15.488 (8055)	0	162 ± 12	164 ± 7	-	-

Note: N = total number of analyzed grains. ρ represents track density. P(χ^2) is chi-square probability. "-" is no data. Apatite ages calculated with ζ (zeta) = 410 ± 17.6 (yr cm^2/tr) and zircon ages calculated with ζ (zeta) = 90.9 ± 2.8 (yr cm^2/tr).

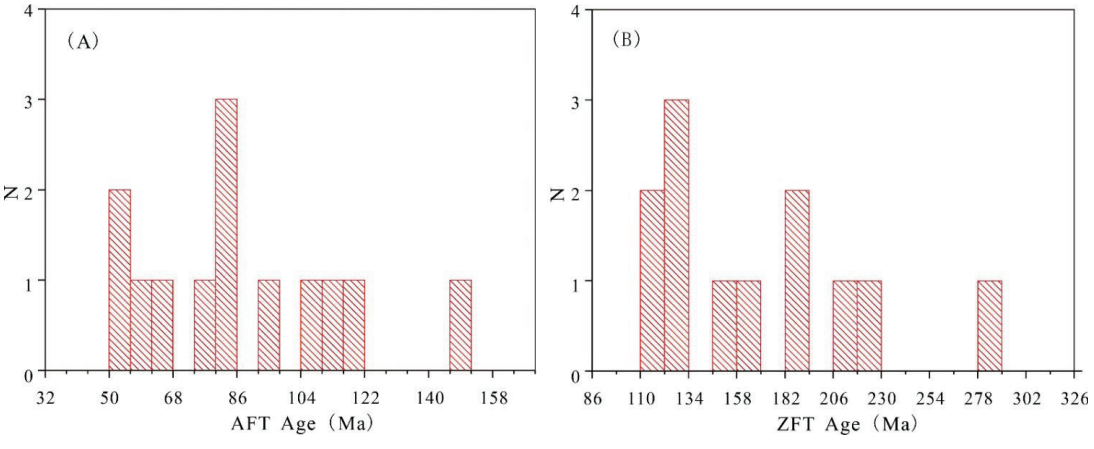

Figure 4. Histogram of the AFT age and ZFT age (N = number of analyzed grains in the correspondent age intervals). (**A**) It is shown that 4 AFT age groups of 147 Ma, 120–109 Ma, 92–77 Ma, and 65–50 Ma. (**B**) It is shown that 5 ZFT age groups of 279 Ma, 222–213 Ma, 193–169 Ma, 151 Ma, and 130–110 Ma.

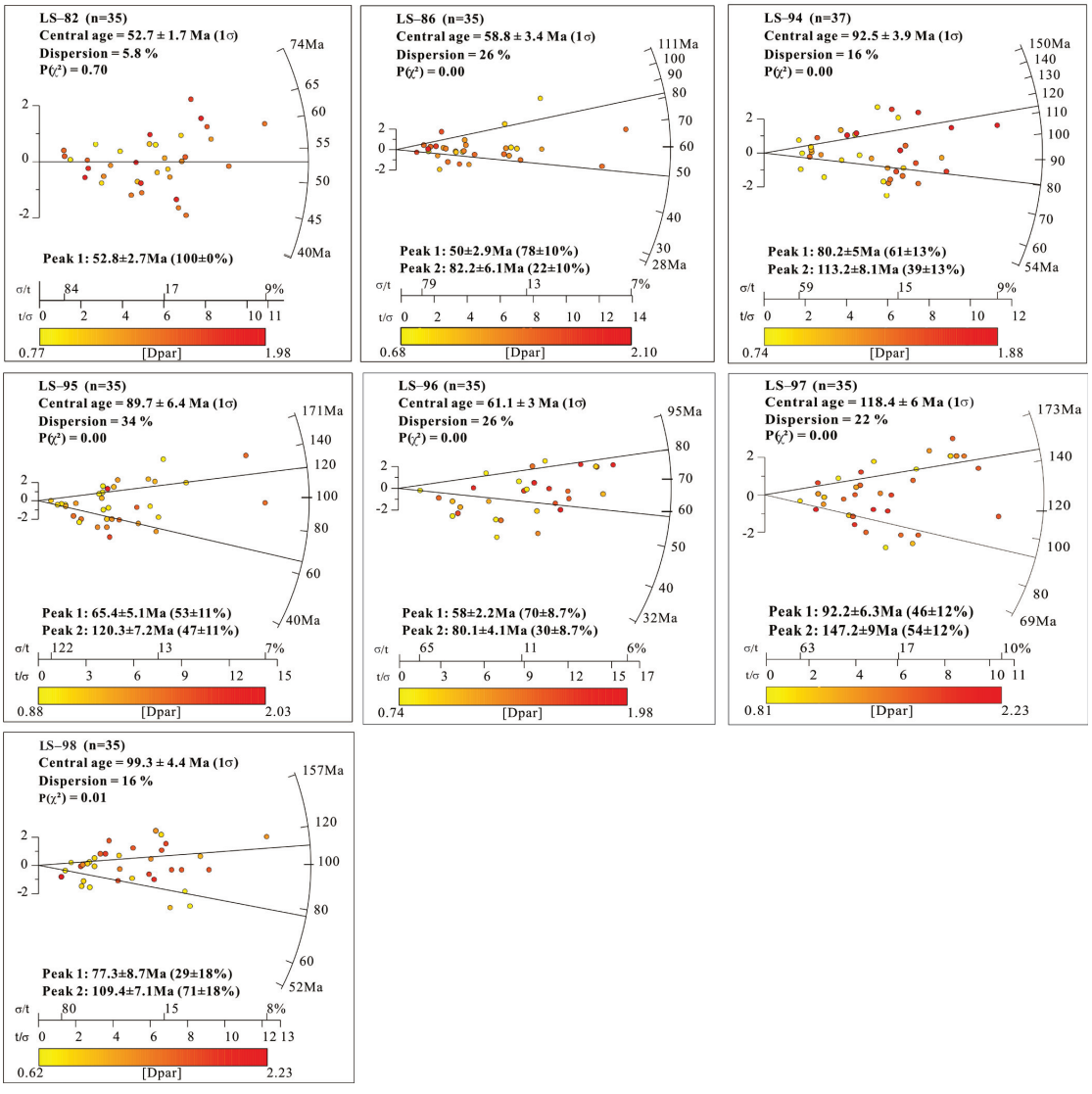

Figure 5. Apatite fission-track radial plots of the study samples from the Radial Plotter (including samples LS–82, LS–86, and LS–94–98).

4.2. ZFT Age Data

The central ages and χ^2 values of the zircon fission track are listed in Table 2. The samples LS–94, LS–95, LS–96, LS–97, LS–98, and LS–99 have been dated with the ZFT methods. ZFT central ages range from 133 to 171 Ma. All ZFT ages are younger than their corresponding strata ages (Figure 4B), indicating that all single-grain ages have been reset. Because the χ^2 value of all zircon samples is <5%, the Radial Plotter [32] with binomial peak-fitting method is used to help us distinguish the cooling age population. Figures 4B and 6 reveal that these six zircon grain ages can be divided into 5 groups: 279 Ma, 222–213 Ma, 193–169 Ma, 151 Ma, and 130–110 Ma.

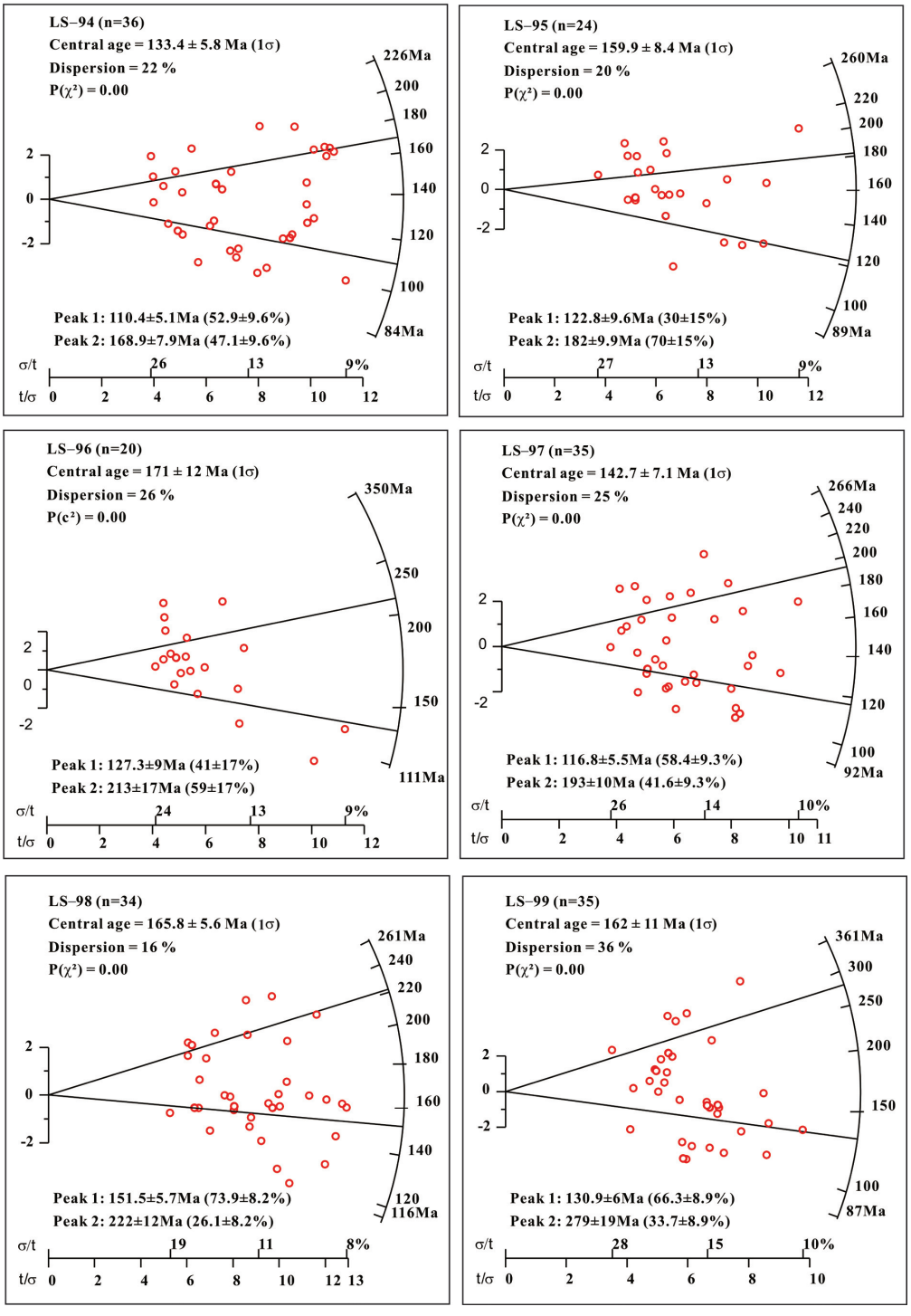

Figure 6. Zircon fission-track radial plots of the study samples (including samples from LS–94 to LS–99).

4.3. FT Age Data

The fission track ages of samples in the HTB were classified into 7 distinct groups: 279 Ma, 222–213 Ma, 193–169 Ma, 151 Ma, 130–109 Ma, 92–77 Ma, and 65–50 Ma, by the integration of AFT and ZFT analysis, facilitated by the utilization of Radial Plotter with a two mixture model.

4.4. Thermal History

Based on the distribution of AFT lengths and age data, the HeFTy software (Version. 1.8.3, Ketchman, 2005) [34] was used to better constrain the exhumation history. The time–temperature (t–t) history was calculated using the multi-kinetic annealing model of Ketchman et al. (2007a) [35] and the c-axis projected length of Ketchman et al. (2007b) [36]. Samples were modeled with at least 100 track-length measurements. The inverse models were executed with 10,000 randomly chosen time–temperature histories for each sample, which in all cases resulted in N > 1000 acceptable paths. A goodness-of-fit parameter (GOF) estimated the degree to which modeled data matched measured values. A path was accepted if the GOF value was >0.05; a good fit was indicated if the GOF value was >0.5 [34]. The initial simulation temperature was set at 130 °C, which is slightly higher than the AFT annealing temperature (120–60 °C). The lower limit of simulation temperature was set at 15 °C, based on the present-day mean surface temperature in the Helanshan Mountains. Because the age of sample LS–97 is old, the fission-track simulation initial time is set at 170 Ma. Furthermore, to explicitly illustrate the temporal pattern of sample LS–98's t–t history spanning from 120 to 110 Ma, the initial time of sample LS–98 is established at 130 Ma, while the other samples start at 120 Ma.

The modeling t–t paths of AFT samples from the central and southern HTB, cooling since 130 °C, are shown in Figure 7. Except for samples LS–82 and LS–86, the cooling paths for most samples share a three-stage cooling history. These three cooling paths include two episodes of rapid cooling that bracket an episode of slow cooling. Samples LS–94 and LS–95 share almost the same t–t history. They have the AFT ages of ~120 Ma when they pass across the upper limit of the partial annealing zone. Samples LS–94 and LS–95 underwent the first rapid cooling until 95 Ma with a cooling rate of 1.6 °C/Ma. Following this rapid cooling stage, a relatively stable episode occurred from 95 Ma to 10~8 Ma at a rate of 0.12 °C/Ma. The third fast cooling existed from 10~8 Ma, which is almost the same time when they entered into the lower limit of partial annealing zone until the present with the rapid cooling rate of 4.5 °C/Ma. The first relatively fast cooling stage of sample LS–97 lasts from 170 Ma to 120 Ma with a cooling rate of 0.47 °C/Ma, and its second rapid cooling episode developed from 10–8 Ma until the present at a rate of 4.5 °C/Ma. The sample LS–98 exhibits two rapid cooling episodes: the first one occurs from 130 Ma to 105 Ma, during which the temperature decreases from 115 to 70 °C with a cooling rate of 1.8 °C/Ma; the second one occurs from ~5 Ma to the present, recorded the temperature drop from 60 °C to 15 °C at a rate of 9 °C/Ma. The LS–82 and LS–86 samples have two- and four-stage cooling histories, respectively. Specifically, sample LS–82 experienced a period of stable cooling from 120 Ma to 60 Ma and entered the rapid cooling path from 60 Ma at a rapid cooling rate of 1.58 °C/Ma. Meanwhile, the sample LS–86 developed two rapid cooling histories from 66 to 60 Ma and from ~8 Ma to the present at a rate of 6.67 °C/Ma and 6.87 °C/Ma, respectively.

Overall, the inverse modeling of AFT revealed four rapid cooling episodes: 170–120 Ma, 120–95 Ma, 66–60 Ma, and ~10–8 Ma to the present. The first episode is mainly developed in the sample LS–97. The second rapid cooling stage occurred between the samples LS–94, LS–95, and LS–97. The third one is derived from the sample LS–86, which aligns with the outcome of AFT obtained using the radial plot. Finally, the majority of samples, except sample LS–82, exhibit the presence of the fourth accelerated cooling interval (8–0 Ma), indicating a widespread cooling event in the Late Miocene.

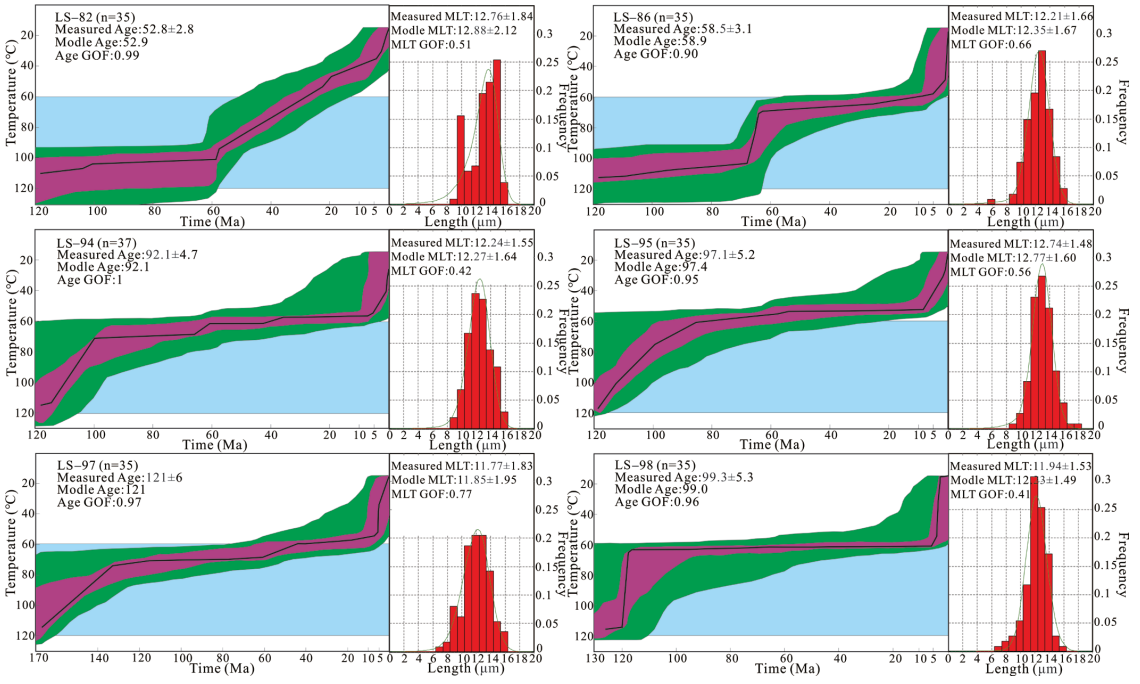

Figure 7. Inverse modeling T–t plot and track length distribution histogram of AFT samples from the central and southern HTB. (The light blue area is the partial annealing zone of apatite. The purple area corresponds to the range of good fits (GOF > 0.5) and the green area shows the range of acceptable fits (GOF = 0.05–0.5). The black line in the purple area represents the best modelled path. N means the number of measured apatite grains. GOF means good-of-fit parameter. MTL represents mean track length).

5. Discussion

5.1. Exhumation and Deformation History

The Ordos Block and its margins (HTB) have exhibited mechanical contrasts since the Early Paleozoic [37]. The transmission of stress from the continent margins to its interior is influenced by mechanical anisotropy, which, once established, localizes strain [1]. The Ordos Block is strong compared to HTB, so the strata in the Ordos Basin remain undeformed. There are three important geological progress around the Eurasian continent: the Paleo-Pacific subduction occurring along the eastern margin of the continent, the subduction/collision zone between the Siberian Plate, and the Mongolia-North China Block to the north of the HTB, involving Qiangtang and Lhasa Blocks to the southwest of the HTB. Due to such a sophisticated tectonic background on the central Eurasian Plate, it is challenging and impractical to connect deformation in the HTB with a single convergent plate boundary. Therefore, the subsequent segmented discussions will try to consider a wide range of geological circumstances surrounding the HTB within the same period.

5.1.1. Early Permian (279 Ma)

Sample LS–99 is the solo specimen in this research with a peak age of 279 Ma from ZFT analysis. Meanwhile, a few relevant age data are found and used in the HTB. However, the extensional back-arc basin was developed in the West Qinling [38], supported by the presence of deep-water sediments and geological structures in the Permian to Middle Triassic [39,40]. The geochronology of this intra-plate extension environment has been better defined by zircon LA-ICP-MS data from a diabase in the southern Alxa Block (276 Ma) [41],

an AFT age of 277–267 Ma in the southwestern Alxa Block [42], and zircon LA-ICP-MS data of 278 Ma in the West Qinling Orogenic Belt [43]. The majority of the northern HTB was deposited with sandstone and shale during the Early Permian, indicating a weak structural environment [23]. Moreover, a series of Permian volcanic interlayers existed in drill holes of the southwestern Ordos Block [23,44]. Consequently, there was a potential reduction in structural intensity from south to north. The activation of the back-arc extension on the south margin of the HTB and southern Alxa Block occurred during the Early–Middle Permian, as a result of the collision between the North China Block and the South China Block [45,46].

5.1.2. Late Triassic (222–213 Ma)

The peak age of Samples 98 and 96, as determined by ZFT analysis with the Radial Plotter, was 222–213 Ma. It is coherent with samples having ZFT ages of 230–210 Ma collected in the central HTB [47], where the Triassic strata were denudated during this interval. Several angular unconformities were observed in the Lower Jurassic Yanan and the Upper Triassic Yanchang Formations [23]. The rapid cooling event in the Late Triassic was revealed as 230–210 Ma in the north of the West Qinling Orogenic Belt with the feldspar multi-diffusion domain method and the AFT method [48]. The adakite and Himalaya-type granite (264–216 Ma) in the West Qinling Orogenic Belt were analyzed using zircon LA-ICP-MS dating, and the results suggested that the thickened crust was formed by continent–continent collision [49]. The presence of the Late Triassic unconformity associated with the NNE–SSE shortening was caused by the Qinling–Dabie orogeny [1,6], a consequence of the collision between the South China Block and the North China Craton.

5.1.3. Early-Middle Jurassic (193–169 Ma)

The Early to Middle Jurassic period was characterized by the development of coal-bearing formations, indicating that the HTB had a period of relative inactivity and experienced extension, with extension direction in the N–S to NNE–SSW [8,9]. Further deformation occurred around the Ordos Basin within the same tectonic context. The E–W-trending extensional basins in the north of Ordos Basin were delineated by normal growth faults along the Daqingshan Mountains [50]. The Early–Middle Jurassic basins in the Alxa Block to the west of the HTB were confined by E–W-striking normal faults [51]. Meanwhile, volcanic activities were developed around 170 Ma in the western Ordos Basin [52], Taihang Mountain [53], and Qinshui Basin [54]. We prefer to attribute this extensional stress regime to the result of post-orogenic collapse, followed by the collision between the North and South China blocks in the Triassic. Meanwhile, this period signifies the tectonic shift from the Triassic period, characterized by a collisional tectonic system with a strong N–S trend, to the Late Jurassic period with nearly E–W-trending compression.

5.1.4. Late Jurassic (151–147 Ma)

By integrating the AFT and ZFT results obtained from the Radial Plotter analysis and the FT data from the prior research, it can be concluded that the Late Jurassic is another important geological episode in the HTB. In the northeastern HTB, Zhuozi Shan and Helanshan Mountain were separated by a left-lateral strike-slip fault system between the Late Jurassic and the Middle Cretaceous [1]. Meanwhile, the Lower Paleozoic carbonates were thrust southeastwards atop the folded Upper Jurassic, composed of sandstone and mudstone. Xiaosongshan thrust nappe places the Early Paleozoic formation upon the Jurassic strata in the north of HTB [55]. The Lower and Upper Jurassic layers exhibited denudation and absence, while the southwest of Ordos Basin displayed the development of complex thrust and reverse faults [56]. The Fengfang River Formation, consisting of sandstone and conglomerate in the Late Jurassic, was discovered in the north part of Ordos Basin by seismic profile [15] and at the base of the Kexue Mountain to the south of the HTB [57]. It denotes that the HTB experienced an intense structural uplift event in the Late Jurassic.

Moreover, various geochronology techniques were employed in the Late Jurassic around the HTB area. The age of 150–140 Ma marked the initiation of structural mechanism conversion, and this conclusion is drawn from a comprehensive analysis, including structural deformation, volcanic activity, and basin migration [58,59]. The 150–145 Ma is one of the peak age intervals from fission track analysis in the west of the Ordos Basin [60]. The study was undertaken in the southwestern Ordos Basin [61] and in the Qilianshan Mountains [62] to determine the similar peak ZFT age of 154–147 Ma and peak AFT age of 153–135 Ma, respectively. The peak FT age of ~145 Ma in the southwestern Ordos Basin is closely connected with the thrust nappe in the Late Jurassic [56]. Zhao et al. [20] conducted the ZFT experiment of samples in the HTB and concluded that the HTB underwent a transition from extensive fault depression to a compression environment during 157–139 Ma. Crust shortening along the HTB in the Late Jurassic caused the shift from the expansion (Early–Middle Jurassic) to the compression environment (Late Jurassic). The eastward migration is indicated by the Xiaosongshan thrust nappe and the left-slip motion of the NW-trending strike fault. Therefore, the dominant factor responsible for the Late Jurassic deformation in the HTB is the eastward extrusion resulting from the subduction belt between the Qiangtang and Lhasa blocks in the TP [63,64].

5.1.5. Early Cretaceous (130–109 Ma)

Based on previous analytical procedures (AFT age data, ZFT age data, and the inverse modeling of thermal history), the denudation event between 130 and 110 Ma of HTB is confirmed to represent a significant geological episode in the Late Mesozoic. The Jurassic sandstones are unconformably overlain by the lower Cretaceous strata, constrained by the West Piedmont Fault of the HTB. The Late Jurassic Fengfang River Formation is interbedded with sandstone, and the Lower Cretaceous overlies conglomerate to the southeast of Yinchuan Basin [23]. In addition, a series of angular unconformity interfaces between the pre-Cretaceous and the Late Cretaceous formation is found in the southern HTB [65]. Early Cretaceous strata in Bayinhaote Basin to the west of the HTB were controlled by the West Piedmont Fault of the HTB. Meanwhile, the East Piedmont Fault restricted the development of Cretaceous formation in the Yinchuan Basin [3]. Therefore, both of these two faults were active during the Early Cretaceous. The maximum principal stress direction shifted from a nearly N–S trend in the Mid–Late Jurassic on the eastern margin of Ordos Basin [66], to an E–W oriented extension of the HTB in the Early Cretaceous. Furthermore, the basalt geochronological data obtained from Gugutai in the HTB provides evidence of the extensional tectonic setting and dynamic during the Early Cretaceous [25,67].

In addition to the HTB, the presence of angular unconformity between the Late Jurassic strata and the Early Cretaceous strata has been identified in several adjacent regions, including northern North China Craton [68], South China [69,70], and the Korean Peninsula [71]. Tectonic and geochronological data indicate that the NW–SE-trending extensional event occurred throughout the NCC and its adjacent area during the Early Cretaceous. Liupanshan Basin, restricted by the normal faults, was characterized by the 3 km thickness of sediments, indicating a strong rapid uplift event in the Early Cretaceous, supported by the FT age of ~130 Ma [52]. The Early Cretaceous (140–120 Ma) saw fast cooling events, using the feldspar multi-diffusion domain approach and the AFT method [48] in the West Qinling Orogenic Belt. Meanwhile, the MDD technique revealed the same 140–120 Ma ages in the East Kunlun Orogenic belt [72]. The weak young trend of Late Mesozoic crustal extension initiated in Mongolia and northern China (ca. 150–145 Ma) [73–75], then progressively developed southeastwards (140–130 Ma) [76,77], and finally spread throughout all of NE Asia (130–120 Ma) [78].

Based on the above evidence, the HTB and the North China Craton were affected by uniform geodynamics during the Early Cretaceous. Prior numerous investigations prefer to link the Early Cretaceous extension of the HTB with the northwestward subduction of the Paleo-Pacific Plate ([3,6]). However, the fast conversion of structural settings should not be ignored. Specifically, the lithospheric thickening caused by the Late Jurassic compression

implies the Early Cretaceous extension deformation in North China Craton (including HTB) [8,74,79]. Therefore, we conclude that the Early Cretaceous extension of the HTB and the North China Craton is not influenced by a solitary factor. Since the remote effect from the rollback of the Paleo-Pacific Plate in the east, the collapse of the thickened lithosphere also played a significant role.

5.1.6. Late Cretaceous (92–77 Ma)

The AFT sample analysis from the southern HTB (LS–94, 95, 96, 97, 98) with Radial Plotter suggests that a rapid cooling event was developed during 92–77 Ma. It is almost synchronized with the AFT data from the central HTB samples (90–70 Ma) [4] and Zhao's research [20] in HTB (88–76 Ma). Meanwhile, the nearly identical AFT ages of 104–81 Ma were developed in the Qilianshan Mountains [62]. The strata formed in the Late Cretaceous are absent in the HTB [23] and Alax Block. Additionally, other basins in eastern Asia, such as Hailar Basin [80] and Songliao Basin [81], also experienced an uplift in the Late Cretaceous, resulting in the formation of strata lacuna. The above evidence with lacked strata indicates that this event is prevalent in the eastern North China Plate as well. The findings of the AFT research conducted around 90 Ma were disseminated across several regions in eastern China, such as the Songliao Basin [82], Jiaolai Basin [5,83], and Qinling-Dabie orogenic belts [84]. Due to this extensive deformation that occurred in Eastern China simultaneously, we believe that the exhumation of HTB in the Late Cretaceous is caused by the convergence between the Pacific and Eurasian Plates.

5.1.7. Early Cenozoic (65–50 Ma)

The AFT radial plot results (Figure 5) demonstrate that the HTB has a rapid denudation event during the Early Cenozoic (mainly in 58–50 Ma). Few relevant ages existed in the HTB, but some were located in the periphery of the Ordos Basin. Huang et al. [85] conducted the ZFT and AFT analysis in the southeastern Ordos Basin and East Qinling Orogenic Belt, and their research shows that the AFT had a rapid uplift age of 66–59 Ma. Meanwhile, the apatite and zircon samples collected from the Kou Zhen area in the south of Ordos Basin exhibit a strong correlation in cooling ages ranging from 63 to 59 Ma [56]. The majority of AFT radial plot ages fall into the interval of 58–50 Ma, and they are close to the rapid cooling events derived from AFT and ZFT data in East Kunlun (~56–45 Ma) [86,87] and Qilian Shan Mountains (~60–50 Ma) [88]. Therefore, the presence of comparable FT ages in the southern East Kunlun Orogenic Belt, North Qinling Orogenic Belt, and the northern HTB suggests that this Early Cenozoic deformation can be attributed to the transfer of the far-field stress from the Eurasian and Indian plates collision boundary. Hence, we suggest that the comparable Early Cenozoic event observed in the HTB could be recognized as a correspondence to the far-field effect of the collision between the Eurasian and Indian Plates.

5.1.8. Miocene (10–8 Ma)

According to the t–t plots described above, the majority of samples experienced rapid cooling initiated at ~10–8 Ma. Moreover, this timing agrees with the study of Yang (2018) [3] and Liu (2010) [5]. Although Zhao's (2007) [20] research of uplift time from AFT has many discrepancies from our results, the differences in sampling location and analytical method could be the main causes, as mentioned earlier. However, 15 Ma is one of the key age groups achieved in their study. According to field observations, the Ordovician strata thrust northeastward over the Eocene Sikouzi Formation in the southwest HTB [7]. In the meantime, an open syncline dipping southwest of the Eocene developed in the footwall, indicating a contraction in the NE–SW direction. Based on the regional geology report of BGMRNXHAR [23], the Miocene strata developed several parallel unconformity sections with the lower Oligocene. Since the Cenozoic, the east boundary fault's corresponding wall has distinct lithologic strata. In detail, the upper (east) wall has a different petrological deposit compared to the lower (west) wall, indicating a denudation phase in HTB.

Analysis of apatite fission tracks provides a method to constrain the cooling history of the HTB and adjacent areas. The uplift of Qilianshan Mountains was initiated from the Early Miocene with coarsen sediments and experienced an acceleration event with a higher denudation rate from the Late Miocene to Pliocene [64], implying that Qilian Shan Mountains was affected by the far-field stress between the Indian Plate and Eurasian Plate. The provenance analysis of sediments from the West Hexi Corridor indicates that the uplift of the North Qilian Shan Mountains began in the Late Miocene [89]. The cooling episode in the northwestern Qilian Shan Mountains occurred 20–10 Ma ago [90]. Tapponnier et al. (2001) [91] noted that TP grows along the Altyn Tagh Fault branches from the Miocene. Meanwhile, the underthrusting of the Indian Plate beneath the southern TP after the Middle Miocene could be demonstrated by the seismic and GPS data [92] and the $^{40}Ar/^{39}Ar$ thermochronological constraints [93]. In summary, the contraction of the Indian and Eurasian Plates not only had a significant impact on the solid deformation and the uplift of the southern TP during the Late Miocene, but also accelerated the growth of the northeastern TP. Meantime, the eastward extrusion of the TP squeezed the adjacent areas, including HTB, Qilian Shan Mountains, and the West Hexi Corridor. Therefore, the aforementioned NE-SE direction contraction in HTB could be interpreted as a consequence of the uplift and NE-directed growth of the TP in the Late Miocene caused by the collision between the Indian Plate and the Eurasian Plate.

5.2. Comparative FT Analysis with Previous Study in HTB

This investigation has identified the following eight rapid cooling events as described above: Early Permian (279 Ma), Late Triassic (222–213 Ma), Early–Middle Jurassic (193–169 Ma), Late Jurassic (151–147 Ma), Early Cretaceous (130–109 Ma), Late Cretaceous (92–77 Ma), Early Cenozoic (65–50 Ma), and Late Miocene (10–8 Ma). The comparative FT analysis of the HTB with previous works is necessary to better understand the evolution of the HTB. Liu et al.'s (2010) [5] AFT analysis reveals that the HTB experienced an accelerated exhumation beginning at 12–10 Ma, which is in accordance with our result at 10–8 Ma. They concluded that HTB exhibited a southwestward titling pattern during the Late Miocene, based on the AFT data. Specifically, the date of the rapid uplift event is older in the south and younger in the north. However, our samples collected in the southern HTB exhibited a nearly identical young event of 10–8 Ma to their results (12–10 Ma) from the northern HTB, implicating that their FT evidence of hypothesis is insufficient. Zhao et al. (2007) [20] proposed the 4 fast cooling stages in HTB based on the FT analysis: 157–139 Ma, 121–97 Ma, 88–76 Ma, and 50–37 Ma. The chronology of the other rapid cooling events partially coincided with our research, suggesting a strong coherence as a whole, except for the youngest event in the Eocene (50–37 Ma). While their research indicates an extension or compression geological environment, a comprehensive geodynamic explanation for most episodes is lacking. Shi et al. (2019) [4] discovered two distinct periods of exhumation in HTB using AFT data: the Late Cretaceous (90–70 Ma) and after 30 Ma. The first stage coincides with this study and both of them have a similar geodynamic, resulting from the horizontal shortening transmitted by the subduction between the Pacific and Eurasian Plates. These two studies in the second stage share the same geodynamics (northeastward expansion of the TP) but differ in timing. In summary, the FT ages in the Early Permian (279 Ma), the Late Triassic (222–213 Ma), the Early–Middle Jurassic (193–169 Ma), and the Early Cenozoic (65–50 Ma) have not been extensively convinced in the prior papers. Meanwhile, new ideas or additions to geodynamics are proposed, such as events that happened in the Late Jurassic (151–147 Ma), the Early Cretaceous (130–109 Ma), the Late Cretaceous (92–77 Ma) and the Late Miocene (10–8 Ma).

6. Conclusions

In this study, we conducted AFT and ZFT techniques to study Meso–Cenozoic thermal-tectonic evolution in the central and southern HTB. AFT analysis of 7 samples with the radial plot could be divided into 4 age groups: 147 Ma, 120~109 Ma, 92~77 Ma, and

65~50 Ma. The inverse modeling of AFT suggests the presence of 4 rapid cooling stages: 170–120 Ma, 120–95 Ma, 66–60 Ma, and 8–0 Ma. In addition, based on the ZFT analysis of 6 samples with radial plots, the following 5 age groups could be discovered: 279 Ma, 222~213 Ma, 193 ~169 Ma, 151 Ma, and 130~110 Ma. In summary, the analysis of the ZFT and AFT ages could be categorized into the following 8 age groups: 279 Ma, 222–213 Ma, 193–169 Ma, 151–147 Ma, 130–109 Ma, 92–77 Ma, 65–50 Ma, and ~10–8 to the present.

This FT analysis reveals that the central and southern HTB has undergone a series of tectonic thermal events. The Early Permian of 279 Ma was characterized by a weak structural episode, representing the back-arc extension in the south HTB and southern Alxa block. The Late Triassic age group of 222–213 Ma was marked with NNE–SSE trending contraction between the South China and North China cratons. The weak extension event in the Early–Middle Jurassic of 193–169 Ma corresponded to the post-orogenic collapse after the Triassic strong compression event. The 151–147 Ma event was caused by the eastward extrusion of the Alax and HTB, resulting from the far-field effect of the subduction between the Qiangtang and Lhasa blocks. The Early Cretaceous (130–109 Ma) event has multiple dynamic origins, from the rollback of the Pacific Plate in the east and the collapse of the thickened lithosphere formed in the Late Jurassic. The Late Cretaceous (92–77 Ma) was ascribed to the convergence between the Pacific and Eurasian Plates. The event during 65–50 Ma was a far-field correspondence to the onset subduction of the Indian Plate under the Eurasian Plate. From 10–8 Ma to the present, the progressive collision of the Indian and Eurasian Plates had a significant impact on the northeastern TP. Meanwhile, the growth and eastward escape of TP developed substantial deformation in the HTB.

Author Contributions: C.W., Y.W. and L.Z. designed and initiated the research. C.W. and Y.W. were responsible for fieldwork. All authors were responsible for discussion. C.W., Y.W. and W.Y. prepared the manuscript. All authors have read and agreed to the published version of the manuscript.

Funding: This research is supported by the Chinese NSF (41602213) and the fundamental Research Funds for the Central Universities (2-9-2017-052).

Institutional Review Board Statement: Not applicable.

Informed Consent Statement: Not applicable.

Data Availability Statement: The raw data supporting the conclusions of this article will be made available by the authors on request.

Acknowledgments: We are grateful to Liang Zhang, Yunlei Feng, and Yajuan Huang for their critical advice of this manuscript. And we sincerely thank reviewers and editors for their thoughtful comments to improve the quality of the manuscript.

Conflicts of Interest: The authors declare no conflicts of interest.

References

1. Darby, B.J.; Ritts, B.D. Mesozoic contractional deformation in the middle of the Asian tectonic collage: The intraplate Western Ordos fold-thrust belt, China. *Earth Planet. Sci. Lett.* **2002**, *205*, 13–24. [CrossRef]
2. Zhang, Y.Q.; Ma, Y.S.; Yang, N.; Shi, W.; Dong, S.W. Cenozoic extensional stress evolution in North China. *J. Geodyn.* **2003**, *36*, 591–613.
3. Yang, X.Y.; Dong, Y.P. Mesozoic and Cenozoic multiple deformations in the Helanshan Tectonic Belt, Northern China. *Gondwana Res.* **2018**, *60*, 34–53. [CrossRef]
4. Shi, G.Z.; Shen, C.B.; Zattin, M.; Wang, H.; Yang, C.Q.; Liang, C. Late Cretaceous-Cenozoic exhumation of the Helanshan Mt Range, western Ordos fold-thrust belt, China: Insight from structural and apatite fission track analyses. *J. Asian Earth Sci.* **2019**, *176*, 196–208. [CrossRef]
5. Liu, J.H.; Zhang, P.Z.; Zheng, D.W.; Wan, J.L.; Wang, W.T.; Du, P.; Lei, Q.Y. Pattern and timing of late Cenozoic rapid exhumation and uplift of the Helan Mountain, China. *Sci. China Ser. D-Earth Sci.* **2010**, *53*, 345–355. [CrossRef]
6. Huang, X.F.; Shi, W.; Chen, P.; Li, H.Q. Superposed deformation in the Helanshan Structural Belt: Implications for Mesozoic intracontinental deformation of the North China Plate. *J. Asian Earth Sci.* **2015**, *114*, 140–154. [CrossRef]
7. Bao, X.W.; Xu, M.J.; Wang, L.S.; Mi, N.; Yu, D.Y.; Li, H. Lithospheric structure of the Ordos Block and its boundary areas inferred from Rayleigh wave dispersion. *Tectonophysics* **2011**, *499*, 132–141. [CrossRef]

8. Zhang, Y.Q.; Shi, W.; Dong, S.W. Changes of Late Mesozoic Tectonic Regimes around the Ordos Basin (North China) and their Geodynamic Implications. *Acta Geol. Sin.-Engl. Ed.* **2011**, *85*, 1254–1276.
9. Zhang, Y.Q.; Liao, C.Z.; Shi, W.; Zhang, T.; Guo, F.G. Jurassic Deformation in and Around the Ordos Basin, North China. *Earth Sci. Front.* **2007**, *14*, 182–196. [CrossRef]
10. Lease, O.R.; Burbank, W.D.; Clark, K.M.; Farley, A.K.; Zheng, D.W.; Zhang, H.P. Middle Miocene reorganization of deformation along the northeastern Tibetan Plateau. *Geology* **2015**, *39*, 359–362. [CrossRef]
11. Lu, H.J.; Fu, B.H.; Shi, P.L.; Ma, Y.X.; Li, H.B. Constraints on the uplift mechanism of northern Tibet. *Earth Planet. Sci. Lett.* **2016**, *453*, 108–118.
12. Feng, Z.R.; Yuan, W.M.; Zhao, Z.D.; Dong, G.C.; Li, X.W.; Sun, W.L.; Yang, L.; Hong, S.J.; Zhao, M.M.; Hu, C.X.; et al. Mesozoic-Cenozoic cooling, exhumation and tectonic implications of Chaqiabeishan-Shaliuquan Li-Be ore district in the northeastern Qinghai-Tibet Plateau. *Tectonophysics* **2023**, *866*, 230040. [CrossRef]
13. Yuan, D.Y.; Ge, W.P.; Chen, Z.W.; Li, C.Y.; Wang, Z.C.; Zhang, H.P.; Zhang, P.Z.; Zheng, D.W.; Zheng, W.J.; Craddock, H.W.; et al. The growth of northeastern Tibet and its relevance to large-scale continental geodynamics: A review of recent studies. *Tectonics* **2013**, *32*, 1358–1370. [CrossRef]
14. Hu, C.X.; Yuan, W.M.; Zhao, Z.D.; Yang, L.; Feng, Z.R.; Hong, S.J.; Zhao, M.M.; Li, S.Y. Uplift and exhumation of the Chakabeishan ore district in the northern margin of the Qaidam Basin, China: Constraints from fission track thermochronology. *J. Asian Earth Sci.* **2023**, *247*, 105596. [CrossRef]
15. Liu, C.Y.; Zhao, H.G.; Zhao, J.F.; Wang, J.Q.; Zhang, D.D.; Yang, M.H. Temporo-spatial coordinates of evolution of the Ordos basin and its mineralization responses. *Acta Geol. Sin.* **2008**, *82*, 1229–1243.
16. Xiao, W.Z.; Liu, C.Y.; Tan, K.X.; Duan, X.Z.; Shi, K.T.; Sui, Q.L.; Feng, P.; Sami, M.; Ahmed, M.S.; Zi, F. Two Distinct Fractional Crystallization Mechanisms of A-Type Granites in the Nanling Range, South China: A Case Study of the Jiuyishan Complex Massif and Xianghualing Intrusive Stocks. *Minerals* **2023**, *13*, 605. [CrossRef]
17. Yuan, Y.S.; Hu, S.B.; Wang, H.J.; Sun, F.J. Meso-Cenozoic tectonothermal evolution of Ordos basin, central China: Insights from newly acquired vitrinite reflectance data and a revision of existing paleothermal indicator data. *J. Geodyn.* **2007**, *44*, 33–46. [CrossRef]
18. Zhang, J.; Dickson, C.; Cheng, H.Y. Sedimentary characteristics of Cenozoic strata in central-southern Ningxia, NW China: Implications for the evolution of the NE Qinghai–Tibetan Plateau. *J. Asian Earth Sci.* **2010**, *39*, 740–759.
19. Liu, X.B.; Shi, W.; Hu, J.M.; Fu, J.L.; Yan, J.Y.; Sun, L.L. Magnetostratigraphy and tectonic implications of Paleogene-Neogene sediments in the Yinchuan Basin, western North China Craton. *J. Asian Earth Sci.* **2019**, *173*, 61–69. [CrossRef]
20. Zhao, H.G.; Liu, C.Y.; Wang, F.; Wang, J.Q.; Li, Q.; Yao, Y.M. Uplift and evolution of Helan Mountain. *Sci. China Ser. D-Earth Sci.* **2007**, *50*, 217–226. [CrossRef]
21. Zhao, H.G. Structural Characteristics and the Evolution in Western Ordos Basin. Ph.D. Thesis, Northwest University, Xi'an, China, 2003.
22. Li, T.B. The Characteristics and Evolution of Thrust Nappe Structure in the West Margin of Ordos Basin. Ph.D. Thesis, China University of Geosciences (Beijing), Beijing, China, 2006.
23. BGMRNXHAR. Bureau of Geological and Mineral Resource of Ningxia Hui Autonomous Region. In *Regional Geology of the Ningxia Hui Autonomous Region*; Geology Publishing House: Beijing, China, 1990; pp. 1–522. (In Chinese with English Abstract)
24. Wang, F.; Liu, C.Y.; Yang, X.K.; Su, C.Q. Geologic geochemical features of Basalt in Ruqi Clough of Helan Mountain and its structural environmental significance. *Pet. Geol. Oilfield Dev. Daqing* **2005**, *24*, 25–27.
25. Yang, H.; Fu, J.H.; Ouyang, Z.J.; Sun, L.Y.; Ma, Z.R. U-Pb Zircon Dating of the Daling-Gugutai Basalt in Rujigou on the Western Margin of Ordos Basin. *Acta Geosci. Sin.* **2010**, *31*, 229–236. (In Chinese with English abstract)
26. Carlson, W.D.; Donelick, R.A.; Ketcham, R.A. Variability of apatite fission-track annealing kinetics: I. Experimental results. *Am. Miner.* **1999**, *84*, 1213–1223. [CrossRef]
27. Green, P.F.; Duddy, I.R.; Gleadow, A.J.W.; Tingate, P.R.; Laslett, G.M. Thermal annealing of fission tracks in apatite: 1. A qualitative description. *Chem. Geol.* **1986**, *59*, 237–253. [CrossRef]
28. Galbraith, R.F. On statistical models for fission-track counts. *J. Int. Assoc. Math. Geol.* **1981**, *13*, 471–478. [CrossRef]
29. Hurford, A.J.; Green, P.F. A users' guide to fission track dating calibration. *Earth Planet. Sci. Lett.* **1982**, *59*, 343–354. [CrossRef]
30. Hurford, A.J. Standardization of fission track dating calibration: Recommendation by the Fission Track Working Group of the IUGS Subcommission on Geochronology. *Chem. Geol.* **1990**, *80*, 171–178. [CrossRef]
31. Green, P.F. A new look at statistics in fission-track dating. *Nucl. Tracks* **1981**, *5*, 77–86. [CrossRef]
32. Vermeesch, P. Radial Plotter: A Java application for fission track, luminescence and other radial plots. *Radiat. Meas.* **2009**, *44*, 409–410. [CrossRef]
33. Gleadow, A.J.W.; Duddy, I.R.; Green, P.F.; Lovering, J.F. Confined fission track lengths in apatite: A diagnostic tool for thermal history analysis. *Contrib. Miner. Petrol.* **1986**, *94*, 405–415. [CrossRef]
34. Ketchman, R.A. Forward and inverse modeling of low-temperature thermochronometry data. *Rev. Mineral. Geochem.* **2005**, *58*, 275–314. [CrossRef]
35. Ketchman, R.A.; Carter, A.; Donelick, R.A.; Barbarand, J.; Hurford, A.J. Improved measurement of fission-track annealing in apatite using c-axis projection. *Am. Miner.* **2007**, *92*, 789–798. [CrossRef]

36. Ketchman, R.A.; Carter, A.; Donelick, R.A.; Barbarand, J.; Hurford, A.J. Improved measurement of fission-track annealing in apatite. *Am. Miner.* **2007**, *92*, 799–810. [CrossRef]
37. Lin, C.; Yang, Q.; Li, S. *Basin Filling and Evolution Analysis of Helan Aulacogen, Northwest China*; Geologic Publishing House: Beijing, China, 1995; p. 143. (In Chinese with English summary)
38. Li, X.W.; Mo, X.X.; Huang, X.F.; Dong, G.C.; Yu, X.H.; Luo, M.F.; Liu, Y.B. U–Pb zircon geochronology, geochemical and Sr–Nd–Hf isotopic compositions of the early Indosinian Tongren pluton in west Qinling: Petrogenesis and geodynamic implications. *J. Asian Earth Sci.* **2015**, *97*, 38–50. [CrossRef]
39. Pullen, A.; Kapp, P.; Gehrels, G.E.; Vervoort, J.D.; Ding, L. Triassic continental subduction in central Tibet and Mediterranean-style closure of the Paleo-Tethys Ocean. *Geology* **2008**, *36*, 351–354. [CrossRef]
40. Wu, G.L.; Meng, Q.R.; Duan, L.; Li, L. Early Mesozoic structural evolution of the eastern west Qinling, northwest China. *Tectonophysics* **2014**, *630*, 9–20. [CrossRef]
41. Zhang, Y.P.; Zhang, J.; Chen, X.H.; Wang, Y.N.; Zhao, H.; Nie, F.J.; Zhang, B.H. Late Paleozoic tectonic setting of southern Alxa Block, NW China: Constrained by age and composition of diabase. *Int. Geol. Rev.* **2016**, *59*, 1028–1046. [CrossRef]
42. Song, D.F.; Glorie, S.; Xiao, W.J.; Collins, A.S.; Gillespie, J.; Jepson, G.; Li, Y.C. Tectonic-thermal evolution of the southwestern Alxa Tectonic Belt, NW China: Constrained by apatite U-Pb and fission track thermochronology. *Tectonophysics* **2017**, *722*, 577–594. [CrossRef]
43. Zhang, B.H.; Zhang, J.; Zhao, H.; Nie, F.J.; Wang, Y.N.; Zhang, Y.P. Tectonic evolution of the western Ordos Basin during the Palaeozoic-Mesozoic time as constrained by detrital zircon ages. *Int. Geol. Rev.* **2018**, *61*, 461–480. [CrossRef]
44. Xu, L.M.; Zhou, L.F.; Deng, K.; Yang, W.J. Geochemical characteristics of Permian event strata in western margin of Ordos basin. *Coal Geol. Explor.* **2006**, *34*, 4–8. (In Chinese with English abstract)
45. Zhang, G.W.; Zhang, B.R.; Yuan, X.C.; Xiao, Q.H. *Continental Dynamics of Qinling Orogen*; Science Press: Beijing, China, 2001; pp. 1–855. (In Chinese with English abstract)
46. Meng, Q.R.; Zhang, G.W. Timing of collision of the North and South China blocks: Controversy and reconciliation. *Geology* **1999**, *27*, 123–126. [CrossRef]
47. Shi, G.Z.; Soares, C.J.; Shen, C.B.; Wang, H.; Yang, C.Q.; Liang, C.; Liu, M.H. Combined detrital zircon fission track and U-Pb dating of the Late Paleozoic to Early Mesozoic sandstones in the Helanshan, western Ordos fold-thrust belt: Constrains for provenance and exhumation history. *J. Geodyn.* **2019**, *130*, 57–71. [CrossRef]
48. Zheng, D.W.; Zhang, P.Z.; Wan, J.L.; Li, D.M.; Wang, F.; Yuan, D.Y.; Zhang, G.L. The $^{40}Ar/^{39}Ar$, fission track evidence of Mesozoic tectonic in northern margin of west Qinling mountain. *Acta Petrol.* **2004**, *20*, 697–706. (In Chinese with English abstract)
49. Xu, X.Y.; Chen, J.L.; Gao, T.; Li, P.; Li, T. Granitoid magmatism and tectonic evolution in northern edge of the Western Qinling terrane, NW China. *Acta Petrol. Sin.* **2014**, *30*, 371–389.
50. Ritts, B.D.; Darby, B.J.; Cope, T. Early Jurassic extensional basin formation in the Daqing Shan segment of the Yinshan belt, northern China Block, Inner Mongolia. *Tectonophysics* **2001**, *339*, 239–258. [CrossRef]
51. Li, M.J.; Zheng, M.L.; Cao, C.C. Evolution of superposed Jurassic and Cretaceous basins in Beishan-Alxa area. *Oil Gas. Geol.* **2004**, *25*, 54–57. (In Chinese with English abstract)
52. Gao, F.; Wang, Y.J.; Liu, S.S.; Hu, B.Q. Thermal history study in the west of the Ordos basin using apatite fission track analysis. *Geotecton. Metallog.* **2000**, *24*, 87–91. (In Chinese with English abstract)
53. Zhao, M.W.; Behr, H.J. Vitrinite reflectance in Triassic with relation to geothermal history of Ordos basin. *Acta Pet. Sin.* **1996**, *13*, 1–9. (In Chinese with English abstract)
54. Ren, Z.L.; Zhao, Z.Y.; Chen, G. Tectonic thermal events of Late Mesozoic in Qinshui basin. *Oil Gas. Geol.* **1999**, *20*, 46–48. (In Chinese with English abstract)
55. Huang, X.F.; Qian, Z.Z.; Sun, B.P.; Wu, W.K.; Lu, Y.J.; Wang, C. Characteristics and evolution of the thrust-nappe structure in the area of Xiaosongshan in the north section of Helan Mountain. *J. Northwest Univ. (Nat. Sci. Ed.)* **2011**, *41*, 273–277. (In Chinese with English abstract)
56. Chen, G.; Wang, Z.W.; Bai, G.J.; Sun, J.B.; Zhang, H.R.; Li, X.D. Meso-Cenozoic peak-age events and their tectono-sedimentary response in the Ordos basin. *Geol. China* **2007**, *34*, 375–383. (In Chinese with English abstract)
57. He, Z.X. *Petroleum and Evolution in Ordos Basin*; Petroleum Industry Press: Beijing, China, 2003; pp. 121–123. (In Chinese with English abstract)
58. Zhai, M.G.; Zhu, R.X.; Liu, J.M.; Meng, Q.R.; Hou, Q.L.; Hu, S.B.; Liu, W.; Li, Z.; Zhang, H.F.; Zhang, H.F. Time range of Mesozoic tectonic regime inversion in eastern North China Block. *Sci. China Ser. D Earth Sci.* **2004**, *47*, 151–159. (In Chinese with English abstract). [CrossRef]
59. Zhai, M.G.; Meng, Q.R.; Liu, J.M. Geological features of Mesozoic tectonic regime inversion in Eastern North China and implication for geodynamics. *Earth Sci. Front.* **2004**, *11*, 285–298. (In Chinese with English abstract)
60. Liu, C.Y.; Zhao, H.G.; Wang, F.; Chen, H. Attributes of the Mesozoic structure on the west margin of the Ordos basin. *Acta Geol. Sin.* **2005**, *79*, 737–747.
61. Chen, Y.; Li, J.G.; Miao, P.S.; Chen, L.L.; Zhao, H.L.; Wang, C.; Yang, J. Relationship between the tectono-thermal events and sandstone-type uranium mineralization in the southwestern Ordos Basin, Northern China: Insights from apatite and zircon fission track analyses. *Ore Geol. Rev.* **2022**, *143*, 104792. [CrossRef]

62. Chen, L.H.; Wang, Y.D.; He, P.J.; Song, C.H.; Meng, Q.Q.; Feng, W.; Chen, W.Q.; Wang, X.H. Mesozoic-Cenozoic multistage tectonic deformation of the Qilian Shan constrained by detrital apatite fission track and zircon U-Pb geochronology in the Yumu Shan area. *Tectonophysics* **2021**, *822*, 229151. [CrossRef]
63. Yin, A.; Harrison, T.M. Geologic Evolution of the Himalayan-Tibetan orogen. *Annu. Rev. Earth Planet. Sci.* **2000**, *28*, 211–280. [CrossRef]
64. Jia, C.Z.; Wei, G.Q.; Li, B.L. Yanshanian tectonic features in west-central China and their petroleum geological significance. *Oil Gas. Geol.* **2005**, *26*, 9–15. (In Chinese with English abstract)
65. Ma, J.H.; He, D.F. Meso-Cenozoic tectonic events in the Helanshan Tectonic Belt and its adjacent areas: Constraints from unconformity and fission track data. *Acta Petrol. Sin.* **2019**, *35*, 1121–1142. (In Chinese with English abstract)
66. Li, Z.H.; Dong, S.W.; Qu, H.J. Timing of the initiation of the Jurassic Yanshan movement on the North China Craton: Evidence from sedimentary cycles, heavy minerals, geochemistry, and zircon U–Pb geochronology. *Int. Geol. Rev.* **2014**, *56*, 288–312. [CrossRef]
67. Gao, S.L.; Li, F.; Li, T.B.; Lv, C.G.; Lu, Y.J. Discussion of the relationship between coal metamorphism and the Late Mesozoic basalt in Rujigou Area. *Coal Geol. Explor.* **2003**, *31*, 8–10. (In Chinese with English abstract)
68. Zhao, Y.; Cui, S.Q.; Guo, T.; Xu, G. Evolution of a Jurassic basin of the Western Hills, Beijing, North China and its tectonic implications. *Geol. Bull. China* **2002**, *21*, 211–217. (In Chinese with English abstract)
69. Cui, J.J.; Zhang, Y.Q.; Dong, S.W.; Jahn, B.M.; Xu, X.B.; Ma, L.C. Zircon U–Pb geochronology of the Mesozoic metamorphic rocks and granitoids in the coastal tectonic zone of SE China: Constraints on the timing of Late Mesozoic orogeny. *J. Asian Earth Sci.* **2013**, *62*, 237–252. [CrossRef]
70. Li, J.H.; Zhang, Y.Q.; Dong, S.W.; Johnston, S.T. Cretaceous tectonic evolution of South China: A preliminary synthesis. *Earth-Sci. Rev.* **2014**, *134*, 98–136. [CrossRef]
71. Lim, C.; Cho, M. Two-phase contractional deformation of the Jurassic Daebo Orogeny, Chungnam Basin, Korea, and its correlation with the early Yanshanian movement of China. *Tectonics* **2011**, *31*. [CrossRef]
72. Mock, C.; Arnaud, N.O.; Cantagrel, J.M. An early unroofing in northeastern Tibet? Constraints from $^{40}Ar/^{39}Ar$ thermochronology on granitoids from the eastern Kunlun range (Qinghai, NW China). *Earth Planet. Sci. Lett.* **1999**, *171*, 107–122. [CrossRef]
73. Davis, G.A.; Qian, X.L.; Zheng, Y.D.; Tong, H.M.; Yu, H.; Wang, C.; Gehrels, G.E.; Shafiquallah, M.; Fryxell, J.E. Mesozoic deformation and plutonism in the Yungmeng Shan: A metamorphic core complex north of Beijing, China. In *The Tectonic Evolution of Asia*; Yin, A., Harrison, T.A., Eds.; Cambridge University Press: New York, NY, USA, 1996; pp. 253–280.
74. Davis, G.A.; Darby, B.J. Early Cretaceous overprinting of the Mesozoic Daqing Shan fold-and-thrust belt by the Hohhot metamorphic core complex, Inner Mongolia, China. *Geosci. Front.* **2010**, *1*, 1–20. [CrossRef]
75. Lin, W.; Faure, M.; Monie, P.; Scharer, U.; Panis, D. Mesozoic extensional tectonics in eastern Asia: The South Liaodong Peninsula Metamorphic Core Complex (NE China). *J. Geol.* **2008**, *116*, 134–154. [CrossRef]
76. Zhu, G.; Xie, C.L.; Chen, W.; Xiang, B.W.; Zhao, Q.H. Evolution of the Hongzhen metamorphic core complex: Evidence for Early Cretaceous extension in the eastern Yangtze craton, eastern China. *Geol. Soc. Am. Bull.* **2010**, *122*, 506–516. [CrossRef]
77. Faure, M.; Sun, Y.; Shu, L.; Monie, P.; Charvet, J. Extensional tectonics within a subduction-type orogen. The case study of the Wugongshan dome (Jiangxi Province, SE China). *Tectonophysics* **1996**, *263*, 77–106. [CrossRef]
78. Wang, T.; Guo, L.; Zheng, Y.D.; Donskaya, T.; Gladkochub, D.; Zeng, L.S.; Li, J.B.; Wang, Y.B.; Mazukabzov, A. Timing and processes of late Mesozoic mid-lower crustal extension in continental NE Asia and implications for the tectonic setting of the destruction of the North China Craton: Mainly constrained by zircon U–Pb ages from metamorphic core complexes. *Lithos* **2012**, *154*, 315–345. [CrossRef]
79. Dong, S.W.; Zhang, Y.Q.; Long, C.X.; Yang, Z.Y.; Ji, Q.; Wang, T.; Hu, J.M.; Chen, X.H. Jurassic tectonic revolution and new interpretation of Yanshan Movement. *Acta Geol. Sin.-Engl. Ed.* **2008**, *82*, 334–347.
80. Min-Na, A.; Zhang, F.Q.; Yang, S.F.; Chen, H.L.; Batt, G.E.; Sun, M.D.; Meng, Q.A.; Zhu, D.F.; Cao, R.C.; Li, J.S. Early Cretaceous provenance change in the southern Hailar Basin, northeastern China and its implication for basin evolution. *Cretac. Res.* **2013**, *40*, 21–42.
81. Song, Y.; Ren, J.Y.; Stepashko, A.A.; Li, J.G. Post-rift geodynamics of the Songliao Basin, NE China: Origin and significance of T11 (Coniacian) unconformity. *Tectonophysics* **2014**, *634*, 1–18. [CrossRef]
82. Song, Y.; Stepashko, A.; Liu, K.Y.; He, Q.K.; Shen, C.B.; Shi, B.J.; Ren, J.Y. Post-rift tectonic history of the Songliao Basin, NE China: Cooling events and post-rift unconformities driven by orogenic pulses from plate boundaries. *J. Geophys. Res. Solid Earth* **2018**, *123*, 2363–2395. [CrossRef]
83. Xia, Z.M.; Liu, J.L.; Ni, J.L.; Zhang, T.T.; Shi, X.M.; Wu, Y. Structure, evolution and regional tectonic implications of the Queshan metamorphic core complex in eastern Jiaodong Peninsula of China. *Sci. China Earth Sci.* **2016**, *59*, 997–1013. [CrossRef]
84. Chen, H.; Hu, J.M.; Wu, G.L.; Shi, W.; Geng, Y.Y.; Qu, H.J. Apatite fission-track thermochronological constraints on the pattern of late Mesozoic-Cenozoic uplift and exhumation of the Qinling Orogen, central China. *J. Asian Earth Sci.* **2015**, *114*, 649–673. [CrossRef]
85. Huang, Z.G.; Ren, Z.L.; Gao, L.G. Evidence from detrital zircon and apatite fission track for tectonic evolution since Cretaceous in southeastern margin of Ordos basin. *Chin. J. Geophys.* **2016**, *59*, 3753–3764. (In Chinese with English abstract)
86. Wang, G.C.; Xiang, S.Y.; Wang, A.; Garver, J.I.; Wintsch, R.P. Thermochronological constraint to the processes of the East Kunlun and adjacent areas in Mesozoic–early Cenozoic. *Earth Sci.* **2007**, *32*, 605–614. (In Chinese with English abstract)

87. Wang, A.; Wang, G.; Zhang, K.; John, G.I. An early Cenozoic tectonic event in Eastern Kunlun Orogen, evidence from detrital fission track geochronology. *Earth Sci.* **2010**, *35*, 737–746. (In Chinese with English abstract)
88. He, P.J.; Song, C.H.; Wang, Y.D.; Chen, L.H.; Chang, P.F.; Wang, Q.Q.; Ren, B. Cenozoic exhumation in the Qilian Shan, northeastern Tibetan Plateau, Evidence from detrital fission track thermochronology in the Jiuquan Basin. *J. Geophys. Res. Solid Earth* **2017**, *122*, 6910–6927. [CrossRef]
89. Bovet, P.M.; Ritts, B.D.; Gehrels, G.; Abbink, A.O.; Darby, B.; Hourigan, J. Evidence of Miocene crustal shortening in the North Qilian Shan from Cenozoic stratigraphy of the western Hexi Corridor, Gansu Province, China. *Am. J. Sci.* **2009**, *309*, 290–329. [CrossRef]
90. George, A.D.; Marshallsea, S.J.; Wyrwoll, K.H.; Chen, J.; Lu, Y.C. Miocene cooling in the northern Qilian Shan, northeastern margin of the Tibetan Plateau, revealed by apatite fission-track and vitrinite-reflectance analysis. *Geology* **2001**, *29*, 939–942. [CrossRef]
91. Tapponnier, P.; Xu, Z.Q.; Roger, F.; Meyer, B.; Arnaud, N.; Wittlinger, G.; Yang, J.S. Oblique stepwise rise and growth of the Tibet Plateau. *Science* **2001**, *294*, 1671–1677. [CrossRef]
92. Zhang, X.M.; Wang, Y. Seismic and GPS evidence for the kinematics and the state of stress of active structures in south and south-central Tibetan Plateau. *J. Asian Earth Sci.* **2007**, *29*, 283–295. [CrossRef]
93. Wang, Y.; Li, Q.; Qu, G.S. *$^{40}Ar/^{39}Ar$ Thermochronological Constraints on the Cooling and Exhumation History of the South Tibetan Detachment System, Nyalam Area, Southern Tibetan*; Special Publications; Geological Society: London, UK, 2006; Volume 268, pp. 327–354.

applied sciences

MDPI

Article

The Characteristics of Luminescence from High-Temperature- and High-Pressure-Treated Diamonds

Mu-Lin Huang [1,2], Xue-Mei He [2,*], Ming-Yue Du [2], Peng-Fei Jiang [2] and Xue-Feng Wang [2]

[1] National Gems & Jewelry Testing Group, Beijing Education Technology Co., Ltd., Beijing 100013, China; hmulin@126.com
[2] School of Gemology, China University of Geosciences, Beijing 100083, China; dumingyue0206@163.com (M.-Y.D.); jpf19960402@163.com (P.-F.J.); wangxuefeng0222@163.com (X.-F.W.)
* Correspondence: hexuemei@cugb.edu.cn

Abstract: High-temperature and high-pressure (HTHP)-treated diamonds have attracted attention all over the world due to their vivid colors. In order to explore a new method for the rapid and non-destructive identification of HTHP-treated diamonds, in this paper, five IaAB-type diamonds yielded in Russia were selected as the research object and treated with HTHP. The HTHP-treated diamonds were investigated by DiamondView^{TM}, cathodoluminescence, micro-infrared spectrometry (micro-IR), low-temperature photoluminescence (PL) spectrometry, and three-dimensional (3D) fluorescence spectrometry. The results show that under DiamondView^{TM} and cathode rays, the five samples were all non-phosphorescent with different luminous patterns, such as regular annular bands, multiple groups of intersecting linear stripes, or jagged stripes. In the low-temperature PL spectra, most HTHP-treated diamonds exhibited stronger luminescence peaks at 637 nm compared to 575 nm. But there were also exceptions, such as the purple-red sample showing the opposite luminescence peak. In the 3D fluorescence spectrum of the HTHP-treated diamonds, the fluorescence peak mainly appeared in the range of 440–450 nm, accompanied by a broad band of 350–500 nm and even longer wavelengths. Meanwhile, some samples also exhibited fluorescence peaks at longer wavelengths, such as 353 nm, 676 nm, and 665 nm. These results make it possible to identify HTHP-treated diamonds by using luminescence characteristics, providing a new method for the non-destructive and rapid detection of HTHP-treated diamonds.

Keywords: gem-grade diamonds; HTHP treated; photoluminescence; 3D contour fluorescence plot

Citation: Huang, M.-L.; He, X.-M.; Du, M.-Y.; Jiang, P.-F.; Wang, X.-F. The Characteristics of Luminescence from High-Temperature- and High-Pressure-Treated Diamonds. *Appl. Sci.* **2024**, *14*, 3071. https://doi.org/10.3390/app14073071

Academic Editor: Andrea L. Rizzo

Received: 17 January 2024
Revised: 19 March 2024
Accepted: 1 April 2024
Published: 5 April 2024

1. Introduction

Colored diamonds have always been highly sought after by consumers, and their colors are diverse, including gold, brown, green, and blue. In recent years, with the improvements in high-temperature and high-pressure (HTHP) treatment technology, this technology has also been applied to the field of diamond color modification. In 1999, General Electric (GE) used HTHP treatment technology to turn brown and gray IIa diamonds into colorless to nearly colorless diamonds [1,2]; in the same year, HTHP treatment technology was also used to turn type Ia brown Nova diamonds into a bright yellow-green color [3,4]. Since then, more and more scholars have begun to devote themselves to the research of HTHP treatment experiments [3,5,6]. With the continuous progress of treatment technology, through HTHP treatment, diamonds can present more vivid colors, such as golden yellow, pink, and so on [7,8]. The research of the HTHP treatment of diamonds has also been deepening. HTHP laboratory conditions provided sufficient isotropic pressure and potential energy for treating lattice defects in brown-yellow diamonds, which helped the dislocations in type Ia and IIa brown-yellow diamonds to climb, reorganize, annihilate, proliferate, and slip, finally transforming the diamonds into colorless, yellow-green, and blue diamonds [1,9–11]. In another study, the formation and evolution of lattice defects

jointly restricted diamond color and luminescence [10]. In other experiments, brown diamonds were changed to yellow after HTHP treatment, mainly related to H3, H4, and N3 centers and isolated nitrogen [12–14]. Diamonds becoming green or yellow-green after treatment has been shown to be mainly related to H2 and H3 centers [12,14–16]; after treatment, the red color is mainly related to high concentrations of (N-V) centers [4,12,14,17,18]. In other experiments, the color of type IIa diamonds became white, mainly because no new color centers were formed due to vacancies and the disappearing of interstices [10,14].

However, previous research on HTHP-treated diamonds has mainly focused on the color-changing mechanism and spectroscopic characteristics; there is relatively little research on their luminescence. Therefore, this paper takes HTHP-treated diamonds as samples and conducts research on their luminescence characteristics by DiamondView^{TM}, cathodoluminescence, low-temperature photoluminescence (PL), and three-dimensional (3D) fluorescence spectrometry, and hopes to find a non-destructive and rapid method of identification of HTHP diamonds.

2. Materials and Methods

The samples tested in this study were five natural diamonds from Russia, and they were subjected to high-temperature and high-pressure treatment to change their color (Figure 1). The colors of the samples mainly include yellow-green (R-YG-1), yellow (R-Y-1, R-Y-2), purple-red (R-P-1), and brown (R-B-1). The HTHP treatment of diamonds was carried out in a cubic press. The temperature range was 1600~2400 °C, the pressure range was 5.5~8 GPa, and the time range was 15~30 min. In this paper, the basic gemological properties of the samples were observed by a gemological microscope, crossed polarizers, and ultraviolet fluorescent lamps. Micro-IR was used to identify the type of diamond. Bruker Lumos FTIR was used for spectral analysis, with a wave number range of 600~4000 cm^{-1}, 32 scans, and a resolution was 4 cm^{-1}. DiamondView^{TM} was applied to observe the growth structure and fluorescence from the samples at room temperature using a short-wavelength (<230 nm) ultraviolet light source. The above two tests were completed in the gem laboratory of the School of Gemmology, China University of Geosciences, Beijing. The model of the cathodoluminescence test instrument was RELIONIII, and the test was carried out at the Analtical Laboratory of BRIUG. A DXR Raman Microscope was used to analyze the PL spectrum. The wavelength of the laser was 532 nm, the exposure time was 1 s, and the number of exposures was 30. The 3D fluorescence spectra of the diamond samples were analyzed by the fluorescence spectrometer FL3-TCSPC. The excitation slit was 14.00 nm, the emission slit was 14.00 nm, the integration time was 0.1 s, the excitation wavelength range was 230~400 nm, and the emission wavelength range was 236~1050 nm. PL and 3D contour fluorescence plot (HORIBA Fluorolog-3) tests were completed at the Beijing branch of HORIBA (Beijing, China).

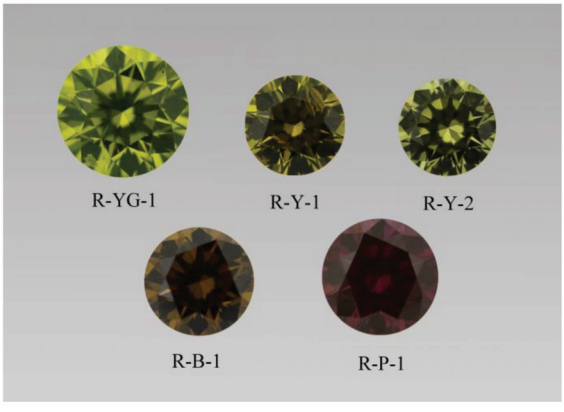

Figure 1. HTHP-treated diamond samples examined in this study.

3. Results and Discussion

3.1. Gemological Properties

Except for sample R-P-1, the color distribution of other samples was more uniform. The local color of sample R-P-1 showed a stripe distribution. The internal characteristics of the samples were observed by a gemological microscope, and black opaque hexagonal sheet inclusions (Figure 2a), rounded colorless crystal inclusions (Figure 2b), and disc-shaped stress fractures (Figure 2c) were observed in some samples. Under orthogonally polarized light, the samples showed obvious anomalous birefringence of parallel bands (Figure 2d) or ripples (Figure 2e). The extinction geometric pattern remained basically unchanged at any rotation angle, accompanied by strong interference color (Figure 2f). The ultraviolet fluorescence characteristics of the samples are shown in Table 1.

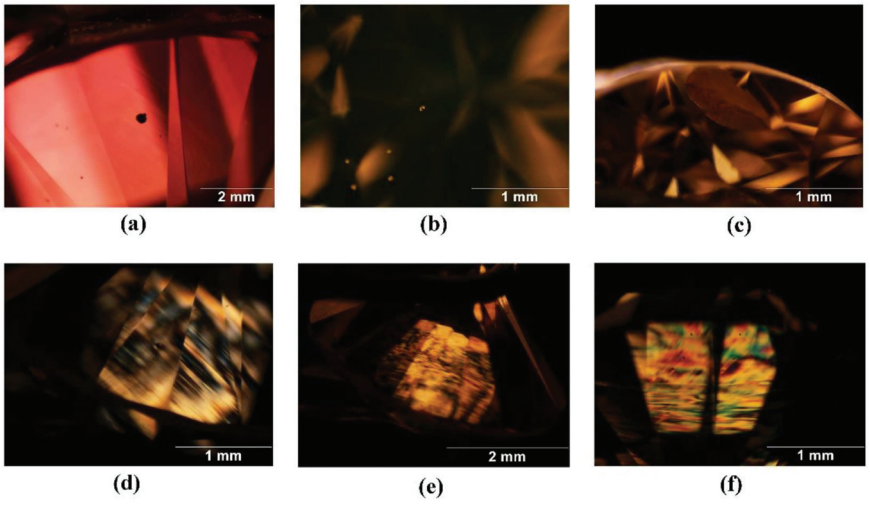

Figure 2. Black hexagonal sheet inclusions in sample R-P-1 (**a**), colorless crystal inclusions in sample R-YG-1 (**b**), and disc-shaped stress cracks in sample R-Y-1 (**c**). Under orthogonal polarized light, the sample showed more obvious parallel bands (**d**) or corrugated abnormal extinction (**e**), accompanied by strong strain interference color (**f**).

Table 1. The ultraviolet fluorescence characteristics of the samples.

Sample	Color	LWUV (Long-Wave Ultraviolet Light: 315–400 nm)	SWUV (Short-Wave Ultraviolet Light: 200–280 nm)
R-YG-1	Yellow-green	Strong yellow-green	Medium yellow-green
R-Y-1	Yellow	Weak green	Weak orange
R-Y-2	Yellow	Medium yellow-green	Strong yellow-green
R-B-1	Brown	-	-
R-P-1	Purple-red	Medium orange	Medium orange-red

3.2. DiamondView™ and Cathodoluminescence

The five samples presented different fluorescence images in DiamondView™, but none of them had phosphorescence. The specific luminous pattern is shown in Figure 3. Sample R-YG-1 emitted medium green fluorescence, presenting a geometric luminescence pattern of a "chip" shape. The growth rings were straight and fine, and some were serrated. The central luminescence was relatively concentrated and uniform, presenting a regular quadrilateral luminescence pattern. Sample R-Y-1 showed weak green and blue fluorescence at the same time, and the whole growth band was fine and straight, with a partial ladder shape. Sample R-Y-2 presented strong yellow-green fluorescence in general,

and blue fluorescence was seen in local areas. The outer part was a lamellar growth ring, and a structure similar to a "growth nucleus" was seen in the center. Sample R-B-1 showed a weak orange fluorescence with blue, straight growth bands. The purple sample R-P-1 showed a strong orange fluorescence, and some showed a yellow and orange fluorescence interphase distribution, which was consistent with the characteristics of the ribbon. In addition, a linear growth pattern was visible, with some of the nearly vertically intersected reticular luminescence patterns.

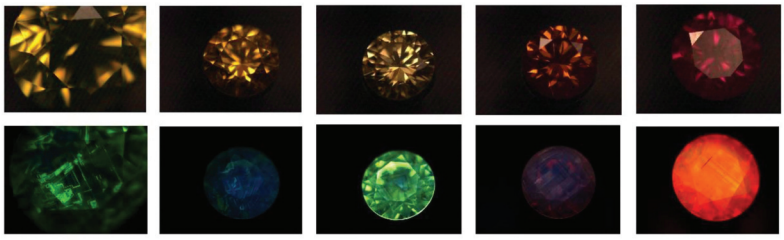

Figure 3. Fluorescence images of samples under DiamondView™.

Cathodoluminescence was used to further observe the color patterns of the samples. Under high-energy cathode rays, the luminescence characteristics of the samples were basically the same as those seen in DiamondView™, but the luminous intensity under the cathode rays was relatively strong, and the image was sharper, thus providing more detail. Jagged growth textures were seen in the sample R-Y-1. In addition, three groups of fine flat linear textures were visible (Figure 4a). In sample R-Y-2, the edge of the part similar to the "growth nucleus" was irregular, and was cut off from the fine, straight, and quadrangular growth ring outside (Figure 4b). In addition to the blue growth ring in the sample R-B-1, a uniform orange luminescence pattern with a regular quadrilateral could be seen (Figure 4c). Sample R-P-1 presented a strip-like luminescence pattern with orange and yellow intersections, and regular laminar growth bands could also be seen inside (Figure 4d). The observation of cathodoluminescence images of diamonds can (1) reveal the internal morphology, growth structure, growth mechanism, growth stage, and process of diamonds; (2) provide the plastic deformation information of diamonds; (3) verify and interpret the results of an infrared spectrum analysis, a stable isotope analysis, and the geological chronology of the diamond microzone; and (4) provide key evidence for distinguishing a natural diamond from a synthetic diamond. It can be seen from the combination of the observation under DiamondView™ and cathodoluminescence that, in the HTHP-treated diamond samples, the yellow-green samples presented yellow-green luminescence, while the yellow samples mainly presented luminescence characteristics of a combination of blue and green, and the brown and purple samples presented a luminescence of orange with different intensities.

In the study of the cathodoluminescence of HTHP-treated diamonds, it has been proposed that the geometric luminous patterns of diamonds before and after HTHP treatment have obvious differences. On the {111} plane of natural brown-yellow diamonds without HTHP treatment, three groups of slip surfaces (lines) are generally developed. The slip band emits a more uniform strong yellow-green luminescence and obviously cuts through and destroys the primary growth ring structure of the diamond, while the locally remaining primary growth ring emits strong blue luminescence, and the sub-deformation transition zone emits uneven strong blue-white luminescence [10,19]. However, HTHP conditions provide sufficient isotropic pressure and potential energy for the crystal defects in these brown and brown-yellow diamonds [10,11]. On the basis of helping the crystal defects to change and achieve the purpose of color change, their luminosity will also be affected. The surface of a yellow-green diamond treated with HTHP shows strong yellow-green luminescence as a whole, and three groups of clear CL slip surfaces (lines) and CL

deformation bands show strong yellow-green luminescence, which constitutes the characteristics of loading-type strong dislocation slip reflected in HTHP-treated yellow-green diamonds [10,19]. Jia and Chen [20] combined HTHP-treated type Ia natural diamond fluorescence images and a PL spectrum analysis and found out that blue fluorescence is mainly caused by N3, while yellow-green fluorescence is related to an H3 center [5]. In addition, Luo and Breeding [21] also proposed that HTHP-treated orange and yellow type Ia natural diamonds show orange-yellow fluorescence, mainly due to the presence of the 480 nm band.

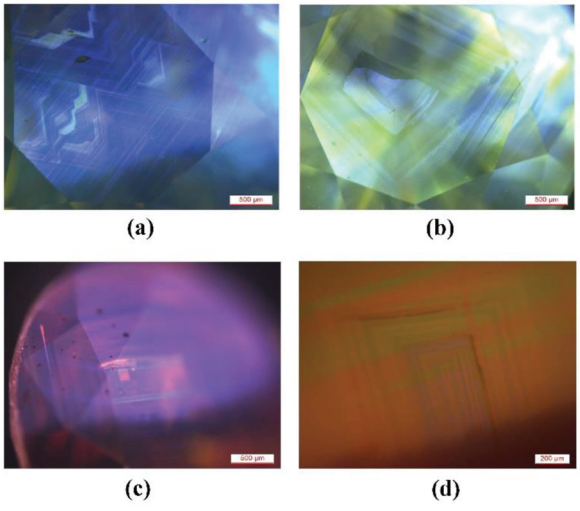

Figure 4. Under the cathode ray, three groups of serrated and fine linear texture could be observed in sample R-Y-1 (**a**). The "growth nucleus" in sample R-Y-2 was cut off from the outer fine growth rings (**b**). Uniform luminescence pattern of regular quadrilateral in sample R-B-1 (**c**). Sample R-P-1 regular layered growth bands (**d**).

From the point of view of the luminous patterns, the samples appeared relatively complicated, and the luminous patterns were mainly divided into three types: regular annulus bands, multiple groups of intersecting linear stripes, and jagged stripes. Bulanova and Milledge [22] studied the cathodoluminescence of the particulate diamond system in Yakut Kimberlite and concluded that there are three main types of diamond growth structure: single octahedral growth bands, complex growth bands, and multi-stage growth bands, and most diamonds are of the single octahedral growth band type. The regular growth bands observed in the samples here belong to this type of growth structure. According to Chen et al. [23], these types of growth bands are straight with different widths and consist of non-luminescent regions and blue-green luminescence regions, arranged parallel from the center to the outside and obviously controlled by the layered growth mechanism. The three groups of fine linear textures observed in the samples are the characteristics of loading-type strong dislocation slip reflected in HTHP-treated diamonds. According to the study of Luo [19], this is the important identification basis of HTHP-treated yellow-green diamonds.

According to the study of Chen et al. [24], the serrated ablation lines or irregular growth pattern and the dense growth pattern in the reaction stage indicate that the diamond grows under pulsating temperature–pressure conditions, and the pulsating characteristics reflect the periodic interaction between the fluid and the melt in an unstable state. Therefore, it can be inferred that the serrated growth texture in the samples observed under cathodoluminescence is an indication of its complex growth environment and process.

3.3. Micro-Infrared Spectroscopy (micro-IR)

The results of the micro-IR test are shown in Figure 5. The main absorption peaks of the five samples were basically the same. They mainly included the strong absorption peaks at 2350, 2157, and 2030 cm^{-1} and the absorption peaks at 1282 and 1175 cm^{-1}. For samples R-YG-1, R-Y-1, and R-B-1, the absorption peaks of 1282 and 1175 cm^{-1} were relatively obvious, and the peak intensity corresponding to 1282 cm^{-1} was greater than that of 1175 cm^{-1}. The two absorption peaks in sample R-Y-2 and R-P-1 were weak, and some samples showed absorption peaks at 1358 cm^{-1}.

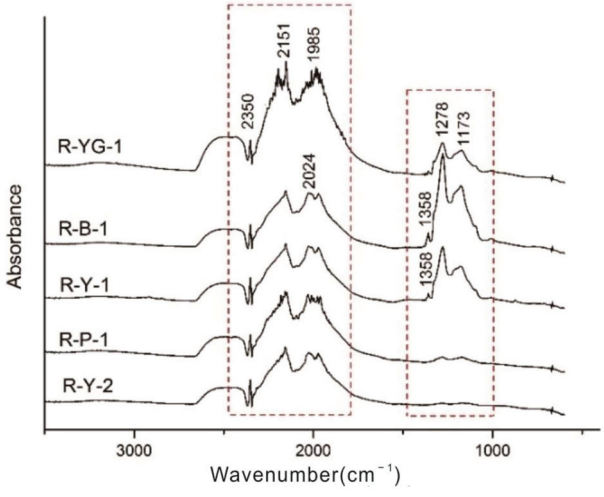

Figure 5. Micro-infrared absorption spectra of samples.

Combining the analysis of the diamond microscopic infrared spectrum by Yang et al. [25], the infrared spectrum of the sample can be divided into two parts: (1) The absorption peak of below 1332 cm^{-1} is a one-phonon absorption region, where the one-phonon absorption caused by the A nitrogen center is located near 1282 cm^{-1}, and the photon absorption caused by the B nitrogen center is located near 1175 cm^{-1}. It can be judged that the five diamond samples are all IaAB diamonds. (2) Next are the absorption peaks around 1973~2500 cm^{-1}, such as the absorption caused by C-C lattice vibration near 1973, 2022, and 2159 cm^{-1}.

3.4. PL Spectroscopy

Using the 532 nm wavelength laser as a light source, the PL spectra of the HTHP-treated diamonds were measured in a liquid nitrogen environment. The PL spectra of the five samples obtained are shown in Figure 6.

It can be seen from Figure 6 that except for the weak emission peak of the sample R-YG-1 at 552 nm, no other samples show emission peaks here. The luminescence peak at 552 nm is the intrinsic peak of the diamond, but because the fluorescence of the diamond sample is too strong, it will weaken or even disappear completely. In addition, the five samples showed luminescence peaks at 637 nm and 575 nm, but the relative intensities of the two peaks were different in different color samples: the yellow (R-Y-1, R-Y-2), yellow-green (R-YG-1), and brown samples (R-B-1) had a stronger emission peak at 637 nm than at 575 nm, while the purple-red sample (R-P-1) showed the opposite phenomenon.

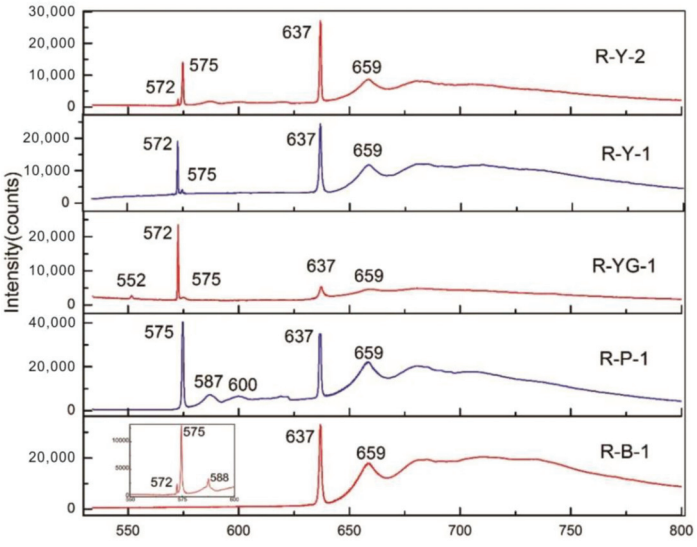

Figure 6. PL spectra of diamond samples.

The peak at 575 nm corresponds to the $(N\text{-}V)^0$ center, and the peak at 637 nm corresponds to the $(N\text{-}V)^-$ center. According to the study of Shi et al. [14], when the temperature of the HTHP treatment is higher than 1960 °C, the aggregate A in the diamond may decompose to produce isolated nitrogen, and isolated nitrogen may combine with a hole to form an uncharged $(N\text{-}V)^0$ center. However, the $(N\text{-}V)^0$ center is very likely to capture an electron during HTHP treatment to form a negatively charged $(N\text{-}V)^-$ center. According to most studies, the peak strength of HTHP-treated diamonds at 637 nm is stronger than that at 575 nm, mainly because more aggregates of nitrogen are decomposed under HTHP treatment, resulting in a higher concentration of the $(N\text{-}V)^-$ center [26]. The reason for the opposite phenomenon in the purple-red samples needs further experimental investigation. In the photoluminescence spectrum test of diamond samples processed by the US Lotus Colors Diamond Company, Qu and Shen [27] also found that the $(N\text{-}V)^0$ center and $(N\text{-}V)^-$ center intensity of purple diamonds did not have an obvious uniform rule, but most of the $(N\text{-}V)^-$ center intensity was stronger. Whether there is an obvious relationship between this phenomenon and color remains to be further confirmed.

3.5. Three-Dimensional Fluorescence Spectroscopy

The 3D fluorescence spectra can provide fluorescence intensity information when the excitation wavelength (EX) and emission wavelength (EM) are changed simultaneously. In this paper, the contour fluorescence spectrum is used to analyze the test results of the samples. In order to more comprehensively display the 3D fluorescence characteristics of the samples, according to the excitation wavelength, it was divided into two wavelength ranges of 250–400 nm and 400–600 nm for testing and analysis.

The yellow sample of R-Y-1 showed two fluorescence peaks in the fluorescence spectrum in the excitation wavelength range of 400–600 nm. One of the fluorescence peaks had an emission wavelength peak at 536 nm (excitation wavelength was 481 nm), and it was accompanied by a relatively wide band. The second fluorescence peak was at 457 nm (excitation wavelength was 403 nm) and was accompanied by a band of 365–510 nm (Figure 7a). The two fluorescence peaks of the other yellow sample R-Y-2 showed at 449 nm (EX = 400 nm) and 535 nm (EX = 490 nm). However, the yellow-green sample R-YG-1 had no obvious fluorescence peak in the excitation wavelength range of 400–600 nm and was mainly concentrated in the range of 250–400 nm. The fluorescence peak of this sample was located at 443 nm, accompanied by a wide fluorescence band of 260–500 nm, and the correspond-

ing excitation wavelength was 397 nm (Figure 7b). For the brown sample R-B-1, a more prominent fluorescence peak appeared at 450 nm, accompanied by a band of ~250–625 nm (Figure 7c). The case of the purple-red sample R-P-1 was different from that of the previous four samples. Three fluorescence peaks appeared in the excitation wavelength range of 250–400 nm, which were located at 441 nm (EX = 394 nm), 676 nm (EX = 313 nm), and 665 nm (EX = ~250) (Figure 7d).

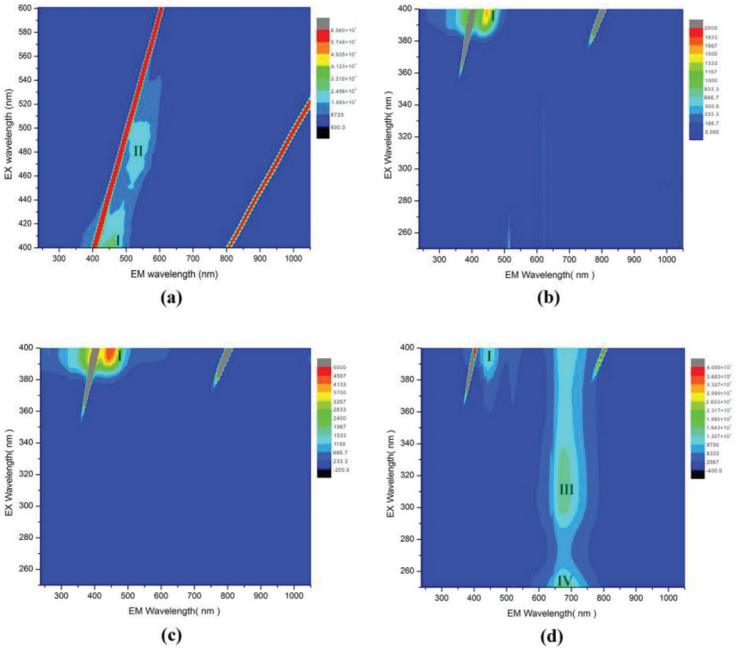

Figure 7. The contour fluorescence spectra of the diamond samples. Sample R-Y-1 shows two fluorescence peaks (I, IV) in the excitation wavelength range of 400–600 nm (**a**); the fluorescence peak of sample R-YG-1 is located at 443 nm (I) (**b**); the brown sample R-B-1 shows a more prominent fluorescence peak at 450 nm (I) (**c**); the purple-red sample R-P-1 shows three fluorescence peaks (I, III, IV) appearing in the excitation wavelength range of 250–400 nm (**d**).

Based on the analysis of the data (Table 2), the fluorescence peaks of the 3D fluorescence spectra of HTHP-treated diamonds have the following characteristics.

Table 2. The 3D fluorescence peak distribution of samples.

Samples	EM (nm)	EX (nm)	Accompanied Band
R-Y-1	536	481	500–590
	457	403	365–510
R-Y-2	535	490	475–610
	449	around 400	390–480
R-YG-1	443	397	260–505
R-B-1	450	around 400	~250–625
R-P-1	441	394	365–545
	676	313	595–785
	665	around 250	575–790

(1) Samples of different colors have fluorescence peaks in the range of 440–450 nm, which are often accompanied by a broad band ranging from 350 to 500 nm, and the excitation wavelength corresponding to the fluorescence peak is around 400 nm. The

brown sample has special characteristics, accompanied by the band extending towards longer wavelengths.

(2) The yellow samples have double fluorescence peaks in the excitation wavelength range of 400–600 nm. In addition to the first characteristic fluorescence peak, there is a second fluorescence peak at 535 nm, and it is accompanied by a 500–600 nm fluorescence band. The corresponding excitation wavelength is around 480 nm. In their research of the luminescence phenomenon caused by optical defects in diamonds, Lou and Breeding [21] pointed out that natural and HTHP-treated yellow-green diamond samples with different saturations show an emission maximum at 520 nm with a wide band extending from ~480 to 650 nm, a feature that manifested itself as a green or yellowish green fluorescence. This emission feature is caused by H3 and has a maximum at 470 nm excitation. And some natural yellow-green samples showed an emission peak centered at 512 nm with a band from ~470 to 630 nm that resulted in a green color from H4 fluorescence. However, this fluorescence peak was not found in the Russian HTHP-treated diamond samples. This may be because the H4 centers are unstable at higher temperatures (greater than 1500 °C) and can be easily decomposed to form H3 centers and isolated nitrogen [14].

(3) The purple-red sample has three fluorescence peaks in the excitation wavelength range of 250–400 nm. In addition to the fluorescence peaks in the range of 440–450 nm, there are two fluorescence peaks at longer wavelengths (in the red wavelength range). According to Lou and Breeding [21], diamond samples affected by the special 480 nm band will present a more complex 3D fluorescence spectrum. It has two main characteristics: (1) a wide band centered at ~653 nm (maximum shifts between 630 and 655 nm), which maximized with a 485 nm excitation wavelength; (2) a ~539 nm band that increased with 420, 345, and 285 nm excitation energies. The combination of both bands ranged from ~500 to 700 nm and produced yellow to orange fluorescence when excited by visible light (near-LWUV) [21]. In this paper, the fluorescence characteristics and ultraviolet fluorescence phenomenon of the purple-red sample are similar, and it is speculated that the fluorescence characteristics of the purple-red sample may be related to the 480 nm band.

4. Conclusions

Through testing and research on HTHP-treated IaAB-type diamonds, the luminescence and fluorescence spectra characteristics can be summarized as follows: Under DiamondView^{TM} and cathode rays, the yellow samples mainly showed a combination of blue and green luminescence, while the brown and purple samples showed a luminescence of orange with different intensities; the luminous patterns could mainly be divided into three types: regular annular bands, multiple groups of intersecting linear stripes, and jagged stripes. In the PL spectra of the yellow, yellow-green, and brown samples, the peaks at 637 nm were stronger than 575 nm, but the opposite phenomenon appeared in the purple-red sample. The 3D fluorescence spectra showed that the fluorescence peaks in the range of 440–450 nm in samples with different colors were accompanied by a wide band ranging from 350 to 500 nm, and in the brown sample, the band extended to the longer wavelength. The second fluorescence peaks at 535 nm appeared in the yellow samples, and in the purple-red sample, there were two peaks of fluorescence at longer wavelengths, which provided a more intuitive detection method for the rapid and non-destructive identification of HTHP-treated diamonds.

Author Contributions: Conceptualization, M.-L.H. and X.-M.H.; methodology, and M.-L.H.; software, M.-Y.D.; validation, M.-L.H., P.-F.J. and X.-F.W.; formal analysis, M.-L.H.; investigation, M.-L.H., P.-F.J. and X.-F.W.; resources, X.-M.H.; data curation, X.-M.H.; writing—original draft preparation, M.-L.H.; writing—review and editing, M.-L.H., X.-M.H., M.-Y.D., P.-F.J. and X.-F.W.; supervision, X.-M.H.; funding acquisition, X.-M.H. All authors have read and agreed to the published version of the manuscript.

Funding: This work has been supported by the project of "Geology of mineral resources in China" from China Geological Survey (Grant Nos. DD20160346, DD20190379).

Institutional Review Board Statement: Not applicable.

Informed Consent Statement: Not applicable.

Data Availability Statement: The original contributions presented in the study are included in the article, further inquiries can be directed to the corresponding author.

Acknowledgments: We are grateful to the editors and anonymous reviewers whose comments improved the quality of the manuscript.

Conflicts of Interest: Author Mu-Lin Huang was employed by the company Beijing Education Technology Co., Ltd. The remaining authors declare that the research was conducted in the absence of any commercial or financial relationships that could be construed as a potential conflict of interest.

References

1. Schmetzer, K. Clues to the process used by generalelectric to enthance the GE Pol diamonds. *Gems Gemmol.* **1999**, *35*, 186–190. [CrossRef]
2. Song, Z.H.; Lu, T.J.; Tang, S.; Gao, B.; Su, J.; Ke, J. Discrimination of HTHP-treated Type Ia Cape Diamonds Using Optical and Photoluminescence Spectroscopic Techniques. *Rock Miner. Anal.* **2020**, *39*, 85–91.
3. Hainschwang, T. HTHP treatment of different classes of type I brown diamond. *J. Gemmol.* **2005**, *29*, 261–273. [CrossRef]
4. Bai, Q. Study of Color enhancement experiment processed on synthetic diamonds and its characteristics. *China Univ. Geosci.* **2019**, *25*, 1–5.
5. Fisher, D.; Spits, R.A. Spectroscopic evidence of GE pol HTHP-treated natural type Iia diamonds. *Gems Gemmol.* **2000**, *36*, 186–190.
6. Reinitz, I.M.; Buerki, P.R.; Shigley, J.E. Identification of HTHP-treated yellow to green diamonds. *Gems Gemmol.* **2000**, *36*, 128–137. [CrossRef]
7. Shen, C.Q. Application of High Temperature with Superhigh Pressure Method to Treatment of Jewelry and Jade. *China Gems Jades* **2004**, *4*, 39–41.
8. Karl, S. High pressure high temperature treatment of diamonds—A review of the patent literature from five decades (1960–2009). *J. Gemmol.* **2010**, *32*, 52–53.
9. Wang, Y.M.; He, B.; Zhao, Z.H. *Diamond*; China University of Geosciences Press: Wuhan, China, 1997.
10. Qi, L.J.; Yuan, X.Q.; Tian, L.G.; Yuan, Z.Z. Evolution and Colouration of Lattice Defects in Diamonds at High Pressure and High Temperature. *J. Gems Gemmol.* **2001**, *3*, 1–7.
11. Mai, X.; Chen, M.H.; Chen, Z. HTHP Treatment Technology of Diamond. *J. Gems Gemmol.* **2004**, *4*, 22–24.
12. Collins, A.T.; Kanda, H.; Kitawaki, H. Colour changes produced in natural brown diamonds by high-pressure, high-temperature treatment. *Diam. Relat. Mater.* **2000**, *9*, 113–122. [CrossRef]
13. Collins, A.T. The colour of diamond and how it may be changed. *J. Gemmol.* **2001**, *27*, 341–359. [CrossRef]
14. Shi, K.; Chen, M.H.; Wang, B.; Wang, H. Structural defects and color change mechanism of HTHP-treated diamond. *Superhard Mater. Eng.* **2010**, *22*, 43–45.
15. Shigley, J.E. Diamonds: High-Pressure-High-Temperature Treatment of Gem Diamonds. *Elements* **2005**, *1*, 101–104. [CrossRef]
16. Wang, J.X.; Chen, M.H.; Wang, L.S. Characteristics of HTHP-Treated Diamonds from Russia. *J. Gems Gemmol.* **2010**, *12*, 5–8+4.
17. Wang, W.Y.; Smith, C.P.; Hall, M.S.; Breeding, C.M.; Moses, T.M. Treated-color pink-to-red diamonds from Lucent Diamonds Inc. *Gems Gemol.* **2005**, *41*, 6–19. [CrossRef]
18. Shan, X.M. *Comparison of Color Modification Experiment and Characteristics of HTHP Synthetic Yellow Diamonds*; University of Geosciences: Beijing, China, 2020.
19. Luo, Y.A. *The Application of Cathodoluminescence Technology in Gemology—A Case Study of Emerald and Diamond*; China University of Geosciences: Wuhan, China, 2002.
20. Jia, Q.; Chen, M.H. Luminescen22ce Characteristics and Fluorescence Spectrum of HTHP-Treated and Irradiated Diamond. *J. Gems Gemmol.* **2018**, *20*, 1–8.
21. Lou, Y.; Breeding, M.C. Fluorescence Produced by Optical Defects in Diamond: Measurement, Characterization, and Challenges. *Gems Gemol.* **2013**, *49*, 82–97.
22. Bulanova, G.P.; Milledge, H.J. Origin and History of Growth of Macro-Diamonds from Yakutian Kimberlites. In *6th International Kimberlite Conference: Extended Abstract*; Siberian Branch of Russian Academy of Science: Novosibirsk, Russia, 1995.
23. Chen, M.H.; Lu, F.X.; Di, J.R.; Zheng, J.P. Cathode Luminescence and Infrared Spectrum Analysis of Diamond in Wafangdian, Liaoning. *Sci. Bull.* **2000**, *45*, 1424–1428. [CrossRef]
24. Chen, M.H.; Lu, F.X.; Zheng, J.P. Cathodoluminescence Features of Diamond in Fuxian Liaoning Provence and Their Implications. *Earth Sci. J. China Univ. Geosci.* **1999**, *24*, 71–74.

25. Yang, Z.J.; Peng, M.S.; Xie, D.X.; Yuan, Z.Z. Mico-Area Analysis of Diamond by Micro-Infrared Spectrometry and Its Significance. *Rock Miner. Anal.* **2002**, *21*, 161–165.
26. Dobrinets, I.A.; Vins, V.G.; Zaitsev, A.M. *HTHP-Treated Diamonds: Diamonds Forever*; Springer: Berlin/Heidelberg, Germany, 2013.
27. Qu, M.W.; Shen, X.T. Spectroscopic Characteristic of Orange Red to Purple Colour-Treated Diamond from Lotus Colors, Inc. U.S.A. *J. Gems Gemmol.* **2019**, *21*, 17–23.

MDPI AG
Grosspeteranlage 5
4052 Basel
Switzerland
Tel.: +41 61 683 77 34

Applied Sciences Editorial Office
E-mail: applsci@mdpi.com
www.mdpi.com/journal/applsci

Academic Open
Access Publishing

mdpi.com

ISBN 978-3-7258-3782-3